ADVANCED DEEP-TRANSFER-LEVERAGED STUDIES ON BRAIN-COMPUTER INTERFACING

EDITED BY: Yizhang Jiang, Yu-Dong Zhang and Mohammad Khosravi
PUBLISHED IN: Frontiers in Neuroscience

frontiers Research Topics

frontiers

ISSN 1664-8714
ISBN 978-2-88971-468-1
DOI 10.3389/978-2-88971-468-1

About Frontiers

Frontiers is more than just an open-access publisher of scholarly articles: it is a pioneering approach to the world of academia, radically improving the way scholarly research is managed. The grand vision of Frontiers is a world where all people have an equal opportunity to seek, share and generate knowledge. Frontiers provides immediate and permanent online open access to all its publications, but this alone is not enough to realize our grand goals.

Frontiers Journal Series

The Frontiers Journal Series is a multi-tier and interdisciplinary set of open-access, online journals, promising a paradigm shift from the current review, selection and dissemination processes in academic publishing. All Frontiers journals are driven by researchers for researchers; therefore, they constitute a service to the scholarly community. At the same time, the Frontiers Journal Series operates on a revolutionary invention, the tiered publishing system, initially addressing specific communities of scholars, and gradually climbing up to broader public understanding, thus serving the interests of the lay society, too.

Dedication to Quality

Each Frontiers article is a landmark of the highest quality, thanks to genuinely collaborative interactions between authors and review editors, who include some of the world's best academicians. Research must be certified by peers before entering a stream of knowledge that may eventually reach the public - and shape society; therefore, Frontiers only applies the most rigorous and unbiased reviews.
Frontiers revolutionizes research publishing by freely delivering the most outstanding research, evaluated with no bias from both the academic and social point of view. By applying the most advanced information technologies, Frontiers is catapulting scholarly publishing into a new generation.

What are Frontiers Research Topics?

Frontiers Research Topics are very popular trademarks of the Frontiers Journals Series: they are collections of at least ten articles, all centered on a particular subject. With their unique mix of varied contributions from Original Research to Review Articles, Frontiers Research Topics unify the most influential researchers, the latest key findings and historical advances in a hot research area! Find out more on how to host your own Frontiers Research Topic or contribute to one as an author by contacting the Frontiers Editorial Office: frontiersin.org/about/contact

ADVANCED DEEP-TRANSFER-LEVERAGED STUDIES ON BRAIN-COMPUTER INTERFACING

Topic Editors:
Yizhang Jiang, Jiangnan University, China
Yu-Dong Zhang, University of Leicester, United Kingdom
Mohammad Khosravi, Persian Gulf University, Iran

Citation: Jiang, Y., Zhang, Y.-D., Khosravi, M., eds. (2021). Advanced Deep-Transfer-Leveraged Studies on Brain-Computer Interfacing. Lausanne: Frontiers Media SA. doi: 10.3389/978-2-88971-468-1

Table of Contents

frontiers in Neuroscience

EDITORIAL
published: 19 August 2021
doi: 10.3389/fnins.2021.733732

Editorial: Advanced Deep-Transfer-Leveraged Studies on Brain-Computer Interfacing

Yizhang Jiang[1]*, *Yu-Dong Zhang*[2] and *Mohammad Khosravi*[3]

[1] School of Artificial Intelligence and Computer Science, Jiangnan University, Wuxi, China, [2] Department of Informatics, University of Leicester, Leicester, United Kingdom, [3] Department of Computer Engineering, Persian Gulf University, Bandar Bushehr, Iran

Keywords: deep learning, transfer learning, brain-computer interfacing, EEG, neuroscience

Editorial on the Research Topic

Advanced Deep-Transfer-Leveraged Studies on Brain-Computer Interfacing

Brain-computer interfacing (BCI) has attracted rapidly increasing research interest in the last decade due to recent advances in neurosciences, wearable/mobile biosensors, and analytics. The ultimate goal is to provide a pathway from the brain to the external world via mapping, assisting, augmenting, or repairing human cognitive or sensory-motor functions. Recently, many advanced machine learning technologies have appeared, such as deep learning, transfer learning, and so on. The deep learning method has achieved great success in the image and the video analysis, the natural language processing, the speech recognition, etc., and recently has also started to find applications in BCI. Transfer learning, which improves learning in a new task by leveraging data or knowledge from other relevant tasks, can be particularly useful in BCI to cope with variability across individuals or tasks, accelerating learning and improving performance. Advanced deep-transfer-leveraged learning technologies can also be integrated to take advantage of both domains.

Although the studies of BCI using advanced deep learning and/or transfer learning methods become more and more popular, there still exist many unsolved fundamental problems so far, such as deep learning representation of some EEG-based BCI data from multiple modalities, mapping data from one modality to another to achieve cross-source BCI data analysis, identifying, and utilizing relations between elements from two or more different signal sources for comprehensive BCI data analysis, fusing information from two or more signal sources to perform a more accurate prediction, transferring knowledge between modalities and their representations, and recovering missing modality data given the observed ones.

In the past decade, several EEG-based BCI methods and technologies have been developed and shown promising results in some real-world examples such as neuroscience, medicine, and rehabilitation, which led to a proliferation of papers showing accuracy/performance and comparison, but most do not advance to real-time, translation, or application. Then, these papers do not fare well, either because of lack of novelty (known technique) or no bio/med/experiment/clinical translation. For all the reasons mentioned above, it inspires us to exploit and develop effective advanced deep learning and/or transfer learning algorithms for addressing fundamental issues in BCI and rehabilitation fields.

This Research Topic (RT) of the Frontiers in Neuroscience (section: Neuroprosthetics) is a selection of 22 papers presented at the RT "Advanced Deep-Transfer-Leveraged Studies on Brain-Computer Interfacing." We provide a brief summary of these papers as follows.

OPEN ACCESS

Edited and reviewed by:
Michela Chiappalone,
Italian Institute of Technology (IIT), Italy

***Correspondence:**
Yizhang Jiang
yzjiang@jiangnan.edu.cn

Specialty section:
This article was submitted to Neuroprosthetics, a section of the journal Frontiers in Neuroscience

Received: *30 June 2021*
Accepted: *22 July 2021*
Published: *19 August 2021*

Citation:
Jiang Y, Zhang Y-D and Khosravi M (2021) Editorial: Advanced Deep-Transfer-Leveraged Studies on Brain-Computer Interfacing. Front. Neurosci. 15:733732. doi: 10.3389/fnins.2021.733732

BCI APPROACHES

The brain computer interface (BCI) is a direct connection between human or animal brain (and brain cell culture) and external devices. In this RT, some scholars proposed many novel methods on BCI technologies. For example, Huang et al. proposed a classification method using sparse representation (SR) and fast compression residual convolutional neural networks (FCRes-CNNs). They obtained the features of the EEG signal through the common spatial patterns algorithm, and they constructed the redundant dictionary with sparse representation based on these features. Subsequently, they used sparse features as the input of fast compression deep learning network to classify EEG signals. Meanwhile, Zhang W. et al. proposed an EEG phase-dependent closed-loop mechanical vibration stimulation method. This novel method is an improvement on traditional vibration stimulation enhancement research and helps to make the stimulation more precise and effective.

BCI has been regarded as a newly developing intervention in promoting motor recovery in stroke survivors. Several studies have been performed in chronic stroke to explore its clinical and subclinical efficacy. However, evidence in subacute stroke was poor, and the longitudinal sensorimotor rhythm changes in subacute stroke after BCI with exoskeleton feedback were still unclear. In this regard, Chen S. et al. studied the longitudinal sensorimotor rhythm changes of BCI with exoskeleton feedback in subacute stroke. The experiments showed that The BCI group showed larger percentage points of improvement and good motor recovery than the control group.

In theory, the BCI system can monitor the signals generated by neural activities through a variety of sensors and other signal acquisition equipment. Through the analysis and processing of the signals, the signals are classified according to separate thinking activities to generate corresponding control commands to complete the interactive tasks between users and external devices. To achieve this goal, Wang et al. explored the classification method of EEG signals based on a multilayered neural network that plays an important role in promoting the practicality of the BCI. In this article, they developed the left-handed and right-handed motor imagination EEG classification model based on convolution neural network, and they achieved 75.3% classification accuracy on the test set of BCI common data set. The designed model can be transplanted to mobile phones, computers, tablets, and other terminal devices, used in BCI technology, medical rehabilitation, the field of healthcare. Meanwhile, Chen Y. et al. developed a knowledge-leverage-based support matrix machine (KL-SMM) to improve the classification performance when only a few labeled EEG data in the target domain (target subject) were available. Different from most current model parameter transfer learning methods, the proposed method can propagate the structural information from the source model to the target model. In addition, the proposed method can afford privacy protection by leveraging only the model knowledge of the source domain.

EEG APPROACHES

Electroencephalogram (EEG) as a biomarker plays an important role in the BCI. The EEG signal can be used as a basis for the prediction of brain behavior and diagnoses of disease. For example, EEG signals are often used to determine the presence and type of epilepsy in clinical diagnosis. In this Research Topic, several papers focus on using different advanced artificial intelligence methods to identify epileptic seizures via EEG signal. Zhou and Li analyzed EEG signal features from linear and non-linear perspectives, and dynamically extract effective features using an improved radial basis function neural network. Moreover, they introduced one against one strategy classifier to reduce the probability of error classification.

Because the responses to EEG signals of different patients in the same cognitive activity show a certain degree of similarity, Zhang Y. et al. leveraged abundant labeled EEG epochs from a related source domain and reused them in the target domain. They proposed an online selective transfer TSK fuzzy classifier underlying joint distribution adaptation and manifold regularization. Their classifier can make use of very few calibration data in the target domain to induce the target predictive function. Using joint distribution adaptation to minimize the marginal distribution distance and conditional distribution distance between the source and target domains, the computational complexity of the classifier can be reduced. Meanwhile, Zhang G. et al. proposed a multi-scale non-local (MNL) network to achieve automatic EEG signal detection. Their MNL-Network is based on 1D convolution neural network involving two specific layers to improve the classification performance. One layer is named the signal pooling layer and the other layer is called a multi-scale non-local layer. The experimental results demonstrate that the MNL-Network could achieve competitive results in the EEG classification task. Additionally, Jiang K. et al. studied how to select effective EEG features to guarantee high-efficiency artificial intelligence-assisted clinical diagnosis. They constructed a stacked deep structure for feature selection in a layer-by-layer manner so as to add random projections into the original features, so that the manifold structure existing in the original feature space was continuously opened in a stacked way. Therefore, according to the stacked generalized principle, the original input feature space became more linearly separable. Moreover, Ni et al. proposed a noise-insensitive Takagi-Sugeno-Kang (TSK) fuzzy system for EEG signal recognition. In particular, they developed a possibilistic clustering in Bayesian framework with interclass competitive learning to determine antecedent parameters of fuzzy rules. To further promote the noise insensitivity of rules, they used the asymmetric expectile term and Ho-Kashyap procedure to learn the consequent parameters of rules. Comprehensive experiments on Bonn EEG dataset revealed that the proposed fuzzy system achieved robust and effective performances for EEG signal recognition. Besides, Xu et al. proposed a one-dimensional convolutional neural network long and short-term memory (1D CNN-LSTM) model to automatically recognizes epileptic seizures through EEG signal analysis. In short, a one-dimensional convolutional neural

network (CNN) and long and short-term memory model are used to extract temporal features from standardized EEG sequence data. Several fully connected layers are used for epilepsy recognition.

To exploit the diversity and complementariness of different feature representations of EEG signals, Xue et al. developed a new auto-weighted multi-view discriminative metric learning method with Fisher discriminative and global structure constraints. On the one hand, they exploited the multiple features of different views in the scheme of the multi-view feature representation. On the other hand, they considered both the Fisher discriminative constraint and global structure constraint into the discriminative metric space, in which the intraclass EEG signals were compact, and the interclass EEG signals were separable as much as possible. Meanwhile, Dong et al. developed a method combining the non-negative matrix factorization technology and transfer learning. They reported that the non-negative matrix factorization can assure to obtain essential information between the testing and the training dataset, and the combination of shared subspace and the original feature space can fully use of the testing signals and the training signals.

Accurate and automatic classification of the speech imagery EEG signals from the BCI system is highly demanded in clinical diagnosis. The key factor in designing an automatic classification system is to extract essential features from the original input. To achieve this goal, Zhang, Luo et al. proposed a dynamic multi-scale network. The whole classification network was based on ResNet, and the input signal first encoded the features by the Short-time Fourier Transform (STFT). Finally, they incorporated a dynamic multi-scale layer to allow the network to learn multi-scale features from different receptive fields at a more granular level.

Currently, the recognition method of EEG signals is one of the important technology for human emotion recognition. The traditional machine learning method has a major disadvantage in that the feature extraction process is usually cumbersome. Zhang Y. et al. focus on emotion recognition based on EEG signals using deep learning model combination. They studied the application of several deep learning models in the research field of EEG-based emotion recognition, including deep neural networks (DNN), convolutional neural networks (CNN), long short-term memory (LSTM), and a hybrid model of CNN and LSTM (CNN-LSTM). Then they used four deep learning models to learn and predict emotion recognition on the DEAP EEG dataset.

Changes in physiological functions during sleep lead to corresponding changes in EEG signals. The acquisition and processing of patients' sleep data at night need the help of automation and digital technology. Wen proposed a sleep quality detection method based on EEG signals. He used the discrete wavelet transform (DWT) for feature extraction and adopted the transfer learning support vector machine (TL-SVM) for classifying the feature data. The proposed method was tested using 60 pieces of data from the National Sleep Research Resource Library of the United States, and the experimental results show that the classification performance of the TL-SVM classifier is significantly higher than other comparison algorithms.

CLINIC APPLICATIONS

In clinic medicine files, the computer-aided diagnosis of brain diseases technology began to use some existing advanced machine learning methods. For example, Cai et al. studied altered patterns of functional connectivity and causal connectivity in salience subnetwork of subjective cognitive decline and amnestic mild cognitive impairment. Meanwhile, Jiang C. et al. studied the numerical evaluation of the influence of skull heterogeneity on transcranial ultrasonic focusing. They investigated how the focus deviates after phase-aberration compensation with ray tracing using time-reversal theory. They simulated the propagation of ultrasound for transcranial focusing with the k-space pseudo spectral method. The results revealed minimal deviation in the focal region and suggested that transcranial focusing deflections are caused mostly by ultrasonic refraction on the surface of the skull bone. Besides, Cai et al. analyzed the altered patterns of phase position connectivity in default mode subnetwork of subjective cognitive decline and amnestic mild cognitive impairment. Vestibular migraine (VM) is a multidisciplinary disease under exploration. Moreover, Yan et al. investigated the clinical features of VM under three temporal patterns. They found that vestibular stimulation could inhibit the trigeminal pain pathway, while painful trigeminal stimulation could excite the vestibular system. This finding may contribute to the clinical identification of VM and further clarification of its pathogenesis. Furthermore, Hong et al. proposed a feature fusion and attention network (FFA-DMRI) is proposed to separate noise from brain magnetic resonance imaging (MRI). Inspired by the attention-guided convolutional neural networks (CNN) network and convolutional block attention module, they designed a spatial attention mechanism to obtain the area of interest in MRI. Furthermore, they marked full use of the multilevel structure and boost the expressive ability of network by the feature fusion block. The comprehensive experiments on Alzheimer's disease neuroimaging initiative dataset demonstrated high effectiveness of FFA-DMRI with maintaining the crucial brain details. Additionally, Ji et al. developed a method to construct dynamic brain functional networks (DBFNs) via hyper-graph manifold regularization (HMR), and employed it to classify mild cognitive impairment (MCI) subjects. Finally, they conduct classification experiments to classify MCI subjects from normal subjects to verify the effectiveness of our method.

CONCLUSION

This Research Topic focuses primarily on novel theories and methods proposed for EEG single and health information processes. New methods can be used to diagnose brain neurological diseases predict and inhibit the onset of epilepsy, and can also be used for some clinic applications. As can be appreciated, these articles covered a wide range of

advances and new insights in our understanding of the brain neuroscience.

AUTHOR CONTRIBUTIONS

All authors listed have made a substantial, direct and intellectual contribution to the work, and approved it for publication.

Conflict of Interest: The authors declare that the research was conducted in the absence of any commercial or financial relationships that could be construed as a potential conflict of interest.

frontiers in Neuroscience

ORIGINAL RESEARCH
published: 20 March 2020
doi: 10.3389/fnins.2020.00185

Altered Patterns of Phase Position Connectivity in Default Mode Subnetwork of Subjective Cognitive Decline and Amnestic Mild Cognitive Impairment

Chunting Cai[1], Chenxi Huang[1], Chenhui Yang[1]*, Xiaodong Zhang[2]*, Yonghong Peng[3], Wenbing Zhao[4], Xin Hong[1], Fujia Ren[1], Dan Hong[1], Yutian Xiao[1] and Jiqiang Yan[1]*

[1] School of Informatics, Xiamen University, Xiamen, China, [2] Department of Ultrasound, The First Affiliated Hospital of Xiamen University, Xiamen, China, [3] Department of Computing and Mathematics, Manchester Metropolitan University, Manchester, United Kingdom, [4] Department of Electrical Engineering and Computer Science, Cleveland State University, Cleveland, OH, United States

OPEN ACCESS

Edited by:
Yizhang Jiang, Jiangnan University, China

Reviewed by:
Wenzheng Bao, Xuzhou University of Technology, China
Tian Wang, Huaqiao University, China

***Correspondence:**
Chenxi Huang
supermonkeyxi@xmu.edu.cn
Chenhui Yang
ych987@126.com
Xiaodong Zhang
zxdon11@163.com

Specialty section:
This article was submitted to Neuroprosthetics, a section of the journal Frontiers in Neuroscience

Received: *02 February 2020*
Accepted: *19 February 2020*
Published: *20 March 2020*

Citation:
Cai C, Huang C, Yang C, Zhang X, Peng Y, Zhao W, Hong X, Ren F, Hong D, Xiao Y and Yan J (2020) Altered Patterns of Phase Position Connectivity in Default Mode Subnetwork of Subjective Cognitive Decline and Amnestic Mild Cognitive Impairment. Front. Neurosci. 14:185. doi: 10.3389/fnins.2020.00185

Alzheimer's disease (AD), which most commonly occurs in the elder, is a chronic neurodegenerative disease with no agreed drugs or treatment protocols at present. Amnestic mild cognitive impairment (aMCI), earlier than AD onset and later than subjective cognitive decline (SCD) onset, has a serious probability of converting into AD. The SCD, which can last for decades, subjectively complains of decline impairment in memory. Distinct altered patterns of default mode network (DMN) subnetworks connected to the whole brain are perceived as prominent hallmarks of the early stages of AD. Nevertheless, the aberrant phase position connectivity (PPC) connected to the whole brain in DMN subnetworks remains unknown. Here, we hypothesized that there exist distinct variations of PPC in DMN subnetworks connected to the whole brain for patients with SCD and aMCI, which might be acted as discriminatory neuroimaging biomarkers. We recruited 27 healthy controls (HC), 20 SCD and 28 aMCI subjects, respectively, to explore aberrant patterns of PPC in DMN subnetworks connected to the whole brain. In anterior DMN (aDMN), SCD group exhibited aberrant PPC in the regions of right superior cerebellum lobule (SCL), right superior frontal gyrus of medial part (SFGMP), and left fusiform gyrus (FG) in comparison of HC group, by contrast, no prominent difference was found in aMCI group. It is important to note that aMCI group showed increased PPC in the right SFGMP in comparison with SCD group. For posterior DMN (pDMN), SCD group showed decreased PPC in the left superior parietal lobule (SPL) and right superior frontal gyrus (SFG) compared to HC group. It is noteworthy that aMCI group showed decreased PPC in the left middle frontal gyrus of orbital part (MFGOP) and right SFG compared to HC group, yet increased PPC was found in the left superior temporal gyrus of temporal pole (STGTP). Additionally, aMCI group exhibited

decreased PPC in the left MFGOP compared to SCD group. Collectively, our results have shown that the aberrant regions of PPC observed in DMN are related to cognitive function, and it might also be served as impressible neuroimaging biomarkers for timely intervention before AD occurs.

Keywords: subjective cognitive decline, amnestic mild cognitive impairment, default mode network, phase position connectivity, neuroimaging biomarkers

INTRODUCTION

Alzheimer's disease (AD), which occurs more commonly in the elder, is a chronic neurodegenerative disease of impaired cognitive and memory (Ren et al., 2019; Wessels et al., 2019). Nevertheless, there are no agreed drugs or treatment protocols for patients with AD. Therefore, the timely detection and treatment of the early stages of AD is an urgent and realistic issue, which can improve symptoms of illness and alleviate the progression of the disease (Yang et al., 2019). Amnestic mild cognitive impairment (aMCI), as the phase close to AD, has a 10–15% probability of converting into AD per annum (Yang et al., 2017). Subjective cognitive decline (SCD) is referring to the fact that impaired cognition appealed by patients is entirely subjective without objective behavior of cognitive decline (Funaki et al., 2019), which has the certain likelihood of the development into aMCI and AD stages (Caillaud et al., 2019; Kim et al., 2020). Thus, from the above, we aim to adopt aMCI and SCD phases which may evolve into AD to explore the neural mechanism of the early stage of AD.

Resting-state functional magnetic resonance imaging (rs-fMRI), as one of the neuroimaging techniques, can offer a noninvasive method for the assessment of the cognitive mechanism of AD to a certain degree (Ferenci et al., 2002). Besides, in most studies of the early stage of AD based on rs-fMRI, the default mode network (DMN) has been emphasized highly for a long time (Banks et al., 2018). Anatomically, it includes the anterior DMN (aDMN) which is primarily composed of the ventromedial prefrontal cortex (vmPFC), and posterior DMN (pDMN) which mainly focuses on the posterior cingulate cortex (PCC) (Xu et al., 2016). Notice that the former mainly concerns memory extinction and self-referential mental idealization, while the latter is closely related to the function of episodic memory retrieval (Yang et al., 2017, 2018). Previously, it has been reported that amyloid deposits are detected with a great probability in the PCC which served as a primary part of DMN (Wang et al., 2013). The previous work has also indicated that the regions of DMN are abnormal and may serve as prominent hallmarks in the early stage of AD such as mild cognitive impairment (MCI) and SCD (Huang et al., 2018a; Scherr et al., 2019; Xie et al., 2019). More specifically, these disconnected areas that are connected from the DMN to the whole brain are considered to be associated with cognitive disorder (Huang et al., 2019; Zhao et al., 2020).

Hilbert transform (HT), which is characterized by rapidly and accurately describing the instantaneous position phase, is suitable for the analysis of non-stationary signals (Peng et al., 2005; Qian et al., 2015). A former study has suggested that frequency domain estimations such as the instantaneous phase position would provide a higher correlation between two signals than time-domain signals (Mandel and Atkins, 2016). Previous studies based on electroencephalography (EEG) have shown that prominently increased and decreased alpha spectral powers are found using HT in patients with AD in comparison with healthy controls (HC) (Babiloni et al., 2006; Fraga et al., 2013; Wang et al., 2020). Furthermore, it has been reported that time series from EEG was employed to obtain the altered instantaneous phase position of DMN using the HT method, which can be served as biomarkers (Thatcher et al., 2014; Wang et al., 2019). A previous investigation has also revealed that the brain activation patterns of DMN measured by HT were altered between the eye open and the closed eye (Wang et al., 2015). Besides, the former work on depressive disorder has indicated that the signals, extracted from the interesting regions of rs-fMRI, can reveal the aberrant brain regions using the HT method (Yu et al., 2018). Until now no experiments of HT in AD based on rs-fMRI, especially in DMN subnetworks, have been reported, which may be a new way to explore the neural mechanism of the early stage of AD.

Accordingly, our target aims to analyze the altered patterns of instantaneous phase position connectivity (PPC) in DMN subnetworks (include aDMN and pDMN networks) connected to the whole brain, and to explore whether there exists a relationship between the cognitive function and the aberrant regions. We hypothesized that there exist distinct variations of PPC in DMN subnetworks for patients SCD and aMCI, which might act as discriminatory neuroimaging biomarkers.

MATERIALS AND METHODS

Participant

Our experimental participants in this work are briefly summarized as follows: All subjects are obtained from the public database of the second phase of Alzheimer's Disease Neuroimaging Initiative (ADNI-2)[1]. The emphasis of ADNI-2 is to survey neurological biomarkers of cognitive disorder. Furthermore, it was announced in 2011 which had been lasting for 5 years to implement. To further explore the gap between the healthy subjects and patients with MCI, consider joining the subjects with SCD for the first time in ADNI-2. All recruited subjects are consist of three parts, HC ($n = 28$), SCD ($n = 23$), and aMCI ($n = 29$), respectively. It deserves to be further mentioned that we have precluded three subjects as the result of undue head movement (cumulative translation or rotation >1.5 mm or 1.5 degrees were executed in our work, $n = 3$). At the same time, we strictly control registration quality relying on artificial

[1]http://adni.loni.usc.edu/

visual recognition due to the poor registration of certain subjects ($n = 2$). To sum up, we recruited 75 subjects, including 27 HC, 20 SCD, and 28 aMCI participants. The detail data selection process is shown in **Figure 1**.

MRI Data Acquisition

The obtained participants underwent rs-fMRI on a clinical 3.0 tesla (T) scanner (Philips Medical Systems). The echo-plane imaging (EPI) sequence consists of 140 volumes in which subjects were required to lie flat, close eyes, avoid conceptual work, and not turn the head during the process of data acquisition. Here, the specific parameters can be briefly described as: flip angle (FA) = 80 degree, matrix = 64 × 64, voxel size = 3.31 mm × 3.31 mm × 3.31 mm, repetition time (TR) = 3000 ms, echo time (TE) = 30 ms, slice thickness = 3.3 mm, respectively. T1-weighted structural MRI were acquired from magnetization-prepared rapid gradient-echo (MPRAGE) sequence (Chen et al., 2016), likewise, detailed parameters are represented as: matrix = 256 × 256, layer thickness = 1.2 mm, voxel size = 1 × 1 × 1.2 mm^3, TR = 6.81 ms, FA = 9 degree, TE = 3.16 ms, respectively.

Data Preprocessing

The data preprocessing with aspect to the rs-fMRI of this work adopted Resting-State fMRI Data Analysis Toolkit plus (RESTplus)[2], which is based on MATLAB2012a[3] and Statistical Parametric Mapping (SPM12)[4]. Briefly steps on data preprocessing involving as follows: We discarded the first 5 of 140 points in time for each subject as the result of the instability of MRI signal induced by machine or human. Then, the remaining volumes were calibrated for controlling the effects of between slices or between subject volumes. It is stressed that we have ruled out the data on the condition of cumulative translation more than 1.5 mm or angular motion more than 1.5 degrees. Next in the normalization process, registration from the original space to Montreal Neurological Institute (MNI) space using T1-weight volumes was implemented to reduce the diversities between various subjects. To directly circumvent the subject variations, the images generated above have been smoothed using a Gaussian kernel of 6 × 6 × 6 of full width at half maximum (FWHW). Following this, to eliminate the influence of nuisance variables (Fox et al., 2009; Huang et al., 2018b), comprising of six head motion parameters, global mean signal, white matter signal and cerebrospinal fluid signal, were ruled out, respectively. At last, subject volumes were filtered at 0.01–0.08 Hz due to noise interferences, which may be induced by heartbeat and breathing.

Statistical Analysis

For this study, the variance (ANOVA) and the chi-square test within the Statistical Package for the Social Sciences (SPSS) software version 22.0 were conducted to determine whether there exist prominent differences ($p < 0.05$) as to the data of demographic and neurocognitive between the HC, SCD and aMCI groups.

To better illustrate the differences of PPC in aDMN and pDMN networks between HC, SCD, and aMCI groups, one-way ANOVA, which is integrated into the software of Data Processing and Analysis for Brain Imaging (DPABI)[5], was adopted after controlling the gender and age. As mentioned in former literature, multiple comparisons at cluster level using non-parametric permutation test can availably control the false positive rate existing in statistics (Winkler et al., 2016), and 1000 permutation times and the prominent cluster size >30 voxels (810 mm^3, $p < 0.05$) were performed in this work. We have employed the two-sample *T*-test for calculating the differences between two groups (i.e., SCD and HC groups, aMCI and HC groups, aMCI and SCD groups), and that mask used in two-sample *T*-test was derived from ANOVA analysis. Besides, according to the recent report, there have identified that the

[2]http://restfmri.net/forum/RESTplusV1.2

[3]http://www.mathworks.com/products/matlab/

[4]https://www.fil.ion.ucl.ac.uk/spm/

[5]http://rfmri.org/dpabi

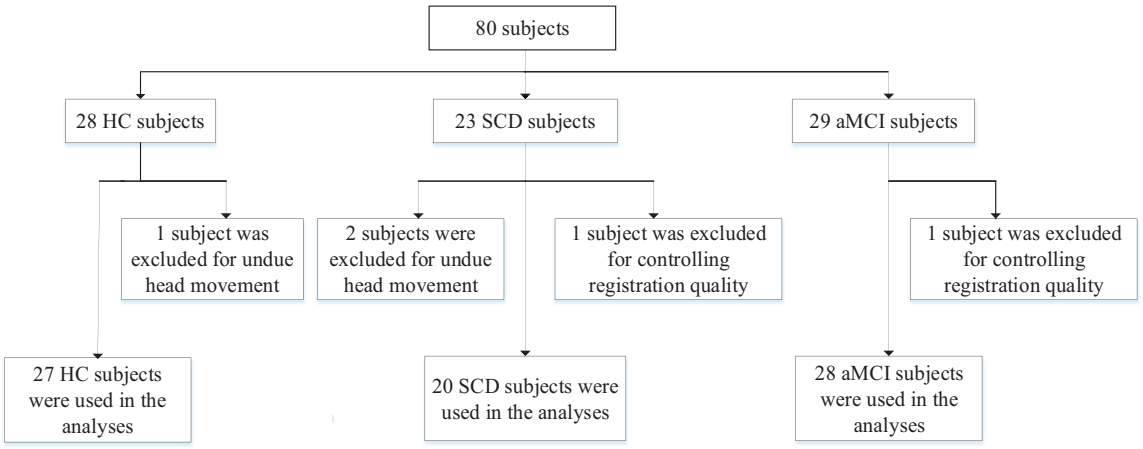

FIGURE 1 | A flow chart depicting the data selection process. HC, healthy controls; SCD, subjective cognitive decline; aMCI, amnestic mild cognitive impairment.

non-parametric permutation test with Threshold-Free Cluster Enhancement (TFCE) can effectively achieve a good balance between family wise error (FWE) rate and reliability (Chen et al., 2018). Therefore, permutation test associated with TFCE, all integrated into PLAM module of DPABI, were employed as the method of multiple comparisons of this work, and we set cluster size >10 voxels (270 mm^3, $p < 0.05$) as a prominent cluster (Xue et al., 2019).

PPC of Two Time Series Using Hilbert Transform

The HT can analyze nonlinear and non-stationary signals, and it is fully self-adaptive and suitable for mutation signals. Besides, it is characterized by rapidly and accurately describing the instantaneous phase position which was adopted to explore the altered patterns of PPC of DMN subnetworks in this work (Martis et al., 2012). Hence, the HT was adopted using complex demodulation to compute the instantaneous phase position difference between each pair of the time series. Among them, one series is extracted from aDMN (or pDMN), the other series is extracted from the voxel within the whole brain. The HT that we follow can be briefly described as follows: Given a time series name as $x(t)$, and the HT later referred to as $H(t)$, is shown in formula (1).

$$H(t) = \frac{1}{\pi}\int_{-\infty}^{+\infty}\frac{x(\tau)}{\pi(t-\tau)}d(\tau) = x(t) * \frac{1}{\pi t} \quad (1)$$

We first take two time series which represent aDMN (or pDMN) signal and the voxel signal of the brain as inputs to the formula (1) respectively. Next, using analytic signal $Z(t)$ of $x(t)$ to generate information about the phase position and amplitude, as shown in formula (2). Therefore, two analytic signals of aDMN (or pDMN) and the voxel of the brain are obtained.

$$Z(t) = x(t) + iH(t) = A(t)e^{-j\phi_x(t)} \quad (2)$$

where $A(t)$ represents signal amplitude, and $\phi_x(t)$ is the instantaneous phase position of the signal. Then, we obtain phase difference $D(t)$ according to phase positions of two signals, consisting of $\phi_{x_1}(t)$ and $\phi_{x_2}(t)$, and it is shown in formula (3). Here, we set the phase lock ratio as $m = n = 1$, and it indicates that the increase phase of two phase position is consistent.

$$D(t) = m\varphi_{x_1}(t) - n\varphi_{x_2}(t) \quad (3)$$

Phase synchronization exponent of two signals can be seen from the formula (4).

$$\lambda = \left| < e^{iD(t)} >_t \right| = \sqrt{< \cos D(t) >_t^2 + < \sin D(t) >_t^2} \quad (4)$$

Note that $< \cdot >_t$ is the average at each time point with values ranging from 0 to 1. Furthermore, $\lambda = 0$ indicates no phase synchronization of two signals, whereas $\lambda = 1$ shows phase synchronization of two signals. That is, the larger the value of λ, the stronger the synchronization between two signals. Moreover, the seed-based method was conducted to analyze the altered PPC of DMN subnetworks. To identify the seed regions about aDMN and pDMN, 10-mm spherical regions of interest in aDMN (MNI space: 0, 52, −6) and pDMN (MNI space: 0, −53, 26) were adopted in our work (Zhang and Raichle, 2010; Xue et al., 2019). Collectively, we applied phase position synchronization generated by HT to investigate the altered connectivity between the DMN subnetworks and the whole brain, and aim to explore the relationship between the aberrant regions and cognitive function.

RESULTS

Demographic and Neurocognitive Characteristics

Here, the demographic and neurocognitive characteristics of experimental participants were described in **Table 1**. The prominent differences verified by ANOVA analysis were the Age ($F = 8.248$, $p = 0.016$), the MMSE score ($F = 9.129$, $p < 0.01$), and CDR score ($F = 68.98$, $p < 0.01$), respectively, yet no prominent difference on the Gender ($F = 2.026$, $p > 0.05$). The results showed that the MMSE values of the HC group (29.14 ± 1.49), SCD group (28.94 ± 0.83) and aMCI group (26.87 ± 2.72) decreased successively. It is noteworthy that lower MMSE scores suggest the severe form of cognitive impairment, whereas higher CDR scores show much more serious for dementia.

The Aberrant PPC of aDMN Network in Patients With SCD and aMCI

The studies we have performed indicated that eight prominent clusters, comprising of right superior cerebellum lobule (SCL), right rectus (REC), left fusiform gyrus (FG), left inferior frontal gyrus of triangular part (IFGTP), left middle temporal gyrus (MTG), right middle frontal gyrus (MFG), left MFG and right superior frontal gyrus of medial part (SFGMP), were revealed according to one-way ANOVA analysis. Besides, patients with SCD exhibited aberrant PPC in the clusters of right SCL, right SFGMP and left FG as compared with HC group, by contrast, no significant difference was found in patients with aMCI resulted from two-sample T-test. Notably, aside from decreased PPC found in the left FG, the clusters of increased PPC were involved in the right SCL and right SFGMP. It is important to note that patients with aMCI showed increased PPC in the right SFGMP in comparison with the SCD group (TFCE-FWE corrected, cluster size ≥ 10 voxels, $p < 0.05$). In particular, we emphasize that our

TABLE 1 | Demographics and clinical measures of HC, SCD, and aMCI groups.

Group	HC (n = 27)	SCD (n = 20)	aMCI (n = 28)	p-values
Gender	20F/7M	10F/10M	10F/18M	0.139[a]
Age (years)	72.63 ± 4.50	72.38 ± 5.31	69.71 ± 7.26	0.016[b]
MMSE scores	29.14 ± 1.49	28.94 ± 0.83	26.87 ± 2.72	<0.01[b]
CDR scores	0.03 ± 0.11	0.12 ± 0.22	0.52 ± 0.10	<0.01[b]

Numbers are given as means ± standard deviation (SD) unless otherwise stated. MMSE, Mini-Mental State Examination; CDR, Clinical Dementia Rating; [a]The p-values were obtained by the chi-square test. [b]The p-value was obtained by one-way ANOVA analysis.

TABLE 2 | The aberrant PPC in aDMN network.

Region	Peak/MNI			*T*-score	Cluster size
	x	*y*	*z*		
ANOVA					
R Superior cerebellum lobule	−15	−99	−3	10.0818	323
R Rectus	3	33	−18	10.3223	45
L Fusiform gyrus	−30	−72	−12	9.5211	69
L Inferior frontal gyrus of triangular part	−48	51	3	9.9487	167
L Middle temporal gyrus	−51	−63	6	6.7590	37
R Middle frontal gyrus	54	39	15	10.7230	98
L Middle frontal gyrus	−36	27	12	7.8551	102
R Superior frontal gyrus of medial part	12	60	36	8.9812	204
SCD > HC					
R Superior cerebellum lobule	21	−93	−27	4.0315	227
R Superior frontal gyrus of medial part	12	48	51	3.9014	10
HC > SCD					
L Fusiform gyrus	−30	−72	−12	4.369	28
aMCI > SCD					
R Superior frontal gyrus of medial part	3	42	39	3.9141	24

The x, y, z coordinates are the primary peak locations in the MNI space. Cluster size >30 voxels in one-way ANOVA analysis, $p < 0.05$. Cluster size >10 voxels in two-sample T-test, $p < 0.05$, TFCE-FWE corrected; L, left; R, right.

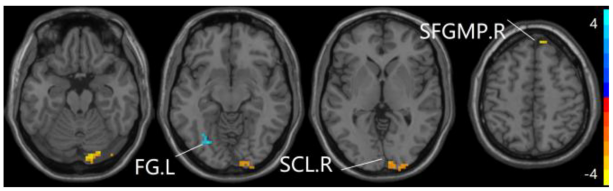

FIGURE 3 | Compared to HC group, the SCD group exhibits prominent differences in PPC of the aDMN network based on two-sample *T*-test. L, left; R, right; FG, fusiform gyrus; SCL, superior cerebellum lobule; SFGMP, superior frontal gyrus of medial part.

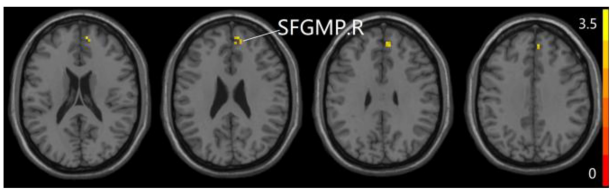

FIGURE 4 | Compared to SCD group, the aMCI group exhibits prominent differences in PPC of the aDMN network based on two-sample *T*-test. R, right; SFGMP, superior frontal gyrus of medial part.

experiments are after controlling the effects of age and gender (see **Table 2** and **Figures 2–4**).

The Aberrant PPC of pDMN Network in Patients With SCD and aMCI

For pDMN network, the one-way ANOVA analysis we have done suggested the prominent differences in four clusters, consisting of the left superior temporal gyrus of temporal pole (STGTP), left MFL, left superior parietal lobule (SPL) and right superior frontal gyrus (SFG). Compared to HC group, patients with SCD showed decreased PPC in the left SPL and right SFG. It is noteworthy that aMCI group showed decreased PPC in the left middle frontal gyrus of orbital part (MFGOP) and right SFG, yet increased PPC was found in the left STGTP. Additionally, aMCI group exhibited decreased PPC in the left MFGOP as the comparison with SCD group (TFCE-FWE corrected, cluster size $\geq$ 10 voxels, $p < 0.05$). The experimental data used in the PPC analysis are after controlling the influences of gender and age (see **Table 3** and **Figures 5–8**).

DISCUSSION

The work presented in this paper is that it focuses on investigating aberrant patterns of PPC of the DMN subnetworks connected to the whole brain between HC, SCD, and aMCI groups, and analyzing whether the aberrant areas are related with cognitive function. The result was consistent with the hypothesis that the SCD and aMCI groups exhibited distinct abnormal PCC in DMN subnetworks and the alerted regions were related to cognitive function. Besides, the altered regions in DMN subnetworks might regard as neuroimaging biomarkers and may be used to better understand the neural mechanism for the early stages of AD.

For aDMN, patients with SCD have prominently altered regions of the right SCL, right SFGMP and left FG resulted from the two-sample *T*-test. Based on earlier finds, SCL is involved in articulatory control and non-motor cognitive function (Ferenci et al., 2002). The left FG plays a critical role in semantic dementia and is repeatedly reported to be involved in visual word processing (Peterburs et al., 2019). SFG, which is located on top of the brain, plays a role in several higher-level cognitive processes

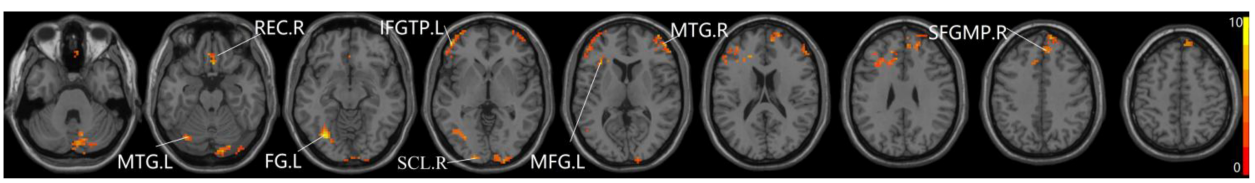

FIGURE 2 | The prominent differences of the brain in PPC of the aDMN network using one-way ANOVA analysis. L, left; R, right; MTG, middle frontal gyrus; REC, rectus; FG, fusiform gyrus; IFGTP, inferior frontal gyrus of triangular part; SCL, superior cerebellum lobule; MFG, middle frontal gyrus; SFGMP, superior frontal gyrus of medial part.

TABLE 3 | The aberrant PPC in pDMN network.

Region	Peak/MNI			*T*-score	Cluster size
	x	*y*	*z*		
ANOVA					
L Superior temporal gyrus of temporal pole	−48	0	−15	11.6797	40
L Middle frontal lobule	−36	63	3	12.6064	94
L Superior parietal lobule	−15	−60	69	9.1601	32
R Superior frontal gyrus	18	−12	72	12.0896	52
HC > SCD					
L Superior parietal lobule	−15	−60	69	3.8077	25
R Superior frontal gyrus	12	−15	75	3.9821	36
aMCI > HC					
L Superior temporal gyrus of temporal pole	−48	0	−15	4.5391	31
HC > aMCI					
L Middle frontal gyrus of orbital part	−36	63	3	3.8683	16
R Superior frontal gyrus	18	−12	72	4.4364	18
SCD > aMCI					
L Middle frontal gyrus of orbital part	−36	63	3	4.7242	90

The x, y, z coordinates are the primary peak locations in the MNI space. Cluster size > 30 voxels in one-way ANOVA analysis, $p < 0.05$; Cluster size > 10 voxels in two-sample T-test, $p < 0.05$, TFCE-FWE corrected; L, left; R, right.

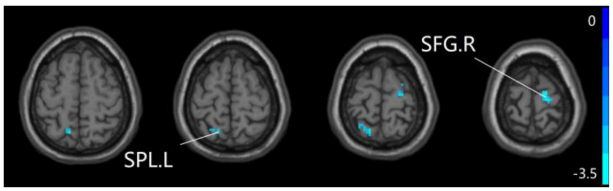

FIGURE 6 | Compared to HC group, the SCD group exhibits prominent differences in PPC of the pDMN network based on two-sample *T*-test. L, left; R, right; SPL, superior parietal lobule; SFG, superior frontal gyrus.

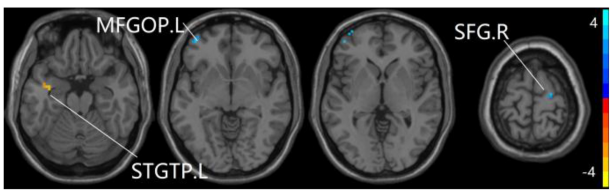

FIGURE 7 | Compared to HC group, the aMCI group exhibits prominent differences in PPC of the pDMN network based on two-sample *T*-test. L, left; R, right; STGTP, superior temporal gyrus of temporal pole; SFG, superior frontal gyrus; MFGOP, middle frontal gyrus of orbital part.

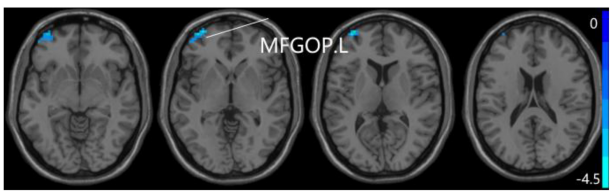

FIGURE 8 | Compared to SCD group, the aMCI group exhibits prominent differences in PPC of the pDMN network based on two-sample *T*-test. L, left; MFGOP, middle frontal gyrus of orbital part.

and working memory according to a previous report (Alagapan et al., 2019). Combining the altered regions mentioned above, these regions are related to language and memory, which are consistent with the manifestation of cognitive function (Samaras et al., 2014). Interestingly, no prominent regions were found in aDMN network in aMCI group, while aMCI group exhibited prominent regions in left STGTP, left MFGOP and right SFG in pDMN. A former study has reported that STG is anchored in the auditory association cortex involving spoken word recognition and MFG is related to working memory (Fegen et al., 2015; Kajikawa et al., 2015). Hence, the altered regions we found might involve in language cognitive disorder, and pDMN first appears abnormal connections compared to aDMN, which might suggest that the aDMN and pDMN have different manifestations in the early stages of AD.

We found that both aMCI and SCD groups showed a prominent region in SFG that is connected to DMN subnetworks, and according to the previous research that the altered functional connectivity between the pDMN and the SFG might be a compensatory response of brain (Xue et al., 2019). We assume that the aberrant PPC in SFG connected to the DMN may also be caused by the brain's compensation. Compared to HC group, aMCI group showed a prominent region in STG which did not belong to the altered region of SCD group, while SCD group showed prominent regions in SCL which did not belong to the altered region of aMCI group. It can be deduced that SCL and STG, related to articulatory control and working memory, respectively, are sensitive and might as neuroimaging biomarkers to distinguish the SCD and aMCI. Interestingly, compared to patients with SCD, DMN subnetworks in aMCI group showed obvious differences in right SFGMP and left MFGOP belonging

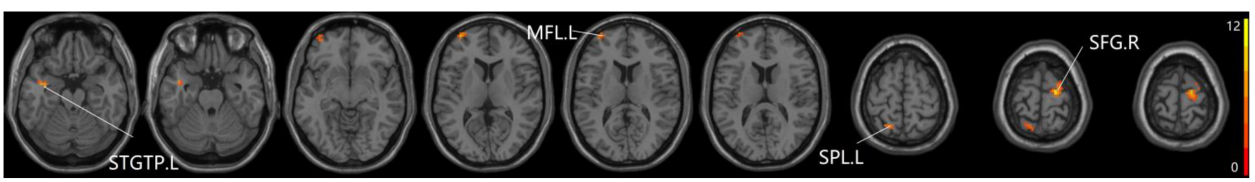

FIGURE 5 | The prominent differences of the brain in PPC of the pDMN network based on one-way ANOVA analysis. L, left; R, right; STGTP, superior temporal gyrus of temporal pole; MFL, middle frontal lobule; SPL, superior parietal lobule; SFG, superior frontal gyrus.

to FG. In previous studies, aMCI group showed more widespread topological changes involving the frontal lobes (Barban et al., 2017), and aberrant connectivity was also found in patients with SCD between DMN and FG due to cognitive impairment (Xue et al., 2019). Besides, an increasing trend of values of amplitude of low-frequency fluctuation (ALFF) and fractional ALFF were detected in FG (Yang et al., 2018). Therefore, changes in FG may be related to cognitive dysfunction.

CONCLUSION

Our study mainly shows that the PPC of the DMN subnetworks which are connected to the whole brain has different disconnection patterns in SCD and aMCI stages. Moreover, the significant difference in DMN subnetworks varies considerably, which might act as neuroimaging biomarkers of sensitivity for timely detection of the early stage of AD.

DATA AVAILABILITY STATEMENT

Publicly available datasets were analyzed in this study. This data can be found here: http://adni.loni.usc.edu/.

AUTHOR CONTRIBUTIONS

CC was responsible for writing the manuscript and doing the experiment. CH, CY, and XZ instructed the experiment. WZ, XH, FR, DH, YX, and JY participated in the experiment of manuscript and checked the English grammar. YP developed the idea for the study and analyzed most of the data.

FUNDING

This work was supported by the Natural Science Foundation of Fujian Province, China (No. 2017J01372) and the Foundation of Fujian Educational Committee (No. JK2015019).

REFERENCES

Alagapan, S., Lustenberger, C., Hadar, E., Shin, H. W., and Frhlich, F. (2019). Low-frequency direct cortical stimulation of left superior frontal gyrus enhances working memory performance. *Neuroimage* 184, 697–706. doi: 10.1016/j.neuroimage.2018.09.064

Babiloni, C., Binetti, G., Cassetta, E., Dal Forno, G., Del Percio, C., Ferreri, F., et al. (2006). Sources of cortical rhythms change as a function of cognitive impairment in pathological aging: a multicenter study. *Clin. Neurophysiol.* 117, 252–268. doi: 10.1016/j.clinph.2005.09.019

Banks, S. J., Zhuang, X., Bayram, E., Bird, C., Cordes, D., Caldwell, J. Z. K., et al. (2018). Default mode network lateralization and memory in healthy aging and Alzheimer's disease. *J. Alzheimers Dis.* 66, 1223–1234. doi: 10.3233/jad-180541

Barban, F., Mancini, M., Cercignani, M., Adriano, F., Perri, R., Annicchiarico, R., et al. (2017). A pilot study on brain plasticity of functional connectivity modulated by cognitive training in mild Alzheimer's disease and mild cognitive impairment. *Brain Sci.* 7:50. doi: 10.3390/brainsci7050050

Caillaud, M., Hudon, C., Boller, B., Brambati, S., Duchesne, S., Lorrain, D., et al. (2019). Evidence of a relation between hippocampal volume, white matter hyperintensities, and cognition in subjective cognitive decline and mild cognitive impairment. *J. Gerontol. B Psychol. Sci. Soc. Sci.* 26:gbz120. doi: 10.1093/geronb/gbz120

Chen, J., Duan, X., Shu, H., Wang, Z., Long, Z., Liu, D., et al. (2016). Differential contributions of subregions of medial temporal lobe to memory system in amnestic mild cognitive impairment: insights from fMRI study. *Sci. Rep.* 6:26148. doi: 10.1038/srep26148

Chen, X., Lu, B., and Yan, C. G. (2018). Reproducibility of R-fMRI metrics on the impact of different strategies for multiple comparison correction and sample sizes. *Hum. Brain Mapp.* 39, 300–318. doi: 10.1002/hbm.23843

Fegen, D., Buchsbaum, B. R., and D'Esposito, M. (2015). The effect of rehearsal rate and memory load on verbal working memory. *Neuroimage* 105, 120–131. doi: 10.1016/j.neuroimage.2014.10.034

Ferenci, P., Lockwood, A., Mullen, K., Tarter, R., Weissenborn, K., and Blei, A. T. (2002). Hepatic encephalopathy–definition, nomenclature, diagnosis, and quantification: final report of the working party at the 11th World Congresses of Gastroenterology, Vienna, 1998. *Hepatology* 35, 716–721. doi: 10.1053/jhep.2002.31250

Fox, M. D., Zhang, D., Snyder, A. Z., and Raichle, M. E. (2009). The global signal and observed anticorrelated resting state brain networks. *J. Neurophysiol.* 101, 3270–3283. doi: 10.1152/jn.90777.2008

Fraga, F. J., Falk, T. H., Kanda, P. A., and Anghinah, R. (2013). Characterizing Alzheimer's disease severity via resting-awake EEG amplitude modulation analysis. *PLoS One* 8:e72240. doi: 10.1371/journal.pone.0072240

Funaki, K., Nakajima, S., Noda, Y., Wake, T., Ito, D., Yamagata, B., et al. (2019). Can we predict amyloid deposition by objective cognition and regional cerebral blood flow in patients with subjective cognitive decline? *Psychogeriatrics* 19, 325–332. doi: 10.1111/psyg.12397

Huang, C., Tian, G., Lan, Y., Peng, Y., Ng, E. Y. K., Hao, Y., et al. (2019). A new pulse coupled neural network (PCNN) for brain medical image fusion empowered by shuffled frog leaping algorithm. *Front. Neurosci.* 13:210. doi: 10.3389/fnins.2019.00210

Huang, C., Xiaoying, S., Yisha, L., Lu, L., Haidong, C., Wenliang, C., et al. (2018a). A hybrid active contour segmentation method for myocardial D-SPECT images. *IEEE Access* 6, 39334–39343. doi: 10.1109/access.2018.2855060

Huang, C., Xie, Y., Lan, Y., Hao, Y., Chen, F., Cheng, Y., et al. (2018b). A new framework for the integrative analytics of intravascular ultrasound and optical coherence tomography images. *IEEE Access* 6, 36408–36419. doi: 10.1109/access.2018.2839694

Kajikawa, Y., Frey, S., Ross, D., Falchier, A., Hackett, T. A., and Schroeder, C. E. (2015). Auditory properties in the parabelt regions of the superior temporal gyrus in the awake macaque monkey: an initial survey. *J. Neurosci.* 35, 4140–4150. doi: 10.1523/JNEUROSCI.3556-14.2015

Kim, J. G., Ahn, C., Shin, H., Kim, W., Lim, T. H., Jang, B. H., et al. (2020). Efficacy of the cooling method for targeted temperature management in post-cardiac arrest patients: a systematic review and meta-analysis. *Resuscitation* 148, 14–24. doi: 10.1016/j.resuscitation.2019.12.025

Mandel, J. E., and Atkins, J. H. (2016). Hilbert-Huang transform yields improved minute volume estimates from respiratory inductance plethysmography during transitions to paradoxical breathing. *Anesth. Analg.* 122, 126–131. doi: 10.1213/ANE.0000000000000969

Martis, R., Acharya, U. R., Tan, J. H., Petznick, A., Yanti, R., Chua, K., et al. (2012). Application of empirical mode decomposition (EMD) for automated detection of epilepsy using EEG signals. *Int. J. Neural Syst.* 22:1250027. doi: 10.1142/S012906571250027X

Peng, Z. K., Tse, P. W., and Chu, F. L. (2005). A comparison study of improved Hilbert–Huang transform and wavelet transform: application to fault diagnosis for rolling bearing. *Mech. Syst. Signal Process.* 19, 974–988. doi: 10.1016/j.ymssp.2004.01.006

Peterburs, J., Blevins, L. C., Sheu, Y. S., and Desmond, J. E. (2019). Cerebellar contributions to sequence prediction in verbal working memory. *Brain Struct. Funct.* 224, 485–499. doi: 10.1007/s00429-018-1784-0

Qian, L., Zhang, Y., Zheng, L., Shang, Y., Gao, J. H., and Liu, Y. (2015). Frequency dependent topological patterns of resting-state brain networks. *PLoS One* 10:e0124681. doi: 10.1371/journal.pone.0124681

Ren, C., Li, D., Zhou, Q., and Hu, X. (2019). Mitochondria-targeted TPP-MoS2 with dual enzyme activity provides efficient neuroprotection through M1/M2 microglial polarization in an Alzheimer's disease model. *Biomaterials* 232:119752. doi: 10.1016/j.biomaterials.2019.119752

Samaras, K., Lutgers, H. L., Kochan, N. A., Crawford, J. D., Campbell, L. V., Wen, W., et al. (2014). The impact of glucose disorders on cognition and brain volumes in the elderly: the Sydney memory and ageing study. *Age (Dordr.)* 36, 977–993. doi: 10.1007/s11357-013-9613-0

Scherr, M., Utz, L., Tahmasian, M., Pasquini, L., Grothe, M. J., Rauschecker, J. P., et al. (2019). Effective connectivity in the default mode network is distinctively disrupted in Alzheimer's disease-A simultaneous resting-state FDG-PET/fMRI study. Hum. Brain Mapp. doi: 10.1002/hbm.24517 [Epub ahead of print].

Thatcher, R. W., North, D. M., and Biver, C. J. (2014). LORETA EEG phase reset of the default mode network. *Front. Hum. Neurosci.* 8:529. doi: 10.3389/fnhum.2014.00529

Wang, T., Luo, H., Zheng, X., and Xie, M. (2019). Crowdsourcing mechanism for trust evaluation in CPCS based on intelligent mobile edge computing. *ACM Trans. Intell. Syst. Technol.* 10:62.

Wang, T., Mei, Y., Jia, W., Zheng, X., Wang, G., and Xie, M. (2020). Edge-based differential privacy computing for sensor-cloud systems. *J. Parallel Distrib. Comput.* 136, 75–85. doi: 10.1016/j.jpdc.2019.10.009

Wang, X. H., Li, L., Xu, T., and Ding, Z. (2015). Investigating the temporal patterns within and between intrinsic connectivity networks under eyes-open and eyes-closed resting states: a dynamical functional connectivity study based on phase synchronization. *PLoS One* 10:e0140300. doi: 10.1371/journal.pone.0140300

Wang, Y., Risacher, S. L., West, J. D., McDonald, B. C., Magee, T. R., Farlow, M. R., et al. (2013). Altered default mode network connectivity in older adults with cognitive complaints and amnestic mild cognitive impairment. *J. Alzheimers Dis.* 35, 751–760. doi: 10.3233/JAD-130080

Wessels, A. M., Tariot, P. N., Zimmer, J. A., Selzler, K. J., Bragg, S. M., Andersen, S. W., et al. (2019). Efficacy and safety of lanabecestat for treatment of early and mild Alzheimer disease: the AMARANTH and DAYBREAK-ALZ randomized clinical trials. *JAMA Neurol.* [Epub ahead of print].

Winkler, A. M., Ridgway, G. R., Douaud, G., Nichols, T. E., and Smith, S. M. (2016). Faster permutation inference in brain imaging. *Neuroimage* 141, 502–516. doi: 10.1016/j.neuroimage.2016.05.068

Xie, Y., Liu, T., Ai, J., Chen, D., Zhuo, Y., Zhao, G., et al. (2019). Changes in centrality frequency of the default mode network in individuals with subjective cognitive decline. *Front. Aging Neurosci.* 11:118. doi: 10.3389/fnagi.2019.00118

Xu, X., Yuan, H., and Lei, X. (2016). Activation and connectivity within the default mode network contribute independently to future-oriented thought. *Sci. Rep.* 6:21001. doi: 10.1038/srep21001

Xue, C., Yuan, B., Yue, Y., Xu, J., Wang, S., Wu, M., et al. (2019). Distinct disruptive patterns of default mode subnetwork connectivity across the spectrum of preclinical Alzheimer's disease. *Front. Aging Neurosci.* 11:307. doi: 10.3389/fnagi.2019.00307

Yang, H., Wang, C., Zhang, Y., Xia, L., Feng, Z., Li, D., et al. (2017). Disrupted causal connectivity anchored in the posterior cingulate cortex in amnestic mild cognitive impairment. *Front. Neurol.* 8:10. doi: 10.3389/fneur.2017.00010

Yang, J., Zeng, F., Ge, Y., Peng, K., Li, X., Li, Y., et al. (2019). Development of near-infrared fluorescent probes for use in Alzheimer's disease diagnosis. *Bioconjug. Chem.* 31, 2–15. doi: 10.1021/acs.bioconjchem.9b00695

Yang, L., Yan, Y., Wang, Y., Hu, X., Lu, J., Chan, P., et al. (2018). Gradual disturbances of the amplitude of low-frequency fluctuations (ALFF) and fractional ALFF in Alzheimer spectrum. *Front. Neurosci.* 12:975. doi: 10.3389/fnins.2018.00975

Yu, H., Li, F., Wu, T., Li, R., Yao, L., Wang, C., et al. (2018). Functional brain abnormalities in major depressive disorder using the Hilbert-Huang transform. *Brain Imaging Behav.* 12, 1556–1568. doi: 10.1007/s11682-017-9816-6

Zhang, D., and Raichle, M. E. (2010). Disease and the brain's dark energy. *Nat. Rev. Neurol.* 6, 15–28.

Zhao, T., Quan, M., and Jia, J. (2020). Functional connectivity of default mode network subsystems in the presymptomatic stage of autosomal dominant Alzheimer's disease. *J. Alzheimers Dis.* 73, 1435–1444. doi: 10.3233/jad-191065

Conflict of Interest: The authors declare that the research was conducted in the absence of any commercial or financial relationships that could be construed as a potential conflict of interest.

frontiers in Neuroscience

ORIGINAL RESEARCH
published: 15 April 2020
doi: 10.3389/fnins.2020.00341

Temporal Patterns of Vertigo and Migraine in Vestibular Migraine

Manyun Yan[1], Xiaoning Guo[1], Wei Liu[1], Jiajie Lu[1], Jingwen Wang[2], Lan Hu[2], Kaijian Xia[3], Jianqiang Ni[1], Haifeng Lu[1] and Hongru Zhao[1]**

[1] Department of Neurology, The First Affiliated Hospital of Soochow University, Suzhou, China, [2] Department of Neurology, Ninth People's Hospital, Suzhou, China, [3] Changshu No. 1 People's Hospital, Suzhou, China

Vestibular migraine (VM) is a multidisciplinary disease under exploration. Multiple temporal patterns of vertigo and migraine make it difficult to diagnose VM, and their effect on the clinical features of VM is still unclear. Here we investigated the clinical features of VM under three temporal patterns. 172 VM patients were enrolled in this study and divided into three groups: 86 patients in group A had an earlier onset of migraine than vertigo, 35 patients in group B had an earlier onset of vertigo than migraine, and 51 patients in group C had concurrent vertigo and migraine. No significant difference was found among three groups regarding types, intensity and accompanying symptoms of the vestibular attack. Patients in group C presented higher frequency and longer duration of vertigo than group A and B, while patients in group A presented lower frequency and shorter duration of headaches than group B and C. Additionally, the frequency, duration, intensity and accompanying symptoms of headache in group A decreased significantly after the onset of vertigo, especially in women around menopause. We hypothesized that vestibular stimulation could inhibit the trigeminal pain pathway, while painful trigeminal stimulation could excite the vestibular system. Our findings may contribute to the clinical identification of VM and further clarification of its pathogenesis.

Keywords: vestibular migraine, temporal patterns, vestibular symptoms, migraine features, interaction

OPEN ACCESS

Edited by:
Mohammad Khosravi, Persian Gulf University, Iran

Reviewed by:
Kaiming Liu, Zhejiang University, China
Yonggang Wang, Capital Medical University, China

****Correspondence:***
Haifeng Lu
lu.haifeng110@163.com
Hongru Zhao
tiantan11@163.com

Specialty section:
This article was submitted to Neuroprosthetics, a section of the journal Frontiers in Neuroscience

Received: *02 March 2020*
Accepted: *23 March 2020*
Published: *15 April 2020*

Citation:
Yan M, Guo X, Liu W, Lu J, Wang J, Hu L, Xia K, Ni J, Lu H and Zhao H (2020) Temporal Patterns of Vertigo and Migraine in Vestibular Migraine. Front. Neurosci. 14:341. doi: 10.3389/fnins.2020.00341

INTRODUCTION

Vertigo and migraine are both very common complaints among patients, and a strong link between them has been proved. The co-occurrence of migraine and vertigo in the same individual was expected in 1% of the population based on the prevalence of migraine and vestibular vertigo, but the actual percentage was about three times higher than expected (Neuhauser et al., 2006). Moreover, migraine patients had a two- or three-fold higher risk for vertigo than those without headache (Vukovic et al., 2007). In 1999, Dieterich and Brandt introduced the term "vestibular migraine" (VM) to describe the clinical condition that associated with vestibular symptoms and migraine headache (Dieterich and Brandt, 1999). In recent years, VM, including definite VM and probable VM, has been considered as an independent diagnostic entity and one of the most common causes of vertigo (Lempert et al., 2012; Arnold, 2018; Huang et al., 2020).

However, VM has been remained underdiagnosed despite ongoing studies in recent years. Only 8–20% of VM patients were correctly diagnosed in practice (Neuhauser et al., 2006; Geser and Straumann, 2012; Formeister et al., 2018). A big challenge for diagnosis is multiple

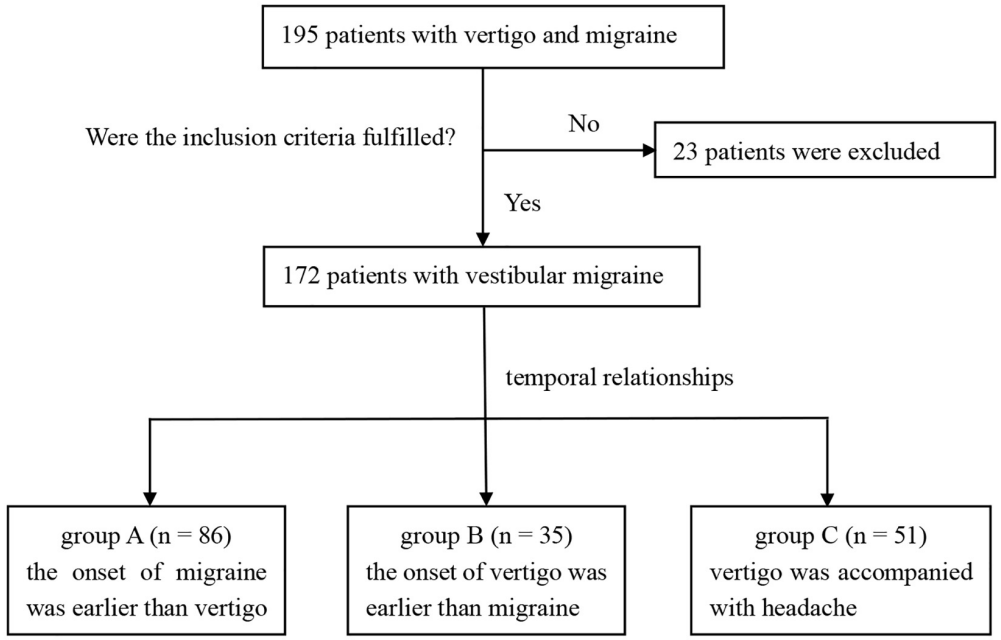

FIGURE 1 | Flow diagram of participants' selection.

temporal patterns of vertigo and migraine in VM. 51–65.6% of VM patients suffered from migraine before the onset of vertigo (Morganti et al., 2016; Zhang et al., 2016; Beh et al., 2019), and there was an interval of 8–20 years between the two symptoms (Cohen et al., 2011; Pagnini et al., 2014). 10.2–13% of patients had an earlier onset of vertigo than migraine (Qiu et al., 2014; Zhang et al., 2016). 34–49.6% of patients had migraine headaches during vestibular attacks (Zhang et al., 2016; Beh et al., 2019). Since most of VM patients experienced vertigo separately from headache, and even some patients had vestibular symptoms years after the headache disappeared, they often did not actively report headache history. One study showed that only 9.8% of VM patients reported headache symptoms before being carefully asked (Ren et al., 2014). Likewise, clinicians often neglect to ask the history or associated symptoms of migraine in patients complaining with vertigo, which often results in misdiagnosis or missed diagnosis. Therefore, the investigation of temporal patterns of vertigo and migraine and their impact on patients with VM is very important for understanding and management of VM.

The aim of this study was to describe and compare the clinical features of VM patients with different temporal patterns, and investigate the interaction between vertigo and migraine headache in VM.

MATERIALS AND METHODS

Participants

Patients who met diagnostic criteria of definite VM (Arnold, 2018) or probable VM (Lempert et al., 2012) in neurology and headache clinics of First Affiliated Hospital of Soochow University from January 2018 to April 2019 were enrolled (**Figure 1**). The exclusion criteria were as follows: other causes of vestibular attack such as benign paroxysmal positional vertigo (BPPV), Meniere's disease or transient ischemic attack of posterior circulation; history of head trauma; severe physical illness; abnormal computed tomography or magnetic resonance imaging (MRI); history of alcohol or drugs abuse; other primary or secondary headaches; dizziness associated with chronic anxiety; history of intracranial infection.

Data Collection

A structured questionnaire was used to interview the participants regarding the following aspects: Demographics, familial history of headache or vertigo, age of onset of vertigo and migraine, vertigo intensity (Arnold, 2018) (moderate: vestibular symptoms interfere with but do not prevent daily activities; severe: daily activities cannot be continued), pain intensity [visual analog scale (VAS)], frequency (number of attacks within 3 months before enrolled), duration (minutes to hours), accompanying symptoms of vertigo (nausea, vomiting, phonophobia, photophobia, tinnitus), accompanying symptoms of headache (nausea, vomiting, phonophobia, photophobia, osmophobia, neck stiffness, scalp allodynia). Vestibular attacks included spontaneous vertigo (internal or external vertigo), positional vertigo (occurring after a change of head position), visually induced vertigo (triggered by a complex or large moving visual stimulus), head motion-induced vertigo (occurring during head motion), head motion-induced dizziness with nausea (dizziness is characterized by a sensation of disturbed spatial orientation) (Arnold, 2018). Furthermore, psychiatric comorbid

disorders [anxiety, depression, persistent postural-perceptual dizziness (PPPD) (Staab et al., 2017) and sleep disorders] were assessed at enrollment.

We defined the temporal patterns between migraine and vertigo as follows: (A) the onset of migraine was earlier than vertigo: (i) between migraine and vertigo there was a symptom-free interval (at least one year), (ii) migraine shifted directly into vertigo without a free interval (iii) migraine gradually changed into vertigo; (B) the onset of vertigo was earlier than migraine; (C) vertigo was accompanied with headache. Moreover, headache features before the onset of vertigo in group A were additionally collected, including frequency, duration, intensity and accompanying symptoms.

Statistical Analyses

All statistical analyses were performed in SPSS software version 22.0. Categorical variables were compared using Chi-square test and presented as frequency counts and percentages. As all continuous variables in this study were non-normal distribution, they were presented as the median and interquartile range, and the Mann–Whitney *U* test was used for comparison between two groups or the Kruskal–Wails H test among three groups. Statistically significance was set at a two-sided p-value < 0.05.

RESULTS

172 VM patients were enrolled in this study and divided into three groups based on the temporal patterns of vertigo and migraine as shown in **Figure 2**. In group A, 86 patients (50.0%) had an earlier onset of migraine than vertigo. Nine patients (5.2%) reported vertigo attacks after the migraine headaches disappeared, with a symptom-free interval of 1–10 years. Six patients (3.5%) reported that vertigo occurred immediately after the disappearance of headaches without any interval. 71 cases (41.3%) reported the gradual shift of the two symptoms, with a partial overlap. In group B, 35 patients (20.3%) had an earlier onset of vertigo than migraine. In group C, 51 patients (29.7%) had concurrent vertigo and migraine headache. Among them, thirty patients (17.4%) initially presented with vertigo and headache simultaneously, and 21 patients (12.2%) complained that vertigo occurred together with headache after a period of migraine headache attacks alone.

Three groups were female-dominated, but more female subjects in group A developed vertigo around menopause than in group B ($p < 0.05$) and C ($p = 0.084$). Patients in group B presented a lower age of onset of vertigo compared to group A and C ($p < 0.01$) as expected. Patients in group A presented a lower age of onset of migraine compared to group B ($p < 0.05$), but similar age of onset to group C [p: not significant (NS)]. The proportion of familial history of migraine in group B was lower than that in group A and C ($p < 0.05$). The proportion of motion sickness history in group C was higher than that in group B ($p < 0.05$) (**Table 1**).

No significant difference was found among groups regarding types, intensity and accompanying symptoms of vestibular attack (p: NS). Patients in group C presented higher frequency and longer duration of vertigo than group A and B. (**Table 2**).

Patients in group A presented lower frequency and shorter duration of migraine headaches than group B and C ($p < 0.05$) (**Table 3**). Furthermore, the frequency, duration, intensity and accompanying symptoms of headache in group A decreased significantly after the onset of vertigo (**Table 4**). Patients in group C presented stronger intensity of headache and reported nausea and vomiting during headache attacks more often compared to patients in group A ($p < 0.001$) and B ($p < 0.05$) (**Table 3**).

Following the onset of vestibular or headache symptoms, many were diagnosed with anxiety (36.6%), depression (47.7%), PPPD (34.9%) and sleep disorders (70.3%). Except that the proportion of anxiety in group C was higher than that in group A ($p < 0.05$), no significant difference in the proportion of psychiatric comorbid disorders was found among groups (p: NS) (**Table 5**).

DISCUSSION

Temporal patterns of vertigo and migraine in VM patients and how they affect the clinical features of VM have not yet been systematically described. In this study, we investigated the clinical features of VM under three temporal patterns and found that patients with vertigo and migraine occurred simultaneously presented higher frequency and longer duration of vertigo, while patients with earlier onset of migraine than vertigo presented lower frequency and shorter duration of headache.

Previous studies have suggested that headaches significantly decreased in frequency and strength or disappeared after the onset of vertigo in VM patients (von Brevern and Lempert, 2016; Teggi et al., 2018). This phenomenon was more common in women around menopause (Lempert et al., 2009; Park and Viirre, 2010). A 13-year observational study showed that headaches

TABLE 1 | Demographic data among subjects in group A, B, and C.

	A (n = 86)	B (n = 35)	C (n = 51)
Age at inclusion (years)	49 (37, 59)	43 (33, 60)	47 (33, 57)
Sex (female %)	69 (80%)	30 (86%)	41 (80%)
Vertigo occurred around menopause (of females)	28 (41%)	5 (17%)*	10 (24%)
Age of onset of vertigo (years)	43 (33, 54)	29 (22, 37)*	40 (30, 49)†
Age of onset of migraine (years)	32 (25, 41)	37 (31, 42)*	32 (25, 43)
Familial history of vertigo	21 (24%)	9 (26%)	18 (35%)
Familial history of migraine	36 (42%)	7 (20%)*	21 (41%)†
Motion sickness history	50 (58%)	17 (49%)	37 (73%)†

*A: the onset of migraine was earlier than vertigo; B: the onset of vertigo was earlier than migraine; C: vertigo was accompanied with headache. *$p < 0.05$ vs. group A; †$p < 0.05$ vs. group B.*

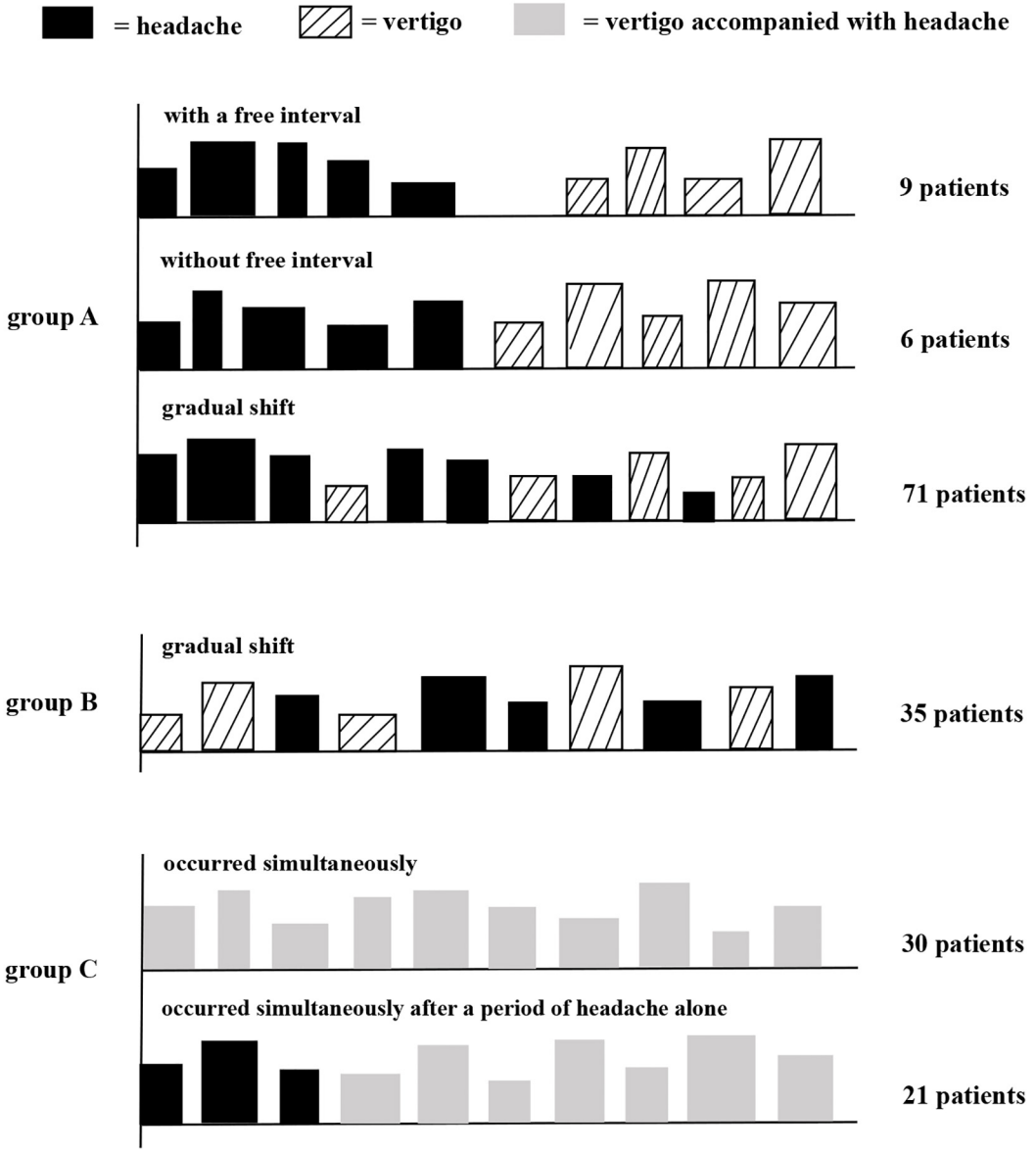

FIGURE 2 | Schematic diagram of temporal patterns of vertigo and migraine in VM patients. Group A, patients had an earlier onset of migraine than vertigo; group B, patients had an earlier onset of vertigo than migraine; and group C, patients had concurrent vertigo and migraine. Height and width of rectangles indicate, respectively, the strength and duration of headache or vertigo.

completely ceased after vertigo attacked in 57% of patients and substantially improved in 43% (Pagnini et al., 2014). However, there were no detailed data to clarify the specific changes in migraine headache features before and after the onset of vertigo. In our cases, we noticed a 50% reduction in frequency and duration of headache after the onset of vertigo, a 17% reduction in pain intensity and a 22–50% reduction in accompanying symptoms such as nausea, vomiting, photophobia, phonophobia, osmophobia, neck stiffness, and scalp allodynia. The difference between our study and the previous study (Pagnini et al., 2014) was that only 19 patients (22%) reported complete cessation of headache in this study, 35% noticed a considerable reduction in frequency of headache after vertigo, 23% got relief for duration, intensity or accompanying symptoms, but in 20% cases, headache symptoms were unaffected by vertigo, which was partly due to the different inclusion criteria. We included all patients diagnosed with VM, and the previous study (Pagnini et al., 2014) only included patients who developed vestibular symptoms after the disappearance or remarkable reduction of headache. Another reason was that this study was not a longitudinal study, and there was recall bias in the features of migraine headache prior to the onset of vertigo.

The mechanisms of disappearance or attenuation of headache after recurrent vertigo in VM are unclear. We hypothesized

TABLE 2 | Vestibular symptoms among subjects in group A, B, and C.

Vestibular symptoms	A (*n* = 86)	B (*n* = 35)	C (*n* = 51)
Vestibular attack			
Spontaneous vertigo	38 (44%)	14 (40%)	15 (29%)
Positional vertigo	26 (30%)	11 (31%)	15 (29%)
Head motion dizziness with nausea	24 (28%)	12 (34%)	22 (43%)
Head-motion vertigo or visual vertigo	4 (5%)	1 (3%)	1 (2%)
Frequency (times/3 months)	3 (1, 9)	3 (0.6, 10.5)	6 (3, 12)*†
Duration (h)	2 (0.3, 18.5)	2.5 (0.5, 30)	18 (2.5, 24)*
5 min–1 h	33 (38%)	14 (40%)	9 (18%)*†
1–24 h	38 (44%)	13 (37%)	25 (49%)
24–72 h	15 (17%)	8 (23%)	17 (33%)*
Intensity (severe %)	33 (38%)	11 (31%)	13 (26%)
Accompanying symptoms			
Nausea	61 (71%)	20 (57%)	37 (73%)
Vomiting	51 (59%)	17 (49%)	26 (51%)
Photophobia	42 (49%)	18 (51%)	21 (41%)
Phonophobia	57 (66%)	23 (66%)	33 (65%)
Tinnitus	20 (23%)	6 (17%)	11 (22%)

*A: the onset of migraine was earlier than vertigo; B: the onset of vertigo was earlier than migraine; C: vertigo was accompanied with headache. *p < 0.05 vs. group A; †p < 0.05 vs. group B.*

TABLE 3 | Headache symptoms among subjects in group A, B, and C.

Headache symptoms	A (*n* = 86)	B (*n* = 35)	C (*n* = 51)
Frequency (times/3 months)	3 (0.3, 7.9)	6 (3, 12)*	7.5 (3, 16.5)*
Duration (h)	12 (2, 24)	24 (5, 36)*	24 (4.5, 36)*
Intensity (VAS)	5 (3, 6)	5 (4, 7)	5 (5, 7)*†
Accompanying symptoms			
Nausea	34 (40%)	18 (51%)	38 (75%)*†
Vomiting	20 (23%)	10 (29%)	27 (53%)*†
Photophobia	26 (30%)	17 (49%)	21 (41%)
Phonophobia	47 (55%)	23 (66%)	35 (69%)
Osmophobia	4 (5%)	4 (11%)	6 (12%)
Neck stiffness	13 (15%)	9 (26%)	14 (27%)
Scalp allodynia	14 (16%)	5 (14%)	5 (10%)

*A: the onset of migraine was earlier than vertigo; B: the onset of vertigo was earlier than migraine; C: vertigo was accompanied with headache. VAS: visual analog scale. *p < 0.05 vs. group A; †p < 0.05 vs. group B.*

TABLE 4 | Headache symptoms before and after the onset of vertigo in group A.

Headache symptoms	Before (*n* = 86)	After (*n* = 86)	*p*-value
Frequency (times/3 months)	6 (3, 9)	3 (0, 8)	0.015
Duration (h)	24 (7.5, 36)	12 (2, 24)	0.001
Intensity (VAS score)	6 (5, 7)	5 (3, 6)	< 0.001
Accompanying symptoms			
Nausea	44 (51%)	34 (40%)	0.126
Vomiting	29 (34%)	20 (23%)	0.128
Photophobia	38 (44%)	26 (30%)	0.058
Phonophobia	60 (70%)	47 (55%)	0.041
Osmophobia	8 (9%)	4 (5%)	0.369
Neck stiffness	23 (27%)	13 (15%)	0.061
Scalp allodynia	22 (26%)	14 (16%)	0.134
Number of accompanying symptoms	2 (2, 4)	2 (0, 3)	0.002

Group A: the onset of migraine was earlier than vertigo; VAS: visual analog scale.

TABLE 5 | Psychiatric comorbid disorders among subjects in group A, B, and C.

Disorders	A (*n* = 86)	B (*n* = 35)	C (*n* = 51)
Anxiety	24 (28%)	13 (37%)	26 (51%)*
Depression	40 (47%)	15 (43%)	27 (53%)
PPPD	30 (35%)	15 (43%)	15 (29%)
Sleep disorders	56 (65%)	29 (83%)	36 (71%)

*A: the onset of migraine was earlier than vertigo; B: the onset of vertigo was earlier than migraine; C: vertigo was accompanied with headache. PPPD: persistent postural-perceptual dizziness. *p < 0.05 vs. group A.*

that one potential mechanism was the interaction of the vestibular and trigeminal systems. The main mechanism of VM is currently considered as the connection of trigeminal caudal nucleus with vestibular nucleus (Furman et al., 2013; Huang et al., 2020), so the vestibular stimulation and migraine headache could interact with each other. A study showed that headaches completely disappeared or reduced in strength after vestibular thermal stimulation during migraine attacks (Kolev, 1990), which suggested that the painful conduction pathway might be inhibited after the activation of the vestibular pathway. On the other hand, both the prevalence of migraine and VM was significantly higher in females than males, and the conversion from headache to vertigo was more common around menopause (Lempert et al., 2009; Park and Viirre, 2010; Pagnini et al., 2014), which has been confirmed in our data. Moreover, migraine tended to improve when sex hormone levels stabilized after menopause (Vetvik and MacGregor, 2017), and hormone fluctuations during the perimenopausal period were associated with an increased risk of vertigo (Park and Viirre, 2010). Hence, another possible hypothesis was the role of female sex hormones as a facilitating factor for the transformation of migraine headaches into vestibular attacks.

An interesting aspect verified in our study was that VM patients with vertigo and headache occurred simultaneously presented higher frequency and longer duration of vertigo. Similarly, this phenomenon might be due to the interaction of the vestibular and trigeminal systems. A study showed that trigeminal stimulation induced nystagmus in patients with migraine but not controls, which suggested increased vestibular excitability in migraine patients (Marano et al., 2005). Functional imaging of the brain showed that the activation of temporo-parieto-insular areas and bilateral thalami was increased during vertigo attacks in VM patients (Shin et al., 2014), and the magnitude of thalamic activation was positively correlated with the frequency of migraine attacks (Russo et al., 2014). Based on this, we hypothesized that vestibular excitability increased when vertigo occurred together with migraine headaches, and the thalamus and other brain regions might be activated more

significantly after both vestibular and painful stimulation. That is to say, painful trigeminal stimulation might enhance the excitability of the vestibular system, and the threshold of vestibular perception of VM patients decreases and the sensitivity increases, similar to the central sensitization effect. In addition, patients with concurrent vertigo and headache experienced severer headaches accompanied with nausea and vomiting more often, which might be associated with more frequent attacks of vertigo. But no significant correlations were found between other clinical features of migraine (e.g., disease duration, pain intensity, migraine disability) and thalamic activation, except for the frequency (Russo et al., 2014). And the influence of migraine symptoms on vestibular attacks remains to be further studied. Other factors that should be considered were the contributions of motion sickness history and anxiety, which were more common in VM patients with concurrent vertigo and migraine. Anxiety was associated with significantly increased recurrence of VM (Formeister et al., 2018) and motion sickness could enhance motion intolerance (Wang and Lewis, 2016).

The special temporal patterns of vertigo and migraine make it difficult for many clinicians to accurately diagnose VM, and patients usually undergo a painful and protracted course until they visit a headache or vertigo specialist. During the course, VM patients are usually anxious about unexpected and intense vertigo attacks, afraid of falling and avoid going out or entering various environments triggering dizziness (Kutay et al., 2017). Additionally, many of them complain of decreased daily activities and nearly constant dizziness and lightheaded (von Brevern and Lempert, 2016). Many studies suggested that VM patients were prone to psychiatric comorbidities, such as anxiety (19.8–70.2%) (Langhagen et al., 2014; Beh et al., 2019), depression (21.8–40.5%) (Vuralli et al., 2018; Beh et al., 2019), PPPD (32.8–41%) (Neff et al., 2012; Eggers et al., 2014; Beh et al., 2019) and sleep disorders (29–67.4%) (Vuralli et al., 2018; Beh et al., 2019; Wu et al., 2019), regardless of the frequency of vertigo. Our study showed that VM patients also had high rates of psychiatric comorbidities regardless of the temporal patterns. Vestibular attacks increase the incidence of psychiatric comorbidities, and psychiatric disorders aggravate the severity of vestibular symptoms. Then a vicious circle is formed, and the disease becomes deferred. Therefore, we should make an effort to understand these temporal patterns in VM, in order to give patients correct diagnosis and timely treatment.

This study had several potential limitations. Firstly, we lacked data on the features of vertigo before the onset of migraine in group B to further support our hypothesis that migraine headaches could increase the vestibular excitability and aggravate the manifestations of vertigo. Moreover, we only described the clinical features of VM by a cross-sectional study. A long-term longitudinal study will be of great help to understand the temporal patterns of VM and identify this entity. Secondly, we enrolled patients with probable VM, the diagnostic criteria of which have not been included in the International Classification of Headache Disorders 3rd edition (ICHD-3). But some studies have shown that there was no significant difference between definite and probable VM (Eggers et al., 2011; Van Ombergen et al., 2015; Cho et al., 2016), and most probable VM patients would develop definite VM over time during long-term follow up (Radtke et al., 2011).

CONCLUSION

We found that the temporal patterns of vertigo and migraine affected the clinical features of VM. Migraine headaches usually disappeared or relieved after recurrent vertigo attacks, especially in women around menopause, while vestibular vertigo was more frequent and lasted longer when accompanied with migraine headaches. The underlying mechanism might be that vestibular stimulation inhibits the trigeminal pain pathway, while painful trigeminal stimulation could excite the vestibular system.

DATA AVAILABILITY STATEMENT

All datasets generated for this study are included in the article/supplementary material.

ETHICS STATEMENT

The studies involving human participants were reviewed and approved by the Institutional Review Board of The First Affiliated Hospital of Soochow University. The patients/participants provided their written informed consent to participate in this study.

AUTHOR CONTRIBUTIONS

HZ, HL, JN, and MY designed the study. HZ, MY, XG, WL, JL, LH, JW, and KX evaluated the subjects and collected the data. MY and XG analyzed the data. MY wrote the initial draft, with HL and HZ participating in revising the manuscript.

FUNDING

This study was funded by the National Natural Science Foundation of China (NSFC, No. 81701309 to HL).

ACKNOWLEDGMENTS

We would like to thank Prof. Xingshun Xu for valuable comments on this manuscript.

REFERENCES

Arnold, M. (2018).Headache classification committee of the international headache society (ihs) the international classification of headache disorders, 3rd edition. *Cephalalgia* 38, 1–211. doi: 10.1177/0333102417738202

Beh, S. C., Masrour, S., Smith, S. V., and Friedman, D. I. (2019). The spectrum of vestibular migraine: clinical features, triggers, and examination findings. *Headache* 59, 727–740. doi: 10.1111/head.13484

Cho, S. J., Kim, B. K., Kim, B. S., Kim, J. M., Kim, S. K., Moon, H. S., et al. (2016). Vestibular migraine in multicenter neurology clinics according to the appendix criteria in the third beta edition of the International classification of headache disorders. *Cephalalgia* 36, 454–462. doi: 10.1177/0333102415597890

Cohen, J. M., Bigal, M. E., and Newman, L. C. (2011). Migraine and vestibular symptoms–identifying clinical features that predict "vestibular migraine". *Headache* 51, 1393–1397. doi: 10.1111/j.1526-4610.2011.01934.x

Dieterich, M., and Brandt, T. (1999). Episodic vertigo related to migraine (90 cases): vestibular migraine? *J.* 246, 883–892. doi: 10.1007/s004150050478

Eggers, S. D., Neff, B. A., Shepard, N. T., and Staab, J. P. (2014). Comorbidities in vestibular migraine. *J. Vestib. Res.* 24, 387–395. doi: 10.3233/VES-140525

Eggers, S. D., Staab, J. P., Neff, B. A., Goulson, A. M., Carlson, M. L., and Shepard, N. T. (2011). Investigation of the coherence of definite and probable vestibular migraine as distinct clinical entities. *Otol. Neurotol.* 32, 1144–1151. doi: 10.1097/MAO.0b013e31822a1c67

Formeister, E. J., Rizk, H. G., Kohn, M. A., and Sharon, J. D. (2018). The epidemiology of vestibular migraine: a population-based survey study. *Otol. Neurotol.* 39, 1037–1044. doi: 10.1097/MAO.0000000000001900

Furman, J. M., Marcus, D. A., and Balaban, C. D. (2013). Vestibular migraine: clinical aspects and pathophysiology. *Lancet Neurol.* 12, 706–715. doi: 10.1016/s1474-4422(13)70107-8

Geser, R., and Straumann, D. (2012). Referral and final diagnoses of patients assessed in an academic vertigo center. *Front. Neurol.* 3:169. doi: 10.3389/fneur.2012.00169

Huang, T. C., Wang, S. J., and Kheradmand, A. (2020). Vestibular migraine: an update on current understanding and future directions. *Cephalalgia* 40, 107–121. doi: 10.1177/0333102419869317

Kolev, O. (1990). How caloric vestibular irritation influences migraine attacks. *Cephalalgia* 10, 167–169. doi: 10.1046/j.1468-2982.1990.1004167.x

Kutay, O., Akdal, G., Keskinoglu, P., Balci, B. D., and Alkin, T. (2017). Vestibular migraine patients are more anxious than migraine patients without vestibular symptoms. *J. Neurol.* 264(Suppl. 1), 37–41. doi: 10.1007/s00415-017-8439-6

Langhagen, T., Lehrer, N., Borggraefe, I., Heinen, F., and Jahn, K. (2014). Vestibular migraine in children and adolescents: clinical findings and laboratory tests. *Front. Neurol.* 5:292. doi: 10.3389/fneur.2014.00292

Lempert, T., Neuhauser, H., and Daroff, R. B. (2009). Vertigo as a symptom of migraine. *Ann. N. Y. Acad. Sci.* 1164, 242–251. doi: 10.1111/j.1749-6632.2009.03852.x

Lempert, T., Olesen, J., Furman, J., Waterston, J., Seemungal, B., Carey, J., et al. (2012). Vestibular migraine: diagnostic criteria. *J. Vestib. Res.* 22, 167–172. doi: 10.3233/VES-2012-0453

Marano, E., Marcelli, V., Di Stasio, E., Bonuso, S., Vacca, G., Manganelli, F., et al. (2005). Trigeminal stimulation elicits a peripheral vestibular imbalance in migraine patients. *Headache* 45, 325–331. doi: 10.1111/j.1526-4610.2005.05069.x

Morganti, L. O., Salmito, M. C., Duarte, J. A., Bezerra, K. C., Simoes, J. C., and Gananca, F. F. (2016). Vestibular migraine: clinical and epidemiological aspects. *Braz. J. Otorhinolaryngol.* 82, 397–402. doi: 10.1016/j.bjorl.2015.06.003

Neff, B. A., Staab, J. P., Eggers, S. D., Carlson, M. L., Schmitt, W. R., Van Abel, K. M., et al. (2012). Auditory and vestibular symptoms and chronic subjective dizziness in patients with Meniere's disease, vestibular migraine, and Meniere's disease with concomitant vestibular migraine. *Otol. Neurotol.* 33, 1235–1244. doi: 10.1097/MAO.0b013e31825d644a

Neuhauser, H. K., Radtke, A., von Brevern, M., Feldmann, M., Lezius, F., Ziese, T., et al. (2006). Migrainous vertigo: prevalence and impact on quality of life. *Neurology* 67, 1028–1033. doi: 10.1212/01.wnl.0000237539.09942.06

Pagnini, P., Vannucchi, P., Giannoni, B., and Pecci, R. (2014). Epigone migraine vertigo (EMV): a late migraine equivalent. *Acta Otorhinolaryngol. Ital.* 34, 62–70.

Park, J. H., and Viirre, E. (2010). Vestibular migraine may be an important cause of dizziness/vertigo in perimenopausal period. *Med. Hypotheses* 75, 409–414. doi: 10.1016/j.mehy.2009.04.054

Qiu, F., Huang, X., Wang, X., Liu, J., and Qi, X. (2014). An analysis of clinical features of 226 vestibular migraine patients. *Zhonghua Nei Ke Za Zhi* 53, 961–963. doi: 10.3760/cma.j.issn.0578-1426.2014.12.009

Radtke, A., Neuhauser, H., von Brevern, M., Hottenrott, T., and Lempert, T. (2011). Vestibular migraine–validity of clinical diagnostic criteria. *Cephalalgia* 31, 906–913. doi: 10.1177/0333102411405228

Ren, T., Dai, C., and Wang, W. (2014). Clinical characteristics of vestibular migraine in 102 patients. *Chin. J. Ophthalmol. Otorhinolaryngol.* 14, 146–150. doi: 10.14166/j.issn.1671-2420.2014.03.003

Russo, A., Marcelli, V., Esposito, F., Corvino, V., Marcuccio, L., Giannone, A., et al. (2014). Abnormal thalamic function in patients with vestibular migraine. *Neurology* 82, 2120–2126. doi: 10.1212/WNL.0000000000000496

Shin, J. H., Kim, Y. K., Kim, H. J., and Kim, J. S. (2014). Altered brain metabolism in vestibular migraine: comparison of interictal and ictal findings. *Cephalalgia* 34, 58–67. doi: 10.1177/0333102413498940

Staab, J. P., Eckhardt-Henn, A., Horii, A., Jacob, R., Strupp, M., Brandt, T., et al. (2017). Diagnostic criteria for persistent postural-perceptual dizziness (PPPD): consensus document of the committee for the classification of vestibular disorders of the barany society. *J. Vestib. Res.* 27, 191–208. doi: 10.3233/VES-170622

Teggi, R., Colombo, B., Albera, R., Asprella Libonati, G., Balzanelli, C., Batuecas Caletrio, A., et al. (2018). Clinical features of headache in patients with diagnosis of definite vestibular migraine: the VM-Phenotypes projects. *Front. Neurol.* 9:395. doi: 10.3389/fneur.2018.00395

Van Ombergen, A., Van Rompaey, V., Van de Heyning, P., and Wuyts, F. (2015). Vestibular migraine in an otolaryngology clinic: prevalence, associated symptoms, and prophylactic medication effectiveness. *Otol. Neurotol.* 36, 133–138. doi: 10.1097/MAO.0000000000000596

Vetvik, K. G., and MacGregor, E. A. (2017). Sex differences in the epidemiology, clinical features, and pathophysiology of migraine. *Lancet Neurol.* 16, 76–87. doi: 10.1016/S1474-4422(16)30293-9

von Brevern, M., and Lempert, T. (2016). Vestibular migraine. *Handb. Clin. Neurol.* 137, 301–316. doi: 10.1016/B978-0-444-63437-5.00022-4

Vukovic, V., Plavec, D., Galinovic, I., Lovrencic-Huzjan, A., Budisic, M., and Demarin, V. (2007). Prevalence of vertigo, dizziness, and migrainous vertigo in patients with migraine. *Headache* 47, 1427–1435. doi: 10.1111/j.1526-4610.2007.00939.x

Vuralli, D., Yildirim, F., Akcali, D. T., Ilhan, M. N., Goksu, N., and Bolay, H. (2018). Visual and postural motion-evoked dizziness symptoms are predominant in vestibular migraine patients. *Pain. Med.* 19, 178–183. doi: 10.1093/pm/pnx182

Wang, J., and Lewis, R. F. (2016). Contribution of intravestibular sensory conflict to motion sickness and dizziness in migraine disorders. *J. Neurophysiol.* 116, 1586–1591. doi: 10.1152/jn.00345.2016

Wu, J., Liu, C., Yu, H., Li, H., Jia, Y., Zhang, D., et al. (2019). Clinical characteristics of sleep disorders in patients with vestibular migraine. *Sleep Breath* doi: 10.1007/s11325-019-01994-1

Zhang, Y., Kong, Q., Chen, J., Li, L., Wang, D., and Zhou, J. (2016). International classification of headache disorders 3rd edition beta-based field testing of vestibular migraine in China: demographic, clinical characteristics, audiometric findings and diagnosis statues. *Cephalalgia* 36, 240–248. doi: 10.1177/0333102415587704

Conflict of Interest: The authors declare that the research was conducted in the absence of any commercial or financial relationships that could be construed as a potential conflict of interest.

frontiers in Neuroscience

ORIGINAL RESEARCH
published: 15 April 2020
doi: 10.3389/fnins.2020.00317

Numerical Evaluation of the Influence of Skull Heterogeneity on Transcranial Ultrasonic Focusing

*Chen Jiang[1], Dan Li[1], Feng Xu[1], Ying Li[1], Chengcheng Liu[2] and Dean Ta[1,3,4]**

[1] Department of Electronic Engineering, Fudan University, Shanghai, China, [2] Institute of Acoustics, Tongji University, Shanghai, China, [3] State Key Laboratory of ASIC and System, School of Microelectronics, Fudan University, Shanghai, China, [4] Key Laboratory of Medical Imaging Computing and Computer Assisted Intervention (MICCAI) of Shanghai, Shanghai, China

In transcranial penetration, ultrasound undergoes refraction, diffraction, multi-reflection, and mode conversion. These factors lead to phase aberration and waveform distortion, which impede the realization of transcranial ultrasonic imaging and therapy. Ray tracing has been used to correct the phase aberration and is computationally more efficient than traditional full-wave simulation. However, when ray tracing has been used for transcranial investigation, it has generally been on the premise that the skull medium is homogeneous. To find suitable homogeneity that balances computational speed and accuracy, the present work investigates how the focus deviates after phase-aberration compensation with ray tracing using time-reversal theory. The waveforms are synthetized with ray tracing for phase aberration, by which the properties of the skull bone are simplified for refraction calculation as those of either (i) the cortical bone or (ii) the mean of the entire skull bone, and the focusing accuracy is evaluated for each hypothesis. The propagation of ultrasound for transcranial focusing is simulated with the elastic model using the k-space pseudospectral method. Unlike the fluid model, the elastic model does not omit shear waves in the skull bones, and the influence of that omission is investigated, with the fluid model resulting in a focal deflection of 0.5 mm. The focusing deviations are huge when the properties of the skull bone are idealized with ray tracing as those of the mean of the entire skull bone. The focusing accuracy improves when the properties of the skull bone are idealized as those of the cortical bone. The results reveal minimal deviation (8.6, 3.9, and 3.2% in the three Cartesian coordinates) in the focal region and suggest that transcranial focusing deflections are caused mostly by ultrasonic refraction on the surface of the skull bone. A heterogeneous skull bone causes wave bending but minimal focusing deflection. The proposed simplification of a homogeneous skull bone is more accurate for transcranial ultrasonic path estimation and offers promising applications in transcranial ultrasonic focusing and imaging.

Keywords: transcranial focusing, k-space pseudospectral method, ray tracing, time-reversal theory, skull heterogeneity

OPEN ACCESS

Edited by:
Yizhang Jiang,
Jiangnan University, China

Reviewed by:
Jing Xue,
Wuxi People's Hospital Affiliated to Nanjing Medical University, China
Yuanpeng Zhang,
Nantong University, China

***Correspondence:**
Dean Ta
tda@fudan.edu.cn

Specialty section:
This article was submitted to Neuroprosthetics, a section of the journal Frontiers in Neuroscience

Received: *18 January 2020*
Accepted: *17 March 2020*
Published: *15 April 2020*

Citation:
Jiang C, Li D, Xu F, Li Y, Liu C and Ta D (2020) Numerical Evaluation of the Influence of Skull Heterogeneity on Transcranial Ultrasonic Focusing. Front. Neurosci. 14:317. doi: 10.3389/fnins.2020.00317

INTRODUCTION

The transmission of ultrasound through the human cranial bone is very important for non-invasive transcranial acoustic imaging (Errico et al., 2016; Jordan et al., 2017), therapeutic applications such as the ablation of brain tumors (Pernot et al., 2007; Colen and Jolesz, 2010; Mcdannold et al., 2010; Damianou, 2019), and mechanical brain thrombosis ablation angioplasty (Behrens et al., 2001; Liu et al., 2014; Lee et al., 2016; Levinsky et al., 2016). Recently, transcranial ultrasound becomes an alternative approach for neuromodulation techniques, as ultrasound can non-invasively transmit to deep targeted brain circuits (Darrow, 2019; Li et al., 2019). The focusing capability of transcranial ultrasound determines the region and volume of neuron stimulation in deep brain (Tyler, 2011; Ibsen et al., 2015). In addition, it shows capability to detect mental activity based on transcranial acoustic images and functional images (Myrden et al., 2011).

The above applications suggest that transcranial ultrasound can be a promising modality for brain computer interface (BCI) systems. However, the irregular geometrical shape and complicated composition of the cranial bones lead to inevitable distortions in ultrasonic waves, such as propagation-path deflection and phase aberration (Pernot et al., 2003; Kyriakou et al., 2013). Therefore, phase-aberration correction is an important aspect of transcranial ultrasound focusing and imaging.

Over the years, researchers have presented diverse models for studying transcranial ultrasound. For instance, the skull has been idealized as a spherical shell, thereby making it easier to calculate the acoustic speed and thickness in the skull (Hatakeyama et al., 2002). The skull has also been idealized as a shell with non-parallel boundaries, thereby facilitating investigation of the transmission of shear waves in the skull bones by using spectral decomposition (Clement et al., 2004). By considering the irregular surfaces and complex inner structure of the skull, full-wave simulation guided by magnetic resonance imaging and computed tomography (CT) is close to reality (Hayner and Hynynen, 2001; Connor et al., 2002). Different types of full-wave simulation have been used for transcranial ultrasound. The finite-difference time-domain (FDTD) method, which is a conventional full-wave simulation method (Yılmaz and Çiftçi, 2013), has been used to estimate the velocity of longitudinal and shear waves in the human skull (Hughes and Hynynen, 2017). The Fourier pseudospectral time-domain method, utilizing fast Fourier transform to solve acoustic equations, tends to be more efficient in solving large-scale problems (Liu, 1998; Muñoz and Hornikx, 2017). The *k*-space method, which is accurate for weak scattering media, has also been applied in transcranial studies (Mast et al., 2001; Robertson et al., 2017).

However, three-dimensional acoustic full-wave simulations are limited by excessive time consumption and memory requirements (Pichardo et al., 2017). Recently, ray tracing (RT) has been implemented in long-bone structure imaging (Renaud et al., 2018) and phase compensation for B-mode image reconstruction (Szostek and Piórkowski, 2016). It shows potential for wave-path prediction and phase-aberration compensation for transcranial ultrasonic focusing. Commonly used in vision graphics and seismic tomography (Wei et al., 2014), RT is more efficient and requires less computational capability than full-wave simulation. However, the spatially varying porosity of the skull limits the use of RT because the acoustic properties differ spatially even in one ultrasound wavelength, which is beyond the ray regime. Consequently, the skull is generally idealized as being either homogenous or less heterogeneous to satisfy the RT requirements (Jin et al., 2008; Wang and Jing, 2013; Vassilevski et al., 2016). In previous papers, several transcranial ultrasound models have treated the skull as a homogenous medium, for which the ultrasound speed was simplified as the average of the entire skull (Jin et al., 2008; Renaud et al., 2018). However, the validity of that simplification is yet to be discussed.

In the present study, to satisfy the RT requirements, the porosity of the skull bone is simplified and the heterogeneous skull bone is regarded as being homogenous. In turn, for refraction calculation with Snell's law (SL), the homogeneous properties of the skull bone are simplified as those of either (i) the cortical portion of the skull or (ii) the mean of the entire skull. For each simplification, the transcranial focusing deflections are evaluated and compared with those obtained using the time-reversal method. The paper is organized as follows: in methods section, RT method, *k*-space pseudospectral based full wave-simulation and time-reversal theory are introduced. Then, the numerical implement is introduced, including CT-based heterogeneous assumption of skull bone, homogeneous assumption in RT and simulation setup. In the simulation setup, focusing deflections caused by (i) the shear wave neglection after phase correction, (ii) the presence of skull with conventional focusing algorithm and (iii) homogeneity assumption in RT are investigated. In the discussion section, the focusing deflections of the simulations are given and corresponding discussion is presented. The present investigation of transcranial focusing deflection with RT should (i) improve the understanding of directional wave deflection for ultrasound transmission and (ii) help in choosing optimal acoustic properties to reduce wave-path estimation errors. The present results have meaning for fast and accurate transcranial phase-aberration calculation with RT.

MATERIALS AND METHODS

Ray Tracing for Transcranial Ultrasound

There are two ways to implement RT numerically. The gridded-velocity model, which is based on the Fourier plane-wave assumption, details the velocity field in two or three dimensions; the ray trajectories are then found by solving the geometrical spreading equation $\frac{A}{2}\nabla^2 A - \nabla A \nabla T = 0$, where A and T are the amplitude and the travel time functions, respectively, both of which vary with position (Kendall and Thomson, 1989). The alternative model, which assumes multiple layers, specifies the geometrical boundary between different velocity layers and implements SL calculations at the boundary (Waltham, 1988;

Clement and Hynynen, 2003). The gridded-velocity model is the simpler of the two models because the RT calculation is reduced to the geometrical spreading equation that incorporates SL; however, computer memory consumption and computational inefficiency impede its use for three-dimensional simulation. The second approach requires complex geometrical calculations for the detailed boundary confirmation and is suitable only in cases of relatively few layers. In the present work, the skull bone is idealized as an isotropic homogenous medium for RT, and a three-layer model is solved by using the latter method for transcranial ultrasonic transmission.

Transmission Coefficient

When the spherical wave generated by a point source refracts at a liquid–solid boundary, the ultrasound energy decreases and the amplitude of the velocity potential decreases to approximately (Teng and Zhang, 1997).

$$Q_2 = (Q_{ref} l_{ref}/l_1) T_r l_2'/(l_2' + l_{2r}). \quad (1)$$

Here, we have $l_2' = l_1 \sin\alpha\cos^2\beta/(\sin\beta\cos^2\alpha)$, where l_1 and l_{2r} are the lengths of the incoming and refracted rays, respectively, α and β are the incoming and refracted angles, respectively, Q_{ref} is the velocity potential reference, and l_{ref} is the corresponding distance between the reference and the source. As shown in the **Appendix**, T_r is the plane-wave transmission coefficient. For the three-layer model, the amplitude of the velocity potential decreases approximately as

$$Q_p = Q_2' T l_3'/(l_3' + l_3). \quad (2)$$

Here, we have $l_{2t} = l_2 + l_2'$ and $l_3' = l_{2t}\sin\alpha'\cos^2\beta'/(\sin\beta'\cos^2\alpha')$, where α' and β' are the incoming and refracted angles, respectively, on the second layer, l_2 is the ray length between the two layers, l_3 is the refracted ray length on the second layer, and Q_2' is the velocity potential of the incoming ray at the second intersection.

Phase Calculation and Waveform Synthesis

Based on the ray shooting method of RT theory, the optimal refraction positions on the two layers can be acquired and the corresponding travel time can be calculated as $t = \sum_{i=1}^{3}(l_i/c_i)$, where c_i is the wave speed in layer i. The frequency deviation caused by the acoustic attenuation can be calculated in the frequency domain. The distorted waveform and the amplitude of the velocity potential can thus be predicted as $P(t) = \mathcal{F}^{-1}\{\mathcal{F}\left(P_{ref}(t)\right) A(\omega)\}$, where $\mathcal{F}$ and $\mathcal{F}^{-1}$ are the forward and inverse Fourier transforms, respectively, and $A(\omega)$ is the frequency-dependent attenuation coefficient. The ultrasound amplitude after refraction can be acquired with the transmission coefficient as shown in the section entitled "Transmission coefficient." The multi-reflection at the middle layer can be neglected when the attenuation there is high compared with those at the adjacent layers. The first transmissive waves are considered with the RT method. Because longitudinal and shear waves exist in the middle layer, two rays are derived separately and combined to synthesize the final waveform.

Full-Wave Simulation

As the theoretical model of ultrasonic propagation, we choose the Kelvin–Voigt elastic wave equation, which includes basic elastic properties such as density, Lamé constants, and attenuation. The corresponding time-domain numerical solutions are acquired using the *k*-space pseudospectral method. In a previous study, various *k*-space algorithms were applied for acoustic wave simulation. The simplest version, which is based on the second-order wave equation, applies to isotropic and homogeneous or weakly homogeneous media (Mast et al., 2001). The second version, which is based on coupled first-order equations, suits sharper-varying materials and requires additional memory to store the displacement vector or the velocity vector (Tabei et al., 2002). Compared with the FDTD method, the second version is more efficient because it requires fewer grid points for the same simulation accuracy. For instance, it is perfectly accurate for homogenous media, even with the two grid points per wavelength that are used in the second version of the *k*-space algorithm, whereas at least six grid points per wavelength are required with the FDTD method (Liu, 1998). The *k*-space pseudospectral algorithm, which is a combination of the two versions, is suitable for large-scale wave simulation because it saves memory and increases computing speed by requiring fewer grids.

Kelvin–Voigt Model

In the linear acoustic regime, coupled first-order equations determine the wave propagation in a viscoelastic medium. In temporal differential form, the coupled equations are given as (Carcione et al., 2004).

$$\begin{aligned}
&\sigma_{ij}(r, t+\Delta t) \\
&= \Delta t\Bigg\{\lambda(r)\,\delta_{ij}\sum_{k=1}^{3}\frac{\partial v_i(r,t)}{\partial x_i} + \mu(r)\left(\frac{\partial v_i(r,t)}{\partial x_j} + \frac{\partial v_j(r,t)}{\partial x_i}\right) \\
&\quad + \lambda'(r)\,\delta_{ij}\sum_{k=1}^{3}\frac{\partial^2 v_i(r,t)}{\partial x_i \partial t} \\
&\quad + \mu'(r)\left(\frac{\partial^2 v_i(r,t)}{\partial x_j \partial t} + \frac{\partial^2 v_j(r,t)}{\partial x_i \partial t}\right)\Bigg\}\sigma_{ij}(r,t), \\
&\qquad\qquad i,j = 1,2,3, \quad (3)
\end{aligned}$$

$$\begin{aligned}
v_i(r, t+\Delta t) &= \frac{\Delta t}{\rho(r)}\left(\sum_{j=1}^{3}\frac{\partial \sigma_{ij}(r,t)}{\partial x_j} + f(r,t)\right) \\
&\quad + v_i(r,t), \quad i = 1,2,3, \quad (4)
\end{aligned}$$

where σ_{ij} and v_i are the stress and velocity vectors, respectively, f is the external stress, $\delta_{ij} = \begin{cases} 1 & i = j \\ 0 & i \neq j \end{cases}$ is the delta function, and x_i and x_j are spatial directions as $x = \{x_1, x_2, x_3\}$ in Cartesian coordinates. Moreover, $\rho(r)$ is the density, $\lambda(r)$ and $\mu(r)$ are the first and second Lamé constants, respectively, $\lambda'(r)$ and $\mu'(r)$ are the

attenuation coefficients, and Δt is the temporal differential step. Note that the second-order derivation in Eq. 3 can be simplified to

$$\frac{\partial^2 v_i(r,t)}{\partial x_j \partial t} = \partial\left(\frac{\partial v_i(r,t)}{\partial t}\right)/\partial x_j = \partial\left\{\frac{1}{\rho(r)}\left(\sum_{j=1}^{3}\frac{\partial \sigma_{ij}(r,t)}{\partial x_j}\right)+f(r,t)\right\}/\partial x_j, \quad i,j=1,2,3. \quad (5)$$

K-Space Pseudospectral Method

The first-order derivation of variables (σ or v) can be obtained by using the *forward* and inverse Fourier transforms of the variables

$$\frac{\partial(\cdot)}{\partial x_i} = \mathcal{F}^{-1}\left\{ik_i \mathrm{sinc}\left(c_m k \Delta t/2\right)\mathcal{F}(\cdot)\right\}, \quad (6)$$

where c_m is the maximum wave velocity and $\mathcal{F}$ and $\mathcal{F}^{-1}$ are the three-dimensional forward and inverse spatial Fourier transforms, respectively. The operator ik_i is generated from the conventional pseudospectral method. The scalar Green's function operator $\mathrm{sinc}\left(c_m k \Delta t/2\right)$ is derived from the dyadic Green's function solution of the second-order elastic wave equation (Liu, 1998). This is an improvement from the pseudospectral method. The elastic wave equations are divided into compressional and shear wave components. The compressional stress matrix σ_{ij}^{p} and the shear stress matrix σ_{ij}^{s} are calculated independently in Eq.3, while the total stress σ_{ij} in Eq. 4 is the sum of σ_{ij}^{p} and σ_{ij}^{s}. Although staggered grids are not necessary in this method, they are used to improve the stability and efficiency (Firouzi et al., 2012).

When the shear modulus matrix μ is set to zero, the coupled viscoelastic first-order equations degenerate into the acoustic wave equations for a fluid medium. Under that hypothesis, the stress vector σ in the elastic equations is equivalent to the sound pressure p in the fluid medium. During transcranial ultrasonic propagation, the stress vector σ and the sound pressure p are continuous at the boundary between solid and liquid, whereas the velocities are continuous at the boundary. Therefore, the viscoelastic model is applicable for simulating ultrasound transcranial transmission.

Time-Reversal Theory

For conventional ultrasonic focusing with a phased-array probe, the phase aberrations are based on the assumption of constant sound velocity in soft tissue. However, the wave velocity difference between soft tissue and bone impedes its application in transcranial focusing. Phase correction with time-reversal theory is a valid way to compensate for the distortion that is caused by the skull. Time-reversal theory, which is based on the reciprocity principle, takes advantage of the invariance of the wave equation and assumes that forward and backward ultrasonic propagation have the same time–frequency response. Ultrasound from a virtual or real source that is located at the desired focal point should be recorded by each channel of the phased array (**Figure 1**). The time-reversed wave that propagates backward to the source will focus optimally on the source (Thomas and Fink, 1996). For conventional time-reversal theory, when the source transmits a pulsed signal, the receivers must record all of the temporal waveforms. The signals are time-reversed and transmitted backward to the source to guarantee the optimal pulse waveform at the focal point. However, transmitting ultrasonic signals with the source deep inside the skull *in vivo* tends to be difficult, especially for clinical trials. An alternative option is to use geometrical information about the skull bone to estimate the waveforms with a virtual source (VS) transmitting a signal inside the skull. For the RT method in the present work, diffraction and multilayer reflections are neglected. Diffractions are omitted because diffraction is weak with the assumption that microstructure (trabecular bone) is not considered and thickness of bone is significantly larger than wavelength. Multilayer reflections are omitted because the energy of reflected waves is neglectable compared with that of the wavefront as a result of attenuation in bone and reflectional energy loss at the tissue-bone boundary. The longitudinal–longitudinal–longitudinal and longitudinal–shear–longitudinal transmission modes are calculated separately and then combined as the signal received by the phased array, while the remaining temporal waveforms are set to zero.

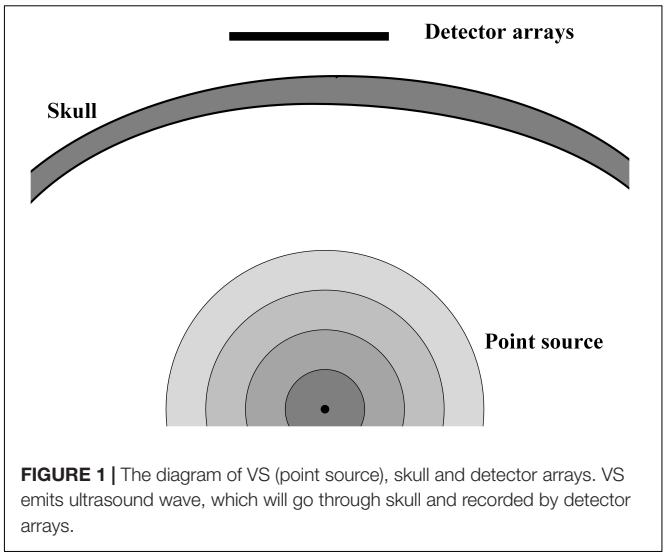

FIGURE 1 | The diagram of VS (point source), skull and detector arrays. VS emits ultrasound wave, which will go through skull and recorded by detector arrays.

NUMERICAL IMPLEMENT

CT-Based Heterogeneous Plastic Material Properties for *k*-Space Pseudospectral Full-Wave Simulation

In transcranial ultrasonic investigations, the assumption that the skull's elastic properties vary along with Hounsfield unit in CT-images has been verified experimentally for transcranial focusing (Top et al., 2016; Pichardo et al., 2017). Under that hypothesis, the elastic properties of the computational region, such as density,

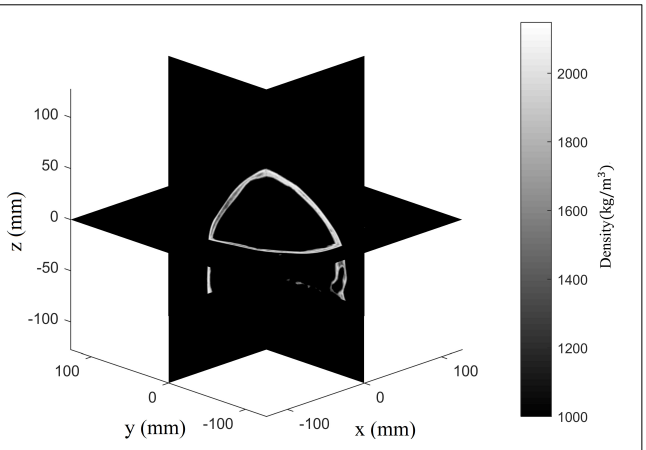

FIGURE 2 | Density distribution of skull and degassed water in vertically spaced slice mode.

wave velocity, and attenuation, can be acquired with the following equations (Pichardo et al., 2011, 2017; Top et al., 2016):

$$\begin{aligned} \psi &= 1 - \frac{Hu}{Hu_w}, \\ \rho &= \rho_{min}\psi + \rho_{max}\left(1-\psi\right), \\ c_L &= c_w\psi + c_b\left(1-\psi\right), \\ \lambda' &= \lambda'_{min} + \left(\lambda'_{max} - \lambda'_{min}\right) \times \psi^{\beta}, \end{aligned} \tag{7}$$

where Hu is the Hounsfield unit, Hu_w represents the Hounsfield windowing of CT data, ψ is the porosity matrix, which is relevant to the bone trabecular density, and ρ is the density matrix, with $\rho_{min} = 1000\text{kg/m}^3$ as the density of water and $\rho_{max} = 2100\text{kg/m}^3$ as the maximum density of the skull. The density distribution can be acquired for the entire computational region (**Figure 2**). In addition, c_L is the longitudinal wave speed matrix, with $c_w = 1500\text{m/s}$ as the sound speed in water and $c_b = 2900\text{m/s}$ as the maximum longitudinal wave speed in the skull. The shear wave speed is approximated as $c_s = 7c_l/11$ in the skull (Pichardo et al., 2017). The term λ' is the frequency-dependent longitudinal wave attenuation matrix, with $\lambda'_{min} = 12\text{Npm}^{-1}$ as the minimum attenuation coefficient and $\lambda'_{max} = 460\text{Npm}^{-1}$ as the maximum attenuation coefficient (Pichardo et al., 2011). The shear wave attenuation matrix is set to $20\lambda'/19$ (Top et al., 2016), with $\beta = 0.5$.

Homogeneous Models for Ray Tracing

In the idealization of using conventional homogeneous elastic properties for transcranial focusing and imaging, a uniform velocity has been treated as being the average for the entire skull, whereas the focusing accuracy remains to be evaluated (Tretbar et al., 2009). However, we consider the velocity in the cortical bone as being superior to an average velocity, this being because the cortical bone covers the skull and refraction occurs at the boundary. We investigate the accuracy of the two idealizations. For the first case, the constant ultrasonic longitudinal velocity in the skull layer is taken as $c_{al} = 2358\text{m/s}$ and shear velocity is taken as $c_{as} = 1500\text{m/s}$, which is the average velocity of the skull. The constant density is taken as the average value, namely $\rho = 1656\text{kg/m}^3$. For the second case, the velocity on the surface of the skull layer is taken to be that in the cortical bone, namely $c_{cl} = 2900\text{m/s}$ and shear velocity is taken as $c_{cs} = 1845\text{m/s}$. The density is taken as being the maximum density, namely $\rho = 2100\text{kg/m}^3$, which is used for the SL-based refraction calculation. The internal skull velocity is taken as being the average value on the ray paths, namely $c = 2358\text{m/s}$, which influences the travel time in the skull layer.

Simulation Setup

Because the acoustic properties of soft tissue, such as the scalp, cerebral spinal fluid, and intracranial soft tissues, are comparable with those of water, all the soft tissues are treated as water. An *in vitro* skull is assumed to be immersed in degassed water to avoid the adverse effects of bubbles, such as acoustic scattering, energy attenuation, and non-linearity. The pixel interval for the whole computational region is interpolated to be 0.5 mm to meet the minimum demand of full-wave simulation, that the mesh size (pixel interval) is approximately one-fourth the wavelength λ = 1.93 mm in water. The corresponding grid size is $512 \times 512 \times 512$, with the skull placed in the central region. With a central frequency of 0.8 MHz and an active element spacing of 10 mm for transcranial focusing, the planar phased array is located 5 mm above the upper surface of the skull and comprises 10×10 elements. Although the relatively large element spacing leads to grating lobes, it does not interfere with the main lobe, which is the present emphasis. The default VS is located at the center of the grid of the computation region, which is also the origin of the rectangular coordinate system. In addition, the axial line of the entire computation region, namely the z axis of the rectangular coordinate system, runs perpendicularly through the middle of the planar phased array. However, we do not consider the size and direction sensitivity of each element or the bandwidth of the phase array (Hu et al., 1988).

The k-space pseudospectral method based on the elastic model tends to be superior to the conventional fluid model because neglecting shear waves in the latter influences the transcranial ultrasonic focusing position and intensity even when the incoming incident wave does not exceed the critical angle for shear-wave omission. The transcranial propagations in this section are calculated with the CT-based heterogeneous-medium assumption, and simulations are implemented to evaluate the impact of neglecting shear waves. In the first case, longitudinal and shear waves in the skull are considered both for the VS to array receiver (VS2AR) process and the array receiver to VS (AR2VS) process. In the second case, longitudinal and shear waves in the skull are considered for the VS2AR process, whereas the shear waves are neglected for the AR2VS process. The neglecting of shear waves is discussed in this section only; in all other sections, longitudinal and shear waves are considered by default for wave-propagation simulations. Note also that in all other sections, transcranial propagation is calculated with the heterogeneous-medium assumption using the elastic model based on the k-space pseudospectral method for the AR2VS process.

Focusing zone deflection of transcranial ultrasound has been investigated with spherically focusing phased array (Hughes and Hynynen, 2017). However, deflection with planar phase array remains to be investigated. Thus, simulations are implemented to evaluate the tremendous impact on focusing zone of skull-induced distortion. Firstly, temporal waveforms are derived with the conventional focusing algorithm without considering the skull's presence for the VS2AR process. The waveforms are time-reversed and transmitted backward toward the VS. Secondly, the skull is not considered for the AR2VS process in the first case but is located between the transducer array and the VS in the complementary case.

In order to evaluate the influence of middle layer (cancellous bone) on focusing zone deflection. Simulations were implemented where temporal waveforms are derived with different homogenous idealizations by using the RT method for the VS2AR process. Re-focusing the deviations with the two homogenous idealizations, the mean velocity value of the entire skull and of the cortical bone are evaluated separately, as mentioned previously. The purpose is to investigate the optimal choice for efficient and accurate RT-based transcranial focusing. Groups of simulations are implemented with VSs other than the default one. The focusing deviations, whose temporal waveforms are calculated by using RT when the homogenous properties of the skull are idealized as those of the cortical bone for the AR2VS process, are measured and compared with those of the conventional time-reversal method. When the temporal waveforms are derived with RT, the time-reversed signal that is emitted from each array element is normalized according to the channel with the highest intensity. The waveform is also set as that for the channel with the highest intensity. This normalization makes sense because the present concern is the focusing deviation, not the power.

RESULTS

Accuracy and Calculation Efficiency

The *k*-space pseudospectral method, the pseudospectral method, and the FDTD method are compared to evaluate the accuracy of the full-wave simulation. The waveform with the *k*-space pseudospectral method ($\lambda = 4\Delta x, u_{max}\Delta t/\Delta x = 0.1$) has a phase-error ratio of 0.7% compared with that with the FDTD method ($\lambda = 16\Delta x, u_{max}\Delta t/\Delta x = 0.015$), where λ is the wavelength, Δx is the grid width, Δt is the time interval. Phase-error ratio is represented by $\Delta\varphi/2\pi \times 100\%$, where $\Delta\varphi$ is the phase difference. The waveform with the pseudospectral method has a phase-error ratio of 7.3% compared with that with the FDTD method under the same setting. The *k*-space pseudospectral method is suitable for the present simulation as it has better accuracy under the same sparse spatial and temporal grids compared with the pseudospectral method. After refraction at the liquid–solid boundary, the waveforms of the acoustic velocity are calculated using RT and the *k*-space pseudospectral method separately (**Figure 3**). The results confirm the feasibility of RT with an amplitude error $\left(\frac{A}{A_{FDTD}} - 1\right) \times 100\%$ of 5.35% and a phase-error ratio of 1.2%, where A is the amplitude with *k*-space pseudospectral method or with pseudospectral method and A_{FDTD} is the reference amplitude with FDTD. The computational time is reduced from 23 h 35 min 13 s with the *k*-space pseudospectral method to 37 min 24 s with RT (Intel® Xeon® E7-4830 v4; MATLAB 2017; 12 cores for parallel computation).

Focusing Deviation Caused by Omission of Shear Waves

The angles between the incident incoming waves from the array elements to the VS and skull surfaces are less than 20°, which meets the demand of shear-wave omission. The acoustic pressure

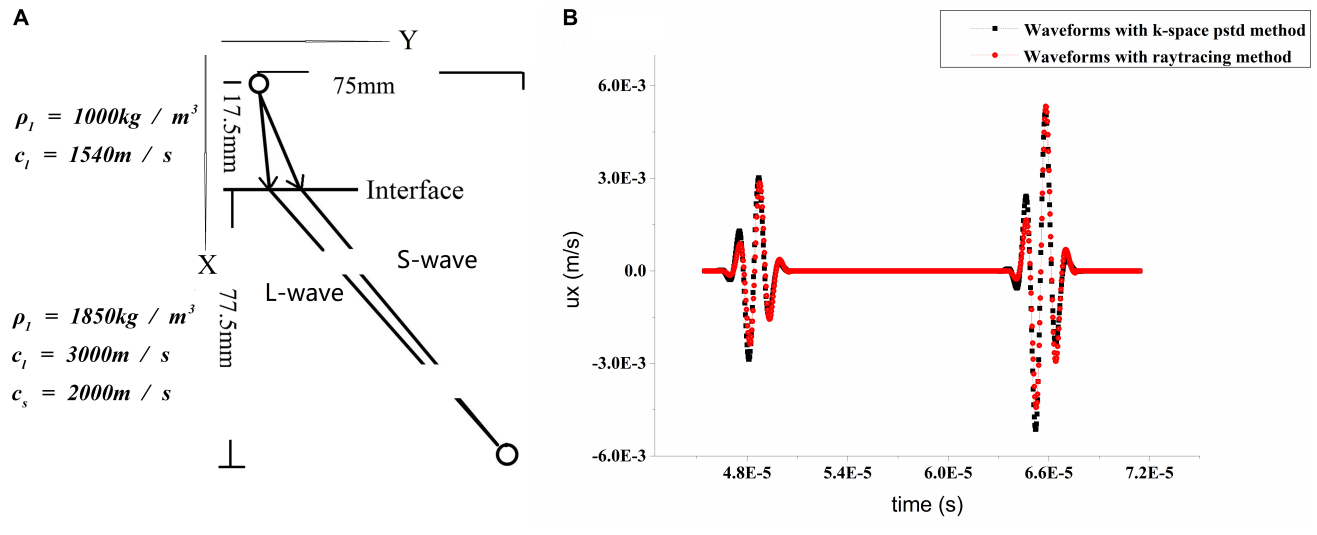

FIGURE 3 | (A) Diagram of ultrasonic refraction at liquid–solid boundary. **(B)** Corresponding waveforms of velocity in *x* direction with *k*-space pseudospectral method (black) and ray tracing (RT) (red). The first pulse is caused by a longitudinal wave and the second pulse is caused by a shear wave.

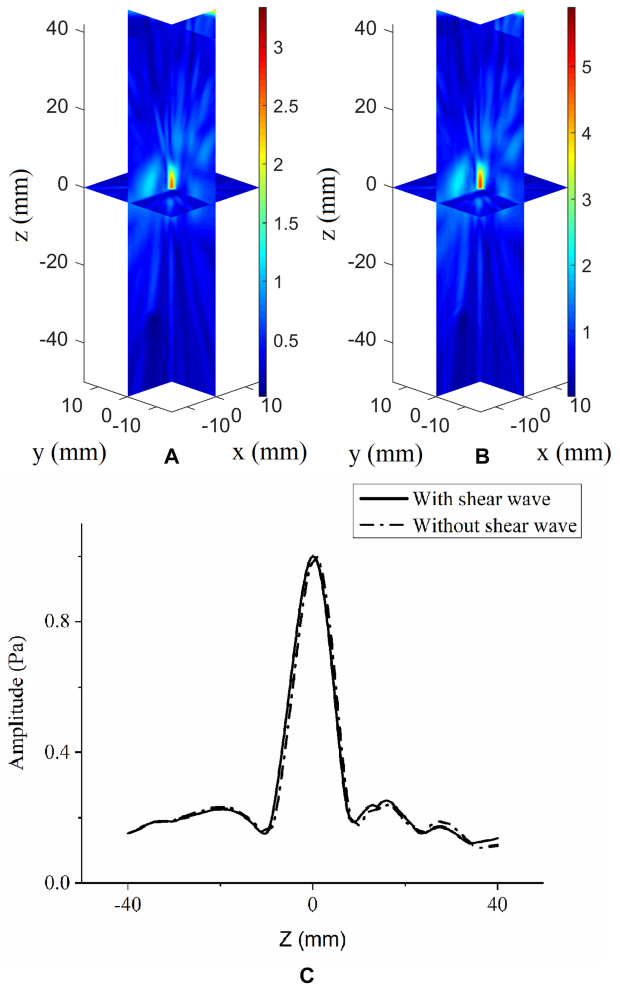

FIGURE 4 | Three-dimensional pressure distributions using conventional time-reversal method considering **(A)** and without considering **(B)** the shear wave for the virtual source to array receiver (VS2AR) process. **(C)** The corresponding normalized pressure distribution in the axial direction.

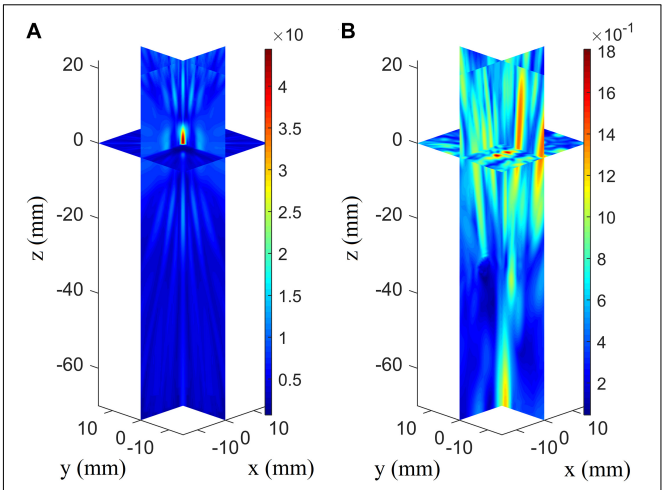

FIGURE 5 | Three-dimensional pressure distributions using conventional focusing algorithm without the skull's presence **(A)** and with the skull's presence for the array receiver to virtual source (AR2VS) process **(B)**.

distributions are illustrated in vertically spaced slice mode, and the deviations in focal position are small compared with the large ultrasonic field space when shear waves are considered (**Figure 4A**) and when they are not (**Figure 4B**). The maximum pressure in the focusing area when shear waves are considered is approximately 3.65 Pa, while that when shear waves are not considered is approximately 4.85 Pa. The normalized pressure distributions in the axial direction are illustrated for better distinction (**Figure 4C**); they reveal an overall distortion of 0.5 mm beyond the VS when shear waves are not considered and perfection at the VS when shear waves are considered.

Presence of Skull-Induced Focusing Error With Conventional Phased Array Focusing

When evaluating the tremendous impact of skull-induced distortion, the focusing deviations are illustrated better by showing them with their coordinates moving up in the axial direction (**Figure 5**). The phased array achieves optimal focusing using the conventional phased-array focusing algorithm without the presence of the skull, while the focusing position with the presence of the skull shows deflections of 79.0 mm in the axial direction and 3.5 mm in the focal plane. For conventional focusing without the skull, the maximum pressure in the focusing area is approximately 46.5 Pa, whereas that with the skull is approximately 1.95 Pa. The pressure in the focusing area is low because the ultrasound transmitted from phased array are normalized according to the maximum. The phenomenon of focusing-area elongation compared with the ideal focusing zone is attributed to the acoustic field of the phased array, which elongates the main lobe with increasing focusing depth. Note that the attenuation disparity leads to the difference in pressure amplitude between the two cases.

Focusing Deviation After Phase-Aberration Correction With Ray Tracing

When the temporal waveforms are derived with RT under the assumption that the homogenous properties of the skull are simplified as those of the cortical bone for refraction calculation, the focusing distribution reveals deflections of 0.5 mm in the axial direction and 0.5 mm in the focal plane compared with the VS (**Figure 6A**). By contrast, the focusing distribution reveals deflections of 9.5 mm in the axial direction and 1.5 mm in the focal plane when the homogenous properties of the skull layer are simplified as those of the mean of the entire skull (**Figure 6B**). The focusing deflections are evaluated when the homogenous properties of the skull are those of the cortical bone for refraction calculation with RT (**Figure 6A**) and are compared with those of the conventional time-reversal method (**Figure 4A**). The normalized pressures are extracted and reveal a quasi-Gaussian distribution with a main-lobe width of 11 mm

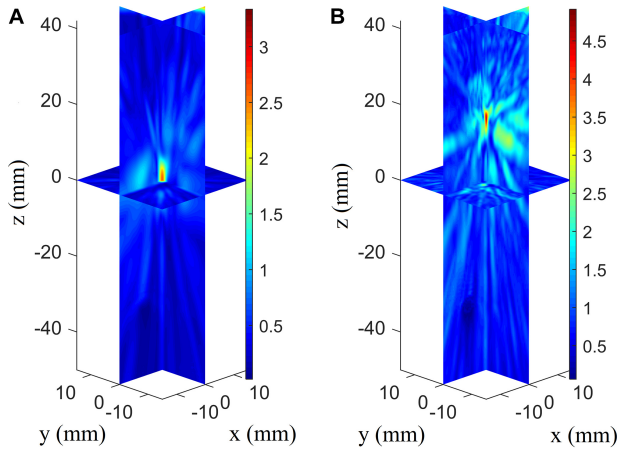

FIGURE 6 | Three-dimensional pressure distributions with temporal waveforms derived using RT when the homogenous properties of the skull are simplified as those of the cortical bone **(A)** and the whole-skull average **(B)** for refraction calculation for the VS2AR process.

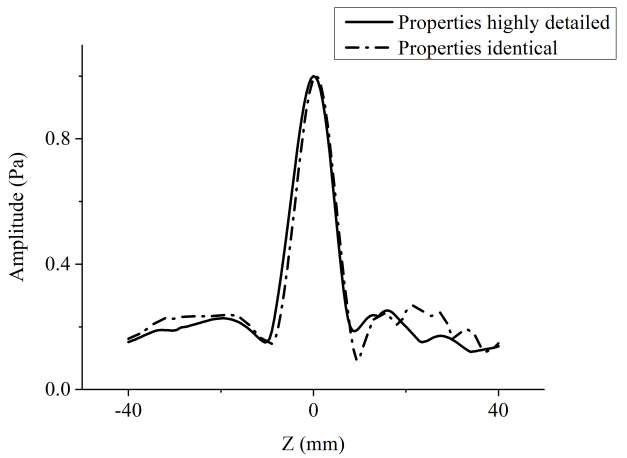

FIGURE 7 | Normalized pressure distribution in axial direction when temporal waveforms are calculated using RT with homogenous properties of the skull idealized as those of the cortical bone for refraction calculation (broken line), and the conventional time-reversal method (solid line) for the VS2AR process.

in the axial direction (**Figure 7**) and a two-dimensional quasi-Gaussian distribution with a main-lobe width of 1.5 mm in the focal plane (**Figure 8**). The focusing deviations, including source position, spatial deviation, main-lobe width, and deviation ratio in each direction, are given in **Table 1** to illustrate the influence of homogeneous idealization using RT. The deviation ratio is the result of dividing the spatial deviation by the main-lobe width.

DISCUSSION

For the AR2VS process, the ultrasonic pressure and focusing position differ slightly depending on whether shear waves are considered. To some extent, the results show that shear waves can be neglected in less-rigorous cases in which the incident wave does not exceed the critical angle for shear-wave omission. However, neglecting the shear waves influences the focusing accuracy and is better when using the elastic model rather than the fluid model. The deviations can be interpreted as the fact that the longitudinal wave in the skull plays a major role as that of the small incident wave, and a small portion of ultrasound energy in fluid medium is transformed into shear waves in solid medium during longitudinal–shear–longitudinal transmission. Different velocities of longitudinal and shear waves in the skull lead to different refractions and wave paths if the longitudinal–shear–longitudinal and longitudinal–longitudinal–longitudinal transmission models are considered separately. In the present work, the focusing position of the longitudinal–shear–longitudinal model happens to be lower than that of the VS, while the focusing position of the longitudinal–longitudinal–longitudinal model is higher than that of the VS. The two focuses are mixed to form the VS. So, the focusing position is a little above the VS if shear wave in bone is not considered. In addition, the maximum amplitude of the focus region with shear waves considered is smaller than that with shear waves neglected, this being because shear waves are attenuated more than are longitudinal waves. It is predictable that this phenomenon should become more obvious as the VS moves closer to the skull, which is equivalent to increasing the angle of the incident wave. The extensive applicability of the elastic model shows its advantages in transcranial investigation, especially for rigorous circumstances. Certain studies have discussed how neglecting shear waves influences transcranial investigations. For example, neglecting the refraction and mode conversion of shear waves in the skull layer for transcranial ultrasonic imaging has led to the images of the absorbers being blurred and dislocated; such phenomena become more evident as the absorbers move closer to the skull both in simulations and in experiments (Jin et al., 2008). Also, the effects of shear-wave propagation in three layer models have been investigated to estimate the compensation of Fourier components in plane-wave representation for image reconstructions using photoacoustic tomography (Schoonover et al., 2012). In conclusion, the elastic model based on the *k*-space pseudospectral method is superior in both computational efficiency and accuracy and is optimized for the transcranial ultrasonic scenario.

The illustrations in **Figure 5** reveal the distinct influence of skull-induced distortion on transcranial focusing. The high attenuation of the skull bone is attributed to the marked difference in the focusing amplitude. In addition, the focusing deviations are large—especially in the axial direction—compared with the results of some studies on transcranial focusing therapy (Kyriakou et al., 2013). That is because focused array transducers are generally used for ultrasonic therapy, and the corresponding distortion was not intense, especially when the VS was not far from its self-focus point (Kyriakou et al., 2013). In ultrasound imaging, using the conventional delay-and-sum reconstruction algorithm for transcranial imaging is expected to give either erroneous or distorted images of brain tissue.

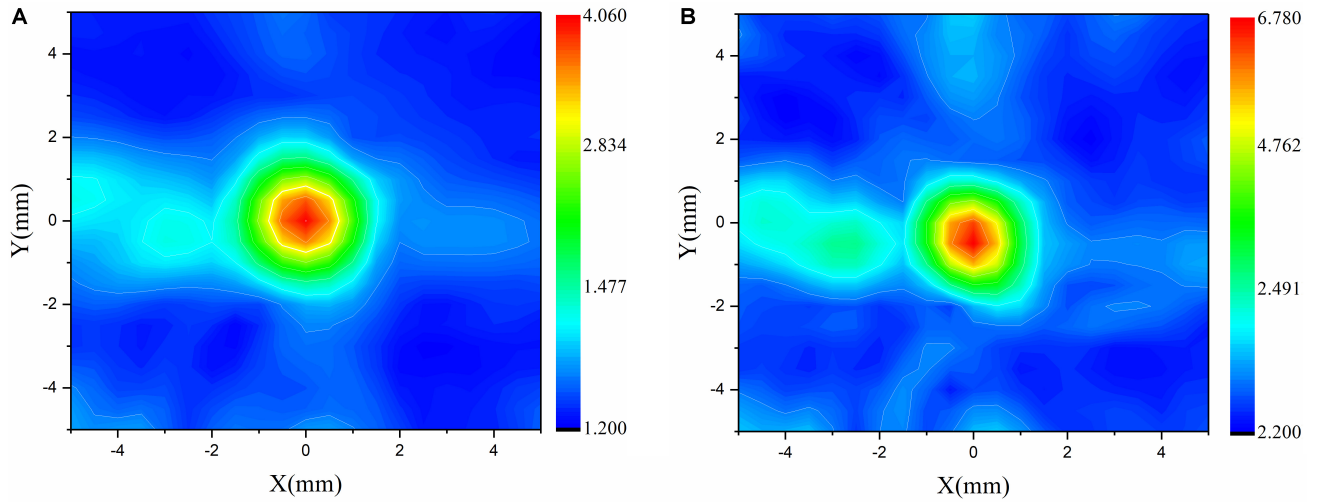

FIGURE 8 | Normalized pressure distribution in focal plane when temporal waveforms are calculated using the conventional time-reversal method **(A)** and RT with the homogenous properties of the skull idealized as those of the cortical bone for refraction calculation **(B)** for the VS2AR process.

Wang and Jing (2013) discussed transcranial imaging with skull aberration, where the positions rising of wire phantom images in the axial direction considering the skull without phase correction is caused by a sound-speed mismatch between skull and tissue. The shape disorder and image deflection in the radial direction are caused by the deflection of the focusing position in the radial plane. There are some unexpected wire phantom artifacts that can be interpreted as the influence of side-focuses (or sidelobes) from skull-induced ultrasonic distortion (**Figure 5B**). The related studies indicate that phase-correction algorithms are required to solve the skull-induced distortion.

Comparing the focusing deviations indicates that the velocity value of cortical bone, instead of the average velocity value, is more suitable for temporal waveform estimation with RT for refraction calculation. The reason is that the skull comprises three layers, namely (i) the upper cortical layer, (ii) the cancellous layer, and (iii) the lower cortical layer. The cortical layer, which is the hardest portion of the skull, is likely to play a decisive role in ultrasonic refraction at the skull–liquid boundary. Cancellous bone, which has a trabecular structure, will not change the ultrasonic propagation path significantly. In this idealization, the fine structure of cancellous bone (heterogenous medium) is simplified as homogenous medium, where refraction-induced ray-path deflections inside the skull are neglected. The focusing deviations indicate that heterogeneity inside the skull has limited influence on the ultrasonic path deflection. The focusing deviation result also supplements the discussion of how the fine structure influences phase aberration, namely that the phase of the ultrasound rarely changes even if the fine structure in the skull is down sampled to half-wavelength resolution (Jing et al., 2012). To investigate the feasibility of the homogenous idealization with RT, deviations with diverse VSs were examined. The focal positions and widths were always integers in multiples of 0.5 mm, as a result of the fixed spatial resolution and the locations. The deviation lengths for different VSs are random and less than 1 mm, revealing average deviation ratios of 8.6% in the *x* direction, 3.9% in the *y* direction, and 3.2% in the *z* direction. The deviation ratios in the focal plane are higher than their counterparts on the axial line because the semi major axis of the ellipsoidal focal area lies in the axial direction. The deviations reveal the reliability of using RT to estimate the temporal waveforms when the skull surfaces are idealized as cortical bone for refraction calculation. The present results contribute to the analysis of unpredictable bending of wave trajectories caused by the trabecular layer and thus provide further insight into major and minor factors of transcranial wave directional deflection, which can be meaningful for fast and accurate phase-aberration correction calculation.

TABLE 1 | Focusing deviations with different VSs (mm).

	Deviation in each direction		
Virtual source	***x***	***Y***	***z***
(0.0, 0.0, 0.0)	(1.0, 4.0, 25)	(0, 4.0, 0)	(0.5, 16.0, 3.0)
(10.0, 0.0, −10.0)	(0.5, 4.0, 12.5)	(0, 4.5, 0)	(0.5, 17.0, 3.0)
(−10.0, 0.0, −10.0)	(0, 3.5, 0)	(0, 4.5, 0)	(0.5, 16.5, 6.7)
(0.0, 0.0, −10.0)	(0, 3.0, 0)	(0, 3.5, 0)	(0.5, 16.5, 3.1)
(10.0, 10.0, 0.0)	(1.0, 3.5, 14.3)	(1.0, 4.0, 12.5)	(0.5, 14.5, 3.5)
(10.0, −10.0, 0.0)	(1.0, 3.5, 14.3)	(1.0, 4.0, 12.5)	(0.5, 14.5, 3.5)

Format of deviations in each direction is as follows: focusing-position deviation (mm), main-lobe width (mm), deviation ratio (%).

CONCLUSION

Transcranial focusing deviations are evaluated when the phase aberrations are corrected with RT. The homogenous properties of the skull are idealized as those of either the cortical bone

or the average of the whole skull. The results reveal that the cortical bone, instead of the average of the whole skull, should be used for homogenous idealization with RT. The deviations also indicate that the heterogeneity inside the skull bone plays a marginal role in transcranial aberration, which can be neglected if precise calculation is not demanded. The transcranial ultrasonic transmission process was implemented with the Kelvin–Voigt viscoelastic model using the *k*-space pseudospectral method, where longitudinal waves, shear waves, and attenuation are all considered. The model shows extensive applicability and accuracy compared to the regularly used fluid model, offering guaranteed reliability of transcranial investigation. The present results could help with estimating wave paths for fast and accurate phase correction using RT, which contribute to application of transcranial ultrasound in brain computer interface systems. Our future work will focus on the *in vivo* experiments of transcranial ultrasound focusing and neuromodulation with the focused ultrasound.

DATA AVAILABILITY STATEMENT

The datasets generated for this study are available on request to the corresponding author.

AUTHOR CONTRIBUTIONS

CJ and DT conceived the idea of the study. CJ, DL, FX, YL, and CL analyzed the data, interpreted the results and wrote the manuscript. All authors discussed the results and revised the manuscript.

FUNDING

This work was supported by the National Natural Science Foundation of China (Grant Nos. 11804056, 11827808, 11525416, 11504057, 11604054, and 11874289) and the China Postdoctoral Science Foundation (Grant No. 2018M641924), as a Shanghai Municipal Science and Technology Major Project (Grant No. 2017SHZDZX01), by the Shanghai Talent Development Fund (Grant No. 2018112) and the State Key Laboratory of ASIC, and as a System Project (Grant No. 2018MS004).

ACKNOWLEDGMENTS

The authors would like to thank Bradley Treeby for his open-source *k*-wave toolbox.

REFERENCES

Behrens, S., Spengos, K., Daffertshofer, M., Schroeck, H., Dempfle, C. E., and Hennerici, M. (2001). Transcranial ultrasound-improved thrombolysis: diagnostic vs. therapeutic ultrasound. *Ultrasound Med. Biol.* 27, 1683–1689. doi: 10.1016/s0301-5629(01)00481-1

Carcione, J. M., Poletto, F., and Gei, D. (2004). 3-D wave simulation in anelastic media using the Kelvin–Voigt constitutive equation. *J. Comput. Phys.* 196, 282–297. doi: 10.1016/j.jcp.2003.10.024

Clement, G., and Hynynen, K. (2003). Forward planar projection through layered media. *IEEE Trans. Ultrason. Ferroelectr. Freq. Control* 50, 1689–1698. doi: 10.1109/tuffc.2003.1256310

Clement, G. T., White, P. J., and Hynynen, K. (2004). Enhanced ultrasound transmission through the human skull using shear mode conversion. *J. Acosut. Soc. Am.* 115, 1356–1364. doi: 10.1121/1.1645610

Colen, R. R., and Jolesz, F. A. (2010). Future potential of MRI-guided focused ultrasound brain surgery. *Neuroimag. Clin. N. Am.* 20, 355–366. doi: 10.1016/j.nic.2010.05.003

Connor, C. W., Clement, G. T., and Hynynen, K. (2002). A unified model for the speed of sound in cranial bone based on genetic algorithm optimization. *Phys. Med. Biol.* 47, 3925–3944. doi: 10.1088/0031-9155/47/22/302

Damianou, C. (2019). The role of phantoms in magnetic resonance imaging-guided focused ultrasound surgery. *Digit. Med.* 5:52. doi: 10.4103/digm.digm_13_19

Darrow, D. P. (2019). Focused ultrasound for neuromodulation. *Neurotherapeutics* 16, 88–99. doi: 10.1007/s13534-016-0007-y

Errico, C., Osmanski, B.-F., Pezet, S., Couture, O., Lenkei, Z., and Tanter, M. (2016). Transcranial functional ultrasound imaging of the brain using microbubble-enhanced ultrasensitive Doppler. *Neuroimage* 124, 752–761. doi: 10.1016/j.neuroimage.2015.09.037

Firouzi, K., Cox, B., Treeby, B., and Saffari, N. (2012). A first-order k-space model for elastic wave propagation in heterogeneous media. *J. Acosut. Soc. Am.* 129, 2611–2611. doi: 10.1121/1.3588669

Hatakeyama, R., Tagawa, N., Yoshizawa, M., and Moriya, T. (2002). Measurement of speed of sound in skull bone and its thickness using a focused ultrasonic wave. *Jpn J. App. Phys.* 41, 3327–3330. doi: 10.1143/jjap.41.3327

Hayner, M., and Hynynen, K. (2001). Numerical analysis of ultrasonic transmission and absorption of oblique plane waves through the human skull. *J. Acosut. Soc. Am.* 110, 3319–3330. doi: 10.1121/1.1410964

Hu, J. K., Zhang, Q. L., and Hutchins, D. A. (1988). Directional characteristics of electromagnetic acoustic transducers. *Ultrasonics* 26, 5–13. doi: 10.1016/0041-624X(88)90042-X

Hughes, A., and Hynynen, K. (2017). Design of patient-specific focused ultrasound arrays for non-invasive brain therapy with increased trans-skull transmission and steering range. *Phys. Med. Biol.* 62, L9–L19. doi: 10.1088/1361-6560/aa7cd5

Ibsen, S., Tong, A., Schutt, C., Esener, S., and Chalasani, S. H. (2015). Sonogenetics is a non-invasive approach to activating neurons in *Caenorhabditis elegans*. *Nat. Commun.* 6:8264. doi: 10.1038/ncomms9264

Jin, X., Li, C., and Wang, L. V. (2008). Effects of acoustic heterogeneities on transcranial brain imaging with microwave-induced thermoacoustic tomography. *Med. Phys.* 35, 3205–3214. doi: 10.1118/1.2938731

Jing, Y., Meral, F. C., and Clement, G. T. (2012). Time-reversal transcranial ultrasound beam focusing using a k-space method. *Phys. Med. Biol.* 57, 901–917. doi: 10.1088/0031-9155/57/4/901

Jordan, M. P., Bennoui, A. B., Molnar-Fenton, A. A., and White, P. J. (2017). Transcranial ultrasound detection of intracranial hemorrhages: time-frequency analysis with empirical and variational mode decomposition. *J. Acosut. Soc. Am.* 141, 3956–3956. doi: 10.1121/1.4988994

Kendall, J.-M., and Thomson, C. J. (1989). A comment on the form of the geometrical spreading equations, with some numerical examples of seismic ray tracing in inhomogeneous, anisotropic media. *Geophys. J. Int.* 99, 401–413. doi: 10.1111/j.1365-246x.1989.tb01697.x

Kyriakou, A., Neufeld, E., Werner, B., Paulides, M. M., Szekely, G., and Kuster, N. (2013). A review of numerical and experimental compensation techniques for skull-induced phase aberrations in transcranial focused ultrasound. *Int. J. Hyperther.* 30, 36–46. doi: 10.3109/02656736.2013.861519

Lee, H. I., Park, J. H., Park, M. Y., Kim, N. G., Park, K.-J., Choi, B. T., et al. (2016). Pre-conditioning with transcranial low-level light therapy reduces neuroinflammation and protects blood-brain barrier after focal cerebral ischemia in mice. *Restor. Neurol. Neurosci.* 34, 201–214. doi: 10.3233/rnn-150559

Levinsky, A., Papyan, S., Weinberg, G., Stadheim, T., and Eide, P. K. (2016). Non-invasive estimation of static and pulsatile intracranial pressure from transcranial acoustic signals. *Med. Eng. Phys.* 38, 477–484. doi: 10.1016/j.medengphy.2016.02.009

Li, X., Yang, H., Yan, J., Wang, X., Li, X., and Yuan, Y. (2019). Low-intensity pulsed ultrasound stimulation modulates the nonlinear dynamics of local field

potentials in temporal lobe epilepsy. *Front. Neurosci.* 13:287. doi: 10.3389/fnins.2019.00287

Liu, H.-L., Jan, C.-K., Chu, P.-C., Hong, J.-C., Lee, P.-Y., Hsu, J.-D., et al. (2014). Design and experimental evaluation of a 256-channel dual-frequency ultrasound phased-array system for transcranial blood–brain barrier opening and brain drug delivery. *IEEE Trans. Biomed. Eng.* 61, 1350–1360. doi: 10.1109/tbme.2014.2305723

Liu, Q. H. (1998). The pseudospectral time-domain (PSTD) algorithm for acoustic waves in absorptive media. *IEEE Trans. Ultrason. Ferroelectr. Freq. Control* 45, 1044–1055. doi: 10.1109/58.710587

Mast, T., Souriau, L., Liu, D.-L., Tabei, M., Nachman, A., and Waag, R. (2001). A k-space method for large-scale models of wave propagation in tissue. *IEEE Trans. Ultrason. Ferroelectr. Freq. Control* 48, 341–354. doi: 10.1109/58.911717

Mcdannold, N., Clement, G. T., Black, P., Jolesz, F., and Hynynen, K. (2010). Transcranial magnetic resonance imaging– guided focused ultrasound surgery of brain tumors. *Neurosurgery* 66, 323–332. doi: 10.1227/01.neu.0000360379.95800.2f

Muñoz, R. P., and Hornikx, M. (2017). Hybrid fourier pseudospectral/discontinuous Galerkin time-domain method for wave propagation. *J. Comput. Phys.* 348, 416–432. doi: 10.1016/j.jcp.2017.07.046

Myrden, A. J., Kushki, A., Sejdić, E., Guerguerian, A. M., and Chau, T. (2011). A brain-computer boundary based on bilateral transcranial doppler ultrasound. *PLoS One* 6:e24170. doi: 10.1371/journal.pone.0024170

Pernot, M., Aubry, J.-F., Tanter, M., Boch, A.-L., Marquet, F., Kujas, M., et al. (2007). In vivo transcranial brain surgery with an ultrasonic time reversal mirror. *J. Neurosci.* 106, 1061–1066. doi: 10.3171/jns.2007.106.6.1061

Pernot, M., Aubry, J.-F., Tanter, M., Thomas, J.-L., and Fink, M. (2003). High power transcranial beam steering for ultrasonic brain therapy. *Phys. Med. Biol.* 48, 2577–2589. doi: 10.1088/0031-9155/48/16/301

Pichardo, S., Hynynen, K., Hynynen, K., and Souquet, J. (2011). Multi-frequency characterization of speed of sound for longitudinal transmission on freshly excised human skulls. *Phys. Med. Biol.* 56, 219–250. doi: 10.1063/1.3367161

Pichardo, S., Moreno-Hernández, C., Drainville, R. A., Sin, V., Curiel, L., and Hynynen, K. (2017). A viscoelastic model for the prediction of transcranial ultrasound propagation: application for the estimation of shear acoustic properties in the human skull. *Phys. Med. Biol.* 62, 6938–6962. doi: 10.1088/1361-6560/aa7ccc

Renaud, G., Kruizinga, P., Cassereau, D., and Laugier, P. (2018). In vivo ultrasound imaging of the bone cortex. *Phys. Med. Biol.* 63:125010. doi: 10.1088/1361-6560/aac784

Robertson, J. L. B., Cox, B. T., Jaros, J., and Treeby, B. E. (2017). Accurate simulation of transcranial ultrasound propagation for ultrasonic neuromodulation and stimulation. *J. Acosut. Soc. Am.* 141, 1726–1738. doi: 10.1121/1.4976339

Schoonover, R. W., Wang, L. V., and Anastasio, M. A. (2012). Numerical investigation of the effects of shear waves in transcranial photoacoustic tomography with a planar geometry. *J. Biomed. Opt.* 17:61215. doi: 10.1117/1.jbo.17.6.061215

Shuey, R. T. (1985). A simplification of the zoeppritz equations. *Geophysics* 50, 609–614. doi: 10.1190/1.1441936

Szostek, K., and Piórkowski, A. (2016). Real-time simulation of ultrasound refraction phenomena using ray-trace based wavefront construction method. *Comput. Methods Program. Biomed.* 135, 187–197. doi: 10.1016/j.cmpb.2016.07.034

Tabei, M., Mast, T. D., and Waag, R. C. (2002). A k-space method for coupled first-order acoustic propagation equations. *J. Acosut. Soc. Am.* 111, 53–63. doi: 10.1121/1.1421344

Teng, Y. P., and Zhang, H. S. (1997). Calculation of spherical wave refraction and its application to angle probes (Chinese Edition). *J. North J. Univ.* 21, 113–116.

Thomas, J.-L., and Fink, M. (1996). Ultrasonic beam focusing through tissue inhomogeneities with a time reversal mirror: application to transskull therapy. *IEEE Trans. Ultrason. Ferroelectr. Freq. Control.* 43, 1122–1129. doi: 10.1109/58.542055

Top, C. B., White, P. J., and Mcdannold, N. J. (2016). Nonthermal ablation of deep brain targets: a simulation study on a large animal model. *Med. Phys.* 43, 870–882. doi: 10.1118/1.4939809

Tretbar, S., Plinkert, P., and Federspil, P. (2009). Accuracy of ultrasound measurements for skull bone thickness using coded signals. *IEEE Trans. Biomed. Eng.* 56, 733–740. doi: 10.1109/tbme.2008.2011058

Tyler, W. J. (2011). Noninvasive neuromodulation with ultrasound? A continuum mechanics hypothesis. *Neuroscientist* 17, 25–36. doi: 10.1177/1073858409348066

Vassilevski, Y. V., Beklemysheva, K. A., Grigoriev, G. K., Kazakov, A. O., Kulberg, N. S., Petrov, I. B., et al. (2016). Transcranial ultrasound of cerebral vessels in silico: proof of concept. *Russ. J. Numer. Anal.* 31, 317–328. doi: 10.1515/rnam-2016-0030

Waltham, D. A. (1988). Two-point ray tracing using fermats principle. *Geophys. J. Int.* 93, 575–582. doi: 10.1111/j.1365-246x.1988.tb03883.x

Wang, T., and Jing, Y. (2013). Transcranial ultrasound imaging with speed of sound-based phase correction: a numerical study. *Phys. Med. Biol.* 58, 6663–6681. doi: 10.1088/0031-9155/58/19/6663

Wei, Q., Patkar, S., and Pai, D. K. (2014). Fast ray-tracing of human eye optics on graphics processing units. *Comput. Methods Programs Biomed.* 114, 302–314. doi: 10.1016/j.cmpb.2014.02.003

Yılmaz, B., and Çiftçi, E. (2013). An FDTD-based computer simulation platform for shock wave propagation in electrohydraulic lithotripsy. *Comput. Methods Programs Biomed.* 110, 389–398. doi: 10.1016/j.cmpb.2012.11.011

Conflict of Interest: The authors declare that the research was conducted in the absence of any commercial or financial relationships that could be construed as a potential conflict of interest.

APPENDIX

According to the Zoeppritz equations (Shuey, 1985), the plane-wave transmission coefficients can be derived for the liquid–solid boundary. A longitudinal wave in the liquid material will transform into shear and longitudinal waves in the solid material. The reflection and transmission coefficients are presented as

$$\begin{pmatrix} A_1 & B_1 & C_1 \\ A_2 & B_2 & C_2 \\ A_3 & B_3 & C_3 \end{pmatrix} \begin{pmatrix} R_{ll} \\ T_{ll} \\ T_{ls} \end{pmatrix} = \begin{pmatrix} D_1 \\ D_2 \\ D_3 \end{pmatrix},$$

where $A_1 = -1, B_1 = \rho_2/\rho_1 \cos(2\theta_{ts}), C_1 = -\rho_2/\rho_1 \cos(2\theta_{ts}), D_1 = 1; A_2 = 0, B_2 = \sin(2\theta_{tl})/c_{2l}^2, C_2 = \cos(2\theta_{ts})/c_{2t}^2, D_2 = 0; A_3 = \cos(\theta_i)/c_{1l}, B_3 = \cos(\theta_{tl})/c_{2l}, C_3 = -\sin(\theta_{ts})/c_{2s}, D_3 = \cos(\theta_i)/c_{1l}$, and R_{ll}, T_{ll}, and T_{ls} are the longitudinal-wave reflection coefficient, longitudinal-wave refraction coefficient, and shear-wave refraction coefficient, respectively. Here, ρ_1 and c_{1l} are the density and longitudinal wave speed, respectively, of the liquid material, ρ_2, c_{2l}, and c_{2s} are the density, longitudinal wave speed, and shear wave speed, respectively, of the solid material, and θ_i, θ_{tl}, and θ_{ts} are the angles of the incoming wave, refracted longitudinal wave, and refracted shear wave, respectively.

The longitudinal wave transforms into longitudinal and shear waves after reflection in the solid material while remaining a longitudinal wave in the liquid material. The reflection and transmission coefficients are presented as

$$\begin{pmatrix} A_1 & B_1 & C_1 \\ A_2 & B_2 & C_2 \\ A_3 & B_3 & C_3 \end{pmatrix} \begin{pmatrix} R_{ll} \\ R_{ls} \\ T_{ll} \end{pmatrix} = \begin{pmatrix} D_1 \\ D_2 \\ D_3 \end{pmatrix},$$

where $A_1 = cos(\theta_i)/c_{1l}, B_1 = -\sin(\theta_{rs})/c_{1s}, C_1 = \cos(\theta_{tl})/c_2, D_1 = \cos(\theta_i)/c_{1l}; A_2 = -\cos(2\theta_{rs}), B_2 = \sin(2\theta_{rs}), C_2 = \rho_2/\rho_1, D_2 = \cos(2\theta_{rs}); A_3 = c_{1s}^2/c_{1l}^2 \sin^2(\theta_i), B_3 = \cos(2\theta_{rs}), C_3 = 0, D_3 = c_{1s}^2/c_{1l}^2 \sin^2(\theta_i)$, and R_{ll}, R_{ls}, and T_{ll} are the longitudinal-wave reflection coefficient, shear-wave reflection coefficient, and longitudinal-wave refraction coefficient, respectively. Here, ρ_1, c_{1l}, and c_{1s} are the density, longitudinal wave speed, and shear wave speed, respectively, of the solid material, ρ_2 and c_{2l} are the density and longitudinal wave speed, respectively, of the liquid material, and θ_i, θ_{tl}, and θ_{rs} are the angles of the incoming wave, the refracted longitudinal wave, and the reflected shear wave, respectively.

e shear wave transforms into longitudinal and shear waves after reflection in the solid material and transform into a longitudinal wave in the liquid material. The reflection and transmission coefficients are presented as

$$\begin{pmatrix} A_1 & B_1 & C_1 \\ A_2 & B_2 & C_2 \\ A_3 & B_3 & C_3 \end{pmatrix} \begin{pmatrix} R_{ss} \\ R_{sl} \\ T_{sl} \end{pmatrix} = \begin{pmatrix} D_1 \\ D_2 \\ D_3 \end{pmatrix},$$

where $A_1 = -\sin(\theta_i)/c_{1s}, B_1 = -\cos(\theta_{rl})/c_{1l}, C_1 = \cos(\theta_{tl})/c_2, D_1 = \sin(\theta_i)/c_{1s}; A_2 = 0, B_2 = \rho_1 \cos(2\theta_i), C_2 = \rho_2, D_2 = 0; A_3 = -\cos(2\theta_i), B_3 = \sin(2\theta_{rl}) c_{1s}^2/c_{1l}^2, C_3 = 0, D_3 = \cos(2\theta_i)$, and R_{ll}., R_{ls}, and T_{ll} are the longitudinal-wave reflection coefficient, shear-wave reflection coefficient, and longitudinal-wave refraction coefficient, respectively. Here, ρ_1, c_{1l}, and c_{1s} are the density, longitudinal wave speed, and shear wave speed, respectively, of the solid material, ρ_2 and c_{2l} are the density and longitudinal wave speed, respectively, of the, and θ_i, θ_{tl}, and θ_{rs} are the angles of the incoming wave, the refracted longitudinal wave, and the reflected shear wave, respectively.

frontiers in Neuroscience

ORIGINAL RESEARCH
published: 21 April 2020
doi: 10.3389/fnins.2020.00288

Altered Patterns of Functional Connectivity and Causal Connectivity in Salience Subnetwork of Subjective Cognitive Decline and Amnestic Mild Cognitive Impairment

Chunting Cai[1], Chenxi Huang[1], Chenhui Yang[1]*, Haijie Lu[2]*, Xin Hong[1,3], Fujia Ren[1], Dan Hong[1] and Eyk Ng[4]*

[1] School of Informatics, Xiamen University, Xiamen, China, [2] Department of Radiation Oncology, Zhongshan Hospital of Xiamen University, Xiamen, China, [3] College of Computer Science and Technology, Huaqiao University, Xiamen, China, [4] School of Mechanical and Aerospace Engineering, Nanyang Technological University, Singapore, Singapore

OPEN ACCESS

Edited by:
Yizhang Jiang, Jiangnan University, China

Reviewed by:
Lei Cao, Shanghai Maritime University, China
Heye Zhang, Sun Yat-sen University, China

***Correspondence:**
Chenxi Huang
supermonkeyxi@xmu.edu.cn
Chenhui Yang
ych987@126.com
Haijie Lu
luhaijiedr@163.com

Specialty section:
This article was submitted to Neuroprosthetics, a section of the journal Frontiers in Neuroscience

Received: *02 January 2020*
Accepted: *12 March 2020*
Published: *21 April 2020*

Citation:
Cai C, Huang C, Yang C, Lu H, Hong X, Ren F, Hong D and Ng E (2020) Altered Patterns of Functional Connectivity and Causal Connectivity in Salience Subnetwork of Subjective Cognitive Decline and Amnestic Mild Cognitive Impairment. Front. Neurosci. 14:288. doi: 10.3389/fnins.2020.00288

The subjective cognitive decline (SCD) may last for decades prior to the onset of dementia and has been proposed as a risk population for development to amnestic mild cognitive impairment (aMCI) and Alzheimer disease (AD). Disruptions of functional connectivity and causal connectivity (CC) in the salience network (SN) are generally perceived as prominent hallmarks of the preclinical AD. Nevertheless, the alterations in anterior SN (aSN), and posterior SN (pSN) remain unclear. Here, we hypothesized that both the functional connectivity (FC) and CC of the SN subnetworks, comprising aSN and pSN, were distinct disruptive in the SCD and aMCI. We utilized resting-state functional magnetic resonance imaging to investigate the altered FC and CC of the SN subnetworks in 28 healthy controls, 23 SCD subjects, and 29 aMCI subjects. In terms of altered patterns of FC in SN subnetworks, aSN connected to the whole brain was significantly increased in the left orbital superior frontal gyrus, left insula lobule, right caudate lobule, and left rolandic operculum gyrus (ROG), whereas decreased FC was found in the left cerebellum superior lobule and left middle temporal gyrus when compared with the HC group. Notably, no prominent statistical differences were obtained in pSN. For altered patterns of CC in SN subnetworks, compared to the HC group, the aberrant connections in aMCI group were separately involved in the right cerebellum inferior lobule (CIL), right supplementary motor area (SMA), and left ROG, whereas the SCD group exhibited more regions of aberrant connection, comprising the right superior parietal lobule, right CIL, left inferior parietal lobule, left post-central gyrus (PG), and right angular gyrus. Especially, SCD group showed increased CC in the right CIL and left PG, whereas the aMCI group showed decreased CC in the left pre-cuneus, corpus callosum, and right SMA when compared to the SCD group. Collectively, our results suggest that analyzing the altered FC and CC observed in SN subnetworks, served as impressible neuroimaging biomarkers, may supply novel insights for designing preclinical interventions in the preclinical stages of AD.

Keywords: subjective cognitive decline, amnestic mild cognitive impairment, salience network, functional connectivity, causal connectivity

INTRODUCTION

Alzheimer disease (AD) is a chronic neurodegenerative disorder presented in elderly individuals with conspicuous decline in cognitive deterioration and lapse of memory (Huang et al., 2019; Wessels et al., 2019; Zhang et al., 2019). As one of the phases between normal aging and dementia, amnestic mild cognitive impairment (aMCI) subjects have a 10–15% possibility of developing into AD per year (Petersen et al., 2002; Yang et al., 2017). Subjective cognitive decline (SCD) is the stage referring to the elderly subjects that can last for decades earlier than the onset of dementia when persons subjectively complain of memory impairment without corresponding objective clinical manifestations, while person's scores are in the normal scope through standardized neuropsychological tests (Huang et al., 2018a; Funaki et al., 2019; Yu et al., 2019). Furthermore, converging evidence suggests that SCD poses risk for developing into MCI and AD, although it may likewise be of early preclinical stages of other neurodegeneration diseases (Berger-Sieczkowski et al., 2019; Caillaud et al., 2019). Thus, it stands to reason that SCD can be utilized in conjunction with aMCI to explore the mechanism of the early phases of AD and to detect it timely.

Numerous authors have applied resting-state functional magnetic resonance imaging (rs-fMRI) as one of the principal means to clarify the cognitive mechanism of AD (Yang et al., 2017; Marchitelli et al., 2018; Passamonti et al., 2019). Besides, the brain network researches relying on rs-fMRI serve the purpose of revealing the mechanism of neural activity in the brain, which have also important application value and significance in exploring the pathogenesis of AD (Donofry et al., 2019; Lee J. et al., 2019). Among them, plentiful works have been examined by scholars involving in the relationships between salience network (SN) and other networks in the brain (Fredericks et al., 2019; Lee S. E. et al., 2019). More specifically, the SN, which is typically involved in detecting stimulus salience, is a large-scale brain network within the human brain (Cai et al., 2019). Anatomically, it can be spilt into anterior SN (aSN) and posterior SN (pSN) and is primarily anchored in frontoinsular cortices and dorsal anterior cingulate cortex (dACC) (Menon and Uddin, 2010). Recent large-scale works of literature point at the altered patterns of FC and causal connectivity (CC) between SN and other networks. A published study has confirmed that individuals with AD exhibit decreased FC within and between the default mode networks (DMNs) and SN in comparison with healthy controls (HCs) (Liu et al., 2019). Additionally, patients with MCI showed increased FC in the right insula lobule (IL) and claustrum within the SN when compared to the HC group. Similarly, for the aMCI subjects, the FC of the SN-centered model [includes SN, DMN, executive control network (ECN)] is impaired compared to the patients with AD, and these alterations in SN-centered model may result in a decline in cognitive disorder (Aguirre et al., 2019). The basic idea of Granger causality analysis (GCA) is based on multiple linear regression to explore whether there is a causal relationship between the two time series; it helps to accurately forecast the current value of another series and is widely utilized to brain science research field (McBride et al., 2015; Xue J. et al., 2019). A recent study using GCA to analyze CC patterns of aMCI has revealed that CC alterations observed in the SN, ECN, and DMN networks may be regarded as impressible neuroimaging biomarkers for the preclinical intervention and detection of aMCI (Zhang et al., 2019). Former investigation has also revealed that pathological alterations existed in the CC of dACC within SN of AD (Petersen et al., 1985). So far, the majority of SN studies have almost focused on the SN network or between SN and other networks, yet very few researches have previously examined whether CC and FC based on SN subnetworks can be used as neuroimaging biomarkers for identifying aMCI and SCD and to explore how the altered regions of FC and CC relate to cognitive function.

Herein, the objective of our work is to analyze the disruptions observed in FC and CC of SN subnetworks for SCD and aMCI. We hypothesized that there be distinct alterations of the FC and CC in SN subnetworks, and they might be regarded as sensitive neuroimaging markers.

MATERIALS AND METHODS

Participant

Data recruited in this article were acquired from the second phase of the Alzheimer's Disease Neuroimaging Initiative (ADNI-2) database[1]. ADNI-2's primary goal is to focus on finding biomarkers of cognitive impairment and measures of outcome. ADNI-2 was announced and implemented in 2011 and began with a $67 million foundation. Furthermore, it lasted about 5 years. To investigate the gap between the HC and MCI, patients with SCD were included in ADNI-2 for the first time; detailed descriptions of ADNI-2 can be found in www.adni-info.org. Subjects with HC (n = 28), SCD (n = 23), and aMCI (n = 29) were recruited in the present work. Additionally, five individuals were excluded because of excessive head motion (we controlled cumulative translation or rotation $>$ 1.5 mm or 1.5°, n = 3) and quality control in normalization (n = 2). Ultimately, a total of 75 subjects were recruited, comprising 27 HC, 20 SCD, and 28 aMCI subjects.

MRI Data Acquisition

All participants recruited in our work underwent rs-fMRI of 3.0-T Philips Medical Systems (Amsterdam, Netherlands) scanner. The echo-planar imaging sequence contained 140 volumes, and the subjects were separately required to lay subjects on their back, with eyes closed, avoid mentally active brain, and maintain head position during data acquisition. The specific parameters of the scan were as follows: each subject contains 140 time points, flip angle (FA) = 80°, matrix = 64 × 64 × 48, voxel size = 3.31 × 3.31 × 3.31 mm^3, repetition time (TR) = 3,000 ms, echo time (TE) = 30 ms, slice thickness = 3.3 mm. T1-weighted image volumes were obtained by using magnetization-prepared rapid gradient-echo sequence (Chen et al., 2016), and the parameters were as follows: matrix = 256 × 256 × 170, slice thickness = 1.2 mm, acquisition plane = sagittal, TE = 3.16 ms, TR = 6.81 ms, voxel size = 1 × 1 × 1.2 mm^3, FA = 9°. All

[1]http://adni.loni.usc.edu/

the data involved in this article are universally available to the scientific community.

Data Pre-processing

For rs-fMRI data, Resting-State fMRI Data Analysis Toolkit plus (RESTplus)[2] was applied for data pre-processing, which is based on MATLAB2012a[3] and Statistical Parametric Mapping (SPM12)[4]. Pre-processing for rs-fMRI data involved the following steps: the first five volumes in 140 volumes for each subject were removed for possible instability of rs-fMRI signal, and the remaining 135 points in time were corrected for controlling time differences between slices and head motion effects of volumes. Cumulative translation of more than 1.5 mm or angular motion of more than 1.5° was excluded. Next, normalization was adopted to register the original space to the Montreal Neurological Institute (MNI) space by T1 images to mitigate the differences in brain structure between different individuals. Then, the normalized brain volumes were smoothed using Gaussian kernel of $6 \times 6 \times 6$ full width at half maximum in order to reduce individual variations. Following this, nuisance variables, such as six head motion parameters, global mean signal, white matter signal, and cerebrospinal fluid signal, were severally removed to reduce the effect on the dependent variable (Fox et al., 2009; Huang et al., 2018b). Finally, to control noise interferences such as heartbeat and breathing, the subjects' brains generated in the previous step were filtered at 0.01–0.08 Hz.

Statistical Analysis

The distinctions between the HC, SCD, and aMCI groups of demographic and neurocognitive data were estimated by employing analysis of variance (ANOVA) and the χ^2-test within the Statistical Package for the Social Sciences (SPSS) software version 22.0 (IBM, Armonk, NY, United States), and then $p < 0.05$ was set to indicate significant difference in our work.

Comparison and analysis for differences between HC, SCD, and aMCI groups, one-way ANOVA, implemented in the Data Processing and Analysis for Brain Imaging (DPABI)[5] software, was performed through voxel-by-voxel way within the brain mask after regression of age and gender covariates. As suggested in former research, the false-positive rate can be effectively controlled for multiple comparisons using the non-parametric permutation test at the cluster level (Winkler et al., 2016). Here we adopt 1,000 permutation times, and a cluster size $>$ 30 voxels (810 mm^3) was set as the significant cluster. Besides, the significance level was set at 0.05 in the permutation test process. The two-sample t-test was employed to calculate differences between two groups within the mask generated by ANOVA. Previous study has identified that the non-parametric permutation test with Threshold-Free Cluster Enhancement (TFCE) can strike a good and strict balance between family-wise error rate and reliability (Chen et al., 2018). Consequently, permutation tests with TFCE, implemented in PLAM within DPABI, were utilized to perform multiple comparisons in this work, and then a cluster size $>$ 10 voxels (270 mm^3) was adopted as the significant cluster, and the significance level was set at 0.05 (Xue C. et al., 2019).

Independent Component Analysis

Independent component analysis (ICA) is a data-driven and robust analysis technique for separating statistically independent signal sources, which is desirable in exploring neuroimaging data (Beckmann, 2012). Based on former researches, we aimed to use GIFT toolbox (v4.0b)[6] and the infomax algorithm to obtain SN subnetwork components of all subjects (Duc et al., 2019; Liu et al., 2019). To obtain more accurate aSN and pSN components, we first split the data into 20, 25, 30, 35, 40, 45, and 50 components. It is noted that the aSN and pSN templates were acquired by pre-decessors' research (Shirer et al., 2012). A previous study has shown that the component with the highest spatial correlation value is most similar to the template (Cai et al., 2017), and then mean spatial maps of each component were severally utilized to run spatial correlations with SN subnetworks templates (Aguirre et al., 2019). Furthermore, a former study has reported that visual recognition of components through observation and comparison of three researchers was the same as or better than machine recognition approaches (Cherubini et al., 2009). Taken together, we obtained 40 independent components through the collaboration of three researchers and ICA for subsequent analysis, and the components most corresponding to aSN and pSN were 34 and 14, respectively. Since the intensity values in the ICA spatial map have been converted to z-values, we directly performed one-sample t-test ($p = 0.05$, TFCE-FWE corrected, cluster size $>$ 10 voxels) of all subjects to ascertain the aSN and pSN components, respectively.

Functional Connectivity Analysis

Two types of masks, comprising aSN and pSN masks, were obtained according to the ICA analysis. Then, mask-based FC analysis was carried out to examine the alteration patterns between SN subnetworks and the whole brain. Following this, Fisher r-to-z transformation was applied in generated FC brains to further improve normal distribution and facilitate subsequent statistical analysis.

Causal Connectivity Analysis

In the present work, GCA, implemented in Resting-State fMRI Data Analysis Toolkit (REST)[7] and as one of the effective methods for inferring causal relationships, was applied to measure the CC between the two time series based on the previous researches (Wang et al., 2015). We first extracted time series of each subject from the SN subnetwork masks mentioned above and voxel in the brain, respectively, and the CC result can be then obtained using GCA. A brief introduction of GCA based on coefficient is provided below. For two given rs-fMRI series $x(t)$ and $y(t)$, supposing that it is more accurate to predict $x(t)$ using the past time points of $x(t)$ and $y(t)$ than to predict x using x, then there

[2]http://restfmri.net/forum/RESTplusV1.2

[3]http://www.mathworks.com/products/matlab/

[4]https://www.fil.ion.ucl.ac.uk/spm/

[5]http://rfmri.org/dpabi

[6]http://icatb.sourceforge.net

[7]http://www.restfmri.net/forum/REST_V1.8

exists a causal relationship between x and y, where y is called the cause and x is the effect. This is also analogous to other case analysis. The mathematical formula is constructed in the following form:

$$x(t) = a_{x,0} + \sum_{i=1}^{p} a_{xx,i}x(t-i) + \sum_{i=1}^{p} a_{yx,i}y(t-i) + \sum_{i=1}^{p} b_{x,i}z_j(t-i) + \xi_x(t)$$

$$y(t) = a_{y,0} + \sum_{i=1}^{p} a_{xy,i}x(t-i) + \sum_{i=1}^{p} a_{yy,i}y(t-i) + \sum_{i=1}^{p} b_{y,i}z_j(t-i) + \xi_y(t) \quad (1)$$

where p is the model order to measure the lag of time series, and it was set to 1 in our work; ξ represents forecast error regression coefficient. a_{xx} and a_{yy} are the autoregressive coefficient, whereas a_{xy} and a_{yx} are regression coefficients that we used in our work; z denotes noise signal, and the covariate effect coefficient is denoted by b. In consequence, the problem mentioned above aimed to explore the CC alterations between the selected SN subnetworks and the whole brain across three groups.

RESULTS

Demographic and Neurocognitive Characteristics

The demographic and neurocognitive data of all subjects are summarized in **Table 1**. One-way ANOVA presented the significant differences on age ($F = 8.248$, $p = 0.016$), Mini-Mental State Examination (MMSE) score ($F = 9.129$, $p < 0.01$), and CDR score ($F = 68.98$, $p < 0.01$). Nonetheless, it showed no significant difference on gender ($F = 2.026$, $p = 0.139$). Whereas lower MMSE scores indicate a greater degree of cognitive impairment, higher CDR scores show greater dementia. For the MMSE scores, the order from high to low was as follows: HC group (29.14 ± 1.49), SCD group (28.94 ± 0.83), and aMCI group (26.87 ± 2.72). Compared to the HC group (0.03 ± 0.11), the CDR scores increased in the SCD group and the aMCI group successively.

TABLE 1 | Demographics and clinical measures of HC, SCD, and aMCI groups.

Group	HC (n = 27)	SCD (n = 20)	aMCI (n = 28)	p
Gender, female/male	20/7	10/10	10/18	0.139[a]
Age (years)	72.63 ± 4.50	72.38 ± 5.31	69.71 ± 7.26	0.016[b]
MMSE scores	29.14 ± 1.49	28.94 ± 0.83	26.87 ± 2.72	<0.01[b]
CDR scores	0.03 ± 0.11	0.12 ± 0.22	0.52 ± 0.10	<0.01[b]

Numbers are given as means ± standard deviation (SD) unless otherwise stated. MMSE, Mini-Mental State Examination; CDR, Clinical Dementia Rating. [a]The p-values were obtained by χ^2-test. [b]The p-value was obtained by one-way ANOVA.

Identified Regions of SN Subnetworks Using ICA

The SN subnetworks, including aSN and pSN networks, were extracted by ICA of all subjects. Spatial correlations of ICA indicated that the 34th component ($r = 0.34$) was the component most closely related to the aSN network; similarly, the 14th component ($r = 0.36$) was the component corresponding to the pSN. Subsequently, we obtained five clusters within the aSN and six clusters within the pSN of all subjects using one-sample t-test separately, consisting of two clusters of right IL, left IL, right supplementary motor area (SMA), left middle frontal gyrus (MFG), right MFG, left superior temporal gyrus (STG), right supramarginal gyrus (SG), left SG, right middle cingulum, and left pre-cuneus (PreCU), respectively ($p < 0.05$, TFCE-FWE corrected, cluster size > 10 voxels) (**Table 2**).

Altered FC Patterns of SN Subnetworks in the SCD and aMCI Groups

In the aSN, one-way ANOVA revealed four distinct clusters within the brain of three groups, including the left cerebellum superior lobule (CSL), left inferior temporal gyrus (ITG), right orbital inferior frontal gyrus, right lingual gyrus. Besides, compared to HC group within the mask after ANOVA, the aSN connected to the whole brain were separately increased in left orbital superior frontal gyrus, left IL, right caudate lobule (CL), left rolandic operculum gyrus (ROG), whereas decreased FC was found in the left CSL and left middle temporal gyrus (MTG) using two-sample t-test. Compared to the SCD group, the aMCI group exhibited decreased FC in the left MTG. Notably, compared to the HC group, decreased and increased FCs were both found in the SCD group, whereas no significant differences were found in the aMCI group (TFCE-FWE corrected, cluster size $\geq$ 10 voxels, $p < 0.05$). Moreover, the influences of age and gender were controlled in all of the results. At last for the pSN, we found no obvious differences at the 0.05 level using two-sample t-test (**Table 3**).

Altered CC Patterns of SN Subnetworks in SCD and aMCI Groups

At first, we assumed that the selected aSN network was the cause, and the whole brain was the effect to explore the altered CC patterns between the aSN and the whole brain. The ANOVA demonstrated that the prominent differences have focused on the regions of right cerebellum inferior lobule (CIL), left CSL and right superior parietal lobule (SPL), respectively. In comparison with the HC group, the SCD group showed increased CC in the right SPL, whereas aMCI group exhibited decreased CC in the right CIL region. It is worth noting that we found no prominently significant differences within the brain between the aMCI and SCD groups in aSN (TFCE-FWE corrected, cluster size $\geq$ 10 voxels, $p < 0.05$) (**Table 4**).

We next presumed that the whole brain was the cause, and the selected aSN network was the effect. The cluster of left CSL was given by the ANOVA. We found that compared to the HC group the SCD group exhibited decreased CC in the region of the right CIL, yet increased CC in the aMCI group.

TABLE 2 | Five significant clusters of the aSN and six significant clusters of pSN using one-sample *t*-test, respectively.

Subnetwork	Region	Peak/MNI			*t*-Score	Cluster size
		x	*Y*	*z*		
aSN	R IL	39	12	0	6.1223	69
	L IL	−51	12	−3	7.4987	45
	R SMA	3	9	57	20.2433	809
	R MFG	30	39	30	6.6647	73
	L MFG	−30	45	30	4.8756	65
pSN	R IL	39	−9	−9	8.4505	40
	L STG	−36	−12	−9	5.9294	25
	R SG	60	−36	27	20.1412	266
	L SG	−60	−30	27	20.4620	339
	R MC	12	−33	45	8.107	20
	L PreCU	−6	−54	57	11.2489	29

The x, y, and z coordinates are the primary peak locations in the MNI space. $p < 0.05$, TFCE-FWE corrected, cluster size > 10 voxels. L, left; R, right; IL, insula lobule; SMA, supplementary motor area; MFG, middle frontal gyrus; STG, superior temporal gyrus; SG, supramarginal gyrus; MC, middle cingulum; PreCU, pre-cuneus.

TABLE 3 | The significant differences in FC in aSN network.

Region	Peak/MNI			*t*-Score	Cluster size
	x	*y*	*z*		
ANOVA					
L cerebellum superior lobule	−45	−72	−30	7.063	462
L inferior temporal gyrus	−57	−54	33	10.8394	3060
R orbital inferior frontal gyrus	30	18	−24	11.4223	908
R lingual gyrus	−3	−63	6	7.7562	265
SCD > HC					
L orbital superior frontal gyrus	−24	42	−15	4.2171	29
L insula lobule	−33	12	6	3.7921	127
R caudate lobule	12	18	−9	3.9469	22
L rolandic operculum gyrus	−42	−6	12	3.8651	42
HC > SCD					
L cerebellum superior lobule	−51	−66	−39	3.6833	25
L middle temporal gyrus	−57	−9	−24	3.893	114
aMCI > SCD					
L middle temporal gyrus	30	18	−24	4.6672	42

The x, y, and z coordinates are the primary peak locations in the MNI space. Cluster size > 200 voxels in one-way ANOVA, $p < 0.05$; cluster size > 10 voxels in two-sample t-test, $p < 0.05$, TFCE-FWE corrected. L, left; R, right.

Further, compared to the SCD group, the aMCI group exhibited no prominent differences within the brain in aSN (TFCE-FWE corrected, cluster size $\geq$ 10 voxels, $p < 0.05$) (**Table 5**).

Then, we supposed that the selected pSN was the cause, and the whole brain was the effect. The ANOVA exhibited prominently significant differences in the right ITG, right inferior parietal lobule (IPL), right angular gyrus (AG), and right SMA, respectively. In comparison with the HC group, the SCD group exhibited decreased CC in the left IPL, left post-central gyrus (PG), and right AG, whereas the aMCI group exhibited decreased CC in right SMA. Compared to the SCD group, the aMCI group exhibited decreased CC in the left PreCU, corpus callosum (CCA), and right SMA. Interestingly, the SCD and aMCI groups all showed decreased CC in aSN when compared to the HC group (TFCE-FWE corrected, cluster size $\geq$ 10, $p < 0.05$) (**Figure 1** and **Table 6**).

TABLE 4 | The significant differences in CC in aSN network when the selected aSN network is the cause and the whole brain is the effect.

Region	Peak/MNI			*t*-Score	Cluster size
	x	*y*	*z*		
ANOVA					
R cerebellum inferior lobule	−6	−54	−51	8.2648	296
L cerebellum superior lobule	−15	−60	−18	7.4053	243
R superior parietal lobule	30	−72	57	12.7877	251
SCD > HC					
R superior parietal lobule	48	−51	54	4.8878	198
HC > aMCI					
R cerebellum inferior lobule	−6	−57	−51	4.063	165

The x, y, and z coordinates are the primary peak locations in the MNI space. Cluster size > 200 voxels in one-way ANOVA, $p < 0.05$; cluster size > 10 voxels in two-sample t-test, $p < 0.05$, TFCE-FWE corrected. L, left; R, right.

TABLE 5 | The significant differences in CC in aSN network when the whole brain is the cause and the selected aSN network is the effect.

Region	Peak/MNI			*t*-Score	Cluster size
	x	*y*	*z*		
ANOVA					
L cerebellum superior lobule	42	−36	−33	10.1827	680
HC > SCD					
R cerebellum inferior lobule	15	−30	33	−3.9058	519
aMCI > SCD					
R cerebellum inferior lobule	27	−54	−33	3.6655	32

The x, y, and z coordinates are the primary peak locations in the MNI space. Cluster size > 200 voxels in one-way ANOVA, $p < 0.05$; cluster size > 10 voxels in two-sample t-test, $p < 0.05$, TFCE-FWE corrected. L, left; R, right.

And finally, we assumed that the whole brain was the cause, and the selected pSN was the effect. The ANOVA showed a statistically significant difference in the left STG. By comparison with the HC group, we found the regions of decreased CC in SG in the SCD group, whereas the aMCI group showed decreased CC and increased CC in the left IPL and left ROG, respectively. It is interesting that decreased CC was found in IPL, yet increased CC in ROG. Compared to the SCD group, the aMCI group exhibited a significant difference of increased CC in left post-central gyrus (LPG). It is noticeable that all of the results have been controlled for the influences of age and gender (**Table 7**).

DISCUSSION

We mainly aimed to explore the alteration patterns of FC and CC of the aSN and pSN networks to the whole brain in the aMCI and SCD groups and to investigate how this altered the

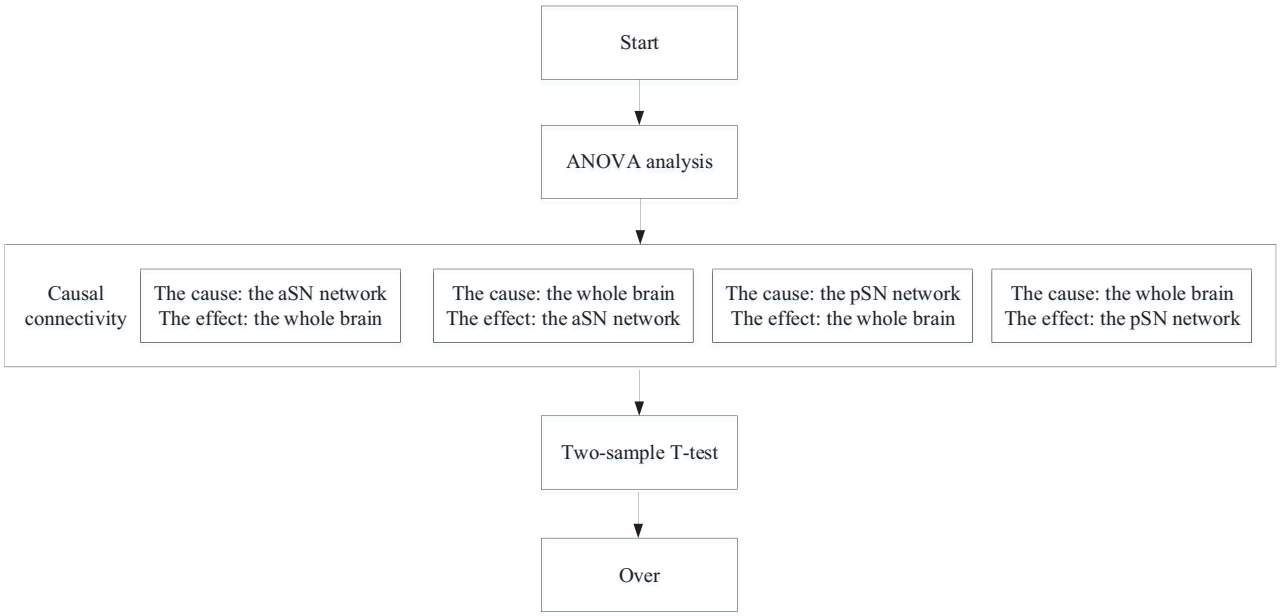

FIGURE 1 | A flowchart depicting the CC process.

regions of FC and CC to cognitive function. The novel aspect of our research is that we demonstrated the FC and CC alterations of SN subnetworks in the SCD and aMCI groups, accompanied by significant brain region analysis. Our results support the hypothesis that was put forward before to a great extent, and the research in this work also provides a new way to understand the stages of aMCI and SCD.

Over the years, the analysis in altered FC and CC of SN and other networks has been a research hotspot, but rarely investigations in SN subnetworks connected with the whole brain. Consistent with previous studies, the hub regions of aSN and pSN networks in this article using ICA, such as IL and cingulum, have been frequently reported to be the major hub regions of SN (Seeley et al., 2007; Menon and Uddin, 2010; Gao et al., 2020a,b, Wang et al., 2020). Then, for FC analysis, we found an interesting phenomenon that only aSN network showed the altered FC using a two-sample *t*-test across groups, proving that aSN might have more disruptive FC when compared to pSN. Notably for aSN, the patients with SCD have more brain regions with remarkable abnormalities than the aMCI group. Compared with the HC group, the patients with SCD have prominently altered CC in both left IL and right CL, which is consistent with previous studies that IL and CL are activated simultaneously (Postuma and Dagher, 2006). Besides, combining the prior research that CL plays a critical role in the brain's learning and memory system and IL is closely related to somatosensory and motor functions (Murray et al., 1984; Bick et al., 2019). Taken together, the altered CC in left IL and right CL where patients with SCD showed prominent differences within the brain might lead to abnormal cognitive functions such as auditory processing, somatosensory, motor, and memory. Specifically, the region where the SCD group patients showed decreased FC in the left MTG in SCD compared to the HC group was similar to that in the aMCI group compared to the SCD group, yet only the former FC was reduced, and the latter FC was increased. According to a previously reported study, the MTG brain region is primarily involved in verbal or semantic cognition and is also associated with oral short-term memory (Vandenberghe et al., 1996). Moreover, the MTG brain region of the AD group showed increased FC, and it has been proved that function involved in semantic knowledge extraction is preserved and may be owed to the compensation mechanism to address memory and cognitive impairment (Peters et al., 2009; Cha et al., 2013). Hence, the alteration in the FC of left MTG found in this study may be explained by a compensation mechanism that exists in the human brain, and left MTG's compensation mechanism of SCD may be stronger than aMCI. Interestingly, patients with SCD primarily appeared to have a decreased FC in left CSL when compared to the HC group, whereas no significant difference was found in patients with aMCI. The cerebellum is involved in motor and balance as well as advanced cognitive functions according to previous research (Gottwald et al., 2003), suggesting that the cerebellar-related cognitive functions of SCD might be subject to a potential effect inferred by the altered FC of aSN to the whole brain. A previous study has indicated that the SN is mainly responsible for cognition-related aspects and is the key interface for the cognitive system (La Corte et al., 2016). Meanwhile, according to the previous relevant studies, there exists obvious cognitive impairment in patients with aMCI when compared to SCD (Yan et al., 2018). Consequently, our results reveal that there might be a different impairment in FC of aSN in cognitive function across the aMCI and SCD.

TABLE 6 | The significant differences in CC in pSN network when the selected pSN is the cause and the whole brain is the effect.

Region	Peak/MNI			*t*-Score	Cluster size
	x	*y*	*z*		
ANOVA					
R inferior temporal gyrus	48	−9	−39	8.0983	212
R inferior parietal lobule	−24	−57	36	9.5386	858
R angular	39	−63	36	9.4243	308
R supplementary motor area	9	−24	60	10.0099	282
HC > SCD					
L inferior parietal lobule	−24	−57	36	4.0374	30
L post-central gyrus	−39	−34	36	3.7147	13
R angular gyrus	39	−63	36	4.0322	42
HC > aMCI					
R supplementary motor area	0	−27	63	4.0201	85
SCD > aMCI					
L pre-cuneus	−18	−45	9	3.8167	21
Corpus Callosum	−15	−39	24	3.3527	49
R supplementary motor area	3	−21	63	3.7881	10

The x, y, and z coordinates are the primary peak locations in the MNI space. Cluster size > 200 voxels in one-way ANOVA, $p < 0.05$; cluster size > 10 voxels in two-sample t-test, $p < 0.05$, TFCE-FWE corrected. L, left; R, right.

TABLE 7 | The significant differences in CC in pSN network when the whole brain is cause and the selected pSN is the effect.

Region	Peak/MNI			*t*-Score	Cluster size
	x	*y*	*z*		
ANOVA					
L superior temporal gyrus	−45	−39	24	12.0664	606
HC > SCD					
Supramarginal gyrus	−36	−39	30	3.8585	17
HC > aMCI					
L inferior parietal lobule	−39	−48	39	3.4764	20
aMCI > HC					
L rolandic operculum gyrus	−45	−39	24	4.8525	137
aMCI > SCD					
L post-central gyrus	−45	−18	27	3.8486	12

The x, y, and z coordinates are the primary peak locations in the MNI space. Cluster size > 200 voxels in one-way ANOVA, $p < 0.05$; cluster size > 10 voxels in two-sample t-test, $p < 0.05$, TFCE-FWE corrected. L, left; R, right.

A recent study has indicated that within-SN CC between the dACC and the striatum is abnormal in aMCI when compared to the HC group (Yu et al., 2019), yet there are only a few studies on the altered CC patterns between the SN subnetworks (aSN and pSN networks) and the whole brain. Then, a previous study has proven that directed connectivity, implemented in GCA within DPABI, can reveal the compensatory or pathological mechanisms of AD to some extent (Menon, 2011). Thus, in this follow-up, we analyzed the alterations of directed CC between the SN subnetworks and the whole brain. Compared to the HC group, in patients with aMCI, it was shown that aberrant connections are separately involved in the right CIL, right SMA, and left ROG, whereas patients with SCD exhibited more aberrant connection regions, comprising the right SPL, right CIL, left IPL, left PG, and right AG. Except for the right CIL region, the regions of significant difference between aSN and pSN were all different, proving that there might exist different communications for information between the SN subnetworks and other brain regions. Compared to the HC group, patients with SCD showed increased CC in the right CIL and left PG, whereas patients with aMCI showed decreased CC in the left PreCU, CCA, and right SMA. The PreCU is associated with many high levels of cognitive functions, such as episodic memory and the processing of self-related information (Herbet et al., 2019). The CCA is mainly connected with motor language center, bilateral visual hearing center, and so on, which is the communication channel of bilateral cerebral hemisphere cognitive function (Prendergast et al., 2018). In addition, PG is located in the parietal lobe of the cerebral cortex, between the central sulcus and the central posterior sulcus, corresponding to the somatosensory center (Yoshino et al., 2017). Thus, the aberrant CC in this article indicates that both the SCD group and aMCI group have different degrees of cognitive impairment, which is consistent with the findings of a previous study (Yan et al., 2018), and the altered CC may be affected by the brain's compensation mechanism. Our research suggests, whether the aSN is the cause or effect, both exhibited statistical differences in the right CIL region, and no prominent difference for pSN was found. Also, no matter the pSN is the cause or effect, both showed statistical differences in the left PG region, and no difference for aSN was seen. Therefore, according to the aforementioned cerebellum involved in motor and balance, as well as advanced cognitive functions, and the PG involved in the somatosensory center, it can be deduced that CIL and left PG are sensitive and might be used as neuroimaging biomarkers to distinguish the cognitive function impairment of aSN and pSN. Interestingly, we also find that the altered CC of pSN is found prominently outnumbering that of aSN, signifying that pSN may have far more serious functional impairment and more compensation requirements and can be used as neuroimaging biomarkers for diagnosis of the early preclinical AD.

In conclusion, our findings show that both the FC and CC of the SN subnetworks (aSN and pSN) are distinctively disruptive in the early preclinical stages of AD consisting of SCD and aMCI. Moreover, the prominent difference in the distribution of aSN and pSN varies considerably, which may be used as neuroimaging biomarkers for diagnosis of the early preclinical AD.

CONCLUSION

This study mainly reveals that the SCD and aMCI groups exhibit distinct alternations in aSN and pSN networks compared to the HC group. It turns out that the altered FC and CC in SCD and aMCI groups may reflect the changes in cognitive function, and there may be a compensation mechanism. Further, the sensitive neuroimaging biomarkers found in the FC and CC of SN subnetworks may provide new insight for the early detection of AD.

DATA AVAILABILITY STATEMENT

Publicly available datasets were analyzed in this study. This data can be found here: http://adni.loni.usc.edu/.

AUTHOR CONTRIBUTIONS

CH, CY, and HL guided experiments and correspondingly proposed some thesis writing strategies for the manuscript. EN, XH, FR, and DH checked for grammatical errors of manuscript, and discussed difficult problems in manuscript with CC.

FUNDING

This work was supported by the Natural Science Foundation of Fujian Province, China (No. 2017J01372), Foundation of Fujian Educational Committee (No. JK2015019).

REFERENCES

Aguirre, N., Costumero-Ramos, V., Marin-Marin, L., Escudero-Torrella, J., Belloch, V., Parcet, M., et al. (2019). Activity in memory brain networks during encoding differentiates mild cognitive impairment converters from non-converters. *J. Alzheimer's Dis.* 71, 1–13. doi: 10.3233/JAD-190421

Beckmann, C. F. (2012). Modelling with independent components. *Neuroimage* 62, 891–901. doi: 10.1016/j.neuroimage.2012.02.020

Berger-Sieczkowski, E., Gruber, B., Stogmann, E., and Lehrner, J. (2019). Differences regarding the five-factor personality model in patients with subjective cognitive decline and mild cognitive impairment. *Neuropsychiatr* 33, 35–45. doi: 10.1007/s40211-018-0292-z

Bick, S. K., Patel, S. R., Katnani, H. A., Peled, N., Widge, A., Cash, S. S., et al. (2019). Caudate stimulation enhances learning. *Brain* 142, 2930–2937. doi: 10.1093/brain/awz254

Cai, S., Peng, Y., Chong, T., Zhang, Y., von Deneen, K. M., Huang, L., et al. (2017). Differentiated effective connectivity patterns of the executive control network in progressive MCI: a potential biomarker for predicting AD. *Curr. Alzheimer Res.* 14, 937–950. doi: 10.2174/1567205014666170309120200

Cai, W., Griffiths, K., Korgaonkar, M. S., Williams, L. M., and Menon, V. (2019). Inhibition-related modulation of salience and frontoparietal networks predicts cognitive control ability and inattention symptoms in children with ADHD. *Mol. Psychiatry* doi: 10.1038/s41380-019-0564-4

Caillaud, M., Hudon, C., Boller, B., Brambati, S., Duchesne, S., Lorrain, D., et al. (2019). Evidence of a relation between hippocampal volume, white matter hyperintensities, and cognition in subjective cognitive decline and mild cognitive impairment. *J. Gerontol. B Psychol. Sci. Soc. Sci.* (in press). doi: 10.1093/geronb/gbz120

Cha, J., Jo, H. J., Kim, H. J., Seo, S. W., Kim, H. S., Yoon, U., et al. (2013). Functional alteration patterns of default mode networks: comparisons of normal aging, amnestic mild cognitive impairment and Alzheimer's disease. *Eur. J. Neurosci.* 37, 1916–1924. doi: 10.1111/ejn.12177

Chen, J., Duan, X., Shu, H., Wang, Z., Long, Z., Liu, D., et al. (2016). Differential contributions of subregions of medial temporal lobe to memory system in amnestic mild cognitive impairment: insights from fMRI study. *Sci. Rep.* 6:26148. doi: 10.1038/srep26148

Chen, X., Lu, B., and Yan, C. G. (2018). Reproducibility of R-fMRI metrics on the impact of different strategies for multiple comparison correction and sample sizes.*Hum. Brain Mapp.* 39, 300–318. doi: 10.1002/hbm.23843

Cherubini, A., Peran, P., Caltagirone, C., Sabatini, U., and Spalletta, G. (2009). Aging of subcortical nuclei: microstructural, mineralization and atrophy modifications measured in vivo using MRI. *Neuroimage* 48, 29–36. doi: 10.1016/j.neuroimage.2009.06.035

Donofry, S. D., Stillman, C. M., and Erickson, K. I. (2019). A review of the relationship between eating behavior, obesity, and functional brain network organization. *Soc. Cogn. Affect. Neurosci.* doi: 10.1093/scan/nsz085

Duc, N. T., Ryu, S., Qureshi, M. N. I., Choi, M., Lee, K. H., and Lee, B. (2019). 3D-Deep learning based automatic diagnosis of Alzheimer's Disease with joint MMSE prediction using resting-state fMRI. *Neuroinformatics* 18, 71–86. doi: 10.1007/s12021-019-09419-w

Fox, M. D., Zhang, D., Snyder, A. Z., and Raichle, M. E. (2009). The global signal and observed anticorrelated resting state brain networks.*J. Neurophysiol.* 101, 3270–3283.

Fredericks, C. A., Brown, J. A., Deng, J., Kramer, A., Ossenkoppele, R., Rankin, K., et al. (2019). Intrinsic connectivity networks in posterior cortical atrophy: a role for the pulvinar? *Neuroimage Clin.* 21:101628. doi: 10.1016/j.nicl.2018.101628

Funaki, K., Nakajima, S., Noda, Y., Wake, T., Ito, D., Yamagata, B., et al. (2019). Can we predict amyloid deposition by objective cognition and regional cerebral blood flow in patients with subjective cognitive decline? *Psychogeriatrics* 19, 325–332. doi: 10.1111/psyg.12397

Gao, Z., Xu, C., Zhang, H., Li, S., and Albuquerque, V. H. C. D. (2020a). Trustful internet of surveillance things based on deeply-represented visual Co-saliency detection. *IEEE Int. Things J.* (in press). doi: 10.1109/JIOT.2019.2963701

Gao, Z., Zhang, H., Dong, S., Sun, S., Wang, X., Yang, G., et al. (2020b). Salient object detection in the distributed cloud-edge intelligent network. *IEEE Network* 34, 216–224. doi: 10.1109/MNET.001.1900260

Gottwald, B., Mihajlovic, Z., Wilde, B., and Mehdorn, H. M. (2003). Does the cerebellum contribute to specific aspects of attention? *Neuropsychologia* 41, 1452–1460.

Herbet, G., Lemaitre, A. L., Moritz-Gasser, S., Cochereau, J., and Duffau, H. (2019). The antero-dorsal precuneal cortex supports specific aspects of bodily awareness. *Brain* 142, 2207–2214. doi: 10.1093/brain/awz179

Huang, C., Tian, G., Lan, Y., Peng, Y., Ng, E. Y. K., Hao, Y., et al. (2019). A New Pulse Coupled Neural Network (PCNN) for brain medical image fusion empowered by shuffled frog leaping algorithm. *Front. Neurosci.* 13:210. doi: 10.3389/fnins.2019.00210

Huang, C., Xiaoying, S., Yisha, L., Lu, L., Haidong, C., Wenliang, C., et al. (2018a). A hybrid active contour segmentation method for myocardial D-SPECT Images. *IEEE Access.* 6, 39334–39343.

Huang, C., Xie, Y., Lan, Y., Hao, Y., Chen, F., Cheng, Y., et al. (2018b). A New framework for the integrative analytics of intravascular ultrasound and optical coherence tomography images. *IEEE Access.* 6, 36408–36419.

La Corte, V., Sperduti, M., Malherbe, C., Vialatte, F., Lion, S., Gallarda, T., et al. (2016). Cognitive decline and reorganization of functional connectivity in healthy aging: the pivotal role of the salience network in the prediction of age and cognitive performances. *Front. Aging Neurosci.* 8:204. doi: 10.3389/fnagi.2016.00204

Lee, J., Eun, S., Kim, J., Lee, J. H., and Park, K. (2019). Differential influence of acupuncture somatosensory and cognitive/affective components on functional brain connectivity and pain reduction during low back pain state. *Front. Neurosci.* 13:1062. doi: 10.3389/fnins.2019.01062

Lee, S. E., Sias, A. C., Kosik, E. L., Flagan, T. M., Deng, J., Chu, S. A., et al. (2019). Thalamo-cortical network hyperconnectivity in preclinical progranulin mutation carriers. *Neuroimage Clin.* 22:101751. doi: 10.1016/j.nicl.2019.101751

Liu, J., Ji, J., Jia, X., and Zhang, A. (2019). Learning brain effective connectivity network structure using ant colony optimization combining with voxel activation information. *IEEE J. Biomed. Health Inform.* (in press). doi: 10.1109/JBHI.2019.2946676

Marchitelli, R., Aiello, M., Cachia, A., Quarantelli, M., Cavaliere, C., Postiglione, A., et al. (2018). Simultaneous resting-state FDG-PET/fMRI in Alzheimer Disease: relationship between glucose metabolism and intrinsic activity. *Neuroimage* 176, 246–258. doi: 10.1016/j.neuroimage.2018.04.048

McBride, J. C., Zhao, X., Munro, N. B., Jicha, G. A., Schmitt, F. A., Kryscio, R. J., et al. (2015). Sugihara causality analysis of scalp EEG for detection of early Alzheimer's disease. *Neuroimage Clin.* 7, 258–265. doi: 10.1016/j.nicl.2014.12.005

Menon, V. (2011). Large-scale brain networks and psychopathology: a unifying triple network model. *Trends Cogn. Sci.* 15, 483–506. doi: 10.1016/j.tics.2011.08.003

Menon, V., and Uddin, L. Q. (2010). Saliency, switching, attention and control: a network model of insula function. *Brain Struct. Funct.* 214, 655–667. doi: 10.1007/s00429-010-0262-0

Murray, E., Mishkin, M., Murray, E. A., and Mishkin, M. (1984). Relative contributions of SII and area 5 to tactile discrimination in monkeys. *Behav. Brain Res.* 11, 67–83.

Passamonti, L., Tsvetanov, K. A., Jones, P. S., Bevan-Jones, W. R., Arnold, R., Borchert, R. J., et al. (2019). Neuroinflammation and functional connectivity in Alzheimer's Disease: interactive influences on cognitive performance. *J. Neurosci.* 39, 7218–7226.

Peters, F., Collette, F., Degueldre, C., Sterpenich, V., Majerus, S., and Salmon, E. (2009). The neural correlates of verbal short-term memory in Alzheimer's disease: an fMRI study. *Brain* 132(Pt 7), 1833–1846. doi: 10.1093/brain/awp075

Petersen, R., Doody, R., Kurz, A., Mohs, R., Morris, J., Rabins, P., et al. (2002). Current concepts in mild cognitive impairment. *Arch. Neurol.* 58, 1985–1992.

Petersen, R. C., Doody, R., Kurz, A., Mohs, R. C., Morris, J. C., Rabins, P. V., et al. (1985). Current concepts in mild cognitive impairment. *Arch. Neurol.* 58:1985.

Postuma, R. B., and Dagher, A. (2006). Basal ganglia functional connectivity based on a meta-analysis of 126 positron emission tomography and functional magnetic resonance imaging publications. *Cereb. Cortex* 16, 1508–1521.

Prendergast, D. M., Karlsgodt, K. H., Fales, C. L., Ardekani, B. A., and Szeszko, P. R. (2018). Corpus callosum shape and morphology in youth across the psychosis spectrum. *Schizophr. Res.* 199, 266–273. doi: 10.1016/j.schres.2018.04.008

Seeley, W. W., Menon, V., Schatzberg, A. F., Keller, J., Glover, G. H., Kenna, H., et al. (2007). Dissociable intrinsic connectivity networks for salience processing and executive control. *J. Neurosci.* 27, 2349–2356.

Shirer, W. R., Ryali, S., Rykhlevskaia, E., Menon, V., and Greicius, M. D. (2012). Decoding subject-driven cognitive states with whole-brain connectivity patterns. *Cereb. Cortex* 22, 158–165. doi: 10.1093/cercor/bhr099

Vandenberghe, R., Price, C., Wise, R., Josephs, O., and Frackowiak, R. S. (1996). Functional anatomy of a common semantic system for words and pictures. *Nature* 383, 254–256.

Wang, C., Dong, S., Zhao, X., Papanastasiou, G., Zhang, H., and Yang, G. (2020). SaliencyGAN: deep learning semisupervised salient object detection in the fog of iot. *IEEE Trans. Ind. Inform.* 16, 2667–2676.

Wang, T., Chen, N., Zhan, W., Liu, J., Zhang, J., Liu, Q., et al. (2015). Altered effective connectivity of posterior thalamus in migraine with cutaneous allodynia: a resting-state fMRI study with Granger causality analysis. *J. Headache Pain* 17:17. doi: 10.1186/s10194-016-0610-4

Wessels, A. M., Tariot, P. N., Zimmer, J. A., Selzler, K. J., Bragg, S. M., Andersen, S. W., et al. (2019). Efficacy and safety of lanabecestat for treatment of early and mild Alzheimer disease: the AMARANTH and DAYBREAK-ALZ randomized clinical trials. *JAMA Neurol.* 77, 199–209. doi: 10.1001/jamaneurol.2019.3988

Winkler, A. M., Ridgway, G. R., Douaud, G., Nichols, T. E., and Smith, S. M. (2016). Faster permutation inference in brain imaging. *Neuroimage* 141, 502–516. doi: 10.1016/j.neuroimage.2016.05.068

Xue, C., Yuan, B., Yue, Y., Xu, J., Wang, S., Wu, M., et al. (2019). Distinct disruptive patterns of default mode subnetwork connectivity across the spectrum of preclinical Alzheimer's Disease. *Front. Aging Neurosci.* 11:307. doi: 10.3389/fnagi.2019.00307

Xue, J., Guo, H., Gao, Y., Wang, X., Cui, H., Chen, Z., et al. (2019). Altered directed functional connectivity of the hippocampus in mild cognitive impairment and Alzheimer's Disease: a resting-state fMRI study. *Front. Aging Neurosci.* 11:326. doi: 10.3389/fnagi.2019.00326

Yan, T., Wang, W., Yang, L., Chen, K., Chen, R., and Han, Y. (2018). Rich club disturbances of the human connectome from subjective cognitive decline to Alzheimer's disease. *Theranostics* 8, 3237–3255. doi: 10.7150/thno.23772

Yang, H., Wang, C., Zhang, Y., Xia, L., Feng, Z., Li, D., et al. (2017). Disrupted causal connectivity anchored in the posterior cingulate cortex in amnestic mild cognitive impairment. *Front. Neurol.* 8:10. doi: 10.3389/fneur.2017.00010

Yoshino, A., Okamoto, Y., Doi, M., Okada, G., Takamura, M., Ichikawa, N., et al. (2017). Functional alterations of postcentral gyrus modulated by angry facial expressions during intraoral tactile stimuli in patients with burning mouth syndrome: a functional magnetic resonance imaging study. *Front. Psychiatry* 8:224. doi: 10.3389/fpsyt.2017.00224

Yu, E., Liao, Z., Tan, Y., Qiu, Y., Zhu, J., Han, Z., et al. (2019). High-sensitivity neuroimaging biomarkers for the identification of amnestic mild cognitive impairment based on resting-state fMRI and a triple network model. *Brain Imaging Behav.* 13, 1–14. doi: 10.1007/s11682-017-9727-6

Zhang, T., Ke, W., Zhou, X., Qian, Y., Feng, S., Wang, R., et al. (2019). Human neural stem cells reinforce hippocampal synaptic network and rescue cognitive deficits in a mouse model of Alzheimer's Disease. *Stem Cell Rep.* 13, 1022–1037. doi: 10.1016/j.stemcr.2019.10.012

Conflict of Interest: The authors declare that the research was conducted in the absence of any commercial or financial relationships that could be construed as a potential conflict of interest.

frontiers in Neuroscience

ORIGINAL RESEARCH
published: 11 June 2020
doi: 10.3389/fnins.2020.00496

Seizure Classification From EEG Signals Using an Online Selective Transfer TSK Fuzzy Classifier With Joint Distribution Adaption and Manifold Regularization

Yuanpeng Zhang[1,2], *Ziyuan Zhou*[1], *Heming Bai*[2], *Wei Liu*[2] *and Li Wang*[1,2]*

[1] *Department of Medical Informatics of Medical (Nursing) school, Nantong University, Nantong, China,* [2] *Research Center for Intelligence Information Technology, Nantong University, Nantong, China*

To recognize abnormal electroencephalogram (EEG) signals for epileptics, in this study, we proposed an online selective transfer TSK fuzzy classifier underlying joint distribution adaption and manifold regularization. Compared with most of the existing transfer classifiers, our classifier has its own characteristics: (1) the labeled EEG epochs from the source domain cannot accurately represent the primary EEG epochs in the target domain. Our classifier can make use of very few calibration data in the target domain to induce the target predictive function. (2) A joint distribution adaption is used to minimize the marginal distribution distance and the conditional distribution distance between the source domain and the target domain. (3) Clustering techniques are used to select source domains so that the computational complexity of our classifier is reduced. We construct six transfer scenarios based on the original EEG signals provided by the Bonn University to verify the performance of our classifier and introduce four baselines and a transfer support vector machine (SVM) for benchmarking studies. Experimental results indicate that our classifier wins the best performance and is not very sensitive to its parameters.

Keywords: seizure classification, brain-computer interface, transfer learning, joint distribution adaption, manifold regularization, TSK fuzzy classifier

OPEN ACCESS

Edited by:
Mohammad Khosravi, Persian Gulf University, Iran

Reviewed by:
Xiaoqing Gu, Changzhou University, China
Wenhao Ying, Changshu Institute of Technology, China

***Correspondence:**
Li Wang
wangli@ntu.edu.cn

Specialty section:
This article was submitted to Neuroprosthetics, a section of the journal Frontiers in Neuroscience

Received: *28 March 2020*
Accepted: *21 April 2020*
Published: *11 June 2020*

Citation:
Zhang Y, Zhou Z, Bai H, Liu W and Wang L (2020) Seizure Classification From EEG Signals Using an Online Selective Transfer TSK Fuzzy Classifier With Joint Distribution Adaption and Manifold Regularization. Front. Neurosci. 14:496. doi: 10.3389/fnins.2020.00496

INTRODUCTION

The maturity of the brain–computer interface (BCI) technology has provided an important channel for the human to use artificial intelligence (AI) to explore the cognitive activities of the brain. For example, many AI methods have been proposed for an intelligent diagnosis of epilepsy instead of neurological physicians through electroencephalogram (EEG) signals (Ghosh-Dastidar et al., 2008; Van Hese et al., 2009; Wang et al., 2016). In this study, we also focus on the intelligent diagnosis of epilepsy through EEG signals. The classic diagnostic procedure for epilepsy by using intelligent models is illustrated in **Figure 1**. We observe that, for an emerging task, a large number of labeled EEG epochs are required to train an intelligent model. Therefore, it needs to consume a lot of effort to manually label EEG epochs. Because the responses to EEG signals of different patients in the same cognitive activity show a certain degree of similarity, we expect to leverage abundant labeled EEG epochs, which are available in a related source domain for training an accurate

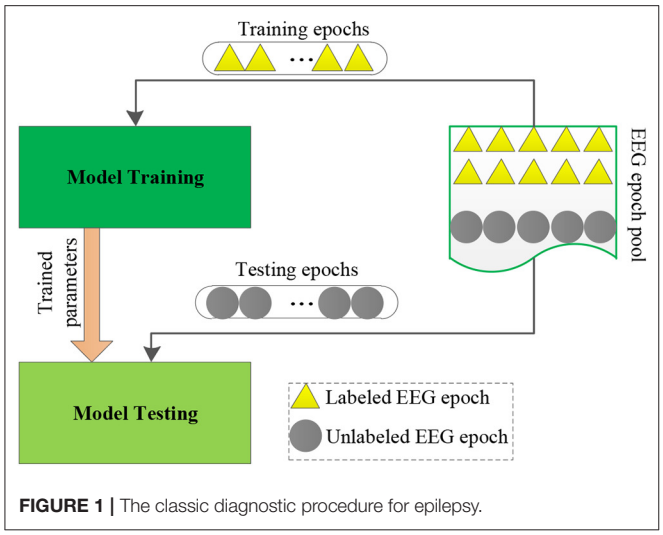

FIGURE 1 | The classic diagnostic procedure for epilepsy.

intelligent model to be reused in the target domain. To this end, transfer learning is often used, which has been proven to be promising for epilepsy EEG signal recognition. For example, Yang et al. (2014) proposed a transfer model LMPROJ for epilepsy EEG signal recognition underlying the support vector machine (SVM) framework. In LMPROJ, the marginal probability distribution distance measured by the maximal mean discrepancy (MMD) between the source domain and the target domain is used to minimize the distribution difference. Jiang et al. (2017c) improved LMPROJ and generated a model A-TL-SSL-TSK for epilepsy EEG signal recognition underlying the TSK fuzzy system framework. Comparing with LMPROJ, A-TL-SSL-TSK not only used the marginal probability distribution consensus as a transfer principle but also introduced semisupervised learning (cluster assumption) for regularization. Additionally, in our previous work (Jiang et al., 2020), we proposed an online multiview and transfer model O-MV-T-TSK-FS for EEG-based drivers' drowsiness estimation. It minimized not only the marginal distribution differences but also the conditional distribution differences between the source domain and the target domain. But it did not derive any information from unlabeled data. More references about transfer learning for epilepsy EEG signal recognition can be found in Jiang et al. (2019) and Parvez and Paul (2016).

Although existing intelligent models, for example, LMPROJ and A-TL-SSL-TSK, underlying the transfer learning framework are effective for epilepsy EEG signal recognition, there still exist some issues that should be further addressed.

- To tolerate the distribution difference between the source domain and the target domain, it is not enough to only minimize the marginal distribution difference between the two domains.
- Most of the existing models use only one source domain for knowledge transfer. That is to say, all available labeled data in the source domain are leveraged for model training. However, some labeled data may cause negative transfer.

TABLE 1 | Epilepsy EEG data archive and collection condition.

Volunteers	Groups	#Group	Collection conditions
Health	A	100	Volunteers with eyes open
	B	100	Volunteers with eyes closed
Epileptic	C	100	From hippocampal formation during seizure free intervals
	D	100	From within epileptogenic zone during seizure free intervals
	E	100	During seizure activity

Sampling rate: 173.6 Hz; duration: 23.6 s.

Therefore, in this study, by overall considering the above two issues, we propose a new intelligent TSK fuzzy classifier (online selective transfer TSK fuzzy classifier with joint distribution adaption and manifold regularization, OS-JDA-MR-T-TSK-FC) for epilepsy EEG signal recognition. First, it further explores the marginal probability distribution adaption between the source domain and the target domain from two aspects. One is that it additionally introduces conditional probability distribution adaption to further minimize the distribution difference. The second is that it preserves manifold consistency underlying the marginal probability distribution. Second, it can selectively leverage knowledge from multiple source domains.

The following sections are organized as follows: in *Data and Methods*, we give the EEG data and our proposed method. In *Results*, we report the experimental results. Discussions about experimental results are presented in *Discussions*, and the whole conclusions are summarized in the last section.

DATA AND METHODS

Data

In this study, we download very commonly used epilepsy EEG[1] data to verify our proposed intelligence model. The data from the University of Bonn is open to the public for scientific research. **Table 1** gives the data archive and collection conditions. Additionally, **Figure 2** illustrates the amplitudes during the collection procedure of one volunteer in each group. The original EEG data cannot be directly used for model training (Jiang et al., 2017b; Tian et al., 2019). We should employ feature extraction methods to extract robust features before model training.

Feature Extraction

Three feature extraction algorithms, that is, wavelet packet decomposition (WPD) (Li, 2011), short-time Fourier transform (STFT) (Pei et al., 1999), and kernel principal component analysis (KPCA) (Li et al., 2005), are employed to extract three kinds of features from the original epilepsy EEG signals.

- Wavelet Packet Decomposition

Wavelet packet decomposition is used to extract time-frequency features from epilepsy EEG signals. More specifically, the

[1]http://www.meb.unibonn.de/epileptologie/science/physik/eegdata.html.

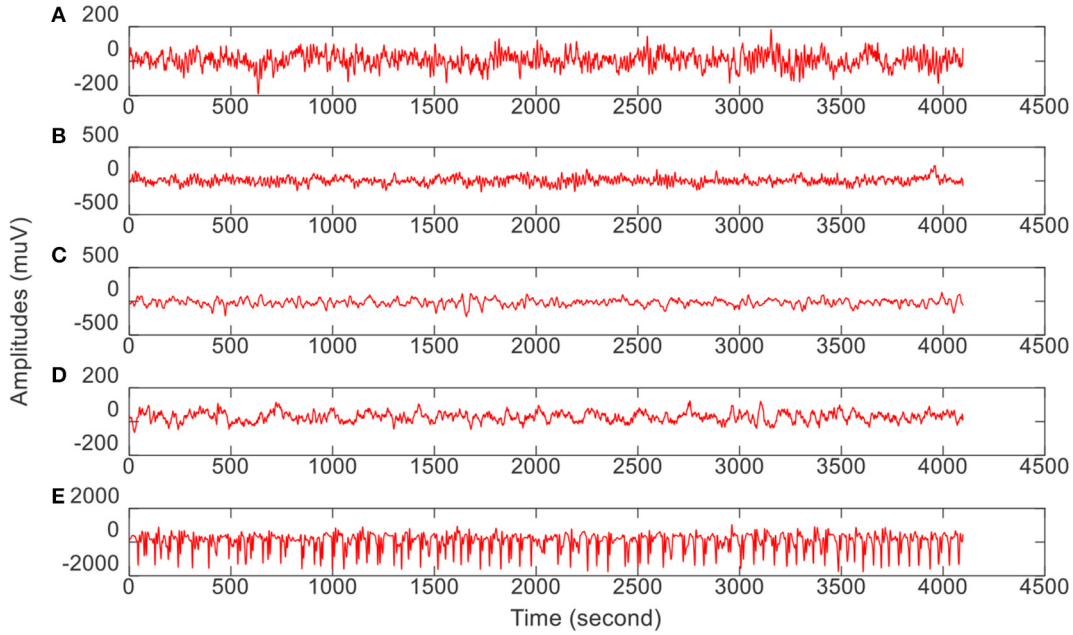

FIGURE 2 | The amplitude of one volunteer in each group during the collection procedure. From top to bottom corresponds to **(A–E)**, respectively.

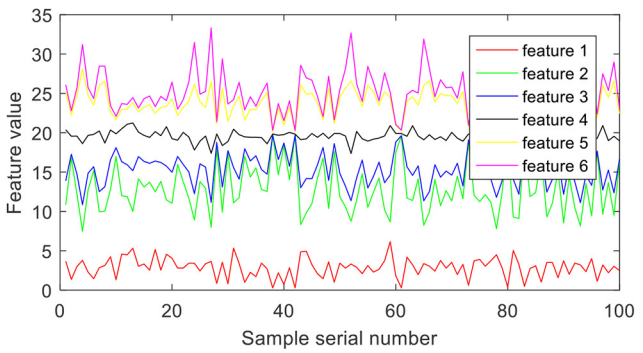

FIGURE 3 | Features extracted by wavelet packet decomposition.

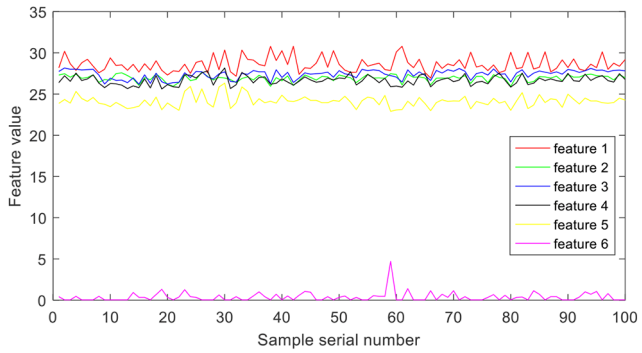

FIGURE 4 | Features extracted by short time Fourier transform.

epilepsy EEG signals are disassembled into six different frequency bands with the Daubechies 4 wavelet coefficients. Each band is considered as one feature. **Figure 3** illustrates the six features of group A.

- Short-Time Fourier Transform

Short-time Fourier transform is used to extract frequency-domain features from epilepsy EEG signals. More specifically, the epilepsy EEG signals are disassembled into different local stationary signal segments, and then the Fourier transform is used to extract a group of spectra of the local segments, which are with evident time-varying characteristics at different times. Finally, six frequency bands are extracted from each group of spectra. **Figure 4** illustrates the six features of group A.

- Kernel Principal Component Analysis

Kernel principal component analysis is used to extract time-domain features from epilepsy EEG signals. More specifically, the Gaussian function is chosen as the kernel to map the original features nonlinearly. Then six kinds of features are selected from the top six PC eigenvectors. **Figure 5** illustrates the six features of group A.

Online Transfer Scenario Construction

We construct six online transfer scenarios from the EEG data after feature extraction (**Table 2**). Each scenario consists of five source domains as multiple source domains and one target domain. Specifically, two healthy groups (A, B) and three epileptic groups (C, D, E) are combined to generate six different

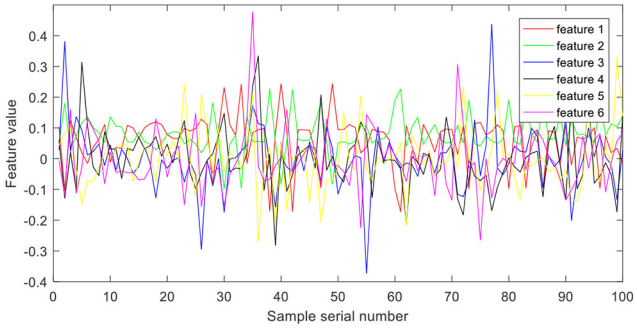

FIGURE 5 | Features extracted by kernel principal component analysis.

TABLE 2 | Six online transfer scenarios.

Scenarios	Source domains	Target domain	No. of subject-specific objects
SC-1	BD, BC, AE, AD, AC	BE	20
SC-2	BE, BC, AE, AD, AC	BD	20
SC-3	BE, BD, AE, AD, AC	BC	20
SC-4	BE, BD, BC, AD, AC	AE	20
SC-5	BE, BD, BC, AE, AC	AD	20
SC-6	BE, BD, BC, AE, AD	AC	20

pairs of combinations, that is, AC, AD, AE, BC, BD, and BE. Five pairs are alternatively selected from the six combinations as source domains, and the rest one is taken as the target domain such that each pair has the opportunity to become the target domain.

In general, calibration in BCIs can be divided into two types, that is, offline calibration and online calibration (Jiang et al., 2020). Offline calibration means that we have obtained a pool of unlabeled EEG epochs. Some of unlabeled EEG epochs were labeled by experts to train a classifier. The unseen epochs then were classified by the trained classifier. Online calibration means that the training EEG epochs were obtained on-the-fly. That is to say, the classifier was trained online. Both calibration methods have their own advantages and disadvantages. For example, in offline calibration, unlabeled EEG epochs can be used to assist labeled ones to achieve classifier training, for example, semisupervised learning (Mallapragada et al., 2009; Zhang et al., 2013; Dornaika and El Traboulsi, 2016). Additionally, if necessary, we can easily obtain the label of any EEG epochs at any time. In online calibration, we not only have no unlabeled EEG epochs to be used for classifier training but also have little control on which epochs to see next. However, online calibration is more attractive because it is more in line with the needs of practical application scenarios. Therefore, in this study, we only consider online calibration for seizure classification. To simulate online calibration in the aforementioned six transfer scenarios, we first generate $M = 20$ subject-specific objects from the target domain. The online calibration flowchart is shown in **Figure 6**. We repeat all rounds 10 times to obtain statistically meaningful results, where each time has a random starting position m_0.

Methods

In this section, we will elaborate the method we proposed for seizure classification. We first mathematically state the transfer problem, and then we give the online transfer learning framework and hence the online transfer TSK fuzzy classifier (OS-JDA-MR-T-TSK-FC). Lastly, we give the detailed algorithm steps of OS-JDA-MR-T-TSK-FC including how to select source domains.

Problem Statement

A domain $\Psi = \{X, P(\mathbf{x})\}$ in the transfer learning or domain adaption scenario consists of a d-dimensional feature space $\in R^d$ and a marginal distribution $P(\mathbf{x})$, and a task $\Gamma = \{Y, P(y|\mathbf{x})\}$ in the similar scenario consists of a one-dimensional label space Y and a conditional distribution $P(y|\mathbf{x})$, where $y \in Y$. Suppose that Ψ_s and Ψ_t are two domains derived from Ψ, they are deemed to be different when $X_s \neq X_t$ and/or $P_s(\mathbf{x}) \neq P_t(\mathbf{x})$. Homoplastically, two tasks Γ_s and Γ_t derived from Γ are different when $Y_s \neq Y_t$ and/or $P_s(y|\mathbf{x}) \neq P_t(y|\mathbf{x})$.

Based on the above definitions, the target of OS-JDA-MR-T-TSK-FC is to train a predictive function on a source domain Ψ_s having N-labeled EEG epochs $\{(\mathbf{x_i}, y_i)\}_{i=1}^{N}$ and a target domain Ψ_t having M-labeled EEG subject-specific epochs $\{(\mathbf{x_i}, y_i)\}_{i=1}^{M}$ to predict the class label of a unseen epoch in the target domain with a low expected error under the hypotheses that $\Psi_s = \Psi_t$, $Y_s = Y_t$, $P_s(\mathbf{x}) \neq P_t(\mathbf{x})$, and $P_s(y|\mathbf{x}) \neq P_t(y|\mathbf{x})$.

OS-JDA-MR-T-TSK-FC

- Online Transfer Learning Framework

Because the classic one-order TSK fuzzy classifier (1-TSK-FC) (Deng et al., 2015; Jiang Y. et al., 2017a; Zhang J. et al., 2018; Zhang et al., 2019) is considered as the basic component of our online transfer learning framework, we first give some details about 1-TSK-FC before introducing our framework.

The kth fuzzy rule involved in 1-TSK-FC is formulated as the following *if–then* form:

$$\begin{aligned} &\text{If } x_{i1} \text{ is } A_1^k \wedge x_{i2} \text{ is } A_2^k \wedge \ldots \wedge x_{id} \text{ is } A_d^k, \\ &\text{then } f^k(\mathbf{x_i}) = p_0^k + p_1^k x_{i1} + \ldots + p_d^k x_{id}, \end{aligned} \tag{1}$$

where $k = 1, 2, \ldots, K$, K represents the total number of fuzzy rules 1-TSK-FC uses. $\mathbf{x_i} = [x_{i1}, x_{i2}, \ldots, x_{id}]^T$ represents the ith object contains d features. A_j^k in (1) represents a fuzzy set subscribed by x_{ij} for the kth fuzzy rule, and $\wedge$ represents a fuzzy conjunction operator. Each fuzzy rule is premised on the feature space and maps the fuzzy sets in the feature space into a varying singleton represented by $f^k(\mathbf{x_i})$. After the steps of inference and defuzzification, the predictive function $y^o(\bullet)$ for an unseen object $\mathbf{x}$ is formulated as the following form:

$$y^o(\mathbf{x}) = \sum_{k=1}^{K} \left(\mu^k(\mathbf{x}) / \sum_{k'=1}^{K} \mu^{k'}(\mathbf{x}) \right) f^k(\mathbf{x}) = \sum_{k=1}^{K} \left(\tilde{\mu}(\mathbf{x}) \right) f^k(\mathbf{x}), \tag{2}$$

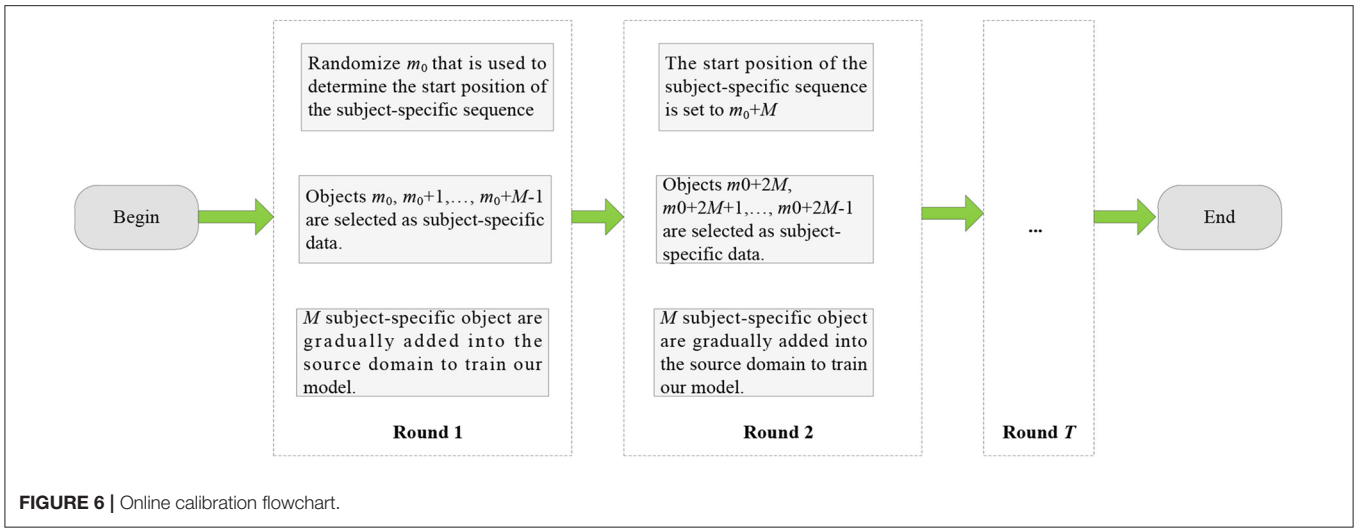

FIGURE 6 | Online calibration flowchart.

in which the $\mu^k(\mathbf{x})$ is expressed as

$$\mu^k(\mathbf{x}) = \prod_{j=1}^{d} \mu_{A_j^k}(x_j), \tag{3}$$

where $\mu_{A_j^k}(x_j)$ can be expressed as the following form when the Gaussian kernel function is employed:

$$\mu_{A_j^k}(x_j) = exp\left(-\left(x_j - c_j^k\right)^2 / 2\left(\delta_j^k\right)^2\right), \tag{4}$$

where c_j^k and δ_j^k are two parameters representing the kernel center and kernel width, respectively. Therefore, training of 1-TSK-FC means to find optimal c_j^k, δ_j^k in the *if* parts, and $\mathbf{p}^k = [p_0^k, p_1^k, \ldots, p_d^k]^T$ in the *then* parts. Referring to the literature (Zhang et al., 2019), we know that parameters in the *if* parts can be trained by clustering techniques. For instance, c_j^k and δ_j^k can be trained by fuzzy *c*-means (FCM) (Gu et al., 2017) as

$$c_j^k = \sum_{i=1}^{N} \mu_{ik} x_{ij} / \sum_{i=1}^{N} \mu_{ik} \tag{5}$$

$$\delta_j^k = h \sum_{i=1}^{N} \mu_{ik} (x_{ij} - c_j^k)^2 \sum_{i=1}^{N} \mu_{ik}, \tag{6}$$

where μ_{ik} is the fuzzy membership degree of $\mathbf{x}_i$ belonging to the kth cluster. h is a regularized parameter that can be always set to 0.5 according to the suggestions in Jiang Y. et al. (2017a). When c_j^k and δ_j^k in the *if* parts are determined by FCM or other similar techniques, for an object $\mathbf{x}_i$ in the training set, let

$$\mathbf{x}_e = (1, (\mathbf{x_i})^T)^T, \tag{7.a}$$

$$\tilde{\mathbf{x}}_i^k = \tilde{\mu}^k(\mathbf{x}_i)\mathbf{x}_e, \tag{7.b}$$

$$\mathbf{x}_{gi} = \left(\left(\tilde{\mathbf{x}}_i^1\right)^T, \left(\tilde{\mathbf{x}}_i^2\right)^T, \ldots, \left(\tilde{\mathbf{x}}_i^K\right)^T\right)^T, \tag{7.c}$$

$$\mathbf{p}^k = (p_0^k, p_1^k, \ldots, p_d^k)^T, \tag{7.d}$$

$$\mathbf{p}_g = ((\mathbf{p}^1)^T, (\mathbf{p}^2)^T, \ldots, (\mathbf{p}^K)^T)^T, \tag{7.e}$$

then we can rewrite the predictive function $y^o(\cdot)$ in (2) as the following form:

$$y^o(\mathbf{x}_i) = \mathbf{p}_\mathbf{g}^T \mathbf{x}_{gi} \tag{8}$$

Referring to Zhou et al. (2017) and Zhang Y. et al. (2018), we formulate an objective function as follows to solve $\mathbf{p}_g$:

$$J_{1-order-TSK-Fc}(\mathbf{p}_g) = \frac{1}{2}(\mathbf{p}_{g,c})^T \mathbf{p}_{g,c} + \frac{\eta}{2} \sum_{i=1}^{N} \left\| (\mathbf{p}_g)^T \mathbf{x}_{gi} - y_i \right\|^2, \tag{9}$$

where the first $\frac{1}{2}(\mathbf{p}_g)^T \mathbf{p}_g$ is a generalization term, the second is a square error term, and $\eta > 0$ is balance parameter used to control the tolerance of errors and the complexity of 1-TSK-FC. By setting the partial derivative of the objective function w.r.t $\mathbf{p}_g$ to zero, that is, $\partial J_{1-order-TSK-FS}(\mathbf{p}_g)/\partial \mathbf{p}_g = 0$, we can compute $\mathbf{p}_g$ analytically as

$$\mathbf{p}_g = \left(\mathbf{I}_{k(d+1)\times k(d+1)} + \sum_{i=1}^{N} \mathbf{x}_{gi}(\mathbf{x}_{gi})^T\right)^{-1} \times \left(\eta \sum_{i=1}^{N} \mathbf{x}_{gi} y_i\right). \tag{10}$$

In this study, 1-TSK-FC is taken as the basic learning component to support the transfer learning framework. Many previous works (Yang et al., 2014; Jiang et al., 2017c) explored the marginal distribution adaption between the source domain and the target domain for transfer learning. In our framework, we introduce conditional distribution adaption to further minimize the distribution difference. Additionally, we impose manifold

consistency on the marginal distribution. Therefore, the transfer learning framework can be formulated as

$$f = \arg\min_{f} [\sum_{i=1}^{N} \ell(f(\mathbf{x}_i), y_i) + \omega_t \sum_{i=N+1}^{N+M} \ell(f(\mathbf{x}_i), y_i)] + \lambda_1[D(J_s, J_t)] + \lambda_2[M(P_s, P_t)], \quad (11)$$

where ω_t in the first term is the overall weights of the specific-subject objects. Generally, ω_t should be larger than 1 so that more emphasis is given to objects in Ψ_s than Ψ_t. Therefore, we set ω_t to $\omega_t = \max(2, \sigma \cdot N/M)$. λ_1 and λ_2 are regularization parameters. The first term contains two parts: the first is to measure the loss on Ψ_s, and the second is to measure the loss in Ψ_t. The second one is the joint distribution adaption term, and the third one is the manifold regularization term. Below, we will explain how to embody them formally.

- Objective function of OS-JDA-MR-T-TSK-FC

Under the framework shown in (11), we specify each term to get the objective function of our online transfer TSK fuzzy classifier OS-JDA-MR-T-TSK-FC.

Loss Function

The squared loss is taken as the loss function to measure the sum of squared training errors on both Ψ_s and Ψ_t; hence, the first term in (11) can be formulated as

$$\sum_{i=1}^{N} (f(\mathbf{x}_i) - y_i)^2 + \omega_t \sum_{i=N+1}^{N+M} (f(\mathbf{x}_i) - y_i)^2 = \sum_{i=1}^{N} (\mathbf{p}_g^T \mathbf{x}_{gi} - y_i)^2 + \omega_t \sum_{i=N+1}^{N+M} (\mathbf{p}_g^T \mathbf{x}_{gi} - y_i)^2, \quad (12)$$

where $f(\mathbf{x}) = \mathbf{p}_g^T \mathbf{x}_{gi}$ is the predictive function of 1-TSK-FC. Suppose we have a diagonal matrix Θ in which each element is defined as

$$\Theta(i,i) = \begin{cases} 1 & 1 \le i \le N \\ \omega_t & N+1 \le i \le N+M \end{cases}. \quad (13)$$

By submitting (13) to (12), then (12) can be rewritten as

$$\sum_{i=1}^{N} (\mathbf{p}_g^T \mathbf{x}_{gi} - y_i)^2 + \omega_t \sum_{i=N+1}^{N+M} (\mathbf{p}_g^T \mathbf{x}_{gi} - y_i)^2 = \sum_{i=1}^{N+M} \Theta(i,i)(\mathbf{p}_g^T \mathbf{x}_{gi} - y_i)^2 = (\mathbf{y}^T - \mathbf{p}_g^T \mathbf{X}_g^T)\Theta(\mathbf{y} - \mathbf{X}_g \mathbf{p}_g), \quad (14)$$

where $\mathbf{X}_g = [\mathbf{x}_{g1}, ..., \mathbf{x}_{gN}, ..., \mathbf{x}_{g(N+M)}]^T$ in which each element $\mathbf{x}_{gi}$ is derived from $\mathbf{x}_i$ by using (7.c).

Joint distribution adaptation

As all we know that even EEG epoch features in Ψ_s and Ψ_t are extracted in the same way, the joint distributions (marginal and conditional distributions) between Ψ_s and Ψ_t are generally different. In order to meet practical requirements, we assume that $P_s(\mathbf{x}) \neq P_t(\mathbf{x})$ and $P_s(y|\mathbf{x}) \neq P_t(y|\mathbf{x})$. Therefore, a joint distribution adaptation should be designed to minimize the distribution similarity (distance) $D(J_s, J_t)$ between Ψ_s and Ψ_t.

First, the projected MMD (Gangeh et al., 2016; Jia et al., 2018; Lin et al., 2018) is employed to the marginal distribution similarity $D(P_s, P_t)$ between Ψ_s and Ψ_t. As a result, $D(P_s, P_t)$ can be expressed as

$$D(P_t, P_s) = \left[\frac{1}{N} \sum_{i=1}^{N} f(\mathbf{x}_i) - \frac{1}{M} \sum_{i=N+1}^{N+M} f(\mathbf{x}_i) \right]^2 = \mathbf{p}_g^T \mathbf{X}_g \Phi \mathbf{X}_g \mathbf{p}_g, \quad (15)$$

where Φ is the MMD matrix, which can be defined as

$$\Phi(i,j) = \begin{cases} 1/N^2, & 1 \le i \le N, 1 \le j \le N \\ 1/M^2, & N+1 \le i, j \le N+M \\ -1/NM & \text{otherwise.} \end{cases} \quad (16)$$

Second, we suppose that $\Psi_{s,c}$ belongs to Ψ_s and its objects are selected by $\{\mathbf{x_i} | \mathbf{x_i} \in \Psi_s \wedge y_i = c\}$, and $\Psi_{t,c}$ belongs to Ψ_t and its objects are selected by $\{\mathbf{x_i} | \mathbf{x_i} \in \Psi_t \wedge y_i = c\}$, where c means the cth class in one domain. Also, for the source domain, N_c is used to denote the number of objects in the cth class, and for the specific-subject objects in the target domain, M_c is used to denote the number of objects in the cth class. Hence, $D(Q_s, Q_t)$ can be expressed as

$$\begin{aligned} D(Q_t, Q_s) &= \sum_{c=1}^{2} [\frac{1}{N_c} \sum_{\mathbf{x}_i \in \Omega_{s,c}} f(\mathbf{x}_i) - \frac{1}{M_c} \sum_{\mathbf{x}_j \in \Omega_{t,c}} f(\mathbf{x}_j)]^2 \\ &= \sum_{c=1}^{2} [\frac{1}{N_c} \sum_{\mathbf{x}_i \in \Omega_{s,c}} \mathbf{p}_g^T \mathbf{x}_{gi} - \frac{1}{M_c} \sum_{\mathbf{x}_j \in \Omega_{t,c}} \mathbf{p}_g^T \mathbf{x}_{gj}]^2, \\ &= \sum_{c=1}^{2} \mathbf{p}_g^T \mathbf{X}_g \Delta_c \mathbf{X}_g \mathbf{p}_g, \\ &= \mathbf{p}_g^T \mathbf{X}_g \Delta \mathbf{X}_g \mathbf{p}_g, \end{aligned} \quad (17)$$

where $\Delta = \sum_{c=1}^{2} \Delta_c$ and Δ_c is an MMD matrix defined as follows:

$$\Delta_c(i,j) = \begin{cases} 1/N_c^2 & \mathbf{x}_i, \mathbf{x}_j \in \Omega_{s,c} \\ 1/M_c^2 & \mathbf{x}_i, \mathbf{x}_j \in \Omega_{t,c} \\ -1/N_c M_c & \mathbf{x}_i \in \Omega_{s,c}, \mathbf{x}_j \in \Omega_{t,c} \\ & \text{or } \mathbf{x}_i \in \Omega_{t,c}, \mathbf{x}_j \in \Omega_{s,c} \\ 0 & \text{otherwise} \end{cases} \quad (18)$$

According to the probability theory, the joint adaption $D(J_s, J_t) = D(P_s, P_t) + D(Q_s, Q_t)$ so that the joint distribution adaptation can be formulated as

$$\begin{aligned} D(J_s, J_t) &= D(P_t, P_s) + D(Q_t, Q_s) \\ &= \mathbf{p}_g^T \mathbf{X}_g \Phi \mathbf{X}_g \mathbf{p}_g + \mathbf{p}_g^T \mathbf{X}_g \Delta \mathbf{X}_g \mathbf{p}_g, \\ &= \mathbf{p}_g^T \mathbf{X}_g (\Phi + \Delta) \mathbf{X}_g \mathbf{p}_g. \end{aligned} \quad (19)$$

Manifold regularization

In the manifold assumption (Lin and Zha, 2008; Chen and Wang, 2011; Geng et al., 2012), it is assumed that if two objects $\mathbf{x_i}$ and $\mathbf{x_j}$ are very close in the intrinsic geometry in terms of $P(\mathbf{x_i})$ and $P(\mathbf{x_j})$, then the corresponding $Q(y_i|\mathbf{x_i})$ and $Q(y_j|\mathbf{x}_j)$ are considered as being similar. That is to say, for the objects in Ψ_s and the calibration objects in Ψ_t, if they are in a manifold, it is expected that their output (conditional probability distribution) differences should be as small as possible. Therefore, the manifold regularization can be formulated as follows under geodesic smoothness,

$$\begin{aligned} M(P_s, P_t) &= \sum_{i=1}^{N+M}\sum_{j=1}^{N+M}(f(\mathbf{x}_i) - f(\mathbf{x}_j))^2 w_{ij} \\ &= \sum_{i=1}^{N+M}\sum_{j=1}^{N+M} f(\mathbf{x}_i) l_{ij} f(\mathbf{x}_j) \\ &= \sum_{i=1}^{N+M}\sum_{j=1}^{N+M} \mathbf{p}_g^T \mathbf{x}_{gi} l_{ij} \mathbf{p}_g^T \mathbf{x}_{gj} \\ &= \mathbf{p}_g^T \mathbf{X}_g \mathbf{L} \mathbf{X}_g \mathbf{p}_g, \end{aligned} \tag{20}$$

Where, $\mathbf{W} = [w_{ij}]_{(N+M)\times(N+M)}$ is the graph affinity matrix in which each element is defined as

$$w_{ij} = \begin{cases} \cos(\mathbf{x}_i, \mathbf{x}_j) & \text{if } \mathbf{x}_i \in \xi_v(\mathbf{x}_j) \text{ or } \mathbf{x}_j \in \xi_v(\mathbf{x}_i) \\ 0 & \text{otherwise} \end{cases}, \tag{21}$$

Where, $\xi_v(\mathbf{x}_i)$ represents a set of v-nearest neighbors of object $\mathbf{x}_i$. $\mathbf{L} = [l_{ij}]_{(N+M)\times(N+M)}$ is the corresponding normalized graph Laplacian matrix of $\mathbf{W}$, which can be computed by $\mathbf{L} = \mathbf{I} - \mathbf{D}^{-1/2}\mathbf{W}\mathbf{D}^{-1/2}$, where $\mathbf{D}$ is the degree matrix in which each diagonal element d_{ii} is computed by $\sum_{j=1}^{N+M} w_{ij}$.

By embedding the manifold regularization into the transfer learning framework, the marginal probability distributions of objects in the target domain and the source domain are fully utilized to guarantee the consistency between the predictive structure of the decision function f and the intrinsic manifold data structure.

By substituting (14), (19), and (20) into our transfer learning framework shown in (12), we can obtain a transfer learning model, that is, OS-JDA-MR-T-TSK-FC as

$$\begin{aligned} f &= \arg\min_f [(\mathbf{y}^T - \mathbf{p}_g^T \mathbf{X}_g^T)\Theta(\mathbf{y} - \mathbf{X}_g \mathbf{p}_g) \\ &\quad + \mathbf{p}_g^T \mathbf{X}_g \lambda_1 (\Phi + \Delta) \mathbf{X}_g \mathbf{p}_g + \mathbf{p}_g^T \mathbf{X}_g \lambda_2 \mathbf{L} \mathbf{X}_g \mathbf{p}_g], \\ &= \arg\min_f [(\mathbf{y}^T - \mathbf{p}_g^T \mathbf{X}_g^T)\Theta(\mathbf{y} - \mathbf{X}_g \mathbf{p}_g) \\ &\quad + \mathbf{p}_g^T \mathbf{X}_g (\lambda_1 (\Phi + \Delta) + \lambda_2 \mathbf{L}) \mathbf{X}_g \mathbf{p}_g]. \end{aligned} \tag{22}$$

We can deduce a closed-form solution of $\mathbf{p}_g$ for the objective function in (26) by setting its derivative w.r.t $\mathbf{p}_g$ to zero as

$$\mathbf{p}_g = [\mathbf{X}_g^T(\Theta + \lambda_1\Phi + \lambda_1\Delta + \lambda_2\mathbf{L})\mathbf{X}_g]^{-1}\mathbf{X}_g^T\Theta\mathbf{y}. \tag{23}$$

Algorithm of OS-JDA-MR-T-TSK-FC

Different from most of the existing transfer models, OS-JDA-MR-T-TSK-FC can leverage knowledge from multiple source domains. However, as we know, too many source domains will improve computational complexity. Additionally, some source domains having significant differences with the target domain may bring some negative transfer knowledge. Therefore, according to Wu et al. (2017), we adopt a distance-based schema to select relative source domains.

We use $\mathbf{v}_{z,c}$ to denote the mean vector of each class in the zth source domain, where $z = 1,2,\ldots, Z$. Similarly, $\mathbf{v}_{t,c}$ is used to denote the mean vector of each class in the target domain. The Euclidean distance between the zth source domain and the target domain can be computed as

$$d(z,t) = \sum_c \left\| \mathbf{v}_{z,c} - \mathbf{v}_{t,c} \right\|^2. \tag{24}$$

With (24), we can get a distance set $\{d(1,t), d(2,t), ..., d(Z,t)\}$ that contains Z domain distances. The distance set then is partitioned by k-means to k groups (in this study, k is set to 2), and the source domains are selected from the cluster who has the smallest center.

As a whole, the training of OS-JDA-MR-T-TSK-FC contains three parts: the first one is source domain selection, the second one is model training on a source domain combining with the target domain, and the last is classifier combination. Algorithm 1 shows the detailed training steps of OS-JDA-MR-T-TSK-FC.

OS-JDA-MR-T-TSK-FC can also be used for multiclassification tasks. According to Zhou et al. (2017), we can convert $\mathbf{y}$ from the space R to the space R^C by that $y_{ij} = 1$ if $y(\mathbf{x}_i) = j$, and $y_{ij} = 0$ otherwise, where $i = 1, 2, ..., N + M$, $j = 1, 2, ..., C$, and C represents the number of classes. Thus, the label space becomes $\mathbf{Y} = [\mathbf{y}_1, ..., \mathbf{y}_N, ..., \mathbf{y}_{N+M}]^T \in R^C$, and $\mathbf{p}_g$ is also converted from R^{d+1} to $R^{(d+1)\times C}$.

Algorithm 1: OS-JDA-MR-T-TSK-FC

Input:

1. $[(\mathbf{x}_1, y_1), (\mathbf{x}_2, y_2), \ldots, (\mathbf{x}_N, y_N), \ldots, (\mathbf{x}_{N+M}, y_{N+M})]^T$
2. ω_t, λ_1, λ_2 and the number of fuzzy rules K;

Output:

1. Training accuracy α_z of each classifier;
2. Final decision function f;

Procedure:

For $z = 1$ to Z

Calculate the Euclidean distance $d(z,t)$ between the zth source domain and the target domain by (24).

End

Partition the distance set $\{d(1,t), d(2,t), ..., d(Z,t)\}$ into two groups.

Select $Z/2$ (as Z') source domains from Z source domains.

For $z = 1$ to Z'

Map $\mathbf{X}$ to $\mathbf{X}_g$ by (7.c);

Calculate Θ, Φ, Δ, and $\mathbf{L}$ by (13), (16), and (18), respectively.

Calculate $\mathbf{p}_g$ and record it as $(\mathbf{p}_g)_z$ by (23);

Use $(\mathbf{p}_g)_z$ to predict $N_z + M$ objects the record the training accuracy as α_z;

End

Return $f(\mathbf{x}) = \alpha_1(\mathbf{p}_g^T)_1\mathbf{x}_g + \alpha_2(\mathbf{p}_g^T)_2\mathbf{x}_g + ... + \alpha_{Z'}(\mathbf{p}_g^T)_{Z'}\mathbf{x}_g$;

TABLE 3 | Average classification performance of the six scenarios in three feature spaces.

	M	0	4	8	12	16	20
KPCA	BL1	0.7962	0.7962	0.7962	0.7962	0.7962	0.7962
	BL2	—	0.6837	0.7460	0.7899	0.8270	0.8536
	BL3	0.7881	0.7761	0.8016	0.8086	0.8048	0.8174
	TSVM	**0.8723**	0.8765	0.8810	0.8864	0.8811	0.8927
	ARRLS	0.8684	0.8217	0.8742	0.8684	0.8821	0.8823
	OS-JDA-MR-T-TSK-FC	0.8701	**0.8943**	**0.9164**	**0.9191**	**0.9214**	**0.9251**
PWD	BL1	0.8618	0.8618	0.8618	0.8618	0.8618	0.8618
	BL2	—	0.7151	0.8597	0.8867	0.9057	0.9176
	BL3	0.8505	0.8503	0.8661	0.8685	0.8751	0.8795
	TSVM	**0.9232**	**0.9271**	0.9269	0.9312	0.9292	0.9344
	ARRLS	0.9157	0.9204	0.9224	0.9287	0.9312	0.9336
	OS-JDA-MR-T-TSK-FC	0.8864	0.9073	**0.9278**	**0.9314**	**0.9332**	**0.9376**
STFT	BL1	0.9129	0.9129	0.9129	0.9129	0.9129	0.9129
	BL2	—	0.7619	0.8531	0.8674	0.8873	0.8962
	BL3	0.9011	0.8923	0.8924	0.8951	0.8989	0.9107
	TSVM	0.9365	**0.9459**	0.9467	0.9502	0.9581	0.9524
	ARRLS	**0.9425**	0.9410	0.9356	0.9478	0.9452	0.9550
	OS-JDA-MR-T-TSK-FC	0.9031	0.9214	**0.9500**	**0.9517**	**0.9585**	**0.9619**

The best performance is marked in bold.

RESULTS

Experiment setups and comparison results will be reported in this section.

Setups

For fair, we introduce three baselines and one transfer learning algorithm for comparison study. The three baselines all use 1-TSK-FC for training. But their training sets are different.

(1) Baseline 1 (BL1). Its training set consists of the five source domains directly connected, and its testing set is the target domain. Therefore, BL1 is considered as a calibration-independent classifier, which does not use the subject-specific data in the target domain for training.
(2) Baseline 2 (BL2). It uses only subject-specific calibration EEG data in the target domain for training. Its testing set is the unlabeled data in the target domain. Therefore, BL2 is considered as a source domain-independent classifier, which does not consider the EEG data in the source domains at all.
(3) Baseline 3 (BL3). BL3 is trained on five training sets, receptively. Each set consisted of a source domain and the subject-specific data in the target domain. The five trained models are finally combined by a weight schema that is also used in Algorithm 1. Its testing set is the unlabeled data in the target domain
(4) Transfer support vector machine (TSVM) (Chapelle et al., 2008). It trains five TSVM classifiers by combining unlabeled EEG data in the target domain for semisupervised learning. The five trained models are finally combined by a weight schema that is also used in Algorithm 1.
(5) ARRLS (Long et al., 2014). It trains five ARRLS classifiers by combining unlabeled EEG data in the target domain for supervised learning. The five trained models are finally combined by a weight schema that is also used in Algorithm 1.

Experimental Results

In this section, we report the experimental results from several aspects, that is, classification performance, interpretability, and robustness.

- Classification Performance

Table 3 shows the average classification performance of the six scenarios in the KPCA feature space, PWD feature space, and STFT feature space, respectively. **Table 4** shows the classification performance on KPCA features. **Table 5** shows the classification performance on PWD features, and **Table 6** shows the classification performance on STFT features. The best results are marked in bold.

- Interpretability

Unlike TSVM that works in a black-box manner, the proposed OS-JDA-MR-T-TSK-FC has high interpretability because 1-TSK-FC is taken as the basic component. **Table 7** shows the five trained fuzzy rules (antecedent and consequent parameters) on SC-1 in the KPCA feature space.

- Robustness

From the objective function of OS-JDA-MR-T-TSK-FC, we see that there are three parameters, that is, ω_t (σ), λ_1, and λ_2 that should be fixed before a classification task. So, we should consider

TABLE 4 | Classification performance on six scenarios in the KPCA feature space.

	M	0	4	8	12	16	20
SC-1	BL1	0.7254	0.7254	0.7253	0.7253	0.7253	0.7253
	BL2	—	0.6507	0.6949	0.7285	0.7438	0.8124
	BL3	0.7845	0.7899	0.8283	0.8535	0.8332	0.8404
	TSVM	0.8527	0.8564	0.8661	0.8675	0.8684	0.8690
	ARRLS	0.8455	0.8631	0.8874	0.8584	0.8632	0.8741
	OS-JDA-MR-T-TSK-FC	0.8835	0.9124	0.9187	0.9123	0.9201	0.9206
SC-2	BL1	0.8050	0.8050	0.8050	0.8050	0.8050	0.8050
	BL2	—	0.6031	0.7458	0.8727	0.9242	0.9447
	BL3	0.7811	0.7912	0.8821	0.8642	0.8097	0.8358
	TSVM	0.9231	0.9305	0.9289	0.9359	0.9399	0.9378
	OS-JDA-MR-T-TSK-FC	0.9187	0.9364	0.9397	0.9415	0.9434	0.9439
SC-3	BL1	0.9045	0.9045	0.9045	0.9045	0.9045	0.9045
	BL2	—	0.8079	0.8689	0.8667	0.8418	0.9191
	BL3	0.8008	0.7838	0.8037	0.8165	0.7804	0.8239
	TSVM	0.9235	0.9214	0.9298	0.9311	0.9287	0.9324
	ARRLS	0.9154	0.9200	0.9147	0.9228	0.9142	0.9364
	OS-JDA-MR-T-TSK-FC	0.9111	0.9125	0.9341	0.9399	0.9421	0.9433
SC-4	BL1	0.6657	0.6657	0.6657	0.6657	0.6657	0.6657
	BL2	—	0.7132	0.7819	0.7745	0.8431	0.8397
	BL3	0.7944	0.7564	0.7506	0.7587	0.7988	0.7993
	TSVM	0.8789	0.8897	0.8942	0.8864	0.8911	0.9001
	ARRLS	0.8654	0.8412	0.8553	0.8631	0.8745	0.8924
	OS-JDA-MR-T-TSK-FC	0.8542	0.8596	0.9241	0.9321	0.9365	0.9387
SC-5	BL1	0.8498	0.8498	0.8498	0.8498	0.8498	0.8498
	BL2	—	0.6349	0.7119	0.7333	0.7425	0.7773
	BL3	0.7751	0.7607	0.7758	0.7677	0.8121	0.8364
	TSVM	0.9024	0.9354	0.9142	0.9321	0.9368	0.9410
	ARRLS	0.8963	0.9224	0.9021	0.9361	0.9556	0.9254
	OS-JDA-MR-T-TSK-FC	0.8654	0.8684	0.9023	0.9234	0.9257	0.9341
SC-6	BL1	0.8267	0.8267	0.8267	0.8267	0.8267	0.8267
	BL2	—	0.6921	0.6723	0.7636	0.8667	0.8283
	BL3	0.7926	0.7743	0.7689	0.7908	0.7946	0.7683
	TSVM	0.8756	0.8632	0.8786	0.8801	0.8698	0.8841
	ARRLS	0.8654	0.8604	0.8552	0.8742	0.8536	0.8774
	OS-JDA-MR-T-TSK-FC	0.8120	0.8763	0.8796	0.8652	0.8605	0.8697

the robustness OS-JDA-MR-T-TSK-FC to them. The sensitivity analysis results are shown in **Figure 7**.

DISCUSSIONS

We observe from **Table 3** that the proposed OS-JDA-MR-T-TSK-FC wins the best average performance across the six transfer scenarios in all feature spaces when the number of specific-subject objects is more than 4. Especially compared with the three baselines, the advantages are more obvious.

Moreover, the classification results in **Tables 4–6** also exhibit the following four characteristics:

- BL1 does not use the specific-subject objects, so its accuracy is independent on *M*, whereas the other four classifiers depend on *M*, and it is intuitive that they gradually perform better than BL1 with the increasing of *M*.
- BL2 is only trained by the subject-specific objects. Therefore, BL2 becomes unusable when *M* is set to 0. But BL1, BL3, TSVM, and OS-JDA-MR-T-TSK-FC can work because, except subject-specific objects, they also leverage training objects from the source domains. Compared with other algorithms,

TABLE 5 | Classification performance on six scenarios in the WPD feature space.

	M	0	4	8	12	16	20
SC-1	BL1	0.9711	0.9711	0.9711	0.9711	0.9711	0.9711
	BL2	—	0.6718	0.9166	0.9142	0.9243	0.9513
	BL3	0.8632	0.7986	0.8542	0.8611	0.8511	0.8442
	TSVM	0.9735	0.9653	0.9842	0.9811	0.9765	0.9647
	ARRLS	0.9632	0.9553	0.8745	0.9567	0.9651	0.9663
	OS-JDA-MR-T-TSK-FC	0.9271	0.9365	0.9654	0.9689	0.9714	0.9736
SC-2	BL1	0.8626	0.8626	0.8626	0.8626	0.8626	0.8626
	BL2	—	0.5873	0.8135	0.8363	0.8627	0.8751
	BL3	0.7895	0.8463	0.8468	0.8532	0.8324	0.8574
	TSVM	0.9021	0.9234	0.9145	0.9310	0.9256	0.9345
	ARRLS	0.8954	0.9321	0.9236	0.9524	0.9125	0.9263
	OS-JDA-MR-T-TSK-FC	0.8852	0.9024	0.9210	0.9253	0.9356	0.9363
SC-3	BL1	0.8388	0.8388	0.8388	0.8388	0.8388	0.8388
	BL2	—	0.8095	0.8067	0.8327	0.8287	0.8865
	BL3	0.7986	0.8023	0.8235	0.8310	0.8352	0.8298
	TSVM	0.8836	0.8896	0.8658	0.8874	0.8697	0.8920
	ARRLS	0.8759	0.8963	0.8741	0.8523	0.8478	0.8623
	OS-JDA-MR-T-TSK-FC	0.7968	0.8541	0.8553	0.8687	0.8723	0.8852
SC-4	BL1	0.9024	0.9024	0.9024	0.9024	0.9024	0.9024
	BL2	—	0.7778	0.9830	0.9818	0.9882	0.9957
	BL3	0.9123	0.9089	0.9189	0.9214	0.9241	0.9298
	TSVM	0.9436	0.9426	0.9463	0.9500	0.9431	0.9498
	ARRLS	0.9355	0.9664	0.9354	0.9632	0.9311	0.9522
	OS-JDA-MR-T-TSK-FC	0.8936	0.9214	0.9386	0.9399	0.9289	0.9400
SC-5	BL1	0.7930	0.7930	0.7930	0.7930	0.7930	0.7930
	BL2	—	0.9047	0.8757	0.8460	0.9454	0.9091
	BL3	0.8826	0.8854	0.8898	0.8754	0.9356	0.9367
	TSVM	0.9241	0.9265	0.9321	0.9222	0.9412	0.9398
	ARRLS	0.9021	0.9214	0.8954	0.8857	0.9145	0.9236
	OS-JDA-MR-T-TSK-FC	0.9311	0.9354	0.9512	0.9568	0.9612	0.9544
SC-6	BL1	0.8029	0.8029	0.8029	0.8029	0.8029	0.8029
	BL2	—	0.5397	0.7627	0.9090	0.8849	0.8879
	BL3	0.8569	0.8601	0.8635	0.8686	0.8720	0.8789
	TSVM	0.9124	0.9154	0.9187	0.9156	0.9189	0.9257
	ARRLS	0.9214	0.9220	0.9201	0.9258	0.9361	0.9123
	OS-JDA-MR-T-TSK-FC	0.8845	0.8942	0.9354	0.9289	0.9298	0.9364

when M is too small, BL2 performs so badly because it cannot get enough training patterns from subject-specific objects.

- When M is set to 0, TSVM always achieves the best performance. With the subject-specific objects gradually added into the training set, OS-JDA-MR-T-TSK-FC soon performs better than TSVM, which indicates that significant differences exist among the domains. Hence, a domain-dependent classifier, for example, TSVM is not very expected in our online transfer scenarios.
- When one batch (four subject-specific objects are taken as a batch in our experiments) or at most two batches of subject-specific objects are added into the training set, the classification performance of OS-JDA-MR-T-TSK-FC becomes stable. That is to say, the number of subject-specific objects OS-JDA-MR-T-TSK-FC needs is very small. So, OS-JDA-MR-T-TSK-FC meets the practical requirements because subject-specific objects are very few in real-world applications.

TABLE 6 | Classification performance on six scenarios in the STFT feature space.

	M	0	4	8	12	16	20
SC-1	BL1	0.8915	0.8915	0.8915	0.8915	0.8915	0.8915
	BL2	—	0.6825	0.7627	0.8400	0.8248	0.8680
	BL3	0.8469	0.8500	0.8598	0.8541	0.8745	0.9021
	TSVM	0.9235	0.9265	0.9211	0.9365	0.9410	0.9389
	ARRLS	0.9123	0.9025	0.9145	0.9452	0.9321	0.9225
	OS-JDA-MR-T-TSK-FC	0.9231	0.9212	0.9536	0.9456	0.9589	0.9610
SC-2	BL1	0.9572	0.9572	0.9572	0.9572	0.9572	0.9572
	BL2	—	0.8412	0.9152	0.8363	0.9215	0.9148
	BL3	0.9356	0.9398	0.9410	0.9369	0.9459	0.9502
	TSVM	0.9578	0.9689	0.9712	0.9754	0.9741	0.9710
	ARRLS	0.9421	0.9532	0.9456	0.9623	0.9456	0.9361
	OS-JDA-MR-T-TSK-FC	0.9241	0.9254	0.9698	0.9789	0.9874	0.9863
SC-3	BL1	0.9452	0.9452	0.9452	0.9452	0.9452	0.9452
	BL2	—	0.8730	0.8983	0.9600	0.9346	0.9148
	BL3	0.9563	0.9541	0.9568	0.9642	0.9687	0.9610
	TSVM	0.9478	0.9620	0.9536	0.9587	0.9641	0.9638
	ARRLS	0.9361	0.9521	0.9357	0.9430	0.9347	0.9637
	OS-JDA-MR-T-TSK-FC	0.9147	0.9689	0.9700	0.9453	0.9432	0.9564
SC-4	BL1	0.9004	0.9004	0.9004	0.9004	0.9004	0.9004
	BL2	—	0.7619	0.8813	0.8363	0.8823	0.9078
	BL3	0.9214	0.9154	0.9354	0.9410	0.9258	0.9320
	TSVM	0.9425	0.9489	0.9631	0.9562	0.9511	0.9468
	ARRLS	0.9364	0.9258	0.9567	0.9412	0.9368	0.9387
	OS-JDA-MR-T-TSK-FC	0.9023	0.9128	0.9587	0.9599	0.9610	0.9632
SC-5	BL1	0.9064	0.9064	0.9064	0.9064	0.9064	0.9064
	BL2	—	0.7778	0.9322	0.8727	0.9424	0.9177
	BL3	0.8921	0.8525	0.8651	0.8621	0.8547	0.8854
	TSVM	0.9257	0.9365	0.9278	0.9421	0.9532	0.9544
	ARRLS	0.9025	0.9236	0.9123	0.9367	0.9458	0.9422
	OS-JDA-MR-T-TSK-FC	0.8789	0.9024	0.9268	0.9541	0.9587	0.9635
SC-6	BL1	0.8766	0.8766	0.8766	0.8766	0.8766	0.8766
	BL2	—	0.6349	0.7288	0.8593	0.8183	0.8539
	BL3	0.8541	0.8423	0.7963	0.8125	0.8236	0.8333
	TSVM	0.9214	0.9325	0.9432	0.9323	0.9654	0.9398
	ARRLS	0.9123	0.9236	0.9347	0.9415	0.9523	0.9225
	OS-JDA-MR-T-TSK-FC	0.8756	0.8974	0.9214	0.9265	0.9421	0.9412

In addition to classification performance, interpretability is also a main characteristic of the proposed OS-JDA-MR-T-TSK-FC. From **Table 7**, we see that it generates five interpretable fuzzy rules on SC-1 in the KPCA feature space. Each feature in a fuzzy rule can be interpreted as the energy of an EEG signal band, and each fuzzy membership function is endowed with a linguistic description. For example, "x_1 is A_1^k" in the antecedent of a fuzzy rule can be interpreted as "the energy of an EEG band is a litter high," where the term "a little high" can be replaced by others such as "a litter low," "medium," or "high." In this way, suppose I am an expert from the field of EEG signal analysis, I assign five kinds of linguistic descriptions to each fuzzy membership function, that is, "low," "a little low," "medium," "a little high," and "high." Therefore, for the first fuzzy rule in **Table 7**, it can be interpreted as follows:

If the energy of an EEG signal band (band 1) is "high," and the energy of an EEG signal band (band 2) is "a little low," and the energy of an EEG signal band (band 3) is "low," and the energy of an EEG signal band (band 4) is "low," and the energy of an EEG signal band (band 5) is "low," and the energy of an EEG signal band

TABLE 7 | Fuzzy rules trained on SC-1 in the KPCA feature space.

OS-JDA-MR-T-TSK-FC			
Fuzzy rules: If x_1 is $A_1^k \wedge x_2$ is $A_2^k \wedge \ldots \wedge x_d$ is A_d^k, then $f^k(\mathbf{x}) = p_0^k + p_1^k x_1 + \ldots + p_d^k x_d, k = 1, 2, \ldots, K$			
SC-1	Rule No.	Antecedent parameters $\mathbf{c}^k = [c_1^k, c_2^k, \ldots, c_d^k]^T, \delta^k = [\delta_1^k, \delta_2^k, \ldots, \delta_d^k]^T$	Consequent parameters $\mathbf{p}^k = [p_0^k, p_1^k, \ldots, p_d^k]^T$
	1	$\mathbf{c}^1$ = [0.0081,-0.0014,-0.0027,-0.0032,-0.0043,-0.0031], δ^1 = [0.0023,0.0055,0.0036,0.0041,0.0021,0.0028]	$\mathbf{p}^1$ = [0.2531, 0.4321, −0.5123, 025623, 0.2415, −0.0423, 0.0012; 0.3135, 0.5287, 0.4452, −0.5342, 0.2342, −0.9734, −0.3244]^T
	2	$\mathbf{c}^2$ = [0.0055,0.0031, -0.0023,0.0022,-0.0098,-0.0021], δ^2 = [0.0050,0.0036,0.0043,0.0044,0.0041,0.0033]	$\mathbf{p}^2$ = [0.1213, −0.5354, 0.5653, −0.1243, 0.3452, 0.0642, 0.0043; 0.0633, −0.6342, 0.1453, 0.3345, −0.0234, 0.0078, −0.0015]^T
	3	$\mathbf{c}^3$ = [0.0498,0.0411,0.0014,0.0056,0.0016,-0.0028], δ^3 = [0.0046,0.0034,0.0057,0.0057,0.0046,0.0037]	$\mathbf{p}^3$ = [0.2342, −0.8456, −0.6345, −0.0134, −0.0267, 0.0111, −0.0042; −0.0534, 0.0324, 0.0434, 0.0116, 0.0362, −0.0632, 0.0027]^T
	4	$\mathbf{c}^4$ = [0.0673,0.0432,0.0014,0.0057,0.0014,-0.0033], δ^4 = [0.0041,0.0032,0.0032,0.0011,0.0034,0.0015]	$\mathbf{p}^4$ = [0.0454, −0.4345, −0.2563, −0.0412, 0.0345, 0.0163, 0.0423; 0.0123, −0.0532, 0.1634, 0.2134, −0.0745, 0.0122, 0.0011]^T
	5	$\mathbf{c}^5$ = [0.0042,0.0098,0.0015,0.0034,0.0047,-0.0011], δ^5 = [0.0047,0.0032,0.0044,0.0076,0.0034,0.0043]	$\mathbf{p}^5$ = [0.0177, 0.0134, 0.0214, 0.0034, −0.0045, 0.0023, −0.0013; 0.0034, 0.0053, −0.0123, 0.0054, 0.0053, 0.0016, 0.0014]^T

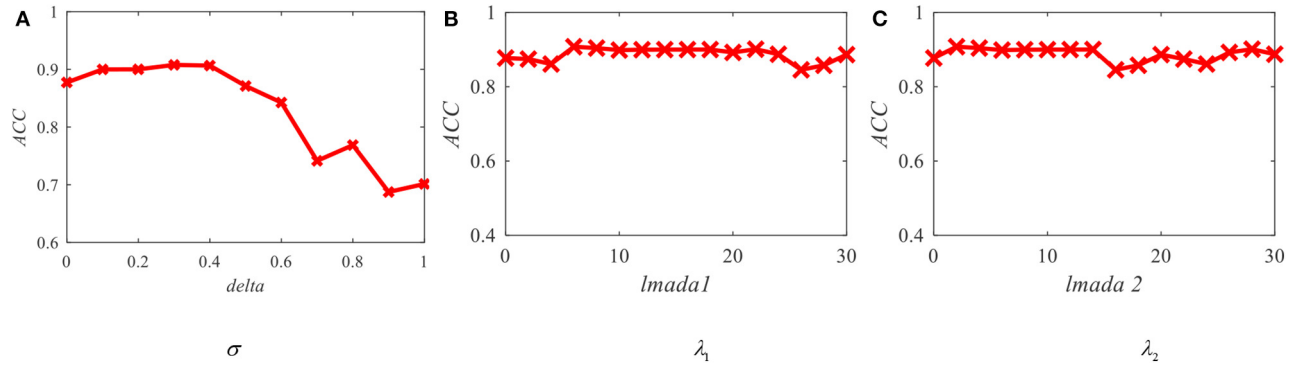

FIGURE 7 | Average accuracy of OS-JDA-MR-T-TSK-FC in the KPCA feature space with different parameters. **(A)** Robustness w.r.t delta; **(B)** robustness w.r.t lmada 1; **(C)** robustness w.r.t lmada 2.

*(band 6) is "low," **then** the consequent of the first fuzzy rule can be expressed as:*

$$f^1(\mathbf{x}) = 0.2531 + 0.4321x_1 - 0.5123x_2 + 0.2562x_3 + 0.2415x_4 - 0.0423x_5 + 0.0012x_6 + 0.3153 - 0.5278x_1 + 0.4452x_2 - 0.5342x_3 + 0.2342x_4 - 0.9734x_5 - 0.3244x_6.$$

From **Figure 6**, we observe that O-T-TSK-FC is robust to σ in the range of [0.1, 0.4], to λ_1 in the range of (Geng et al., 2012; Jiang et al., 2017c), and to λ_2 in the range of (Ghosh-Dastidar et al., 2008; Mallapragada et al., 2009), respectively.

CONCLUSIONS

In this study, we propose a seizure classification model OS-JDA-MR-T-TSK-FC using an online selective transfer TSK fuzzy classifier with a joint distribution adaption and manifold regularization. We use epilepsy EEG signals provided by the University of Bonn as the original data and construct six transfer scenarios in three kinds of feature spaces to demonstrate the promising performance of OS-JDA-MR-T-TSK-FC. We also generate four baselines and introduce a transfer SVM model for fair comparison. The experimental results show that OS-JDA-MR-T-TSK-FC performs better than baselines and the introduced two transfer models. However, in this study, we only consider how to select the source domains. Recent studies show that dynamically selecting useful samples from the source domain can effectively induce the learning on the target domain. Therefore, in our future work, we will try to develop a mechanism, for example, classification error consensus to select most useful samples from the source domain.

DATA AVAILABILITY STATEMENT

The original EEG data are available in http://www.meb.unibonn.de/epileptologie/science/physik/eegdata.html.

AUTHOR CONTRIBUTIONS

YZ designed the whole algorithm and experiments. ZZ, HB, and WL contributed on code

implementation, and LW gave some suggestions to the writing.

FUNDING

This work was supported in part by the National Natural Science Foundation of China under Grants No. 81873915, 817017938, by Ministry of Science and Technology Key Research and Development Program of China under Grants no. 2018YFC0116902.

ACKNOWLEDGMENTS

We thank the reviewers whose comments and suggestions helped improve this manuscript.

REFERENCES

Chapelle, O., Sindhwani, V., and Keerthi, S. S., (2008) Optimization techniques for semi-supervised support vector machines. *J. Mach. Learn. Res.* 9, 203–233.

Chen, K., and Wang, S. (2011). Semi-supervised learning via regularized boosting working on multiple semi-supervised assumptions. *IEEE Trans. Pattern Anal. Mach. Intell.* 33, 129–143. doi: 10.1109/TPAMI.2010.92

Deng, Z., Cao, L., Jiang, Y., and Wang, S. (2015). Minimax probability TSK fuzzy system classifier: a more transparent and highly interpretable classification model. *IEEE Trans. Fuzzy Systems* 23, 813–826. doi: 10.1109/TFUZZ.2014.2328014

Dornaika, F., and El Traboulsi, Y. (2016). Learning flexible graph-based semi-supervised embedding. *IEEE Trans. Cybern.* 46, 206–218. doi: 10.1109/TCYB.2015.2399456

Gangeh, M. J., Tadayyon, H., Sannachi, L., Sadeghi-Naini, A., Tran, W., T., and Czarnota, G., J. (2016). Computer aided theragnosis using quantitative ultrasound spectroscopy and maximum mean discrepancy in locally advanced breast cancer. *IEEE Trans. Med. Imaging* 35, 778–790. doi: 10.1109/TMI.2015.2495246

Geng, B., Tao, D., Xu, C., Yang, L., and Hua, X. (2012). Ensemble manifold regularization. *IEEE Trans. Pattern Anal. Mach. Intell.* 34, 1227–1233. doi: 10.1109/TPAMI.2012.57

Ghosh-Dastidar, S., Adeli, H., and Dadmehr, N. (2008). Principal component analysis-enhanced cosine radial basis function neural network for robust epilepsy and seizure detection. *IEEE Trans. Biomed. Eng.* 55, 512–518. doi: 10.1109/TBME.2007.905490

Gu, X., Chung, F., Ishibuchi, H., and Wang, S. (2017). Imbalanced TSK fuzzy classifier by cross-class bayesian fuzzy clustering and imbalance learning. *IEEE Trans. Systems Man Cybern. Systems* 47, 2005–2020. doi: 10.1109/TSMC.2016.2598270

Jia, X., Zhao, M., Di, Y., Yang, Q., and Lee, J. (2018). Assessment of data suitability for machine prognosis using maximum mean discrepancy. *IEEE Trans. Ind. Electron.* 65, 5872–5881. doi: 10.1109/TIE.2017.2777383

Jiang, Y., Deng, Z., Chung, F., and Wang, S. (2017a). Realizing two-view TSK fuzzy classification system by using collaborative learning. *IEEE Trans. Systems Man Cybern. Systems* 47, 145–160. doi: 10.1109/TSMC.2016.2577558

Jiang, Y., Deng, Z., Chung, F. L., Wang, G., Qian, P., Choi, K. S., et al. (2017b). Recognition of Epileptic EEG Signals Using a Novel Multiview TSK Fuzzy System. *IEEE Trans. Fuzzy Systems* 25, 3–20. doi: 10.1109/TFUZZ.2016.2637405

Jiang, Y., Wu, D., Deng, Z., Qian, P., Wang, J., Wang, G., et al. (2017c). Seizure classification from EEG signals using transfer learning, semi-supervised learning and TSK fuzzy system. *IEEE Trans. Neural Sys. Rehabil. Eng.* 25, 2270–2284. doi: 10.1109/TNSRE.2017.2748388

Jiang, Y., Zhang, Y., Lin, C., Wu, D., and Lin, C. (2020). EEG-based driver drowsiness estimation using an online multi-view and transfer TSK fuzzy system. *IEEE Trans. Intell. Transportation Systems*. 1–13. doi: 10.1109/TITS.2020.2973673

Jiang, Z., Chung, F., and Wang, S. (2019). Recognition of multiclass epileptic EEG signals based on knowledge and label space inductive transfer. *IEEE Trans. Neural Sys. Rehabil. Eng.* 27, 630–642. doi: 10.1109/TNSRE.2019.2904708

Li, J., Tao, D., Hu, W., and Li, X. (2005). "Kernel principle component analysis in pixels clustering," in *The 2005 IEEE/WIC/ACM International Conference on Web Intelligence (WI'05),* (Compiegne: IEEE). 786–789.

Li, S. (2011). "Speech Denoising Based on Improved Discrete Wavelet Packet Decomposition," in *2011 International Conference on Network Computing and Information Security* (Guilin: IEEE), 415–419. doi: 10.1109/NCIS.2011.182

Lin, T., and Zha, H. (2008). Riemannian manifold learning. *IEEE Trans. Pattern Anal. Mach. Intell.* 30, 796–809. doi: 10.1109/TPAMI.2007.70735

Lin, W., Mak, M., and Chien, J. (2018). Multisource I-vectors domain adaptation using maximum mean discrepancy based autoencoders. *IEEE/ACM Trans. Audio Speech Lang. Proc.* 26, 2412–2422. doi: 10.1109/TASLP.2018.2866707

Long, M., Wang, J., Ding, G., Pan, S. J., and Yu, P., S. (2014). Adaptation regularization: a general framework for transfer learning. *IEEE Trans. Knowl. Data Eng.* 26, 1076–1089. doi: 10.1109/TKDE.2013.111

Mallapragada, P. K., Jin, R., Jain, A., K., and Liu, Y. (2009). SemiBoost: boosting for semi-supervised learning. *IEEE Trans. Pattern Anal. Mach. Intell.* 31, 2000–2014. doi: 10.1109/TPAMI.2008.235

Parvez, M. Z., and Paul, M. (2016). Epileptic seizure prediction by exploiting spatiotemporal relationship of EEG signals using phase correlation. *IEEE Trans. Neural Systems Rehabil. Eng.* 24, 158–168. doi: 10.1109/TNSRE.2015.2458982

Pei, S. C., Yeh, M. H., and Luo, T. L. (1999). Fractional Fourier series expansion for finite signals and dual extension to discrete-time fractional Fourier transform. *IEEE Trans. Signal Proc.* 47, 2883–2888. doi: 10.1109/78.790671

Tian, X., Deng, Z., Ying, W., Choi, K. S., Wu, D., Qin, B., et al. (2019). Deep multi-view feature learning for EEG-based epileptic seizure detection. *IEEE Trans. Neural Systems Rehabil. Eng.* 27, 1962–1972. doi: 10.1109/T.N.S.R.E.2019.2940485

Van Hese, P., Martens, J., Waterschoot, L., Boon, P., and Lemahieu, I. (2009). Automatic detection of spike and wave discharges in the EEG of genetic absence epilepsy rats from strasbourg. *IEEE Trans. Biomed. Eng.* 56, 706–717. doi: 10.1109/TBME.2008.2008858

Wang, Y., Chen, Y., Su, A., W., Shaw, F., and Liang, S. (2016). Epileptic pattern recognition and discovery of the local field potential in amygdala kindling process. *IEEE Trans. Neural Systems Rehabil. Eng.* 24, 374–385. doi: 10.1109/TNSRE.2015.2512258

Wu, D., Lawhern, V., J., Gordon, S., Lance, B. J., and Lin, C. (2017). Driver drowsiness estimation from EEG signals using online weighted adaptation regularization for regression (OwARR). *IEEE Trans. Fuzzy Systems* 25, 1522–1535. doi: 10.1109/TFUZZ.2016.2633379

Yang, C., Deng, Z., Choi, K. S., Jiang, Y., and Wang, S. (2014). Transductive domain adaptive learning for epileptic electroencephalogram recognition. *Artif. Intell. Med.* 62, 165–177. doi: 10.1016/j.artmed.2014.10.002

Zhang, J., Deng, Z., Choi, K., and Wang, S. (2018). Data-driven elastic fuzzy logic system modeling: constructing a concise system with human-like inference mechanism. *IEEE Trans. Fuzzy Sys.* 26, 2160–2173. doi: 10.1109/TFUZZ.2017.2767025

Zhang, Y., Dong, J., Zhu, J., and Wu, C. (2019). Common and special knowledge-driven TSK fuzzy system and its modeling and application for epileptic EEG signals recognition. *IEEE Access* 7, 127600–127614. doi: 10.1109/ACCESS.2019.2937657

Zhang, Y., Ishibuchi, H., and Wang, S. (2018). Deep takagi–sugeno–kang fuzzy classifier with Shared Linguistic Fuzzy Rules. *IEEE Trans. Fuzzy Systems* 26, 1535–1549. doi: 10.1109/TFUZZ.2017.2729507

Zhang, Z., Chow, T. W. S., and Zhao, M. (2013). Trace ratio optimization-based semi-supervised nonlinear dimensionality reduction for marginal manifold visualization. *IEEE Trans. Knowl. Data Eng.* 25, 1148–1161. doi: 10.1109/TKDE.2012.47

Zhou, T., Chung, F., and Wang, S. (2017). Deep TSK fuzzy classifier with stacked generalization and triplely concise interpretability guarantee for large data. *IEEE Trans. Fuzzy Sys.* 25, 1207–1221. doi: 10.1109/TFUZZ.2016.2604003

Conflict of Interest: The authors declare that the research was conducted in the absence of any commercial or financial relationships that could be construed as a potential conflict of interest.

frontiers in Neuroscience

ORIGINAL RESEARCH
published: 23 June 2020
doi: 10.3389/fnins.2020.00606

Epilepsy EEG Signal Classification Algorithm Based on Improved RBF

Dongmei Zhou[1]* *and Xuemei Li*[2]

[1] College of Information Science and Technology, Chengdu University of Technology, Chengdu, China, [2] Xijing Hospital, Air Force Medical University, Xi'an, China

Epilepsy is a chronic recurrent transient brain dysfunction syndrome. It is characterized by recurrent epilepsy caused by abnormal discharge of brain neurons. Epilepsy is one of the common diseases in nervous system. The analysis of EEG signals is a hot topic in current research. In order to solve the problem of epileptic EEG signals classification accurately, we carry out in-depth research on epileptic EEG signals, analyze features from linear and non-linear perspectives, input them into the improved RBF model to dynamically extract effective features, and introduce one against one strategy classifier to reduce the probability of error classification. Experiments show that the proposed algorithm has strong robustness and high epileptic signal recognition rate.

Keywords: epilepsia, EEG signal, convolution neural network, RBF, one-against-one

OPEN ACCESS

Edited by:
Yizhang Jiang,
Jiangnan University, China

Reviewed by:
Bin Li,
Northwest University, China
Cao Yaoguang,
Beihang University, China

***Correspondence:**
Dongmei Zhou
winwin111111@sina.com

Specialty section:
This article was submitted to Neuroprosthetics, a section of the journal Frontiers in Neuroscience

Received: *23 April 2020*
Accepted: *18 May 2020*
Published: *23 June 2020*

Citation:
Zhou D and Li X (2020) Epilepsy EEG Signal Classification Algorithm Based on Improved RBF. Front. Neurosci. 14:606. doi: 10.3389/fnins.2020.00606

INTRODUCTION

Epilepsy is a transient brain dysfunction caused by sudden abnormal over discharge of brain neurons, which has a high incidence rate (Jiang et al., 2020). The detection and recognition of EEG signal are the most important means to diagnose epilepsy. The method of multi-feature extraction and intelligent recognition has been applied to the recognition of epileptic EEG signals (Ojha et al., 2020). Guo et al. (2010) realizes EEG signal classification based on intelligent network. Faust et al. (2010) analyzes EEG information of epilepsy in frequency domain. Wang et al. (2011) establishes wavelet model to classify signals. Hubsch et al. (2011) establishes a model for EEG analysis from the perspective of video. Chua et al. (2011) uses high-order features to realize epilepsy signal recognition. Kumar et al. (2012) proposes the classification of epileptic signals by relative wave energy and wave entry. Tzallas et al. (2012) reviews the history of epileptic brain signal recognition. Khan et al. (2012) uses multi-dimensional wavelet transform to detect epileptic signals. Murugavel et al. (2013) establishes SVM classifier to realize EEG classification. Zhu et al. (2013) analyzes the distribution of EEG signals from the perspective of energy. Wang et al. (2013) extracts fractal features for EEG analysis. Kumar et al. (2014) analyzes EEG based on fuzzy set. Yuan et al. (2014) uses different kernel functions to classify epileptic signals. Xie and Krishnan (2014) introduces sliding window to block EEG analysis. Kaya (2015) analyzes EEG signals based on local binary patterns. Faust et al. (2015) uses computer-aided means to identify EEG signals. Martis et al. (2015) uses multiple frequency bands to analyze EEG signals of epilepsy. Djemili et al. (2016) introduces artificial mode to distinguish epileptic signals from ordinary signals. Al Ghayab et al. (2016) extracts features from EEG signals by random sampling. Murugavel and Ramakrishnan (2016) establishes SVM classifier to classify EEG signals. Li et al. (2017) extracts the non-linear structure of EEG to realize the automatic identification of EEG signals. Tibdewal et al. (2017) carries out research on the basis of multichannel epileptic EEG signals. Sharma and Pachori (2017) establishes a model from the time and space dimensions for analysis. Sharma et al. (2018) uses iterative filtering to recognize EEG signals. Prabhakar and Rajaguru (2018) establishes AdaBoost classifier to realize

multi-dimensional EEG analysis. Zhou et al. (2018) introduces CNN to analyze EEG signals. Buettner et al. (2019) extracts higher-order features for EEG analysis. Raghu et al. (2019) realizes the signal recognition of epileptic seizure based on matrix terminator. Hossain et al. (2019) establishes a deep learning network to visualize brain imaging. Parija et al. (2020) establishes a model from the perspective of multi-core to analyze EEG. Li et al. (2020) analyzes the instantaneous signal strength. Seo et al. (2020) establishes a dynamic model to recognize EEG signals.

The main problems of epilepsy recognition by EEG are as follows: (1) Limited single feature leads to difficult extraction of signal feature. (2) Single layer neural network has limited ability to distinguish strong correlation signals. (3) Poor performance of single classifier has poor classification performance.

Thus, we carried out in-depth study on EEG signals of epilepsy. (1) Establish a multi-dimensional information fusion model. (2) The RBF model is improved to realize the accurate feature representation mechanism. (3) OAO strategy is introduced to carry out the research of classifiers to realize the recognition of epileptic EEG signals accurately.

ALGORITHM

According to above problems, we design the algorithm flow chart, as shown in **Figure 1**. First, EEG signal is input. Then, it is extracted from linear feature and non-linear feature. Wave coefficients are extracted from linear features. Approximate entropy, sample entropy and multi-scale permutation entropy are extracted from non-linear features to analyze from the energy point of view. On the basis of RBF, convolution neural network is constructed to extract signal features. OAO strategy classifier is established to recognize epileptic signals.

Feature Extraction

Human brain signal contains linear information, mainly including time-domain, frequency-domain and time-domain analysis, which focus on EEG sequence waveform and amplitude statistics.

Wave coefficient $F_i(n)$ can measure the amplitude change of EEG sequence:

$$F_i(n) = \frac{1}{M-1}\sum_{j=1}^{M-1}\left|a_n(j+1) - a_n(j)\right| \tag{1}$$

where a_n is the amplitude of n-th EEG data after wavelet transform; M is the signal length.

EEG signal has chaotic features. Only linear features of EEG signal cannot completely describe the signal. Therefore, we extract non-linear features of EEG sequence.

Entropy is used to express the uniformity of energy distribution in space. The more uniform the energy distribution, the greater the entropy. When the energy of a system is completely evenly distributed, the entropy of the system reaches the maximum (Longo, 2020). Thus, we measure the non-linear features of signal from the perspective of entropy.

Approximate entropy uses short data to distinguish different types of time series accurately. Considering different states of healthy period, epileptic intermittence period and epileptic period, the waveform, frequency, amplitude and other manifestations of EEG sequence are different, so this feature is used to identify EEG sequence.

Given there are N EEG data and similarity tolerance N. Approximate entropy $AE(m,r)$ represents the probability that two sequences of adjacent m points are still adjacent after mapping to $m+1$ dimensional space on the basis of r in the original sequence of N sample points.

$$AE(m,r) = \phi^m(r) - \phi^{m+1}(r) \tag{2}$$

$$\begin{cases} \phi^m(r) = \frac{1}{N-m}\sum_{i=1}^{N-m}\ln C_i^m(r) \\ C_i^m(r) = \frac{Q}{N-m-1}; \\ d_{ij} = \max_{k=0!\ m-1}\left[\left|x(i+k) - x(j+k)\right|\right] \end{cases} \tag{3}$$

were $\phi^m(r)$, $C_i^m(r)$, and d_{ij} are the intermediate variables.

Approximate entropy can express the similarity of signals, but it is difficult to explain the complexity of signals, which reduces

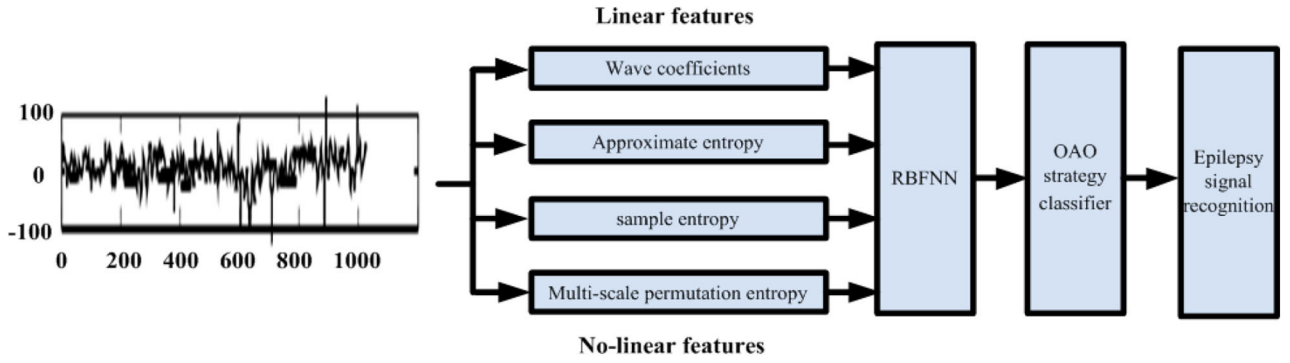

FIGURE 1 | The algorithm flow chart.

the ability of analyzing problems. For this reason, sample entropy is introduced:

$$SE(m,r) = -\ln \frac{B^{m+1}(r)}{B^{m}(r)} \tag{4}$$

$$\begin{cases} B^{m}(r) = \frac{1}{N-m} \sum_{i=1}^{N-m} B_i^m(r) \\ B_i^m(r) = \frac{1}{N-m-1} \sum_{j=1, j\neq i}^{N-m} \ln \frac{Q}{N-m-1} \end{cases} \tag{5}$$

where $B_i^m(r)$ is the energy contained in single signal.

Compared with approximate entropy, sample entropy eliminates the comparison of its own data, has strong independence and overcomes the dependence on other data; the consistency of sample entropy is good. When m and r are changed, the relationship of sample entropy size of different EEG sequences will not be changed; Compared with approximate entropy, sample entropy needs less data and even loses a part of data, which can still obtain reliable results.

Multiscale permutation entropy is improved on the basis of permutation entropy. The basic idea is to calculate multiscale coarse-grained time series, and then calculate permutation entropy. Suppose that the time series with length L is coarsely granulated as follows:

$$y_j^s = \frac{1}{s} \sum_{i=(j-1)s+1}^{js} x_i, \ j \in [1, L/s] \tag{6}$$

where s is the scale factor; y_j^s is the multi-scale time series. When s=1, it is the original time series. The calculated entropy is the permutation entropy. After the multi-scale calculation of the visual sequence, the permutation entropy is estimated to calculate the multi-scale permutation entropy of the time sequence.

Time series y_j^s is reconstructed as $Y_t^s = \left\{ y_t^s, y_{t+\tau}^s, ...y_{t+(m-1)\tau}^s \right\}$, where m is the embedding dimension, τ is the delay factor, and the pairs are arranged in ascending order. The probability of the permutation is calculated:

$$P_l^s = \frac{N_l}{n/s - m + 1} \tag{7}$$

Then the entropy of multiscale arrangement is:

$$H_P^s = \sum_{l=1}^{m!} P_l^s \ln P_l^s \tag{8}$$

When H_P^s reaches the maximum value, the permutation entropy is normalized:

$$h_P^s = H_P^s / \ln(m!) \tag{9}$$

Improved RBFNN

RBFNN (radial basis function neural network) has good generalization ability, and can approach the specified continuous function with any precision. When dealing with the classification problem, the linear non-separable problem in the original feature space is transformed into the linear separable problem in the high-dimensional feature space through the non-linear mapping of the hidden layer.

$$y = \varphi^T(\mathbf{x})\,\boldsymbol{\omega} - b \tag{10}$$

where d is the number of neurons; b is the threshold; $\mathbf{x}$ is the input vector; ω is the weight of the output layer.

$$\begin{cases} \varphi(x) = \left[f_1(x), f_2(x), ...f_K(x) \right]^T \\ \mathbf{x} = [x_1, x_2...x_d]^T \\ \boldsymbol{\omega} = [\omega_1, \omega_2...\omega_d]^T \end{cases} \tag{11}$$

f_k represents the radial basis function of the k-th neuron in the hidden layer:

$$f_k(x) = \exp\left(-\frac{\|x - c_k\|}{2\sigma_k^2} \right) \tag{12}$$

where c_k and σ_k are the center and width of radial basis function, respectively.

The minimax probability machine (MPM) is a binary classification model based on the minimization of upper bound of misclassification probability. It is defined as:

$$\begin{aligned} &\max_{\alpha, w\neq 0, b} \alpha, \ s.t. \inf_{x\sim(u_+, \sum_+)} \mathrm{pr}\left(\mathbf{w}^T\mathbf{x} \geq b\right) \geq \alpha, \\ &\inf_{x:(u_-, \sum_-)} \mathrm{pr}\left(\mathbf{w}^T\mathbf{x} \leq b\right) \geq \alpha \end{aligned} \tag{13}$$

where $\inf_{x\sim(u_+, \sum_+)} \mathrm{pr}\left(\mathbf{w}^T\mathbf{x} \geq b\right)$ represents the lower bound of probability when the condition is $\mathbf{w}^T\mathbf{x} \geq b$, $x:\left(u_+, \sum_+\right)$. For the same reason, $\inf_{x:(u_-, \sum_-)} \mathrm{pr}\left(\mathbf{w}^T\mathbf{x} \leq b\right)$.

For two kinds of data subject to different distributions, there is an optimal hyperplane $(\mathbf{w}^*)^T x = b^*$, which maximizes the lower bound α of the correct classification probability. When $\mu_+ = \mu_-$, by solving:

$$\begin{aligned} &\gamma(\alpha)^{-1} = \min_w \left(\sqrt{w^T \sum\nolimits_+ w} + \sqrt{w^T \sum\nolimits_- w} \right) \\ &w^T(\mu_+ - \mu_-) = 1 \end{aligned} \tag{14}$$

The optimal solution is $\mathbf{w}^*$, then the optimal solution of b can be set as:

$$b^* = \left(w^*\right)^T \mu_+ - \gamma^*(\alpha) \sqrt{(w^*)^T \sum\nolimits_+ (w^*)} \tag{15}$$

The lower bound of correct classification probability can be obtained by using the optimal solution:

$$\alpha^* = \frac{1}{1 + \left(\sqrt{(w^*)^T \sum\nolimits_+ (w^*)} + \sqrt{(w^*)^T \sum\nolimits_- (w^*)} \right)^2} \tag{16}$$

The value of α fully reflects the separability between two types of data. When it is closer to 1, the classification model is more

reliable. It indicates that the stronger the separability between two types of data.

Considering the equivalence of RBF neural network and TSK fuzzy system under certain conditions, the objective function is defined as:

$$\max_{\alpha,w\neq 0,b} \alpha, s.t. \inf_{\psi(w)-\left(u_{\phi(+)},\sum_{\psi(+)}\right)} \mathrm{pr}\left(\mathbf{w}^T\psi\left(\mathbf{x}\right)\geq b\right)\geq\alpha, \inf_{\psi(w)-\left(u_{\phi(-)},\sum_{\psi(-)}\right)} \mathrm{pr}\left(\mathbf{w}^T\psi\left(\mathbf{x}\right)\leq b\right)\geq\alpha \quad (17)$$

It represents the corresponding vector of x in the new feature space obtained by RBF neural network mapping. The covariance of the mapped data samples can be estimated from the data sample set $\psi(x)$.

$$\sum\nolimits_{\psi} = \left(X_\psi - \mu_\psi\right)\left(X_\psi - \mu_\psi\right)^T/N \quad (18)$$

The optimization objective function is as follows:

$$\gamma(\alpha)^{-1} = \min_{w}\left(\sqrt{w^T\sum\nolimits_{\psi(+)}w} + \sqrt{w^T\sum\nolimits_{\psi(-)}w}\right) \quad w^T\left(\mu_{\psi(+)} - \mu_{\psi(-)}\right) = 1 \quad (19)$$

where α can describe the separability between two kinds of data and measure the reliability of classification model. According to the complexity of classification problem, by adjusting the number of neurons in hidden layer, the balance between the improvement of classification accuracy and the complexity of control model can be achieved.

One against one (OAO) strategy can resolve a complete multi-classification problem into multiple sub classification problems, and finally train the finite element classifier (Setiawan et al., 2020). Compared with one against rest (OAR) strategy, each subcategory is less difficult and easy to find a simple and effective interface to explain. The "voting method" is generally adopted, when OAO strategy test is applied. However, the problem of voting method is that the same number of votes of multiple classes will lead to the phenomenon of classification rejection, and each input data needs to be compared multiple times.

In order to avoid the classification rejection of voting method and improve the efficiency of classification model, we use exclusion method to build classification decision tree. Each internal node of the tree is a binary classifier, which means the method of exclusion along the direction of tree growth only needs M-1 comparison to get the classification results. In order to reduce the inherent "error accumulation" of tree structure, in this paper, we will make full use of the index provided by the minimum maximum probability technology. The binary classifier with large index has priority to do the classification with high assurance first. We normalize all signals and send

TABLE 1 | Date set description.

Sate	Serial number	Description
Healthy	1	EEG signal when opening eyes
	2	EEG signal when closing eyes
Sick	3	EEG signal in hippocampus during intermission
	4	EEG signal in epileptic area during intermission
	5	EEG signal in the onset period

TABLE 2 | DATA 1 comparison of feature extraction performance.

Index	Linear kernel	Non-linear kernel	Fusion kernel
SPE	0.802 ± 0.042	0.932 ± 0.023	0.951 ± 0.021
SEN	0.841 ± 0.019	0.946 ± 0.019	0.965 ± 0.047
ACC	0.843 ± 0.021	0.932 ± 0.024	0.963 ± 0.024
α((1, 2):(3, 4, 5))	0.456 ± 0.012	0.951 ± 0.031	0.963 ± 0.013

TABLE 3 | DATA 2 comparison of feature extraction performance.

Index	Linear kernel	Non-linear kernel	Fusion kernel
SPE	0.946 ± 0.022	0.945 ± 0.013	0.963 ± 0.009
	0.973 ± 0.026	0.956 ± 0.022	0.923 ± 0.015
	0.932 ± 0.012	0.962 ± 0.013	0.912 ± 0.009
SEN	0.943 ± 0.045	0.965 ± 0.032	0.951 ± 0.018
	0.890 ± 0.055	0.935 ± 0.021	0.953 ± 0.037
	0.973 ± 0.048	0.942 ± 0.034	0.910 ± 0.056
ACC	0.918 ± 0.019	0.943 ± 0.013	0.960 ± 0.024
α((1,2):(3,4))	0.813 ± 0.015	0.702 ± 0.007	0.775 ± 0.001
α((1,2):(5))	0.951 ± 0.014	0.762 ± 0.011	0.973 ± 0.001
α((3,4):(5))	0.926 ± 0.009	0.783 ± 0.023	0.949 ± 0.003

TABLE 4 | DATA 3 comparison of feature extraction performance.

Index	Linear kernel	Non-linear kernel	Fusion kernel
SPE	0.963 ± 0.012	0.971 ± 0.023	0.944 ± 0.031
	0.981 ± 0.021	0.961 ± 0.024	0.983 ± 0.015
	0.933 ± 0.026	0.923 ± 0.017	0.893 ± 0.051
	0.931 ± 0.024	0.901 ± 0.012	0.919 ± 0.048
	0.987 ± 0.013	0.961 ± 0.032	0.998 ± 0.061
SEN	0.791 ± 0.031	0.810 ± 0.062	0.910 ± 0.063
	0.921 ± 0.042	0.891 ± 0.120	0.823 ± 0.056
	0.581 ± 0.123	0.651 ± 0.130	0.713 ± 0.166
	0.589 ± 0.120	0.661 ± 0.067	0.613 ± 0.114
	0.981 ± 0.031	0.953 ± 0.035	0.865 ± 0.067
ACC	0.813 ± 0.036	0.769 ± 0.035	0.784 ± 0.056
α(1:2)	0.753 ± 0.015	0.621 ± 0.022	0.701 ± 0.031
α(1:3)	0.856 ± 0.007	0.765 ± 0.012	0.758 ± 0.007
α(2:3)	0.920 ± 0.006	0.841 ± 0.010	0.895 ± 0.008
α(1:4)	0.821 ± 0.013	0.761 ± 0.010	0.776 ± 0.031
α(2:4)	0.901 ± 0.006	0.812 ± 0.005	0.893 ± 0.008
α(3:4)	0.381 ± 0.031	0.273 ± 0.032	0.351 ± 0.033
α(1:5)	0.978 ± 0.003	0.813 ± 0.013	0.983 ± 0.003
α(2:5)	0.953 ± 0.004	0.790 ± 0.012	0.972 ± 0.012
α(3:5)	0.957 ± 0.009	0.789 ± 0.013	0.968 ± 0.005
α(4:5)	0.913 ± 0.011	0.743 ± 0.018	0.912 ± 0.007

them to RBFNN at a uniform scale. It is shown that the number of neurons is 1,024 and the size of nuclear function is 5 × 5 indicated through experiments and related references.
Training process:

1) Specify the number of neurons to get the center and width of each radial basis function.
2) Trained data is mapped to new feature space through RBF.
3) Train binary classifier with OAO strategy.
4) The classifier with the largest α is used as the root node of the classification tree.
5) If the classification result is that the sample does not belong to class *i*, then the available classifier of its child nodes is $C = C\backslash I$, and the classifier used is the one with the largest index related to *j* in *C*;

Repeat all the process until traversing all child nodes.

EXPERIMENTAL RESULTS AND ANALYSIS

Experiment Data and Experiment Platform

All data come from the epileptic EEG signal data experiment provided by the University of Bonn, Germany. This data set is divided into five groups. Each group of data contains 100 EEG signal segments of 23.6 s. Sampling frequency is 173.61 Hz with 4,097 sampling points, as shown in **Table 1**. All data come from the epileptic EEG signal data experiment provided by the University of Bonn, Germany. This data set is divided into five groups, where the ratio of training to testing is 1:1. We use different sampling evaluation rates to sample the sequence randomly and normalize it, which has increased the number of positive samples.

The experiment is based on WinXP, VC++ program and core dual core processor. Based on the above database, three groups of experiments are designed: DATA: EEG signals of the healthy and the sick are divided into two categories. Data 2: EEG signals of the healthy, the sick interval and the disease attack are divided into three categories. Data 3: each group of EEG signal is divided into one category.

Feature Extraction Performance

Based on the traditional RBFNN, linear kernel, non-linear kernel and the proposed fusion kernel are compared. In the form of "mean ± standard deviation," the test sensitivity (*SEN*), specificity (*SPE*) and accuracy (*ACC*) of each algorithm for data

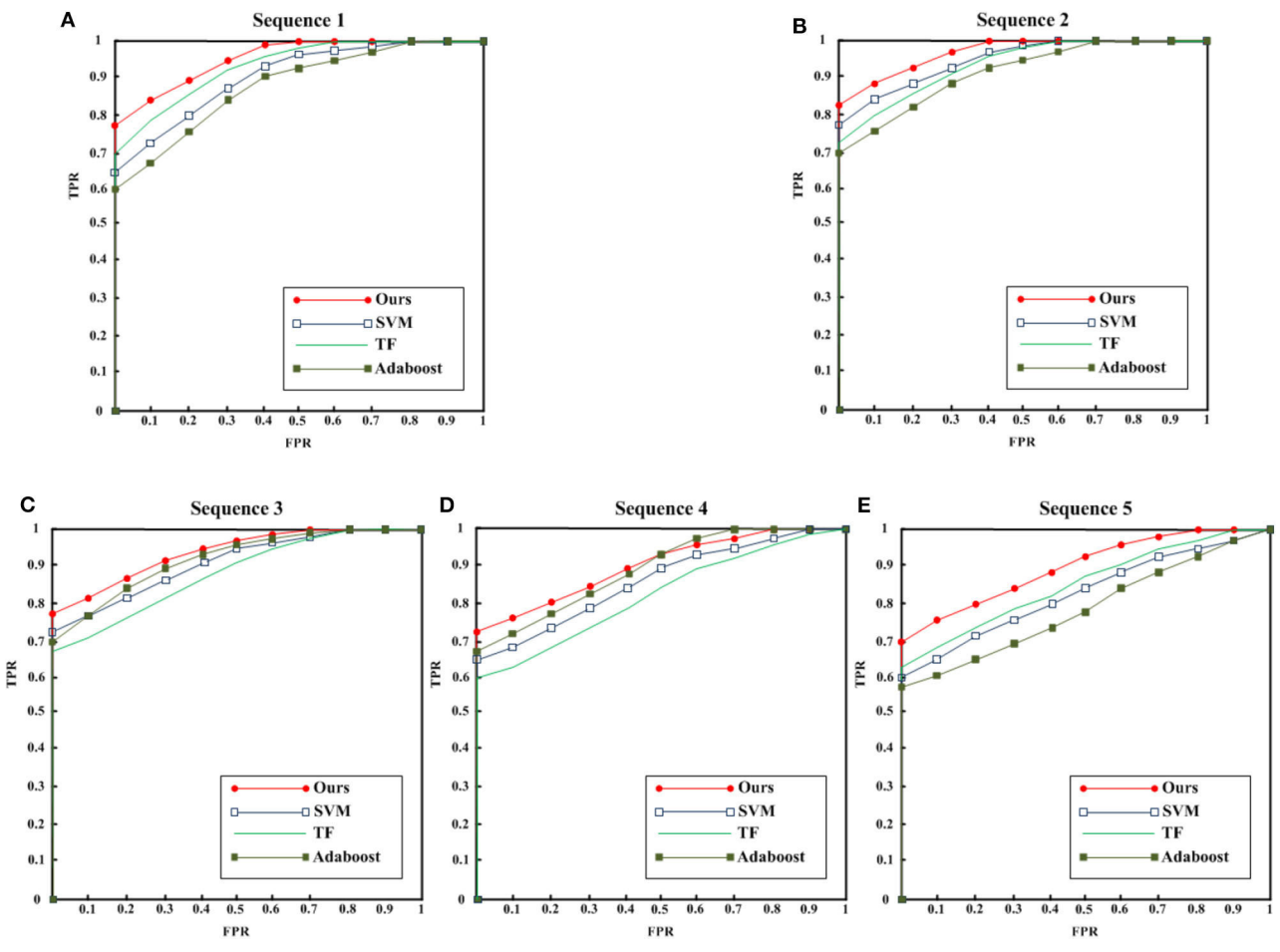

FIGURE 2 | ROC curves. **(A)** Sequence 1, **(B)** sequence 2, **(C)** sequence 3, **(D)** sequence 4, and **(E)** sequence 5.

set classification are given:

$$SEN = \frac{TP}{TP + FN} \tag{20}$$

$$SPE = \frac{TN}{TN + FP} \tag{21}$$

$$ACC = \frac{TP + TN}{TP + FP + TN + FN} \tag{22}$$

As well as the α index in this paper to measure the performance of feature extraction.

As shown in **Tables 2–4**, the linear and non-linear combined feature model proposed in this paper has achieved good results in all data sets. the α index is related to *SPE* and *SEN*, and is closely related to missed diagnosis rate and misdiagnosis rate in medical diagnosis. When using decision tree classification, the significance of choosing the classifier with large α index is to reduce the accumulation error. In Group 5, the signal is easy to recognize; α index is large; specificity is high and misdiagnosis rate is low. Therefore, we can distinguish the epileptic patients in the onset period, and then further diagnose whether the subjects are healthy or in the seizure interval. The proposed algorithm has strong non-linear classification ability, and has the advantages of simplicity, high efficiency and strong interpretation. In the training stage, we can find the differences of the distribution relations of all kinds of data, and build an effective classification tree model, without having to calculate the sensitivity and specificity in the test stage before doing comparative analysis.

Performance Comparison of Classification Algorithms

We use different algorithms to statistic ROC curves of all data, as shown in **Figure 2**. Generally, the proposed algorithm achieve better effect. We use the corresponding algorithm in the references. Based on the particularity of the EEG signal and the parameters setting mentioned in the references, we perform fine tuning experiment to ensure the performance of the proposed algorithm. As shown in **Figures 2A,B**, all algorithms for healthy EEG signals have achieved good results. Due to the multi-scale nature of AdaBoost algorithm cannot fully show the features of EEG signal, the detection effect is slightly low. For the EEG signal **Figures 2C–E**, during the onset, the detection effect is lower than that of healthy EEG signal because of the short onset time and limited display of EEG signal. SVM (Murugavel and Ramakrishnan, 2016) is classified by time-domain features. TF (time frequency) (Sharma and Pachori, 2017) algorithm establishes the relationship between time and frequency for analysis. Andrzejak et al. (2001) establishes a multi-scale classification framework. Because of the classification tree structure used in the decision-making stage, the proposed method is simple and efficient. Compared with traditional algorithms, the proposed method combines RBF neural network, so it has better non-linear approximation ability and generalization performance to achieve the best detection effect.

CONCLUSIONS

Aiming at the difficulty of classification of epileptic EEG signals, this paper analyzes the problem from the feature level, and proposes the feature structure combining linearity and non-linearity. In order to better represent the epileptic signal, the RBF algorithm is improved, and the one-again-one (OAO) strategy is introduced to realize the classification of epileptic signal by computer means, which is better than the current mainstream algorithm.

DATA AVAILABILITY STATEMENT

The raw data supporting the conclusions of this article will be made available by the authors, without undue reservation.

AUTHOR CONTRIBUTIONS

All authors listed have made a substantial, direct and intellectual contribution to the work, and approved it for publication.

FUNDING

This work was supported by Light of West China (Grant No. XAB2016B23), Chinese Academy of Sciences, the Open Project Program of the State Key Lab of CAD and CG (Grant No. A2026), and Zhejiang University, National Natural Science Foundation of China (Grant No. 61561040).

ACKNOWLEDGMENTS

We are very grateful to the editor and peer reviewers and all those people who helped us a lot during the writing of this article.

REFERENCES

Al Ghayab, H. R., Li, Y., Abdulla, S., Diykh, M., and Wan, X. (2016). Classification of epileptic EEG signals based on simple random sampling and sequential feature selection. *Brain Inform.* 3, 85–91. doi: 10.1007/s40708-016-0039-1

Andrzejak, R. G., Lehnertz, K., Mormann, F., Rieke, C., David, P., and Elger, C. E. (2001). Indications of non-linear deterministic and finite-dimensional structures in time series of brain electrical activity: dependence on recording region and brain state. *Phys. Rev. E* 64:061907. doi: 10.1103/PhysRevE.64.061907

Buettner, R., Frick, J., and Rieg, T. (2019). "High-performance detection of epilepsy in seizure-free EEG recordings: A novel machine learning approach using very specific epileptic EEG sub-bands," in *Fortieth International Conference on Information Systems* (Munich), 1–16.

Chua, K. C., Chandran, V., Acharya, U. R., and Lim, C. M. (2011). Application of higher order spectra to identify epileptic EEG. *J. Med. Syst.* 35, 1563–1571. doi: 10.1007/s10916-010-9433-z

Djemili, R., Bourouba, H., and Korba, M. A. (2016). Application of empirical mode decomposition and artificial neural network for the classification of normal and epileptic EEG signals. *Biocyb. Biomed. Eng.* 36, 285–291. doi: 10.1016/j.bbe.2015.10.006

Faust, O., Acharya, U. R., Adeli, H., and Adeli, A. (2015). Wavelet-based EEG processing for computer-aided seizure detection and epilepsy diagnosis. *Seizure* 26, 56–64. doi: 10.1016/j.seizure.2015.01.012

Faust, O., Acharya, U. R., Min, L. C., and Sputh, B. H. (2010). Automatic identification of epileptic and background EEG signals using frequency domain parameters. *Int. J. Neural Syst.* 20, 159–176. doi: 10.1142/S0129065710002334

Guo, L., Rivero, D., Dorado, J., Rabunal, J. R., and Pazos, A. (2010). Automatic epileptic seizure detection in EEGs based on line length feature and artificial neural networks. *J. Neurosci. Methods* 191, 101–109. doi: 10.1016/j.jneumeth.2010.05.020

Hossain, M. S., Amin, S. U., Alsulaiman, M., and Muhammad, G. (2019). Applying deep learning for epilepsy seizure detection and brain mapping visualization. *ACM Trans. Mult. Comp. Commun. Appl.* 15, 1–17. doi: 10.1145/3241056

Hubsch, C., Baumann, C., Hingray, C., Gospodaru, N., Vignal, J. P., Vespignani, H., et al. (2011). Clinical classification of psychogenic non-epileptic seizures based on video-EEG analysis and automatic clustering. *J. Neurol. Neurosur. Psychiatry* 82, 955–960. doi: 10.1136/jnnp.2010.235424

Jiang, Y., Chen, W., and Li, M. (2020). Symplectic geometry decomposition-based features for automatic epileptic seizure detection. *Comput. Biol. Med.* 116:103549. doi: 10.1016/j.compbiomed.2019.103549

Kaya, Y. (2015). Hidden pattern discovery on epileptic EEG with 1-D local binary patterns and epileptic seizures detection by grey relational analysis. *Austr. Phys. Eng. Sci. Med.* 38, 435–446. doi: 10.1007/s13246-015-0362-5

Khan, Y. U., Rafiuddin, N., and Farooq, O. (2012). "Automated seizure detection in scalp EEG using multiple wavelet scales," in *2012 IEEE International Conference on Signal Processing, Computing and Control* (Waknaghat Solan: IEEE), 1–5. doi: 10.1109/ISPCC.2012.6224361

Kumar, Y., Dewal, M. L., and Anand, R. S. (2012). Relative wavelet energy and wavelet entropy based epileptic brain signals classification. *Biomed. Eng. Lett.* 2, 147–157. doi: 10.1007/s13534-012-0066-7

Kumar, Y., Dewal, M. L., and Anand, R. S. (2014). Epileptic seizure detection using DWT based fuzzy approximate entropy and support vector machine. *Neurocomputing* 133, 271–279. doi: 10.1016/j.neucom.2013.11.009

Li, M., Chen, W., and Zhang, T. (2017). Automatic epileptic EEG detection using DT-CWT-based non-linear features. *Biomed. Signal Process. Control* 34, 114–125. doi: 10.1016/j.bspc.2017.01.010

Li, Y., Liu, Y., Cui, W. G., Guo, Y. Z., Huang, H., and Hu, Z. Y. (2020). Epileptic seizure detection in EEG signals using a unified temporal-spectral squeezeand-excitation network. *IEEE Trans. Neural Syst. Rehabil. Eng.* 28, 782–794. doi: 10.1109/TNSRE.2020.2973434

Longo, R. (2020). Entropy distribution of localised states. *Commun. Math. Phys.* 373, 473–505. doi: 10.1007/s00220-019-03332-8

Martis, R. J., Tan, J. H., Chua, C. K., Loon, T. C., YEO, S. W. J., and Tong, L. (2015). Epileptic EEG classification using non-linear parameters on different frequency bands. *J. Mech. Med. Biol.* 15:1550040. doi: 10.1142/S0219519415500402

Murugavel, A. M., and Ramakrishnan, S. (2016). Hierarchical multi-class SVM with ELM kernel for epileptic EEG signal classification. *Med. Biol. Eng. Comp.* 54, 149–161. doi: 10.1007/s11517-015-1351-2

Murugavel, A. M., Ramakrishnan, S., Maheswari, U., and Sabetha, B. S. (2013). "Combined seizure index with adaptive multi-class SVM for epileptic EEG classification," in *2013 International Conference on Emerging Trends in VLSI, Embedded System, Nano Electronics and Telecommunication System (ICEVENT)* (Tiruvannamalai: IEEE), 1–5.

Ojha, A. D., Navelkar, A., Gore, M., and Kalbande, D. (2020). "Methodologies for epilepsy detection: survey and review," in *International Conference on Innovative Computing and Communications* (Singapore: Springer), 207–22. doi: 10.1007/978-981-15-1286-5_18

Parija, S., Dash, P. K., and Bisoi, R. (2020). Multi-kernel-based random vector functional link network with decomposed features for epileptic EEG signal classification. *IET Signal Proc.* 14, 162–174. doi: 10.1049/iet-spr.2019.0277

Prabhakar, S. K., and Rajaguru, H. (2018). Adaboost "Classifier with dimensionality reduction techniques for Epilepsy Classification from EEG," in *Precision Medicine Powered by pHealth and Connected Health* (Singapore: Springer), 185–189. doi: 10.1007/978-981-10-7419-6_31

Raghu, S., Sriraam, N., Hegde, A. S., and Kubben, P. L. (2019). A novel approach for classification of epileptic seizures using matrix determinant. *Expert Syst. Appl* 127, 323–341. doi: 10.1016/j.eswa.2019.03.021

Seo, J. H., Tsuda, I., Lee, Y. J., Ikeda, A., Matsuhashi, M., Matsumoto, R., et al. (2020). Pattern recognition in epileptic EEG signals via dynamic mode decomposition. *Mathematics* 8:481. doi: 10.3390/math8040481

Setiawan, B., Djanali, S., and Ahmad, T. (2020). Analyzing the performance of intrusion detection model using weighted one-against-one support vector machine and feature selection for imbalanced classes. *Int. J. Intell. Eng. Syst.* 13, 151–160. doi: 10.22266/ijies2020.0430.15

Sharma, R. R., and Pachori, R. B. (2017). Time–frequency representation using IEVDHM–HT with application to classification of epileptic EEG signals. *IET Sci. Measur. Technol.* 12, 72–82. doi: 10.1049/iet-smt.2017.0058

Sharma, R. R., Varshney, P., Pachori, R. B., and Vishvakarma, S. K. (2018). Automated system for epileptic EEG detection using iterative filtering. *IEEE Sens. Lett.* 2, 1–4. doi: 10.1109/LSENS.2018.2882622

Tibdewal, M. N., Dey, H. R., Mahadevappa, M., Ray, A., and Malokar, M. (2017). Multiple entropies performance measure for detection and localization of multi-channel epileptic EEG. *Biomed. Signal Process. Control* 38, 158–167. doi: 10.1016/j.bspc.2017.05.002

Tzallas, A. T., Tsipouras, M. G., Tsalikakis, D. G., Karvounis, E. C., Astrakas, L., Konitsiotis, S., et al. (2012). "Automated epileptic seizure detection methods: a review study," *in Epilepsy - Histological, Electroencephalographic and Psychological Aspects*, ed D. Stevanovic (InTech), 75–98. doi: 10.5772/31597

Wang, D., Miao, D., and Xie, C. (2011). Best basis-based wavelet packet entropy feature extraction and hierarchical EEG classification for epileptic detection. *Expert Syst. Appl.* 38, 14314–14320. doi: 10.1016/j.eswa.2011.05.096

Wang, Y., Zhou, W., Yuan, Q., Li, X., Meng, Q., Zhao, X., et al. (2013). Comparison of ictal and interictal EEG signals using fractal features. *Int. J. Neural Syst.* 23:1350028. doi: 10.1142/S0129065713500287

Xie, S., and Krishnan, S. (2014). Dynamic principal component analysis with nonoverlapping moving window and its applications to epileptic EEG classification. *Scientific World J.* 2014:419308. doi: 10.1155/2014/419308

Yuan, Q., Zhou, W., Yuan, S., Li, X., Wang, J., and Jia, G. (2014). Epileptic EEG classification based on kernel sparse representation. *Int. J. Neural Syst.* 24, 1450015. doi: 10.1142/S0129065714500154

Zhou, M., Tian, C., Cao, R., Wang, B., Niu, Y., Hu, T., et al. (2018). Epileptic seizure detection based on EEG signals and CNN. *Front. Neuroinform* 12:95. doi: 10.3389/fninf.2018.00095

Zhu, G., Li, Y., Wen, P. P., Wang, S., and Xi, M. (2013). "Epileptogenic focus detection in intracranial EEG based on delay permutation entropy," in *AIP Conference Proceedings,* Vol. 1559 (Sydney, NSW: American Institute of Physics), 31–36. doi: 10.1063/1.4824993

Conflict of Interest: The authors declare that the research was conducted in the absence of any commercial or financial relationships that could be construed as a potential conflict of interest.

frontiers in Neuroscience

ORIGINAL RESEARCH
published: 06 August 2020
doi: 10.3389/fnins.2020.00829

EEG Feature Selection via Stacked Deep Embedded Regression With Joint Sparsity

Kui Jiang[1], Jiaxi Tang[1], Yulong Wang[1], Chengyu Qiu[1], Yuanpeng Zhang[1] and Chuang Lin[2]**

[1] Department of Medical Informatics of Medical (Nursing) School, Nantong University, Nantong, China, [2] Shenzhen Institutes of Advanced Technology, Chinese Academy of Sciences, Shenzhen, China

In the field of brain-computer interface (BCI), selecting efficient and robust features is very seductive for artificial intelligence (AI)-assisted clinical diagnosis. In this study, based on an embedded feature selection model, we construct a stacked deep structure for feature selection in a layer-by-layer manner. Its promising performance is guaranteed by the stacked generalized principle that random projections added into the original features can help us to continuously open the manifold structure existing in the original feature space in a stacked way. With such benefits, the original input feature space becomes more linearly separable. We use the epilepsy EEG data provided by the University of Bonn to evaluate our model. Based on the EEG data, we construct three classification tasks. On each task, we use different feature selection models to select features and then use two classifiers to perform classification based on the selected features. Our experimental results show that features selected by our new structure are more meaningful and helpful to the classifier hence generates better performance than benchmarking models.

Keywords: brain-computer interface, feature selection, stacked deep structure, stacked generalized principle, EEG

OPEN ACCESS

Edited by:
Mohammad Khosravi, Persian Gulf University, Iran

Reviewed by:
Shan Zhong, Changshu Institute of Technology, China
Hongru Zhao, Soochow University, China

****Correspondence:***
Yuanpeng Zhang
maxbirdzhang@ntu.edu.cn
Chuang Lin
chuang.lin@siat.ac.cn

Specialty section:
This article was submitted to Neuroprosthetics, a section of the journal Frontiers in Neuroscience

Received: *12 June 2020*
Accepted: *16 July 2020*
Published: *06 August 2020*

Citation:
Jiang K, Tang J, Wang Y, Qiu C, Zhang Y and Lin C (2020) EEG Feature Selection via Stacked Deep Embedded Regression With Joint Sparsity. Front. Neurosci. 14:829. doi: 10.3389/fnins.2020.00829

INTRODUCTION

Electroencephalogram (EEG) as a biomarker plays an important role in the brain-computer interface (BCI) (Wang et al., 2013; Zheng, 2017; Mammone et al., 2019; Nakamura et al., 2020). For example, EEG signals are often used to determine the presence and type of epilepsy in clinical diagnosis (Rieke et al., 2003; Yetik et al., 2005; Adeli et al., 2007; Lopes da Silva, 2008; Coito et al., 2016; Parvez and Paul, 2016; Peker et al., 2016; Panwar et al., 2019). In recent years, with the rapid development of artificial intelligence technology, AI-assisted diagnosis has attracted more and more attention and achieved unprecedented success in many scenarios including BCI (Agarwal et al., 2018; Wu et al., 2018). In general, a standard EEG-based AI-assisted diagnosis flowchart is illustrated in **Figure 1**, which contains signal acquisition, signal processing, feature extraction, feature selection and model training and testing. As we know that original features extracted from EEG signals cannot be directly used for model training because they are often represented in very high-dimensional feature space. Therefore, feature selection is usually performed before model training. In this study, we focus on how to selection effective features to guarantee high-efficiency AI-assisted clinical diagnosis.

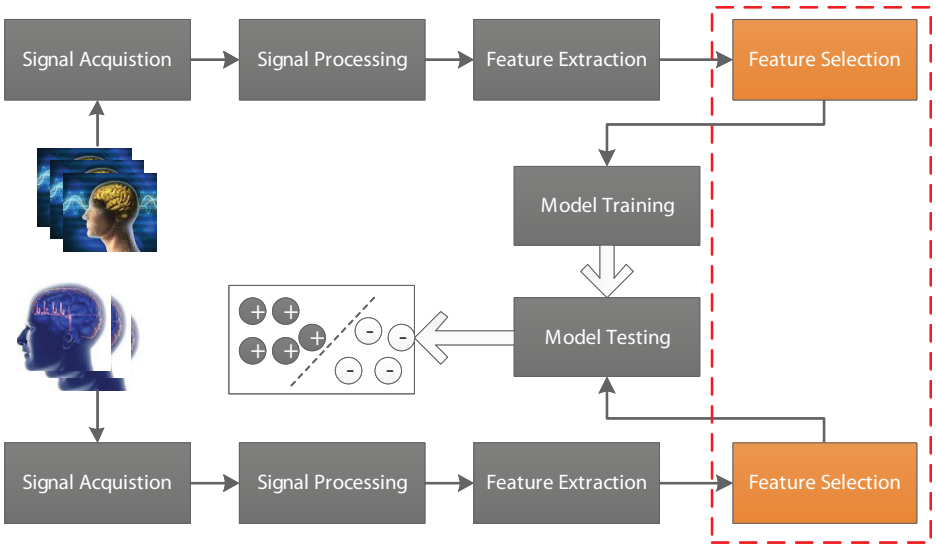

FIGURE 1 | EEG-based AI-assisted diagnosis flowchart containing signal acquisition, signal processing, feature extraction, feature selection, and model training and testing.

To the best of our knowledge, most of the existing feature selection models belong to one of three main catalog, i.e., filter, embedded, and wrapper (Visalakshi and Radha, 2014; Ang et al., 2016; Shah and Patel, 2016; Saputra Rangkuti et al., 2018). In filter models, feature selection depends on the intrinsic properties and the relevancies existing among features. That is to say, filter models are independent of classifiers. Some of the most commonly-used filter models include mRMR (Peng et al., 2005), F-statistic (Habbema and Hermans, 1977), Chi-square and information gain (Raileanu and Stoffel, 2004), *t*-test (Raileanu and Stoffel, 2004) and Relief (Kira and Rendell, 1992), etc. All of them perform feature selection by making use of global statistical information such as the relevance/sensitivity/correlation of a feature w.r.t the class label distribution of the data. In wrapper models, feature selection is around classifiers providing them subsets of features and receiving their feedback. Different from filter models, wrapper models are tightly coupled with a specific classifier. Some representative models include CFS (Hall and Smith, 1999) and RFE-SVM (Guyon et al., 2002), etc. In embedded models, feature selection is considered as an optimization problem and integrating into a specific classifier so that the selected features have a seductive effect on the corresponding classification task. For example, Nie et al. (2010) integrated l_2, $_1$-norm into a robust loss function and proposed an efficient and robust model (renamed as E-JS-Regression) to perform feature selection. Their experimental results on several biomedical data indicated that E-JS-Regression won better performance than both filter models and wrapper models.

In ensemble learning (Webb and Zheng, 2004; Minku et al., 2010; Chen et al., 2017; Liu et al., 2019; Zhu et al., 2020), stacking is a popular classifier combination strategy which takes the outputs of other classifier as input to train a generalizer. In Wolpert (1992) proposed the stacked generalization principle which indicated that the outputs can help to open the manifold of data distribution. In our previous work (Zhang et al., 2018), we made use of this principle and proposed a deep TSK fuzzy system. Therefore, in this study, based on this principle and by taking E-JS-Regression as the basic component, we will construct a layer-by-layer stacked deep structure for feature extraction. The new model is termed as SDE-JS-Regression. In SDE-JS-Regression, each component is connected in a layer-by-layer manner, the output of the previous layer is transformed by random projection as a random shift and then added into the input space. The new input space is considered as the input to the next component. In such a way, the manifold in the training space is continuously opened. The contribution of this study is summarized as follows:

(i) Based on E-JS-Regression proposed by Nie et al. we construct a stacked deep structure for feature selection in a layer-by-layer manner so as to add random projections into the original features so that the manifold structure existing in the original feature space is continuously opened in a stacked way. Therefore, according to the stacked generalized principle, the original input feature space becomes more linearly separable.

(ii) We build three classification tasks from epilepsy EEG data provided by the University of Bonn and introduce different kinds of feature selection methods to demonstrate the promising performance of our proposed method.

DATA AND METHODS

Data

The epilepsy EEG data downloaded from the University of Bonn will be used to evaluate our proposed feature selection

model. This dataset consists of 5 groups of subsets (from group A to group E), where each group is composed of 100 single channel EEG segments during 23.6 s duration. Segments in group A and group B are collected from 5 healthy subjects, while segments in the rest groups are collected from epileptics. **Table 1** lists the data structure and collection conditions. Additionally, **Figure 2** (Zhang et al., 2020) illustrates the amplitudes during the collection procedure of one subject in each group.

Methods

In this section, we will give technical details of our proposed method including its framework, optimization, and algorithm steps. Before we do that, we first summarize the following used notations and some commonly-used definitions.

Notations and Definitions

We use $\mathbf{X} = [\mathbf{x}_1, \mathbf{x}_2, \ldots, \mathbf{x}_n] \in R^{d\times n}$ and $\mathbf{Y} = [\mathbf{y}_1, \mathbf{y}_2, \ldots, \mathbf{y}_n]^T \in R^{n\times c}$ to represent a training set, where $\mathbf{x}_i = [x_1, x_2, \ldots, x_d]^T \in R^d$ represents a training sample and $y_i \in R^c$ is the corresponding label vector of $\mathbf{x}_i$, $1 \leq i \leq n$. For matrix $\mathbf{B}$, we use b_{ij} to represent its element in the i-th row and j-th column, b^i and b_j to represent its i-th row and j-th column, respectively. The l_2,$_1$-norm of matrix $\mathbf{B}$ is defined as:

$$\| \mathbf{B}_{2,1} \| = \sum_{i=1}^{n} \left(\sum_{j=1}^{m} \mathbf{b}_{ij}^2 \right)^{1/2} = \sum_{i=1}^{n} \| \mathbf{b}_2^i \| \tag{1}$$

Structure of SDE-JS-Regression

In Nie et al. (2010) proposed an efficient and robust embedded regression model for feature selection via joint l_2,$_1$-norm sparsity (simplified as E-JS-Regression). Since l_2-norm based loss function is sensitive to outlies, they used a l_2,$_1$-norm based loss function to remove outlies. Additionally, they also used a l_2,$_1$-norm to regularize the transformation matrix to select features with joint sparsity. That is to say, each feature either has small scores for all samples or has large scores for all samples. The objective function is defined as:

$$\min_{\mathbf{W}} J(\mathbf{W}) = \| \mathbf{X}^T\mathbf{W} - \mathbf{Y} \|_{2,1} + \theta \| \mathbf{W} \|_{2,1} \tag{2}$$

where θ is the regularized parameter, $\mathbf{W} \in R^{d\times c}$. The stacked generalized principle as an ensemble learning strategy can provide an efficient way for model combination. Although the stacked generalized principle is not as widely used as boosting and bagging, its great innovation has been successful in many application scenarios. In this study, we take E-JS-Regression as a basic component to construct a stacked deep embedded regression model for EEG feature selection. **Figure 3** illustrates the stacked deep structure of our proposed model.

The stacked deep structure is composed of m basic components linked in a layer-by-layer manner. To be specific, when the first component is fixed, the input to the subsequent components consists of two parts: the original input features and the output of the previous layer/component. How to fuse these two parts is very important in this study. Referring to the stacked generalized principle, we randomly generate a project of the output of the previous layer as a random shift and then integrate the random shift into the original input features. Therefore, the input of component s $(1 < s \leq m)$ $\mathbf{X}_s$ can be obtained by the following equation,

$$\mathbf{X}_s^T = \mathbf{X}^T + \sigma\mathbf{Y}_{s-1}\mathbf{Z} \tag{3}$$

where $\mathbf{Z} \in R^{c\times d}$ is a random projection matrix in which each element is in the range of [0, 1], σ is a positive regularized parameter. By virtue of this structure, all components (E-JS-Regression) are stacked and bridged by adding the original features to a continuous random shift to form the proposed feature selection model SDE-JS-Regression.

The benefits we inherit from the stacked deep structure lie in that the random projections added into the original features can help us to continuously open the manifold structure existing in the original feature space in a stacked way. With such benefits, the input feature space becomes more linearly separable.

Optimization of SDE-JS-Regression

By substituting (3) into (2), the optimization of SDE-JS-Regression can be considered as solving m subproblems. The s-th subproblem can be formulated as follows,

$$\min_{\mathbf{W}} J(\mathbf{W}) = \frac{1}{\theta} \| (\mathbf{X}^T + \sigma\mathbf{Y}_{s-1}\mathbf{Z})\mathbf{W} - \mathbf{Y} \|_{2,1} + \| \mathbf{W} \|_{2,1} \tag{4}$$

which is equivalent to the following problem,

$$\min_{\mathbf{W},\mathbf{Q}} J(\mathbf{W}) = \| \mathbf{Q} \|_{2,1} + \| \mathbf{W} \|_{2,1} \tag{5}$$

$$\text{s.t.} (\mathbf{X}^T + \sigma\mathbf{Y}_{s-1}\mathbf{Z})\mathbf{W} + \theta\mathbf{Q} = \mathbf{Y} \tag{6}$$

TABLE 1 | Data structure and collection conditions of epilepsy EEG segments.

Volunteers	Groups	#Channels	#Features	Collection conditions
Health	A	100	4097	Signals were recorded when volunteer subjects were relaxed in awaken state with eyes open.
	B	100	4097	Signals were recorded when volunteer subjects were relaxed in awaken state with eyes closed.
Epileptic	C	100	4097	Signals were recorded from the hippocampal formation of the opposite hemisphere of brain.
	D	100	4097	Signals were recorded within epileptogenic zone during seizure free intervals.
	E	100	4097	Signals were recorded during seizure activity.

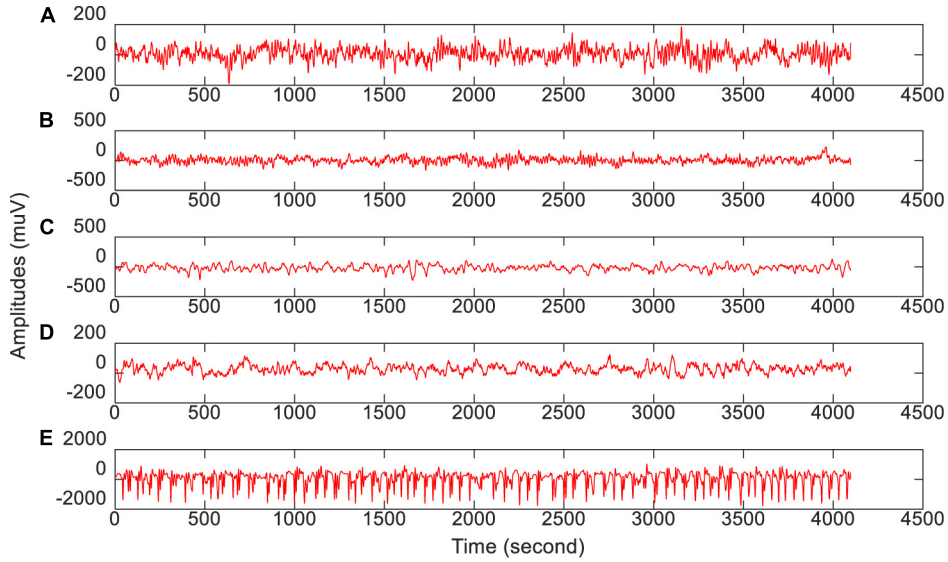

FIGURE 2 | The amplitude of one subject in each group during the collection procedure. From top to bottom corresponds to **(A–E)**, respectively.

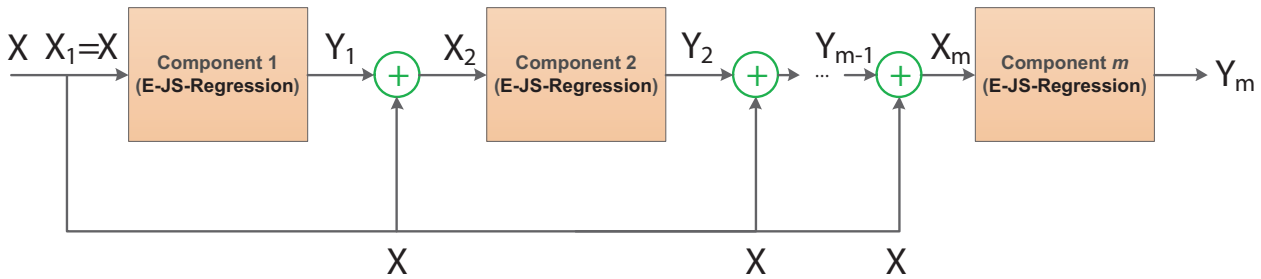

FIGURE 3 | Stacked deep structure of SDE-JS-Regression.

By equivalent transformation, we have:

$$\min_{\mathbf{W},\mathbf{Q}} J(\mathbf{W}) = \left\| \begin{bmatrix} \mathbf{W} \\ \mathbf{Q} \end{bmatrix} \right\|_{2,1} \tag{7}$$

$$\text{s.t.} \left[\mathbf{X}^T + \sigma \mathbf{Y}_{s-1} \mathbf{Z}\ \theta \mathbf{I} \right] \begin{bmatrix} \mathbf{W} \\ \mathbf{Q} \end{bmatrix} = \mathbf{Y} \tag{8}$$

where $\mathbf{I} \in R^{n \times n}$ is a identity matrix. Let $h = n + d$, $\mathbf{K} = \left[\mathbf{X}^T + \sigma \mathbf{Y}_{s-1} Z\ \theta \mathbf{I} \right] \in R^{n \times h}$ and $\mathbf{V} = \begin{bmatrix} \mathbf{W} \\ \mathbf{Q} \end{bmatrix} \in R^{h \times c}$, then the optimization problem in (7) can be updated as follows,

$$\min_{\mathbf{V}} J(\mathbf{V}) = \| \mathbf{V} \|_{2,1} \tag{9}$$

$$\text{s.t. } \mathbf{KV} = \mathbf{Y} \tag{10}$$

By introducing Lagrangian multiplies Δ, the corresponding Lagrangian function of (9) is formulated as follows,

$$L(\mathbf{V}) = \| \mathbf{V} \|_{2,1} - Tr\left(\Delta^T (\mathbf{KV} - \mathbf{Y}) \right) \tag{11}$$

By setting the partial derivative of $L(\mathbf{V})$ w.r.t $\mathbf{V}$ to 0, i.e.,

$$\frac{\partial L(\mathbf{V})}{\partial \mathbf{V}} = 2\mathbf{GV} - \mathbf{K}^T \Delta = 0 \tag{12}$$

where $\mathbf{G} \in R^{h \times h}$ is a diagonal matrix in which the i-th diagonal element is:

$$g_{ii} = \frac{1}{2 \| v^i \|_2} \tag{13}$$

Thus, by multiplying the two sides of (12) by $\mathbf{KG}^{-1}$, and making use of the constraint $\mathbf{KV} = \mathbf{Y}$, we have:

$$\begin{aligned} &2\mathbf{KV} - \mathbf{KG}^{-1}\mathbf{K}^T\mathbf{\Delta} = 0 \\ &\Rightarrow 2\mathbf{Y} - \mathbf{KG}^{-1}\mathbf{K}^T\mathbf{\Delta} = 0 \\ &\Rightarrow \mathbf{\Delta} = 2(\mathbf{KG}^{-1}\mathbf{K}^T)^{-1}\mathbf{Y} \end{aligned} \tag{14}$$

By substituting (14) into (12), we obtain $\mathbf{V}$ as:

$$\mathbf{V} = \mathbf{G}^{-1}\mathbf{K}^T(\mathbf{KG}^{-1}\mathbf{K}^T)^{-1}\mathbf{Y} \tag{15}$$

Algorithm of SDE-JS-Regression

The detailed algorithm steps of SDE-JS-Regression are listed in Algorithm 1. When the transformation matrix $\mathbf{W} \in R^{d \times c}$ is

obtained by SDE-JS-Regression, we compute the sum of each column vector $\mathbf{w}_j$, then sort the elements in the final column vector from largest to smallest. In such a way, we obtain the feature ranking list, which can guide feature selection.

RESULTS

In this section, we will report our experimental settings and results.

Setups

To fairly evaluate the feature selection performance of SDE-JS-Regression, we introduce serval types of feature selection models, i.e., E-JS-Regression (Nie et al., 2010), mRMR (Peng et al., 2005), RFE-SVM (Guyon et al., 2002), and Relief (Kira and Rendell, 1992) for benchmarking testing. A brief introduction of each benchmarking model is summarized as follows.

- E-JS-Regression: It is an embedded feature selection model and also the basic component of our proposed method. Its involved regularized parameter γ will be determined by 5-CV in our experiments.
- mRMR: It is a filtering feature selection model based on minimum redundancy and maximum relevancy. The redundancy is measured by mutual information.
- RFE-SVM: It is a wrapper feature selection model combining with the SVM classifier to achieve recursive feature elimination. Parameters in SVM are all determined by 5-CV.
- Relief: It is also a filtering feature selection model, which assigns a weight to each feature depending on the relevance between features and classes. The number of nearest neighbors is set to 10 in our experiments.

Algorithm 1: SDE-JS-Regression
Input:
$\mathbf{X} = [\mathbf{x}_1, \mathbf{x}_2, \ldots, \mathbf{x}_n] \in R^{d\times n}$ and
$\mathbf{Y} = [\mathbf{y}_1, \mathbf{y}_2, \ldots, \mathbf{y}_n]^T \in R^{n\times c}$
θ, σ and m
Output:
$\mathbf{W}$
Procedure:
Set $t \leftarrow 0$
Initialize $\mathbf{G}^{(t)} \in R^{h\times h}$ as an identity matrix
Set $s \leftarrow 1$
Set $\mathbf{Y}_0 = \mathbf{0}$
Compute $\mathbf{K} = \left[\mathbf{X}^T + \sigma\mathbf{Y}_0\mathbf{Z}\ \theta\mathbf{I}\right] \in R^{n\times h}$
Repeat
  Compute $\mathbf{V}^{(t+1)} = (\mathbf{G}^{(t)})^{-1}\mathbf{K}^T(\mathbf{K}(\mathbf{G}^{(t)})^{-1}\mathbf{K}^T)^{-1}\mathbf{Y}$
  Compute $\mathbf{G}^{(t+1)}$, where the i-th diagonal element is $g_{ii} = \frac{1}{2\|v^{i(t+1)}\|_2}$
  Set $t \leftarrow t+1$
Until $\left|J^{(t+1)}(\mathbf{V}) - J^{(t)}(\mathbf{V})\right| <$
Extract $\mathbf{W}$ from $\mathbf{V}$
Compute $\mathbf{Y}_1 = \mathbf{X}^T\mathbf{W}$
For $s = 1$ *to* m
  Set $t \leftarrow 0$
  Initialize $\mathbf{G}^{(t)} \in R^{h\times h}$ as an identity matrix
  Randomly generate $\mathbf{Z} \in R^{c\times d}$, where each element is in the range of [0, 1]
  Compute $\mathbf{K} = \left[\mathbf{X}^T + \sigma\mathbf{Y}_s\mathbf{Z}\ \theta\mathbf{I}\right] \in R^{n\times h}$
  Repeat
    Compute $\mathbf{V}^{(t+1)} = (\mathbf{G}^{(t)})^{-1}\mathbf{K}^T(\mathbf{K}(\mathbf{G}^{(t)})^{-1}\mathbf{K}^T)^{-1}\mathbf{Y}$
    Compute $\mathbf{G}^{(t+1)}$, where the i-th diagonal element is $g_{ii} = \frac{1}{2v_2^{i(t+1)}}$
    Set $t \leftarrow t+1$
  Until $\left|J^{(t+1)}(\mathbf{V}) - J^{(t)}(V)\right| < \epsilon$
  Extract $\mathbf{W}$ from $\mathbf{V}$
  Compute $\mathbf{Y}_s = \mathbf{X}^T\mathbf{W}$
End

When the feature ranking list generated by each model is obtained, the Gaussian kernel based SVM (Chang and Lin, 2011) and Ridge regression (Ridge) (Yang and Wen, 2018) are employed to perform classification tasks. Based on the epilepsy EEG data shown in **Table 1**, we construct 3 classification tasks (see **Table 2**).

For each task, 75% samples are used for training and 25% samples are used for testing. Parameters (kernel width and slack variable) in the Gaussian kernel based SVM and the regularized parameter in Ridge are determined by 5-CV on the training set. Testing procedure is repeated 100 times and the average results in terms of *Accuracy* are recorded, where *Accuracy* is defined as the ratio of the number of correctly classified samples to the number of all samples.

Experimental Results

In this section, we report our experimental results from two main aspects, i.e., classification performance of selected features and the parameter analysis. **Figures 4**, **5** show the classification performance of five models with different numbers of features (from 5 to 100, step size is 5) selected from the corresponding

TABLE 2 | Three classification tasks for selected features.

No. of tasks	Volunteers	Groups	#Sizes	#Classes	Task description
Task 1	Health	A, B	200	2	Classify healthy subjects to the eye-opening group and the eye-closing group.
Task 2	Epileptic	C, D and E	300	3	Classify epileptic subjects to non-seizure period, interseizure period and seizure period.
Task 3	Health/Epileptic	A, B, C, D and E	500	2	Classify all subjects into healthy group and epileptic group.

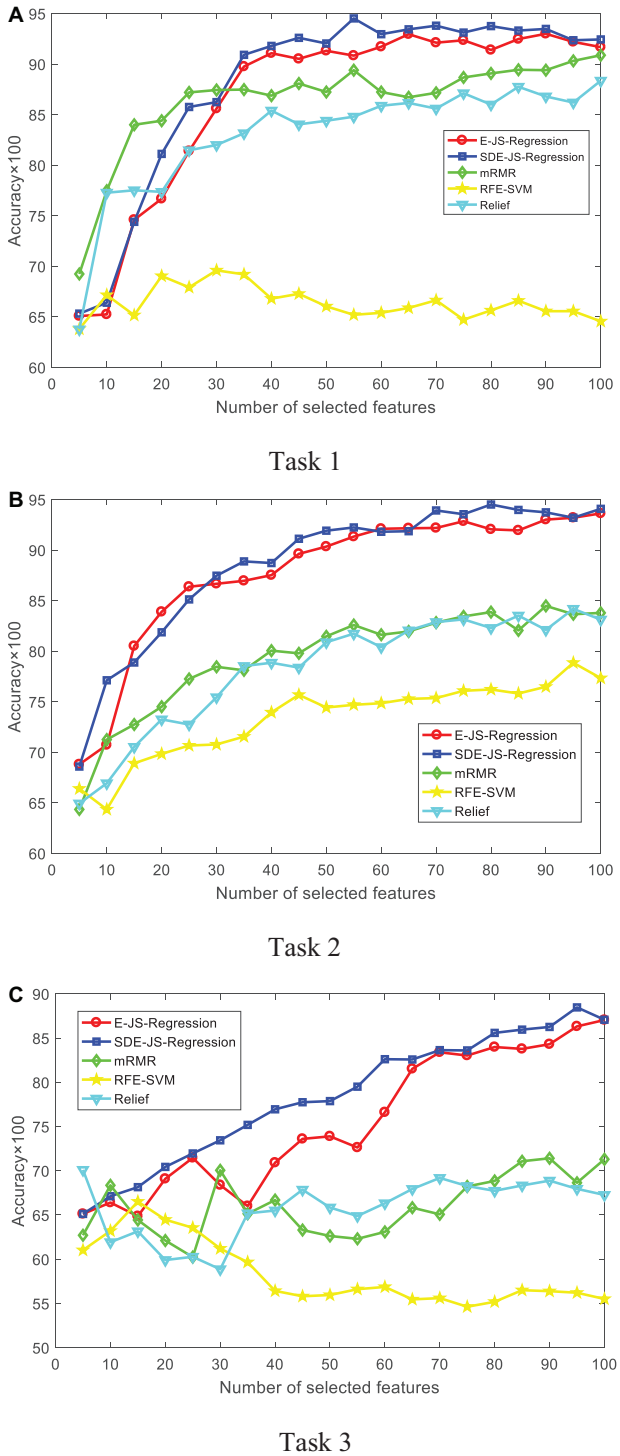

FIGURE 4 | Classification performance by SVM. SDE-JS-Regression is our method. **(A)** Task 1. **(B)** Task 2. **(C)** Task 3.

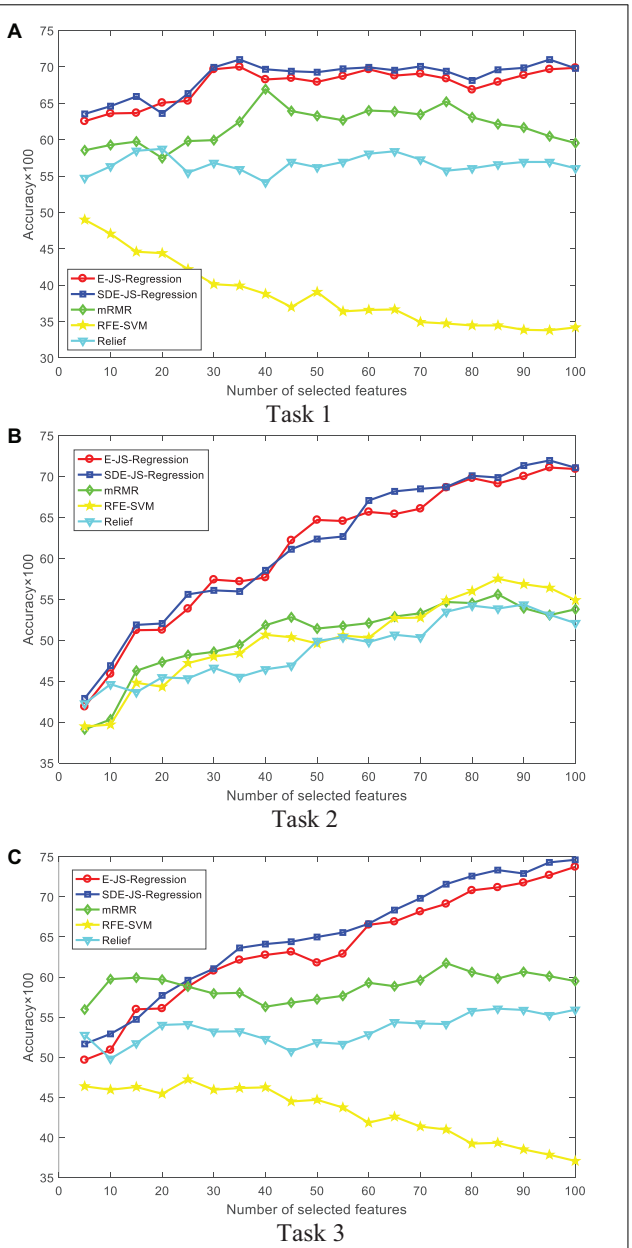

FIGURE 5 | Classification performance by Ridge. SDE-JS-Regression is our method. **(A)** Task 1. **(B)** Task 2. **(C)** Task 3.

ranking list. **Figure 6** shows parameter analysis results w.r.t the regularized parameter θ and the number of components m, where θ is searched from the range [0.001, 0.005, 0.01, 0.05, 0.1, 0.5, 1, 1.5, 2, 2.5] and m is searched from the range [1–10]. Accuracy of each task is obtained on the top 55 features selected from the ranking feature list.

DISCUSSION

From the comparative results of three classification tasks shown in **Figures 4**, **5**, we observe that SDE-JS-Regression performs better than the benchmarking models, especially mRMR, RFE-SVM, and Relief. On task 3, regardless of SVM or Ridge,

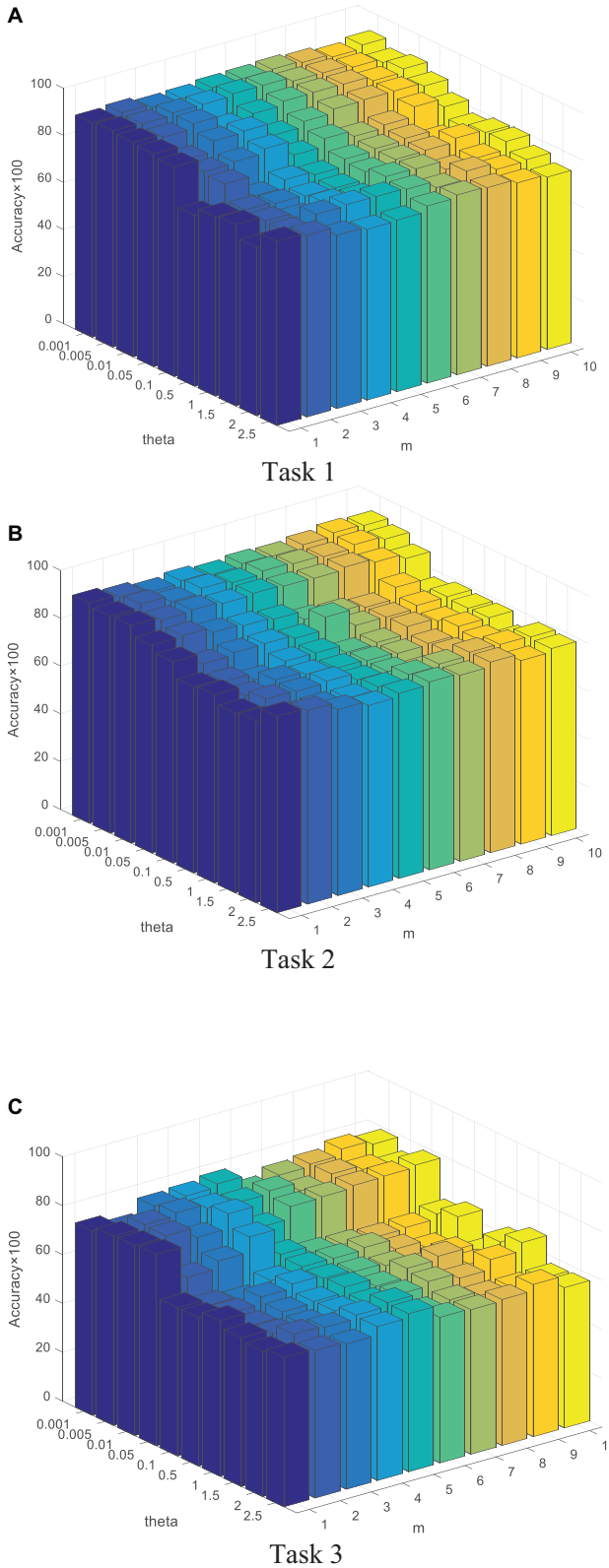

FIGURE 6 | Parameter analysis w.r.t θ and *m*. Accuracy of each task is obtained on the top 55 features selected from the ranking feature list. **(A)** Task 1. **(B)** Task 2. **(C)** Task 3.

SDE-JS-Regression always perform better than E-JS-Regression when the number of selected top features is bigger than 15. More characteristics are exhibited from the following aspects.

- From our experimental results, we find that features obtained from embedded feature selection models (SDE-JS-Regression and E-JS-Regression) are more inductive to the classifier than filter models (mRMR and Relief) and wrapper models (RFE-SVM). This is because embedded feature selection models minimize the classification training errors during the procedure of feature selection. Therefore, for our epilepsy classification tasks via EEG signals, embedded feature selection models are more suitable.
- On the three classification tasks, especially task 3, SDE-JS-Regression achieves better performance than E-JS-Regression, which indicates that our stacked deep structure can indeed help to select more classification addictive features and hence improve the classification performance. As we stated before, the benefits we inherit from the stacked deep structure lie in that the random projections added into the original features can help us to continuously open the manifold structure existing in the original feature space in a stacked way. With such benefits, the input feature space becomes more linearly separable.
- From **Figure 5**, with respect to θ, we observe that SDE-JS-Regression performs well in its range of [0.001, 0.05]. With the further increase of θ from 0.05 to 2.5, the classification performance begins to decrease. However, although the performance begins to decline when θ is in the range of [0.05, 2.5], the performance of SDE-JS-Regression does not show a significant change. Therefore, our proposed SDE-JS-Regression seems to be robust to θ. For our three EEG classification tasks, θ can be set from 0.001 to 0.05.
- The number of layers (components) in the structure of SDE-JS-Regression determines the number of random shifts added into the input feature space. As we can see from **Figure 5** that "the more layers the better performance" is not holds. On the three tasks, 4–6 layers can guarantee a relatively good performance. Too many random shifts can lead to distribution distortion of the training set.

CONCLUSION

In this study, we propose a feature selection model SDE-JS-Regression for AI-assisted clinical diagnosis through EEG signals. SDE-JS-Regression is quite different from the existing embedded models due to its stacked deep structure that is constructed in a layer-by-layer manner based on the stacked generalized principle. SDE-JS-Regression is derived from E-JS-Regression but performs better than E-JS-Regression since that random projections added into the original features can help us to continuously open the manifold structure existing in the original feature space in a stacked way so that the original input feature space becomes more linearly separable. We construct three classification tasks based on the selected features to evaluate the

effectiveness of SDE-JS-Regression. Experimental results show that features selected by SDE-JS-Regression are more meaningful and helpful to the classifier hence generates better performance than benchmarking models. This study is not without limitations. For example, how to effectively determine the number of layers is very important. Therefore, in addition to CV, a new finding strategy will be desired in our coming studies.

DATA AVAILABILITY STATEMENT

Publicly available datasets were analyzed in this study. This data can be found here: http://www.meb.unibonn.de/epileptologie/science/physik/eegdata.html.

AUTHOR CONTRIBUTIONS

YZ, KJ, and CL designed the whole algorithm and experiments. JT, YW, and CQ contributed on code implementation. All authors contributed to the article and approved the submitted version.

FUNDING

This work was supported in part by the National Natural Science Foundation of China under Grant No. 817017938, by Jiangsu Post-doctoral Research Funding Program under Grant No. 2020Z020, and by the Shenzhen Basic Research under Grant Nos. JCYJ20170413152804728 and JCYJ2018050718250885.

ACKNOWLEDGMENTS

We thank the reviewers whose comments and suggestions helped improve this manuscript. We also thank Feiping Nie for sharing the source code of E-JS-Regression.

REFERENCES

Adeli, H., Ghosh-Dastidar, S., and Dadmehr, N. (2007). A Wavelet-Chaos Methodology for Analysis of EEGs and EEG Subbands to Detect Seizure and Epilepsy. *IEEE Trans. Biomed. Eng.* 54, 205–211. doi: 10.1109/tbme.2006.886855

Agarwal, A., Dowsley, R., McKinney, N. D., and Wu, D. (2018). Privacy-preserving linear regression for brain-computer interface applications, in *Proceedings of the 2018 IEEE International Conference on Big Data (Big Data)*, Seattle, WA, 5277–5278.

Ang, J. C., Mirzal, A., Haron, H., and Hamed, H. N. A. (2016). Supervised, unsupervised, and semi-supervised feature selection: a review on gene selection. *IEEE/ACM Trans. Comput. Biol. Bioinform.* 13, 971–989. doi: 10.1109/tcbb.2015.2478454

Chang, C. C., and Lin, C. J. (2011). LIBSVM: a library for support vector machines. *ACM Trans. Intell. Syst. Technol. (TIST)* 2, 1–27. doi: 10.1145/1961189.1961199

Chen, C., Dong, D., Qi, B., Petersen, I. R., and Rabitz, H. (2017). Quantum ensemble classification: a sampling-based learning control approach. *IEEE Trans. Neural Netw. Learn. Syst.* 28, 1345–1359. doi: 10.1109/tnnls.2016.2540719

Coito, A., Michel, C. M., van Mierlo, P., Vulliémoz, S., and Plomp, G. (2016). Directed functional brain connectivity based on EEG source imaging: methodology and application to temporal lobe epilepsy. *IEEE Trans. Biomed. Eng.* 63, 2619–2628. doi: 10.1109/tbme.2016.2619665

Guyon, I., Weston, J., Barnhill, S., and Vapnik, V. (2002). Gene selection for cancer classification using support vector machines. *Mach. Learn.* 46, 389–422.

Habbema, J., and Hermans, J. (1977). Selection of variables in discriminant analysis by F-statistic and error rate. *Technometrics* 19, 487–493. doi: 10.1080/00401706.1977.10489590

Hall, M. A., and Smith, L. A. (1999). "Feature selection for machine learning: comparing a correlation-based filter approach to the wrapper," in *Proceedings of the FLAIRS Conference*, Hollywood, FL, 235–239.

Kira, K., and Rendell, L. A. (1992). "A Practical Approach to Feature Selection," in *Proceedings of the Ninth International Workshop on Machine Learning*, San Francisco, CA, 249–256. doi: 10.1016/b978-1-55860-247-2.50037-1

Liu, W., Wu, W., Wang, Y., Fu, Y., and Lin, Y. (2019). Selective ensemble learning method for belief-rule-base classification system based on PAES. *Big Data Mining Anal.* 2, 306–318. doi: 10.26599/bdma.2019.9020008

Lopes da Silva, F. H. (2008). The Impact of EEG/MEG Signal Processing and Modeling in the Diagnostic and Management of Epilepsy. *IEEE R0ev. Biomed. Eng.* 1, 143–156. doi: 10.1109/rbme.2008.2008246

Mammone, N., De Salvo, S., Bonanno, L., and Ieracitano, C. (2019). Brain Network Analysis of Compressive Sensed High-Density EEG Signals in AD and MCI subjects. *IEEE Trans. Indus. Inform.* 15, 527–536. doi: 10.1109/tii.2018.2868431

Minku, L. L., White, A. P., and Yao, X. (2010). The impact of diversity on online ensemble learning in the presence of concept drift. *IEEE Trans. Knowledge Data Eng.* 22, 730–742. doi: 10.1109/tkde.2009.156

Nakamura, T., Alqurashi, Y. D., Morrell, M. J., and Mandic, D. P. (2020). Hearables: automatic overnight sleep monitoring with standardized in-ear EEG sensor. *IEEE Trans. Biomed. Eng.* 67, 203–212. doi: 10.1109/tbme.2019.2911423

Nie, F., Huang, H., Cai, X., and Ding, C. H. (2010). Efficient and robust feature selection via joint l2, 1-norms minimization, in *Advances in Neural Information Processing Systems*, eds M. I. Jordan, Y. LeCun, and S. A. Solla (Cambridge, MA: MIT Press), 1813–1821.

Panwar, S., Joshi, S. D., Gupta, A., and Agarwal, P. (2019). Automated epilepsy diagnosis Using EEG with test set evaluation. *IEEE Trans. Neural Syst. Rehabil. Eng.* 27, 1106–1116. doi: 10.1109/tnsre.2019.2914603

Parvez, M. Z., and Paul, M. (2016). Epileptic seizure prediction by exploiting spatiotemporal relationship of EEG signals using phase correlation. *IEEE Trans. Neural Syst. Rehabil. Eng.* 24, 158–168. doi: 10.1109/tnsre.2015.2458982

Peker, M., Sen, B., and Delen, D. (2016). A novel method for automated diagnosis of epilepsy using complex-valued classifiers. *IEEE J. Biomed. Health Inform.* 20, 108–118. doi: 10.1109/jbhi.2014.2387795

Peng, H., Long, F., and Ding, C. H. Q. (2005). Feature selection based on mutual information: criteria of max-dependency, max-relevance, and min-redundancy. *IEEE Trans. Pattern Anal. Mach. Intell.* 27, 1226–1238. doi: 10.1109/tpami.2005.159

Raileanu, L. E., and Stoffel, K. (2004). Theoretical comparison between the gini index and information gain criteria. *Ann. Math. Artif. Intell.* 41, 77–93. doi: 10.1023/b:amai.0000018580.96245.c6

Rieke, C., Mormann, F., Andrzejak, R. G., Kreuz, T., David, P., Elger, C. E., et al. (2003). Discerning nonstationarity from nonlinearity in seizure-free and preseizure EEG recordings from epilepsy patients. *IEEE Trans. Biomed. Eng.* 50, 634–639. doi: 10.1109/tbme.2003.810684

Saputra Rangkuti, F. R., Fauzi, M. A., Sari, Y. A., and Sari, E. D. L. (2018). "Sentiment analysis on movie reviews using ensemble features and pearson correlation based feature selection," in *Proceedings of the 2018 International Conference on Sustainable Information Engineering and Technology (SIET)*, Malang, 88–91.

Shah, F. P., and Patel, V. (2016). "A review on feature selection and feature extraction for text classification," in *Proceedings of the 2016 International*

Conference on Wireless Communications, Signal Processing and Networking (WiSPNET), Chennai, 2264–2268.

Visalakshi, S., and Radha, V. (2014). "A literature review of feature selection techniques and applications: review of feature selection in data mining," in *Proceedings of the 2014 IEEE International Conference on Computational Intelligence and Computing Research*, Coimbatore, 1–6.

Wang, D., Miao, D., and Blohm, G. (2013). A New Method for EEG-Based Concealed Information Test. *IEEE Trans. Inform. Forensics Security* 8, 520–527. doi: 10.1109/tifs.2013.2244884

Webb, G. I., and Zheng, Z. (2004). Multistrategy ensemble learning: reducing error by combining ensemble learning techniques. *IEEE Trans. Knowledge Data Eng.* 16, 980–991. doi: 10.1109/tkde.2004.29

Wolpert, D. H. (1992). Stacked generalization. *Neural Netw.* 5, 241–259.

Wu, D., King, J., Chuang, C., Lin, C., and Jung, T. (2018). Spatial Filtering for EEG-Based Regression Problems in Brain–Computer Interface (BCI). *IEEE Trans. Fuzzy Syst.* 26, 771–781. doi: 10.1109/tfuzz.2017.2688423

Yang, X., and Wen, W. (2018). Ridge and Lasso Regression Models for Cross-Version Defect Prediction. *IEEE Trans. Reliabil.* 67, 885–896. doi: 10.1109/tr.2018.2847353

Yetik, I. S., Nehorai, A., Lewine, J. D., and Muravchik, C. H. (2005). Distinguishing between moving and stationary sources using EEG/MEG measurements with an application to epilepsy. *IEEE Trans. Biomed. Eng.* 52, 471–479. doi: 10.1109/tbme.2004.843289

Zhang, Y., Ishibuchi, H., and Wang, S. (2018). Deep takagi–sugeno–kang fuzzy classifier with shared linguistic fuzzy rules. *IEEE Trans. Fuzzy Syst.* 26, 1535–1549. doi: 10.1109/tfuzz.2017.2729507

Zhang, Y., Zhou, Z., Bai, H., Liu, W., and Wang, L. (2020). Seizure classification from EEG signals using an online selective transfer TSK fuzzy classifier with joint distribution adaption and manifold regularization. *Front. Neurosci.* 11:496. doi: 10.3389/fnins.2020.00496

Zheng, W. (2017). Multichannel EEG-based emotion recognition via group sparse canonical correlation analysis. *IEEE Trans. Cogn. Dev. Syst.* 9, 281–290. doi: 10.1109/tcds.2016.2587290

Zhu, Z., Wang, Z., Li, D., Zhu, Y., and Du, W. (2020). Geometric structural ensemble learning for imbalanced problems. *IEEE Trans. Cybernet.* 50, 1617–1629. doi: 10.1109/tcyb.2018.2877663

Conflict of Interest: The authors declare that the research was conducted in the absence of any commercial or financial relationships that could be construed as a potential conflict of interest.

frontiers in Neuroscience

ORIGINAL RESEARCH
published: 14 August 2020
doi: 10.3389/fnins.2020.00809

Longitudinal Electroencephalography Analysis in Subacute Stroke Patients During Intervention of Brain–Computer Interface With Exoskeleton Feedback

Shugeng Chen[1], Lei Cao[2], Xiaokang Shu[3], Hewei Wang[1], Li Ding[1], Shui-Hua Wang[4,5] and Jie Jia[1,6]**

[1] Department of Rehabilitation Medicine, Huashan Hospital, Fudan University, Shanghai, China, [2] Department of Computer Science and Technology, Shanghai Maritime University, Shanghai, China, [3] School of Mechanical Engineering, Shanghai Jiao Tong University, Shanghai, China, [4] School of Architecture Building and Civil Engineering, Loughborough University, Loughborough, United Kingdom, [5] School of Mathematics and Actuarial Science, University of Leicester, Leicester, United Kingdom, [6] National Clinical Research Center for Aging and Medicine, Huashan Hospital, Fudan University, Shanghai, China

OPEN ACCESS

Edited by:
Yizhang Jiang, Jiangnan University, China

Reviewed by:
Juan Yang, Suzhou University, China
Jing Jin, East China University of Science and Technology, China

***Correspondence:**
Shui-Hua Wang
shuihuawang@ieee.org
Jie Jia
shannonjj@126.com

Specialty section:
This article was submitted to Neuroprosthetics, a section of the journal Frontiers in Neuroscience

Received: *27 May 2020*
Accepted: *10 July 2020*
Published: *14 August 2020*

Citation:
Chen S, Cao L, Shu X, Wang H, Ding L, Wang S-H and Jia J (2020) Longitudinal Electroencephalography Analysis in Subacute Stroke Patients During Intervention of Brain–Computer Interface With Exoskeleton Feedback. Front. Neurosci. 14:809. doi: 10.3389/fnins.2020.00809

Background: Brain–computer interface (BCI) has been regarded as a newly developing intervention in promoting motor recovery in stroke survivors. Several studies have been performed in chronic stroke to explore its clinical and subclinical efficacy. However, evidence in subacute stroke was poor, and the longitudinal sensorimotor rhythm changes in subacute stroke after BCI with exoskeleton feedback were still unclear.

Materials and Methods: Fourteen stroke patients in subacute stage were recruited and randomly allocated to BCI group (n = 7) and the control group (n = 7). Brain–computer interface training with exoskeleton feedback was applied in the BCI group three times a week for 4 weeks. The Fugl–Meyer Assessment of Upper Extremity (FMA-UE) scale was used to assess motor function improvement. Brain–computer interface performance was calculated across the 12-time interventions. Sensorimotor rhythm changes were explored by event-related desynchronization (ERD) changes and topographies.

Results: After 1 month BCI intervention, both the BCI group (p = 0.032) and the control group (p = 0.048) improved in FMA-UE scores. The BCI group (12.77%) showed larger percentage of improvement than the control group (7.14%), and more patients obtained good motor recovery in the BCI group (57.1%) than did the control group (28.6%). Patients with good recovery showed relatively higher online BCI performance, which were greater than 70%. And they showed a continuous improvement in offline BCI performance and obtained a highest value in the last six sessions of interventions during BCI training. However, patients with poor recovery reached a platform in the first six sessions of interventions and did not improve any more or even showed a decrease. In sensorimotor rhythm, patients with good recovery showed an enhanced ERD along with time change. Topographies showed that the ipsilesional hemisphere presented stronger activations after BCI intervention.

Conclusion: Brain–computer interface training with exoskeleton feedback was feasible in subacute stroke patients. Brain–computer interface performance can be an index to evaluate the efficacy of BCI intervention. Patients who presented increasingly stronger or continuously strong activations (ERD) may obtain better motor recovery.

Keywords: BCI performance, event-related desynchronization, motor recovery, longitudinal change, stroke

INTRODUCTION

Brain–computer interface (BCI) is increasingly developing in the neurological treatment, especially in stroke rehabilitation (López-Larraz et al., 2018). It is an intervention focused on the central nerve system, which played a role in both treatment and assessment. Recently, a meta-analysis (Cervera et al., 2018) has revealed its clinical efficacy in stroke motor rehabilitation. More and more studies have been performed to verify the positive effects in motor recovery by BCI training and to explore its possible mechanism as for promoting related cortical plasticity.

Brain–computer interface intervention has been applied to train stroke patients both in chronic and subacute stages for motor rehabilitation. Some scholars focused on chronic stroke. Ander et al. (Ramos-Murguialday et al., 2013) first reported a significant improvement in upper-limb motor function of the chronic stroke patients after 8 weeks in a randomized controlled trial. Leeb et al. (2016) also showed motor recovery through 10 sessions' BCI training. Ang et al. (2014) applied 12-session BCI training in chronic stroke and reported motor improvements.

Literature reported that stroke patients might obtain more motor recovery in subacute than chronic stage (Buma et al., 2013). It suggested the possibility and value to add BCI intervention in subacute stage. As a result, studies of BCI intervention in subacute stroke were performed by several other scholars. Li et al. (2014) applied 24 sessions' BCI training with functional electrical stimulation (FES) feedback in stroke patients of subacute stage and reported an improvement in hand function by the Action Research Arm Test. Pichiorri et al. (2015) reported an improvement in the Fugl–Meyer Assessment of Upper Extremity (FMA-UE) after 12-session BCI training. Mihara et al. (2013) applied six sessions' BCI training and found improvement in the hand/finger subscale of FMA-UE. All above studies suggested the feasibility and efficacy to apply BCI intervention in both chronic and subacute stroke to promote motor recovery.

Brain–computer interface performance is a parameter used to judge the interaction effects when applying BCI training. Tam et al. (2011) tried to improve BCI performance to make it more user-friendly and reliable for stroke rehabilitation. Higher BCI performance was reported to be along with good motor recovery in stroke patients. Li et al. (2014) reported that BCI performance improved as the intervention times increased and the patients obtained motor recovery. Tung et al. (2013) reported that the number of sessions correlated with the change in the FMA scores. Brain–computer interface performance may be used to evaluate the applicability of BCI intervention for stroke individuals. Prasad et al. (2009) showed a range of 60–75% of online BCI performance in chronic stroke patients, which suggested the feasibility of BCI training in neurorehabilitation.

Sensorimotor rhythm changes were commonly explored by many BCI studies. Event-related desynchronization (ERD) (Pfurtscheller, 1979) was calculated from the electroencephalography (EEG) data to describe sensorimotor rhythm changes. It also stands for the cortical activities of the stroke patients during motor tasks (Pfurtscheller, 1999; Takemi et al., 2013; Kaiser et al., 2014). Stronger ERD was reported to present in the sensorimotor cortex of patients with good motor function (Bartur et al., 2019), and the location of ERD became focused on sensorimotor cortex after rehabilitation training (Tam et al., 2011; Liu et al., 2014). The longitudinal changes of cortical activities during a long-term BCI intervention are of great importance to show the time-varying effects. However, the longitudinal sensorimotor rhythm changes of patients with different levels of motor recovery under BCI intervention in subacute stroke are unclear. In subacute stage, the cortical activities varied quickly along time. During BCI training, it is valuable to clarify the longitudinal cortical activities, which may help explore the mechanism of BCI intervention.

The application of BCI intervention in subacute stroke patients could be useful in motor rehabilitation. The aim of this study was to explore the characteristics of BCI performance and longitudinal sensorimotor rhythm changes in subacute stroke patients. We hypothesized that the continuous results of BCI performance could be used to evaluate the clinical effects of motor recovery. Patients presented different longitudinal sensorimotor rhythm changes with different levels of motor recovery.

MATERIALS AND METHODS

Research Subjects

Patients were recruited from the Department of Rehabilitation Medicine of Huashan Hospital affiliated to Fudan University. Inclusion criteria for the study were as follows: (1) unilateral subcortical stroke (ischemia or hemorrhage) diagnosed by computer tomography or magnetic resonance imaging (MRI); (2) first onset of stroke; (3) age between 25 and 75 years; (4) the onset was more than 4 weeks and less than 6 months; (5) the level of cognitive impairment: Mini-Mental State Examination score >25; (6) and being able to sit in a chair for at least 1 h. Exclusion criteria were as follows: (1) patients with previous history of epilepsy; severe failure of vital organs such as heart, lung, liver, and kidney; uncontrollable hypertension; arrhythmia; severe coronary heart disease; and

diabetes complications; (2) unilateral neglect or vision problems; (3) allergic to conductive paste; (4) received other non-invasive brain stimulation interventions during the study period; and (5) cannot complete basic treatment. Fourteen subacute stroke patients were enrolled in the study and randomly allocated to BCI group (n = 7) and the control group (n = 7). Baseline demographic data and clinical characteristics of patients were presented in **Table 1**. This study was approved by the Ethics Committee of Huashan Hospital (KY2017-005) and performed according to the Declaration of Helsinki. All the patients signed the informed consent.

Experimental Procedure

Group Allocation

In addition to the BCI intervention, the other parts of the basic treatment were maintained consistent in the two groups (BCI group and control group). Basic treatment included the following: (1) drug: following the rehabilitation physician's advice; (2) routine rehabilitation therapy: physical therapy (20 min, five times a week), low-frequency electrical stimulation (20 min, five times a week), occupational therapy (20 min, five times a week).

The BCI intervention was three sessions a week lasting 1 month, with a total of 12 sessions. To keep the consistency of rehabilitation with the experimental group, the control group was instructed with the same hand motor imagery training tasks. All patients in the control group were instructed to attempt motion of wrist extension by the same therapist. The tasks were combined with three sets, 30 motions for one set. And the instructions were maintained the same as it were in the BCI group. Patients in the control group did not use the Omega device, and they were blind to what the patients did in the BCI group.

TABLE 1 | The demographic and baseline clinical characteristics of the subjects.

	Sex	Age (years)	AL	TI	TSI (m)	SI	FMA-UE
BCI group							
OME1	M	31	R	I	5	L, basal ganglia	36
OME2	M	40	L	H	4	R, basal ganglia	30
OME3	M	42	R	H	1	L, basal ganglia	50
OME4	M	47	R	I	1	L, paracele	37
OME5	M	36	R	I	3	L, basal ganglia	28
OME6	M	30	R	I	5	L, paracele, basal ganglia	25
OME7	M	65	L	I	3	R, brainstem	13
Mean (*SD*)	–	41.6 (12.0)	–	–	3.1 (1.7)	–	31.3 (11.5)
Control group							
CG1	F	72	R	I	1	L, paracele	19
CG2	M	37	R	H	4	L, basal ganglia	28
CG3	F	43	L	I	3	R, basal ganglia	29
CG4	M	64	R	I	4.5	L, paracele, corona radiata	26
CG5	M	47	R	H	2	L, basal ganglia	28
CG6	M	64	R	I	6	L, brainstem, basal ganglia, paracele	42
CG7	M	42	L	I	4	R, basal ganglia	54
Mean (*SD*)	–	52.0 (11.1)	–	–	3.9 (1.5)	–	32.3 (11.8)
p	–	0.13	–	–	0.70	–	0.87

AL, affected limb; TI, type of injury; TSI, time since injury; SI, site of injury; M, male; F, female; R, right; L, left; I, ischemia; H, hemorrhage; FMA-UE, the Fugl–Meyer Assessment of Upper Extremity; SD, standard deviation; p, results of t-test between groups.

Protocol for BCI Intervention

Figure 1A shows the overview of the BCI intervention system principle. Brain–computer interface training was conducted in a quiet room. The Omega force feedback device was placed on the table and controlled by the BCI system. The patients sat in front of a computer screen with their affected hands fixed on the Omega device. Electroencephalography were collected using 32 channels consisting of Ag/AgCl electrode of EEG cap (actiCAP; Brain Products, Gilching, Germany) according to the configuration of 10–20 International System (Klem et al., 1999). The signal is amplified by the amplifier (Brain Products). The reference electrode was located in the right mastoid process, and the ground electrode was located in the forehead. The electrode impedance was kept below 5 k**Ω**. The original EEG signals was recorded at a sampling rate of 200 Hz and filtered by a bandpass filter between 1 and 100 Hz.

There was approximately 11 s for one trial, 30 trials as a set with a total of three sets for one-session BCI training. Patients in the process of BCI training were required to attempt motion of wrist extension as far as possible but not to have compensatory movements (e.g., to move the head and shoulders, etc.). When the BCI system correctly recognized the intention of the patients' motor attempt, it would output command and manipulate the Omega force feedback device and drive the patients' affected hands to complete the wrist extension motion. When the patients' motion intention was not successfully recognized, the Omega device would not produce any movement.

Figure 1B shows the experimental setup of one trial. During one trial, there was a white cross presenting on the center of the screen from 0 to 3 s. The patients kept still and rest. After the task began 1 s, vibrations appeared on the Omega device to give tips for the patients. And then a red square or a red rectangle appeared. The red square represented a static task, whereas a red rectangle represented the motor task. When the patients were performing motor task, they were required to maintain the motion as far as they could until the white cross disappeared. When there was a static task, patients just rested and did nothing. The rest time interval was adopted randomly in order to prevent the patients' adaptability in the training process. There were rest intervals between each set (totally three sets for 1 day's BCI training) generally for 1 min, depending on the patients' status.

BCI Performance Calculation

Brain–computer interface performance was evaluated between the task and idle states. The idle state was defined at [−4, −1] s prior to task cues and the task state was defined at [1, 4] s post-task cues. Common spatial pattern (CSP) was used for feature extraction of EEG data (Blankertz et al., 2006). Electroencephalography data were filtered by the band from alpha–beta frequency (8–30 Hz).

For online BCI performance, all 31 channels (FP1, FZ, F3, F7, FT9, FC5, FC1, C3, T7, TP9, CP5, CP1, PZ, P3, P7, O1, O2, P4,

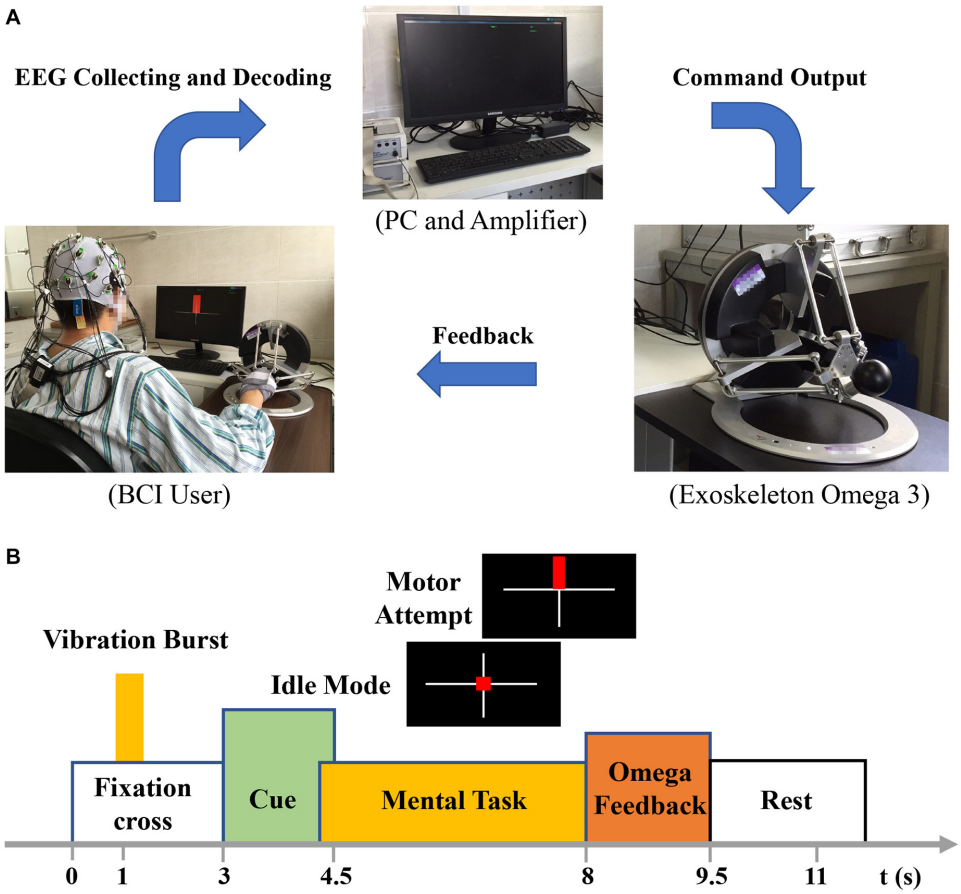

FIGURE 1 | (A) Overview of the BCI system principle. **(B)** Experimental setup of one trial.

P8, TP10, CP6, CP2, CZ, C4, T8, FT10, FC6, FC2, F4, F8, FP2) were used for calculation. In each online test, the first run of 30 times of the task state and static state were used for training the classifier. In the second run of tests, at the end of each task, single-trial classification was performed with 31 channels of EEG signals. In order to better adapt to the nonstationarity of EEG signals, supervised online adaptation was implemented in the online decoding. In the second online feedback training, the CSP filter and linear discriminant analysis classifier were retrained after each test using the previous 30 test results.

For offline BCI performance calculation, all 31 and 7 channels (FC1, FC2, C3, CZ, C4, CP1, and CP2) were selected for data analysis. The first and last three rows of the CSP transformation matrix could be used for maximizing the difference of two groups of data. And then the transformed features were trained by random forest classifier. The 90 trials were divided into three pieces. Thus, a 3-fold cross-validation was applied to pick an optimal classifier.

EEG Processing

Electroencephalography data from 31 channels were used in processing. The power spectrum of channels C3 and C4 was computed at the frequency of 8–30 Hz to identify ERD on motor tasks of the affected hands. Time–frequency distributions of EEG trials were estimated using a windowed Fourier transform (Peng et al., 2019) with a fixed 200 ms Hanning window. Windowed Fourier transform yielded, for each trial, a complex time–frequency estimate F(t,f) at each time–frequency point (t,f), extending from −2,000 to 6,000 ms (in steps of 5ms) in the time domain, and from 1 to 30 Hz (in steps of 1Hz) in the frequency domain. Power spectrum (P), $P(t,f) = |F(t,f)|^2$, was obtained. The percentage of relative power change was calculated to obtain the ERD with respect to a resting-state baseline ([−2, 0] s) before the red triangle cue. The interest time was set at [1, 4] s after the cue, during which the patient was performing the motor tasks of wrist extension. The power spectrum of interest in the period after the event is given by A, whereas that of the preceding baseline period is given by R. Event-related desynchronization/event-related synchronization (ERS) (E) was calculated according to Eq. (1):

$$E = \frac{A - R}{R} \times 100\% \quad (1)$$

Under this definition, ERD was expressed as a negative value, and ERS was a positive value. The topographies were drawn with an

interest time of [1.4, 1.6] s after the task onset, with respect to a resting-state baseline ([−2, 0] s).

Statistical Analysis

Analyses were conducted using SPSS version 23.0 (IBM Inc., Chicago, IL, United States). Continuous variables are presented as the mean ± standard deviation. A *t*-test was performed to compare the difference of age, time since injury, and baseline FMA-UE between the BCI group and the control group. Two-way repeated-measures analysis of variance (ANOVA) was performed for the FMA-UE with time as the within-subject factor (i.e., before and after therapy) and group as the between-subject factor (i.e., BCI and control groups). If a significant interaction was identified through two-way repeated measures ANOVA, then a paired *t*-test was adopted for *post hoc* analysis to compare FMA-UE score before and after BCI intervention. A *t*-test was conducted to compare the effects between groups. Two-way repeated-measures ANOVA was performed for the ERD with time (i.e., before and after therapy) and channel (i.e., C3 and C4) as the within-subject factors. A paired *t*-test was applied

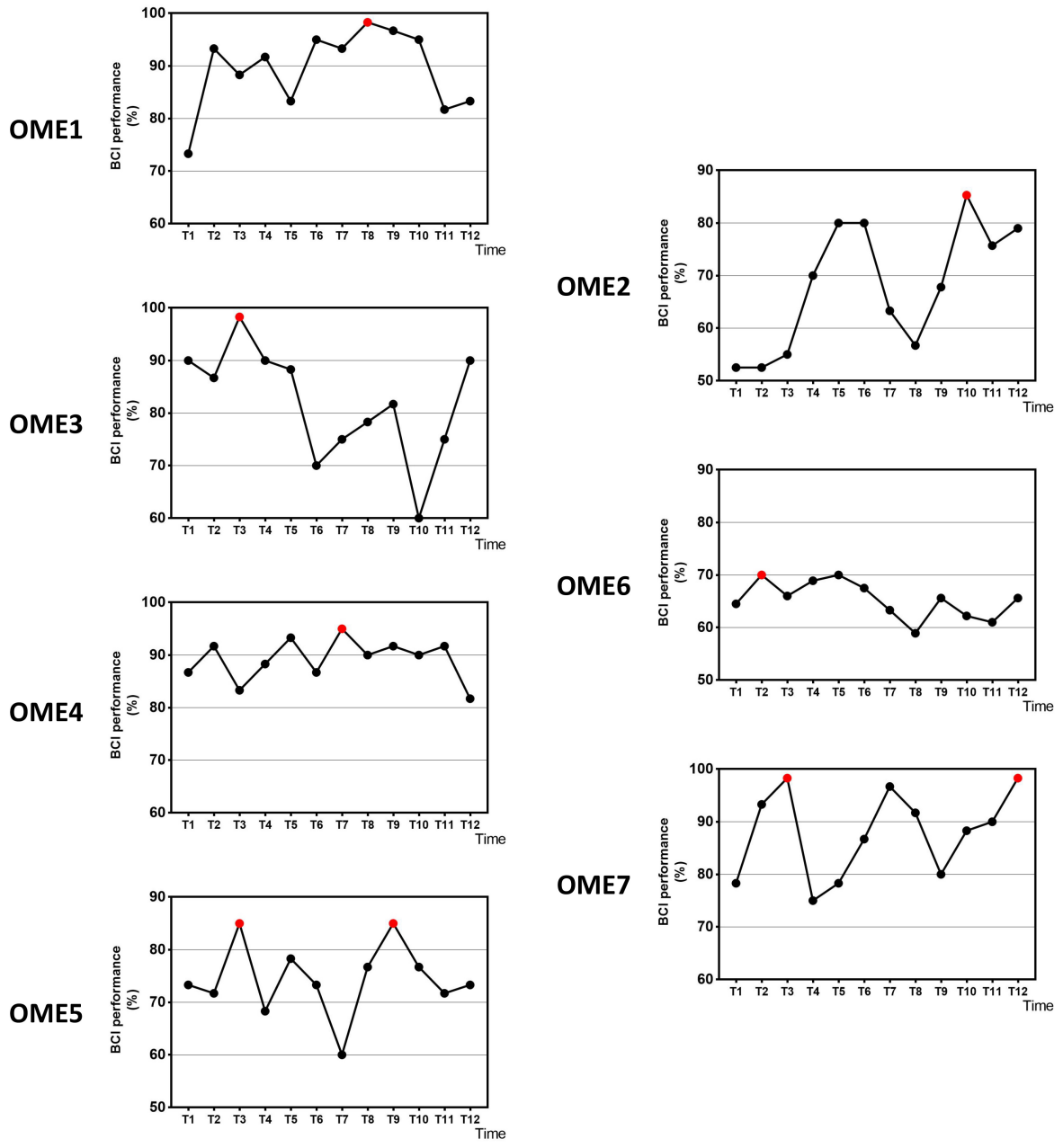

FIGURE 2 | The online BCI performance with 31 channels of the seven subjects during the 12-session BCI training in the BCI group. The red point means the highest value.

for *post hoc* analysis to compare the ERD before and after BCI intervention in the BCI group. $p < 0.05$ (two-sided) was considered to indicate a significant result.

RESULTS

BCI Performance

Figure 2 shows the online performance of BCI tasks for all subjects. The data were acquired from 31 channels of EEG signals. Three patients (OME1, OME4, and OME7) maintained a level of greater than 70% in BCI performance across the 12 training sessions. Two patients (OME3 and OME5) presented a BCI performance of more than 70% in most of the 12 training sessions. Two patients (OME2 and OME6) showed poor BCI performance during the 12 training sessions.

Figure 3 shows the offline performance of BCI tasks for all subjects. The data were acquired from 31 channels of EEG signals. Three subjects (OME1, OME4, and OME5) were included into a subgroup, which obtained the highest BCI performance in

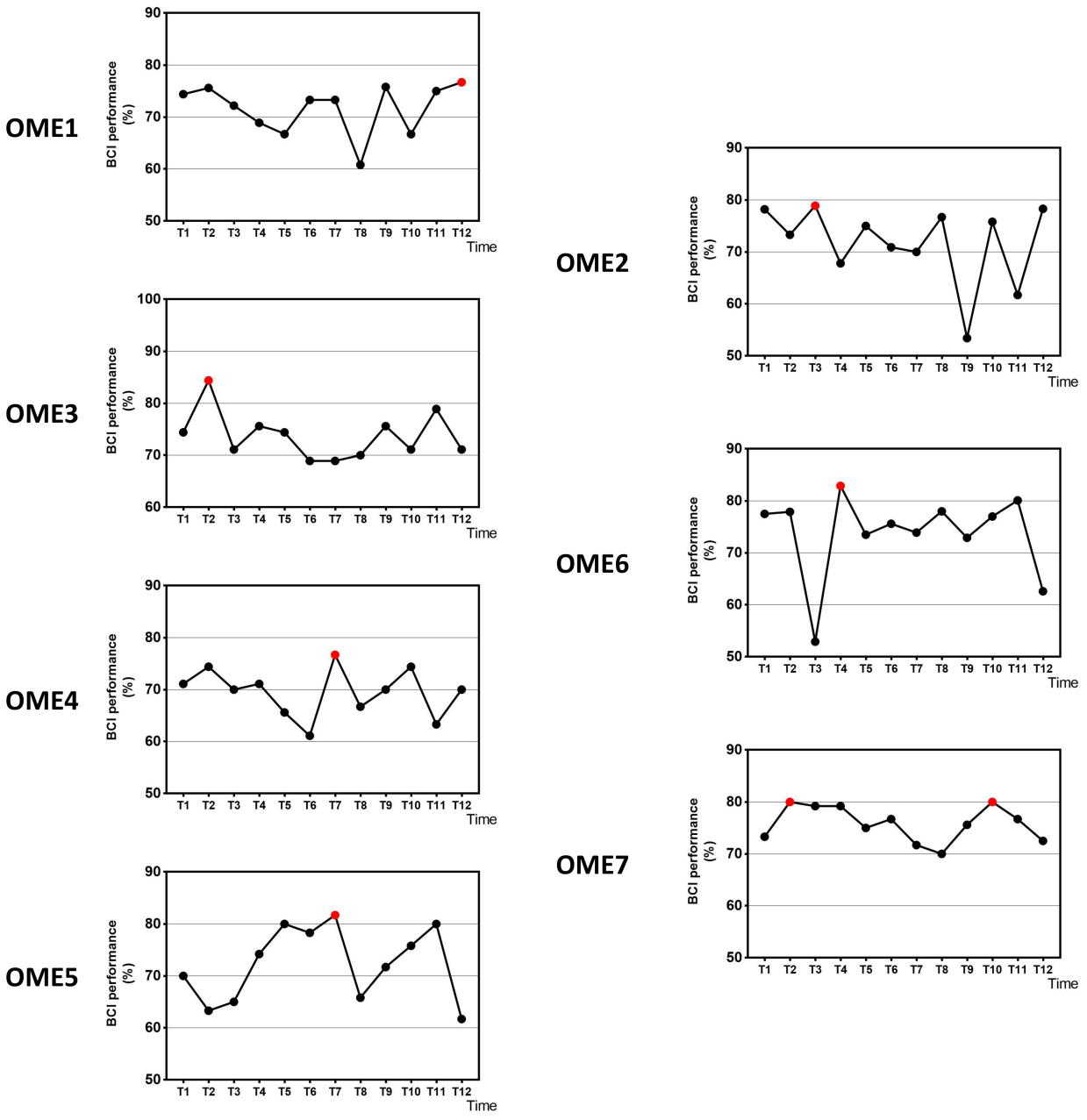

FIGURE 3 | The offline BCI performance with 31 channels of the seven subjects during the 12-session BCI training in the BCI group. The red point means the highest value.

the last six sessions. Three subjects (OME2, OME6, and OME7) were included into another subgroup, which obtained the highest BCI performance in the first six sessions. **Figure 4** shows the offline performance of BCI tasks of for all subjects. The data were acquired from seven channels (FC1, FC2, C3, CZ, C4, CP1, and CP2). Three subjects (OME1, OME3, and OME4) were included into a subgroup, which obtained the highest BCI performance in the last six sessions. Three subjects (OME2, OME6, and OME7) were included into another subgroup, which obtained the highest BCI performance in the first six sessions.

Figure 5 shows the average BCI performance of online 31 channels, offline 31 channels, and offline 7 channels. The online accuracies were higher than the offline accuracies in five patients (OME1, OME3, OME4, OME5, and OME7) and lower in two patients (OME2 and OME6). OME2 and OME6 showed average online BCI performance that were lower than 70%. For offline 7 channels and 31 channels analysis, all subjects almost achieved the criterion level of mean accuracy (70%) that rendered the control of BCI application. It was suggested that the pattern of motor attempt could be detected for BCI recognition. However, the mean accuracies used in 7 channels were higher than those used in all 31 channels in six subjects except OME7. It was inferred that the effective features of neural pattern were mainly evoked in the area of motor cortex.

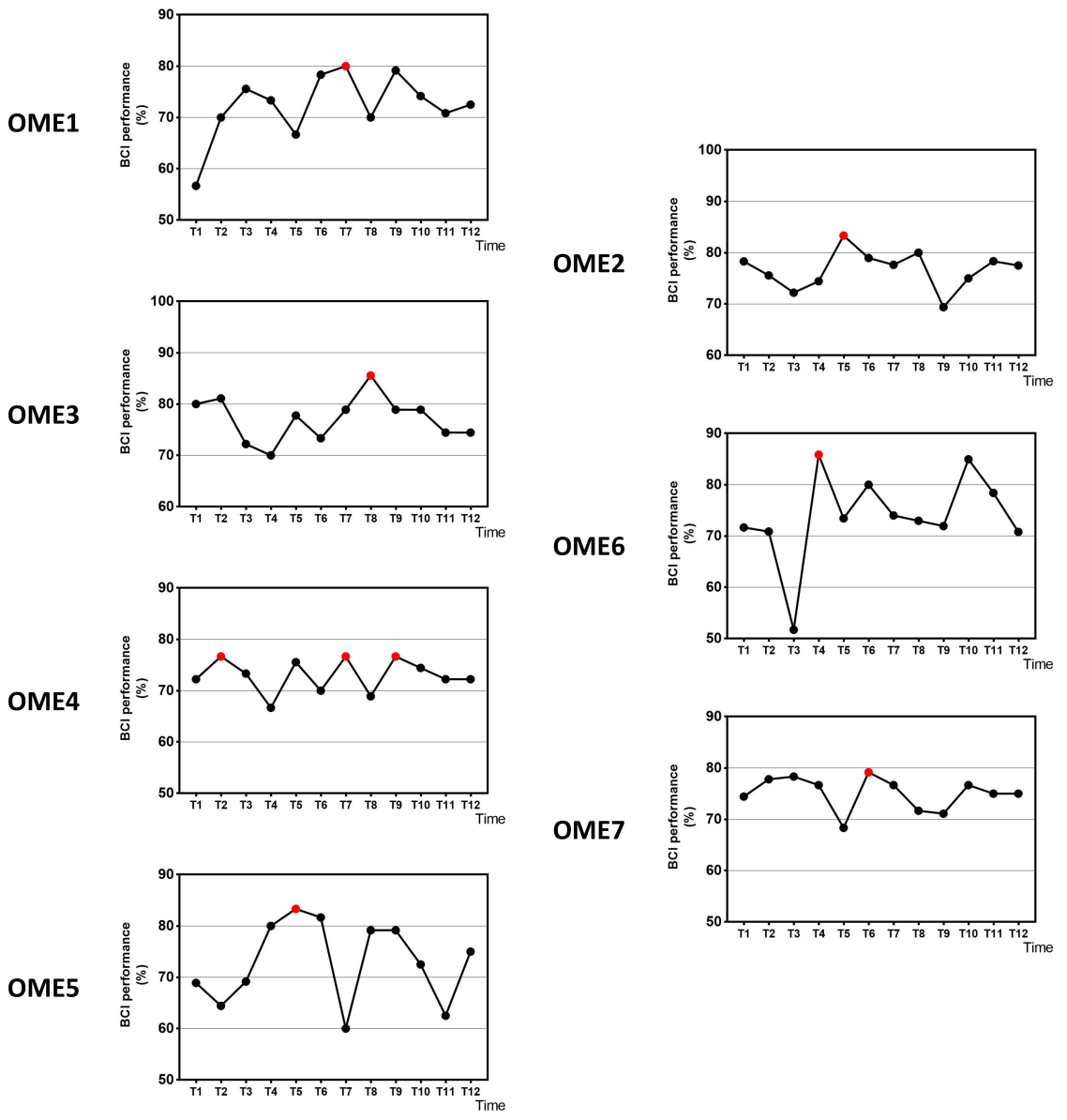

FIGURE 4 | The offline BCI performance with seven channels of the seven subjects during the 12-session BCI training in the BCI group. The red point means the highest value.

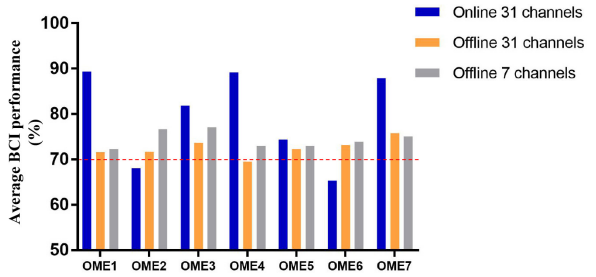

FIGURE 5 | The average BCI performance of 12 sessions with online 31 channels, offline 31 channels, and offline 7 channels of the seven subjects in the BCI group.

Rehabilitation Outcomes

Two-way repeated-measures ANOVA results for the FMA-UE showed no significant time and group interaction [$F_{(1,\ 6)} = 1.209$, $p = 0.314$]. The main effect analysis showed that time had a significant effect on FMA-UE [$F_{(1,\ 6)} = 12.115$, $p = 0.013$], but no significant effect on FMA-UE for group [$F_{(1,\ 6)} = 0.009$, $p = 0.926$]. Further analysis showed that, after the 1 month intervention, the FMA-UE of the BCI group and that of the control group were both significantly improved. The percentage of improvement of the BCI group (12.77%, $p = 0.032$) was more than that of the control group (7.14%, $p = 0.048$) before and after intervention. The results are shown in **Figure 6A**. Four (OME1, OME3, OME4, and OME5) of the seven patients (57.1%) in the BCI group obtained more than five scores in FMA-UE improvement, and only two of the seven patients (28.6%) in the control group had improvement of more than five scores in FMA-UE. The detailed improvement of every individual is shown in **Table 2**.

ERD and Topography Changes

The detailed ERD changes (in T1 and T12 intervention) of every individual are shown in **Table 3**. It showed that the averaged ERD of ipsilesional (channel C3) and the contralesional (channel C4) hemisphere of seven subjects became stronger after the 12-session BCI training. Two-way repeated-measures ANOVA results for the ERD of channels C3 and C4 showed no significant time and channel interaction [$F_{(1,\ 6)} = 0.319$, $p = 0.593$]. The main effect analysis showed that time had a significant effect on ERD [$F_{(1,\ 6)} = 8.927$, $p = 0.024$], but no significant effect on ERD for channel [$F_{(1,\ 6)} = 0.188$, $p = 0.680$]. Further analysis showed that ERD of both channels C3 ($p = 0.032$) and C4 ($p = 0.029$) became significantly stronger after the 12-session BCI interventions. The results are shown in **Figure 6B**.

Topographies in **Figure 7** show that OME1 and OME3 presented with increasingly stronger ERD, especially in the ipsilesional sensorimotor cortex (around channel C3) as the training sessions went on. OME4 and OME5 presented continuously activations (ERD) in the left ipsilesional hemisphere across most of the training sessions. OME2 and OME7, who had injury in the right contralesional hemisphere (around channel C4), showed limited or even no activation in the sensorimotor cortex in more than six training sessions. OME6 presented ERD or ERS in the bilateral hemispheres in the 12 training sessions.

DISCUSSION

Our study obtained more motor function improvement after 12-session BCI intervention in the BCI group than in the control group. Patients with good recovery showed relatively higher online BCI performance, which were greater than 70%. And they showed a continuous improvement in offline BCI performance and obtained a highest value in the last six sessions of interventions during BCI training, whereas patients with poor recovery reached a platform in the first six sessions of interventions and did not improve any more or even show a decrease. Stronger ERD appeared along with motor recovery. Topographies showed that the locations of ERD transferred to be focused on the sensorimotor cortex after BCI intervention.

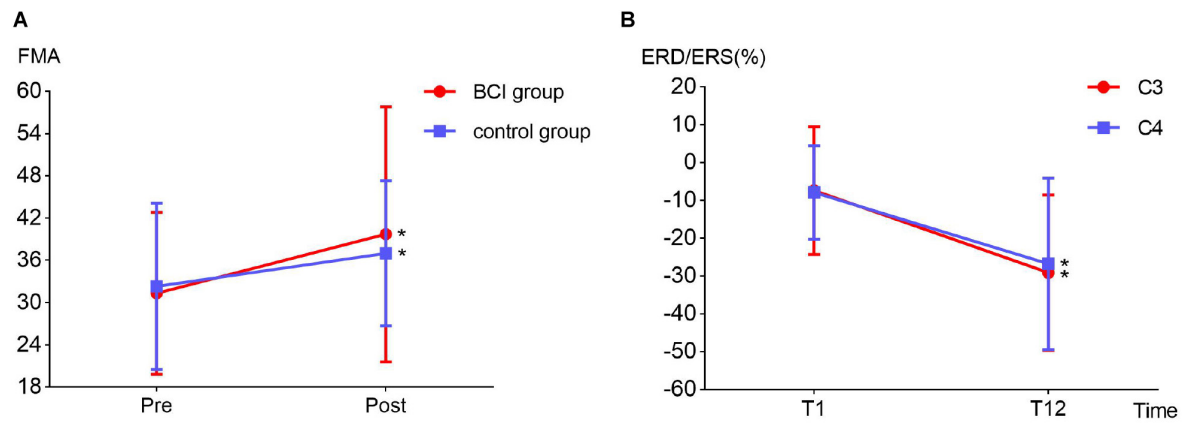

FIGURE 6 | (A) Fugl–Meyer assessment improvement between BCI group (12.77%, $p = 0.032$) and the control group (7.14%, $p = 0.048$) before (T1) and after (T12) the intervention. **(B)** Event-related desynchronization change in the ipsilesional (channel C3, $p = 0.032$) and contralesional (channel C4, $p = 0.029$) hemispheres before (T1) and after (T12) the intervention in the BCI group.

TABLE 2 | Fugl–Meyer assessment scores change between the BCI group and the control group.

FMA-UE	Pre-intervention	Post-intervention	Improvement
BCI group			
OME1	36	45	9
OME2	30	32	2
OME3	50	65	15
OME4	37	60	23
OME5	28	34	6
OME6	25	28	3
OME7	13	14	1
Control group			
CG1	19	34	15
CG2	28	31	3
CG3	29	36	7
CG4	26	28	2
CG5	28	30	2
CG6	42	42	0
CG7	54	58	4

TABLE 3 | Event-related desynchronization values before (T1) and after (T12) the BCI intervention of the ipsilesional hemisphere and contralesional hemisphere in the BCI group.

ERD	T1		T12	
BCI group	**Ipsilesional**	**Contralesional**	**Ipsilesional**	**Contralesional**
OME1	0.103	0.018	−0.554	−0.505
OME2	0.055	−0.007	−0.126	−0.111
OME3	−0.008	−0.059	−0.242	−0.120
OME4	−0.392	−0.314	−0.607	−0.587
OME5	−0.092	0.024	−0.155	−0.106
OME6	−0.182	−0.176	−0.245	−0.416
OME7	−0.002	−0.040	−0.110	−0.034
Mean	−0.074	−0.079	−0.291	−0.268

Brain–computer interface performance was an important parameter of BCI system. Higher BCI accuracies have been correlated with larger excitability in healthy people (Niazi et al., 2012) and better motor recovery in hemiplegic patients (Biasiucci et al., 2018). During BCI training, it would change with the sessions increasing (Li et al., 2014). Many BCI researchers were studying the effects of BCI performance on the motor recovery of stroke patients. Feedback was an essential part of BCI system, and it could promote brain plasticity. Frolov et al. (2017) demonstrated motor function improvements in both subacute and chronic stroke patients with exoskeleton feedback of BCI intervention compared to a control group. Ang et al. (2014) reported that 136 times of BCI exoskeleton feedback could obtain similar recovery effects as 1,040 times of traditional robotic training, which has shown the value of BCI feedback. Higher BCI performance could increase the correct numbers of feedback, which was good for the stroke patients to get motor recovery.

It has been reported in several BCI studies that BCI performance were significantly associated with the improvement of upper limb motor function (Li et al., 2014) or even related to the rehabilitation efficacy of the stroke patients (Bundy et al., 2017; Frolov et al., 2017). In the current study, the rehabilitation process was observed by BCI performance. The group (OME1, OME3, and OME4) that had more improvements in FMA-UE got the highest precision of BCI control in last six sessions of BCI training. While the other group with poor motor recovery (OME2, OME6, and OME7) got it in first six sessions (**Figure 4**). Among the three patients, OME2 presented poor online BCI performance across the 12 training sessions, with an average accuracy of less than 70%. It was implied that rehabilitation effect was correlated with the performance of BCI control. The steadily rising BCI performance suggested a good learning effect, which might be the source of enhance brain plasticity and motor recovery. The continuous improvements of patients could be reflected by the raise of BCI classification accuracy. And the patients of weak recovery performed more poorly after first several BCI training sessions. It was meaningful for clinical evaluation of recovery effects according to the continuous results of BCI performance.

The power change of EEG during motor task of BCI training was a symbol of brain function. Event-related desynchronization represented the cortical activation state, and stronger ERD suggested better brain function and brain plasticity (Ono et al., 2015). After the 12-session BCI intervention, ERD became significantly stronger in the 12th session compared to the first session. Two patients (OME1 and OME3) obtained obviously strong ERD in the third and fourth weeks. Moreover, the ipsilesional hemisphere presented more power decrease than the contralesional hemisphere did (**Table 3**). This was consistent with the study in healthy subjects that motor task was mainly activating the contralateral hemisphere (Pfurtscheller, 1999; Wolpaw, 2000). In functional MRI studies, activation on the ipsilateral side was also reported in stroke recovery (Erik Ween, 2008). This also suggested that BCI could facilitate ipsilesional cortical activations, and these activations might lead to motor recovery in subacute stroke patients. Interestingly, one patient (OME7) presented a relatively acceptable online BCI performance (mostly ranking from 70 to 80%). However, he showed poor activations in the right ipsilesional hemisphere, especially around the C4 channel. Thus, OME7 showed poor motor recovery. In addition, OME2 showed poor online BCI performance along with poor activations (ERD) in bilateral hemispheres, especially in the right ipsilesional hemisphere, in most of the 12 training sessions. These might also show poor motor recovery. It suggested that both BCI performance and sensorimotor rhythm (ERD) were important in reflecting motor recovery in subacute stroke patients during BCI training.

The locations of ERD changed as the intervention sessions increased, and specific characteristics were shown by topographies. A patient (OME1), who showed activations in the contralesional hemisphere in the first week, had focal ERD in the ipsilesional hemisphere after several BCI sessions. It was reasonable because the sensorimotor areas should be mostly involved in motor-related tasks (Li et al., 2014; Wang et al., 2016). Patients, who presented with extensive activations at the very start, became focused on the sensorimotor cortex

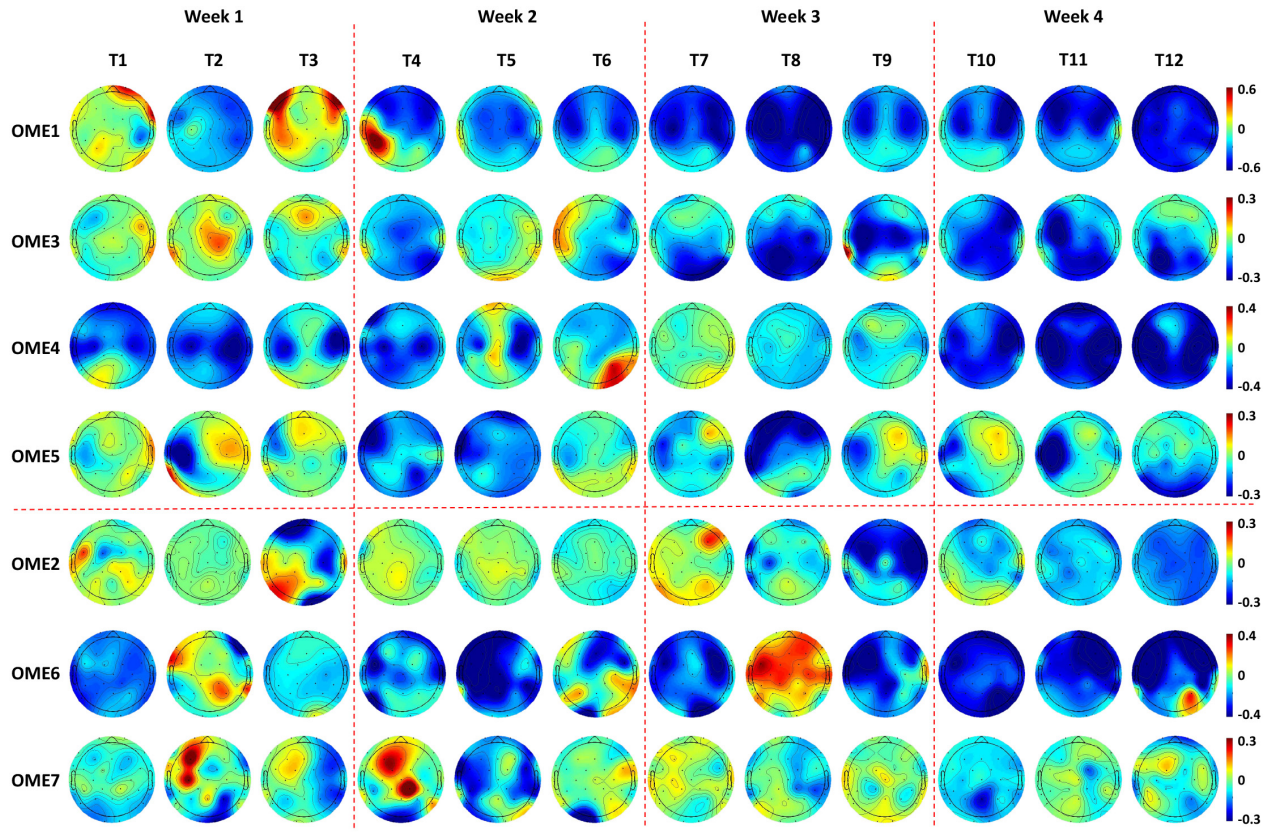

FIGURE 7 | Topographies of 1.4–1.6 s after the task onset of the seven subjects during the 12-session BCI training in the BCI group. Two patients (OME1 and OME3) presented increasingly stronger ERD in the bilateral hemispheres as the training sessions went on. Two patients (OME4 and OME5) presented continuously strong activations (ERD) in the left ipsilesional hemisphere across most of the training sessions. Two patients (OME2 and OME7) presented weak or even no activation in the right ipsilesional hemisphere in more than six training sessions. One patient (OME6) presented ERD or ERS in the bilateral hemispheres in the 12 training sessions.

after BCI training. This suggested that as the BCI intervention continuously proceeded, neural plasticity might enhance with stronger ERD in the sensorimotor cortex, which might lead to better motor recovery. Additionally, a patient (OME6) who presented with strong ERD but poor motor recovery could be at a subclinical efficacy. He also presented poor online BCI performance of less than 70%. Actually, he got an improvement of 3 in FMA-UE, which was lower than did the other patients with good motor recovery. He might have a slower improvement than others but might be further improved with more training.

The limitations of our study included a small sample size and no EEG data collected from the control group. This led to a lack of EEG comparison between groups and a more moderate conclusion of the clinical efficacy of BCI intervention. Based on this pilot study, a further study with a larger sample size is needed to contribute a stronger and clearer result.

CONCLUSION

This study explored the longitudinal sensorimotor rhythm changes in subacute stroke patients after 1 month BCI training with exoskeleton feedback. Clinical improvement was found in FMA-UE scores. Brain–computer interface performance was a good index to evaluate the clinical efficacy during the long-term BCI intervention. Patients who presented increasingly stronger or continuously strong activations (ERD) may obtain better motor recovery.

DATA AVAILABILITY STATEMENT

The raw data supporting the conclusions of this article will be made available by the authors, without undue reservation.

ETHICS STATEMENT

The studies involving human participants were reviewed and approved by the Ethics Committee of Huashan Hospital. The patients/participants provided their written informed consent to participate in this study. Written informed consent was obtained from the individuals for the publication of any potentially identifiable images or data included in this article.

AUTHOR CONTRIBUTIONS

SC and XS designed and performed the study. SC and LC organized the data, performed the data analysis, and wrote the manuscript. LC, XS, HW, LD, S-HW, and JJ reviewed and edited the manuscript. All authors read and approved the submitted manuscript.

FUNDING

This study was supported by the National Key Research and Development Program Project of China (Grant Nos. 2018YFC2002300 and 2018YFC2002301) and the National Natural Science Foundation of China (Grant Nos. 81672252 and 81702229).

REFERENCES

Ang, K. K., Chua, K. S. G., Phua, K. S., Wang, C., Chin, Z. Y., Kuah, C. W. K., et al. (2014). A randomized controlled trial of EEG-based motor imagery brain-computer interface robotic rehabilitation for stroke. *Clin. EEG Neurosci.* 46, 310–320. doi: 10.1177/1550059414522229

Bartur, G., Pratt, H., and Soroker, N. (2019). Changes in mu and beta amplitude of the EEG during upper limb movement correlate with motor impairment and structural damage in subacute stroke. *Clin. Neurophysiol.* 130, 1644–1651. doi: 10.1016/j.clinph.2019.06.008

Biasiucci, A., Leeb, R., Iturrate, I., Perdikis, S., Al-Khodairy, A., Corbet, T., et al. (2018). Brain-actuated functional electrical stimulation elicits lasting arm motor recovery after stroke. *Nat. Commun.* 9:2421. doi: 10.1038/s41467-018-04673-z

Blankertz, B., Muller, K. R., Krusienski, D. J., Schalk, G., Wolpaw, J. R., Schlogl, A., et al. (2006). The BCI competition III: validating alternative approaches to actual BCI problems. *IEEE Trans. Neural Syst. Rehabil. Eng.* 14, 153–159. doi: 10.1109/TNSRE.2006.875642

Buma, F., Kwakkel, G., and Ramsey, N. (2013). Understanding upper limb recovery after stroke. *Restorat. Neurol. Neurosci.* 31, 707–722. doi: 10.3233/RNN-130332

Bundy, D. T., Souders, L., Baranyai, K., Leonard, L., Schalk, G., Coker, R., et al. (2017). Contralesional brain–computer interface control of a powered exoskeleton for motor recovery in chronic stroke survivors. *Stroke* 48, 1908–1915. doi: 10.1161/STROKEAHA.116.016304

Cervera, M. A., Soekadar, S. R., Ushiba, J., Millán, J. D. R., Liu, M., Birbaumer, N., et al. (2018). Brain−computer interfaces for post−stroke motor rehabilitation: a meta−analysis. *Ann. Clin. Transl. Neurol.* 5, 651–663. doi: 10.1002/acn3.544

Erik Ween, J. (2008). Functional imaging of stroke recovery: an ecological review from a neural network perspective with an emphasis on motor systems. *J. Neuroimag.* 18, 227–236. doi: 10.1111/j.1552-6569.2007.00180.x

Frolov, A. A., Mokienko, O., Lyukmanov, R., Biryukova, E., Kotov, S., Turbina, L., et al. (2017). Post-stroke rehabilitation training with a motor-imagery-based brain-computer interface (BCI)-controlled hand exoskeleton: a randomized controlled multicenter trial. *Front. Neurosci.* 11:400. doi: 10.3389/fnins.2017.00400

Kaiser, V., Bauernfeind, G., Kreilinger, A., Kaufmann, T., Kübler, A., Neuper, C., et al. (2014). Cortical effects of user training in a motor imagery based brain–computer interface measured by fNIRS and EEG. *NeuroImage* 85, 432–444. doi: 10.1016/j.neuroimage.2013.04.097

Klem, G. H., Luders, H. O., Jasper, H. H., and Elger, C. (1999). The ten-twenty electrode system of the international federation. the international federation of clinical neurophysiology. *Electroencephalogr. Clin. Neurophysiol. Suppl.* 52, 3–6.

Leeb, R., Biasiucci, A., Schmidlin, T., Corbet, T., Vuadens, P., and Millán, J. D. R. (2016). "BCI controlled neuromuscular electrical stimulation enables sustained motor recovery in chronic stroke victims," in *Proceedings of the 6th International Brain-Computer Interface Meeting*, At Asilomar, CA.

Li, M., Liu, Y., Wu, Y., Liu, S., Jia, J., and Zhang, L. (2014). Neurophysiological substrates of stroke patients with motor imagery-based brain-computer interface training. *Int. J. Neurosci.* 124, 403–415. doi: 10.3109/00207454.2013.850082

Liu, Y., Li, M., Zhang, H., Wang, H., Li, J., Jia, J., et al. (2014). A tensor-based scheme for stroke patients' motor imagery EEG analysis in BCI-FES rehabilitation training. *J. Neurosci. Methods* 222, 238–249. doi: 10.1016/j.jneumeth.2013.11.009

López-Larraz, E., Sarasola-Sanz, A., Irastorza-Landa, N., Birbaumer, N., and Ramos-Murguialday, A. (2018). Brain-machine interfaces for rehabilitation in stroke: a review. *NeuroRehabilitation* 43, 77–97. doi: 10.3233/NRE-172394

Mihara, M., Hattori, N., Hatakenaka, M., Yagura, H., Kawano, T., Hino, T., et al. (2013). Near-infrared spectroscopy–mediated neurofeedback enhances efficacy of motor imagery–based training in poststroke victims. *Stroke* 44, 1091–1098. doi: 10.1161/STROKEAHA.111.674507

Niazi, I. K., Mrachacz-Kersting, N., Jiang, N., Dremstrup, K., and Farina, D. (2012). Peripheral electrical stimulation triggered by self-paced detection of motor intention enhances motor evoked potentials. *IEEE Trans. Neural Syst. Rehabil. Eng.* 20, 595–604. doi: 10.1109/TNSRE.2012.2194309

Ono, T., Tomita, Y., Inose, M., Ota, T., Kimura, A., Liu, M., et al. (2015). Multimodal sensory feedback associated with motor attempts alters BOLD responses to paralyzed hand movement in chronic stroke patients. *Brain Topogr.* 28, 340–351. doi: 10.1007/s10548-014-0382-6

Peng, W. W., Tang, Z. Y., Zhang, F. R., Li, H., Kong, Y. Z., Iannetti, G. D., et al. (2019). Neurobiological mechanisms of TENS-induced analgesia. *NeuroImage* 195, 396–408. doi: 10.1016/j.neuroimage.2019.03.077

Pfurtscheller, G. A. A. (1979). Evaluation of event-related desynchronization (ERD) preceding and following voluntary self-paced movements. *Electroenceph. Clin. Neurophysiol.* 46, 138–146. doi: 10.1016/0013-4694(79)90063-4

Pfurtscheller, G. L. D. S. (1999). Event-related EEG/MEG synchronization and desynchronization: basic principles. *Clin. Neurophysiol* 11, 1842–1857. doi: 10.1016/s1388-2457(99)00141-8

Pichiorri, F., Morone, G., Petti, M., Toppi, J., Pisotta, I., Molinari, M., et al. (2015). Brain-computer interface boosts motor imagery practice during stroke recovery. *Ann. Neurol.* 77, 851–865. doi: 10.1002/ana.24390

Prasad, G., Herman, P., Coyle, D., McDonough, S., and Crosbie, J. (2009). "Using motor imagery based brain-computer interface for post-stroke rehabilitation," in *Proceedings of the 4th International IEEE/EMBS Conference on Neural Engineering* (Antalya: IEEE), 258–262.

Ramos-Murguialday, A., Broetz, D., Rea, M., Läer, L., Yilmaz, Ö, Brasil, F. L., et al. (2013). Brain-machine interface in chronic stroke rehabilitation: a controlled study. *Ann. Neurol.* 74, 100–108. doi: 10.1002/ana.23879

Takemi, M., Masakado, Y., Liu, M., and Ushiba, J. (2013). Event-related desynchronization reflects downregulation of intracortical inhibition in human primary motor cortex. *J. Neurophysiol.* 110, 1158–1166. doi: 10.1152/jn.01092.2012

Tam, W., Tong, K., Meng, F., and Gao, S. (2011). A minimal set of electrodes for motor imagery BCI to control an assistive device in chronic stroke subjects: a multi-session study. *IEEE Trans. Neural Syst. Rehabil. Eng.* 19, 617–627. doi: 10.1109/TNSRE.2011.2168542

Tung, S. W., Guan, C., Ang, K. K., Phua, K. S., Wang, C., Zhao, L., et al. (2013). "Motor imagery BCI for upper limb stroke rehabilitation: an evaluation of the EEG recordings using coherence analysis," in *Proceedings of the 35th Annual International Conference of the IEEE Engineering in Medicine and Biology Society (EMBC)* (Osaka: IEEE), 261.

Wang, L., Zhang, J., Zhang, Y., Yan, R., Liu, H., and Qiu, M. (2016). Conditional granger causality analysis of effective connectivity during motor imagery and motor execution in stroke patients. *BioMed Res. Int.* 2016, 1–9. doi: 10.1155/2016/3870863

Wolpaw, D. J. M. A. (2000). Mu and beta rhythm topographies during motor imagery and actual movements. *Brain Topogr.* 12, 177–186.

Conflict of Interest: The authors declare that the research was conducted in the absence of any commercial or financial relationships that could be construed as a potential conflict of interest.

frontiers in Neuroscience

ORIGINAL RESEARCH
published: 04 September 2020
doi: 10.3389/fnins.2020.00837

An Intelligence EEG Signal Recognition Method via Noise Insensitive TSK Fuzzy System Based on Interclass Competitive Learning

Tongguang Ni, Xiaoqing Gu and Cong Zhang*

School of Computer Science and Artificial Intelligence, Changzhou University, Changzhou, China

Epilepsy is an abnormal function disease of movement, consciousness, and nerve caused by abnormal discharge of brain neurons in the brain. EEG is currently a very important tool in the process of epilepsy research. In this paper, a novel noise-insensitive Takagi–Sugeno–Kang (TSK) fuzzy system based on interclass competitive learning is proposed for EEG signal recognition. First, a possibilistic clustering in Bayesian framework with interclass competitive learning called PCB-ICL is presented to determine antecedent parameters of fuzzy rules. Inherited by the possibilistic *c*-means clustering, PCB-ICL is noise insensitive. PCB-ICL learns cluster centers of different classes in a competitive relationship. The obtained clustering centers are attracted by the samples of the same class and also excluded by the samples of other classes and pushed away from the heterogeneous data. PCB-ICL uses the Metropolis–Hastings method to obtain the optimal clustering results in an alternating iterative strategy. Thus, the learned antecedent parameters have high interpretability. To further promote the noise insensitivity of rules, the asymmetric expectile term and Ho–Kashyap procedure are adopted to learn the consequent parameters of rules. Based on the above ideas, a TSK fuzzy system is proposed and is called PCB-ICL-TSK. Comprehensive experiments on real-world EEG data reveal that the proposed fuzzy system achieves the robust and effective performance for EEG signal recognition.

Keywords: noise insensitive, TSK fuzzy system, Bayesian framework, possibilistic clustering, Ho–Kashyap procedure, asymmetric expectile term

OPEN ACCESS

Edited by:
Mohammad Khosravi, Persian Gulf University, Iran

Reviewed by:
Shan Zhong, Changshu Institute of Technology, China
Juan Yang, Suzhou University, China

****Correspondence:***
Xiaoqing Gu
guxq@cczu.edu.cn

Specialty section:
This article was submitted to Neuroprosthetics, a section of the journal Frontiers in Neuroscience

Received: *21 June 2020*
Accepted: *20 July 2020*
Published: *04 September 2020*

Citation:
Ni T, Gu X and Zhang C (2020) An Intelligence EEG Signal Recognition Method via Noise Insensitive TSK Fuzzy System Based on Interclass Competitive Learning. Front. Neurosci. 14:837. doi: 10.3389/fnins.2020.00837

INTRODUCTION

Epilepsy occurs randomly and may occur multiple times in a day. In the case of epileptic seizures, the patients have a sudden physical convulsions and loss of consciousness, which bring great physical and psychological pain to patients (Ahmadlou and Adeli, 2011; Gummadavelli et al., 2018; Cury et al., 2019). Seizures will lead to brain cell death, affect brain function, and even threaten patients' lives in serious cases. The incidence of epilepsy is high, and the age range is very wide, including children, adolescents, and the elderly, but the incidence of children and adolescents is the highest. Both men and women are likely to have the disease, and men are more likely to have this disease than women. As an important clinical means of monitoring and diagnosing epilepsy, EEG provides a more rapid and stable low-cost and non-invasive technology in monitoring the brain activity of the cerebral cortex. It provides information that other physiological methods

cannot provide. The specific waveforms such as spike, sharp, and complex wave can be reflected by EEG. Therefore, the prevention and treatment of epilepsy research for epilepsy patients is of great significance. In the process of diagnosis and treatment of epilepsy, EEG plays an irreplaceable role. Doctors usually judge the condition of patients by observing their EEG.

The traditional way to judge the EEG signal is not only inefficient, but also because of the difference of experts' subjective experience, the automatic detection of EEG signal is still one of the hot issues in biomedical research (Jiang et al., 2017a; Martinez-Vargas et al., 2017; Li et al., 2019). An automatic epilepsy detection method can help doctors improve the accuracy of epilepsy diagnosis and also greatly save time. The research of automatic epilepsy detection is of great value to the prevention, diagnosis, and treatment of epilepsy. At present, epilepsy can be detected by machine learning and data mining. Firstly, the effective feature information is extracted from EEG and preprocessed for data analysis; secondly, the preprocessed EEG data are sent to the classifier for analysis and detection of epileptic and non-epileptic EEG data. In the above implementation process, the key research is to design an effective prediction and discrimination method that can be applied to normal EEG signal and epileptic EEG signal. Many effective methods have been successfully applied to automatic epilepsy detection system, including extreme learning machine (ELM), artificial neural network, Bayesian linear discriminant analysis, support vector machine (SVM), and fuzzy system (Kabir and Zhang, 2016; Qi et al., 2017; Akhavan and Moradi, 2018; Truong et al., 2018; Hossain et al., 2019; Liu et al., 2019; Sreej and Samanta, 2019; Xia et al., 2020). The fuzzy system is a model constructed to deal with the thinking, analysis, reasoning, and decision-making processes in production and practice. It can directly translate natural language into computer language. Due to its ability to process uncertain and ambiguous information, it has a high degree of interpretability and strong learning ability (Juang et al., 2007; Gu et al., 2017a; Jiang et al., 2017b,c; Gu and Wang, 2018). However, the traditional fuzzy system has poor robustness and anti-interference ability, and the classification accuracy is not high in data noise scenarios. But in real life, the classification of noise data is widely used. For example, in actual application scenarios, due to differences in machine advices or scanning technology, such as different rotation angles and noise, the quality of medical images may vary greatly (Siuly and Li, 2015; Hussein et al., 2019; Razzak et al., 2019).

Based on key technology of fuzzy system modeling, this paper proposes a novel noise-insensitive Takagi–Sugeno–Kang (TSK) fuzzy system. How to determine the antecedent and consequent parameters is the key to modeling the noise-insensitive fuzzy system (Takagi and Sugeno, 1985; Jiang et al., 2015). For the antecedent part of fuzzy rules, clustering is one kind of a commonly used strategy, such as fuzzy c-means (FCM) clustering (Bezdek et al., 1984), fuzzy $(c + p)$ clustering (Leski, 2015), Bayesian fuzzy clustering (BFC) (Glenn et al., 2015), and possibilistic c-means (PCM) clustering (Krishnapuram and Keller, 1993). However, FCM, fuzzy $(c + p)$, and BFC are sensitive to noise and will lead to unsatisfactory partition in noisy scenarios. PCM inherits the practicability and flexibility of fuzzy clustering and greatly enhances the clustering performance of data with noise or outliers. However, the unsupervised nature of PCM makes it unable to use the class label information of samples, which easily causes the insufficient fuzzy space partition, thus further affecting the learning of antecedent parameters of fuzzy rules. The principle of antecedent parameter learning using PCM clustering is shown in **Figure 1A**. PCM clustering is directly used on whole datasets or on samples in each class, and then the antecedent parameters are learned using the obtained clustering results. Then the data samples are simply divided into several clusters, without fully taking advantage of the geometry of data and the label information of samples. In this case, in the data overlapping regions, the distance between clustering centers may be too small or the centers may overlap.

In this paper, we first propose a noise-insensitive possibilistic clustering in Bayesian framework with interclass competitive learning called PCB-ICL. Inherited by PCB, PCB-ICL is noise insensitive; meanwhile, different classes of cluster centers will produce a competitive relationship during the learning process. That is, in the sample overlapping area, the clustering centers are attracted by the samples of the same class and also excluded by the samples of other classes and pushed away from the heterogeneous data. The principle of antecedent parameter learning using PCB-ICL clustering is shown in **Figure 1B**. PCB-ICL integrates the competitive learning mechanism of clustering centers among different classes in the Bayesian framework. PCB-ICL considers the structure information of samples in the clustering procedure and realizes the competition between clustering centers among different classes. We obtain the antecedent part of fuzzy rules by performing PCB-ICL alternatively on each class samples. Then, a Ho–Kashyap procedure (Leski, 2003) with an asymmetric expectile term (Huang et al., 2014a,b) is adopted to estimate the consequent parameters of fuzzy rules. Due to the statistical characteristics of the asymmetric expectile term, it is insensitive to noise; so the asymmetric expectile term is used to measure the misclassification error. Based on the above idea, the TSK fuzzy system called PCB-ICL-TSK is developed, which learns antecedent parameters by PCB-ICL clustering and consequent parameters by the Ho–Kashyap procedure with an asymmetric expectile term. We apply the proposed algorithm on the Bonn EEG dataset, and the experimental results on several noisy classification tasks demonstrate that PCB-ICL-TSK can achieve satisfactory performance in EEG signal classification. The novelty of our study is as follows. (1) Both the PCB-ICL and Ho–Kashyap procedure with an asymmetric expectile term are insensitive to noise; thus, the obtained antecedent and consequent parameters are noise insensitive. (2) With the Bayesian framework, the clustering results of PCB-ICL are globally optimal. In addition, the competitive relationship strategy between cluster centers enhances the interpretability of the antecedents of fuzzy rules. (3) The experiments on real-word EEG datasets confirm the effectiveness of PCB-ICL-TSK.

The detailed chapters are arranged as follows. Section Backgrounds introduces the TSK fuzzy system and PCM clustering. Section Possibilistic Clustering in Bayesian With Interclass Competitive Learning explores PCB-ICL clustering. Section Noise-Insensitive TSK Fuzzy System via Interclass

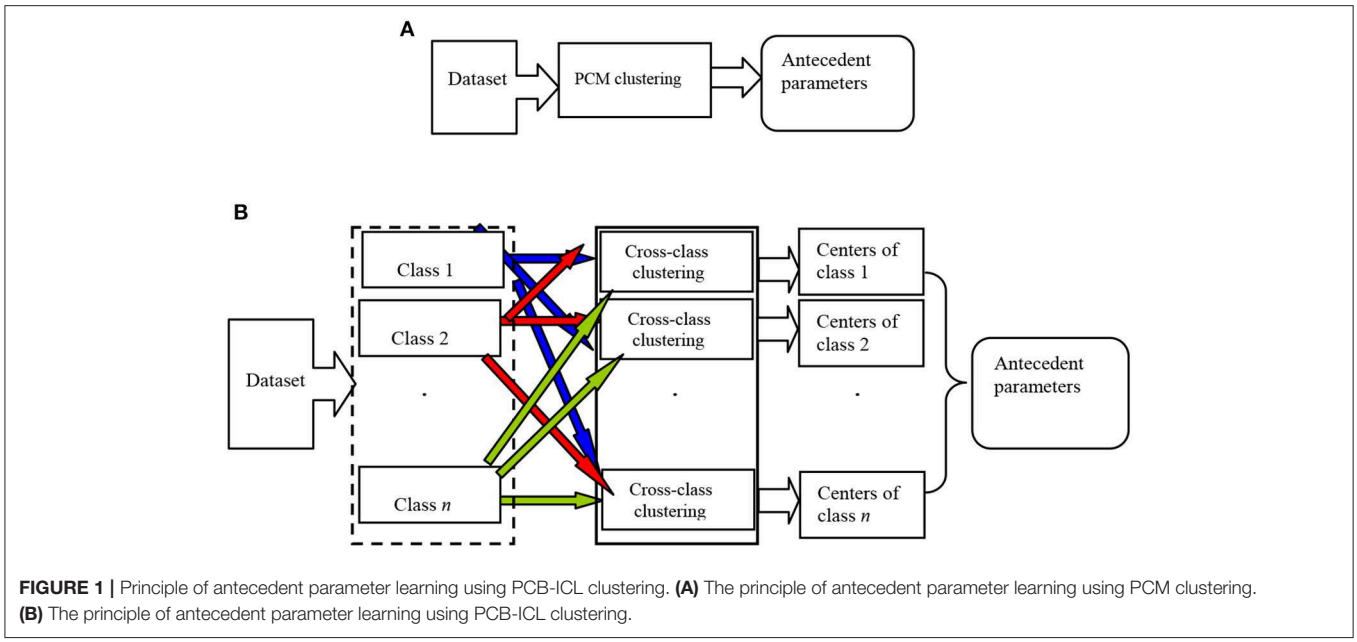

FIGURE 1 | Principle of antecedent parameter learning using PCB-ICL clustering. **(A)** The principle of antecedent parameter learning using PCM clustering. **(B)** The principle of antecedent parameter learning using PCB-ICL clustering.

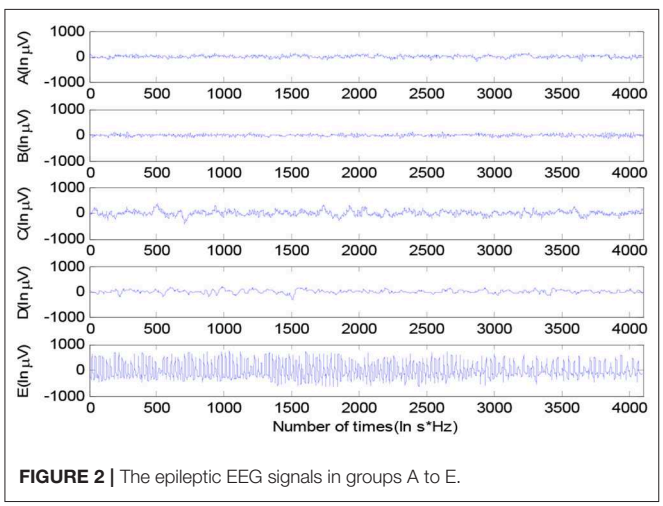

FIGURE 2 | The epileptic EEG signals in groups A to E.

Competitive Learning explores the noise-insensitive TSK fuzzy system PCB-ICL-TSK. Section Experiment is experiments on noisy EEG data. Section Conclusion is the conclusion.

BACKGROUNDS

Dataset

The epileptic EEG in the experiment is the Bonn dataset from Bonn University, Germany (Tzallas et al., 2009). The Bonn EEG dataset consists of five groups of data, namely, A to E, shown in **Figure 2**. Each group of data contains 100 EEG signal segments of 23.6 s, which were selected from continuous single-channel EEG recordings. The EEG signals were recorded under different conditions with five patients and five healthy volunteers. The basic information of groups A–E is shown in **Table 1**.

TABLE 1 | The basic information of EEG data groups of A–E.

	Group	Description
Healthy volunteers	A	EEG signals of healthy volunteers in an awakened state with eyes open
	B	EEG signals of healthy volunteers in an awakened state with eyes closed
Patients	C	EEG signals of patients in hippocampal formation of the opposite hemisphere of the brain
	D	EEG signals of patients in the epileptogenic zone during periodic lulls
	E	EEG signals of patients during seizure activity

TSK Fuzzy System

The most commonly used rule in the zero-order TSK fuzzy system can be represented by

Rule R_k: IF x_1 is $A_{k,1}$ and x_2 is $A_{k,2}$ and … and x_d is $A_{k,d}$,

$$then\, f_k(\mathbf{x}) = P_{k,0}, (k = 1, 2, \ldots, K) \tag{1}$$

where $x_1, x_2, \ldots, x_d$ are input variables, $A_{k,i}$ is a fuzzy subset, and K is the number of fuzzy rules. For an input vector $\mathbf{x}$, the output of the corresponding TSK fuzzy system is represented by

$$y_{\,output} = \frac{\sum_{k=1}^{K} \mu_k(\mathbf{x}) p_{k,0}}{\sum_{k=1}^{K} \mu_k(\mathbf{x})} = \sum_{k=1}^{K} \tilde{\mu}_k(\mathbf{x}) p_{k,0}, \tag{2}$$

where the fuzzy membership $\mu_k(\mathbf{x})$ and the normalized fuzzy membership $\tilde{\mu}_k(\mathbf{x})$ is

$$\mu_k(\mathbf{x}) = \prod_{i=1}^{d} \mu_{A_{k,i}}(x_i), \tag{3}$$

$$\tilde{\mu}_k(\mathbf{x}) = \frac{\mu_k(\mathbf{x})}{\sum_{k'=1}^{K} \mu_{k'}(\mathbf{x})}. \tag{4}$$

For the sample $\mathbf{x}_i$, we can rewrite it by

$$d(\mathbf{x}_i) = [\tilde{\mu}_1(\mathbf{x}_i), \tilde{\mu}_2(\mathbf{x}_i), \ldots, \tilde{\mu}_K(\mathbf{x}_i)]^T, \tag{5}$$

Generally, antecedent and consequent parameters of rules are determined separately. A popular way to estimate antecedent parameters is to use a certain fuzzy clustering method (Takagi and Sugeno, 1985; Gu et al., 2017b; Salgado et al., 2017). Then $\mu_{A_{k,i}}(x_i)$ can be computed by

$$\mu_{A_{k,i}}(x_i) = \exp(-\frac{(x_i - y_{k,i})^2}{2\delta_{k,i}}), \tag{6}$$

where the width parameter $\delta_{k,i}$ can be obtained by

$$\delta_{k,i} = \frac{h \cdot \sum_{j=1}^{N} u_{k,j}(x_{ji} - y_{k,i})^2}{\sum_{j=1}^{N} u_{k,j}}, \tag{7}$$

where h is the scale parameter and $u_{k,j}$ is the fuzzy membership of the jth input sample $\mathbf{x}_j$ belonging to the kth cluster.

Then the learning of consequent parameters can be represented by

$$\min_{\mathbf{p}} \sum_{i=1}^{N} |l_i d(\mathbf{x}_i)^T \mathbf{p} - 1| \tag{8}$$

Using the least square solution to minimize the squared loss, Equation (8) can be written by

$$\min_{\mathbf{p}} J(\mathbf{p}) = (\mathbf{D}\mathbf{p} - \mathbf{1}_{N\times 1})^T \mathbf{H}(\mathbf{D}\mathbf{p} - \mathbf{1}_{N\times 1}) + \tau \mathbf{p}^T \mathbf{p}, \tag{9}$$

where $\mathbf{D} = [l_1 d(\mathbf{x}_1)^T, \ldots, l_N d(\mathbf{x}_N)^T]^T$, the matrix $\mathbf{H} = \text{diag}(h_1, h_2, \ldots, h_N)$, $h_i = 1/|l_i d(\mathbf{x}_i)^T \boldsymbol{p} - 1|$ for $l_i d(\mathbf{x}_i)^T \boldsymbol{p} - 1 < 0$, and $h_i = 0$ otherwise. τ is the regularization parameter. Using the Ho–Kashyap iterative method (Leski, 2003), $\mathbf{p}$ can be computed by

$$\mathbf{p} = (\mathbf{D}^T \mathbf{H} \mathbf{D} + \tau \mathbf{I})^{-1} \mathbf{D}^T \mathbf{H} \mathbf{1}, \tag{10}$$

where $\mathbf{I}$ is the identify matrix.

PCM Clustering

PCM clustering is a probability clustering based on FCM. Based on the framework of possibility theory, PCM not only takes into account the general criteria of clustering with the minimum distance within one class and the maximum distance between classes but also emphasizes the principle of the maximum membership value to avoid ordinary solution problems. The objective function of PCM is

$$\min_{\mathbf{U},\mathbf{Y}} \sum_{n=1}^{N}\sum_{c=1}^{C} u_{nc}^m (\mathbf{x}_n - \mathbf{y}_c)^2 + \sum_{n=1}^{N}\sum_{c=1}^{C} \eta_c (1 - u_{nc})^m, \quad s.t.\ u_{nc} \in [0,1], \forall n, c \tag{11}$$

The closed solution of $\mathbf{U}$ and $\mathbf{Y}$ can be obtained by minimizing the objective function with respect to u_{nc} and $\mathbf{y}_c$ by.

$$\mathbf{y}_c = \frac{\sum_{n=1}^{N} u_{nc}^m \mathbf{x}_n}{\sum_{n=1}^{N} u_{nc}^m} \tag{12}$$

$$u_{nc} = \frac{1}{1 + (\frac{(\mathbf{x}_n - \mathbf{y}_c)^2}{\eta_c})^{\frac{1}{m-1}}} \tag{13}$$

POSSIBILISTIC CLUSTERING IN BAYESIAN WITH INTERCLASS COMPETITIVE LEARNING

Objective Function

A clustering method implements data partition with some certain degree of similarity. In the clustering process, the samples of one class will have a repulsive effect on the clustering center of other classes, especially in the overlapping regions of different classes of samples; the greater the overlap density, the greater the repulsive force. In these sample overlapping regions, clustering centers of different classes form the competitive learning relationship. On the one hand, the clustering centers are attracted by samples of this class; on the other hand, the clustering centers are excluded by different classes of samples and far away from the overlapping region. In this paper, this idea is embedded into PCM clustering. Based on the Bayesian framework, we propose the possibilistic clustering in Bayesian with interclass competitive learning.

Suppose a given binary classification dataset $\mathbf{X} = \{\mathbf{x}_n, l_n\}_{n=1}^{N}$, in which $\mathbf{X}_1 = \{\mathbf{x}_n, l_n\}_{n=1}^{N_1}$ and $\mathbf{X}_2 = \{\mathbf{x}_n, l_n\}_{n=N_1+1}^{N}$ represent two class samples and $l_n \in \{+1, -1\}$ is the class label of the nth sample. Let the cluster number of one class samples be C_1 and the cluster centers of the other class $\mathbf{Z}$ be priorly known $\mathbf{Z} = [\mathbf{z}_1, \mathbf{z}_2, \ldots, \mathbf{z}_{\mathbf{c}_2}]^T$, where the cluster number is C_2. We suppose data $\mathbf{X}$ follows the normal distribution, and each sample $\mathbf{x}_i$ has an independent probability distribution. The maximum

posterior estimation of data and parameters in $\mathbf{X}_1$ is expressed by

$$\begin{aligned} p(\mathbf{X}_1, \mathbf{U}, \mathbf{Y}) &= p(\mathbf{X}_1|\mathbf{U}, \mathbf{Y})p(\mathbf{U}|\mathbf{Y})p(\mathbf{Y}) \\ &\propto exp\left\{-\frac{1}{2}(\sum_{n=1}^{N_1}\sum_{c=1}^{C_1} u_{nc}^m||\mathbf{x}_n - \mathbf{y}_c||^2 + \sum_{n=1}^{N_1}\sum_{c=C_1+1}^{C_1+C_2} u_{nc}^m||\mathbf{x}_n - \mathbf{z}_c||^2)\right\} \times \\ &\left[\prod_{n=1}^{N_1}\prod_{c=1}^{C_1+C_2} \exp(-\frac{1}{2}\eta_c(1-u_{nc})^m) \times \exp\left\{-\frac{1}{2}\sum_{c=1}^{C_1}(\mathbf{y}_c - \boldsymbol{\mu}_y)^T\sum\nolimits_y^{-1}(\mathbf{y}_c - \boldsymbol{\mu}_y)\right\}\right], \end{aligned} \tag{14}$$

where $\mathbf{Y} = \left[\mathbf{y}_1, \mathbf{y}_2, \ldots, \mathbf{y}_{c_1}\right]^T$ is the unknown cluster center matrix of one class sample. By taking the logarithm of Equation (14), the objective function of PCB-ICL method can be obtained as

$$\begin{aligned} J(\mathbf{X}_1, \mathbf{U}, \mathbf{Y}) &= \sum_{n=1}^{N_1}\sum_{c=1}^{C_1} u_{nc}^m||\mathbf{x}_n - \mathbf{y}_c||^2 + \sum_{n=1}^{N_1}\sum_{c=C_1+1}^{C_1+C_2} u_{nc}^m||\mathbf{x}_n - \mathbf{z}_c||^2 \\ &+ \sum_{n=1}^{N_1}\sum_{c=1}^{C_1+C_2}\eta_c(1-u_{nc})^m \\ &+ \sum_{c=1}^{C_1}(\mathbf{y}_c - \boldsymbol{\mu}_y)^T\sum_y^{-1}(\mathbf{y}_c - \boldsymbol{\mu}_y). \end{aligned} \tag{15}$$

From Equations (14) and (15), we can see that (1) the PCB-ICL method shows the competition relationship between clustering centers of different classes. Different from the traditional PCM clustering method, PCB-ICL not only considers the label information of samples but also considers the competition relationship between clustering centers, as shown in the first two items. On the premise that the clustering centers of the other class are priorly known, the clustering centers of the current class will inevitably have a competition relationship with these known clustering centers in the overlapping region. (2) Due to simultaneously utilizing the global distribution structure and the discrimination information of the samples, the obtained antecedent part of fuzzy rules by PCB-ICL can realize the clarity of fuzzy space partition and enhance the interpretability of the fuzzy rules.

Parameter Learning

To obtain the optimal fuzzy partition matrix $\mathbf{U}$, the PCB-ICL method uses the Metropolis–Hastings method (Chib and Greenberg, 1995; Elvira et al., 2017) to construct a Markov chain to make $p(\mathbf{U}|\mathbf{X}_1, \mathbf{Y})$ stable. The conditional distribution $p(\mathbf{U}|\mathbf{X}_1, \mathbf{Y})$ is proportional to the joint distribution $p(\mathbf{X}_1, \mathbf{U}, \mathbf{Y})$ when the sample and clustering center are known and also is proportional to the conditional distribution $p(\mathbf{U}|\mathbf{X}_1, \mathbf{Y})$. Therefore, we only need compute $p(\mathbf{x}_n, \mathbf{u}_n|\mathbf{Y})$ of the sample $\mathbf{x}_n$:

$$\begin{aligned} p(\mathbf{x}_n, \mathbf{u}_n|\mathbf{Y}) &= p(\mathbf{x}_n|\mathbf{u}_n, \mathbf{Y})p(\mathbf{u}_n|\mathbf{Y}) \\ &\propto exp\left\{-\frac{1}{2}(\sum_{c=1}^{C_1} u_{nc}^m||\mathbf{x}_n - \mathbf{y}_c||^2 + \sum_{c=C_1+1}^{C_1+C_2} u_{nc}^m||\mathbf{x}_n - \mathbf{z}_c||^2)\right\} \\ &\times \prod_{c=1}^{C_1+C_2}\exp(-\frac{1}{2}\eta_c(1-u_{nc})^m). \end{aligned} \tag{16}$$

Thus, the process of the ith iteration of the Markov chain is

1) Generate a new state $\mathbf{u}_n^+$ of $\mathbf{u}_n$ with a uniform distribution as

$$\mathbf{u}_n^+ \sim \text{Uniform}(0, 1), \forall n \tag{17}$$

2) The newly generated membership $\mathbf{u}_n^+$ is accepted by the probability $a_{\boldsymbol{u}}$ as

$$a_{\mathbf{u}} = \min\left\{1, \frac{p(\mathbf{x}_n, \mathbf{u}_n^+|\mathbf{Y})}{p(\mathbf{x}_n, \mathbf{u}_n|\mathbf{Y})}\right\} \tag{18}$$

Then accepting $a_{\boldsymbol{u}}$ as the current state with probability $\mathbf{u}_n$,

$$\mathbf{u}_n = \begin{cases} \mathbf{u}_n^+, & \mu \le \alpha_{\mathbf{u}} \\ \mathbf{u}_n, & \mu > \alpha_{\mathbf{u}} \end{cases} \tag{19}$$

where μ is a random number in [0, 1]. The distribution of the new state $\mathbf{u}_n^+$ obtained by sampling is independent of the current sample, and the state $\mathbf{u}_n^+/\mathbf{u}_n$ is independent, so a_{u} does not need Hasting correction.

3) Compare $p(\mathbf{x}_n, \mathbf{u}_n^+|\mathbf{Y}^*)$ and $p(\mathbf{x}_n, \mathbf{u}_n^*|\mathbf{Y}^*)$, where $\mathbf{Y}^*$ and $\mathbf{u}_n^*$ are the optimal values of $\mathbf{Y}$ and $\mathbf{u}_n$. If, $p(\mathbf{x}_n, \mathbf{u}_n^+|\mathbf{Y}^*) > p(\mathbf{x}_n, \mathbf{u}_n^*|\mathbf{Y}^*)$ $\mathbf{u}_n^+$ is replaced by $\mathbf{u}_n^*$.

When the matrix $\mathbf{U}$ is fixed, we use Metropolis–Hastings to sample the conditional distribution $p(\mathbf{Y}|\mathbf{X}, \mathbf{U})$. In this case, $p(\mathbf{Y}|\mathbf{X}, \mathbf{U})$ is proportional to the joint distribution $p(\mathbf{X}, \mathbf{U}, \mathbf{Y})$. We estimate $\mathbf{y}_c$ by using the Gaussian distribution as

$$\mathrm{y}_c^+ \sim \mathcal{N}\left(\mathrm{y}_c, \frac{1}{\sigma}\sum\nolimits_y\right) \tag{20}$$

where $\mathbf{y}_c^+$ centers on the current value $\mathbf{y}_c$. σ is a positive number and is used to control the compactness of cluster centers. In the experiment, we empirically set σ to 10.

For the newly generated $\mathbf{y}_c^+$, it is independent of other clustering centers. Then the conditional distribution $p(\mathbf{X}, \mathbf{y}_c|\mathbf{U})$ is represented by

$$\begin{aligned} p(\mathbf{X}, \mathbf{y}_c|\mathbf{U}) &= p(\mathbf{X}|\mathbf{U}, \mathbf{y}_c)p(\mathbf{y}_c) \\ &\propto \exp\left\{-\frac{1}{2}\sum_{n=1}^{N_1} u_{nc}^m||\mathbf{x}_n - \mathbf{y}_c||^2\right\} \\ &\times \exp\left\{-\frac{1}{2}(\mathbf{y}_c - \mu_y)^T\sum\nolimits_y^{-1}(\mathbf{y}_c - \mu_y)\right\}. \end{aligned} \tag{21}$$

Similarly, the newly generated membership $\mathbf{y}_c^+$ is accepted by the probability a_{y} as

$$a_{\mathbf{y}} = \min\left\{1, \frac{p(\mathbf{X}, \mathbf{y}_c^+|\mathbf{U})}{p(\mathbf{X}, \mathbf{y}_c|\mathbf{U})}\right\} \tag{22}$$

Since the Gaussian distribution is symmetric, a_{y} does not need Hasting correction.

Finally, we compute $p(\mathbf{X}, \mathbf{U}^*, \mathbf{Y}^*)$ using Equation (15) and compare it with the current $p(\mathbf{X}, \mathbf{U}, \mathbf{Y})$. If $p(\mathbf{X}, \mathbf{U}, \mathbf{Y}) > p(\mathbf{X}, \mathbf{U}^*, \mathbf{Y}^*)$, the $\{\mathbf{U}, \mathbf{Y}\}$ is replaced by $\{\mathbf{U}^*, \mathbf{Y}^*\}$.

Based on the above analysis, we give the procedure of the PCB-ICL method in **Algorithm 1**.

Algorithm 1 | PCB-ICL method.

Input: Dataset X_1 of one class, the number of clustering C, priorly known clustering center matrix $\mathbf{Z}$ of the other class;

Output: Fuzzy partition matrix $\mathbf{U}^*$ and clustering center matrix $\mathbf{Y}^*$.

Step 1 Initiate $\mathbf{u}_n^+ \sim Uniform(0, 1), \forall n$;
Step 2 Initiate $\mathbf{y}_c^+ \sim \mathcal{N}(\mathbf{y}_c, \frac{1}{\sigma}\sum_y), \forall c$;
Step 3 Set $\mathbf{u}_n^* = \mathbf{u}_n^+$, $\mathbf{y}_c^* = \mathbf{y}_c^+$;
For $iter = 1, 2, \ldots, N_{iter}$
  For $n = 1, 2, \ldots, N$
  Step 4 Sample $\mathbf{u}_n^+$ using Equation (17) and accept it as $\mathbf{u}_n$ using Equations (18) and (19);
  Step 5 If $p(\mathbf{x}_n, \mathbf{u}_n^+|\mathbf{Y}^*) > p(\mathbf{x}_n, \mathbf{u}_n^*|\mathbf{Y}^*)$, then $\mathbf{u}_n^* = \mathbf{u}_n^+$;
  Endfor
  For $c = 1, 2, \ldots, C$
  Step 6 Sample $\mathbf{y}_c^+$ using Equation (20) and accept it as $\mathbf{y}_c^*$ using Equations (21) and (22);
  Step 7 If $p(\mathbf{X}, \mathbf{y}_c^+|\mathbf{U}^*) > p(\mathbf{X}, \mathbf{y}_c^*|\mathbf{U}^*)$, then $\mathbf{y}_c^* \leftarrow \mathbf{y}_c^+$;
  Endfor
Step 8 If $p(\mathbf{X}, \mathbf{U}^*, \mathbf{Y}^*) > p(\mathbf{X}, \mathbf{U}, \mathbf{Y})$, then $\mathbf{U}^* \leftarrow \mathbf{U}$, $\mathbf{Y}^* \leftarrow \mathbf{Y}$;
Endfor.

Algorithm 2 | Fuzzy partition on the whole data.

Input: Two class samples $\mathbf{X}_1$ and $\mathbf{X}_2$, the numbers of clustering C_1 and C_2 in two classes;

Output: Fuzzy partition matrix $\mathbf{U}^{(1)^*}$, $\mathbf{U}^{(2)^*}$ and clustering center matrix $\mathbf{Y}^{(1)^*}$, $\mathbf{Y}^{(2)^*}$.

Step 1 Initiate $\mathbf{u}_n^{(1)}$ ($\mathbf{u}_n^{(2)}$) $\sim$ Uniform(0, 1) in two classes;
Step 2 Initiate in two classes;
Step 3 Set $\mathbf{u}_n^{(1)*} = \mathbf{u}_n^{(1)}$, $\mathbf{u}_n^{(2)*} = \mathbf{u}_n^{(2)}$, $\mathbf{y}_{c_1}^{(1)*} = \mathbf{y}_{c_1}^{(1)}$, $\mathbf{y}_{c_2}^{(2)*} = \mathbf{y}_{c_2}^{(2)}$;
  $iter = 0$;
Do
  Step 4 Perform **Algorithm 1** on $\mathbf{X}_1$;
  Step 5 Perform **Algorithm 1** on $\mathbf{X}_2$;
  $iter = iter + 1$;
Until $\mathbf{Y}^{(1)^*}$ is $|\mathbf{Y}^{(1)^*}(\nu) - \mathbf{Y}^{(1)^*}(\nu - 1)| \le \varepsilon$ or $iter > N_{iter}$

NOISE-INSENSITIVE TSK FUZZY SYSTEM VIA INTERCLASS COMPETITIVE LEARNING

Antecedent Parameter Learning in PCB-ICL-TSK

In this section, we compute the antecedent parameters in PCB-ICL-TSK. The premise of PCB-ICL clustering in **Algorithm 1** is that the clustering centers of other class are priorly known, which is obviously not feasible in practical application. To perform the fuzzy partition on the whole data set, we take the strategy of an alternating cycle to perform **Algorithm 1** on different classes. In this case, the clustering results of one class influence the ones of the other class. Taking binary classification as an example, we perform **Algorithm 1** on positive class $\mathbf{X}_1$ and negative class $\mathbf{X}_2$ alternately. The detailed fuzzy partition of the whole data is shown in **Algorithm 2**.

The numbers of clustering in two classes are C_1 and C_2, and the cluster centers in two classes are $\mathbf{Y}_1$ and $\mathbf{Y}_2$, respectively. After applying **Algorithm 2** on the whole data, the center matrix $\mathbf{Y}$ can be described by $\mathbf{Y}^* = [\mathbf{Y}^{(1)*}; \mathbf{Y}^{(2)*}]$.

Consequent Parameter Learning in PCB-ICL-TSK

In this section, we compute the noise-insensitive consequent parameters in PCB-ICL-TSK. As discussed before, using the obtained the antecedent parameters, the dataset $\mathbf{X} = \{\mathbf{x}_i, l_i\}_{i=1}^N$ is represented as $S = \{(\tilde{\mu}(\mathbf{x}_i), l_i)\}_{i=1}^N$, where $\tilde{\mu}(\mathbf{x}_i) = [\tilde{\mu}_1(\mathbf{x}_i)^T, \tilde{\mu}_2(\mathbf{x}_i)^T, \ldots, \tilde{\mu}_{(C_1+C_2)}(\mathbf{x}_i)^T]^T$. Defining the vector $d(\mathbf{x}_i) = [\tilde{\mu}_1(\mathbf{x}_i)^T, \tilde{\mu}_2(\mathbf{x}_i)^T, \ldots, \tilde{\mu}_{(C_1+C_2)}(\mathbf{x}_i)^T, 1]^T$, the consequent vector $\mathbf{p}^* = [p_0^1, p_0^2, ..., p_0^{(C_1+C_2)}, w]^T$ can be computed by

$$f(\mathbf{x}_i) = (\mathbf{p}^*)^T d(\mathbf{x}_i) = \mathbf{p}_0{}^T \tilde{\mu}(\mathbf{x}_i) + w \begin{cases} \ge 0, & \mathbf{x}_i \in \mathbf{X}_1 \\ < 0, & \mathbf{x}_i \in \mathbf{X}_2 \end{cases} \quad (23)$$

where the vector $\mathbf{p}_0 = [p_0^1, p_0^2, ..., p_0^{(C_1+C_2)}]^T$ and w is the decision threshold. If we multiply Equation (23) by the class label, Equation (23) is represented as $l_i(\mathbf{p}^*)^T d(\mathbf{x}_i) \ge 0$ ($i = 1, \ldots, N$). Then, the vector $\mathbf{p}^*$ can be computed by

$$l_i(\mathbf{p}^*)^T d(\mathbf{x}_i) \ge \varepsilon_0 \quad (24)$$

In particular, $\varepsilon_0 = 1$ leads to the classical SVM. For simplicity, we set $\varepsilon_0 = 1$, and Equation (24) can be written as $l_i(\mathbf{p}^*)^T d(\mathbf{x}_i) \ge 1$. Thus, Equation (24) can be written as

$$J(\mathbf{p}^*) = \sum_{i=1}^{N} (l_i(\mathbf{p}^*)^T d(\mathbf{x}_i) - 1)^2 \quad (25)$$

Denote the matrix $\mathbf{D} = [l_1 d(\mathbf{x}_1)^T, l_2 d(\mathbf{x}_2)^T, \ldots, l_N d(\mathbf{x}_N)^T]^T$ and the error vector $\mathbf{e} = \mathbf{D}^*\mathbf{p}^* - \mathbf{1}$. Equation (25) can be rewritten as

$$\min_{\mathbf{p}^*} J(\mathbf{p}^*) = \frac{1}{2}(\mathbf{D}\mathbf{p}^* - \mathbf{1})^T \mathbf{H}(\mathbf{D}\mathbf{p}^* - \mathbf{1}) \quad (26)$$

where the matrix $\mathbf{H} = (\lambda/N)\mathrm{diag}(h_1, h_2, \ldots, h_N)$, with $h_i = 0$ for error $e_i \ge 0$ and 1 otherwise.

However, the misclassification error in Equation (24) is noise sensitive. To further improve the robustness of the TSK fuzzy system, we use the asymmetric expectile term, which is noise insensitive, especially to noise around the decision boundary. The weight h_i of the ith sample can be expressed by

$$h_i = \begin{cases} q, & e_i \ge 0 \\ (1 - q), & e_i < 0 \end{cases} \quad (27)$$

where h_i is the q (lower) expectile parameter. Obviously, when $q = 0$, the loss term obtained in Equation (27) is equal to the

Algorithm 3 | Learning algorithm for consequent parameters.

Input: The dataset $\mathbf{X}$; the number of clusters ($C_1 + C_2$); the cluster centers $\mathbf{Y}_1$, $\mathbf{Y}_2$ and the membership matrix $\mathbf{U}_1$, $\mathbf{U}_2$; the expectile parameter q; and the regularization parameter τ;

Output: Consequent parameters $\mathbf{p}_0$.

Step 1 Run **Algorithm 2** to obtain the antecedent parameters;
Step 2 Compute the membership function $d(\mathbf{x}_i)=[\tilde{\mu}_1(\mathbf{x}_i)^T, \tilde{\mu}_2(\mathbf{x}_i)^T, \ldots, \tilde{\mu}_{(C_1+C_2)}(\mathbf{x}_i)^T, 1]^T$ by using Equations (5)–(7);
$k = 0$;
Do
Step 3 Obtain the parameters $(\mathbf{p}^*)^{(k)}$ using Equation (29);
Step 4 Compute the parameter $\mathbf{e}^{(k)}$ using $\mathbf{e}^{(k)} = \mathbf{D}(\mathbf{p}^*)^{(k)} - \mathbf{1}$;
Step 5 Compute the parameter $\mathbf{H}^{(k+1)}$ using Equation (27);
$k = k + 1$;
Until $\mathbf{p}^*$ is convergence or $k > k_{\max}$.

hinge loss, and when $q = 0.5$, the loss term is equal to the l_2 loss in Huang et al. (2014a,b).

At the same time, considering the regularization term, Equation (26) can be rewritten as

$$\min_{\mathbf{p}^*} J(\mathbf{p}^*)^{(k)} = \frac{1}{2}(\mathbf{D}^*(\mathbf{p}^*)^{(k)} - \mathbf{1})^T \mathbf{H}^{(k)}(\mathbf{D}^*(\mathbf{p}^*)^{(k)} - \mathbf{1}) + \frac{\tau}{2}(\mathbf{p}_0{}^{(k)})^T \mathbf{p}_0{}^{(k)} \quad (28)$$

where τ is the regularization parameter. $\mathbf{p}^{*(k)}$, $\mathbf{H}^{(k)}$, and $\mathbf{e}^{(k)}$ are the kth iteration of $\mathbf{p}^*$, $\mathbf{H}$, and $\mathbf{e}$, respectively.

The condition for optimality of Equation (28) in the kth iteration is obtained by setting $dJ/d\mathbf{p}^* = 0$:

$$(\mathbf{p}^*)^{(k)} = ((\mathbf{D}^*)^T \mathbf{H}^{(k)} \mathbf{D}^* + \tau\, \tilde{\mathbf{I}})^{-1} (\mathbf{D}^*)^T \mathbf{H}^{(k)} \mathbf{1} \quad (29)$$

where $\tilde{\mathbf{I}}$ is the identity matrix with the last element on the main diagonal set to 0.

The consequent parameter learning in IB-TSK-FC on dataset $\mathbf{X}$ is shown in **Algorithm 3**.

EXPERIMENT

Experimental Settings

The real-world EEG signals have characters of high dimensionality and instability. Feature extraction is a necessary stage before classification for EEG signal recognition. In general, time domain and frequency domain feature extractions are two types of feature extraction methods (Wen and Zhang, 2017). In our experiments, we extract EEG features using kernel principal component analysis (KPCA) and short-time Fourier transform (STFT) (Blanco et al., 1997). The former is the time domain feature extraction, and the latter is the frequency domain feature extraction. In the experiment, we design eight classification tasks, namely, four binary classification and four three-class classification tasks, as shown in **Table 2**. We corrupt the original datasets with different amounts of random noises at 5, 10, and 15% noise levels.

TABLE 2 | EEG classification tasks in the experiment.

Tasks	Number of classes	Datasets
T1	Two classes	A and C
T2		A and E
T3		B and D
T4		B and E
T5	Three classes	A, C and E
T6		A, D, and E
T7		B, C, and E
T8		B, D, and E

TABLE 3 | Parameter settings for all methods in the experiment.

Methods	Parameter settings
ε-margin-TSK-FS FS-FCSVM	Number of rules$\in \{1, 2, \ldots, 12\}$, regularization parameter $\in \{10^{-3}, 10^{-2}, \ldots, \ldots, 10^3\}$, scale parameter $\in \{0.4^2, 0.6^2, \ldots, 3^2\}$, fuzzy index = 2
IB-TSK-FC	Model sparsity parameter $\in \{1, 2, \ldots, 6\}$, fuzzy index = 2, number of particles = 10, convergence thresholds = 10^{-3}, convergence threshold = 10–^{3}, strength parameter = 3
CS-SVM	Gaussian kernel parameter $\in \{10^{-2}, 10^{-1}, \ldots, \ldots, 10^2\}$, regularization parameter $\in \{10^{-3}, 10^{-2}, \ldots, \ldots, 10^3\}$
FRSVM-ANCH	Gaussian kernel parameter $\in \{10^{-2}, 10^{-1}, \ldots, \ldots, 10^2\}$, regularization parameter $\in \{10^{-3}, 10^{-2}, \ldots, \ldots, 10^3\}$, pinball loss parameter = 0.05
PCB-ICL-TSK	Fuzzy index = 2, number of rules $\in \{1, 2, \ldots, 12\}$, convergence threshold = 10^{-3}, strength parameter = 3, expectile parameter = 0.05, maximum number of iterations = 1,000 and 200 in **Algorithms 1** and **2**, respectively

The experimental environment in this study is a computer with Intel Core i3-3317U 3.40-GHz CPU and 8-GB RAM. To validate the performance of MST-TSK, we compare three fuzzy systems (FS-FCSVM; et al., 2007, ε-margin-TSK-FS; Leski, 2005, and IB-TSK-FC; Gu et al., 2017b) and two robust classification methods (CS-SVM; Iranmehr et al., 2019 and FRSVM-ANCH; Gu et al., 2019). The Gaussian kernel is used for two SVM methods. The parameter settings for all methods are listed in **Table 3**. All parameters are obtained by a 5-fold cross-validation strategy.

Classification Performance Comparison

In this section, eight EEG classification tasks are used to verify the classification performance of PCB-ICL-TSK. **Tables 4**, **5** show the experimental results of six classification algorithms using STFT and KPCA feature extraction methods at the 5% noise level. **Tables 6**, **7** show the experimental results of six

TABLE 4 | The classification accuracy for the 5% noise level using STFT features.

Tasks	FS-FCSVM	ε-margin-TSK-FS	IB-TSK-FC	CS-SVM	FRSVM-ANCH	PCB-ICL-TSK
Task 1	94.56	94.69	95.22	96.27	96.73	**96.74**
Task 2	94.88	94.81	95.34	96.19	96.51	**96.62**
Task 3	94.64	94.57	95.39	96.45	**96.70**	96.69
Task 4	94.21	94.34	95.57	96.58	96.54	**96.67**
Task 5	93.46	93.25	93.98	96.27	**96.32**	96.29
Task 6	93.37	93.42	93.96	95.89	**96.14**	96.12
Task 7	93.25	93.34	93.86	95.78	95.97	**96.04**
Task 8	93.38	93.29	93.75	95.86	96.09	**96.10**

The bold values indicate the best classification performance in the tasks.

TABLE 5 | The classification accuracy for the 5% noise level using KPCA features.

Tasks	FS-FCSVM	ε-margin-TSK-FS	IB-TSK-FC	CS-SVM	FRSVM-ANCH	PCB-ICL-TSK
Task 1	94.53	94.70	95.23	96.28	96.63	**96.75**
Task 2	94.92	94.78	95.39	96.23	96.50	**96.59**
Task 3	94.62	94.55	95.40	96.42	**96.72**	96.72
Task 4	94.23	94.33	95.56	96.62	96.51	**96.65**
Task 5	93.47	93.25	93.95	96.26	**96.33**	96.31
Task 6	93.38	93.44	93.97	95.94	96.11	**96.19**
Task 7	93.23	93.36	93.85	95.79	95.95	**96.01**
Task 8	93.37	93.34	93.76	95.89	96.10	**96.11**

The bold values indicate the best classification performance in the tasks.

TABLE 6 | The classification accuracy for the 10% noise level using STFT features.

Tasks	FS-FCSVM	ε-margin-TSK-FS	IB-TSK-FC	CS-SVM	FRSVM-ANCH	PCB-ICL-TSK
Task 1	92.79	92.84	93.44	94.64	95.09	**95.29**
Task 2	93.12	93.01	93.58	94.57	95.21	**95.28**
Task 3	92.76	92.76	93.59	94.86	**95.39**	95.30
Task 4	92.48	92.52	93.76	95.03	94.99	**95.21**
Task 5	91.60	91.45	92.16	94.63	94.66	**94.93**
Task 6	91.61	91.65	92.23	94.23	**94.71**	94.70
Task 7	91.44	91.58	92.09	94.18	94.61	**94.68**
Task 8	91.58	91.55	91.94	94.19	94.56	**94.67**

The bold values indicate the best classification performance in the tasks.

TABLE 7 | The classification accuracy for the 10% noise level using KPCA features.

Tasks	FS-FCSVM	ε-margin-TSK-FS	IB-TSK-FC	CS-SVM	FRSVM-ANCH	PCB-ICL-TSK
Task 1	92.75	92.80	93.39	94.61	95.24	**95.27**
Task 2	93.12	92.98	93.53	94.56	**95.21**	**95.21**
Task 3	92.77	92.72	93.63	94.85	95.14	**95.26**
Task 4	92.49	92.58	93.84	95.08	94.95	**95.20**
Task 5	91.63	91.42	92.20	94.66	94.77	**94.96**
Task 6	91.53	91.66	92.22	94.24	94.58	**94.69**
Task 7	91.45	91.52	92.10	94.24	94.51	**94.68**
Task 8	91.61	91.58	91.87	94.19	94.54	**94.69**

The bold values indicate the best classification performance in the tasks.

TABLE 8 | The classification accuracy for the 15% noise level using STFT features.

Tasks	FS-FCSVM	ε-margin-TSK-FS	IB-TSK-FC	CS-SVM	FRSVM-ANCH	PCB-ICL-TSK
Task 1	90.73	90.77	91.39	92.98	93.48	**93.88**
Task 2	91.13	90.94	91.49	92.84	93.85	**93.90**
Task 3	90.70	90.76	91.53	93.18	93.70	**93.88**
Task 4	90.48	90.57	91.84	93.33	**93.85**	93.84
Task 5	89.68	89.39	90.19	92.91	93.07	**93.57**
Task 6	89.55	89.74	90.20	92.59	92.92	**93.33**
Task 7	89.49	89.48	90.05	92.48	93.04	**93.28**
Task 8	89.62	89.67	89.85	92.50	93.28	**93.32**

The bold values indicate the best classification performance in the tasks.

TABLE 9 | The classification accuracy for the 15% noise level using KPCA features.

Tasks	FS-FCSVM	ε-margin-TSK-FS	IB-TSK-FC	CS-SVM	FRSVM-ANCH	PCB-ICL-TSK
Task 1	90.73	90.77	91.39	92.96	93.47	**93.87**
Task 2	91.13	90.94	91.49	92.86	93.34	**93.82**
Task 3	90.70	90.76	91.53	93.20	93.73	**93.90**
Task 4	90.48	90.57	91.84	93.33	**93.82**	**93.82**
Task 5	89.68	89.39	90.19	92.93	93.12	**93.49**
Task 6	89.55	89.74	90.20	92.52	92.91	**93.32**
Task 7	89.49	89.48	90.05	92.47	92.99	**93.24**
Task 8	89.62	89.67	89.85	92.49	93.20	**93.22**

The bold values indicate the best classification performance in the tasks.

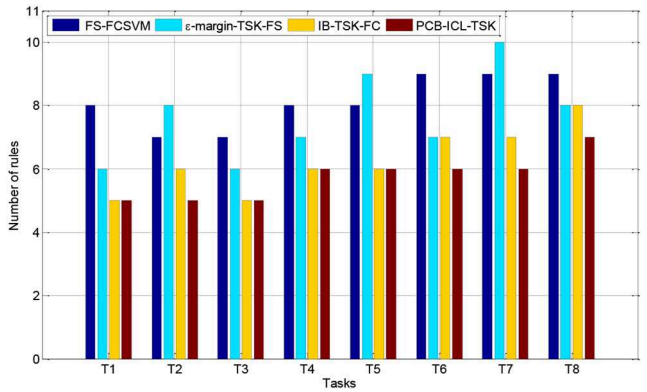

FIGURE 3 | The rules obtained by four fuzzy systems on the 5% noise level using KPCA features.

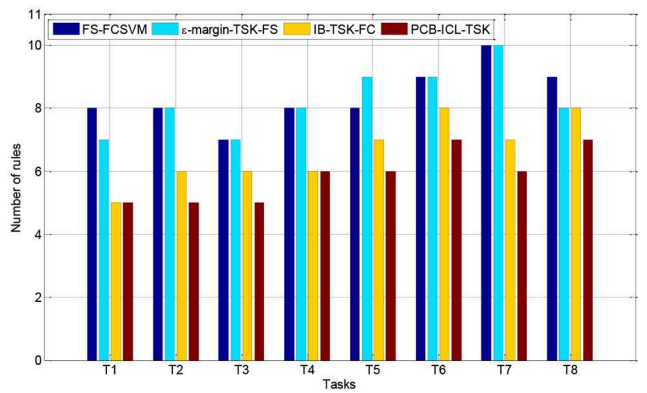

FIGURE 5 | The rules obtained by four fuzzy systems on the 5% noise level using STFT features.

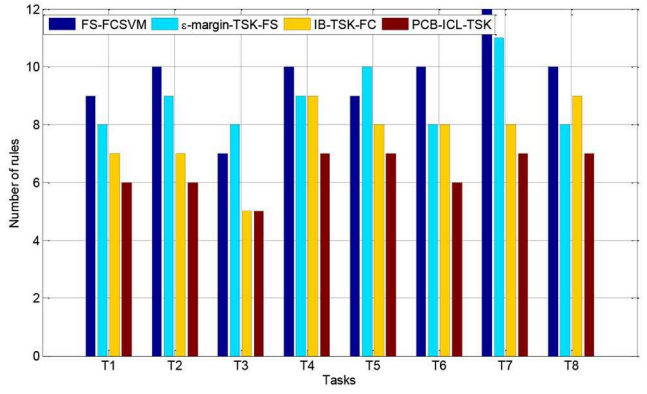

FIGURE 4 | The rules obtained by four fuzzy systems on the 15% noise level using KPCA features.

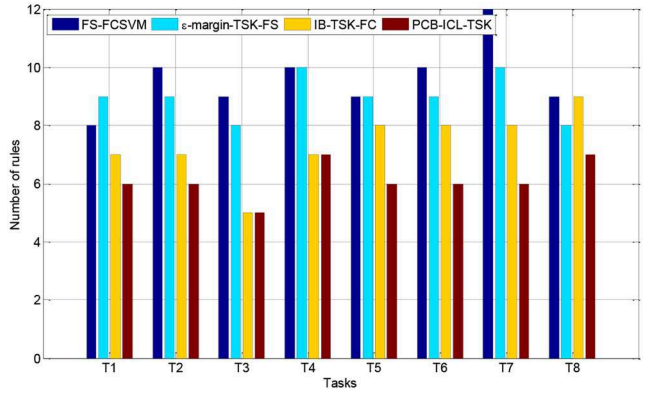

FIGURE 6 | The rules obtained by four fuzzy systems on the 15% noise level using STFT features.

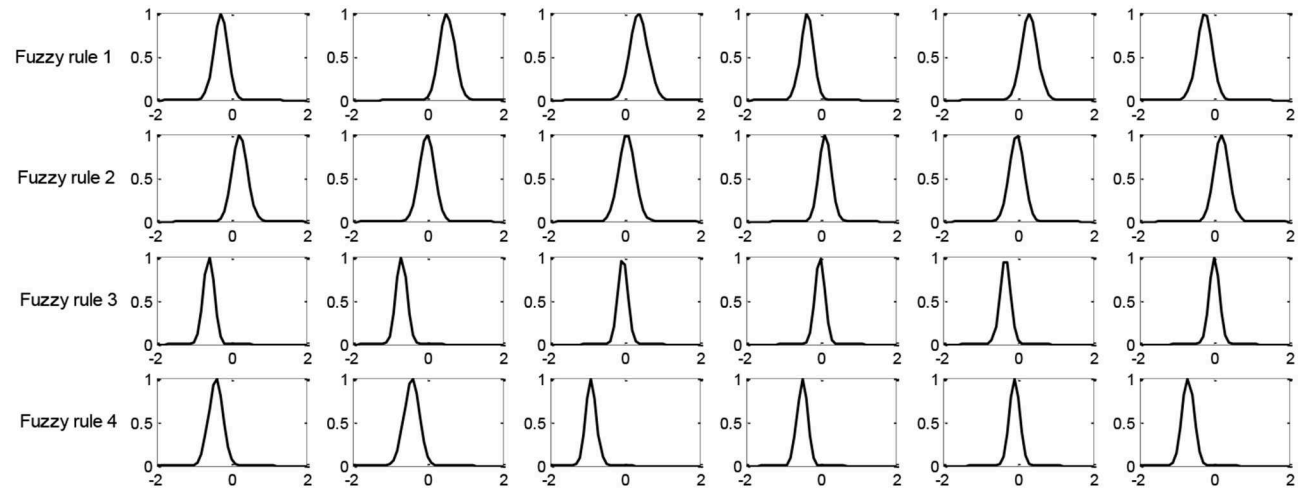

FIGURE 7 | Fuzzy membership functions obtained by PCB-ICL on Task 1 with the 5% noise level using KPCA features.

classification methods using STFT and KPCA feature extraction methods at the 10% noise level. **Tables 8**, **9** show the experimental results of six classification methods using STFT and KPCA feature extraction methods at the 15% noise level. From the experimental results, it can be seen that the noise data seriously affect the classification performance of the method. During the learning process, considering the noise of the data is helpful to promote the classification performance. Therefore, the performances of FS-FCSVM, ε-margin-TSK-FS, and IB-TSK-FC are poor. CS-SVM, FRSVM-ANCH, and PCB-ICL-TSK are not sensitive to noise, and they can achieve good classification results. In particular, PCB-ICL-TSK shows excellent classification performance in different levels of noise occasions, and it reflects strong robustness. Since PCB-ICL-TSK uses the PCB-ICL and Ho–Kashyap procedure with an asymmetric expectile term to compute antecedent and consequent parameters of fuzzy rules, it is noise insensitive. In addition, in the Bayesian framework, PCB-ICL obtains global optimal clustering results, and the strategy of competitive relationship of clustering centers can enhance the interpretability of the antecedents of fuzzy rules.

Interpretability Comparison

In this section, we compare the number of fuzzy rules of four fuzzy systems in Task 8. **Figures 3**, **4** show the number of fuzzy rules on the 5 and 15% noise levels for four fuzzy systems using KPCA features. **Figures 5**, **6** show the number of fuzzy rules on the 5 and 15% noise levels for four fuzzy systems using STFT features. From the results in **Figures 3**–**6**, compared with the three fuzzy systems, the number of fuzzy rules obtained by PCB-ICL-TSK is the least in all EEG classification tasks. It is known that for fuzzy systems, the interpretability of fuzzy rules is related to the number of fuzzy rules and the definition of fuzzy subsets. The fuzzy membership function obtained by PCB-ICL on Task 1 at the 5% noise level using KPCA features is shown in **Figure 7**. Because PCB-ICL clustering considers the influence of clustering centers of different classes in the process of clustering, that is, the competition relationship between different classes of clustering centers, PCB-ICL clustering can obtain clustering centers with a large interval, which guarantees the partition clarity of feature space and the classification accuracy of the obtained fuzzy system and the interpretation of rules.

CONCLUSION

The noise-insensitive PCB-ICL-TSK fuzzy system is proposed in this paper. In the learning of rule antecedent parameters, the proposed noise-insensitive PCB-ICL clustering based on the Bayesian probability model is used. PCB-ICL clustering considers the repulsion between different clustering centers, which can ensure the interpretability of the rule antecedent. PCB-ICL can learn the global optimal solution of clustering results by using the Markov model. PCB-ICL-TSK learns consequent parameters using the Ho–Kashyap procedure with an asymmetric expectile term. Thus, it not only has strong noise resistance but also has high classification performance. The experimental results of a real EEG dataset show that PCB-ICL-TSK has achieved satisfactory results in classification performance and high interpretability. Our future work is to further improve its practicability when the sample dimension is large.

DATA AVAILABILITY STATEMENT

Publicly available datasets were analyzed in this study. This data can be found here: The dataset analyzed for this study can be found in the Department of Epileptology University of Bonn [http://epileptologie-bonn.de/cms/upload/workgroup/lehnertz/eegdata.html].

AUTHOR CONTRIBUTIONS

TN and XG conceived and developed the theoretical framework of the manuscript. All authors carried out the experiment and data process and drafted the manuscript.

FUNDING

This work was supported in part by the National Natural Science Foundation of China under Grant 61806026 and by the Natural Science Foundation of Jiangsu Province under Grant BK20180956.

REFERENCES

Ahmadlou, M., and Adeli, H. (2011). Functional community analysis of brain: a new approach for EEG-based investigation of the brain pathology. *Neuroimage* 58, 401–408. doi: 10.1016/j.neuroimage.2011.04.070

Akhavan, A., and Moradi, M. H. (2018). Detection of concealed information using multichannel discriminative dictionary and spatial filter learning. *IEEE Trans. Inform. Foren. Secur*. 13, 2616–2627. doi: 10.1109/TIFS.2018.2825940

Bezdek, J., Ehrlich, R., and Full W. (1984). FCM: the fuzzy c-means clustering algorithm. *Comp. Geosci*. 10, 191–203. doi: 10.1016/0098-3004(84)90020-7

Blanco, S., Kochen, S., Rosso, O. A., and Salgado,. P. (1997). Applying time frequency analysis to seizure EEG activity. *IEEE Eng. Med. Biol. Mag*. 16, 64–71. doi: 10.1109/51.566156

Chib, S., and Greenberg, E. (1995). Understanding the metropolis-hastings algorithm. *Am. Stat*. 49, 327–335. doi: 10.1080/00031305.1995.10476177

Cury, C., Maurel, P., Gribonval, R., and Barillot, C. (2019). A sparse EEG-informed fMRI model for hybrid EEG-fMRI neurofeedback prediction. *Front. Neurosci.* 13:1451. doi: 10.3389/fnins.2019.01451

Elvira, V., Míguez, J., and Djurić, P. M. (2017). Adapting the number of particles in sequential Monte Carlo methods through an online scheme for convergence assessment. *IEEE Trans. Signal Process.* 65, 1781–1794. doi: 10.1109/TSP.2016.2637324

Glenn, T. C., Zare, A., and Gader, P. D. (2015). Bayesian fuzzy clustering. *IEEE Trans. Fuzzy Syst*. 23, 1545–1561. doi: 10.1109/TFUZZ.2014.2370676

Gu, X., Chung, F., and Wang, S. (2017a). Bayesian Takagi-Sugeno-Kang fuzzy classifier. *IEEE Trans. Fuzzy Syst*. 25, 1655–1671. doi: 10.1109/TFUZZ.2016.2617377

Gu, X., Chung, F. L., Ishibuchi, H., and Wang, S. (2017b). Imbalanced TSK fuzzy classifier by cross-class Bayesian fuzzy clustering and imbalance learning, IEEE Trans. *Syst. Man Cybernet. Syst*. 47, 2005–2020. doi: 10.1109/TSMC.2016.2598270

Gu, X., Ni, T., and Fan, Y. (2019). A fast and robust support vector machine with anti-noise convex hull and its application in large-scale ncRNA data classification. *IEEE Access*. 7, 134730–134741. doi: 10.1109/ACCESS.2019.2941986

Gu, X., and Wang, S. (2018). Bayesian Takagi-Sugeno-Kang Fuzzy model and its joint learning of structure identification and parameter estimation. *IEEE Trans. Indust. Inform*. 14, 5327–5337. doi: 10.1109/TII.2018.2813977

Gummadavelli, A., Zaveri, H. P., Spencer, D. D., and Gerrard, J. L. (2018). Expanding brain-computer interfaces for controlling epilepsy networks: novel thalamic responsive neurostimulation in refractory epilepsy. *Front. Neurosci.* 12:474. doi: 10.3389/fnins.2018.00474

Hossain, M. S., Amin, S. U., Alsulaiman, M., and Muhammad, G. (2019). Applying deep learning for epilepsy seizure detection and brain mapping visualization, ACM Trans. *Multimed. Comput. Commun. Appl.* 15, 1–17. doi: 10.1145/3241056

Huang, X. L., Shi, L., Pelckmansb, K., and Suykens, J. A. K. (2014a). Asymmetric ν-tube support vector regression. *Comput. Stat. Data Anal*. 77, 371–382. doi: 10.1016/j.csda.2014.03.016

Huang, X. L., Shi, L., and Suykens, J. A. K. (2014b). Support vector machine classifier with pinball loss. *IEEE Trans. Pattern Anal. Mach. Intell*. 36, 984–997. doi: 10.1109/TPAMI.2013.178

Hussein, R., Palangi, H., Ward, R. K., and Wang, Z. J. (2019). Optimized deep neural network architecture for robust detection of epileptic seizures using EEG signals. *Clin. Neurophysiol.* 130, 25–37. doi: 10.1016/j.clinph.2018.10.010

Iranmehr, A., Shirazi, H. M., and Vasconcelos, N. (2019). Cost-sensitive support vector machines. *Neurocomputing* 343, 50–64. doi: 10.1016/j.neucom.2018.11.099

Jiang, Y., Deng, Z., Chung, F., Wang, G., Qian, P., Choi, K. S., et al. (2017c). Recognition of epileptic EEG signals using a novel multiview TSK fuzzy system. *IEEE Trans. Fuzzy Syst*. 25, 3–20. doi: 10.1109/TFUZZ.2016.2637405

Jiang, Y., Deng, Z., Chung, F., and Wang, S. (2015). Multi-task TSK fuzzy system modeling using inter-task correlation information. *Inform. Sci*. 298, 512–533. doi: 10.1016/j.ins.2014.12.007

Jiang, Y., Deng, Z., Chung, F., and Wang, S. (2017b). Realizing two-view TSK fuzzy classification system by using collaborative learning. *IEEE Transac. Syst. Man Cybernet. Syst*. 47, 145–160. doi: 10.1109/TSMC.2016.2577558

Jiang, Y., Wu, D., Deng, Z., Qian, P., Wang, J., Wang, G., et al. (2017a). Seizure classification from EEG signals using transfer learning, semi-supervised learning and TSK fuzzy system. *IEEE Trans. Neural Syst. Rehabil. Eng*. 25, 2270–2284. doi: 10.1109/TNSRE.2017.2748388

Juang, C. F., Chiu, S. H., and Shiu, S. J. (2007). Fuzzy system learned through fuzzy clustering and support vector machine for human skin color segmentation. *IEEE Trans. Syst. Man Cybernet. Part A Syst. Hum*. 37, 1077–1087. doi: 10.1109/TSMCA.2007.904579

Kabir, E., and Zhang, Y. (2016). Epileptic seizure detection from EEG signals using logistic model trees. *Brain Inform*. 3, 93–100. doi: 10.1007/s40708-015-0030-2

Krishnapuram, R., and Keller, J. M. (1993). A possibilistic approach to clustering. *IEEE Trans. Fuzzy Syst*. 1, 98–110. doi: 10.1109/91.227387

Leski, J. M. (2003). Ho-Kashyap classifier with generalization control. *Pattern Recogn. Lett*. 24, 2281–2290. doi: 10.1016/S0167-8655(03)00054-0

Leski, J. M. (2005). TSK-fuzzy modeling based on ε - insensitive learning. *IEEE Trans. Fuzzy Syst*. 13, 181–193. doi: 10.1109/TFUZZ.2004.840094

Leski, J. M. (2015). Fuzzy (c+p)-means clustering and its application to a fuzzy rule-based classifier: towards good generalization and good interpretability. *IEEE Trans. Fuzzy Syst*. 23, 802–812. doi: 10.1109/TFUZZ.2014.2327995

Li, X., Yang, H., Yan, J., Wang, X., Li, X., and Yuan, Y. (2019). Low-intensity pulsed ultrasound stimulation modulates the nonlinear dynamics of local field potentials in temporal lobe epilepsy. *Front. Neurosci.* 13:287. doi: 10.3389/fnins.2019.00287

Liu, C. L., Xiao, B., Hsaio,W. H., and Tseng, V. S. (2019). Epileptic seizure prediction with multi-view convolutional neural networks. *IEEE Access*. 7, 170352–170361. doi: 10.1109/ACCESS.2019.2955285

Martinez-Vargas, J. D., Strobbe, G., Vonck, K., Van Mierlo, P., and Castellanos-Dominguez, G. (2017). Improved localization of seizure onset zones using spatiotemporal constraints and time-varying source connectivity. *Front. Neurosci.* 11:156. doi: 10.3389/fnins.2017.00156

Qi, F., Li, Y., and Wu, W. (2017). RSTFC: a novel algorithm for spatio-temporal filtering and classification of single-trial EEG. *IEEE Trans. Neural Netw. Learn. Syst*. 26, 3070–3082. doi: 10.1109/TNNLS.2015.2402694

Razzak, I., Hameed, I. A., and Xu, G. D. (2019). Robust sparse representation and multiclass support matrix machines for the classification of motor imagery EEG signals. *IEEE J. Transl. Eng. Health Med*. 7, 2168–2372. doi: 10.1109/JTEHM.2019.2942017

Salgado, C. M., Viegas, J. L., Azevedo, C. S., Ferreira, M. C., Vieira, S. M., and Sousa, J. M. C. (2017). Takagi-Sugeno fuzzy modeling using mixed fuzzy clustering. *IEEE Trans. Fuzzy Syst*. 25, 1417–1429. doi: 10.1109/TFUZZ.2016.2639565

Siuly, S., and Li, Y. (2015). Designing a robust feature extraction method based on optimum allocation and principal component analysis for epileptic EEG signal classification. *Comput. Methods Prog. Biomed*. 119, 29–42. doi: 10.1016/j.cmpb.2015.01.002

Sreej, S. R., and Samanta, D. (2019). Classification of multiclass motor imagery EEG signal using sparsity approach. *Neurocomputing* 368, 133–145. doi: 10.1016/j.neucom.2019.08.037

Takagi, T., and Sugeno, M. (1985). Fuzzy identification of systems and its application to modeling and control,. *Trans. Syst. Man Cybernet.* 15, 116–132. doi: 10.1109/TSMC.1985.6313399

Truong, N. D., Nguyen, A., Kuhlmann, D. L., Bonyadi, M. R., Yang, J. W., Ippolito, S., et al. (2018). Integer convolutional neural network for seizure detection. *IEEE J. Emerg. Select. Top. Circuits Syst.* 8, 849–857. doi: 10.1109/JETCAS.2018.2842761

Tzallas, A. T., Tsipouras, M. G., and Fotiadis, I. D. (2009). Epileptic seizure detection in EEGs using time-frequency analysis. *IEEE Trans. Inform. Technol. Biomed.* 13, 703–710. doi: 10.1109/TITB.2009.2017939

Wen, T., and Zhang, Z. (2017). Effective and extensible feature extraction method using genetic algorithm-based frequency-domain feature search for epileptic EEG multiclassification. *Medicine* 96:e6879. doi: 10.1097/MD.0000000000006879

Xia, K., Ni, T., Yin, H., and Chen, B. (2020). Cross-domain classification model with knowledge utilization maximization for recognition of epileptic EEG signals. *IEEE/ACM Trans. Comput. Biol. Bioinformatics.* doi: 10.1109/TCBB.2020.2973978. [Epub ahead of print].

Conflict of Interest: The authors declare that the research was conducted in the absence of any commercial or financial relationships that could be construed as a potential conflict of interest.

frontiers in Neuroscience

ORIGINAL RESEARCH
published: 16 September 2020
doi: 10.3389/fnins.2020.577937

FFA-DMRI: A Network Based on Feature Fusion and Attention Mechanism for Brain MRI Denoising

Dan Hong[1], Chenxi Huang[1], Chenhui Yang[1]*, Jianpeng Li[2]*, Yunhan Qian[1] and Chunting Cai[1]*

[1] School of Informatics, Xiamen University, Xiamen, China, [2] Department of Neurology, The First Affiliated Hospital of Xiamen University, Xiamen, China

Magnetic Resonance Imaging (MRI) is an indispensable tool in the diagnosis of brain diseases due to painlessness and safety. Nevertheless, Rician noise is inevitably injected during the image acquisition process, which leads to poor observation and interferes with the treatment. Owing to the complexity of Rician noise, using the elimination method of Gaussian to remove it does not perform well. Therefore, the feature fusion and attention network (FFA-DMRI) is proposed to separate noise from observed MRI. Inspired by the attention-guided CNN network (ADNet) and Convolutional block attention module (CBAM), a spatial attention mechanism has been specially designed to obtain the area of interest in MRI. Furthermore, the feature fusion block concatenates local with global information, which makes full use of the multilevel structure and boosts the expressive ability of network. The comprehensive experiments on Alzheimer's disease neuroimaging initiative dataset (ADNI) have demonstrated high effectiveness of FFA-DMRI with maintaining the crucial brain details. Moreover, in terms of visual inspections, the denoising results are also consistent with human perception.

Keywords: magnetic resonance imaging, brain, denoising, feature fusion, attention mechanism

OPEN ACCESS

Edited by:
Yizhang Jiang,
Jiangnan University, China

Reviewed by:
Qianyi Zhan,
Jiangnan University, China
Juan Yang,
Suzhou University, China

****Correspondence:***
Chenxi Huang
chyang@xmu.edu.cn
Chenhui Yang
ych987@126.com
Jianpeng Li
liwitty@outlook.com

Specialty section:
This article was submitted to Neuroprosthetics, a section of the journal Frontiers in Neuroscience

Received: *30 June 2020*
Accepted: *13 August 2020*
Published: *16 September 2020*

Citation:
Hong D, Huang C, Yang C, Li J, Qian Y and Cai C (2020) FFA-DMRI: A Network Based on Feature Fusion and Attention Mechanism for Brain MRI Denoising. Front. Neurosci. 14:577937. doi: 10.3389/fnins.2020.577937

INTRODUCTION

Magnetic Resonance Imaging (MRI) of brains, with the superior features of non-radiation, non-invasiveness, and high resolution, is notable for diagnosis and treatment (Ikram et al., 2019; Jiang et al., 2019; Yu et al., 2019; Tripathi and Bag, 2020). In clinical practice, high-quality MRI can provide clear structural and functional information on brain tissues. However, noise is introduced into the raw image due to the circulation of magnetic fields and the interaction of magnets in MRI machines, which may hide the details of brain tissues and hinder the auto-computerized analysis (Jiang et al., 2017). Therefore, noise removal is a vital task to recover the clean MRI before the images are applied to diagnosis.

Previous research has established that the noise in MRI is governed by the Rician distribution, in which both real and imaginary parts are corrupted by Gaussian noise with equal variance (Bhadauria and Dewal, 2013; Li et al., 2020). The Rician distribution is signal-dependent as distinct from additive Gaussian noise. In other words, Rician noise is related to the image, and utilizing

Gaussian denoising methods directly to remove it usually yields poor results. Thus, the right way to separate noise from the raw MRI without losing critical details is a huge challenge (Cai et al., 2020a).

With the increasing demand for image quality, a number of methods have been proposed for denoising. Existing methods can be mainly classified into two categories: transform domain methods and filtering methods (Mohan et al., 2014). The purpose of the transform domain method is to convert the original signal into a pattern that can remove noise more easily. For instance, a bilateral filtering scheme was proposed based on wavelets, in which the noise coefficient is expressed effectively by an undecimated wavelet transform (UDWT). There is a nice trade-off between the effect of noise removal and feature retention (Anand and Sahambi, 2010; Cai et al., 2020b). Based on wavelet shrinkage, the iterative scheme estimates the signal wavelet coefficients from the noisy images (Yu and Zhao, 2008). For signal high-dimensional singularities, wavelet transform does not perform well. Curvelet transform makes up for the shortcomings (Mohan et al., 2014). In this transform, edge directions are reproduced using the directivity and anisotropy of the curve (Do and Vetterli, 2005). However, the wavelet transform fails to resolve the curve with smooth edges. To overcome the drawback, a geometrical image transform was proposed, which greatly captures contours and details in MRI.

The filter methods, generally grouped into linear and non-linear parts, are adapted to remove noise in MRI. For linear filters, spatial filters and temporal filters are commonly employed (McVeigh et al., 1985; Mohan et al., 2014). Relatively, a spatial filter decreases the variance in MRI; however, it faces shortcomings in that it introduces the blurring of edges, which results in part of the required information that cannot be restored correctly (Soomro and Gao, 2016). Temporal filters are utilized only to spin-echo images. Furthermore, to prevent the aliasing artifacts, it is essential to select the appropriate filter to match filter sampling intervals. If the filters are too broad or too narrow, the performance is not satisfactory. For non-linear spatial filters, using a linear approach directly is not allowed. There are some typical examples in non-linear filters such as anisotropic diffusion filter (ADF) (Sijbers et al., 1999) and non-local means (NLM) (Coupé et al., 2006). The ADF approach obtains the denoising images efficiently with sharp edges. The filter of NLM employs redundant information to restore noise-free images. On the basis of the filter, unbiased NLM (Manjón et al., 2008) is exploited to improve the SNR in MRI; meanwhile, it does not influence the obvious structures. Nevertheless, the method has the shortcoming of high computational complexity.

Recently, methodologies based on deep learning are used to alleviate the above problem, such as deep plug-and-play super-resolution (DPSR) (Zhang K. et al., 2019), fast and flexible denoising convolutional neural network (FFDNet) (Zhang et al., 2018), and variance-stabilizing transformation inspired networks (VST-net) (Zhang M. et al., 2019). VST-net inherits the structures of traditional variance-stabilizing transformation and optimizes non-linear transformation through the design of a deep learning network. That shows the great potential of deep learning for denoising tasks. It is noted that the denoising convolutional neural network (DnCNN) (Zhang et al., 2017a) utilizes batch normalization and residual learning, which exhibits high effectiveness in JPEG image deblocking, single image super-resolution, and Gaussian denoising. Numerous deep learning methods for denoising have achieved outstanding performance. However, most research up to now has focused on the reduction of Gaussian noise, real noise, and blind noise. To our best knowledge, far too little attention has been paid to removing the Rician noise in MRI.

In this work, we propose a feature fusion and attention network (FFA-DMRI) for removing Rician noise in magnetic resonance (MR) images. Inspired by the structure of attention-guided CNN network (ADNet) (Tian et al., 2020), we have designed the FFA-DMRI network to restore noise-free images while maintaining critical brain tissues to the maximum extent possible. The main contributions of this paper are as follows:

(1) The proposed FFA-DMRI is dedicated to removing Rician noise in MR images. In contrast to other deep leaning methods for denoising, we specifically develop a spatial attention mechanism to focus on the area-of-interest of the brain.
(2) FFA-DMRI network is constructed with three blocks, including the feature extraction block, the feature fusion block, and the attention block. The feature extraction block utilizes the common convolution and the dilated convolution, which expands the receptive field and gains the details effectively. The feature fusion block is designed to combine the local and global features. Consequently, this block obtains more contextual information and promotes the reconstruction of pixels in MR images.
(3) The FFA-DMRI network is very superior for denoising on the ADNI dataset. In comparative experiments, it is competitive in quantitative metrics in terms of SSIM and PSNR. From the visual inspection, the denoising results are also in line with the human sense.

MATERIALS AND METHODS

Rician Noise in MRI

The raw image generated by magnetic resonance equipment is K-space, including the real channel $P_r$and the imaginary channelP_i. Both channels are governed by Gaussian noise with equal variance σ^2 and a mean value of zero (Zhu et al., 2009), which can be given by

$$\begin{cases} P_{\mathrm{r}} = R\cos\alpha + \Re \\ P_i = R\sin\alpha + \Im \end{cases} \tag{1}$$

where R is the amplitude and α is the phase of raw signal. In addition, $\Re$ and $\Im$ denote the independent Gaussian noise which is injected into the real and the imaginary channel, respectively. An inverse discrete Fourier transform (Briggs and Henson, 1995) and the modular operation are exploited to reconstruct the MR

images, which satisfies the human visual sense. The modular operation can be expressed as follows:

$$D = \sqrt{P_r^2 + P_i^2} = \sqrt{(R\cos\alpha + \Re)^2 + (R\sin\alpha + \Im)^2} \quad (2)$$

After the non-linear transformation, the noise distribution is converted from Gaussian to Rician (He and Greenshields, 2008). The probability distribution function (PDF) of Rician noise can be estimated as

$$p(D|R,\sigma) = \frac{D}{\sigma^2} e^{-\frac{D^2+R^2}{2\sigma^2}} I_0\left(\frac{RD}{\sigma^2}\right) \quad (3)$$

where I_0 stands for the zeroth-order modified Bessel function (Sijbers and den Dekker, 2004) when the discrete grid is utilized to define MRI. From the PDF, it can be inferred that Rician noise is associated with images. For images with different signal-to-noise ratios (SNR), the distributions of Rician noise are disparate. If the value of SNR is relatively high, Rician distribution degenerates into a Gaussian distribution. Conversely, it tends to the Rayleigh distribution in low SNR. Therefore, compared with Gaussian noise, Rician noise is more complicated.

Proposed Method

Network Architecture of FFA-DMRI

Inspired by ADNet (Tian et al., 2020), the FFA-DMRI is proposed to eliminate noise in MRI. **Figure 1** illustrates the overall architecture of FFA-DMRI. The network constructed by three sub-networks is as follows: a feature extraction block, a feature fusion block, and an attention block. These blocks correspond to the stages of denoising. Firstly, it employs common convolutions and dilated convolutions to expand the receptive field and acquires the features adequately. Furthermore, the operation of concatenation between global and local information enhances the expressive ability of network. Finally, the attention mechanism guides the network to extract useful information by assigning weights to different spatial positions and channels. The output of the network is the residual MR image and the potential clean image is obtained by subtracting the residual image from the input noisy image.

According to the structure of FFA-DMRI, the input of the network is noisy observed MRI, which is defined as$S$. The FFA-DMRI aims to learn the residual image N as an output rather than the potential clean image$C$. Every block is assumed to be a function; hence the execution process of network is defined as

$$N = g_{at}(g_{fu}(g_{ex}(S),\ S)) \quad (4)$$

where g_{ex}, g_{fu}, and g_{at} denote the functions of the feature extraction, feature fusion, and attention block, respectively. The output N is the mapping of noise in MRI and the potential clean image can be reconstructed by subtracting N from S. The implementations can be expressed as

$$C = S - N \quad (5)$$

Feature Extraction Block

It is known that the crucial structural information in complex images is easily hidden, which leads to poor performance in practice. Therefore, extracting the representative features is notoriously hard but vital in deep learning. To overcome this problem, during the course of training, the network of FFA-DMRI is supposed to focus on the interest area of the brain and suppress the insignificant region. Motivated by that, we have designed the spatial attention mechanism inspired by CBAM (Woo et al., 2018), which is suitable for MR images specifically.

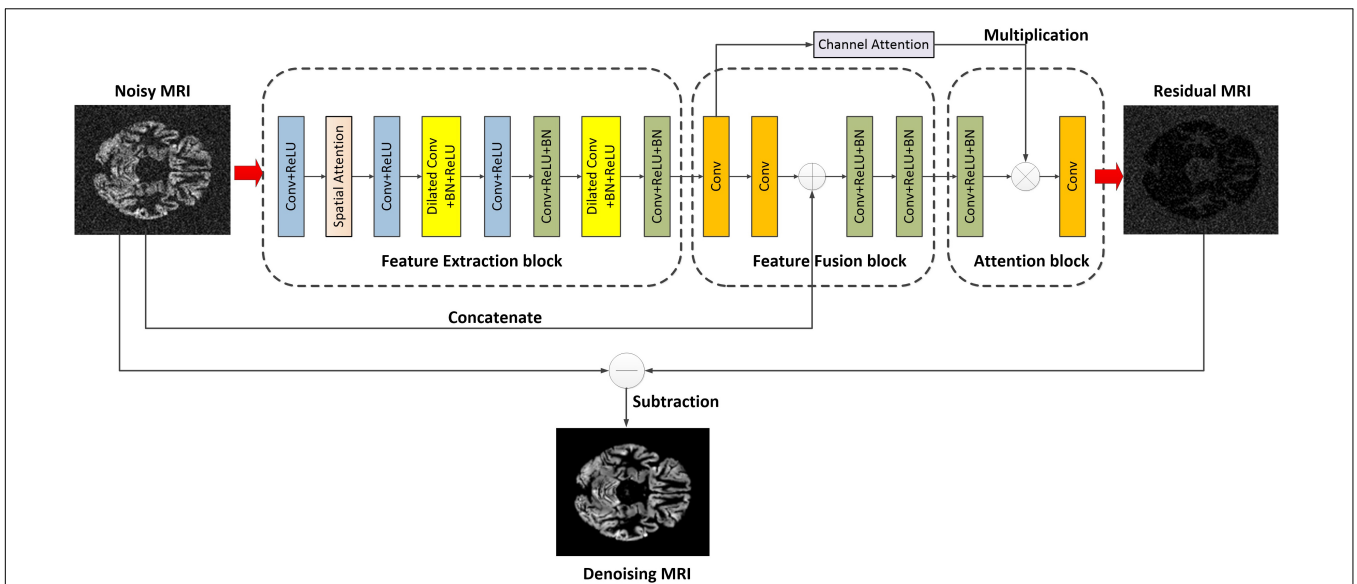

FIGURE 1 | Overall architecture of the proposed FFA-DMRI.

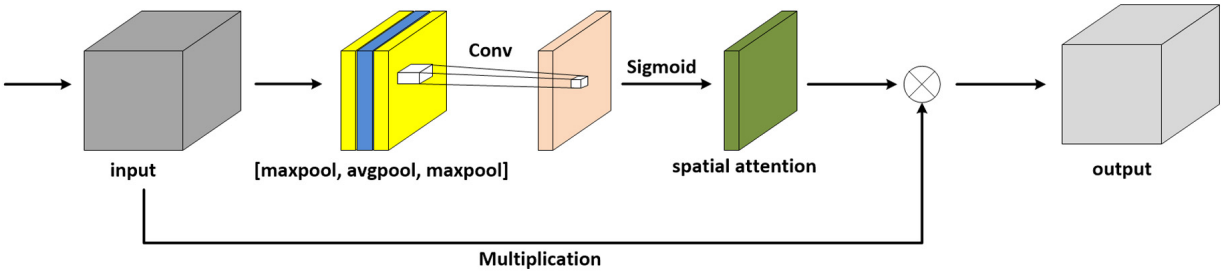

FIGURE 2 | Spatial attention module with an additional layer of maximum pooling.

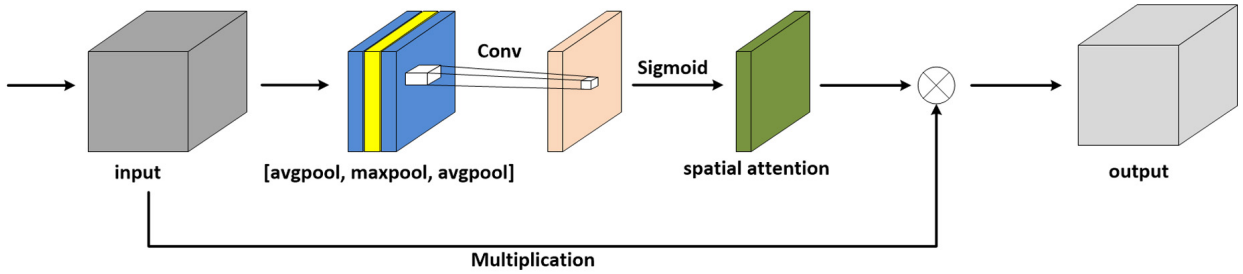

FIGURE 3 | Spatial attention module with an additional layer of average pooling.

Figure 2 depicts the spatial attention module with an additional layer of maximum pooling.

The attention module simulates the prioritization of visual information in human perception. In order to make the network pay more attention to the extraction of brain structure, an additional layer of maximum pooling is concatenated on the original architecture of CBAM. In this work, we consider another situation in which a spatial attention module is added with a layer of average pooling, as shown in **Figure 3**.

In terms of MR images, the pixels in the background are mostly black, and thus the values are zero. With respect to the brain regions, the pixel values are mostly greater than zero. For average pooling, the operation preserves background information and is suitable for the images where all pixels contribute to the prediction. Thus, average pooling is less applicable to MRI denoising. Relatively, maximum pooling is utilized to extract textures and assists the network in focusing on the brain regions, hence maximum pooling is selected in the module. To sum up, we take advantage of spatial attention to enhance the ability to extract brain features, which results in spending a lower amount of computing resources and achieving outstanding effects.

The batch normalization (BN) operation normalizes the input data; hence, it will destroy the original contrast of MR images. Besides, it has been pointed out that BN is more suitable to map data with regular distribution (Li et al., 2020). From the generation of Rician noise, it can be determined that the noise is non-linear. Thus, we do not employ the BN operation in the first two convolutions. Furthermore, the extraction of the context plays a crucial role in computer vision applications. For the denoising task, the construction of pixels is closely related to the context information (Yu and Koltun, 2016). In order to obtain more context, dilated convolution is utilized for the network, which enlarges the receptive field without reducing image resolution and losing details. Numerous works have been reported in the validity of dilated convolution (Yu and Koltun, 2016; Wei et al., 2018). For example, compared with a common convolution-based 3×3 kernel, a dilated convolution can serve a 5×5 or greater receptive field, but no increase in the number of parameters and computations. In FFA-DMRI, we integrate the common convolution and dilated convolution to take full advantage of information.

Feature Fusion Block

AlexNet (Krizhevsky et al., 2012), VGG-Net (Simonyan and Zisserman, 2014), and other deep learning models yield excellent results by increasing network layers. Nevertheless, on the one hand, the deeper network presents the phenomenon of gradient explosion and gradient disappearance. On the other hand, with continuous convolution, the effect of shallow features on a deep layer grows weak gradually. Thus, the way to extract high-quality features is pivotal for denoising tasks. To cope with the problem, we apply a lightweight and efficient feature-fusion module to combine low-level and high-level features. The module concatenates the intermediate feature map with the noisy observed MRI at the same scale, which makes full use of the structural information in the shallow network and boosts the network performance.

At the end of the feature fusion block, the two layers employ convolutions with the Rectified Linear Unit activation function (ReLU) and batch normalization. Compared with the sigmoid function, the ReLU function greatly reduces

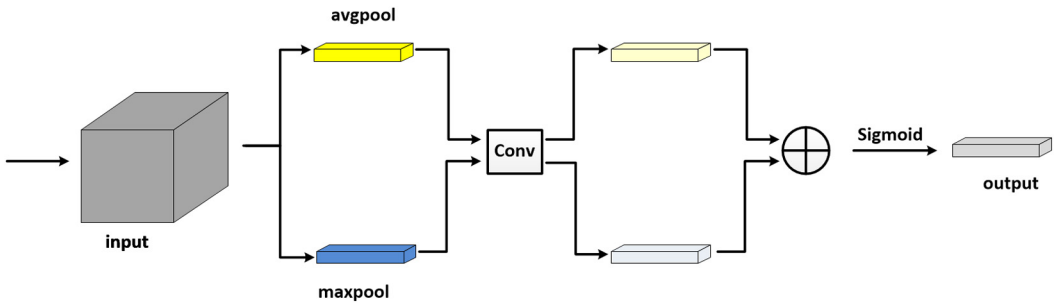

FIGURE 4 | Channel attention module.

network computation and avoids the problem of gradient disappearance. Additionally, the ReLU function increases the non-linear relationship between the network layers, and thus it is appropriate to process the non-linear Rician noise. In this block, BN yields the distribution of images more stable, which greatly simplifies parameter adjustment and alleviates the problem of gradient disappearance.

Attention Block

In computer vision, the attention mechanism improves the efficiency and accuracy of network to a certain extent. It adjusts the weight of each channel through training in order to enhance the influence of useful channels and suppress the unnecessary channels. Exploring the relationship between channels is beneficial to extract more vital content for the results and improve the denoising performance. In this paper, we exploit the maximum pooling and average pooling to the input feature map first. Furthermore, the two pooling layers are convolved separately. Then a sum of the convolutional layers yields the channel weights (Woo et al., 2018). The structure of channel attention is shown in **Figure 4**.

Loss Function

The loss function guides the further training of the network, and thus the selection of a loss function is directly related to the effect of execution. Different from the existing denoising networks that predict potential clean images directly, FFA-DMRI is able to estimate the residual images. Then subtracting the residual image from the input original image can obtain the clean images. Therefore, we use the mean square error (MSE) (Ephraim and Malah, 1984) to calculate the gap between the residual images generated by FFA-DMRI and the desired residual images. The desired residual image is obtained by subtracting noise-free image from noisy observed image. The loss function is described as

$$L(\theta) = \frac{1}{2M}\sum_{k=1}^{M} ||f_{FFA-DMRI}(S_k) - (S_k - G_k)||^2 \quad (6)$$

Where S represents the noisy observed image and G stands for the noise-free image. θ denotes the parameter of FFA-DMRI training. M is the number of noisy-clean training image pairs.

EXPERIMENTS

Data Acquisition and Training Settings

Deep learning is a data-driven technology. In other words, it requires a large amount of data for training to achieve promising performance. The network of FFA-DMRI is evaluated on the public real brain database of the Alzheimer's disease neuroimaging initiative (ADNI)[1]. In our experiments, it consists of 199 three-dimensional (3D) images of brain MRI. We slice each 3D image to get the axial plane and select the slices that range from 37 to 86 due to less information in the head and tail regions. Then Rician noise is injected into images with noise levels of 5, 10, 20, and 30 according to formula (2), respectively. All the images have a resolution of 145×121, and they are divided into three parts; the training set contains 7,800 images, the test set includes 975 images, and the validation set consists of 975 images.

The network is trained with the PyTorch framework in Python and employs the NVIDIA GeForce GTX 960. In some scenarios, adaptive moment estimation (Adam) has better performance than the stochastic gradient descent (SGD) (Zhang, 2018). Thus, the optimizer used in this experiment is Adam (Kingma and Ba, 2014). The initial learning rate is chosen as 0.0001, and it is reduced by 0.5, 0.25, and 0.125 in the following training. The batch size is set to four due to the trade-off between GPU memory and computational speed.

Qualitative Metrics

There are two popular qualitative metrics to evaluate denoising methods, including peak signal-to-noise ratio (PSNR) and structural similarity index measure (SSIM) (Kala and Deepa, 2018; Yu et al., 2019). PSNR calculates the distortion between recovered images $q(x, y)$ and ground truth$p(x, y)$. It can be defined as

$$PSNR(p, q) = 10\log_{10}\frac{255^2 \times M \times N}{\sum_{(x,y\in\Omega)}|p(x, y) - q(x, y)|^2}(dB) \quad (7)$$

where M × N is the size of MR images and higher PSNR means the less distortion in images.

The metrics of SSIM is based on three comparative measurements, including luminance, contrast, and structure. Itis

[1]http://adni.loni.usc.edu/

TABLE 1 | The average PSNR/dB results of different methods on the ADNI dataset at different noise levels.

Noise level λ	BM3D	NLM	Wiener filter	MRF	WNNM	IRCNN	DnCNN	FFA-DMRI (ours)
5	28.57	31.90	21.59	25.92	33.00	39.09	39.72	**39.76**
10	25.52	26.68	20.79	23.89	27.08	34.31	34.83	**35.23**
20	21.05	21.13	18.81	20.28	21.28	29.12	30.24	**30.55**
30	18.27	18.01	17.03	18.27	17.97	26.40	27.32	**27.51**

The best results at each noise level are highlighted in bold.

TABLE 2 | The average SSIM results of different methods on the ADNI dataset at different noise levels.

Noise level λ	BM3D	NLM	Wiener filter	MRF	WNNM	IRCNN	DnCNN	FFA-DMRI (ours)
5	0.5261	0.5477	0.3314	0.4897	0.5633	0.9914	0.9935	**0.9946**
10	0.4439	0.3850	0.2637	0.4117	0.4768	0.9797	0.9815	**0.9850**
20	0.3701	0.4654	0.2125	0.3423	0.3839	0.9320	0.9507	**0.9586**
30	0.3084	0.3143	0.1762	0.3084	0.2700	0.8907	0.9064	**0.9166**

The best results at each noise level are highlighted in bold.

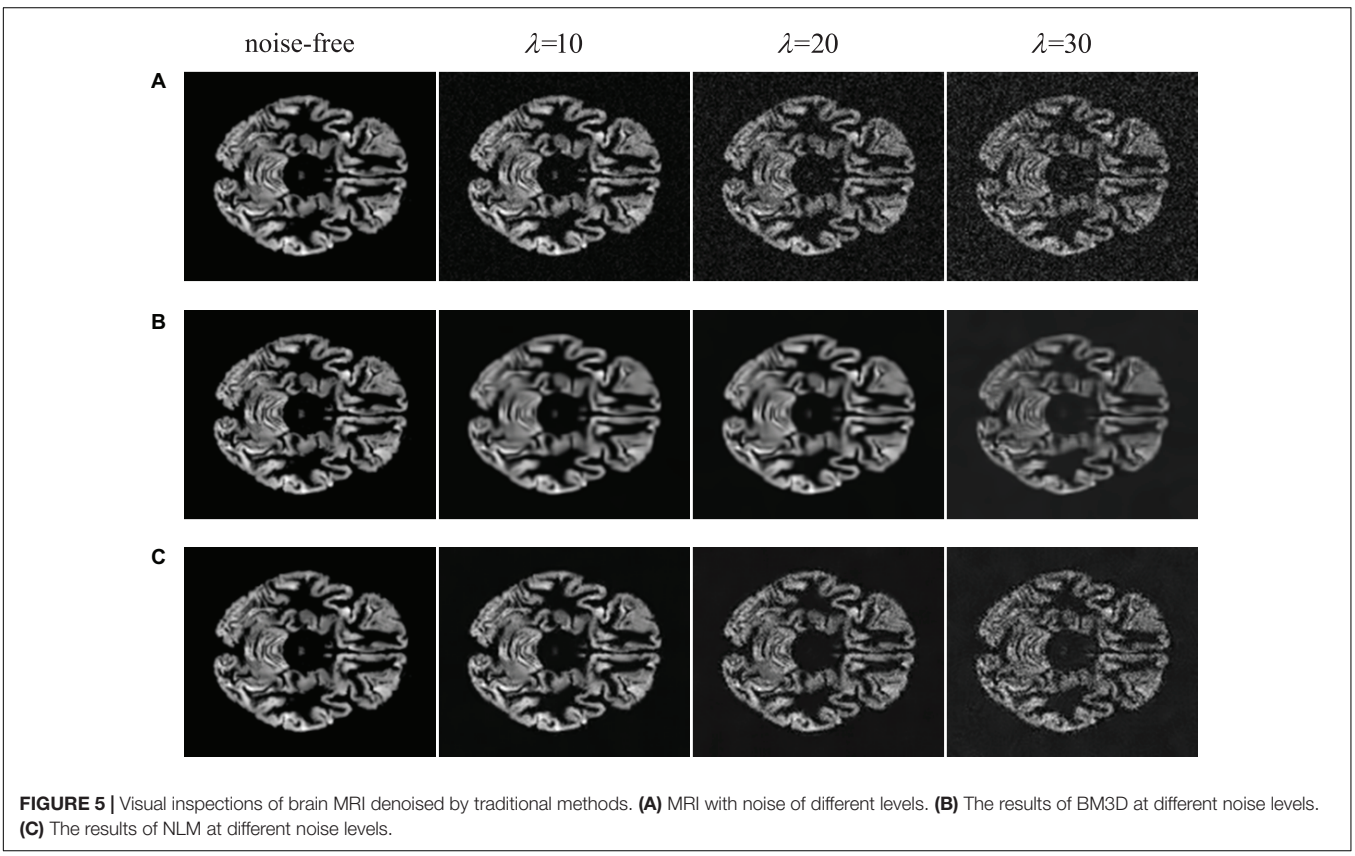

FIGURE 5 | Visual inspections of brain MRI denoised by traditional methods. **(A)** MRI with noise of different levels. **(B)** The results of BM3D at different noise levels. **(C)** The results of NLM at different noise levels.

more consistent with human visual perception (Wang et al., 2004), that can be obtained by

$$SSIM\left(p,q\right)=\frac{\left(2u_pu_q+c_1\right)\left(2\sigma_{pq}+c_2\right)}{\left(u_p^2+u_q^2\right)\left(\sigma_p^2+\sigma_q^2+c_2\right)} \tag{8}$$

where u_p, u_q is the average of p, q, respectively. And σ_p^2 is the variance of p; σ_p^2 denotes the variance of q, and σ_{pq} represents the covariance of p and q. To avoid instability, SSIM appends two constants including c_1 and c_2. The value range of SSIM is [0, 1].

Performance Comparison

In order to verify the effectiveness of the proposed FFA-DMRI, comparative experiments are conducted under the same dataset and parameters to guarantee fairness. The results of different denoising schemes are evaluated in terms of quantitative and qualitative metrics. Collectively, we compare

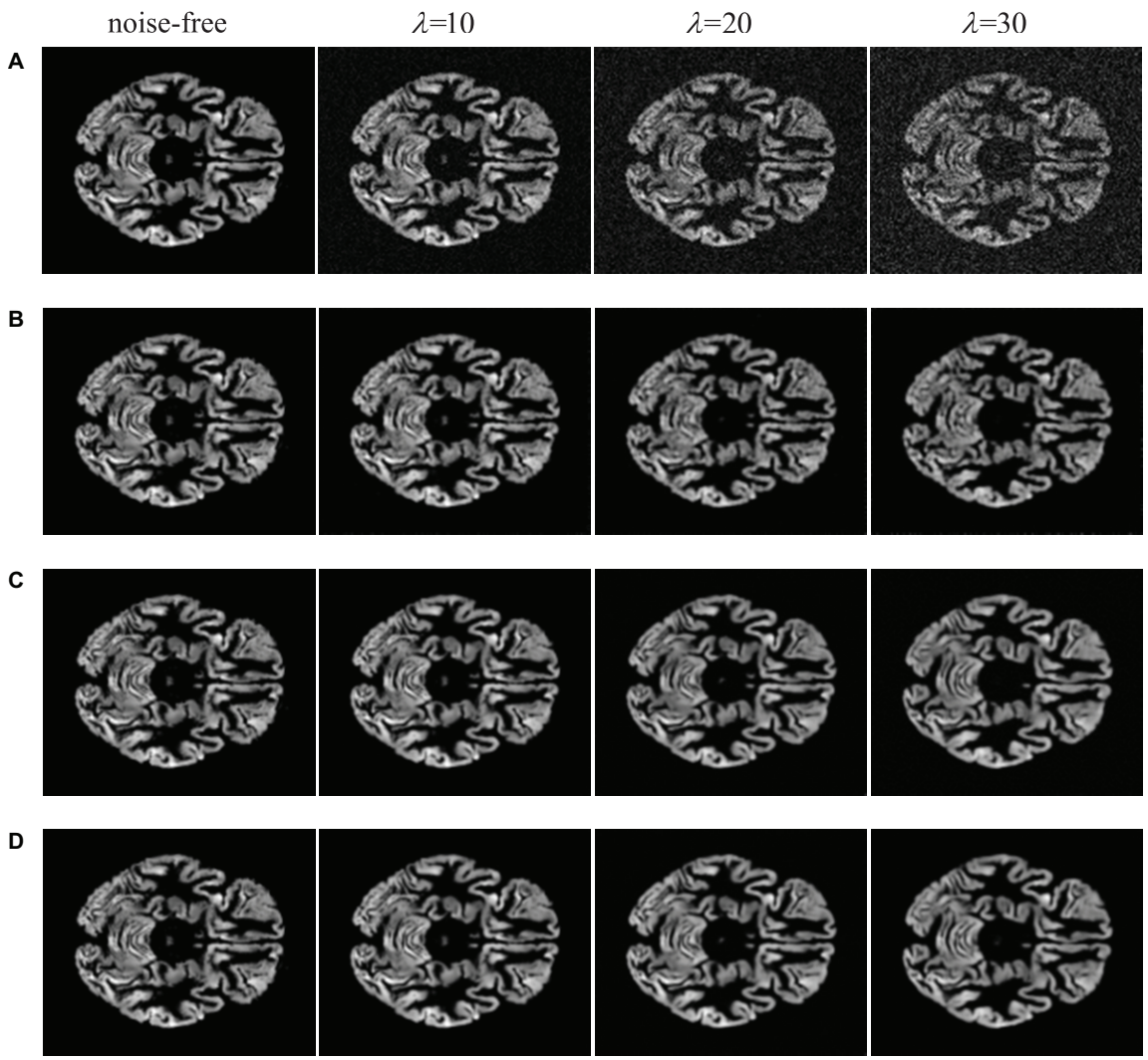

FIGURE 6 | Visual inspections of brain MRI denoised by deep learning methods. **(A)** MRI with noise of different levels. **(B)** The results of IRCNN at different noise levels. **(C)** The results of DnCNN at different noise levels. **(D)** the results of FFA-DMRI at different noise levels.

the proposed network FFA-DMRI with common denoising algorithms, including NLM (Buades et al., 2011), BM3D (Danielyan et al., 2011), MRF (Ji, 2019), Wiener filter (Jang and Kim, 2001), WNNM (Gu et al., 2014), IRCNN (Zhang et al., 2017b) and DnCNN (Zhang et al., 2017a).

Quantitative Metrics

Based on the above Settings, the average PNSR results of different denoising methods are presented in **Table 1**, and the average SSIM results are reported in **Table 2**.

It is known that the Rician noise depends on the images, so removing it is more complicated than Gaussian additive noise. From **Table 1**, the best result of PSNR at each noise level is shown in bold. It can be observed that the proposed FFA-DMRI outperforms other methods tested. For BM3D and NLM methods, it is difficult to match similar regions at higher noise levels. Besides, searching and matching regions consume much time. Therefore, the traditional method does not perform well on the dataset. It is noted that deep learning methods achieve outstanding denoising results. In particular, among the listed deep learning methods, the proposed FFA-DMRI promotes the removing performance at each noise level. On the specifics, FFA-DMRI exceeds IRCNN 1.43 dB at the noise level of 20 and is superior to DnCNN at every noise level. Additionally, we measured the results of the above methods in terms of SSIM.

The metrics of SSIM indicates that the structural similarity between recovered images and ground truth. As described in **Table 2**, FFA-DMRI achieves the best performance. It brings an improvement of 2.66% than IRCNN at the noise level of 20. Note that when the noise level is 5, our method tends to the highest value (the highest value in SSIM is 1), which shows that recovered images perfectly restore noise-free images. Besides, the value of SSIM is over 90% at each noise level for FFA-DMRI.

Consistent with the results of PSNR, the traditional methods are inferior to the deep learning methods in this dataset. In summary, there is a significant improvement in brain MRI denoising, which reconstructs the latent clean image with maintaining the vital structure information. Thus FFA-DMRI is a competitive denoising method in terms of quantitative analysis.

Qualitative Metrics

In practice, it is indispensable to evaluate image quality through the human senses. In some cases, the metrics of SSIM and PSNR are outstanding in computer vision tasks; however, the images that do not satisfy human perception are distorted. In this paper, we list the visual inspections of comparative experiments as illustrated in **Figures 5**, **6**.

From **Figure 5**, we illustrate traditional denoising methods for comparison. It is noticeable that the BM3D and NLM methods can remove a part of noise while generating the blurred structure of brain. Meanwhile, some crucial details in original images are lost. When the concentration of noise increases, the removal effect is worse on speediness with poor visual perception. In **Figure 6**, visual illustrations of deep learning methods are shown. It can be seen that the effect of deep learning methods is superior to traditional methods, which remove background noise and recover most of the complex brain structures.

In comparison with IRCNN, the proposed FFA-DMRI yields clearer brain tissues and sharper edges after noise removal. The method of DnCNN also achieves excellent results in the experiments; however, FFA-DMRI maintains more subtle features of the original image, and the contrast between brain regions and background is stronger than DnCNN. The obvious contrast contributes to enhancing the interpretation and recognition of images and satisfies the needs of clinical analysis. In general, FFA-DMRI we proposed performs well in the quantitative and qualitative analysis.

CONCLUSION

In this article, we propose a network to remove Rician noise from a brain MRI as well as FFA-DMRI. The network is composed of a feature extraction block, a feature fusion block, and an attention block. The feature extraction block exploits the spatial attention mechanism to obtain the area of interest emphatically. Moreover, we utilize dilated convolutions, which expand the receptive fields, and we fuse local and global information to boost the network performance. Then the channel attention mechanism is employed to enhance the influence of essential elements and suppress the useless channels. After the above steps are carried out, FFA-DMRI is trained on the ADNI dataset. In terms of quantitative evaluation, SSIM and PSNR are adopted. Experimental results show that FFA-DMRI can effectively remove Rician noise and maintain most of the crucial details. For quantitative evaluation, it can be seen from visual inspection that the recovered images are more consistent with human senses with obvious contrast, clear brain tissues, and sharp edges. Therefore, the proposed method FFA-DMRI is competitive in brain MRI denoising, which can assist clinicians in diagnosis and treatment.

DATA AVAILABILITY STATEMENT

Publicly available datasets were analyzed in this study. This data can be found here: http://adni.loni.usc.edu/.

AUTHOR CONTRIBUTIONS

DH was responsible for the work of writing the manuscript and doing experiments. CH, CY, JL, and YQ made the experiments. CC modified the English grammar of the article. All authors contributed to the article and approved the submitted version.

REFERENCES

Anand, C. S., and Sahambi, J. S. (2010). Wavelet domain non-linear filtering for MRI denoising. *Magn. Reson. Imaging* 28, 842–861. doi: 10.1016/j.mri.2010.03.013

Bhadauria, H., and Dewal, M. L. (2013). Medical image denoising using adaptive fusion of curvelet transform and total variation. *Comput. Electr. Eng.* 39, 1451–1460. doi: 10.1016/j.compeleceng.2012.04.003

Briggs, W. L., and Henson, V. E. (1995). *The DFT: An Owner's Manual for the Discrete Fourier Transform*. Philadelphia, PA: SIAM. doi: 10.1137/1.9781611971514

Buades, A., Coll, B., and Morel, J.-M. (2011). Non-local means denoising. *Image Process. On Line* 1, 208–212. doi: 10.5201/ipol.2011.bcm_nlm

Cai, C., Huang, C., Yang, C., Lu, H., Hong, X., Ren, F., et al. (2020a). Altered patterns of functional connectivity and causal connectivity in salience subnetwork of subjective cognitive decline and amnestic mild cognitive impairment. *Front. Neurosci.* 14:288. doi: 10.3389/fnins.2020.00288

Cai, C., Huang, C., Yang, C., Zhang, X., Peng, Y., Zhao, W., et al. (2020b). Altered patterns of phase position connectivity in default mode subnetwork of subjective cognitive decline and amnestic mild cognitive impairment. *Front. Neurosci.* 14:185. doi: 10.3389/fnins.2020.00185

Coupé, P., Yger, P., and Barillot, C. (2006). "Fast non local means denoising for 3D MR images," in *Proceedings of the International Conference on Medical Image Computing and Computer-Assisted Intervention*, (Berlin: Springer). doi: 10.1007/11866763_5

Danielyan, A., Katkovnik, V., and Egiazarian, K. (2011). BM3D frames and variational image deblurring. *IEEE Trans. Image Process.* 21, 1715–1728. doi: 10.1109/tip.2011.2176954

Do, M. N., and Vetterli, M. (2005). The contourlet transform: an efficient directional multiresolution image representation. *IEEE Trans. Image Process.* 14, 2091–2106. doi: 10.1109/tip.2005.859376

Ephraim, Y., and Malah, D. (1984). Speech enhancement using a minimum-mean square error short-time spectral amplitude estimator. *IEEE Trans. Acoust. Speech Signal Process.* 32, 1109–1121. doi: 10.1109/tassp.1984.1164453

Gu, S., Zhang, L., Zuo, W., and Feng, X. (2014). "Weighted nuclear norm minimization with application to image denoising," in *Proceedings of the IEEE Conference on Computer Vision and Pattern Recognition*, (Piscataway, NJ: IEEE). doi: 10.1109/CVPR.2014.366

He, L., and Greenshields, I. R. (2008). A nonlocal maximum likelihood estimation method for Rician noise reduction in MR images. *IEEE Trans. Med. Imaging* 28, 165–172. doi: 10.1109/tmi.2008.927338

Ikram, S., Shah, J. A., Zubair, S. I, Qureshi, M., and Bilal, M. (2019). Improved reconstruction of MR scanned images by using a dictionary learning scheme. *Sensors* 19:1918. doi: 10.3390/s19081918

Jang, I.-H., and Kim, N.-C. (2001). Denoising of images using locally adaptive Wiener filter in wavelet domain. *IEICE Trans. Inf. Syst.* 84, 495–501.

Ji, Q. (2019). *Probabilistic Graphical Models for Computer Vision*. Cambridge: Academic Press. doi: 10.1016/B978-0-12-803467-5.00008-3

Jiang, Y., Wu, D., Deng, Z., Qian, P., Wang, J., Wang, G., et al. (2017). Seizure classification from EEG signals using transfer learning, semi-supervised learning and TSK fuzzy system. *IEEE Trans. Neural Syst. Rehabil. Eng.* 25, 2270–2284. doi: 10.1109/tnsre.2017.2748388

Jiang, Y., Zhao, K., Xia, K., Xue, J., Zhou, L., Ding, Y., et al. (2019). A novel distributed multitask fuzzy clustering algorithm for automatic MR brain image segmentation.*J. Med. Syst.* 43:118. doi: 10.1007/s10916-019-1245-1

Kala, R., and Deepa, P. (2018). Adaptive hexagonal fuzzy hybrid filter for Rician noise removal in MRI images. *Neural Comput. Appl.* 29, 237–249. doi: 10.1007/s00521-017-2953-4

Kingma, D. P., and Ba, J. L. (2014). "Adam: a method for stochastic optimization," in *Proceedings of the ICLR 2015: International Conference on Learning Representations 2015*, San Diego, CA.

Krizhevsky, A., Sutskever, I., and Hinton, G. E. (2012). Imagenet classification with deep convolutional neural networks. *Adv. Neural Inf. Process. Syst.* 25, 1097–1105.

Li, S., Zhou, J., Liang, D., and Liu, Q. (2020). MRI denoising using progressively distribution-based neural network. *Magn. Reson. Imaging.* 71, 55–68. doi: 10.1016/j.mri.2020.04.006

Manjón, J. V., Carbonell-Caballero, J., Lull, J. J., García-Martí, G., Martí-Bonmatí, L., and Robles, M. (2008). MRI denoising using non-local means. *Med. Image Anal.* 12, 514–523. doi: 10.1016/j.media.2008.02.004

McVeigh, E. R., Henkelman, R. M., and Bronskill, M. J. (1985). Noise and filtration in magnetic resonance imaging. *Med. Phys.* 12, 586–591. doi: 10.1118/1.595679

Mohan, J., Krishnaveni, V., and Guo, Y. (2014). A survey on the magnetic resonance image denoising methods. *Biomed. Signal Process. Control* 9, 56–69. doi: 10.1016/j.bspc.2013.10.007

Sijbers, J., and den Dekker, A. J. (2004). Maximum likelihood estimation of signal amplitude and noise variance from MR data. *Magn. Reson. Med.* 51, 586–594. doi: 10.1002/mrm.10728

Sijbers, J., den Dekker, A. J., Van der Linden, A., Verhoye, T. M., and Van Dyck, D. (1999). Adaptive anisotropic noise filtering for magnitude MR data. *Magn. Reson. Imaging* 17, 1533–1539. doi: 10.1016/s0730-725x(99)00088-0

Simonyan, K., and Zisserman, A. (2014). "Very deep convolutional networks for large-scale image recognition," in *Proceedings of the ICLR 2015: International Conference on Learning Representations 2015*, San Diego, CA.

Soomro, T. A., and Gao, J. (2016). "Neural network based denoised methods for retinal fundus images and MRI brain images," in *Preoceedings of the 2016 International Joint Conference on Neural Networks (IJCNN)*, (Piscataway, NJ: IEEE). doi: 10.1109/IJCNN.2016.7727327

Tian, C., Xu, Y., Li, Z., Zuo, W., Fei, L., and Liu, H. (2020). Attention-guided CNN for image denoising. *Neural Netw.* 124, 117–129. doi: 10.1016/j.neunet.2019.12.024

Tripathi, P. C., and Bag, S. (2020). CNN-DMRI: a convolutional neural network for denoising of magnetic resonance images. *Pattern Recogn. Lett.* 135 57–63. doi: 10.1016/j.patrec.2020.03.036

Wang, Z., Bovik, A. C., Sheikh, H. R., and Simoncelli, E. P. (2004). Image quality assessment: from error visibility to structural similarity. *IEEE Trans. Image Process.* 13, 600–612. doi: 10.1109/tip.2003.819861

Wei, Y., Xiao, H., Shi, H., Jie, Z., Feng, J., and Huang, T. S. (2018). "Revisiting dilated convolution: A simple approach for weakly-and semi-supervised semantic segmentation," in *Proceedings of the IEEE Conference on Computer Vision and Pattern Recognition*, (Piscataway, NJ: IEEE). doi: 10.1109/CVPR.2018.00759

Woo, S., Park, J., Lee, J.-Y., and So Kweon, I. (2018). "Cbam: convolutional block attention module," *Proceedings of the European Conference on Computer Vision (ECCV)*. Glasgow: ECCV. doi: 10.1007/978-3-030-01234-2_1

Yu, F., and Koltun, V. (2016). "Multi-Scale Context Aggregation by Dilated Convolutions," in *Proceedings of the ICLR 2016: International Conference on Learning Representations 2016*, San Juan.

Yu, H., Ding, M., and Zhang, X. (2019). Laplacian Eigenmaps Network-Based Nonlocal Means Method for MR Image Denoising. *Sensors* 19, 2918. doi: 10.3390/s19132918

Yu, H., and Zhao, L. (2008). "An efficient denoising procedure for magnetic resonance imaging," in *Preoceedings of the 2008 2nd International Conference on Bioinformatics and Biomedical Engineering*, (Piscataway, NJ: IEEE). doi: 10.1109/ICBBE.2008.990

Zhang, K., Zuo, W., Chen, Y., Meng, D., and Zhang, L. (2017a). Beyond a gaussian denoiser: residual learning of deep cnn for image denoising. *IEEE Trans. Image Process.* 26, 3142–3155. doi: 10.1109/tip.2017.2662206

Zhang, K., Zuo, W., Gu, S., and Zhang, L. (2017b). "Learning deep CNN denoiser prior for image restoration," in *Proceedings of the IEEE Conference on Computer Vision and Pattern Recognition*, (Piscataway, NJ: IEEE). doi: 10.1109/tip.2017.2662206

Zhang, K., Zuo, W., and Zhang, L. (2018). FFDNet: Toward a fast and flexible solution for CNN-based image denoising. *IEEE Trans. Image Process.* 27, 4608–4622. doi: 10.1109/tip.2018.2839891

Zhang, K., Zuo, W., and Zhang, L. (2019). "Deep plug-and-play super-resolution for arbitrary blur kernels," in *Proceedings of the IEEE Conference on Computer Vision and Pattern Recognition*, (Piscataway, NJ: IEEE). doi: 10.1109/CVPR.2019.00177

Zhang, M., Zhang, F., Liu, Q., and Wang, S. (2019). VST-net: variance-stabilizing transformation inspired network for Poisson denoising. *J. Vis. Commun. Image Represent.* 62, 12–22. doi: 10.1016/j.jvcir.2019.04.011

Zhang, Z. (2018). "Improved adam optimizer for deep neural networks," in *Proceedings of the 2018 IEEE/ACM 26th International Symposium on Quality of Service (IWQoS)*, (Piscataway, NJ: IEEE). doi: 10.1109/IWQoS.2018.8624183

Zhu, H., Li, Y., Ibrahim, J. G., Shi, X., An, H., Chen, Y., et al. (2009). Regression models for identifying noise sources in magnetic resonance images. *J. Am. Stat. Assoc.* 104, 623–637. doi: 10.1198/jasa.2009.0029

Conflict of Interest: The authors declare that the research was conducted in the absence of any commercial or financial relationships that could be construed as a potential conflict of interest.

frontiers in Neuroscience

ORIGINAL RESEARCH
published: 29 September 2020
doi: 10.3389/fnins.2020.586149

Auto-Weighted Multi-View Discriminative Metric Learning Method With Fisher Discriminative and Global Structure Constraints for Epilepsy EEG Signal Classification

Jing Xue[1], *Xiaoqing Gu*[2] *and Tongguang Ni*[2]*

[1] Department of Nephrology, The Affiliated Wuxi People's Hospital of Nanjing Medical University, Wuxi, China, [2] School of Computer Science and Artificial Intelligence, Changzhou University, Changzhou, China

Metric learning is a class of efficient algorithms for EEG signal classification problem. Usually, metric learning method deals with EEG signals in the single view space. To exploit the diversity and complementariness of different feature representations, a new *a*uto-weighted *m*ulti-view *d*iscriminative *m*etric *l*earning method with Fisher discriminative and global structure constraints for epilepsy EEG signal classification called AMDML is proposed to promote the performance of EEG signal classification. On the one hand, AMDML exploits the multiple features of different views in the scheme of the multi-view feature representation. On the other hand, considering both the Fisher discriminative constraint and global structure constraint, AMDML learns the discriminative metric space, in which the intraclass EEG signals are compact and the interclass EEG signals are separable as much as possible. For better adjusting the weights of constraints and views, instead of manually adjusting, a closed form solution is proposed, which obtain the best values when achieving the optimal model. Experimental results on Bonn EEG dataset show AMDML achieves the satisfactory results.

Keywords: metric learning, multi-view learning, auto-weight, EEG signal classification, epilepsy

OPEN ACCESS

Edited by:
Mohammad Khosravi, Persian Gulf University, Iran

Reviewed by:
Yufeng Yao, Changshu Institute of Technology, China
Hongru Zhao, Soochow University, China

***Correspondence:**
Tongguang Ni
ntg@cczu.edu.cn

Specialty section:
This article was submitted to Neuroprosthetics, a section of the journal Frontiers in Neuroscience

Received: *22 July 2020*
Accepted: *24 August 2020*
Published: *29 September 2020*

Citation:
Xue J, Gu X and Ni T (2020) Auto-Weighted Multi-View Discriminative Metric Learning Method With Fisher Discriminative and Global Structure Constraints for Epilepsy EEG Signal Classification. Front. Neurosci. 14:586149. doi: 10.3389/fnins.2020.586149

INTRODUCTION

Epilepsy is characterized by an unexpected seizure periodicity, where brain temporary dysfunction is caused by abnormal discharge of neurons (Kabir and Zhang, 2016; Gummadavelli et al., 2018; Li et al., 2019). During the seizure, motor dysfunction, intestinal and bladder dysfunction, loss of consciousness, and other cognitive dysfunction often occur. Since the occurrence of epilepsy is often accompanied by changes in spatial organization and temporal dynamics of brain neural neurons, many brain imaging methods are used to reveal abnormal changes in brain neural neurons caused by epilepsy. EEG signal is an important signal to record the activity of neurons in the brain. It uses electrophysiological indicators to record the changes in the electrical wave of the cerebral cortex generated during brain activity. It is the overall reflection of the activity of brain neurons in the cerebral cortex. Many clinical studies have shown that due to abnormal discharge of brain neurons, epilepsy-specific waveforms, such as spikes and sharp waves, appear during or shortly before the onset of seizures, so identifying EEG signals is an effective detection of epilepsy method. Clinically, the detection of seizures based on EEG signals mainly relies on the personal experience

of doctors. However, modern EEG recorders can generate up to 1,000 data points per second, and the standard recording process can last for several days. This procedure will make manual screening require a lot of physical and mental exhaustion, and after a long period of observation, the doctor's judgment is easily affected by fatigue.

With the gradual development of smart healthcare, more and more machine learning algorithms are applied to the detection of epilepsy of EEG signals (Jiang et al., 2017a; Juan et al., 2017; Usman and Fong, 2017; Richhariya and Tanveer, 2018; Cury et al., 2019). In the view of machine learning, the EEG signal recognition contains two stages: feature extraction and classification method. The commonly used feature extraction methods for EEG signals are time-domain feature extractions and frequency-domain feature extractions (Srinivasan et al., 2005; Tzallas et al., 2009; Iscan et al., 2011). Since the original EEG signal is the time series signal, the time-domain feature extractions are generally based on the original EEG signal; then, the relevant statistics of the time series are calculated, and the epilepsy EEG features are extracted, using the kernel principal component analysis (KPCA) (Smola, 1997). The frequency-domain features are to transform the original EEG signal in the time domain to the frequency domain and then extract the relevant frequency-domain features as EEG features (Griffin and Lim, 1984). Although these feature extraction methods provide good performance in some practical applications, there is no feature extraction method that can be applied to all application scenarios. EEG signals are generated by numerous brain neuron activities. Due to the non-linear and non-static nature of EEG signals, how to extract effective features is still an important challenge. For those reasons, the multiple feature based multi-view learning concept has become a hot topic in EEG signal classification (Yuan et al., 2019; Wen et al., 2020). Different from using the single feature type, the multi-view learning method can comprehensively use a set of data features obtained from multiple ways or multiple levels. Each view of the data features may contain specific information not available in other views. Specifically, these independent and diverse features can be extracted from time-domain, frequency-domain, and multilevel features of signals. Appropriately designed multi-view learning can significantly promote the performance of EEG signal classification. For example, Spyrou et al. (2018) proposed a multiple features-based classifier to use spatial, temporal, or frequency EEG data. This classifier performs dimensionality reduction and rejects components through evaluating the classification performance. Two multi-view Takagi–Sugeno–Kang fuzzy systems for epileptic EEG signals classification are proposed in Zhou et al. (2019) and Jiang et al. (2017b), respectively. The former fuzzy system is developed in a deep view-reduction framework, and the latter fuzzy system is developed in a multi-view collaborative learning mechanism.

Besides the multi-view learning, classification algorithm is very important for EEG signal classification. One of the recent trends is the metric learning method. Metric learning method learns a more suitable distance measurement criterion in the feature space from the training data. Metric learning can be used for specific tasks, such as classification and clustering, so as to more accurately represent the similarity between samples. Different from traditional Euclidean distance, such as nearest-neighbors classifiers and K-means, metric learning aims to find the appropriate similarity measures between data pairs to maintain the required distance structure (Cai et al., 2015; Wang et al., 2015; Lu et al., 2016). The appropriately distance metrics can provide a good measure of the similarity and dissimilarity between different samples. For example, Liu et al. (2014) developed a similarity metric-learning in the process of EEG P300 wave recognition. Compared with traditional Euclidean metric, the proposed global Mahalanobis distance metric shows the better discriminative representation. Phan et al. (2013) proposed a metric learning method using the global distance metric from labeled examples. This method successfully applied on single-channel EEG data for sleep staging and does not need artifact removal or boostrapping preprocessing steps. Alwasiti et al. (2020) proposed a deep metric learning model and tested it for motor imagery EEG signals classification. The experimental results show that the proposed deep metric learning model can converge with very small number of training EEG signals.

Inspired by the distance metric and multi-view learning, we present a new auto-weighted multi-view discriminative metric learning method with Fisher discriminative and global structure constraints for EEG signal classification called AMDML. To better exploit the correlation and complementary data features of multiple views, both the Fisher discriminative constraint and global structure constraint are adopted in the construction process of the distance metric matrix. In such common metric space, the intraclass EEG signals are compact, and interclass EEG signals are separable as much as possible. Simultaneously, an auto-weighted learning strategy is developed to automatically adjust constraint and view weights during the model learning process. The contributions of our work are as follows: (1) Both Fisher discriminative and global structure information of multiple view data features are considered in the multi-view metric learning model with the high discriminative performance; (2) in the optimization process, the constraint and view weights can be adjusted auto-weighted by the closed form solution, instead of adjusted manually. Thus, the constraints balance and multiple view collaboration can be optimized; and (3) the experimental results on Bonn EEG dataset justify the applicability of AMDML for EEG signal classification.

RELATED WORK

Metric Learning

Here, we introduce the baseline method in the study. Xing et al. (2003) proposed a distance metric considering side-information (DMSI) method. Using the given similar and dissimilar pairs of samples, DMSI learns a good distance metric to identify the "similar" relationship between all pairs of samples so that similar pairs are close and dissimilar pairs are separated. Let S and D be two sets of pair as

$$S = \{(\boldsymbol{x}_i, \boldsymbol{x}_j) | \boldsymbol{x}_i \textit{ and } \boldsymbol{x}_j \textit{ are similar}\}, \quad (1)$$

$$D = \{(\boldsymbol{x}_i, \boldsymbol{x}_j) | \boldsymbol{x}_i \textit{ and } \boldsymbol{x}_j \textit{ are dissimilar}\}. \quad (2)$$

The optimization problem of DMSI is represented as

$$\begin{aligned} &\min_{\boldsymbol{M}} \sum_{(\boldsymbol{x}_i,\boldsymbol{x}_j)\in S} \left\|\boldsymbol{x}_i-\boldsymbol{x}_j\right\|_{\boldsymbol{M}}^2 \\ &s.t. \sum_{(\boldsymbol{x}_i,\boldsymbol{x}_j)\in D} \left\|\boldsymbol{x}_i-\boldsymbol{x}_j\right\|_{\boldsymbol{M}} \geq 1, \\ &\boldsymbol{M}\geq 0. \end{aligned} \tag{3}$$

A key point in DMSI is that all samples that are not clearly identified as similar are dissimilar. In addition, metric learning tries to find an appropriate measurement to preserve the distance structure. The distance metric considers a positive semidefinite matrix $\boldsymbol{M}$, and $\left\|\boldsymbol{x}_i-\boldsymbol{x}_j\right\|_{\boldsymbol{M}}$ is induced as a Mahalanobis distance

$$\left\|\boldsymbol{x}_i-\boldsymbol{x}_j\right\|_{\boldsymbol{M}}=\sqrt{(\boldsymbol{x}_i-\boldsymbol{x}_j)^T\boldsymbol{M}(\boldsymbol{x}_i-\boldsymbol{x}_j)} \tag{4}$$

When the learned $\boldsymbol{M}$ is a diagonal matrix, **Equation (3)** can be solved by the Newton–Raphson method; when $\boldsymbol{M}$ is a full matrix, **Equation (3)** can be solved by an iterative optimization algorithm with gradient ascent and iterative projection strategies.

Bonn EEG Dataset

The EEG signal data in the experiment is from the website of the Bonn University, Germany (Tzallas et al., 2009). The Bonn EEG dataset contains five groups of EEG signal sets called as groups A–E. The example samples in groups A–E are shown in **Figure 1**. Each EEG data group consists of 100 single-channel EEG signal segments of 23.6 s and 173.6 Hz rate. The basic information of five groups is listed in **Table 1**. EEG signal data in groups A and B is sampled from five healthy volunteers, and EEG signal data in groups C–E is sampled from five patients at different states of epileptic seizure.

PROPOSED METHOD

Objective Function

After collecting a set of EEG signals, we obtain N samples presented as $\{\boldsymbol{x}_i, l_i\}_{i=1}^N$, where l_i is the class label of sample $\boldsymbol{x}_i$. According to the label information, we construct two sets of sample pairs such that $\boldsymbol{X}_s = \{(\boldsymbol{x}_i,\boldsymbol{x}_j)|l_i = l_j\}$ is the intraclass sample set and $\boldsymbol{X}_d = \{(\boldsymbol{x}_i,\boldsymbol{x}_j)|l_i \neq l_j\}$ is the interclass sample set. Then, generating multiple view of data samples, we obtain $\{\boldsymbol{x}_i^m\}_{m=1}^M$ from M different view features of each sample, where $\boldsymbol{x}_i^m$ is the mth view of sample $\boldsymbol{x}_i$. For discriminative projecting, we build the k-nearest neighbor intraclass graph $\{\boldsymbol{G}^m\}_{m=1}^M$ and interclass graph $\{\boldsymbol{P}^m\}_{m=1}^M$ in each view, which use the supervised information to describe the local geometrical structure of the

TABLE 1 | The basic information of EEG data groups of A–E.

Group	Basic information
A	EEG signals of healthy volunteers in awaken state with eyes open
B	EEG signals of healthy volunteers in awaken state with eyes closed
C	EEG signals of patients in hippocampal formation of the opposite hemisphere of brain
D	EEG signals of patients in epileptogenic zone during periodic lulls
E	EEG signals of patients during seizure activity

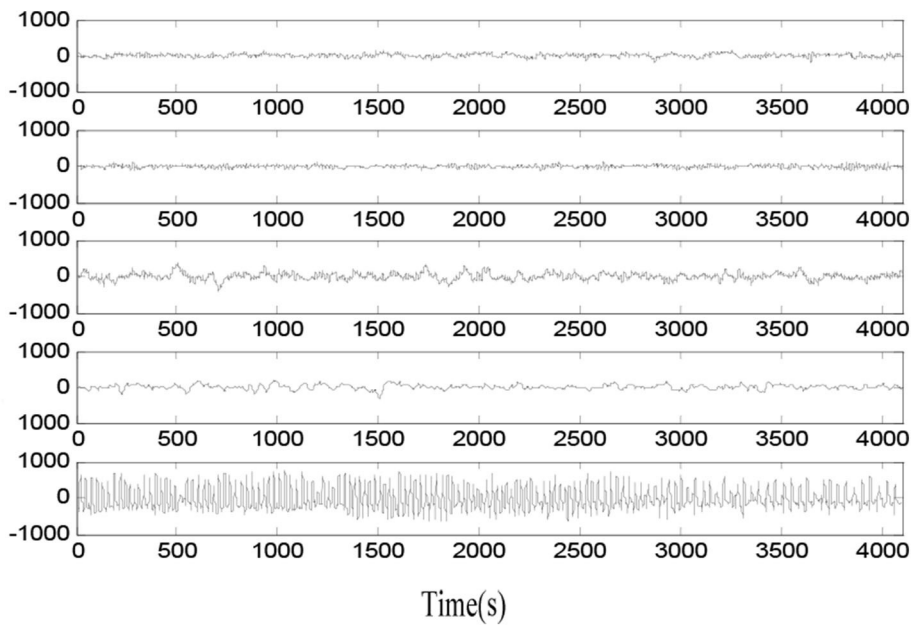

FIGURE 1 | Original epileptic EEG signals in five groups.

data. The intraclass graph $\boldsymbol{G}^m$ can be computed as

$$G_{i,j}^m = \begin{cases} 1/|\boldsymbol{X}_s| & if\ \boldsymbol{x}_i^m \in N_{k_1}(\boldsymbol{x}_j^m)\ or\ \boldsymbol{x}_j^m \in N_{k_1}(\boldsymbol{x}_i^m)\ and\ (\boldsymbol{x}_i, \boldsymbol{x}_j) \in \boldsymbol{X}_s, \\ 0 & otherwise \end{cases} \quad (5)$$

where $N_{k_1}(\boldsymbol{x}_j^m)$ denotes the intraclass sample set containing the k_1 nearest neighbors of $\boldsymbol{x}_i^m$.

The graph $\boldsymbol{P}^m$ can be computed as

$$P_{i,j}^m = \begin{cases} 1/|\boldsymbol{X}_d| & if\ \boldsymbol{x}_i^m \in N_{k_2}(\boldsymbol{x}_j^m)\ or\ \boldsymbol{x}_j^m \in N_{k_2}(\boldsymbol{x}_i^m)\ and\ (\boldsymbol{x}_i, \boldsymbol{x}_j) \in \boldsymbol{X}_d, \\ 0 & otherwise \end{cases} \quad (6)$$

where $N_{k_2}(\boldsymbol{x}_j^m)$ denotes the interclass sample set containing the k_2 nearest neighbors of $\boldsymbol{x}_i^m$.

Then, the intraclass correlation constraint $\boldsymbol{F}_G^m$ from the mth view can be written as

$$\begin{aligned} \boldsymbol{F}_G^m &= \frac{1}{2}\sum_{i,j}^{N} G_{i,j}^m \left\| \boldsymbol{H}^T\boldsymbol{x}_i^m - \boldsymbol{H}^T\boldsymbol{x}_j^m \right\|_2^2 \\ &= \frac{1}{2}\sum_{i,j}^{N} P_{i,j}^m (\boldsymbol{H}^T(\boldsymbol{x}_i^m - \boldsymbol{x}_j^m)(\boldsymbol{x}_i^m - \boldsymbol{x}_j^m)^T\boldsymbol{H}) \\ &= Tr(\boldsymbol{H}^T\boldsymbol{X}^m\boldsymbol{L}_G^m\boldsymbol{X}^{mT}\boldsymbol{H}) \end{aligned} \quad (7)$$

where $\boldsymbol{L}_G^m$ is the Laplacian matrix on $\boldsymbol{G}^m$, and $\boldsymbol{L}_G^m$ is computed as $\boldsymbol{L}_G^m = \boldsymbol{D}_G^m - \boldsymbol{G}^m$. $\boldsymbol{D}_G^m$ is a diagonal matrix, and the element in $\boldsymbol{D}_G^m$ is $D_{G,i,i}^m = \sum_j G_{i,j}^m$. Tr () is for the trace operator.

The interclass correlation constraint $\boldsymbol{F}_P^m$ from the mth view can be written as

$$\begin{aligned} \boldsymbol{F}_P^m &= \frac{1}{2}\sum_{i,j}^{N} P_{i,j}^m \left\| \boldsymbol{H}^T\boldsymbol{x}_i^m - \boldsymbol{H}^T\boldsymbol{x}_j^m \right\|_2^2 \\ &= \frac{1}{2}\sum_{i,j}^{N} P_{i,j}^m (\boldsymbol{H}^T(\boldsymbol{x}_i^m - \boldsymbol{x}_j^m)(\boldsymbol{x}_i^m - \boldsymbol{x}_j^m)^T\boldsymbol{H}) \\ &= Tr(\boldsymbol{H}^T\boldsymbol{X}^m\boldsymbol{L}_P^m\boldsymbol{X}^{mT}\boldsymbol{H}) \end{aligned} \quad (8)$$

where $\boldsymbol{L}_P^m$ is the Laplacian matrix on $\boldsymbol{P}^m$, and $\boldsymbol{L}_P^m$ is computed as $\boldsymbol{L}_P^m = \boldsymbol{D}_P^m - \boldsymbol{P}^m$. $\boldsymbol{D}_P^m$ is a diagonal matrix, and the element in $\boldsymbol{D}_P^m$ is $D_{p,i,i}^m = \sum_j P_{i,j}^m$.

For global structure knowledge of multiple-view data preservation, the following global structure consistency $\boldsymbol{Q}^m$ is employed

$$\begin{aligned} \boldsymbol{Q}^m &= \frac{1}{2}\sum_{i,j}^{N} W_{i,j} \left\| \boldsymbol{H}^T\boldsymbol{x}_i^m - \boldsymbol{H}^T\boldsymbol{x}_j^m \right\|_2^2 \\ &= \frac{1}{2}\sum_{i,j}^{N} W_{i,j} (\boldsymbol{H}^T(\boldsymbol{x}_i^m - \boldsymbol{x}_j^m)(\boldsymbol{x}_i^m - \boldsymbol{x}_j^m)^T\boldsymbol{H}) \\ &= Tr(\boldsymbol{H}^T\boldsymbol{X}^m\boldsymbol{L}_W\boldsymbol{X}^{mT}\boldsymbol{H}) \end{aligned} \quad (9)$$

where $\boldsymbol{W}$ is an adjacent matrix whose element is $W_{i,j} = 1/N^2$. $\boldsymbol{L}_W$ is the Laplacian matrix on $\boldsymbol{W}$, and $\boldsymbol{L}_W$ is computed as $\boldsymbol{L}_W = \boldsymbol{D}_W - \boldsymbol{W}$, $\boldsymbol{D}_W$ is a diagonal matrix, and the element in $\boldsymbol{D}_W$ is $D_{W,i,i}^m = 1/N$.

The basic principle of $\boldsymbol{Q}^m$ is to use the global structural information through cross-view data covariance. The term $\boldsymbol{X}^m\boldsymbol{L}_W\boldsymbol{X}^{mT}$ is equivalent to the centering matrix of the mth view data, i.e., $\boldsymbol{X}^m\boldsymbol{L}_W\boldsymbol{X}^{mT} = E[(\boldsymbol{x} - \frac{1}{N}\sum_i \boldsymbol{x}_i)(\boldsymbol{x} - \frac{1}{N}\sum_i \boldsymbol{x}_i)^T]$. It represents the average squared distance between all samples of the mth view in the metric space. Therefore, $\boldsymbol{Q}^m$ can be considered as a principal component analysis (PCA) (Smola, 1997)—like the regularization term in the mth view.

The goal of AMDML is to find an optimal discriminative distance metric in a multi-view learning model, and in such metric space, it can exploit the complementary information of different view data features and further enforce the proposed method to be more discriminative. To achieve this goal, we learn a metric that maximizes the Fisher analysis constraint (interclass/intraclass correlation ratio), simultaneously maximizing the preservation of the global structure consistency constraint. The objective function of AMDML is designed as

$$\begin{aligned} &\min_{\boldsymbol{H},\Theta} \sum_{m=1}^{M} \Theta_m^r \frac{\boldsymbol{F}_G^m - \boldsymbol{F}_P^m}{\boldsymbol{Q}^m}, \\ &s.t.\ \boldsymbol{H}^T\boldsymbol{H} = \boldsymbol{I}, \\ &\quad \sum_{m=1}^{M} \Theta_m = 1, \Theta_m \geq 0, \end{aligned} \quad (10)$$

The projection matrix $\boldsymbol{H}$ helps to build a discriminative metric space among multiple views, such that the feature correlation and complementary structural information among multiple views can be exploited. The vector $\boldsymbol{\Theta} = [\Theta_1, \Theta_2, ..., \Theta_M]$ is the view weight vector, and its element Θ_m indicates the role importance of the mth view. When Θ_m tends to 0, it means the data features of the mth view are useless for discrimination task. The Θ_m=1 means that only one type of data features from one view is used in AMDML, and in this case, Equation (10) is a single view learning problem. To better utilize the complementary information of multiple features rather than the best feature, we use index parameter r ($r > 1$) on Θ_m.

Equation (10) can be represented as

$$\begin{aligned} &\min_{\boldsymbol{H},\Theta} \sum_{m=1}^{M} \Theta_m^r \frac{Tr(\boldsymbol{H}^T\boldsymbol{X}^m(\boldsymbol{L}_G^m - \boldsymbol{L}_P^m)\boldsymbol{X}^{mT}\boldsymbol{H})}{Tr(\boldsymbol{H}^T\boldsymbol{X}^m\boldsymbol{L}_W\boldsymbol{X}^{mT}\boldsymbol{H})}, \\ &s.t.\ \boldsymbol{H}^T\boldsymbol{H} = \boldsymbol{I}, \\ &\quad \sum_{m=1}^{M} \Theta_m = 1, \Theta_m \geq 0. \end{aligned} \quad (11)$$

However, the optimization of Equation (11) involves a complex operation of inverse. Using a constraint weight parameter γ, we reconstruct Equation (11) into the following weighted optimization model

$$\begin{aligned} &\min_{\boldsymbol{H},\Theta,\gamma} \sum_{m=1}^{M} \Theta_m^t(\gamma^2\boldsymbol{H}^T\boldsymbol{X}^m(\boldsymbol{L}_G^m - \boldsymbol{L}_P^m)\boldsymbol{X}^{mT}\boldsymbol{H} - \gamma\, Tr(\boldsymbol{H}^T\boldsymbol{X}^m\boldsymbol{L}_W\boldsymbol{X}^{mT}\boldsymbol{H})), \\ &s.t.\ \boldsymbol{H}^T\boldsymbol{H} = \boldsymbol{I}, \\ &\quad \sum_{m=1}^{M} \Theta_m = 1, \Theta_m \geq 0. \end{aligned} \quad (12)$$

where γ represents a constraint weight tradeoff Fisher discriminative constraint and global structure constraint. It is noted that the constraint weight γ and view weight Θ are not a manually adjusted parameters. In this study, we adaptively adjust γ and Θ in two closed form solutions, respectively.

Optimization

Because the optimization problem of Equation (12) is a non-linear constrained non-convex problem, in this study, we solve the optimization problem in Equation (12) using the iteratively optimization strategy to obtain the AMDML parameters of $\boldsymbol{H}$, $\boldsymbol{\Theta}$, and γ. First, we tune parameter $\boldsymbol{H}$ while fixing parameters $\boldsymbol{\Theta}$ and γ. The optimization problem in Equation (12) can be reformulated as follows:

$$\begin{aligned} &\min_{\boldsymbol{H}} \sum_{m=1}^{M} \Theta_m^t(\gamma^2 Tr(\boldsymbol{H}^T\boldsymbol{X}^m(\boldsymbol{L}_G^m - \boldsymbol{L}_P^m)\boldsymbol{X}^{mT}\boldsymbol{H}) - \gamma Tr(\boldsymbol{H}^T\boldsymbol{X}^m\boldsymbol{L}_W\boldsymbol{X}^{mT}\boldsymbol{H})), \\ &s.t.\ \boldsymbol{H}^T\boldsymbol{H} = \boldsymbol{I}, \end{aligned} \tag{13}$$

Thus, $\boldsymbol{H}$ can be easily calculated by solving the eigenvalue decomposition problem as follows:

$$(\sum_{m=1}^{M} \Theta_m^t(\gamma^2\boldsymbol{X}^m(\boldsymbol{L}_G^m - \boldsymbol{L}_P^m)\boldsymbol{X}^{mT} - \gamma(\boldsymbol{X}^m\boldsymbol{L}_W\boldsymbol{X}^{mT})))\boldsymbol{H} = \alpha\boldsymbol{H} \tag{14}$$

In terms of the Lagrange optimization, the minimization of Equation (14) can be converted with multiplier as follows:

$$\begin{aligned} J(\Theta,\gamma,\alpha) = &\sum_{m=1}^{M} \Theta_m^t \Big(\gamma^2 Tr(\boldsymbol{H}^T\boldsymbol{X}^m(\boldsymbol{L}_G^m - \boldsymbol{L}_P^m)\boldsymbol{X}^{mT}\boldsymbol{H}) \\ &-\gamma Tr(\boldsymbol{H}^T\boldsymbol{X}^m\boldsymbol{L}_W\boldsymbol{X}^{mT}\boldsymbol{H})\Big) - \alpha(\sum_{m=1}^{M}\Theta_m^t - 1). \end{aligned} \tag{15}$$

Next, we tune parameter $\boldsymbol{\Theta}$ while fixing parameters $\boldsymbol{H}$ and γ.

Let $\frac{\partial J(\boldsymbol{\Theta},\gamma,\alpha)}{\partial\Theta_m} = 0$ and $\frac{\partial J(\boldsymbol{\Theta},\gamma,\alpha)}{\partial\alpha} = 0$, we have

$$\begin{cases} t\Theta_m^{t-1}\gamma^2(Tr(\boldsymbol{H}^T\boldsymbol{X}^m(\boldsymbol{L}_G^m - \boldsymbol{L}_P^m)\boldsymbol{X}^{mT}\boldsymbol{H}) - \gamma Tr(\boldsymbol{H}^T\boldsymbol{X}^m\boldsymbol{L}_W\boldsymbol{X}^{mT}\boldsymbol{H})) - \alpha = 0, \\ \sum_{m=1}^{M}\Theta_m - 1 = 0. \end{cases} \tag{16}$$

We can obtain Θ_m as follows:

$$\Theta_m = \frac{(1/(\gamma^2 Tr(\boldsymbol{H}^T\boldsymbol{X}^m(\boldsymbol{L}_G^m - \boldsymbol{L}_P^m)\boldsymbol{X}^{mT}\boldsymbol{H}) - \gamma Tr(\boldsymbol{H}^T\boldsymbol{X}^m\boldsymbol{L}_W\boldsymbol{X}^{mT}\boldsymbol{H})))^{1/(t-1)}}{\sum_{m=1}^{M}(1/(\gamma^2 Tr(\boldsymbol{H}^T\boldsymbol{X}^m(\boldsymbol{L}_G^m - \boldsymbol{L}_P^m)\boldsymbol{X}^{mT}\boldsymbol{H}) - \gamma Tr(\boldsymbol{H}^T\boldsymbol{X}^m\boldsymbol{L}_W\boldsymbol{X}^{mT}\boldsymbol{H})))^{1/(t-1)}}. \tag{17}$$

Finally, we tune parameter γ while fixing parameters $\boldsymbol{H}$ and $\boldsymbol{\Theta}$. In terms of the Lagrange optimization, the solution of γ is $\frac{\partial J(\boldsymbol{\Theta},\gamma,\alpha)}{\partial\gamma} = 0$; we can obtain γ as follows:

$$\gamma = \frac{\Theta_m^t\sum_{m=1}^{M} Tr(\boldsymbol{H}^T\boldsymbol{X}^m\boldsymbol{L}_W\boldsymbol{X}^{mT}\boldsymbol{H})}{2\Theta_m^t\sum_{m=1}^{M} Tr(\boldsymbol{H}^T\boldsymbol{X}^m(\boldsymbol{L}_G^m - \boldsymbol{L}_P^m)\boldsymbol{X}^{mT}\boldsymbol{H})} \tag{18}$$

Based on the above analysis, the proposed AMDML method is presented in **Algorithm 1**.

Algorithm 1 | The proposed AMDML method.

Input: M views of m pairs of EEG signals;

Output: the best metric $H = H_l$.

Set $\boldsymbol{\Theta} = [1/M, 1/M, ..., 1/M]$ and compute $\boldsymbol{H}$ using **Equation (13)**.
Repeat
$t = t+1$
  Fix $\boldsymbol{H}(t)$, and compute $\boldsymbol{\Theta}(t)$ using **Equation (17)**;
  Fix $\boldsymbol{\Theta}(t)$, and compute $\boldsymbol{H}(t)$ using **Equation (18)**
  Compute L(t) using **Equation (15)**;
Until $\|J(t)\text{-}J(t\text{-}1)\| \le \delta$ or $t \ge t_{max}$

TABLE 2 | Ten EEG classification tasks.

Tasks	EEG signal groups
Task 1	A and C
Task 2	A and D
Task 3	A and E
Task 4	B and C
Task 5	B and D
Task 6	B and E
Task 7	{A, B} and {C, D}
Task 8	{A, B} and E
Task 9	{A, B} and {D, E}
Task 10	{A, B} and {C, E}

EXPERIMENT

Experimental Settings

In the experiment, we extract three types of data feature including KPCA, wavelet packet decomposition (WPD) (Wu et al., 2008), and short-time Fourier transform (STFT) (Griffin and Lim, 1984). We design 10 classification tasks, and the basic information of tasks is as shown in **Table 2**. In order to show the performance of our method, we compare AMDML with four single-view classification methods [including DMSI (Xing et al., 2003), large margin nearest neighbor (LMNN) (Weinberger and Saul, 2009), neighborhood preserving embedding (NPE) (Wen et al., 2010), and RDML-CCPVL (Ni et al., 2018)] and three multi-view methods [including MvCVM (Huang et al., 2015), VMRML-LS (Quang et al., 2013), and DMML (Zhang et al., 2019)]. In the LMNN method, the number of target neighbors k was set to $k = 3$, and the weighting parameter μ is selected within the grid {0, 0.2,..., 1}. In the RDML-CCPVL method, the regularization parameter is selected within the grid [0.01, 0.1, 0.5, 1, 5, 10, 20] and the number of clusters is selected within the grid [2, 3,..., 20]. In the MvCVM method, the regularization parameter is selected within the grid [0.01, 0.1, 0.5, 1, 5, 10, 20]. In VMRML-LS, the regularization parameters $\gamma_A = 10^{-5}$, $\gamma_B = 10^{-6}$, and $\gamma_W = 10^{-6}$, and the element in weight vector is selected in [1,

TABLE 3 | The classification performances of AMDML on 10 classification tasks.

		WPD	STFT	KPCA	Full views
Task 1	LMNN	95.00	96.14	96.19	96.18
	NPE-KNN	95.05	96.29	96.34	96.38
	NPE-SVM	95.08	96.17	96.29	96.49
	RDML-CCPVL	96.07	96.64	96.58	96.97
	DMSI	96.11	96.53	96.52	96.88
	AMDML-KNN	97.75	97.62	97.88	**99.19**
	AMDML-SVM	97.86	97.55	97.86	99.18
Task 2	LMNN	93.92	94.73	95.00	95.88
	NPE-KNN	94.01	95.03	95.21	95.71
	NPE-SVM	94.06	95.00	94.54	96.07
	RDML-CCPVL	94.60	95.06	95.88	96.17
	DMSI	94.45	95.08	94.64	96.22
	AMDML-KNN	97.29	97.86	98.38	99.77
	AMDML-SVM	97.22	98.03	98.30	**99.78**
Task 3	LMNN	94.75	94.92	95.11	95.40
	NPE-KNN	94.01	94.01	95.42	95.72
	NPE-SVM	94.98	94.08	95.41	95.64
	RDML-CCPVL	94.56	95.59	95.88	95.70
	DMSI	94.72	95.34	95.26	96.24
	AMDML-KNN	96.72	98.82	98.35	99.35
	AMDML-SVM	96.83	98.90	98.48	**99.41**
Task 4	LMNN	92.76	92.90	93.07	94.45
	NPE-KNN	94.00	93.02	94.48	94.70
	NPE-SVM	93.00	93.04	93.42	94.65
	RDML-CCPVL	93.52	93.56	93.90	94.92
	DMSI	94.21	94.01	94.45	95.03
	AMDML-KNN	96.71	97.88	97.44	**99.42**
	AMDML-SVM	96.88	97.86	97.42	99.35
Task 5	LMNN	91.81	93.89	94.10	95.46
	NPE-KNN	92.99	93.08	93.43	95.71
	NPE-SVM	92.98	93.13	94.46	95.66
	RDML-CCPVL	94.54	94.66	94.91	95.99
	DMSI	94.50	95.04	95.11	95.37
	AMDML-KNN	98.76	98.87	98.40	99.39
	AMDML-SVM	99.83	98.89	98.39	**99.41**
Task 6	LMNN	96.72	96.92	96.16	97.36
	NPE-KNN	96.05	96.93	97.09	97.22
	NPE-SVM	96.91	97.01	97.22	97.42
	RDML-CCPVL	96.57	97.62	96.90	97.37
	DMSI	96.49	97.49	96.81	97.02
	AMDML-KNN	97.73	98.89	97.39	**99.45**
	AMDML-SVM	97.89	98.94	97.35	99.38
Task 7	LMNN	93.76	93.87	93.05	95.37
	NPE-KNN	93.93	94.06	93.41	95.73
	NPE-SVM	96.03	95.97	95.43	95.68
	RDML-CCPVL	95.54	95.59	94.94	95.94
	DMSI	95.29	95.36	94.73	95.08

(Continued)

TABLE 3 | Continued

		WPD	STFT	KPCA	Full views
	AMDML-KNN	97.74	97.89	97.31	99.39
	AMDML-SVM	97.92	97.81	97.36	**99.44**
Task 8	LMNN	94.79	95.86	95.12	96.40
	NPE-KNN	94.95	96.00	95.44	96.41
	NPE-SVM	94.94	95.99	95.45	96.09
	RDML-CCPVL	95.57	96.09	95.89	96.14
	DMSI	95.63	95.94	96.15	96.18
	AMDML-KNN	97.72	98.82	98.41	99.45
	AMDML-SVM	97.90	98.92	98.45	**99.46**
Task 9	LMNN	92.78	94.94	94.06	95.37
	NPE-KNN	92.93	95.05	94.44	95.68
	NPE-SVM	93.01	95.04	95.43	95.62
	RDML-CCPVL	94.52	95.66	95.94	95.98
	DMSI	94.67	92.51	96.04	96.40
	AMDML-KNN	96.69	97.83	97.37	**99.42**
	AMDML-SVM	96.99	97.90	97.43	99.38
Task 10	LMNN	93.87	93.86	93.13	94.31
	NPE-KNN	94.02	92.97	93.44	94.49
	NPE-SVM	93.04	94.09	94.48	94.66
	RDML-CCPVL	95.57	95.56	94.98	96.01
	DMSI	95.17	94.22	94.10	94.56
	AMDML-KNN	97.78	97.83	96.41	**98.40**
	AMDML-SVM	97.89	97.97	96.38	98.37

The bold values represents mean the best classification performance in the tasks.

5, 10]. In the DMML method, the number of interclass marginal samples is selected within the grid [1, 2,..., 10]. In the proposed AMDML method, the parameters k_1 and k_2 in **Equations (5)** and **(6)** are selected in [2, 3,..., 10]. The widely used K-nearest neighbor (KNN) and support vector machine (SVM) are used as the classifiers for the proposed AMDML, and we name them as AMDML-KNN and AMDML-SVM, respectively. We empirically set the nearest neighborhood number of KNN classifier as [1, 3,..., 9] and train SVM model using LIBSVM (Chang and Lin, 2011). All methods are implemented in MATLAB using a computer with 2.6 GHz dual-core CPU and 8 GB RAM.

Performance Comparisons With Single-View Methods

We first compare the performance of AMDML with several single-view classification methods. NPE using two classifiers KNN and SVM are named as NPE-KNN and NPE-SVM, respectively. **Table 3** shows the classification performance of these methods on Bonn EEG dataset using three signal views (WPD, STFT, and KPCA) and full views. When AMDML uses single-view feature data, the parameter Θ_m is fixed with Θ_m=1 in its objective function. For a fair comparison, three signal views features are combined for four single-view classification methods in full views. We can see that, on the one hand, both AMDML-KNN and AMDML-SVM using full-view features are better than them using only single-view features. For example, the performances of AMDML-KNN with full-view feature are 1.44, 1.57, and 1.31% higher than its performance in WPD, STFT, and KPCA on Task 1, respectively. On the other hand, the classification accuracy of methods AMDML-KNN and AMDML-SVM are better than single-view methods on 10 tasks. These results show that (1) the simple combination of features is limited to improve classification performance for single-view methods, and (2) due to the inherent diversity and complex of EEG signals, it is suitable to exploit multiple view features to better make use of the correlation and complementary EEG data. Thus, the multi-view learning framework can promote the EEG signal classification performance.

Performance Comparisons With Multi-View Methods

In this subsection, we compare AMDML with several multi-view classification methods. The multi-view metric learning method DMML uses KNN and SVM as testing classifiers, and two classifiers are named as DMML-KNN and DMML-SVM, respectively. **Figure 2** shows the classification accuracies of all methods on all EEG classification tasks. In addition, we use balanced loss l_{bal} (Wang et al., 2014; Gu et al., 2020) to

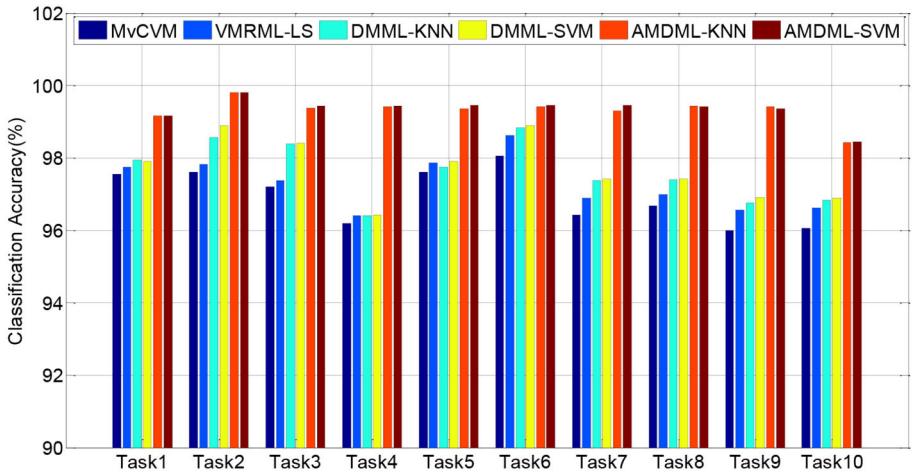

FIGURE 2 | Classification accuracies of six methods on 10 EEG classification tasks.

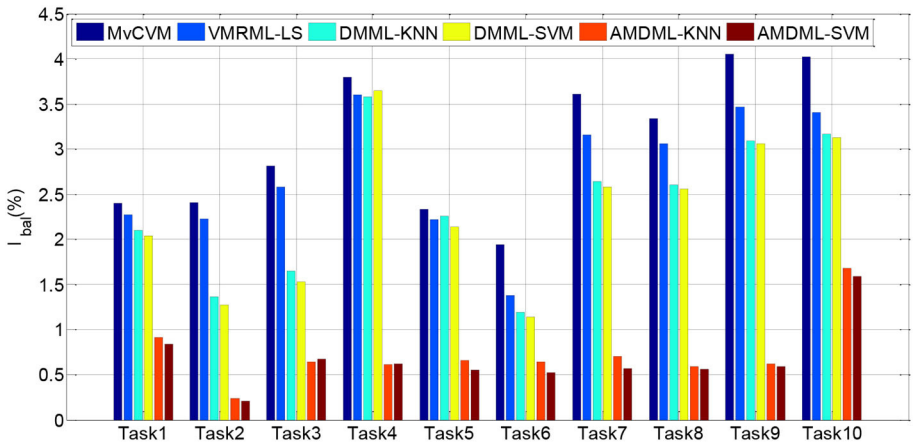

FIGURE 3 | l_{bal} performance of six methods on all EEG classification tasks.

evaluate the classification accuracy on positive class $ACC_{positive}$ and negative class $ACC_{negative}$:

$$l_{bal} = 1 - (ACC_{positive} + ACC_{negative})/2$$

Figure 3 shows l_{bal} performance of all methods on EEG classification tasks. Experiment results show that compared with all multi-view classification methods, both AMDML-KNN and AMDML-SVM have a positive effect on improving classification performance. AMDML-KNN and AMDML-SVM achieve the satisfactory classification performance in almost all of the EEG signal categories. In the framework of multi-view learning and to discriminate each emotion category best from all other categories, AMDML learns discriminative metric space to utilize the global and local information by adopting Fisher discriminative constraint and global structure constraint. Thus, the intraclass compactness and interclass EEG signals separability can perform better in the learned metric space. In addition, the auto-weighted learning strategy used in the proposed method adjusts constraint and view weights. The optimal weights can be obtained adaptively, and multiple feature representation in each view can be collaborative leaned. Similar to the results shown in **Table 3**, the classification accuracies of AMDML-KNN and AMDML-SVM are comparative. To summarize, the results in **Figures 2**, **3** confirm that the AMDML method is effective in EEG signal classification.

Model Analysis

To further validate the effects of performance of AMDML, we discuss the effect of the k_1 in **Equation (5)** and k_2 in **Equation (6)** in AMDML. The parameters k_1 and k_2 build the k-nearest neighbor inter- and intraclass graphs, respectively. For convenience, we set $k_1 = k_2$ in the range {2,..., 10}. **Figure 4** shows the classification accuracy of AMDML-KNN with different values of k_1 for Tasks 1, 4, and 8; meanwhile, the k-nearest neighbor

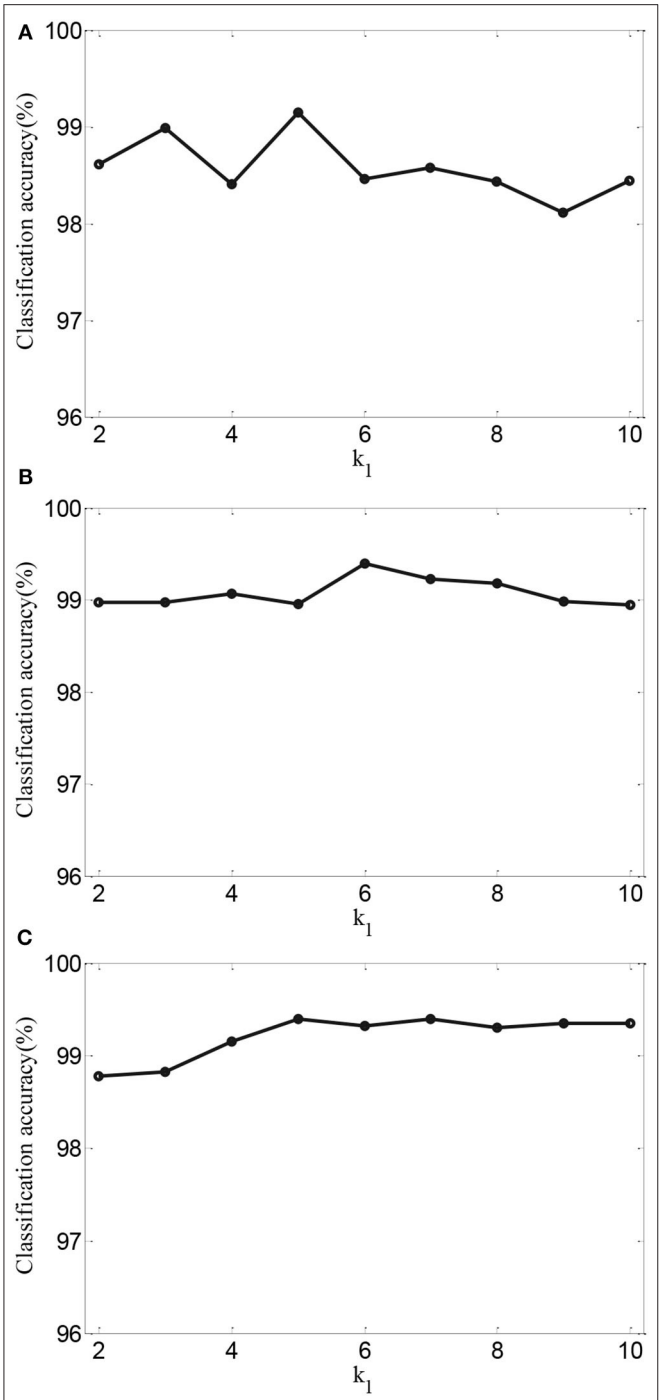

FIGURE 4 | Classification accuracy of AMDML-KNN with different values of k_1 for **(A)** Task 1, **(B)** Task 4, and **(C)** Task 8.

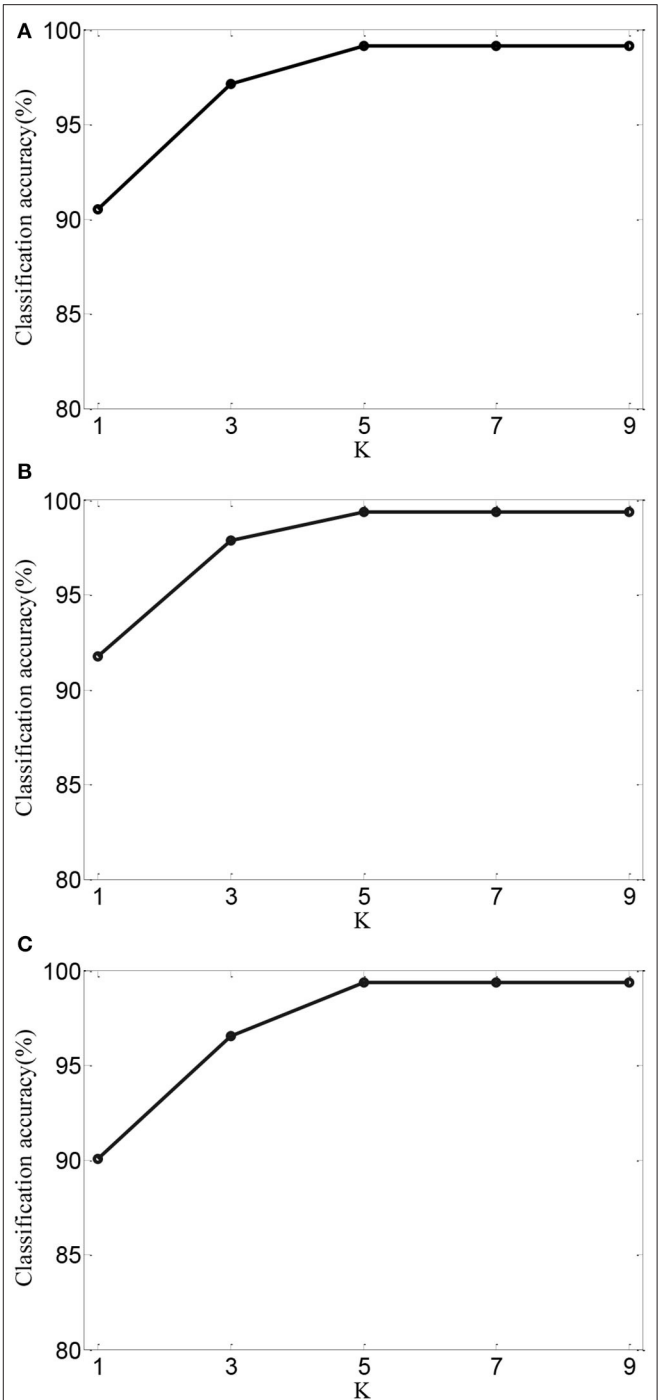

FIGURE 5 | Classification accuracy of AMDML-KNN with different values of K for **(A)** Task 1, **(B)** Task 4, and **(C)** Task 8.

in KNN are fixed with 7. We can see that the performance of AMDML-KNN is not high sensitive to the variation k_1 and k_2.

Next, for AMDML-KNN, we discuss the effect of the K in KNN classifier. In KNN classifier, the class label of the testing sample is determined by the distance from the K nearest training sample. **Figure 5** shows the classification performance of different values of K for all tasks; meanwhile, fixing $k_1 = k_2 = 5$. We can see that the classification accuracy of AMDML-KNN is relatively stable with respect to the variation K. Therefore, we can set K empirically to 7 for Tasks 1, 4, and 8.

CONCLUSION

In this paper, we propose a new multi-views metric learning to achieve the robust distance metric for EEG signal classification. In the scheme of the multi-view data representation, the diversity, and complementariness of features of all views can be exploited; meanwhile, both the Fisher discriminative constraint and global structure constraint are considered, and the learned classifier will obtain high generalization ability. Through learning a discriminative metric space, AMDML shows the higher classification performance. There are several directions of future study. In this paper, we use the *k*-nearest neighbor intra- and interclass graphs to exploit local discriminative information; we will consider other discriminative terms in the multi-view metric learning framework. Second, the gradient descent method used in this study is a simple and common solution method. We may develop a more effective method to speed up the solution of our method. Third, we plan to apply the proposed method for more EEG signal classification applications.

DATA AVAILABILITY STATEMENT

Publicly available datasets were analyzed in this study. This data can be found here: http://epileptologie-bonn.de/cms/upload/workgroup/lehnertz/eegdata.html.

AUTHOR CONTRIBUTIONS

JX and TN conceived and developed the theoretical framework of the manuscript. XG performed the data process, data evaluation, analysis, interpretation, and designed the figures. All authors drafted the manuscript.

FUNDING

This work was supported in part by the National Natural Science Foundation of China under Grant No. 61806026, by the Natural Science Foundation of Jiangsu Province under Grant No. BK20180956.

REFERENCES

Alwasiti, H., Yusoff, M. Z., and Raza, K. (2020). Motor imagery classification for brain computer interface using deep metric learning. *IEEE Access* 8, 109949–109963. doi: 10.1109/ACCESS.2020.3002459

Cai, D., Liu, K., and Su, F. (2015). "Local metric learning for EEG-based personal identification," i*n Proceedings of 2015 IEEE International Conference on Acoustics, Speech and Signal Processing (ICASSP)* (Brisbane, QLD), 842–846. doi: 10.1109/ICASSP.2015.7178088

Chang, C. C., and Lin, C. J. (2011). LIBSVM: a library for support vector machines. *ACM Trans. Intelligent Intellig. Syst. Technol.* 2, 1–27. doi: 10.1145/1961189.1961199

Cury, C., Maurel, P., Gribonval, R., and Barillot, C. (2019). A sparse EEG-informed fMRI model for hybrid EEG-fMRI neurofeedback prediction. *Front. Neurosci.* 13:1451. doi: 10.3389/fnins.2019.01451

Griffin, D., and Lim, J. S. (1984). Signal estimation from modified short-time fourier transform. *IEEE Trans. Acoustics Speech Signal Process.* 32, 236–243. doi: 10.1109/TASSP.1984.1164317

Gu, X., Chung, K., and Wang, S. (2020). Extreme vector machine for fast training on large data. *Int. J. Mach. Learn. Cybernet.* 11, 33–53. doi: 10.1007/s13042-019-00936-3

Gummadavelli, A., Zaveri, H. P., Spencer, D. D., and Gerrard, J. L. (2018). Expanding brain-computer interfaces for controlling epilepsy networks: novel thalamic responsive neurostimulation in refractory epilepsy. *Front. Neurosci.* 12:474. doi: 10.3389/fnins.2018.00474

Huang, C., Chung, F. L., and Wang, S. (2015). Multi-view L2-svm and its multi-view core vector machine. *Neural Netw.* . 75, 110–125. doi: 10.1016/j.neunet.2015.12.004

Iscan, Z., Dokur, Z., and Demiralp, T. (2011). Classification of electroencephalogram signals with combined time and frequency features. *Expert Syst. Appl.* 38, 10499–10505. doi: 10.1016/j.eswa.2011.02.110

Jiang, Y., Deng, Z., Chung, F., Wang, G., Qian, P., Choi, K. S., et al. (2017b). Recognition of epileptic EEG signals using a novel multiview TSK fuzzy system. *IEEE Trans. Fuzzy Syst.* 25, 3–20. doi: 10.1109/TFUZZ.2016.2637405

Jiang, Y., Wu, D., Deng, Z., Qian, P., Wang, J., Wang, G., et al. (2017a). Seizure classification from EEG signals using transfer learning, semi-supervised learning and TSK fuzzy system. *IEEE Trans. Neural Syst. Rehabil. Eng.* 25, 2270–2284. doi: 10.1109/TNSRE.2017.2748388

Juan, D. M. V., Gregor, S., Kristl, V., Pieter, M., German, C., and Dominguez. (2017). Improved localization of seizure onset zones using spatiotemporal constraints and time-varying source connectivity. *Front. Neurosci.* 11:156. doi: 10.3389/fnins.2017.00156

Kabir, E., and Zhang, Y. (2016). Epileptic seizure detection from EEG signals using logistic model trees. *Brain Inform.* 3, 93–100, doi: 10.1007/s40708-015-0030-2

Li, X., Yang, H., Yan, J., Wang, X., Li, X., and Yuan, Y. (2019). Low-intensity pulsed ultrasound stimulation modulates the nonlinear dynamics of local field potentials in temporal lobe epilepsy. *Front. Neurosci.* 13:287. doi: 10.3389/fnins.2019.00287

Liu, Q., Zhao, X., and Hou, Z. (2014). "Metric learning for event-related potential component classification in EEG signals," in *Proceedings of 2014 22nd European Signal Processing Conference (EUSIPCO)* (Lisbon), 2005–2009.

Lu, X., Wang, Y., Zhou, X., and Ling, Z. (2016). A method for metric learning with multiple-kernel embedding. *Neural Process. Lett.* 43, 905–921. doi: 10.1007/s11063-015-9444-3

Ni, T., Ding, Z., Chen, F., and Wang, H. (2018). Relative distance metric leaning based on clustering centralization and projection vectors learning for person Re-identification. *IEEE Access* 6, 11405–11411. doi: 10.1109/ACCESS.2018.2795020

Phan, H., Do, Q., Do, T. L., and Vu, D. L. (2013). "Metric learning for automatic sleep stage classification," i in *Proceedings of 2013 35th Annual International Conference of the IEEE Engineering in Medicine and Biology Society* (EMBC) (Osaka), 5025–5028. doi: 10.1109/EMBC.2013.6610677

Quang, M. H., Bazzani, L., and Murino, V. (2013). "A unifying framework for vector-valued manifold regularization and multi-view learning," in *Proceedings of the 30th International Conference on International Conference on Machine Learning* (Atlanta, GA), 100–108.

Richhariya, B., and Tanveer, M. (2018). EEG signal classification using universum support vector machine. *Expert Syst. Appl.* 106, 169–182. doi: 10.1016/j.eswa.2018.03.053

Smola, A. J. (1997). "Kernel principal component analysis," in *Proceedings of International Conference on Artificial Neural Networks* (Lausanne), 583–588. doi: 10.1007/BFb0020217

Spyrou, L., Kouchaki, S., and Sanei, S. (2018). Multiview classification and dimensionality reduction of scalp and intracranial EEG data through tensor factorisation. *J. Signal Process. Syst.* 90, 273–284. doi: 10.1007/s11265-016-1164-z

Srinivasan, V., Eswaran, C., and Sriraam, N. (2005). Artificial neural network based epileptic detection using time-domain and frequency-domain features. *J. Med. Syst.* 29, 647–660. doi: 10.1007/s10916-005-6133-1

Tzallas, A. T., Tsipouras, M. G., and Fotiadis, I. D. (2009). Epileptic seizure detection in EEGs using time-frequency analysis. *IEEE Trans. Inform. Technol. Biomed.*13, 703–710. doi: 10.1109/TITB.2009.2017939

Usman, S. M., and Fong, S. (2017). Epileptic seizures prediction using machine learning methods. *Computat. Math. Methods Med.* 2017:9074759. doi: 10.1155/2017/9074759

Wang, F., Zuo, W., Zhang, L., Meng, D., and Zhang, D. (2015). A kernel classification framework for metric learning, IEEE Trans. *Neural Netw. Learn. Syst.* 26, 1950–1962. doi: 10.1109/TNNLS.2014.2361142

Wang, S., Wang, J., and Chung, K. (2014). Kernel density estimation, kernel methods, and fast learning in large data sets. *IEEE Trans. Cybernet.* 44, 1–20. doi: 10.1109/TSMCB.2012.2236828

Weinberger, K. Q., and Saul, L. K. (2009). Distance metric learning for large margin nearest neighbor classification. *Mach. Learn. Res.* 10, 207–244.

Wen, D., Li, P., Zhou, Y., Sun, Y., Xu, J., Liu, Y., et al. (2020). Feature classification method of resting-state EEG signals from amnestic mild cognitive impairment with type 2 diabetes mellitus based on multi-view convolutional neural network. *IEEE Trans. Neural Syst. Rehabil. Eng.* 28, 1702–1709. doi: 10.1109/TNSRE.2020.3004462

Wen, J., Tian, Z., She, H., and Yan, W. (2010). "Feature extraction of hyperspectral images based on preserving neighborhood discriminant embedding," in *Proceedings of IEEE Conference: Image Analysis and Signal Processing (IASP)* (Xiamen), 257–262.

Wu, T., Yan, G. Z., Yang, B. H., and Hong, S. (2008). EEG feature extraction based on wavelet packet decomposition for brain computer interface. *Measurement* 41, 618–625. doi: 10.1016/j.measurement.2007.07.007

Xing, E. P., Jordan, M. I., Russell, S. J., and Ng, A. Y. (2003). "Distance metric learning with application to clustering with side-information," in *Advances in Neural Information Processing Systems,* (Cambridge, MA, USA: MIT Press), 521–528.

Yuan, Y., Xun, G., Jia, K., and Zhang, A. (2019). A multi-view deep learning framework for EEG seizure detection. *IEEE J. Biomed. Health Inform.* 23, 83–94. doi: 10.1109/JBHI.2018.2871678

Zhang, L., Shum, H. P. H., Liu, L., Guo, G., and Shao, L. (2019). Multiview discriminative marginal metric learning for makeup face verification. *Neurocomputing* 333, 339–350. doi: 10.1016/j.neucom.2018.12.003

Zhou, Z., Zhang, Y., and Jiang, Y. (2019). "Deep view-reduction TSK fuzzy system: a case study on epileptic EEG signals detection," in *Proceedings of 2019 IEEE Symposium Series on Computational Intelligence (SSCI)* (Xiamen), 387–392. doi: 10.1109/SSCI44817.2019.9002722

Conflict of Interest: The authors declare that the research was conducted in the absence of any commercial or financial relationships that could be construed as a potential conflict of interest.

frontiers in Neuroscience

BRIEF RESEARCH REPORT
published: 30 September 2020
doi: 10.3389/fnins.2020.00808

An Intelligent EEG Classification Methodology Based on Sparse Representation Enhanced Deep Learning Networks

Jing-Shan Huang[1], Yang Li[1], Bin-Qiang Chen[1], Chuang Lin[2]* and Bin Yao[1]*

[1] School of Aerospace Engineering, Xiamen University, Xiamen, China, [2] Shenzhen Institutes of Advanced Technology, Chinese Academy of Sciences, Shenzhen, China

The classification of electroencephalogram (EEG) signals is of significant importance in brain–computer interface (BCI) systems. Aiming to achieve intelligent classification of EEG types with high accuracy, a classification methodology using sparse representation (SR) and fast compression residual convolutional neural networks (FCRes-CNNs) is proposed. In the proposed methodology, EEG waveforms of classes 1 and 2 are segmented into subsignals,and 140 experimental samples were achieved for each type of EEG signal. The common spatial patterns algorithm is used to obtain the features of the EEG signal. Subsequently, the redundant dictionary with sparse representation is constructed based on these features. Finally, the samples of the EEG types were imported into the FCRes-CNN model having fast down-sampling module and residual block structural units to be identified and classified. The datasets from BCI Competition 2005 (dataset IVa) and BCI Competition 2003 (dataset III) were used to test the performance of the proposed deep learning classifier. The classification experiments show that the recognition averaged accuracy of the proposed method is 98.82%. The experimental results show that the classification method provides better classification performance compared with sparse representation classification (SRC) method. The method can be applied successfully to BCI systems where the amount of data is large due to daily recording.

Keywords: electroencephalogram, common spatial patterns, sparserepresentation, residual convolutional neural networks, fast compression

OPEN ACCESS

Edited by:
Yizhang Jiang,
Jiangnan University, China

Reviewed by:
Zhe Yang,
Dongguan University of Technology, China
Hongru Zhao,
Soochow University, China

****Correspondence:***
Bin-Qiang Chen
cbq@xmu.edu.cn
Chuang Lin
chuang.lin@siat.ac.cn

Specialty section:
This article was submitted to Neuroprosthetics, a section of the journal Frontiers in Neuroscience

Received: *29 May 2020*
Accepted: *10 July 2020*
Published: *30 September 2020*

Citation:
Huang J-S, Li Y, Chen B-Q, Lin C and Yao B (2020) An Intelligent EEG Classification Methodology Based on Sparse Representation Enhanced Deep Learning Networks. Front. Neurosci. 14:808. doi: 10.3389/fnins.2020.00808

INTRODUCTION

Brain–computer interface (BCI) is one of the research hotspots in the fields of biomedicine and signal processing in recent years. Brain–computer interface technology is a human–computer interaction method based on brain signals. It provides a communication channel for non-neuromuscular control. Brain–computer interface is a communication system that enables the human brain to interact with the external environment without relying on the peripheral nervous system and muscles.

In the BCI system, electroencephalography (EEG) signal is the manifestation of brain nerve electrical signals. It is also the basis of signal processing in the system. Electroencephalography

signals comprehensively reflect the physical and chemical activities of the nervous system and are powerful tools for analyzing neural activity and brain conditions (Wu et al., 2008). Any changes in brain function and structure caused by neurological brain diseases can lead to abnormal brain electrical signals. In clinical medicine, the information processing of EEG signals not only provides an objective basis for the diagnosis of certain brain diseases, but also provides effective treatment for some brain diseases (Thornton, 2002). For a long time, doctors need to manually detect and analyze the waveform characteristics of EEG, with intensive labor and strong subjectivity. Therefore, the classification of EEG signals is of great significance to the identification, morbid prediction, and prevention of brain diseases.

In the BCI, the EEG signal is the main medium for human–computer interaction. An important part of the BCI system is processing the collected EEG signals to determine the type of commands issued by the brain.Motor imaging (MI) signal is a type of EEG signals. It refers to brain signals generated by imagining limb movement without actual limb movement. By analyzing the MI signal, it is possible to judge the imaginary's movement intention and operate the external device. At present, the motion imaging control has great potential application value in various fields such as sports function rehabilitation, motor function assistance, and so on. Therefore, the MI signal becomes the most commonly used signal in the BCI.It is also the EEG signal studied in this article. Because of the non-stationarity of the EEG signal and the influence of a large number of background waveforms and artifacts, EEG classification is a challenging problem. At present, researchers have done a lot of work in various fields to study the feature extraction and classification of EEG signals.

Common spatial patterns (CSPs) is a popular method of extracting features in EEG studies. The CSP method has been applied successfully in many EEG classification studies (Ramoser et al., 2000; Grossewentrup and Buss, 2008; Mousavi et al., 2011; Keng et al., 2012). Other well-known feature extraction and dimension reduction methods such as principal component analysis and independent component analysis are also used frequently to improve the EEG classification accuracy (Ince et al., 2006; Guo et al., 2008; Talukdar et al., 2014). Autoregressive model and power spectral density estimation are also common feature extraction algorithms for EEG classification (Argunsah and Cetin, 2010; Seth et al., 2017). In the classification part, the frequently used classification methods include linear discriminant analysis (Rajaguru and Prabhakar, 2017), Bayesian method (Bashashati et al., 2016), BP neural network (Gao et al., 2012), support vector machine (SVM) (Liu et al., 2012), and so on (Wang et al., 2006; Yang et al., 2012; Roeva and Atanassova, 2016). The characteristics of EEG signals mainly include the following aspects: randomness, weakness, catastrophe, non-stationarity, low frequency, and non-linearity. Therefore, it is difficult to determine the representation and appropriate description (Gao et al., 2018).

Sparse representation is a fast developing field by constructing sparse linear models. It represents a given input signal as a linear superposition of base signals selected from a predetermined dictionary (Chen, 2016).It can find a suitable dictionary for ordinary densely expressed signal samples, and convert the samples into a suitable sparse expression form. Sparse representation can simplify learning tasks and reduce model complexity. Sparse representation has a large number of applications in the fields of signal acquisition, denoising, and image restoration (Elad and Aharon, 2006; Yang and Li, 2009; Li et al., 2013). The classification of EEG signals based on sparse representation is also developing gradually. Shin et al. (2015) proposed simple adaptive sparse representation-based classification (SRC) schemes for EEG classification, and the proposed adaptive schemes show relatively improved classification accuracy as compared to conventional methods without requiring additional computation. Zhou et al. (2012) proposed a method to learn a new dictionary with smaller size and more discriminative ability for the classification, and the experimental results of the EEG classification show that the proposed method outperforms the SRC method. Sreeja and Samanta (2020) proposed a weighted SRC (WSRC) for classifying MI signals to further boost the proficiency of SRC technique, and the experimental results substantiate that WSRC is more efficient and accurate than SRC.However, there is a contradiction between dictionary size and algorithm recognition accuracy.

Deep learning methodologies show outstanding performances in pattern recognition problems (Huang et al., 2019). Although the traditional pattern recognition method has been widely adopted, there is still a problem of relying on experience and prior knowledge in the process of manually selecting EEG signal features. In addition, feature extraction algorithms and feature classification algorithms use different objective functions so as to affect the pattern recognition accuracy. The deep learning neural network can extract more distinguishable and interpretable features of EEG signals. Meanwhile, the classification method based on deep learning neural network includes feature extraction and feature classification in a frame so as to avoid the loss of signal information caused by separating the two steps. Therefore, EEG classification based on deep learning related techniques has become a research hotspot. A deep belief network model (An et al., 2014)was applied for two class motor imagery (MI) classification, and the proposed model was shown more successful than the SVM method. Tsinalis et al. (2016) used convolutional neural networks (CNNs) to learn a single-channel EEG-based classification task filter for the automatic scoring of the sleep stage.Yang et al. (2015) used CNN to classify MI EEG signals. Chambon et al. (2018) proposed an end-to-end deep learning method to extract information from the EEG channel, which can finally correctly classify 91% of sleep stages from EEG signal.A recurrent CNN architecture was proposed by Bashivan et al. (2015) to model cognitive events from EEG data. A deep learning network with principal component–based covariate shift adaptation was proposed by Jirayucharoensak et al. (2014) for automatic emotion recognition.

Because the EEG signal contains a lot of noise and redundant information, it is not effective to obtain classification information directly from it. The sparse representation method can effectively remove the redundant information and retain the feature information that is beneficial to classification to best express the

signal feature information. Meanwhile, the deep learning neural network has a wide range of applications in pattern recognition. Therefore, we combine the advantages of these two methods. We innovatively use the sparse features of the EEG signal as the input terminal of the deep neural network model and train the deep neural network model parameters to realize the automatic classification of the EEG signal.

In this article,we propose an intelligent EEG classification method based on sparse representation and enhanced deep learning networks.The features of the EEG signal are obtained through the CSP algorithm, and then the redundant dictionary with sparse representation is constructed based on these features. Subsequently, the sparse features were utilized as input of the fast compression deep learning networks to achieve the classification of EEG signals.The dataset downloaded from the website of BCI Competition 2005 (dataset IVa) and BCI Competition 2003 (dataset III) was used as the training and testing data. The classification results using the proposed method can reach an averaged accuracy of 98.82%.

The rest of this article is organized as follows. In *Methods*, we explain the methodology used for the EEG classification, including methodology overview, database and segmentation, and data preprocessing. We also explain the sparse representation classification model and the proposed fast compression deep learning networks. In *Results*, numerical evaluation and experimental results of EEG classification are shown, including evaluation metrics and the experimental classification results. Finally, we give the discussion and conclusion in *Discussion*.

METHODS

Methodology Overview

The overall procedures of the proposed EEG classification method based on sparse representation and fast compression deep learning networks are shown in **Figure 1**. The original EEG signals were shared by the BCI Competition database (Blankertz et al., 2006). First, EEG waveforms are segmented into subsignals. Then the EEG signal features are obtained through the CSP algorithm, and the redundant dictionary with sparse representation is constructed based on these EEG signal features. Subsequently, the sparse features were utilized as input of the fast compression deep learning networks to complete the classification of EEG signals. Finally, EEG types are classified by the fast compression residual CNNs (FCRes-CNNs) classifier intelligently.

Database and Segmentation

The experimental data in this article comes from the databases in BCI Competition 2005 (dataset IVa) and BCI Competition 2003 (dataset III).The databases contain datasets recorded by five different healthy subjects (aa, al, av, aw, ay). All five subjects underwent BCI experiments with three MI exercises of left hand, right hand, and right foot. In this experiment, only two types of right hand (R) and right foot (F) were used for data analysis, and they are named class 1 and class 2. Each EEG signal has 118channels.The common goal of BCI Competitions was to classify these MI tasks by using EEG signals recorded at C3, Cz, and C4 channels.First, the EEG signal is filtered by a bandpass filter of 0.05 to 200 Hz. Then, the EEG signal is digitized at a frequency of 1,000 Hz. Finally, the EEG signal

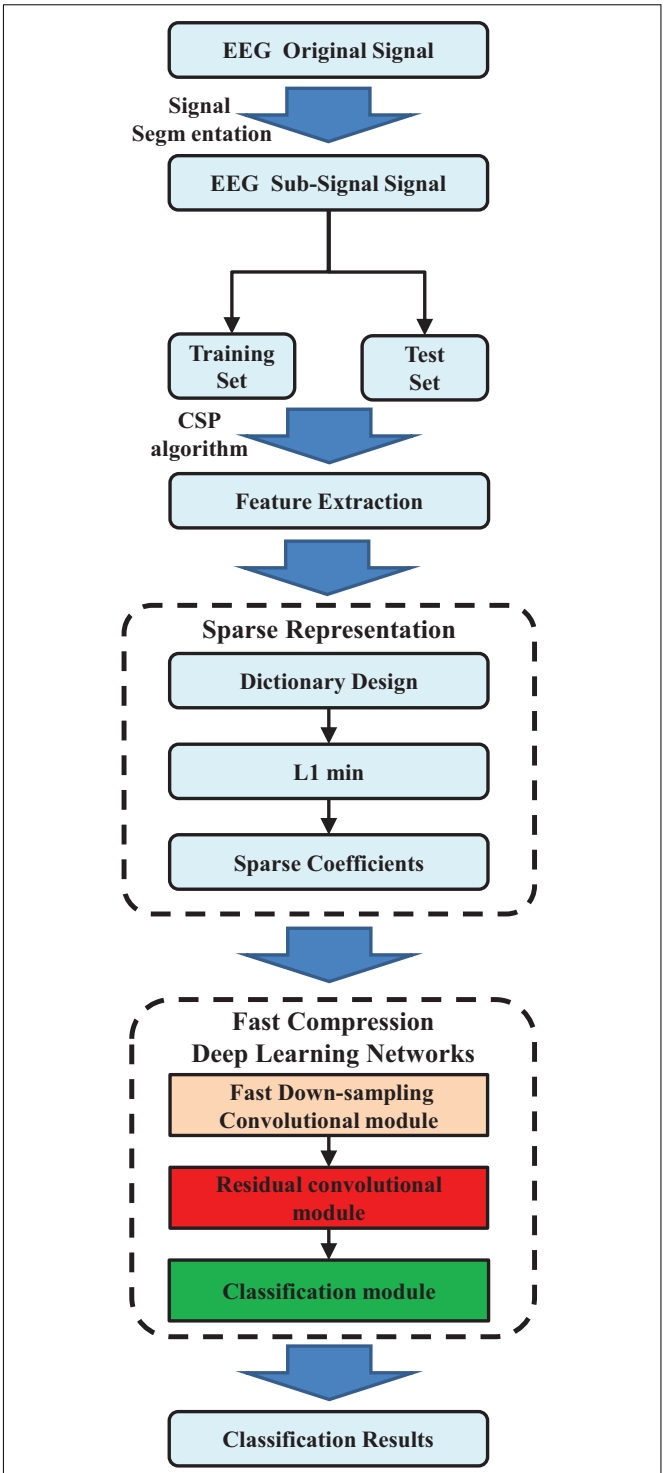

FIGURE 1 | Overall procedures in EEG classification based on the proposed method.

is down-sampled to 100 Hz, and it is analyzed offline by the Berlin research team.

During the experiment, the subjects were seated in a comfortable chair, with their arms resting naturally on the armrests.At the beginning of the experiment, a visual cue in the form of a shoulder appeared in the center of the screen, informing the subjects of the MI task to be performed. The subject's imagination time was 3.5 s.After the end of the MI, the subjects had a short time to rest and the rest time varied randomly from 1.75 to 2.25 s.

Data Preprocessing

First, EEG waveforms need to be segmented to the 3-s time samples, and140 experimental samples can be achieved for each type of EEG signal. To reduce the interference from other sources such as electrooculogramsand electromyograms, 8- to 15-Hz bandpass filters were applied in this article (Gao et al., 2018).The CSP method is an effective method in the feature extraction problem of motion imaging signals.It is suitable for two classes (conditions) of multichannel EEG-baBCIs, so this article adopts the CSP method to filter the EEG signals and extract energy features. When the number of CSP filters is set as 32, after filtering operation, training and testing EEG samples can be converted to 32 CSP eigenvalues, which can be used for data classification.

Sparse Representation Classification Model

Sparse representation represents a given input signal as a linear superposition of a small set of base signals selected from a predetermined dictionary. It can be said that the problem of sparse representation is a problem of representing a given input signal as simply as possible. For the EEG signals, a feature vector can be obtained by CSP (Legendre and Fortin, 1989):

$$asv_i = [\, v_{1i}, v_{2i}, \ldots, v_{mi}] \in R^m \tag{1}$$

where m is the sample dimension. If all the characteristic vector signals from different types of EEG signals are put in A, the matrix A can be written as the following form:

$$A = [\, v_1, v_2, \ldots, v_n] \in R^{m \times n} \tag{2}$$

Rajaguru and Prabhakar (2017) declared that if the training data from the i^{th} category are enough, the test sample y from the same category can be shown as a linear combination of the training set associated with subject :

$$y = \propto_1 v_1 + \propto_2 v_2 + \cdots + \propto_n v_n \tag{3}$$

where $\propto$ is the coefficient vector, and its elements are not all zero. By concatenating A_i, the dictionary matrix A for all k classes can be acquired as $i = 1, 2, \ldots\ldots k$. The dictionary can be given as follows:

$$A = [\, A_1, A_2, \ldots, A_k] \in R^{m \times k} \tag{4}$$

If the EEG feature signal y is the tested signal, y can be written as a linear combination of.

all nk training data.

$$y = Ax = x_{1,1}v_{1,1} + x_{1,2}v_{1,2} + \cdots + x_{1,n}v_{1,n} + x_{2,1}v_{2,1} + \cdots + x_{k,n}v_{k,n} \tag{5}$$

where $x = [v_{1,1}, v_{2,2}, \ldots, v_{k,n}]^T \in R^{nk}$ are the coefficients vectors. In the ideal case,

$x = [\, 0, 0\ldots\ldots, v_{i,1}, v_{i,2}, \ldots, 0, 0\ldots\ldots, 0]$ is a vector, which is mostly zero value except for those elements corresponding to the class of i^{th}; thus, the corresponding class of EEG feature signals can be classified. The two types of sparse presentation classification operations are shown in **Figure 2**.

The test sample feature vector can be expressed as a linear combination of feature vectors of the training sample. The sparse coefficients x are used to encode the identity information of the test sample. The sparse coefficients are obtained by solving the linear equation of (5). Because the number of CSP filters is smaller than the number of training samples, the solution of x is not unique so that Eq.5 is underdetermined. New theories of sparse representation and compressed sensing have pointed out that L1 norm optimization can be used to solve underdetermined linear equations as long as x is sufficiently sparse. Based on the vector x and the test signal y, L1-norm minimization equation can be listed as follows:

$$\widehat{x}_1 = arg\ min||x||_1 subjects.t.Ax = y \tag{6}$$

In the ideal case, when we obtained the estimate, it should have non-zero element corresponding to y. Through analyzing the indices of the non-zero elements in $\widehat{x}_1$, the class of y can be determined. However, because of the modeling limitations and noise, $\widehat{x}_1$ is not exactly zero but is close to zero. To resolve this problem, the following equation will be calculated generally as follows:

$$r1(y) = \left|\left|y - A\delta_i(x)\right|\right|_2 \tag{7}$$

The test samples are classified according to the approximation residuals. The smaller the approximation residual, the closer the test sample is to this category. Therefore, the test sample

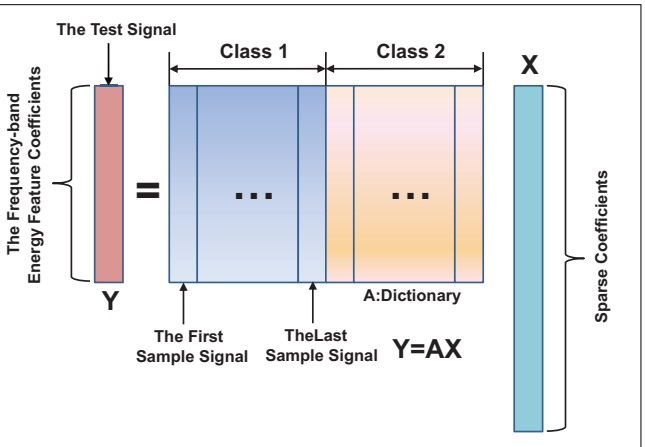

FIGURE 2 | Sparse representation classification model.

is discriminated as the smallest category that approximates the residual. For each class i, $\delta_i(x)$ is obtained by nulling all the elements corresponding to the other class, then class i can be classified by analyzing the residuals, that is:

$$class\,(y) = arg\ min_i r_i(y) \tag{8}$$

Residual Neural Network Theory

Convolutional neural network is a special deep feedforward neural network designed by the inspiration of the concept of "receptive field" in the field of biological neuroscience (Liu, 2018). For traditional CNNs, the learning ability of the network will increase as the depth of the network increases. Meanwhile, the convergence speed of the network will slow down, and the time required for training will also become longer (Huang et al., 2020). The aim of residual networks is to address the degradation problem, which is defined as the decrease in accuracy as depth becomes greater than a certain threshold (He et al., 2016). Convolutional neural networks composed of residual block local deep neural networks units can address the degradation problem by facilitating the learning of identity mappings and solve difficulty in tuning of deep networks.

The residual neural network draws on the ideas of Highway networks (Srivastava et al., 2015). When the number of network layers reaches a certain threshold, the learning rate will decrease, and there is a risk of accuracy rate decline. The input of each layer in the general conventional CNN is derived from the output of the previous layer (Qin, 2019). It will be easily paralyzed if a network with many layers is performed with gradient calculations. The network structure of the residual network is similar to a "short circuit" structure. The output of the previous layers in the residual network does not go through the middle multiple network layers but directly serves as the input part of the network layer behind (Ji, 2019). Therefore, the residual structure has transformed the learning objectives. It no longer learns a complete mapping relationship from input to output, but the difference between the optimal solution $H(x)$ and the input congruent mapping x (Huang et al., 2020). The residual calculation formula is as follows:

$$F(y) = H(x) - x \tag{9}$$

The residual network can be regarded as a type of architecture consisting of a stack of residual blocks. The input data in the residual network come from different combinations of the previous network structure. This method introduces sufficient reference information to extract the effective features of the input EEG signal data (Liu, 2018). Because the paths in the network are relatively independent of each other, the regularity of the deep learning network structure is improved greatly.

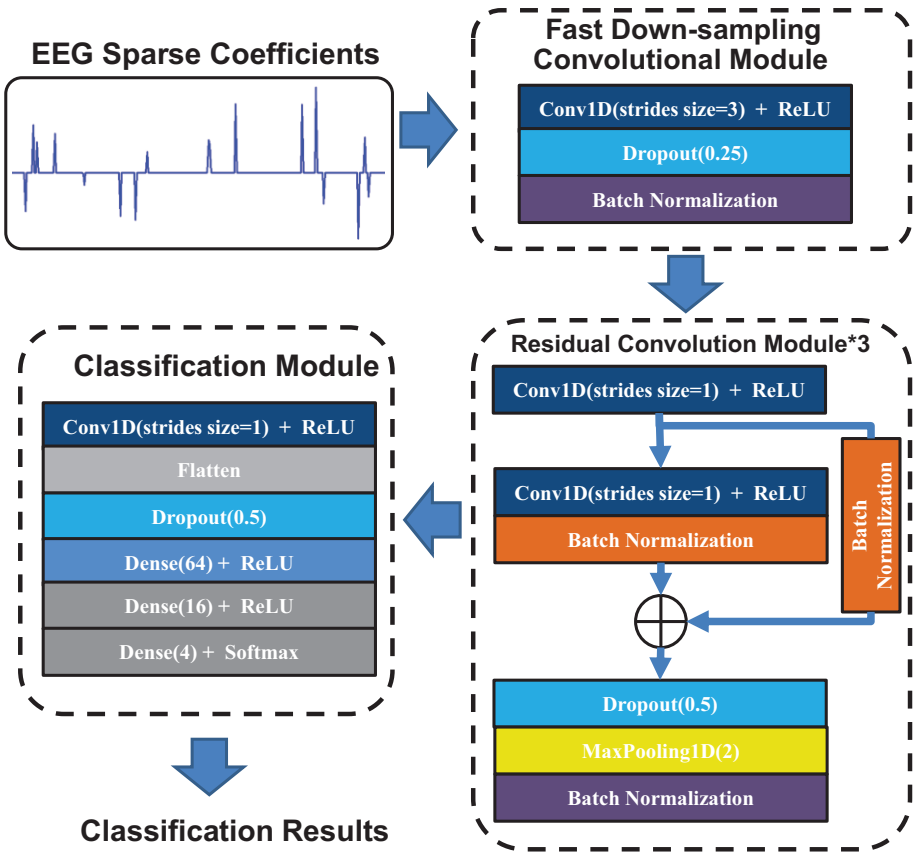

FIGURE 3 | The architecture of the proposed FCRes-CNN.

Proposed Convolutional Networks

In this section, we propose the FCRes-CNNs. As shown in **Figure 3**, the FCRes-CNN is mainly composed of a fast down-sampling module, three residual convolution modules, and a classification module. In the proposed FCRes-CNN model, the learning rate is set as 0.001, and the batch size parameter is set as 2,500.

In the proposed convolutional networks, convolutional layer with a stride of three is applied in the fast down-sampling module. Although a pooling layer also has effect of data compression, reducing overfitting, it will lose most of the original signal information while increasing network depth and spatial information loss due to the averaging nature of the pooling layer. Compared with the pooling layer, the convolutional layer with a large stride can adaptively learn the convolution kernel while compressing the input data (Huang et al., 2020). Therefore, we applied a convolutional layer with a large stride instead of a pooling layer in the fast down-sampling module.

The fast down-sampling module consists of a convolutional layer, a random dropout layer, and a batch-normalization layer. The convolutional layer with a stride of 3 is the main part of the fast down-sampling module. A random dropout layer and a batch-normalization layer follow the convolutional layer to enhance the generalization of the networks model. The fast down-sampling module can effectivelysimplify the calculation of deep network models, reduce data redundancy, and promote model learning (Huang et al., 2020).

Convolutional layers in series are applied in the residual convolution module, which are followed by residual short circuit. Then, a random dropout layer is added after the convolutional layer, and the max-pooling layer is applied to down-sample the EEG signal feature vectors.

In the classification module, a convolution layer is first used to reduce the dimension of the feature vectors. Then, a flattened layer follows the convolution layer. After the flattened layer, a random dropout layer is applied to prevent overfitting.

RESULTS

Evaluation Metrics

The accuracy and loss were used as the evaluation criteria in the pattern recognition field.Therefore, we used the two evaluation criteria for the classification performance of EEG types.The accuracy and loss were calculated through Eqs10 and 11.

$$\text{Accuracy}\ (\%) = \frac{\text{TP+TN}}{\text{TP+TN+FP+FN}} \times 100 \qquad (10)$$

where **TP** stands for true positive, meaning the correct classification as class 1 of EEG; **TN** stands for true negative, meaning correct classification as class 2 of EEG; **FP** stands for false positive, meaning incorrect classification as class 1 of EEG; and **FN** represents false negative, meaning incorrect classification as class 2of EEG (Yin et al., 2016).

As for the metric of loss, it is defined as the difference between the predicted value of the EEG classification model and the true value for aspecific EEG sample (Huang et al., 2020). In this study, the mathematical expressionof categorical cross entropy loss is shown as Eq.11.

$$\text{loss} = -\frac{1}{n}\sum_{i=1}^{n} \hat{y}_{i1} ln y_{i1} + \hat{y}_{i2} ln y_{i2} + \cdots + \hat{y}_{im} ln y_{im} \qquad (11)$$

where n represents the number of EEGsamples; m represents the number of EEG types; $\hat{y}$ represents the predictive output value; and y represents the actual value.

The Experimental Classification Results

In classification for the EEG signals of classes 1 and 2, each class can get 140 groups of 32 eigenvalues after the above data processing. Based on the training samples, the redundant

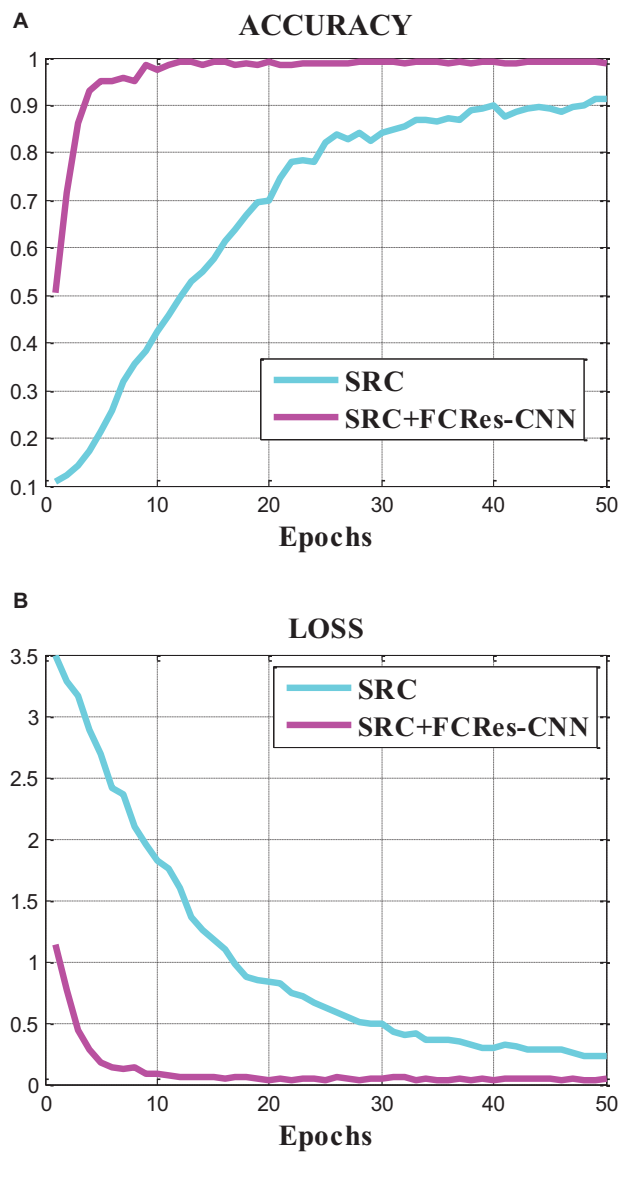

FIGURE 4 | Accuracy and loss curves of the SRC and the proposed method.

dictionaries of sparse classification algorithm were constructed by using the CSP eigenvalues obtained by classes 1 and 2. Then, we scrambled all the EEG training sample data randomly and then selected the last 100 samples as the testing set. This approach ensures that the distribution of the training set and testing set is random and uncertain, and it can better reflect the classification effect of the proposed classifier.

The classification of EEG signals was completed based on the classification algorithm described insection "Methods." The raw EEG waveforms are segmented into subsignals. The features of the EEG signal are obtained through the CSP algorithm. Then the redundant dictionary with sparse representation is constructed based on these features. Finally, the sparse features were utilized as input of the fast compression deep learning networks to complete the classification of EEG signals. The experiment runs on a PC with 16GB of memory and 16GB of GPU memory.

Figure 4 represents the accuracy and loss curves of the sparse representation algorithm (SRC) and the proposed classification method (SRC +FCRes-CNN). From **Figure 4**, we can find that the accuracy value curve convergence rate of the proposed model is faster than that of SRC model, and the final accuracy convergence value of the proposed model is also much higher than that of SRC model. The loss value curve convergence rate of the proposed model is faster than that of SRC model, and the final loss convergence value of the proposed model is also much lower than that of SRC model. From these results, we can conclude that the proposed model achieves a higher average accuracy with lower loss than the SRC model based on the classification results of EEG signals. The proposed model outperforms the SRC model in the EEG classification application.

In the contrast experiment, the SRC model achieved an average accuracy of 88.79% and an average loss of 18.10%. In contrast, the proposed SRC +FCRes-CNN model achieved an average accuracy of 98.82% and an average loss of 4.74%. In this article, the total number of EEG training trials is 280. For the training process of deep learning, the number of samples is still insufficient. If the number of training samples is sufficient, the accuracy of classification will be further improved.

DISCUSSION

In this article, we proposed an EEG classification method based on sparse representation enhanced deep learning networks.

The original EEG signals were shared by the BCI Competition database. In the procedure of the proposed method, EEG waveforms of classes 1 and 2 are segmented into subsignals.The 3-s time samples after the prompt to conduct the classification experiment was applied, and 140 experimental samples can be achieved for each type of EEG signal. The CSP algorithm is used to obtain the features of the EEG signal. Then the redundant dictionary with sparse representation is constructed based on these features. Finally, the sparse features were utilized as input of the fast compression deep learning networks to complete the classification of EEG signal. The EEG classification is performed in the FCRes-CNN classifier automatically and intelligently.

The accuracy result of the proposed method on BCI Competition dataset Iva and dataset III is 98.82%, which is higher than the sparse representation classification method. The proposed method performs higher classification accuracy than other methods in literature by a training even using only a few samples, which is 280 trials in this article.We believe that the proposed method is of great significance for BCI applications that require real-time EEG classification of daily life use.

DATA AVAILABILITY STATEMENT

Publicly available datasets were analyzed in this study. This data can be found here: http://www.bbci.de/competition/iii/, http://www.bbci.de/competition/ii/#datasets.

AUTHOR CONTRIBUTIONS

J-SH, B-QC, and BY conceived and designed the classification method. CL and YL performed the experiment. J-SH preprocess and analyzed the data and wrote the manuscript. BY and B-QC reviewed and edited the manuscript. All authors read and approved the manuscript.

FUNDING

This research was supported financially by the National Natural Science Foundation of China (Grant No. 51605403), the Fundamental Research Funds for the Central Universities under Grant No. 20720190009, International Science and Technology Cooperation Project of Fujian Province of China under Grant No. 2019I0003, the Shenzhen Basic Research Grant No. JCYJ20170413152804728, and the Shenzhen Basic Research Grant No. JCYJ20180507182508857.

REFERENCES

An, X., Kuang, D., Guo, X., Zhao, Y., and He, L. (2014). "A deep learning method for classification of EEG data based on motor imagery," in *Proceedings of the 10th International Conference on Intelligent Computing, ICIC 2014*, Taiyuan, 203–210. doi: 10.1007/978-3-319-09330-7_25

Argunsah, A. O., and Cetin, M. (2010). "AR-PCA-HMM approach for sensorimotor task classification in EEG-based brain-computer interfaces," in *Proceedings of the 20th International Conference on Pattern Recognition*, (Istanbul:IEEE), 113–116.

Bashashati, H., Ward, R. K., and Bashashati, A. (2016). "Bayesian optimization of bci parameters," in *Proceedings of the IEEE Canadian Conference on Electrical and Computer Engineering (CCECE)*, (Vancouver, BC: IEEE), 1–5.

Bashivan, P., Rish, I., Yeasin, M., and Codella, N. (2015). Learning representations from EEG with deep recurrent-convolutional neural networks. *arXiv*[Preprint].

Blankertz, B., Muller, K. R., Krusienski, D. J., Schalk, G., Wolpaw, J. R., Schlögl, A., et al. (2006). The BCI competition III: validating alternative approaches to actual BCI problems. *IEEE Trans. Neural Syst. Rehabil. Eng.*14, 153–159. doi: 10.1109/tnsre.2006.875642

Chambon, S., Galtier, M. N., Arnal, P. J., Wainrib, G., and Gramfort, A. (2018). A deep learning architecture for temporal sleep stage classification using multivariate and multimodal time series. *IEEE Trans. Neural Syst. Rehabil. Eng.*26:758. doi: 10.1109/tnsre.2018.2813138

Chen, S. (2016). *Research on Epilepsy EEG Classification and Recognition Method Based on Sparse Representation and Feature Extraction*. .

Elad, M., and Aharon, M. (2006). "Image denoising via learned dictionaries and sparse representation,". In *Proceedings of the IEEE Computer Society Conference on Computer Vision and Pattern Recognition (CVPR'06)*, (New York, NY: IEEE), Vol. 1, 895–900.

Gao, G., Shang, L., Xiong, K., Fang, J., Zhang, C., and Gu, X. (2018). EEG classification based on sparse representation and deep learning. *NeuroQuantology*16, 789–795.

Gao, X. Z., Wang, J., Tanskanen, J. M. A., Bie, R., and Guo, P. (2012). "BP neural networks with harmony search method-based training for epileptic EEG signal classification," in *Proceedings of the 8th International Conference on Computational Intelligence and Security*, (Guangzhou:IEEE), 252–257.

Grossewentrup, M., and Buss, M. (2008). Multiclass common spatial patterns and information theoretic feature extraction. *IEEE Trans. Biomed. Eng.*55, 1991–2000. doi: 10.1109/tbme.2008.921154

Guo, X., Wang, L., Wu, X., and Zhang, D. (2008). "Dynamic analysis of motor imagery EEG using kurtosis based independent component analysis," in *Advances in Cognitive Neurodynamics ICCN 2007*, edsR.Wang, E.Shen, and F.Gu (Dordrecht: Springer), 381–385. doi: 10.1007/978-1-4020-8387-7_65

He, K., Zhang, X., Ren, S., and Sun, J. (2016). "Deep residual learning for image recognition," in *Proceedings of the IEEE Conference on Computer Vision and Pattern Recognition*, (Las Vegas, NV: IEEE), 770–778.

Huang, J., Chen, B., Yao, B., and He, W. (2019). ECG arrhythmia classification using STFT-based spectrogram and convolutional neural network. *IEEE Access*7, 92871–92880. doi: 10.1109/access.2019.2928017

Huang, J., Chen, B., Zeng, N., Cao, X.-C., and Li, Y. (2020). Accurate classification of ECG arrhythmia using MOWPT enhanced fast compression deep learning networks. *J. Amb. Intell. Hum. Comput.*

Ince, N. F., Arica, S., and Tewfik, A. (2006). Classification of single trial motor imagery EEG recordings with subject adapted non-dyadic arbitrary time–frequency tilings. *J. Neural Eng.*3:235. doi: 10.1088/1741-2560/3/3/006

Ji, T. (2019). *Research on Remote Sensing Image Scene Classification Based on Convolutional Neural Network*. .

Jirayucharoensak, S., Panngum, S., and Israsena, P. (2014). EEG-based emotion recognition using deep learning network with principal component based covariate shift adaptation. *Sci. World J.*2014:627892.

Keng, A. K., Yang, C. Z., Chuanchu, W., Guan, C., and Zhang, H. (2012). Filter bank common spatial pattern algorithm on BCI competition IV datasets 2a and 2b. *Front. Neurosci.*6:39. doi: 10.3389/fnins.2012.00039

Legendre, P., and Fortin, M. J. (1989). Spatial pattern and ecological analysis. *Vegetatio*80, 107–138.

Li, S., Xu, L. D., and Wang, X. (2013). A continuous biomedical signal acquisition system based on compressed sensing in body sensor networks. *IEEE Trans. Indust. Inform.*9, 1764–1771. doi: 10.1109/tii.2013.2245334

Liu, C. (2018). *Research and Design of Handwritten Digit Recognition Based on Convolutional Neural Network*. .

Liu, Y., Zhou, W., Yuan, Q., and Chen, S. (2012). Automatic seizure detection using wavelet transform and SVM in long-term intracranial EEG. *IEEE Trans. Neural Syst. Rehabil. Eng.*20, 749–755. doi: 10.1109/tnsre.2012.2206054

Mousavi, E. A., Maller, J. J., Fitzgerald, P. B., and Lithgow, B. J. (2011). Wavelet common spatial pattern in asynchronous offline brain computer interfaces. *Biomed. Signal Process. Control*6, 121–128.doi: doi: 10.1016/j.bspc.2010.08.003

Qin, S. (2019). *Research on Handwritten Digit Recognition Based on Deep Residual Network*. .

Rajaguru, H., and Prabhakar, S. K. (2017). "Epilepsy classification using fuzzy optimization and Kernel Fisher discriminant analysis," in *Proceedings of the 2nd International Conference on Communication and Electronics Systems (ICCES)*, (Coimbatore: IEEE), 183–186.

Ramoser, H., Mullergerking, J., and Pfurtscheller, G. (2000). Optimal spatial filtering of single trial EEG during imagined hand movement. *IEEE Trans. Rehabil. Eng.*8, 441–446. doi: 10.1109/86.895946

Roeva, O., and Atanassova, V. (2016). Cuckoo search algorithm for model parameter identification. *Algorithms*1:26.

Seth, D., Chakraborty, D., Ghosal, P., and Sanyal, S. K. (2017). "Brain computer interfacing: a spectrum estimation based neurophysiological signal interpretation," in *Proceedings 4th International Conference on Signal Processing and Integrated Networks (SPIN)*, (Noida: IEEE), 534–539.

Shin, Y., Lee, S., Ahn, M., Cho, H., Jun, S. C., and Lee, H.-N. (2015). Simple adaptive sparse representation based classification schemes for EEG based brain–computer interface applications. *Comput. Biol. Med.*66, 29–38. doi: 10.1016/j.compbiomed.2015.08.017

Sreeja, S. R., and Samanta, D. (2020). Distance-based weighted sparse representation to classify motor imagery EEG signals for BCI applications. *Multimed. Tools Appl.*79, 13775–13793. doi: 10.1007/s11042-019-08602-0

Srivastava, R. K., Greff, K., and Schmidhuber, J. (2015). Highway Networks. *Comput. Sci.*

Talukdar, M. T. F., Sakib, S. K., Pathan, N. S., and Fattah, S. A. (2014). "Motor imagery EEG signal classification scheme based on autoregressive reflection coefficients," in *Proceedings of the International Conference on Informatics, Electronics & Vision (ICIEV)*, (Dhaka: IEEE), 1–4.

Thornton, K. E. (2002). Electrophysiological(QEEG) correlates of effective reading: towards a generator/ activation theory of the mind. *J. Neurother.*6, 37–66. doi: 10.1300/j184v06n03_04

Tsinalis, O., Matthews, P. M., Guo, Y., and Zafeiriou, S. (2016). Automatic sleep stage scoring with single-channel EEG using convolutional neural networks. *arXiv*[Preprint].

Wang, Y., Gao, S., and Gao, X. (2006). "Common spatial pattern method for channel selelction in motor imagery based brain-computer interface," in *Proceedings of the 27th Annual Conference IEEE Engineering in Medicine and Biology*, (Shanghai:IEEE), 5392–5395.

Wu, M., Wei, Z., Tang, L., Su Y., and Liu T. (2008). An EEG signal analysis method based on sparse representation model. *Chin. J. Tissue Eng. Res. Clin. Rehabil.*4, 81–84.

Yang, B., and Li, S. (2009). Multifocus image fusion and restoration with sparse representation. *IEEE Trans. Instrument. Meas.*59, 884–892. doi: 10.1109/tim.2009.2026612

Yang, H., Sakhavi, S., Ang, K. K., and Guan, C. (2015). On the use of convolutional neural networks and augmented CSP features for multi-class motor imagery of EEG signals classification. *Conf. Proc. IEEE Eng. Med. Biol. Soc.*2015:2620–2623.

Yang, Y., Yu, Z. L., Gu, Z., and Zhou, W. (2012). "A new method for motor imagery classification based on Hidden Markov Model," in *Proceedings of the 7th IEEE Conference on Industrial Electronics and Applications (ICIEA)*, (Singapore: IEEE), 1588–1591.

Yin, W., Yang, X., Zhang, L., and Oki, E. (2016). ECG monitoring system integrated with 42IR-UWB radar based on CNN. *IEEE Access*4, 6344–6351.

Zhou, W., Yang, Y., and Yu, Z. (2012). "Discriminative dictionary learning for EEG signal classification in Brain-computer interface," in *Proceedings of the 12th International Conference on Control Automation Robotics & Vision (ICARCV)*, (Guangzhou: IEEE), 1582–1585.

Conflict of Interest: The authors declare that the research was conducted in the absence of any commercial or financial relationships that could be construed as a potential conflict of interest.

frontiers in Neuroscience

ORIGINAL RESEARCH
published: 22 October 2020
doi: 10.3389/fnins.2020.595084

Rehabilitation Treatment of Motor Dysfunction Patients Based on Deep Learning Brain–Computer Interface Technology

Huihai Wang, Qinglun Su, Zhenzhuang Yan, Fei Lu, Qin Zhao, Zhen Liu and Fang Zhou*

Department of Rehabilitation Medicine, The First People's Hospital of Lianyungang, Lianyungang, China

In recent years, brain–computer interface (BCI) is expected to solve the physiological and psychological needs of patients with motor dysfunction with great individual differences. However, the classification method based on feature extraction requires a lot of prior knowledge when extracting data features and lacks a good measurement standard, which makes the development of BCI. In particular, the development of a multi-classification brain–computer interface is facing a bottleneck. To avoid the blindness and complexity of electroencephalogram (EEG) feature extraction, the deep learning method is applied to the automatic feature extraction of EEG signals. It is necessary to design a classification model with strong robustness and high accuracy for EEG signals. Based on the research and implementation of a BCI system based on a convolutional neural network, this article aims to design a brain–computer interface system that can automatically extract features of EEG signals and classify EEG signals accurately. It can avoid the blindness and time-consuming problems caused by the machine learning method based on feature extraction of EEG data due to the lack of a large amount of prior knowledge.

Keywords: rehabilitation treatment, motor dysfunction patients, deep learning, brain–computer interface technology, EEG

OPEN ACCESS

Edited by:
Yizhang Jiang,
Jiangnan University, China

Reviewed by:
Juan Yang,
Suzhou University, China
Yuanpeng Zhang,
Nantong University, China

****Correspondence:***
Qinglun Su
18961325969@163.com

Specialty section:
This article was submitted to Neuroprosthetics, a section of the journal Frontiers in Neuroscience

Received: *15 August 2020*
Accepted: *08 September 2020*
Published: *22 October 2020*

Citation:
Wang H, Su Q, Yan Z, Lu F, Zhao Q, Liu Z and Zhou F (2020) Rehabilitation Treatment of Motor Dysfunction Patients Based on Deep Learning Brain–Computer Interface Technology. Front. Neurosci. 14:595084. doi: 10.3389/fnins.2020.595084

INTRODUCTION

Brain–computer interface (BCI) is a communication control system established between the brain and external devices (computers or other electronic devices) through signals generated by brain activity. The system does not depend on muscles and nerves other than the brain and establishes direct communication between the brain and the machine (Wang et al., 2020). It is a new, high-end way of human–computer interaction. The complete BCI system includes four parts: signal acquisition part, the feature extraction part, pattern recognition part, and control command output part (Turgut et al., 2018). The brain's thinking activity mainly depends on the central nervous system. When human beings carry out different thinking activities, the neural activity patterns in the brain are altered, and the signals generated by the neural activity are different. In theory, the BCI system can monitor the signals generated by neural activities through a variety of sensors and other signal acquisition equipment. Through the analysis and processing of the signals, that

is, feature extraction and pattern recognition in the following section, the signals are classified according to separate thinking activities to generate corresponding control commands to complete the interactive tasks between users and external devices. Feedback is not necessary. It is usually used in online BCI systems so that users can see their thinking corresponding to the control results as shown in **Figure 1**. If the consequences are different from expectations, users can adjust their thinking in time and have a better user experience.

The activities of the nervous system in the brain are very complex, including electrophysiological activities, neurochemical reactions, and metabolic phenomena in the central nervous system, such as action potential, postsynaptic potential, neurotransmitter release, oxygen metabolism, and so on. During this period, there are a variety of signals, including electrical signals, magnetic signals, chemical signals, and so on. According to the way of signal acquisition, the BCI system can be divided into two categories: intrusive and non-invasive (Arndt et al., 2017). For the detection of chemical signals, such as the changes of oxygenated hemoglobin or other physiological parameters, it is generally necessary to use an invasive BCI system, that is, to record signals in the brain by implanting sensors into the skull. For magnetic signal detection, magnetoencephalography (MEG) (Zesiewicz et al., 2018) can be utilized, which is a non-invasive device, but it has the advantages of large size, high price, and low time resolution. For the detection of electrical signals, there are two commonly used methods: electrocorticogram (electrocorticography) and electroencephalogram (EEG). Among them, electrocorticogram is an invasive acquisition method (Earnshaw et al., 2019; Levy et al., 2019; Tian et al., 2019), which extracts electrical signals from the cortex by implanting a microelectrode array into the cerebral cortex. The amplitude of the signal extracted by this method is large and the signal-to-noise ratio is high, but because of the craniotomy. The risk coefficient is high. EEG is a non-invasive acquisition method, which detects weak EEG signals by placing electrodes on the scalp, filters and amplifies them, and records the changes of scalp electrical signals during brain nerve activity. The equipment is light and portable, the price is relatively low and easy to operate, but because the process of EEG transmission from the cerebral cortex to the scalp will be greatly weakened, the signal-to-noise ratio of the extracted signal is very low, which increases the difficulty of subsequent feature extraction. At present, the most studied BCI system is the one which collects scalp EEG as the source signal in a non-invasive way. With the continuous maturity of BCI, the BCI system will gradually come into people's everyday life. Considering multiple factors such as dangerous, maneuverability, price, and so on, collecting EEG through wearable equipment will become the main development direction of this technology and get the most extensive application.

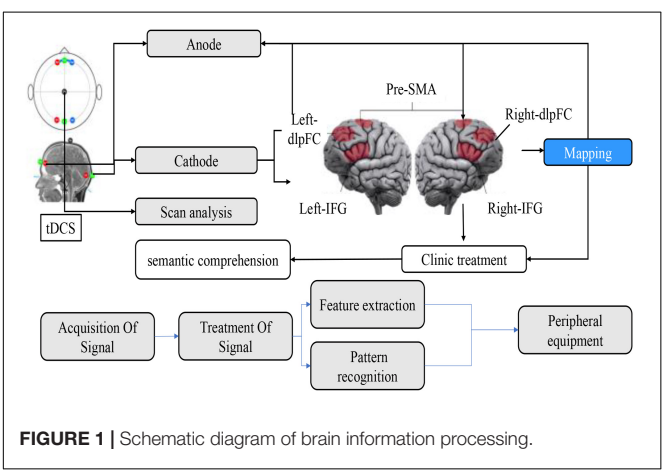

FIGURE 1 | Schematic diagram of brain information processing.

Although human beings have mastered some knowledge about medicine, physiology, and pathology of the brain, for such a complex brain, these are only the tip of the iceberg; anthropological understanding of the brain is not very clear. Through the study of BCI and the analysis of the signals generated by the human brain, it can indirectly help human beings to explore the brain and understand the structure, working principle, and cognitive law of the brain. The knowledge obtained can not only promote the study of the brain–computer interface in turn but also be combined with other scientific directions such as computer and chemistry to promote the development of related disciplines. For example, the law of human brain vision cognition obtained through the study of vision-evoked brain–computer interface has inspired researchers to improve computer vision models and greatly promoted the research progress in the field of machine vision. CI technology is widely used in the medical field, mainly focused on the research and development of medical rehabilitation aid. For patients with epilepsy, a medical device can be designed to identify abnormal brain activity (Shulman et al., 2020). When abnormal brain activity is detected, a pulse signal is directed to destroy the prerequisite for seizures. For patients with insomnia, wearable devices can be developed to improve sleep quality (Drew et al., 2017), to understand the current sleep state by detecting EEG and to introduce auditory stimulation to guide patients into a deep sleep. For people with muscle paralysis, devices such as wheelchairs or robotic arms controlled by EEG signals can be improved to help people with motor disabilities complete movements that they cannot achieve and improve their ability to take care of themselves. Based on the research and implementation of a brain–computer interface system based on a convolutional neural network, this article aims to design a brain–computer interface system that can automatically extract features of EEG signals and classify EEG signals accurately. It can avoid the blindness and time-consuming problems caused by the machine learning method based on feature extraction in feature extraction of EEG data due to the lack of a large amount of prior knowledge. The purpose of this article is to explore the extension of the intense learning method to the field of brain–computer interface. The classification and recognition of EEG signals are the core focus of the development of BCI. Without the classification of EEG signals, the development of BCI is impossible. Therefore, to explore how to use the innate learning method to design an efficient classification model for the classification and recognition of EEG signals under the new situation is helpful to promote

the development of BCI (Jiang et al., 2017). At the same time, exploring the classification method of EEG signals based on a multilayered neural network plays an important role in promoting the practicality of the brain–computer interface. In this article, the left-handed and right-handed motor imagination EEG classification model based on convolution neural network developed by Google machine learning framework contraflow achieves 75.3% classification accuracy on the test set of BCI Competition IV common data set, Data set 2b, and it can be transplanted to mobile phones, computers, tablets, and other terminal devices, used in brain–computer interface technology, in medical rehabilitation in the field of healthcare. For some, physical disabilities but normal brain function, such as muscle atrophy, spinal injury, and limb paralysis, provide a certain degree of convenience in life.

The rest is organized as follows. In Section 2, we review some related works. In Section 3, we state our data and method. In Section 4, we show the experimental results and discuss the results. Lastly, we conclude our study and indicate our future studies.

RELATED WORK

Classification of EEG Signals Based on Machine Learning Method of Feature Extraction

In 1990, Kole proposed the common space template (CSP) method based on the eigenfunction method of Hjorth and Rodin. Kole uses the CSP method to process EEG data, which can distinguish whether the tested object is a patient or not. The accuracy of the test results is between 71% and 85%. Based on Kole's proposal, Gerking, Herbert, and Ramoser put forward the method of solving the optimal value of the spatial template (Ferragut-Garcías et al., 2017). In 2010, Subasi used a new classification method based on his original research results, absorbed the support vector machine (SVM) theory, and introduced independent principal component analysis (ICA), principal component analysis (PCA) and other methods in feature extraction. The accuracy of EEG classification has been improved to more than 98%. In 2011, Deepa used a combination of instance-based (IB1) and alternating decision tree (tree) to classify human EEG signals, using EEG energy data calculated by GS-FHT method, and Chebyshev filter was used for initial signal processing. Deepa confirmed that using the GS-FHT method is 3–4% points more accurate than the FHT method used. Wu Linshang and others have done a lot of research in this area, which shows that in extracting the features of the data, through the CSP (ordinary spatial pattern) method, when classifying the data, the LDA (linear recognition analysis) method is used to get about 80% of the 2 classification results of the motion imagination data. Huang uses the feature extraction methods of surface Laplace transform (SLD) and power spectral density (PSD), combined with the classification method of support vector machine (SVM) to recognize motion imagination EEG data, and applies its results to the control of the two-dimensional mouse. We used a common spatial pattern (CSP) for feature extraction, then used linear discriminant (LDA) for motion imagination data classification, and achieved good results.

Classification of EEG Signals Based on Deep Learning Method

In recent years, with the arrival of the big data era and the popularity of GPU parallel computing, deep learning has received unprecedented attention, and its related theories have been continuously improved and developed. Nowadays, the model built by deep learning method has won the championship in many competitions between pattern recognition and machine learning and has brought breakthroughs in the fields of image recognition, speech recognition, and natural language processing. Deep learning is developed from machine learning and is very good at automatic feature extraction from complex unstructured data. In the early days of artificial intelligence, traditional algorithms such as logical regression and Bayesian classification already have the ability of machine learning, but these algorithms do not learn from the original data but require manual feature representation of the input data. For example, for the problem that the input is X and the expected output is Y, the researchers should first design the Feature (X), and then learn the mapping F from the traditional algorithm to make the Y-shaped feature F. The disadvantages of this kind of methods are obvious, and how to extract the features effectively has become a new problem to be solved. On this basis, representation learning arises at the historic moment (Pin-Yeh and Qiang, 2017). For the problem that the input is X and the expected output is Y, the mapping function is constructed, and the features that need to be extracted manually are also automatically learned by the algorithm through machine learning. Self-encoder belongs to this kind of algorithm, this kind of calculation not only saves manual time and energy, but also the features obtained often have better expression performance than those selected by hand. For some very complex problems, the shallow features obtained by learning can no longer meet the needs of the problem, so deep learning begins to develop. This kind of method constructs complex features through simple features, abstracts them step by step, and finally extracts the high-level features that can solve the problem through multi-layer representation, that is, the process of solving the problem. Although the increase of depth makes the deep learning algorithm have more powerful feature representation ability, it also makes the process of training optimization easily fall into the local extremum and produce the phenomenon of gradient disappearance, and the effect is not ideal. BP network is an example. Later, Hinton and others put forward the concept of deep belief network in 2006, successfully introduced the pre-training process and fine-tuning technology, and used greedy strategy to train the deep architecture composed of restricted Boltzmann machine layer by layer (Barfod et al., 2020; Smith et al., 2020), which not only solved the convergence problem of the depth model but also greatly reduced the time needed for deep network training, which started the wave of deep learning. Nowadays, researchers all over the world have done a lot of research in this field, and deep learning algorithms have been greatly expanded and developed, including convolutional neural networks, cyclic neural networks, stacked self-coding networks,

and deep belief networks. Deep Boltzmann machines have made breakthroughs and have been widely used in different fields. Combined with the characteristics of EEG signals, this article chooses a convolution neural network (convolutional neural networks, CNN) and long-term short-term memory circulation neural network (long short-term memory networks, LSTM) for in-depth research. The following article will focus on the principle, advantages, and reasons for choosing this algorithm.

The convolution neural network model is the first neural network based on the concept of the local receptive field constructed by Fukushima in 1984. This model is inspired by the process of human visual abstraction and is widely used in image and video recognition. In the 2012 Image Net competition, previous work won the competition by relying on the five-layer convolution network model Alex Net constructed by the convolution neural network algorithm and achieved a good result of 1000 classification error rate of 100000 images with an error rate of 15.3% (Zhang et al., 2017). In recent years, through the continuous efforts of a large number of researchers and improving the 152-layer Res Net model designed by He K and others, the error rate has been reduced to 3.6% (Kubota et al., 2019), which makes the image recognition ability of machines surpass that of human beings. In Telles et al. (2019), Deng et al. used CNN to extract different kinds of features from EEG signals. A complete convolution neural network model usually consists of an input layer (picture), multiple alternating convolution layers and pooling layers, a full connection layer, and a final output layer. And the distributed system for the neural network process timing sequence can be seen in **Figure 2**.

The structure of a neuron in the neural network model is shown in **Figure 3**. The first difference between the convolution neural network and the traditional neural network lies in the choice of the activation function σ. In the traditional neural network, σ is usually selected as the sigmoid function or tanh function, while the activation function σ of the convolution neural network is the real function.

Additionally, some deep ensemble methods are also used for EEG classification. For example, Zhang et al. (2019d) proposed a deep view-reduction TSK fuzzy system for epileptic EEG signals recognition. It is a deep ensemble method in which 0-order TSK fuzzy systems are linked in a stacked manner so as to improve the classification performance.

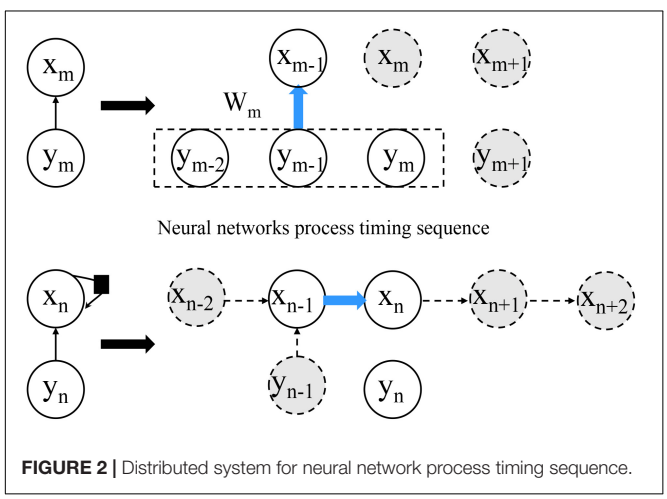

FIGURE 2 | Distributed system for neural network process timing sequence.

Research on Visual Driving Potential System

Visual evoked potential (VEP), also known as visual evoked potential (VEP), is one of the evoked BCI EEG signals. Its principle is to produce measurable potential changes in the visual cortex through visual stimulation (flicker stimulation, change of stimulus brightness, color alternation, etc.). According to the frequency of stimulation, VEP can be divided into transient evoked potential (transient visual evoked potential, TVEP) and steady-state evoked potential (steady state visually evoked potentials, SSVEP). The frequency of TVEP stimulation is low, and the next stimulation will not be carried out until the response produced by a single stimulation in the cerebral cortex disappears, while the stimulation frequency of SSVEP is high, and the next superimposed stimulation will be carried out directly before the response produced by a single stimulation in the cerebral cortex has disappeared (Bober et al., 2018; Whyte et al., 2019). In the BCI system with VEP as the paradigm, there are more researches on the use of SSVEP stimulation, and the system of this paradigm is also the fastest among the non-invasive BCI systems at present. American Calhoun G.L. Using steady-state visual evoked potentials to complete the task of brainwave control to simulate aircraft (Jiang et al., 2017; Zhang et al., 2019b,d) the BCI system based on the SSVEP paradigm developed by, previous work realized the functions of the mind control switch, mobile dialing and so on (Lopes et al., 2017). Because the stimuli and visual evoked potentials have the same rhythm, it is easier to determine the subjects' gaze commands, the EEG signals generated by this paradigm have good stability, high signal-to-noise ratio, and a large number of identifiable classifications. However, this paradigm requires subjects to look at the screen for a long time, which is easy to feel tired, and the scheme needs to select targets with the help of the subjects' eye movements, so it cannot be applied to blind and completely paralyzed patients. The evoked potentials generated based on the SSVEP paradigm were distributed in the occipital lobe of the scalp, the frequency was between 1 Hz and 300 Hz, and the duration was about 200 ms (Skolasky et al., 2020). The evoked potentials were recorded with 1 to 8 electrodes. The EEG power spectrum analysis method commonly used in the single-lead acquisition is (Power Spectral Density, PSD) to extract frequency domain features (Zhang et al., 2018, 2019a, 2020a; Zhao et al., 2019; Zheng et al., 2019), and the typical correlation analysis method (canonical correlation analysis, CCA) in multi-lead acquisition EEG is commonly used to extract spatial features (Pereira et al., 2019). Before feature extraction, it is necessary to filter and fuse the original EEG signal to improve the signal-to-noise ratio (Stan et al., 2019). We use wavelet denoising for preprocessing, and the processing process of pattern classification by CCA achieves 85% accuracy in four classifications. Literature (Dong et al., 2017) adds the processing step of channel selection, which increases the accuracy to 87.5%. Literature (Bai and Fong, 2020) proposes a method of

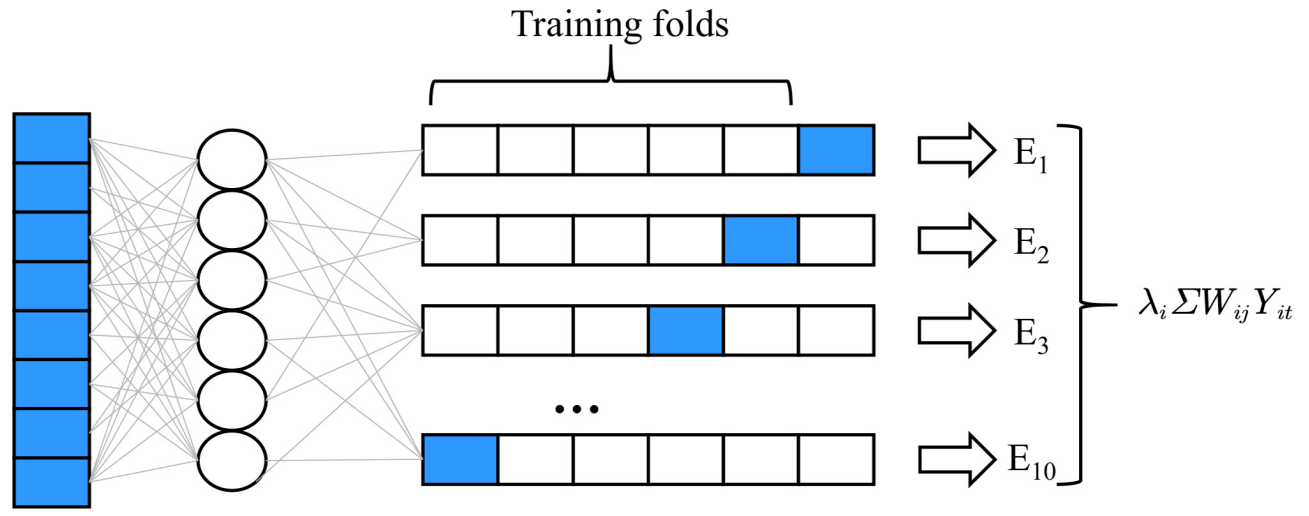

FIGURE 3 | The structure of a neuron in the neural network model.

combining independent component analysis with Hilbert-Huang transform, which can effectively extract features but takes a long time. Literature (Schneider et al., 2017) uses principal component analysis to improve CCA to ensure accuracy and improve the speed of signal recognition at the same time. Previous work (Bober et al., 2020) uses a wavelet packet to improve CCA as shown in **Figure 4**, which improves accuracy by about 5% and gets 82% accuracy. In the literature, a power spectrum Gaussian method based on empirical mode decomposition is proposed to achieve 84% accuracy.

Convolutional Network and Recurrent Neural Network

Convolution Network

The traditional fully connected network has many disadvantages. Taking the problem of image recognition as an example, if we take a picture of 1000 × 1000 pixels as the input of the network and set the number of neurons in the first hidden layer to 100, then only the first layer has 100 biases (b) and 100000000 weights (w) need to be trained, the number of parameters of the network is too many, the training is extremely difficult. On the other hand, the convolution network makes full use of the correlation difference of image pixels in different positions and adopts three methods: local receptive field, weight sharing, and downsampling, which provides an effective solution to the problem of image recognition. For the pixels in the picture, the relationship between the adjacent pixels is larger, and the relationship between the distant pixels is smaller, so it is not necessary to connect the neurons with each pixel in the input image. We only need to connect the local of the previous layer, scan and extract the features in blocks, and then synthesize the local features at a deeper level to get the global features. This process is very similar to the visual process. In the human visual system, each neuron corresponds to a part of the visual domain. In the convolution model, each convolution nucleus is only connected to the part of the neurons in the previous layer to extract a local feature. The connection between neurons through the local receptive field has reduced the parameters by a large part, and weight sharing can further reduce the number of parameters. Take the input picture of 1000 × 1000 pixel as an example, if the convolution kernel size of the first layer is 10 × 10, the meaning of weight sharing means that the weight of 10 × 10 on the convolution kernel is the same to the 1000 × 1000 input layer neurons, that is, there are only 100 parameters of the weight, and the weight trained in a certain location is still valid in other locations. In theory, the features extracted by the convolution kernel can be directly used in the training of the classifier, but the high dimension of the feature vector is not conducive to training, and it is easy to produce over-fitting phenomenon. The convolution network puts forward the process of adding downsampling after convolution, and aggregates and statistics the features of different locations. This process, also known as pooling, can not only reduce the dimension of features to improve training efficiency but also prevent overfitting. The specific pooling methods include maximum pooling, average pooling, and so on. The maximum pooling only retains the maximum value of the pooling window, while the average pooling retains the average value of the pooling window. Although the convolution neural network model is inspired by the visual abstraction process and has made brilliant achievements in the field of picture recognition and computer vision, however, this does not mean that convolution neural networks can only be applied to the recognition and processing of vision-related signals such as pictures and videos. Through the above analysis of the principle and method of the convolution neural network model, it is reasonable to think that the model can also be applied to the feature extraction and classification of EEG signals. Because the convolution neural network model is proposed for the problem of taking pictures as input, the structure of the model is very beneficial to the feature extraction and classification of two-dimensional or multi-dimensional matrix inputs. The EEG

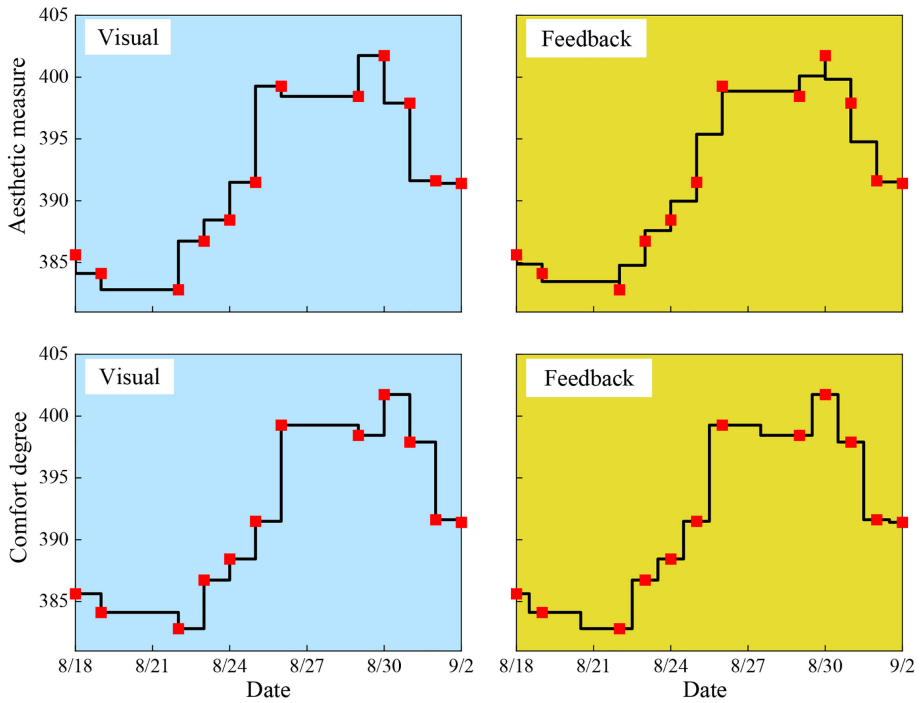

FIGURE 4 | The visual and feedback signals for different dates.

signal collected by the subject is two-dimensional matrix data, which satisfies the input form of a convolution neural network. The use of convolution network not only solves the training difficulties caused by the high dimension of EEG signals but also gives full play to the shape advantage that EEG signals are two-dimensional matrix (Zhang et al., 2016, 2019c, 2020b; Polkey et al., 2018). The structure of the network model is very clear. The convolution network uses the local receptive field to solve the problem of too many parameters of the network. The premise of this method is that the closer the pixel in the picture is, the larger the relationship is, and the farther the distance is, the smaller the relationship is. If the cerebral cortex is regarded as a picture, and the voltage collected by the electrode placed on the cortex is regarded as a pixel, then the EEG signal has a position relationship similar to that of the picture pixel. Therefore, the method of the local receptive field in the convolution network can be used to process EEG signals without losing features (Pavlova et al., 2017). The weight sharing strategy adopted by the convolution neural network makes the network translation invariant, which is shown in the picture, although the extracted feature position has changed after the translation operation of a picture. But the network can still correctly identify the picture. It is shown in the EEG that if the electrode cap used in the collection is not worn, there is a deviation in the distribution position of the conductive electrode, or due to the slow response of the subjects, the acquisition equipment is not sensitive and other factors such as time-shift (Kim et al., 2019) will not affect the classification results of EEG signals. This is consistent with the actual demand, so the weight sharing strategy in the convolution network is also suitable for EEG signal processing. The pooling layer in the convolution network reduces the feature dimension extracted by the convolution layer and aggregates the features in different positions of the image. According to the calculation principle of average pooling, it is known that this method makes the network have certain distortion invariance, that is, a certain amount of distortion operation on the input image will not affect the recognition of the image. The EEG signal has the characteristics of high noise and strong randomness. The motion imagination EEG signal of different people or even the same person at a different time is different every time. Pooling operation can filter noise and increase the robustness of the algorithm to a certain extent. To sum up, although EEG is a voltage signal and image is pixel information, they have many common characteristics, they can share local information, and the features and features are homogeneous. Also, the convolution neural network algorithm has the advantages of fast training speed and strong ability of spatial feature extraction, so the convolution neural network algorithm (CNN) is selected for an in-depth study of MI EEG signals.

Recurrent Neural Network

The recurrent neural network (RNN) model was proposed by Paul Werbos in 1988. To better deal with the sequence data, the concept of loop is added to the structure to persist the information. The unique loop structure of the algorithm enables the network to remember the previously input information and apply the useful information in the memory to the calculation

of the subsequent output, which is very suitable for text, voice, and video. This model has made great achievements in many fields of time series analysis, such as speech recognition, natural language processing, machine translation, and so on. It is called the two most popular deep learning algorithms together with a convolution neural network.

The core of the RNN model lies in the ring structure on the left side, which expands the network in the timing direction and can learn the sequential relationship between the input samples by itself. In RNN, the input X of each hidden layer meets the following conditions:

$$\Phi(Y) = \sum_i \left(\sum_j w_{ij} X_j - X_i \right)^2 \tag{1}$$

$$x_i^{k+1} = \sum_j w_{ij} x_j^k \tag{2}$$

$$x_i^{k+1} = \frac{2}{D_s} \sum_j w_{ij} x_j^k \tag{3}$$

where x_j represents an element of X_j, w_{ij} represents the weight between x_i and x_j. It can be seen in **Figure 5** that the network can theoretically look forward to any number of input nodes, but in the actual deep learning project, the basic cyclic neural network model cannot well deal with long input sequences. The main reason is that in the backpropagation training process of the RNN network loop layer, the longer the input sequence, the faster the error increases or decreases, and the corresponding problems such as gradient explosion or gradient disappearance lead to the network cannot be trained. To solve this problem, a large number of scholars have improved the basic RNN model, among which the most successful one is the long-term and short-term memory network model (LSTM), which was proposed by Hochreiter and Schmidhuber in 1997. It not only perfectly solves the problem of long-term dependence, but also improves the speech recognition performance of Google by nearly 50%.

DATA AND METHODS

Data

The EEG signals used in this subject are from the BCI competition in 2005 and the other part is collected by the laboratory itself. The selection of subjects will have a certain impact on the universality and reliability of the experimental results. The EEG signals used in this study come from 2 women and 3 men, respectively. The subjects are all healthy, mental, and right-handed students. According to the previous physiological knowledge of cerebral cortical division, we can know that the cerebral cortex activated by imagining hand movement is larger and easier to detect, so this experiment stipulates that the subjects' imagination task is left-hand finger movement and right-hand finger movement. Because of the characteristics of low signal-to-noise ratio, strong randomness, some matters must be paid attention to in the process of EEG acquisition.

Electroencephalogram signals are affected by blood glucose factors, so subjects are not recommended to conduct experiments on an empty stomach or in a full stomach, as shown in **Figure 6**. The subjects should wash their hair in advance. Too much scalp oil will lead to excessive scalp resistance and distortion of the acquisition waveform. EEG signals are extremely weak and easy to interfere with, so the process of data acquisition should be far away from electromagnetic interference and ensure a quiet collection environment. Internal factors can also be the interference source of EEG signals, so subjects should not carry out any exercise in the process of collection, keep muscles relaxed and minimize blinking, eye movement, saliva swallowing and other behaviors, to reduce the interference of EMG and ophthalmogram. The acquisition process of BCI competition is described as follows: subjects sit quietly in front of a computer wearing an electrode cap and imagine the movement of their left hand, right hand or right foot according to the on-screen graphics. Each subject had a total of 280 exercise imaginations, of which 140 were left and right.

In the experiment, the EEG voltage of the scalp was collected with a 118 conductive electrode cap. The position distribution of

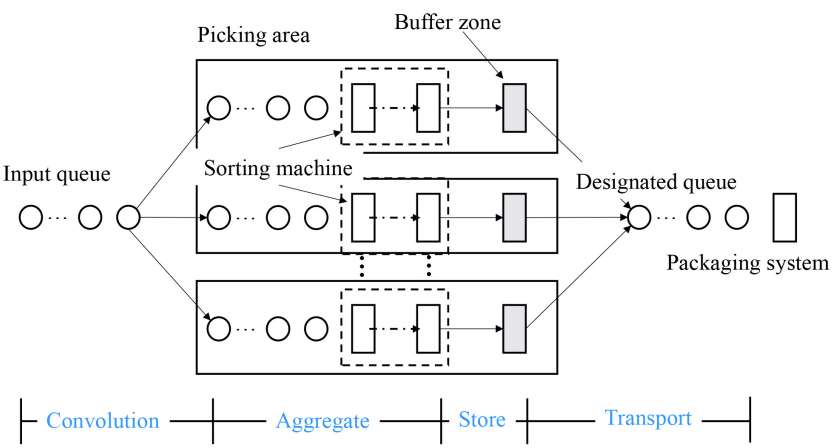

FIGURE 5 | Distributed system for aggregation timing sequence.

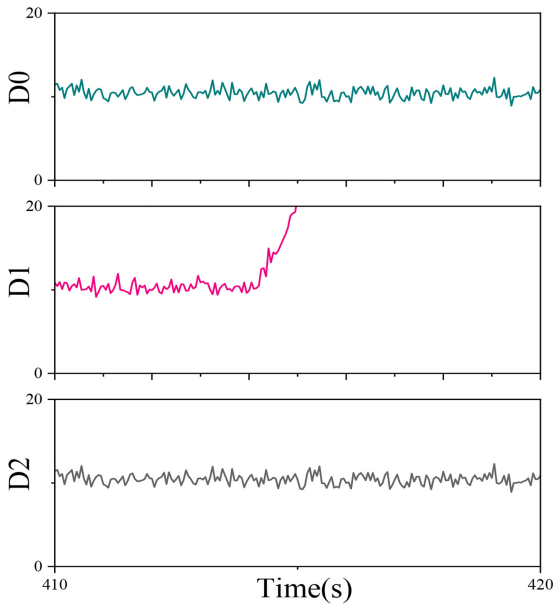

FIGURE 6 | Communication module for different sensors.

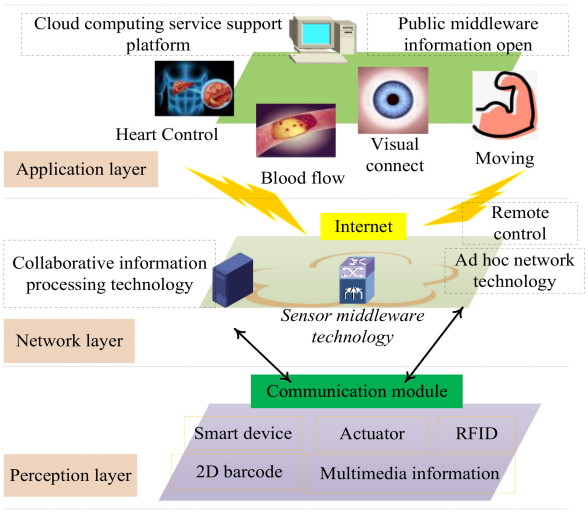

FIGURE 7 | Distribution 0–2 (D0, D1, D2) changes with time.

the 118 conductive electrodes in the cerebral cortex was shown above. The acquisition frequency was 100 Hz. The EEG signals of all the above processes were collected by the system, so the obtained EEG signals were five matrices with 118 rows 280 mm 7 columns, among which the effective EEG signals of each subject for motor imagination task were 118 rows 280 mm 3.5 column matrices. The EEG data collected by the laboratory use different acquisition equipment, and the rest of the process is similar to the above description, but only imagine the movement of the left and right fingers and use fixed arrows to minimize the eye movement interference of the subjects. The equipment used in the laboratory conducts electricity as much as 32 conductors, and the acquisition frequency is 250 Hz. Although the acquisition equipment is different, the principles of data preprocessing, classifier design and training are all the same. Therefore, in the latter description, all of them take BCI competition's 118derivative data set as an example to explain the preprocessing and classifier network structure, and the operation process of 32-lead data is similar.

Methods

Physiological Basis of Brain–Computer Interface

The structure of the human brain can be divided into left and right hemispheres, and each hemisphere can be divided into four lobes according to its location, namely frontal lobe, temporal lobe, parietal lobe, and occipital lobe. The lobar region contains nerve centers that can undertake different tasks, thus forming a phenomenon of zoning specialization in the cerebral cortex.

In the different regions of the cerebral cortex, the somatic motor area and somatosensory area are closely related to motor imagination as shown in **Figure 7**. The somatosensory area is located in the frontal lobe near the central sulcus, which is mainly used to control the movement of the contralateral body. The somatosensory area is located in the parietal lobe near the central sulcus, which is mainly used to receive the sensation of the contralateral body. Although the subjects do not have real body movement in the process of motor imagination, the phenomena and characteristics that occur in these two regions are the same. There are mainly the following three points: (1) The two regions control and feel the contralateral body, that is, the somatomotor area of the left brain controls the movement of the right half of the body, and the somatosensory area of the left brain feels the sensation of the right half of the body, and vice versa. (2) The two areas control and feel the inverted body, that is, the upper part of the body motor area controls the movement of the lower limbs, the middle controls the movement of the upper limbs, the lower part controls the movement of the head, and so does the somatosensory area. (3) The area of different parts of the body mapped to the two areas is inversely proportional to the degree of flexibility and sensitivity of the part. For example, the hand and mouth can complete very complex movements, and their flexibility is much higher than that of the torso. Therefore, their area in the body movement area will be much larger than that of the torso.

There are more than 100 billion neurons in the human brain. When humans are thinking, these neurons will produce synchronous discharges. These potential changes can be collected by placing electrodes on the scalp, which is called EEG signals. The signal can be regarded as the superposition of waves with different frequencies, amplitudes, and phases produced by a large number of neurons. Brain waves can usually be divided into δ waves, θ waves, α waves, β waves, and γ waves. Because the EEG generated by motor imagination belongs to spontaneous EEG, and the frequency of spontaneous EEG is generally between 1 Hz and 30 Hz, so the γ wave can be filtered out directly without considering γ wave in BCI research. Among the five kinds of brain waves mentioned above, the α wave and β wave are closely related to the study of BCI. Specifically, they are the alpha wave

in the middle-frequency band (mu rhythm) and the β wave that appears near the central sulcus. The frequency of mu rhythm is about 10 Hz, if classified according to frequency and amplitude, it can be classified as α wave, but mu rhythm has nothing to do with the state of eye closure, it is a kind of EEG signal which is closely related to somatic motor area. B waves are distributed near the frontal lobe and central sulcus, but the β waves related to mu rhythm often appear near the central sulcus (Mudiganty et al., 2017; Torres-Rodríguez et al., 2018; van Yperen et al., 2018). Therefore, in the study of BCI, we usually focus on the β waves near the central sulcus.

Motion-Dependent Synchronization Phenomenon

Event-related synchronous (ERS) / desynchronized (ERD) phenomenon is an electrophysiological phenomenon that can be used as a feature of motor imagination EEG signals. The specific manifestation of ERD phenomenon is as follows: when the unilateral limb is imagined or the real movement occurs, the somatic motor area and somatosensory area of the contralateral cerebral cortex will be activated, and the increase of blood flow and the acceleration of metabolism in this area will occur the decrease of α wave frequency and amplitude (α wave blocking phenomenon) (Belash et al., 2018). Correspondingly, the ERS phenomenon is shown as follows: because the somatic motor area and somatosensory area of the ipsilateral cerebral cortex are not activated, the frequency and amplitude of α wave will increase (Maceira-Elvira et al., 2019). ERD and ERS phenomena are closely related and can influence each other. Studies have shown that once the ERD phenomenon begins to occur in a certain region, it is accompanied by the ERS phenomenon in the adjacent cortex, and with time, the ERD phenomenon will gradually spread to the somatosensory motor areas on both sides. It shows the ERD/ERS phenomenon. C3 is the guide electrode placed in the somatic motor area of the left hemisphere, and C4 is the guide electrode in the somatic motor area of the right hemisphere. It can be seen that during the left-handed motor imagination task, the energy of alpha wave (12 Hz) in the somatic motor area (C4) of the right hemisphere decreased significantly. Also, this phenomenon can be calculated by the quantitative formula (2−1) (Telles et al., 2019), where E is the energy value of the α-wave band after motion imagination, and R is the energy value of the α-wave band before motion imagination. If ERSERD0/ occurs, the ERD phenomenon occurs, otherwise, the ERS phenomenon occurs.

RESULTS AND DISCUSSION

In this section, we will report our experimental settings and results. Our experiments are conducted on a PC with Intel i7-9700 CPU @3.00 GHz, 32G memory, and RTX 1080ti 11G. All parameters in our method are determined by 5-CV.

Rehabilitation Treatment of Motor Dysfunction

The EEG signals in the previous section are classified according to different motor imagination tasks, in which there are 5140,700 samples of imagining left finger movement and imagining right finger movement, and each sample is a matrix with a dimension. First of all, we make an intuitive time-domain analysis of the EEG signal, and in this process, by observing the average voltage of each guide electrode in different experiments, we can roughly judge the effectiveness of the EEG signal. If there is an obvious difference in amplitude or frequency between the EEG data collected in a certain experiment and the EEG data in most experiments, it can be considered that the EEG data is abnormal in the process of collection and is an invalid sample. After the abnormal data are put forward through macroscopic analysis, the specific electrodes can be further analyzed. The C3 conductive pole located in the somatic motor area of the left hemisphere is taken as an example. The primitive EEG signals collected during left-hand movement imagination and right-hand movement imagination are shown below. It can be seen that the event-related synchronization phenomenon (ERS), with the increase of α-wave amplitude at the (CLASS1) C3 electrode during the left-hand motion imagination and the event-related desynchronization phenomenon (ERD), with the decrease of the α-wave amplitude at the (CLASS2) C3 electrode during the right-hand motion imagination, are consistent with the physiological phenomena introduced before.

Then the EEG signal is analyzed in the frequency domain, and the periodic graph method is used to estimate the power spectrum. The Fourier transform of discrete-time series [x (1), x (2), ..., x (n)] is calculated as equation (4), and the power spectral density function P (w) is shown as equation (5). When the signal sequence is of finite length, the expectation and de-limit operation of the omission formula (6) get the periodic graph estimation.

$$P(w) = \sum_i \left(\sum_j w_{ij} X_1 - X_2 \right)^2 \tag{4}$$

$$F(w) = \sum_i q(n) e^{-jwn} \tag{5}$$

$$P(w) = \sum_i \left(\frac{1}{N_i} (x_1 - x_2) \right)^2 \tag{6}$$

The power spectral density obtained from the power spectrum estimation of the 118-channel EEG signal is shown in **Figure 8**. From this image, we can directly see the distribution of EEG signals on 0–50 Hz, but the result is contrary to the theory in above section. In theory, the delta wave at 0–4 Hz is only visible in deep sleep, while the delta wave shown in the picture accounts for a large proportion in the EEG, even exceeding the alpha wave in the 8–14 Hz band as a feature. Thus it can be seen that a large number of low-frequency noise and 50 Hz power frequency interference in the original EEG data collected cannot be directly used for subsequent feature extraction and classification, so we should first carry out pre-processing operations such as noise reduction or reconstruction.

In this experiment, the sampling frequency of the EEG signal is 100 Hz. According to the Nyquist theorem, the maximum frequency retained in this signal is 50 Hz. Combined with the

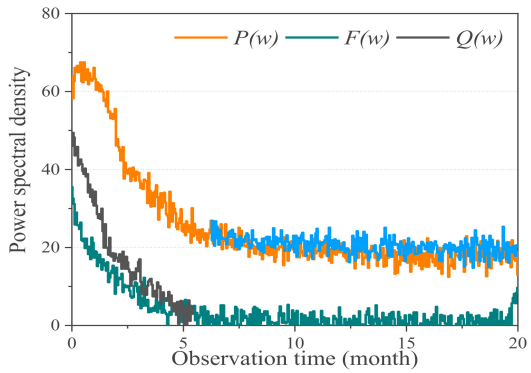

FIGURE 8 | Power spectral density for *P*(*w*), *F*(*w*), and *Q*(*w*).

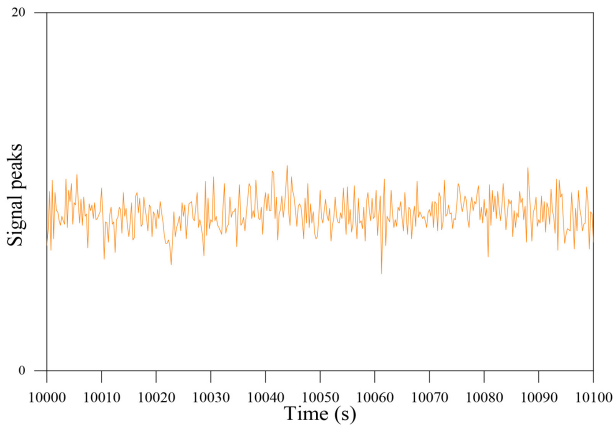

FIGURE 9 | The signal peaks occur after 10000 s.

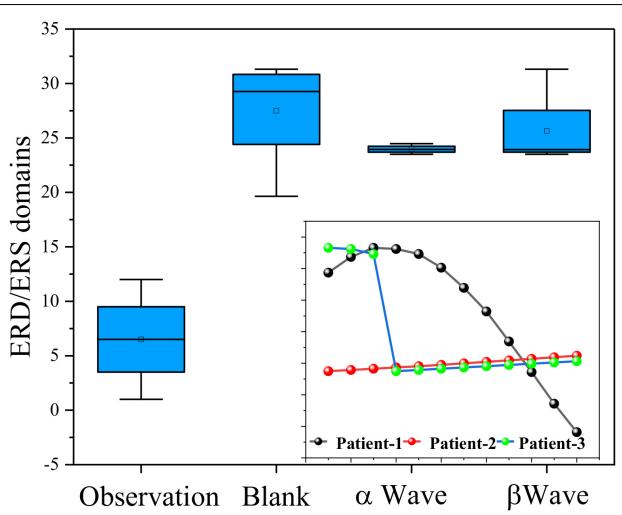

FIGURE 10 | The ERD/ERS domains for α wave and β wave.

classification of 2.1.2 EEG signals according to frequency, the useful information in EEG signals is mainly concentrated in the middle and low-frequency band of 6.5 Hz–25 Hz. The frequency above 25 Hz can be regarded as high-frequency noise, and the frequency below 6.5 Hz has little to do with motor imagination. Therefore, the subject uses the fast algorithm of orthogonal wavelet transform Mallat algorithm for multi-resolution analysis of EEG signals, this algorithm only decomposes the low-frequency part of each layer, and the high resolution in the low-frequency band meets the needs of EEG band classification. After a large number of experiments, the subject uses the db6 function of the Daubechies wavelet system to decompose the original EEG signals in three layers, and the high-frequency and low-frequency parts of each layer are segmented as shown in above section, namely EEG = D1+D2+D3+A3. In the process of EEG reconstruction, only the two main frequency bands, D2 in the second layer and D3 in the third layer, are retained, and the wavelet coefficients of A3 in the low-frequency band and D1 in the first layer are set to 0 to achieve the purpose of noise reduction and enhancement of the signal, as shown in **Figure 9**. Taking the EEG signal collected by the C3 guide electrode during left-hand motion imagination as an example, wavelet analysis is carried out. The decomposed high-frequency coefficient d1murd3 and low-frequency coefficient A1-A3 results are shown above. The delta wave and theta wave between 0 Hz and 6.5 Hz, the α wave between 6.5 Hz and 12.5 Hz, the β wave between 12.5 Hz and 25 Hz, and the γ wave above 25 Hz are reconstructed by wavelet coefficients as shown below.

The above α-wave and β-wave are selected for reconstruction, and the EEG signal with the main frequency band of 6.5–25 Hz is obtained. The EEG signal after the above preprocessing operation is in the frequency domain, and the time domain analysis chart is shown. It can be seen from the picture that the signal is indeed consistent with the prior knowledge in brain theory. There is an obvious ERD/ERS phenomenon in time domain analysis, and the main components in frequency domain analysis are α wave and β wave as shown in **Figure 10**. Therefore, compared with the original data, the EEG preprocessed by wavelet analysis reduces the noise and enhances the features, and can be used for subsequent feature extraction and classification.

Evaluation of Rehabilitation Effect

Through functional electrical stimulation of muscles that are out of nerve control, muscles can contract and can replace or correct the lost motor functions of organs and limbs. Because the nervous system has a certain ability of self-repair and reorganization, according to the principle of human neurophysiology, electrical stimulation of nerves and muscles is used to stimulate afferent nerves and train movement information repeatedly. It will be introduced into the central nervous system, which can form exciting traces in the cerebral cortex and play a great role in promoting the recovery of lost motor function. Limb stroke rehabilitation system is generally divided into upper limb rehabilitation and lower limb rehabilitation, which can be detected by MRI mapping as shown in **Figure 11**. It is very important for the functional rehabilitation of the upper limb, especially for the wrist to complete the activities of the daily life of stroke patients. Therefore, in our experiment, the repeated stimulation of the upper limb is mainly aimed at the wrist flexion

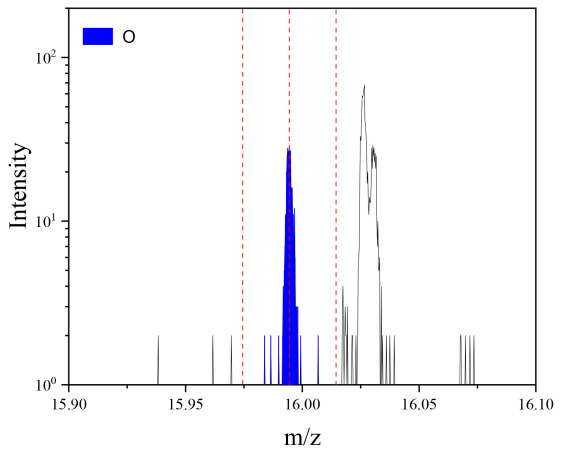

FIGURE 11 | The MRI signal for limb stroke rehabilitation system.

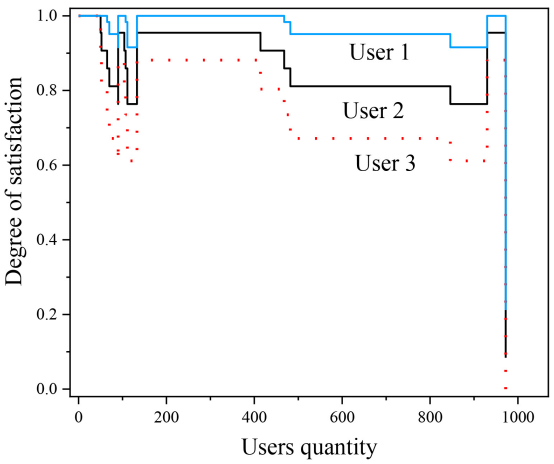

FIGURE 12 | The degree of satisfaction for different users.

and wrist extension, while the lower limb is mainly aimed at the ankle dorsiflexion and metatarsal flexion.

Brain–computer interface technology is a research field that has attracted wide attention and developed rapidly in the past 15 years. With the application of brain–computer interface technology, without relying on the transmission of intermediate neurons, a reliable information transmission channel can be established directly between the brain and external devices, to realize the direct control of EEG information to external devices. By decoding the electrical activity of cortical neurons, brain–computer interface technology provides a new interactive way for people with dyskinesia to acquire the motor ability and environmental control ability. Functional electrical stimulation has been widely used in the field of stroke rehabilitation and has been paid attention to by the majority of rehabilitation workers. Proper FES can cause the contraction of the corresponding muscles, so it can compensate for the lost limb movement. At the same time, the degree of satisfaction for different users is also uploaded to the afferent nerve and finally mapped to the advanced nerve center, which promotes the reconstruction of limb motor function as shown in **Figure 12**. This article makes an exploratory study on the design of a stroke rehabilitation system with the combination of brain–computer interface and functional electrical stimulation, which can show the feasibility of its realization. The EEG signals used in this subject are from the BCI competition in 2005 and the other part is collected by the laboratory itself. The selection of subjects will have a certain impact on the universality and reliability of the experimental results. The EEG signals used in this study come from 2 women and 3 men, respectively. The subjects are all healthy, mental, and right-handed students.

Usually, for stroke hemiplegic patients, they lose the ability of spontaneous movement because the motor nerve cannot receive motor signals, but the muscles they dominate still have the ability of motor contraction, and the upper motor neurons of hemiplegic patients are damaged, losing the ability to control random movement and showing spastic paralysis, but the lower motor neurons are normal, so the pathway exists and has stress function. At this time, appropriate FES can contract the corresponding vision imaging and compensate for the loss of limb motor function as shown in **Figure 13**. At the same time, the stimulation is also uploaded to the afferent nerve and mapped to the higher nerve center through the spinal cord, which promotes the reconstruction of limb function and the recovery of mental state. Too much scalp oil will lead to excessive scalp resistance and distortion of the acquisition waveform. EEG signals are extremely weak and easy to interfere with, so the process of data acquisition should be far away from electromagnetic interference and ensure a quiet collection environment. Internal factors can also be the interference source of EEG signals, so subjects should not carry out any exercise in the process of collection, keep muscles relaxed and minimize blinking, eye movement, saliva swallowing and other behaviors, to reduce the interference of EMG and ophthalmogram. The acquisition process of BCI competition is described as follows: subjects sit quietly in front of a computer wearing an electrode cap and imagine the movement of their left hand, right hand or right foot according to the on-screen graphics. Each subject had a total of 280 exercise imaginations, of which 140 were left and right.

FES can be used for central paralyzes, such as hemiplegia, cerebral palsy, paraplegia, multiple lateral sclerosis of the spinal cord, and paralysis caused by spinal cord injury. It can also be used to relieve pain, treat epilepsy, spinal deformity, urinary incontinence, respiratory dysfunction, but also has the effect of visual aid, hearing aid, and even can be used in midwifery in the process of delivery. For the poor performance of LSTM classifier in the classification of motor imagination EEG signals, one of the reasons for the low accuracy of the test set may be that the experiment did not design a correct network, or did not effectively preprocess the data, wrong preprocessing methods, an insufficient amount of data and so on. Another reason may be that the characteristics of motor imagination EEG itself have little to do with time. Although the imaginative

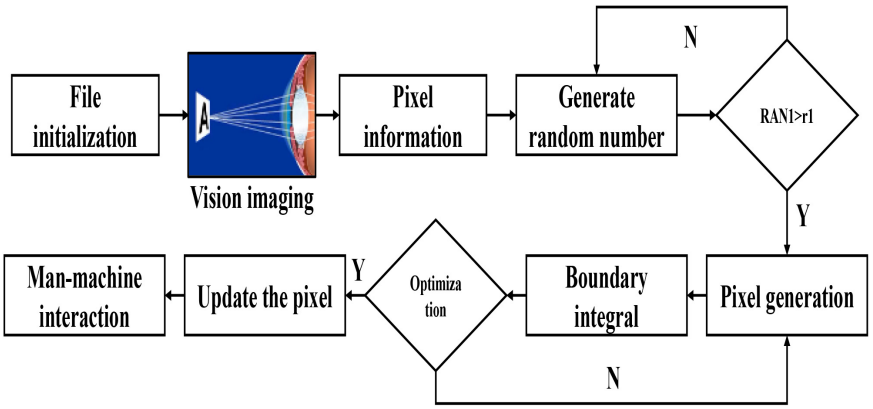

FIGURE 13 | The vision imaging interacted with pixel generation.

process of the subjects was sequential, the original principle of EEG classification by imagining left-handed and right-handed movements was: changes in the energy distribution and intensity of brain waves caused by the ERD/ERS phenomenon in the process of imagination.

$$ERD/ERS = \frac{E - R}{R} \times 100\% \tag{7}$$

That is to say when you imagine the movement of the right hand, the energy in the left brain region increases, and the energy in the right brain region decreases, while when you imagine the left-hand movement, it is just the opposite. These two features are mainly frequency domain features and spatial domain features, while the time domain features are relatively weak, so the classification effect of time series features learned by the LSTM algorithm in the training process is not as obvious as that learned by CNN algorithm. For the phenomenon that the classification accuracy of LSTM classifier when subjects are trained separately is not significantly higher than that when all subjects are trained together, but the accuracy of CNN classifier is quite different under these two methods, this article speculates that the frequency and spatial characteristics of EEG signals may be different because different subjects have different brain shapes and different ways of thinking. There are great differences in many types, such as different active parts of the brain, that is, the characteristics of EEG signals extracted by CNN of single-person network vary from person to person, while the time sequence characteristics of EEG signals are relatively fixed and are not affected by the above-mentioned factors, and the difference may be small among different signal types. The signal intensity for different types can be seen in **Figure 14**. For convolution neural network, the data of different subjects can be trained together because the essence of deep learning is to find commonness in massive data to fit it, so even if there are individual differences in the characteristics of motion imagination among different subjects, the CNN of the multi-person network can also find commonness and extract more universal ERD/ERS features.

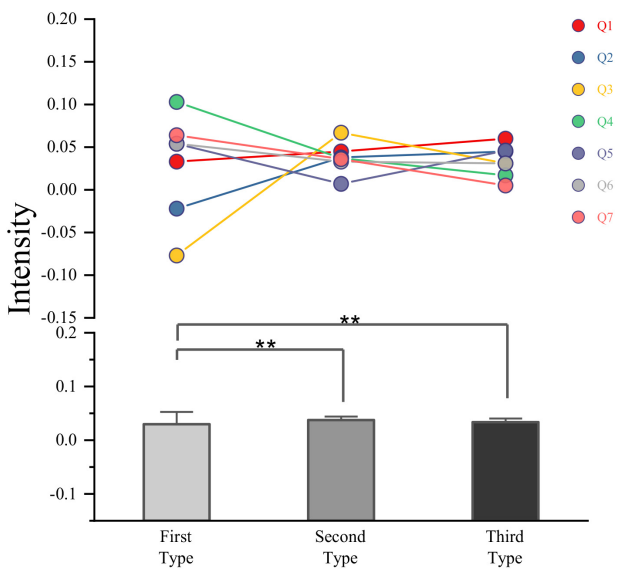

FIGURE 14 | The signal intensity for different types.

CONCLUSION

Electroencephalogram has the characteristics of low signal-to-noise ratio, vulnerable to interference, and obvious differences between different individuals, which makes it difficult for traditional classification methods to find good differentiation and representative characteristics to design a classification model with excellent performance. With the above characteristics, brain–computer interface technology is expected to solve the physiological and psychological needs of patients with motor dysfunction with great individual differences. However, the classification method based on feature extraction requires a lot of prior knowledge when extracting data features and lacks a good measurement standard, which makes the development of brain–computer interface technology. In particular, the development of a multi-classification brain–computer interface is facing a

bottleneck. However, in recent years, with the characteristics of layer-by-layer automatic learning data features, step-by-step abstraction, and good generalization ability, deep learning has achieved great success in the field of image and speech. To avoid the blindness and complexity of EEG feature extraction, the deep learning method is applied to the automatic feature extraction of EEG signals. It is necessary to design a classification model with strong robustness and high accuracy for EEG signals. Based on the research and implementation of a brain–computer interface system based on a convolutional neural network, this article aims to design a brain–computer interface system that can automatically extract features of EEG signals and classify EEG signals accurately. Avoid the blindness and time-consuming problems caused by the machine learning method based on feature extraction in feature extraction of EEG data due to the lack of a large amount of prior knowledge.

This study has several limitations. For example, overfitting often occurs during the classification procedure. Therefore, in our future work, we will try to overcome this problem to improve the generalization ability of our model.

DATA AVAILABILITY STATEMENT

All datasets presented in this study are included in the article/supplementary material.

AUTHOR CONTRIBUTIONS

HW designed the whole algorithm and experiments. ZY, FL, QZ, ZL, and FZ contributed to the code implementation. QS supervised the whole including experiments and manuscript writing. All authors contributed to the article and approved the submitted version.

ACKNOWLEDGMENTS

We thank the reviewers whose comments and suggestions helped improve this manuscript.

REFERENCES

Arndt, S., Laszig, R., Aschendorff, A., Hassepass, F., Beck, R., Wesarg, T., et al. (2017). Cochlear implant treatment of patients with single-sided deafness or asymmetric hearing loss. *Hno* 65, 98–108. doi: 10.1007/s00106-016-0297-5

Bai, Z., and Fong, K. N. K. (2020). Remind-to-move treatment enhanced activation of the primary motor cortex in patients with stroke. *Brain Topogr.* 33, 275–283. doi: 10.1007/s10548-020-00756-7

Barfod, K. W., Hansen, M. S., Hölmich, P., Kristensen, M. T., and Troelsen, A. (2020). ., Efficacy of early controlled motion of the ankle compared with immobilisation in non-operative treatment of patients with an acute achilles tendon rupture: an assessor-blinded, randomised controlled trial. *Br. J. Sports Med.* 54, 719–724. doi: 10.1136/bjsports-2019-100709

Belash, V. O., Mokhov, D. E., and Tregubova, E. S. (2018). The use of the osteopathic correction for the combined treatment and rehabilitation of the patients presenting with the vertebral artery syndrome. *Voprosy Kurortologii Fizioterapii I Lechebnoi Fizicheskoi Kultury* 95, 34–43. doi: 10.17116/kurort20189506134

Bober, S. L., Fine, E., and Recklitis, C. J. (2020). Sexual health and rehabilitation after ovarian suppression treatment (Share-Os): a clinical intervention for young breast cancer survivors. *J. Cancer Survivorsh.* 14, 26–30. doi: 10.1007/s11764-019-00800-x

Bober, S. L., Recklitis, C. J., Michaud, A. L., and Wright, A. A. (2018). Improvement in sexual function after ovarian cancer: effects of sexual therapy and rehabilitation after treatment for ovarian Cancer. *Cancer* 124, 176–182. doi: 10.1002/cncr.30976

Dong, V. A., Fong, K. N. K., Chen, Y.-F., Tseng, S. S., and Wong, L. M. (2017). 'Remind-to-Move' treatment versus constraint-induced movement therapy for children with hemiplegic cerebral palsy: a randomized controlled trial. *Dev. Med. Child Neurol.* 59, 160–167. doi: 10.1111/dmcn.13216

Drew, B. T., Conaghan, P. G., Smith, T. O., Selfe, J., and Redmond, A. C. (2017). The effect of targeted treatment on people with patellofemoral pain: a pragmatic, randomised controlled feasibility study. *BMC Musculoskelet. Disord.* 18:338. doi: 10.1186/s12891-017-1698-7

Earnshaw, V. A., Bogart, L. M., Menino, D. D., Kelly, J. F., Chaudoir, S. R., and Reed, N. M. (2019). Disclosure, stigma, and social support among young people receiving treatment for substance use disorders and their caregivers: a qualitative analysis. *Int. J. Ment. Health Addict.* 17, 11–15.

Ferragut-Garcías, A., Plaza-Manzano, G., Rodríguez-Blanco, C., Velasco-Roldán, O., Pecos-Martín, D., Oliva-Pascual-Vaca, J., et al. (2017). Effectiveness of a treatment involving soft tissue techniques and/or neural mobilization techniques in the management of tension-type headache: a randomized controlled trial. *Arch. Phys. Med. Rehabil.* 98, 211–219. doi: 10.1016/j.apmr.2016.08.466

Jiang, Y., Wu, D., Deng, Z., Qian, P., Wang, J., Wang, G., et al. (2017). Seizure classification from EEG signals using transfer learning, semi-supervised learning and TSK fuzzy system. *IEEE Trans. Neural Syst. Rehabil. Eng.* 25, 2270–2284. doi: 10.1109/tnsre.2017.2748388

Kim, W. S., Lee, K., Kim, S., Cho, S., and Paik, N.-J. (2019). Transcranial direct current stimulation for the treatment of motor impairment following traumatic brain injury. *J. Neuroeng. Rehabil.* 16, 34–45.

Kubota, S., Abe, T., Kadone, H., Shimizu, Y., Funayama, T., Watanabe, H., et al. (2019). Hybrid assistive limb (Hal) treatment for patients with severe thoracic myelopathy due to ossification of the posterior longitudinal ligament (Opel) in the postoperative acute/subacute phase: a clinical trial. *J. Spinal Cord Med.* 42, 517–525. doi: 10.1080/10790268.2018.1525975

Levy, J., Molteni, F., Cannaviello, G., Lansaman, T., Roche, N., Bensmail, D., et al. (2019). Does botulinum toxin treatment improve upper limb active function. *Ann. Phys. Rehabil. Med.* 62, 234–240. doi: 10.1016/j.rehab.2018.05.1320

Lopes, A., Maló, P., Nobre, M. D. A., Sánchez-Fernández, E., and Gravito, I. (2017). The Nobelguide§All-on-4§treatment concept for rehabilitation of edentulous jaws: a retrospective report on the 7-Years clinical and 5-years radiographic outcomes. *Clin. Implant Dent. Relat. Res.* 19, 233–244. doi: 10.1111/cid.12456

Maceira-Elvira, P., Popa, T., Schmid, A.-C., and Hummel, F. C. (2019). Wearable technology in stroke rehabilitation: towards improved diagnosis and treatment of upper-limb motor impairment. *J. Neuroeng. Rehabil.* 16, 8–18.

Mudiganty, S., Daolagupu, A. K., Sipani, A. K., Das, S. K., Alam, J. E., Plumari, S., et al. (2017). Treatment of infected non-unions with segmental defects with a rail fixation system. *Strategies Trauma Limb Reconstr.* 12, 45–51. doi: 10.1007/s11751-017-0278-6

Pavlova, E. L., Lindberg, P., Khan, A. J., O'Donovan, A., Neylan, T. C., Gross, J. J., et al. (2017). Transcranial direct current stimulation combined with visuo-motor training as treatment for chronic stroke patients. *Restorat.Neurol. Neurosci.* 35, 307–317. doi: 10.3233/rnn-160706

Pereira, M. G., Lynch, B., Hall-Faul Pedras, M., and Quality, S. (2019). of Life of women with urinary incontinence in rehabilitation treatment. *J. Health Psychol.* 24, 254–263. doi: 10.1177/1359105316650615

Pin-Yeh, F., and Qiang, W. (2017). Effects of intensive exercise training combined with prophylactic antidepressant treatment on motor function and depression in patients with stroke. *Int. J. Sci.* 6, 81–89. doi: 10.18483/ijsci.1215

Polkey, M. I., Qiu, Z.-H., Zhou, L., Zhu, M.-D., Wu, Y.-X., Chen, Y.-Y., et al. (2018). Tai chi and pulmonary rehabilitation compared for treatment-naive patients with copd: a randomized controlled Trial. *Chest* 153, 1116–1124. doi: 10.1016/j.chest.2018.01.053

Schneider, K. J., Leddy, J. J., Guskiewicz, K. M., Seifert, T., McCrea, M., Silverberg, N. D., et al. (2017). Rest and treatment/rehabilitation following sport-related concussion: a systematic review. *Br. J. Sports Med.* 51, 930–934. doi: 10.1136/bjsports-2016-097475

Shulman, J., Conroy, C., Cybulski, A., Smith, K. R., Jervis, K., Johnson, H., et al. (2020). Does intensive interdisciplinary pain treatment improve pediatric headache-related disability? *Disabil. Rehabi.* 14–28. doi: 10.1080/09638288.2020.1762125

Skolasky, R. L., Wegener, S. T., Aaron, R. V., Ephraim, P., Brennan, G., Greene, T., et al. (2020). The optimize study: protocol of a pragmatic sequential multiple assessment randomized trial of nonpharmacologic treatment for chronic, nonspecific low back pain. *BMC Musculoskelet. Disord.* 21:293. doi: 10.1186/s12891-020-03324-z

Smith, M. M. F., Collins, N. J., Mellor, R., Grimaldi, A., Elliott, J., Hoggarth, M., et al. (2020). Foot exercise plus education versus wait and see for the treatment of plantar heel pain (Feet Trial): a protocol for a feasibility study. *J. Foot Ankle Res.* 13, 34–56.

Stan, J. H. V., Dijkers, M. P., Whyte, J., Hart, T., Turkstra, L. S., Zanca, J. M., et al. (2019). The rehabilitation treatment specification system: implications for improvements in research design, reporting, replication, and synthesis. *Archiv. Phys. Med. Rehabil.* 100, 146–155. doi: 10.1016/j.apmr.2018.09.112

Telles, S., Sayal, N., Nacht, C., Chopra, A., Patel, K., Wnuk, A., et al. (2019). Yoga: can it be integrated with treatment of neuropathic pain? *Ann. Neurosci.* 26, 82–91. doi: 10.5214/ans.0972.7531.260208

Tian, X., Gao, H., Jiang, W., Zhang, H., Yu, X., Liu, E., et al. (2019). Deep multi-view feature learning for eeg-based epileptic seizure detection. *IEEE Trans. Neural Syst. Rehabil. Eng.* 27, 1962–1972. doi: 10.1109/tnsre.2019.2940485

Torres-Rodríguez, A., Griffiths, M. D., and Carbonell, X. (2018). The treatment of internet gaming disorder: a brief overview of the pipatic program. *Int.J. Ment. Health Addict.* 16, 1000–1015. doi: 10.1007/s11469-017-9825-0

Turgut, N., Möller, L., Dengler, K., Steinberg, K., Sprenger, A., Eling, P., et al. (2018). Adaptive cueing treatment of neglect in stroke patients leads to improvements in activities of daily living: a randomized controlled, crossover trial. *Neurorehabil. Neural Repair* 32, 988–998. doi: 10.1177/1545968318807054

van Yperen, D. T., Reijman, M., van Es, E. M., Bierma-Zeinstra, S. M. A., and Meuffels, D. E. (2018). Twenty-year follow-up study comparing operative versus nonoperative treatment of anterior cruciate ligament ruptures in high-level athletes. *Am. J. Sports Med.* 46, 1129–1136. doi: 10.1177/0363546517751683

Wang, J., Shi, W., Khiati, D., Shi, B., Chen, M., Xia, Z., et al. (2020). Acupuncture treatment on the motor area of the scalp for motor dysfunction in children with cerebral palsy: study protocol for a multicenter randomized controlled trial. *Trials* 21, 11–21.

Whyte, J., Dijkers, M. P., Hart, T., Van Stan, J. H., Packel, A., Turkstra, L. S., et al. (2019). The importance of voluntary behavior in rehabilitation treatment and outcomes. *Archiv. Phys. Med. Rehabil.* 100, 156–163. doi: 10.1016/j.apmr.2018.09.111

Zesiewicz, T. A., Wilmot, G., Kuo, S.-H., Perlman, P., Greenstein, P. E., Ying, S. H., et al. (2018). Comprehensive systematic review summary: treatment of cerebellar motor dysfunction and ataxia: report of the guideline development, dissemination, and implementation subcommittee of the american academy of neurology. *Neurology* 90, 464–471. doi: 10.1212/wnl.0000000000005055

Zhang, P., Hu, S., He, F., Fan, J., Wang, Q., He, X., et al. (2017). [He Xingwei's exploration and experience in the pathogenesis and treatment of motor impairment of the trunk after stroke. *Chin. Acupunct. Moxibustion* 37, 191–193.

Zhang, Y., Chung, F., Wang, S. (2019a). A multiview and multiexemplar fuzzy clustering approach: theoretical analysis and experimental studies. *IEEE Trans. Fuzzy Syst.* 27, 1543–1557. doi: 10.1109/tfuzz.2018.2883022

Zhang, Y., Chung, F., and Wang, S. (2019b). Fast reduced set-based exemplar finding and cluster assignment. *IEEE Trans. Syst. ManCybernet.* 49, 917–931. doi: 10.1109/tsmc.2017.2689789

Zhang, Y., Dong, J., Zhu, J., and Wu, C. (2019c). Common and special knowledge-driven TSK fuzzy system and its modeling and application for epileptic EEG signals recognition. *IEEE Access* 7, 127600–127614. doi: 10.1109/access.2019.2937657

Zhang, Y., Li, X., Zhu, J., Wu, C., and Wu, Q. (2019d). Epileptic EEG signals recognition using a deep view-reduction TSK Fuzzy system with high interpretability. *IEEE Access* 7, 137344–137354. doi: 10.1109/access.2019.2942641

Zhang, Y., Chung, F., and Wang, S. (2020a). Fast exemplar-based clustering by gravity enrichment between data objects. *IEEE Trans. Syst. Man Cybernet.* 50, 2996–3009.

Zhang, Y., Zhou, Z., Bai, H., Liu, W., and Wang, L. (2020b). Seizure classification from EEG signals using an online selective transfer TSK fuzzy classifier with joint distribution adaption and manifold regularization. *Front. Neurosci.* 14:496. doi: 10.3389/fnins.2020.00496

Zhang, Y., Ishibuchi, H., and Wang, S. (2018). Deep Takagi–Sugeno–Kang fuzzy classifier with shared linguistic fuzzy rules. *IEEE Trans. Fuzzy Syst.* 26, 1535–1549. doi: 10.1109/tfuzz.2017.2729507

Zhang, Y., Wang, L., Wu, H., Geng, X., Yao, D., and Dong, J. (2016). A clustering method based on fast exemplar finding and its application on brain magnetic resonance images segmentation. *J. Med. Imaging Health Informat.* 6, 1337–1344. doi: 10.1166/jmihi.2016.1923

Zhao, K., Zhou, L., Qian, P., Ding, Y., Jiang, Y., Chen, Y., et al. (2019). A transfer fuzzy clustering and neural network based tissue segmentation method during PET/MR attenuation correction. *J. Med. Imaging Health Informat.* 9, 1491–1497. doi: 10.1166/jmihi.2019.2749

Zheng, J., Cao, J., Wang, Z., Liu, F., Wang, S., Wu, T., et al. (2019). Semi-automatic synthetic computed tomography generation for abdomens using transfer learning and semi-supervised classification. *J. Med. Imaging Health Informat.* 9, 1878–1886. doi: 10.1166/jmihi.2019.2809

Conflict of Interest: The authors declare that the research was conducted in the absence of any commercial or financial relationships that could be construed as a potential conflict of interest.

frontiers in Neuroscience

ORIGINAL RESEARCH
published: 17 November 2020
doi: 10.3389/fnins.2020.00870

MNL-Network: A Multi-Scale Non-local Network for Epilepsy Detection From EEG Signals

Guokai Zhang[1], Le Yang[2], Boyang Li[2], Yiwen Lu[3], Qinyuan Liu[3], Wei Zhao[4], Tianhe Ren[5], Junsheng Zhou[5], Shui-Hua Wang[6,7]* and Wenliang Che[8]**

[1] School of Optical-Electrical and Computer Engineering, University of Shanghai for Science and Technology, Shanghai, China, [2] School of Software Engineering, Tongji University, Shanghai, China, [3] Department of Computer Science and Technology, Tongji University, Shanghai, China, [4] Chengyi University College, Jimei University, Xiamen, China, [5] School of Informatics, Xiamen University, Xiamen, China, [6] School of Architecture Building and Civil Engineering, Loughborough University, Loughborough, United Kingdom, [7] School of Mathematics and Actuarial Science, University of Leicester, Leicester, United Kingdom, [8] Department of Cardiology, Shanghai Tenth People's Hospital, Tongji University School of Medicine, Shanghai, China

Epilepsy is a prevalent neurological disorder that threatens human health in the world. The most commonly used method to detect epilepsy is using the electroencephalogram (EEG). However, epilepsy detection from the EEG is time-consuming and error-prone work because of the varying levels of experience we find in physicians. To tackle this challenge, in this paper, we propose a multi-scale non-local (MNL) network to achieve automatic EEG signal detection. Our MNL-Network is based on 1D convolution neural network involving two specific layers to improve the classification performance. One layer is named the signal pooling layer which incorporates three different sizes of 1D max-pooling layers to learn the multi-scale features from the EEG signal. The other one is called a multi-scale non-local layer, which calculates the correlation of different multi-scale extracted features and outputs the correlative encoded features to further enhance the classification performance. To evaluate the effectiveness of our model, we conduct experiments on the Bonn dataset. The experimental results demonstrate that our MNL-Network could achieve competitive results in the EEG classification task.

Keywords: convolution neural network, EEG, epilepsy, multi-scale, non-local, seizure, ictal, interictal

OPEN ACCESS

Edited by:
Yizhang Jiang,
Jiangnan University, China

Reviewed by:
Yuanpeng Zhang,
Nantong University, China
Xuejing Lan,
Guangzhou University, China

****Correspondence:***
Qinyuan Liu
liuqy@tongji.edu.cn
Shui-Hua Wang
huihuawang@ieee.org
Wenliang Che
chewenliang@tongji.edu.cn

Specialty section:
This article was submitted to Neuroprosthetics, a section of the journal Frontiers in Neuroscience

Received: *01 June 2020*
Accepted: *27 July 2020*
Published: *17 November 2020*

Citation:
Zhang G, Yang L, Li B, Lu Y, Liu Q, Zhao W, Ren T, Zhou J, Wang S-H and Che W (2020) MNL-Network: A Multi-Scale Non-local Network for Epilepsy Detection From EEG Signals. Front. Neurosci. 14:870. doi: 10.3389/fnins.2020.00870

1. INTRODUCTION

As the center of cognitive processes and sensory stimuli, the brain controls the vital functions of the body and has a complicated information processing function (Türk and Özerdem, 2019). When the nervous system is active, the brain emits biopotential signals that can reflect dysfunction or disease. By magnifying and recording the spontaneous biological potential of the brain from the scalp through sophisticated electronic instruments, one can obtain electroencephalography (EEG) signals. Due to its excellent temporal resolution, easy implementation, and low cost, EEG has become one of the most effective techniques in monitoring the brain activity and diagnosing the neurological disorder (Ullah et al., 2018).

Epilepsy is a neurological disorder affecting about 50 million people around the world (Beghi et al., 2005; Megiddo et al., 2016). Epilepsy manifests in the form of seizures, which is an abnormal electrical activity that occurs temporarily in nerve cells (Bancaud, 1973). Since EEG can accurately record the intermittent slow waves, spikes, or irregular spikes during seizures by analyzing the wave

morphology of EEG signals, one can give an explicit evaluation of the presence and level of epilepsy. Unfortunately, the detection of epilepsy from EEG requires signal records over a long-term period, which is a time-consuming and inefficient undertaking. Considering the shortage of professional doctors at present, it is therefore urgent and meaningful to detect epilepsy in an automatic way.

In recent years, the algorithms based on the hand-crafted feature engineering have shown great success in many medical image analysis fields (Jiang et al., 2017; Li et al., 2019; Xu et al., 2020); for EEG signal automatic detection tasks, some early attempts such as Gotman (1982) decomposed the EEG into elementary waves and detected the paroxysmal bursts of rhythmic activity. Furthermore, these works could detect the patterns specific to newborns and then give a warning to patients when a seizure is starting (Gotman, 1999). Recently, Gardner et al. proposed a Support Vector Machine (SVM)-based method in which seizure activity induced distributional changes in feature space that increased the empirical outlier fraction (Gardner et al., 2006). Moreover, an automatic epileptic seizure detection method was developed based on line length feature and artificial neural networks in Guo et al. (2010). After that, a different feature acquisition and classification technique in the diagnosis of both epilepsy and autism spectrum disorder (ASD) was developed by Ibrahim (Ibrahim et al., 2017). Lu's team used Kraskov Entropy based on the Hilbert Huang Transform (HHT) to obtain features. They used the Least Squares Version of Support Vector Machine (LS-SVM) for wavelet transformation (Lu et al., 2018). Although many hand-crafted feature algorithms have been proposed, it is still a challenging problem to identify epilepsy and non-epileptic EEG signals due to the noise and artifacts in the data as well as the inconsistency in seizure morphology of the epilepsy (Tao et al., 2017).

Recently, with the great success of deep learning in computer vision and data mining fields, considerable attention has been focused on the EEG signal classification task. Compared with the hand-crafted feature learning methods, the deep learning methods could generically learn stronger discriminative features with an end-to-end manner. For EEG classification, a Computer-Aided Diagnosis (CAD) system was developed in Acharya et al. (2017), which employed the Convolutional Neural Network (CNN) for analysis of EEG signals. In the follow-up study, the authors in Yuan et al. (2017) transformed EEG signals into EEG scalogram sequences using wavelet transformation, and they then obtained three different EEG features by using Global Principal Component Analysis (GPCA) (Vidal, 2016), Stacked Denoising Autoencoders (SDAE) (Vincent et al., 2010), and EEG segments. After that, the seizure detection was performed by combining all the obtained features and assigning them to the SVM classifier. As for the end-to-end feature learning, Türk et al. obtained two-dimensional (2D) frequency-time scalograms by applying continuous wavelet transform to EEG records, and they then used CNN to learn the properties of these scalogram images to classify the EEG signal (Türk and Özerdem, 2019).

Bhattacharyya et al. analyzed the underlying complexity and nonlinearity of EEG signals by computing a novel multi-scale entropy measure for the classification of seizure, seizure-free, and normal EEG signals (Abhijit et al., 2017). Hussein et al. transformed EEG data into a series of non-overlapping segments to reveal the correlation between consecutive data samples. The Long Short Term Memory (LSTM) network and the softmax classifier were exploited for classification to learn the high-level features of normal and seizure EEG models (Hussein et al., 2018). It should be noted that the majority of the automatic systems perform well in detecting binary epilepsy scenarios, but their performance degrades greatly in classifying the ternary case. To overcome this problem, Ullah et al. proposed an ensemble of pyramidal one-dimensional convolutional neural network (P-1D-CNN) models (Ullah et al., 2018), which could efficiently handle the small available data challenge in classifying the ternary case.

Despite some preliminary results that have been established in the literature, they ignore the multi-scale features which play an important role in the EEG classification task. For example, the long scale of the signal reflects more global representations of the EEG signal, and the short scale of signal embodies the information from the local EEG signal. Thus, those methods based on the single scale of the EEG signal could hinder the model from achieving a better performance due to the absence of multi-scale features. Moreover, the correlations of multi-scale signal features could also be an important factor in this classification task. The learned correlations of multi-scale features are capable of providing correlative dependencies of various lengths' EEG signals, which give more feature information to further improve the classification performance. Based on the discussion above, in this paper, we propose a Multi-scale Non-local (MNL) network to learn multi-scale and correlative features from the input EEG signals. The overview of our designed MNL-Network is illustrated in **Figure 2**. Different from the previous work that directly input the extracted features into the fully connected layer for classification, our MNL-Network developed a signal pooling layer to learn the multi-scale representations through different sizes of 1D max-pooling layers (Zhao et al., 2017) and then input these representations to a Non-local layer (Wang et al., 2018), which aims to encode more correlative features with multi-scale characteristic. To evaluate the performance of the proposed MNL-Network, we conduct comprehensive experiments on the public EEG Bonn dataset. The experimental results show the high classification accuracy of different EEG records, which convinces the effectiveness of our MNL-Network.

In the following section, we will first describe the experimental data in section 2.1. The detailed description of our proposed method is introduced from section 2.2 to section 2.4. The comparison results of different class combinations will be presented in section 3. Finally, we will give an overall discussion of our work in section 4.

2. DATA AND METHODS

2.1. Data Description

Our experiments employ the EEG Bonn dataset (Andrzejak et al., 2001), which is public and widely used. There are five subsets/classes in this Bonn dataset, and they are denoted as set A, B, C, D, and E. Set A and B monitor the surface EEG

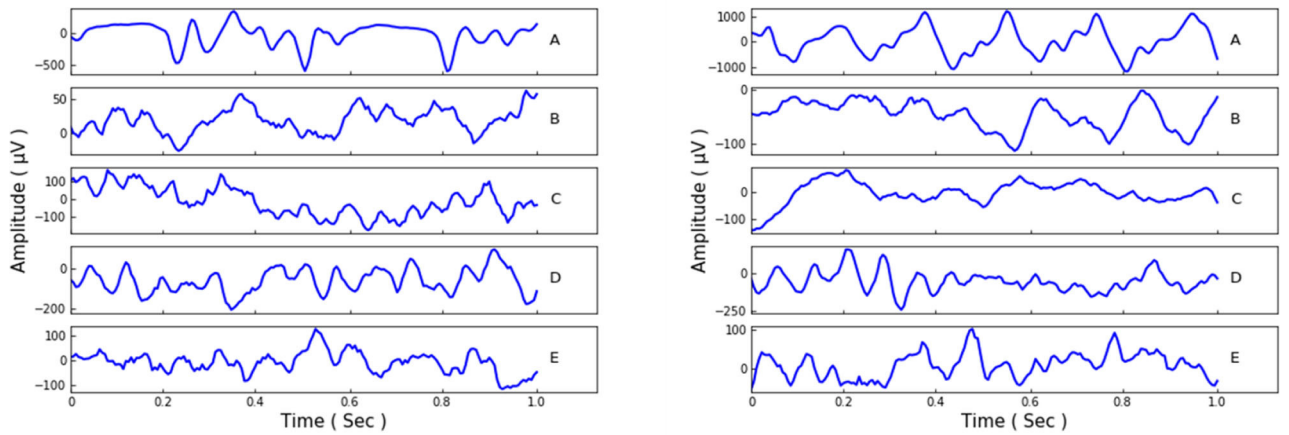

FIGURE 1 | The data samples from the Bonn dataset.

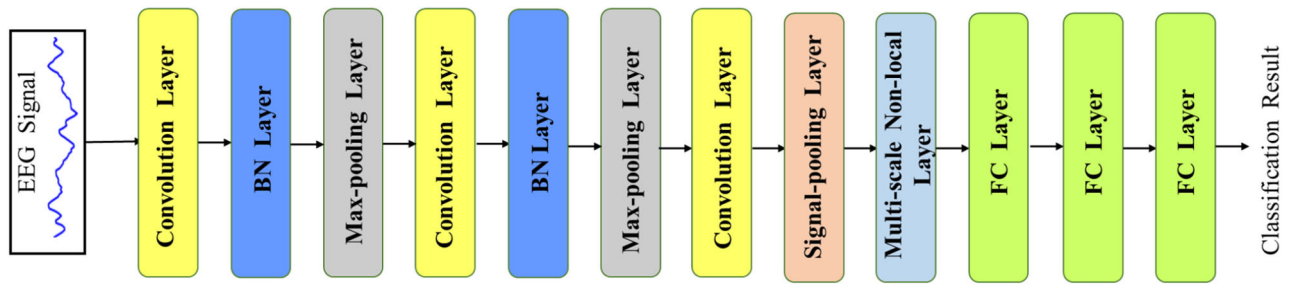

FIGURE 2 | The overview of our MNL-Network. The main backbone is based on a 1D convolution neural network with two additional layers (i.e., signal pooling layer and multi-scale non-local layer), which are developed to learn multi-scale and correlative features from the EEG signals.

records of healthy waking people with eyes open or closed. The other three sets, C, D, and E, are collected from epileptics. Set C it detects the records from the hippocampal formation of the brain during the seizure-free intervals. Set D is gained from the epileptogenic zone with the same intervals as set C, and set E only contains the records of the seizure activities. Each of the five sets is composed of 100 person signals of sampling rate 173.61 Hz and duration 23.6 s. Afterwards, the data samples were made into 4, 097 data points and then divided into 23 chunks for each person signal. Thus, the total record amount of the five sets could be $23 \times 100 \times 5 = 11,500$, and each set contains 2, 300 records. We show some samples of the different sets in **Figure 1**.

2.2. Network Architecture

Recently, the deep convolutional neural network has achieved great success in computer vision and data analysis fields, and it has become the most rapidly developing technology in the machine learning domain. Compared with the traditional hand-defined feature learning methods, the CNN extracts highly sophisticated feature representations by an end-to-end learning mode, which could be more efficient and accurate. Since the EEG signal is a 1D time-series data, our main network is based on a 1D CNN, which mainly consists of the convolution layer, max-pooling layer, batch-normalization (BN) layer, and fully connected (FC) layer. The overview of our proposed network is illustrated in **Figure 2**. The network takes the EEG signal as the input and outputs the final EEG classification prediction result in an end-to-end manner. In order to accelerate the convergence of the network, we first use the z-score normalization to normalize the input EEG signal to $[0, 1]$ range. Denoting the input signal data as s, the z-score normalization could be formulated as the following:

$$s^* = \frac{s - \mu}{\theta} \tag{1}$$

where μ is the mean value of s, the parameter of θ is the standard deviation of s, and the normalized data is s^*.

In our MNL-Network, the first layer is the convolution layer, which is generally used for filtering signals with fixed length to get discriminating features from the input. The filter number denotes the amounts of features that the kernel extracts. For reducing the complexities of the network, we use three convolution layers with the sizes 40, 20, and 10, respectively. Through using different kernels, discriminative categories of features are extracted and then fed into the next layer. Note that in the CNN, the deeper convolution layer usually extracts more

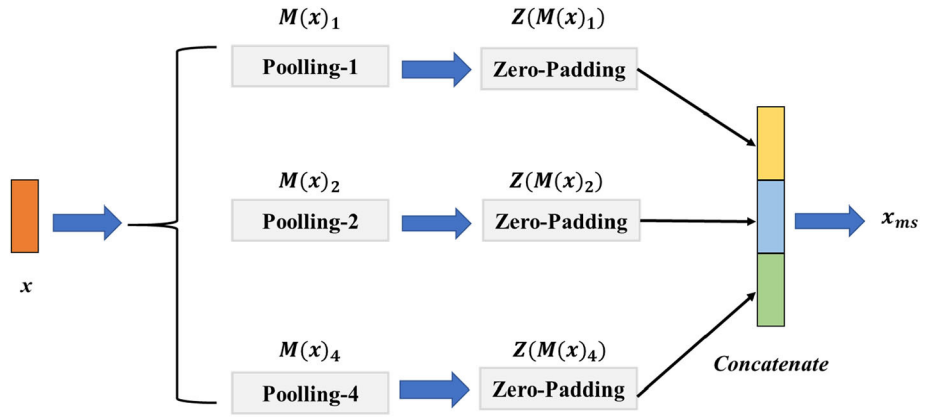

FIGURE 3 | The architecture of the signal pooling layer. The $M(x)_1$, $M(x)_2$, $M(x)_4$ denote the max-pooling operations with the sizes of {1, 2, 4}, respectively, and the $Z(M(x)_1)$, $Z(M(x)_2)$, $Z(M(x)_4)$ is the zero-padding layer with sizes of {1, 2, 4} that aim to reshape the feature map resolution to the same size.

TABLE 1 | The parameters of the MNL-Network.

Layer	Filter numbers	Filter size	Stride	Output size
Convolution layer	20	40	–	178 × 20
BN layer	–	–	–	178 × 20
Max-pooling layer	–	2	2	89 × 20
Convolution layer	40	20	2	35 × 40
BN layer	–	–	–	35 × 40
Max-pooling layer	–	2	2	17 × 40
Convolution layer	80	10	2	4 × 80
BN layer	–	–	–	4 × 80
Signal pooling layer	–	–	–	4 × 80
Multi-scale non-local layer	–	–	–	4 × 80
Flatten	–	–	–	4 × 80
FC layer	64	–	–	64
FC layer	32	–	–	32
FC layer	2	–	–	5

high-level representations, while the lower one learns more tiny-detailed features. For learning more non-linear representations from the EEG signal, the Rectified Linear Unit (RELU) activation function is adopted with the form as follows:

$$f(a) = max(0, a) \tag{2}$$

where $f(a)$ is the activation output of the input feature a. Since the BN layer can accelerate the learning process and maintain training stability, we add it after each convolution layer. After the BN layer, the max-pooling layer is followed to get the maximum signal value from the encoded features, and it is also used to down-sample or pool the input representation. The size of the max-pooling layer in our network is set as 2 with the stride 2. Before input the extracted features into the signal pooling layer, there are two max-pooling layers utilized to extract spatial information and enlarge the receptive field from the signal features. The detailed parameters of the MNL-Network are presented in **Table 1**.

For combining non-linear features from the previous layers, we use three FC layers, and the last FC layer is with a softmax function to output the prediction probability of each class. Mathematically, we denote the class labels as $y_{(i)} \in \{1, 2, \cdots, C\}$, where the data samples have C classes totally. Given the normalized input data s^*, the softmax operation $h_\theta(\mathbf{s}^*)$ could be formulated as the following:

$$\begin{aligned} \boldsymbol{h}_\theta(\mathbf{s}^*) &= \begin{pmatrix} \mathcal{P}(y=1|\mathbf{s}^*;\theta) \\ \mathcal{P}(y=2|\mathbf{s}^*;\theta) \\ \vdots \\ \mathcal{P}(y=C|\mathbf{s}^*;\theta) \end{pmatrix} \\ &= \frac{1}{\sum_{j=1}^{C} \exp\left(\theta_j^{\mathrm{T}}\mathbf{s}^*\right)} \begin{pmatrix} \exp\left(\theta_1^{\mathrm{T}}\mathbf{s}^*\right) \\ \exp\left(\theta_2^{\mathrm{T}}\mathbf{s}^*\right) \\ \vdots \\ \exp\left(\theta_C^{\mathrm{T}}\mathbf{s}^*\right) \end{pmatrix} \end{aligned} \tag{3}$$

where $\theta_1, \theta_2, \cdots, \theta_C$ are the parameters of the softmax operation.

2.3. Signal Pooling Layer

The EEG signal with different scales contains various multi-scale representations. However, the fixed size of the convolution or pooling layer could ignore the multi-scale features and thus hinder the model from achieving a higher classification performance. To address this challenge, we introduce a signal pooling layer that has two main parts: the multi-pooling part and the concatenation part to realize extracting the features from different scales. The detailed structure of the signal pooling layer is illustrated in **Figure 3**. Let $\mathbf{x} \in \mathbb{R}^{w \times c}$ be the output features from the third convolution layer, w the length of $\mathbf{x}$, and c indicate

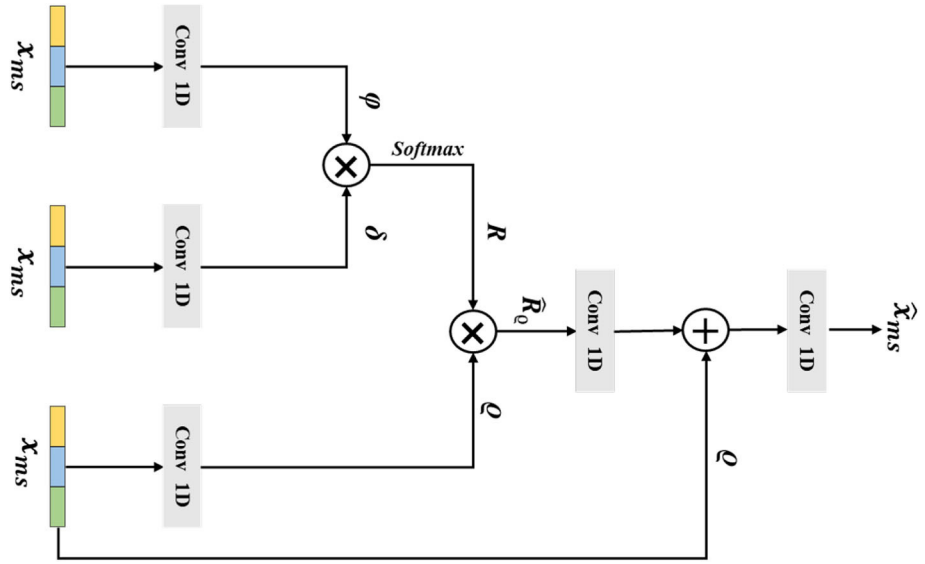

FIGURE 4 | The architecture of the multi-scale non-local layer. The $\mathbf{x}_{ms}$ is the extracted multi-scale features from the previous layer, $\phi, \delta, and \varrho$ are the output features from Conv 1D, the variable of **R** denotes the similarity matrix of ϕ and δ, the $\hat{\mathbf{R}}_{\varrho}$ is gained by multiplying **R** and ϱ, and the final output of the multi-scale non-local layer is $\hat{\mathbf{x}}_{ms}$.

TABLE 2 | The k-10 accuracy performance of double classes classification.

	k1	k2	k3	k4	k5	k6	k7	k8	k9	k10	Mean
A-E	97.82	100	100	99.78	100	99.78	100	100	100	100	99.93
B-E	99.35	100	100	99.35	99.78	99.57	99.78	100	99.35	100	99.72
C-E	98.45	99.57	99.13	99.78	99.78	99.56	99.13	98.91	99.13	100	99.35
D-E	98.70	98.48	99.57	98.91	98.48	99.35	98.70	98.70	98.70	98.04	98.76
AB-E	99.57	100	99.86	99.42	99.71	99.71	99.71	100	99.57	100	99.75
AC-E	99.42	99.42	99.57	99.57	99.42	99.71	99.28	99.28	99.28	99.86	99.48
AD-E	98.99	99.42	99.13	99.28	98.84	98.99	98.70	99.28	98.99	99.42	99.10
BC-E	99.28	99.86	99.42	99.28	98.99	99.28	99.13	99.57	98.99	100	99.38
BD-E	98.84	98.84	98.99	98.84	98.26	98.99	98.99	98.99	98.16	99.57	98.84
CD-E	98.84	99.42	98.99	99.28	98.12	98.99	99.70	98.12	98.70	99.28	98.84
ABC-E	99.57	99.67	99.78	99.24	99.78	99.67	99.57	99.78	99.57	99.24	99.59
ABD-E	99.46	99.13	99.24	99.02	99.57	99.78	99.24	99.57	99.13	99.13	99.33
BCD-E	99.57	98.70	99.24	98.70	99.35	99.35	98.59	99.35	98.91	98.04	98.98
ABCD-E	99.04	99.39	99.39	99.13	98.87	99.48	99.48	98.70	99.48	98.70	99.17

the channels of $\mathbf{x}$. Then, we define the $\mathbf{M}(\cdot)_p$ as the max-pooling operation with the size of $p \in \{1, 2, 4\}$ and the stride as d with the value of 1; the output size of feature o could be calculated as Equation (4).

$$o = (w - p)/d + 1 \tag{4}$$

For merging different sizes of the multi-scale features, we define the operator of $\mathbf{Z}(\cdot)$ is the zero-padding layer with the left and right padding size of l and r, and the value of l, r is calculated as follows:

$$l = \lceil \frac{w - o}{4} \rceil \tag{5}$$

$$r = w - o - l \tag{6}$$

where $\lceil \cdot \rceil$ denotes the round up value operation. Specifically, for the input feature $\mathbf{x}$, we first perform $\mathbf{M}(\cdot)_1, \mathbf{M}(\cdot)_2, \mathbf{M}(\cdot)_4$ parallelly to extract the multi-scale features. We then use the $\mathbf{Z}(\cdot)$ to pad the features to the same size. Finally, a concatenation operation of $\mathbf{Z}(\mathbf{M}(\mathbf{x})_1), \mathbf{Z}(\mathbf{M}(\mathbf{x})_2), \mathbf{Z}(\mathbf{M}(\mathbf{x})_4)$ is conducted before taking them into the multi-scale non-local layer. The final output feature $\mathbf{x}_{ms}$ of the signal pooling layer could be given as follows:

$$\mathbf{x}_{ms} = Concat(\mathbf{Z}(\mathbf{M}(\mathbf{x})_1), \mathbf{Z}(\mathbf{M}(\mathbf{x})_2), \mathbf{Z}(\mathbf{M}(\mathbf{x})_4)) \tag{7}$$

where the $Concat(\cdot)$ represents the concatenation operation of different features.

2.4. Multi-Scale Non-local Layer

The long-range correlations of different scale EEG signals are of a vital importance in the epilepsy classification task. However, the traditional non-local method has been impeded by the lack of considering the multi-scale features. Thus, in this section, we introduce our designed multi-scale non-local layer, which could learn discriminative multi-scale EEG signal features in a non-local manner. The detailed structure of our multi-scale non-local layer is shown in **Figure 4**. Instead of using the hierarchical feature from the network, the input feature of the multi-scale non-local layer is extracted from the signal pooling layer, which contains more discriminative multi-scale representations. By measuring the correlations of different multi-scale features, the final category of the EEG signal could be predicted by learning similarities across different scopes.

Mathematically, we consider that the multi-scale input feature of the multi-scale non-local layer is $\mathbf{x}_{ms} \in \mathbb{R}^{w \times c}$, which is extracted from the previous signal pooling layer. Then, we use three 1D convolutions with the receptive field and filter size of one to transform $\mathbf{x}_{ms} \in \mathbb{R}^{w \times c}$ to embedding space, the output features $\phi \in \mathbb{R}^{w \times \hat{c}}, \delta \in \mathbb{R}^{w \times \hat{c}}, \varrho \in \mathbb{R}^{w \times \hat{c}}$ could be defined as:

$$\phi = Conv_{\phi}(\mathbf{x}_{ms}) \tag{8}$$

$$\delta = Conv_{\delta}(\mathbf{x}_{ms}) \tag{9}$$

$$\varrho = Conv_{\varrho}(\mathbf{x}_{ms}) \tag{10}$$

where $\hat{c}$ is the channel number of $\phi, \delta, and\ \varrho$. After that we flatten the three embeddings and use the matrix multiplication operation $g(\cdot, \cdot)$ between ϕ and δ to calculate the similarity matrix $\mathbf{R}$, which could be formulated as the following:

$$\mathbf{R} = g(\phi, \delta) = \phi^{\mathbf{T}} \times \delta \tag{11}$$

Next, we apply the a softmax operation to $h_{\eta}(\cdot)$ to normalize the similarity matrix $\mathbf{R}$ and gain the attention weight matrix $\hat{\mathbf{R}}$ $=h_{\eta}(\mathbf{R})$; here, η is the parameters of softmax operation. Then, we perform a matrix multiplication between $\hat{\mathbf{R}}$ and ϱ, which is formulated as the following:

$$\hat{\mathbf{R}}_{\varrho} = \hat{\mathbf{R}} \times \varrho^{\mathbf{T}} \tag{12}$$

and the $\hat{\mathbf{R}}_{\varrho} \in \mathbb{R}^{w \times \hat{c}}$ denotes the output feature. Afterward, a residual connection between $\hat{\mathbf{R}}$ and ϱ is performed, and the final output $\hat{\mathbf{x}}_{ms}$ of the multi-scale non-local layer is given as the following:

$$\hat{\mathbf{x}}_{ms} = Conv_{ms}(Conv_{ms}(\hat{\mathbf{R}_{\varrho}}) + \mathbf{x}_{ms}) \tag{13}$$

2.5. Implementation Details

The proposed method is implemented by the Keras with 1 RTX 2070 GPU, and we use the cross-entropy as our loss function to train the model end-to-end. The parameters of the method are optimized by the Adam optimizer, the initial learning rate is set as 0.0005, and we reduce it by 0.1 after the validation accuracy is not improved after 10 epochs. All the training data is trained in a mini-batch size mode, and we set the mini-batch as 100 for each epoch. For each fold, we choose the best checkpoint on the validation accuracy as our final predicted model.

TABLE 3 | The overall performance of double classes classification.

	Accuracy	Sensitivity	Specificity	Precision	F1-score
A-E	99.93	98.96	99.96	99.96	99.45
B-E	99.72	97.96	99.91	99.91	98.92
C-E	99.35	96.70	99.83	99.82	98.23
D-E	98.76	97.09	98.30	98.31	97.68
AB-E	99.75	97.87	99.98	99.96	98.90
AC-E	99.48	96.91	99.85	99.69	98.28
AD-E	99.10	97.04	99.48	98.94	97.98
BC-E	99.38	96.61	99.89	99.78	98.16
BD-E	98.84	95.70	99.48	98.93	97.28
CD-E	98.84	95.30	99.61	99.18	97.20
ABC-E	99.59	96.13	99.97	99.91	97.98
ABD-E	99.33	96.57	99.58	98.72	97.62
BCD-E	98.98	94.39	99.62	98.83	96.53
ABCD-E	99.17	94.65	99.76	99.00	96.77

TABLE 4 | The k-10 performance of multiple classes classification.

	k1	k2	k3	k4	k5	k6	k7	k8	k9	k10	Mean
A-C-E	97.34	97.78	96.81	97.68	97.00	98.12	98.16	98.02	97.20	97.68	97.58
A-D-E	97.68	97.83	98.16	97.83	97.49	97.87	98.36	97.97	97.54	97.39	97.81
B-C-E	98.07	97.83	98.60	97.78	98.16	98.60	98.84	99.42	97.97	99.03	98.43
B-D-E	98.45	98.74	98.79	98.31	98.74	98.36	98.65	98.74	98.55	98.84	98.62
AB-CD-E	97.04	97.39	98.67	97.62	97.68	97.91	97.62	97.97	98.55	97.13	97.76
A-B-C-D-E	94.63	94.35	93.34	93.79	93.98	94.40	94.28	93.11	93.93	94.31	94.01

TABLE 5 | The overall performance of multiple classes classification.

	Accuracy	Sensitivity	Specificity	Precision	F1-score
A-C-E	97.58	95.54	97.77	95.54	95.54
A-D-E	97.81	95.87	97.93	95.87	95.87
B-C-E	98.43	97.00	98.50	97.00	97.00
B-D-E	98.62	97.14	98.57	97.14	97.14
AB-CD-E	97.76	95.95	97.97	95.95	95.95
A-B-C-D-E	94.01	83.49	83.49	95.87	89.46

3. EXPERIMENTAL RESULTS

3.1. Evaluation Metrics

For evaluation, well-known performance metrics, such as accuracy, precision, sensitivity, specificity and F1-score, are adopted. The definitions of these performance metrics are given below:

$$Accuracy = \frac{TP + TN}{TP + TN + FP + FN} \tag{14}$$

$$Precision = \frac{TP}{TP + FP} \tag{15}$$

$$Sensitivity = \frac{TP}{TP + FN} \tag{16}$$

$$Specificity = \frac{TN}{FP + TN} \tag{17}$$

$$F1 - score = 2 \times \frac{Precision \times Sensitivity}{Precision + Sensitivity} \tag{18}$$

where TP (true positives) are the number of the EEG records that are abnormal and actually identified as abnormal; TN (true negatives) are the number of the EEG records that are normal and actually identified as normal; FP (false positives) are the number of the EEG records that are normal but are actually predicted as abnormal; and FN (false negatives) are the number of the EEG records that are abnormal but are actually predicted as normal.

In order to ensure the system is tested over different categories of data, we used 10-fold cross-validation to evaluate all the data in system performance. That is, we randomly divided the 2,300 EEG signals of each class into ten non-overlapping folds. Then each fold, in turn, is used for testing while the other nine folds are used for training the model. We calculated the average values of accuracy, sensitivity, and specificity for 10-folds to get the average performance of the system.

3.2. The Performance of Double Classes Classification

In this section, we conduct the experiment by comparing the double classes classification performance. The combinations of different classes are A-E, B-E, C-E, D-E, AB-E, AC-E, AD-E, BC-E, BD-E, CD-E, ABC-E, ABD-E, BCD-E, and ABCD-E. The accuracy comparison result of k-10 testing is shown in **Table 2**, the best performance is achieved on the A-E classes classification with the performance of 99.93%, and the hardest classification is CD-E with the score of 98.54%. It could explain that the healthy waking with eyes open classes could have a big difference from the seizure epileptic, and thus it could achieve a higher classification performance. We also compare other metrics as shown in **Table 3**. The best overall performance is by classifying A-E classes, which further proves the reasons presented above. Overall, the accuracy performance of different double classes is

TABLE 6 | The overall performance of double classes classification.

	Method	Study	Accuracy	Our accuracy
	1-D-LBP + FT/BN	Kaya et al., 2014	99.50	
	FFT and Decision tree	Polat and Güneş, 2007	98.70	
A-E	Wavelet transform	Lee et al., 2014	98.17	99.93
	Artificial neural networks	Nigam and Graupe, 2004	97.50	
	CWT + CNN	Türk and Özerdem, 2019	99.50	
	Robust CNN	Zhao et al., 2020	99.11	
	CNN + M-V	Ullah et al., 2018	99.6	
B-E	CWT + CNN	Türk and Özerdem, 2019	99.50	99.72
	DTCWT + GRNN	Swami et al., 2016	98.9	
	DWT + NB/KNN	Sharmila, 2016	99.25	
	CWT + CNN	Türk and Özerdem, 2019	98.50	
	CCNN + M-V	Ullah et al., 2018	99.1	
C-E	DTCWT + GRNN	Swami et al., 2016	98.7	99.35
	Robust CNN	Zhao et al., 2020	99.1	
	P-1D-CNN	Ullah et al., 2018	98.02	
	TQWT- K-NN Entropy	Abhijit et al., 2017	98.00	
	CEEMDAN + RF	Jia et al., 2017	98.00	
D-E	DTCWT + GRNN	Swami et al., 2016	98.00	98.76
	Robust CNN	Zhao et al., 2020	97.63	
	WPE + SVM	Tawfik et al., 2016	96.50	
	DWT + NB/KNN	Sharmila, 2016	99.16	
AB-E	DTCWT + GRNN	Swami et al., 2016	99.2	99.75
	Robust CNN	Zhao et al., 2020	99.38	
BC-E	DWT+NB/K-NN	Sharmila, 2016	98.3	99.38
	1-D-LBP + FT/BN	Kaya et al., 2014	97.00	
CD-E	DWT + NB/KNN	Sharmila, 2016	98.75	98.84
	Robust CNN	Zhao et al., 2020	98.03	
	1-D-LBP + FT/BN	Kaya et al., 2014	95.67	
A-D-E	LSP-SVM	Tuncer et al., 2019	95.67	97.81
	TQWT-QSP + 1N	Aydemir et al., 2020	99.67	
	LSP-SVM	Tuncer et al., 2019	93.0	
A-B-C-D-E	Robust CNN	Zhao et al., 2020	93.55	94.01

all above 98%, which indicates that our proposed method could be very generalized in this classification task.

3.3. The k-10 Performance of Multiple Classes Classification

For a more comprehensive comparison, we conduct multiple classes classification in this section. The experimental combinations contain A-C-E, A-D-E, B-C-E, B-D-E, AB-CD-E, and A-B-C-D-E, separately. The accuracy performance of different multiple classes is illustrated in **Table 4**. Compared with the double classes classification, the multiple classes classification tends to be more difficult, and the overall accuracy is lower than the double classes. The reason behind this could be the multiple classes classification having a more complex data distribution than the double classes classification. The overall comparison result of other metrics is shown in **Table 5**. The best performance is gained by the B-D-E combination, and it achieves 98.62% accuracy, 97.14% sensitivity, 98.57% specificity, 97.14% precision, and an F1-score of 97.14%. Meanwhile, the result shows that the A-B-C-D-E five classes combination obtains the lowest performance, and it is mostly because the five classes combination has a more complicated data characteristic from each class data.

3.4. Compare With Other Methods

To further evaluate the effectiveness of our proposed network, we compare our method with other previous works. In **Table 6**, it shows the comparison result of different methods. Since there are multiple combinations of EEG classes, for simplicity, we use the A-E, B-E, C-E, D-E, AB-E, BC-E, CD-E, A-D-E, and A-B-C-D-E combinations to evaluate our MNL-Network performance. The comparison result demonstrates that our method could achieve competitive performance on double classed classification when compared with other previous works. The best performance of the double classes combination is achieved by A-E, and the reason could be that the class A and E have a large gap between each other, and some other combinations also gain high classification accuracy, which are all above 94%. Moreover, the five classes classification result is also reported in **Table 6**, our proposed method has achieved an accuracy classification performance of 94.01%, which is higher than the recent works. In particular, the overall CNN based methods usually have better performance than the traditional hand-crafted ones, which further proves that they can extract stronger discriminative representations thus could perform more prominently in the classification task.

4. CONCLUSION

In this paper, we propose an automatic EEG signal detection network to help the physicians diagnose the epilepsy more efficiently. The whole architecture is based on the 1D convolution neural network, and two additional layers (signal pooling layer and multi-scale non-local layer) are proposed to learn the multi-scale and correlative information. Extensive comparative evaluations on the Bonn dataset are conducted, and they validate the effectiveness of our proposed method. In future works, we will explore the possibilities of incorporating reinforcement learning in this classification task.

DATA AVAILABILITY STATEMENT

Publicly available datasets were analyzed in this study. This data can be found here: https://archive.ics.uci.edu/ml/datasets/Epileptic+Seizure+Recognition.

AUTHOR CONTRIBUTIONS

GZ, LY, and BL conceived the idea and designed the algorithm. GZ conducted the experiments. YL wrote the initial paper. All the remaining authors contributed to refining the ideas and revised the manuscript.

FUNDING

This work was supported by the Fundamental Research Funds for the Central Universities NO.22120190211.

REFERENCES

Abhijit, B., Ram, P., Abhay, U., and Acharya, U. (2017). Tunable-q wavelet transform based multiscale entropy measure for automated classification of epileptic EEG signals. *Appl. Sci.* 7:385. doi: 10.3390/app7040385

Acharya, U. R., Oh, S. L., Hagiwara, Y., Tan, J. H., and Adeli, H. (2017). Deep convolutional neural network for the automated detection and diagnosis of seizure using EEG signals. *Comput. Biol. Med.* 100, 270–278. doi: 10.1016/j.compbiomed.2017.09.017

Andrzejak, R. G., Lehnertz, K., Mormann, F., Rieke, C., David, P., and Elger, C. E. (2001). Indications of nonlinear deterministic and finite-dimensional structures in time series of brain electrical activity: dependence on recording region and brain state. *Phys. Rev. E* 64:061907. doi: 10.1103/PhysRevE.64.061907

Aydemir, E., Tuncer, T., and Dogan, S. (2020). A tunable-q wavelet transform and quadruple symmetric pattern based EEG signal classification method. *Med. Hypothes.* 134:109519. doi: 10.1016/j.mehy.2019.109519

Bancaud, J. (1973). Clinical electroencephalography: L. g. kiloh, a. j. mccomas, j. w. osselton, butterworth, third edition, london 1972. *Neuropsychologia* 11:251. doi: 10.1016/0028-3932(73)90021-3

Beghi, E., Berg, A., Carpio, A., Forsgren, L., Hesdorffer, D. C., Hauser, W. A., et al. (2005). Comment on epileptic seizures and epilepsy: definitions proposed by the international league against epilepsy (ILAE) and the international bureau for epilepsy (IBE). *Epilepsia* 46:1698. doi: 10.1111/j.1528-1167.2005.00273_1.x

Gardner, A. B., Krieger, A. M., Vachtsevanos, G., Litt, B., and Kaelbing, L. P. (2006). One-class novelty detection for seizure analysis from intracranial EEG. *J. Mach. Learn. Res.* 7, 1025–1044. doi: 10.5555/1248547.1248584

Gotman, J. (1982). Automatic recognition of epileptic seizures in the EEG. *Electroencephalogr. Clin. Neurophysiol.* 54:540. doi: 10.1016/0013-4694(82)90038-4

Gotman, J. (1999). Automatic detection of seizures and spikes. *J. Clin. Neurophysiol.* 16, 130–140. doi: 10.1097/00004691-199903000-00005

Guo, L., Rivero, D., Dorado, J., RabuñAl, J. R., and Pazos, A. (2010). Automatic epileptic seizure detection in EEGs based on line length

feature and artificial neural networks. *J. Neurosci. Methods* 191, 101–109. doi: 10.1016/j.jneumeth.2010.05.020

Hussein, R., Elgendi, M., Wang, Z. J., and Ward, R. K. (2018). Robust detection of epileptic seizures based on L1-penalized robust regression of EEG signals. *Expert Syst. Appl.* 104, 153–167. doi: 10.1016/j.eswa.2018.03.022

Ibrahim, S., Djemal, R., and Alsuwailem, A. (2017). Electroencephalography (EEG) signal processing for epilepsy and autism spectrum disorder diagnosis. *Biocybern. Biomed. Eng.* 38, 16–26. doi: 10.1016/j.bbe.2017.08.006

Jia, J., Goparaju, B., Song, J., Zhang, R., and Westover, M. B. (2017). Automated identification of epileptic seizures in EEG signals based on phase space representation and statistical features in the CEEMD domain. *Biomed. Signal Process. Control* 38, 148–157. doi: 10.1016/j.bspc.2017.05.015

Jiang, Y., Wu, D., Deng, Z., Qian, P., Wang, J., Wang, G., et al. (2017). Seizure classification from EEG signals using transfer learning, semi-supervised learning and tsk fuzzy system. *IEEE Trans. Neural Syst. Rehabil. Eng.* 25, 2270–2284. doi: 10.1109/TNSRE.2017.2748388

Kaya, Y., Uyar, M., Tekin, R., and Yildirim, S. (2014). 1d-local binary pattern based feature extraction for classification of epileptic EEG signals. *Appl. Math. Comput.* 243, 209–219. doi: 10.1016/j.amc.2014.05.128

Lee, S.-H., Lim, J. S., Kim, J.-K., Yang, J., and Lee, Y. (2014). Classification of normal and epileptic seizure EEG signals using wavelet transform, phase-space reconstruction, and Euclidean distance. *Comput. Methods Prog. Biomed.* 116, 10–25. doi: 10.1016/j.cmpb.2014.04.012

Li, W., Zhang, L., Qiao, L., and Shen, D. (2019). Toward a better estimation of functional brain network for mild cognitive impairment identification: a transfer learning view. *IEEE J. Biomed. Health Inform.* 24, 1160–1168. doi: 10.1101/684779

Lu, Y., Ma, Y., Chen, C., and Wang, Y. (2018). Classification of single-channel EEG signals for epileptic seizures detection based on hybrid features. *Technol. Health Care* 26(Suppl.), 337–346. doi: 10.3233/THC-174679

Megiddo, I., Colson, A., Chisholm, D., Dua, T., Nandi, A., and Laxminarayan, R. (2016). Health and economic benefits of public financing of epilepsy treatment in India: an agent-based simulation model. *Epilepsia* 57, 464–474. doi: 10.1111/epi.13294

Nigam, V. P., and Graupe, D. (2004). A neural-network-based detection of epilepsy. *Neurol. Res.* 26, 55–60. doi: 10.1179/016164104773026534

Polat, K., and Güneş, S. (2007). Classification of epileptiform EEG using a hybrid system based on decision tree classifier and fast Fourier transform. *Appl. Math. Comput.* 187, 1017–1026. doi: 10.1016/j.amc.2006.09.022

Sharmila, A. E. A. (2016). DWT based detection of epileptic seizure from EEG signals using naive bayes and K-NN classifiers. *IEEE Access* 4, 7716–7727. doi: 10.1109/ACCESS.2016.2585661

Swami, P., Gandhi, T. K., Panigrahi, B. K., Tripathi, M., and Anand, S. (2016). A novel robust diagnostic model to detect seizures in electroencephalography. *Expert Syst. Appl.* 56, 116–130. doi: 10.1016/j.eswa.2016.02.040

Tao, Z., Chen, W., and Li, M. (2017). AR based quadratic feature extraction in the VMD domain for the automated seizure detection of EEG using random forest classifier. *Biomed. Signal Process. Control* 31, 550–559. doi: 10.1016/j.bspc.2016.10.001

Tawfik, N. S., Youssef, S. M., and Kholief, M. (2016). A hybrid automated detection of epileptic seizures in EEG records. *Comput. Electr. Eng.* 53, 177–190. doi: 10.1016/j.compeleceng.2015.09.001

Tuncer, T., Dogan, S., and Akbal, E. (2019). A novel local senary pattern based epilepsy diagnosis system using EEG signals. *Austral. Phys. Eng. Sci. Med.* 42, 939–948. doi: 10.1007/s13246-019-00794-x

Türk, Ö. and Özerdem, M. S. (2019). Epilepsy detection by using scalogram based convolutional neural network from EEG signals. *Brain Sci.* 9:115. doi: 10.3390/brainsci9050115

Ullah, I., Hussain, M., Aboalsamh, H., et al. (2018). An automated system for epilepsy detection using EEG brain signals based on deep learning approach. *Expert Syst. Appl.* 107, 61–71. doi: 10.1016/j.eswa.2018.04.021

Vidal, R. (2016). *Generalized Principal Component Analysis (GPCA)*. New York, NY: Springer. doi: 10.1007/978-0-387-87811-9

Vincent, P., Larochelle, H., Lajoie, I., Bengio, Y., and Manzagol, P. A. (2010). Stacked denoising autoencoders: learning useful representations in a deep network with a local denoising criterion. *J. Mach. Learn. Res.* 11, 3371–3408. doi: 10.5555/1756006.1953039

Wang, X., Girshick, R., Gupta, A., and He, K. (2018). "Non-local neural networks," in *Proceedings of the IEEE Conference on Computer Vision and Pattern Recognition* (Salt Lake City, UT), 7794–7803. doi: 10.1109/CVPR.2018.00813

Xu, X., Li, W., Mei, J., Tao, M., Wang, X., Zhao, Q., et al. (2020). Feature selection and combination of information in the functional brain connectome for discrimination of mild cognitive impairment and analyses of altered brain patterns. *Front. Aging Neurosci.* 12:28. doi: 10.3389/fnagi.2020.00028

Yuan, Y., Xun, G., Jia, K., and Zhang, A. (2017). "A novel wavelet-based model for eeg epileptic seizure detection using multi-context learning," in *2017 IEEE International Conference on Bioinformatics and Biomedicine (BIBM)*, (Kansas City, MO), 694–699. doi: 10.1109/BIBM.2017.8217737

Zhao, H., Shi, J., Qi, X., Wang, X., and Jia, J. (2017). "Pyramid scene parsing network," in *Proceedings of the IEEE Conference on Computer Vision and Pattern Recognition*, (Honolulu, HI), 2881–2890. doi: 10.1109/CVPR.2017.660

Zhao, W., Zhao, W., Wang, W., Jiang, X., Zhang, X., Peng, Y., et al. (2020). A novel deep neural network for robust detection of seizures using EEG signals. *Comput. Math. Methods Med.* 2020:9689821. doi: 10.1155/2020/9689821

Conflict of Interest: The authors declare that the research was conducted in the absence of any commercial or financial relationships that could be construed as a potential conflict of interest.

frontiers in Neuroscience

ORIGINAL RESEARCH
published: 23 November 2020
doi: 10.3389/fnins.2020.606949

A Novel Transfer Support Matrix Machine for Motor Imagery-Based Brain Computer Interface

Yan Chen[1,2†], Wenlong Hang[2†], Shuang Liang[3], Xuejun Liu[1], Guanglin Li[4], Qiong Wang[5], Jing Qin[6] and Kup-Sze Choi[6]*

[1] School of Computer Science and Technology, Nanjing Tech University, Nanjing, China, [2] Key Laboratory of Child Development and Learning Science, Ministry of Education, Southeast University, Nanjing, China, [3] Smart Health Big Data Analysis and Location Services Engineering Lab of Jiangsu Province, Nanjing University of Posts and Telecommunications, Nanjing, China, [4] CAS Key Laboratory of Human-Machine Intelligence-Synergy Systems, Shenzhen Institutes of Advanced Technology, Chinese Academy of Sciences, Shenzhen, China, [5] Guangdong-Hong Kong-Macao Joint Laboratory of Human-Machine Intelligence-Synergy Systems, Shenzhen Institutes of Advanced Technology, Chinese Academy of Sciences, Shenzhen, China, [6] School of Nursing, The Hong Kong Polytechnic University, Hong Kong, China

In recent years, emerging matrix learning methods have shown promising performance in motor imagery (MI)-based brain-computer interfaces (BCIs). Nonetheless, the electroencephalography (EEG) pattern variations among different subjects necessitates collecting a large amount of labeled individual data for model training, which prolongs the calibration session. From the perspective of transfer learning, the model knowledge inherent in reference subjects incorporating few target EEG data have the potential to solve the above issue. Thus, a novel knowledge-leverage-based support matrix machine (KL-SMM) was developed to improve the classification performance when only a few labeled EEG data in the target domain (target subject) were available. The proposed KL-SMM possesses the powerful capability of a matrix learning machine, which allows it to directly learn the structural information from matrix-form EEG data. In addition, the KL-SMM can not only fully leverage few labeled EEG data from the target domain during the learning procedure but can also leverage the existing model knowledge from the source domain (source subject). Therefore, the KL-SMM can enhance the generalization performance of the target classifier while guaranteeing privacy protection to a certain extent. Finally, the objective function of the KL-SMM can be easily optimized using the alternating direction method of multipliers method. Extensive experiments were conducted to evaluate the effectiveness of the KL-SMM on publicly available MI-based EEG datasets. Experimental results demonstrated that the KL-SMM outperformed the comparable methods when the EEG data were insufficient.

Keywords: motor imagery, brain-computer interface, electroencephalography, support matrix machine, transfer learning

OPEN ACCESS

Edited by:
Mohammad Khosravi, Persian Gulf University, Iran

Reviewed by:
Yufeng Yao, Changshu Institute of Technology, China
Juan Yang, Soochow University, China

****Correspondence:***
Qiong Wang
wangqiong@siat.ac.cn

† These authors have contributed equally to this work

Specialty section:
This article was submitted to Neuroprosthetics, a section of the journal Frontiers in Neuroscience

Received: *16 September 2020*
Accepted: *28 October 2020*
Published: *23 November 2020*

Citation:
Chen Y, Hang W, Liang S, Liu X, Li G, Wang Q, Qin J and Choi K-S (2020) A Novel Transfer Support Matrix Machine for Motor Imagery-Based Brain Computer Interface. Front. Neurosci. 14:606949. doi: 10.3389/fnins.2020.606949

INTRODUCTION

Brain-computer interface (BCI) systems enable machines to accurately perceive the mental states of human beings, thereby establishing an effective user interface between humans and machines. There are several kinds of BCI paradigms, such as steady-state visual evoked potentials (Allison et al., 2008), P300 (Salvaris and Sepulveda, 2009), and motor imagery (MI)

(Pfurtscheller and Neuper, 2001). Among them, the MI-based BCI is widely used because of its self-paced fashion, and it does not require any external stimuli (Pfurtscheller and Da Silva, 1999). Electroencephalography (EEG) is the most extensively used technique to record neuronal activity in the brain due to its high temporal resolution, portability, and non-invasiveness. EEG-based motor imagery BCI has shown great potential in many applications, such as rehabilitating the sensory-motor functions of disabled patients (Ang et al., 2011; Al-Qaysi et al., 2018) and facilitating smart living for healthy people (Vourvopoulos et al., 2017; Wang et al., 2019).

Although many machine learning algorithms have been developed to implement MI-based BCI with great success, most of them need to collect a considerable amount of labeled EEG data for model training, which is exceedingly time-consuming and labor-intensive. Insufficient labeled EEG data weaken the generalization capability of the classifier in the prediction. An intuitive solution to this problem is to leverage historical EEG data from the source domain (source subject) in modeling the target domain (target subject). However, this approach may engender some challenges. Owing to the EEG pattern variations between different subjects (Morioka et al., 2015), directly using the EEG data of the source domain may cause performance degradation. Furthermore, because the original EEG data contains personal information, the data of other subjects may not always be available for constructing the classifier for privacy reasons (Agarwal et al., 2019). Thus, exploring an effective knowledge transfer strategy that can protect the personal information of a source subject is highly desirable in the MI-based BCI.

From the perspective of transfer learning (Pan and Yang, 2009), the model knowledge of the source domain can potentially be leveraged to address these problems. Generally, EEG-based learning methods involve two steps: EEG feature extraction and classification. The model knowledge of the source domain can either be integrated into the feature extraction process (Kang et al., 2009; Samek et al., 2013), or be used in modeling the classifier (Azab et al., 2019). Specifically, Kang et al. (2009) proposed leveraging the linear combination of covariance matrices of the source subjects as reference during the feature extraction of the target EEG data. Azab et al. (2019) proposed the construction of multiple-source models and transfer of the weighted multiple-source model knowledge to the target domain. Deng et al. (2013) proposed a knowledge-leverage-based fuzzy system that can leverage the model knowledge from the source domain in order to make up for the lack of labeled target data as well as privacy protection.

Although it has been empirically demonstrated that the aforementioned methods are effective in dealing with EEG classification in scenarios where the labeled data are limited, these methods always need to transform the input data into vectors before classification. It is well known that EEG signals record brain activities over a period of time from multiple channels, which are naturally represented as matrices. Transforming the input matrices into vectors may destroy the correlation of rows or columns within matrix-form EEG features. Thus, several classification methods that can directly handle these matrix-form data have been developed accordingly. For example, Wolf et al. (2007) proposed modeling the regression matrix of a support vector machine (SVM), which is the sum of the k rank-one orthogonal matrices (rank-k SVM). Pirsiavash et al. (2009) proposed a bilinear SVM (BSVM) based on factorizing the regression matrix into the product of two low-rank matrices. Although these methods can capture the correlation within matrix data, pre-determining the rank of the regression matrix requires a tedious tuning procedure. Luo et al. (2015) proposed combining the nuclear norm and squared Frobenius norm of the regression matrix to derive the support matrix machine (SMM). The cornerstone of the SMM uses the nuclear norm of the regression matrix as the convex approximation of the matrix rank; thus, its optimization problem becomes more tractable and can be solved using the alternating direction method of multipliers (ADMM) method. Based on SMM, Zheng et al. proposed multiclass SMM (Zheng et al., 2018c) and sparse SMM (Zheng et al., 2018b) for EEG data. Although existing matrix classification methods can effectively deal with the matrix-form EEG data, they have not taken the transferrable knowledge into consideration to improve EEG classification performance. They may suffer from the weak generalization capability when the available EEG data are insufficient.

We propose a novel knowledge-leverage-based matrix classification method for MI-based EEG classification at the first time. The proposed knowledge-leverage-based SMM (KL-SMM) can address the above-mentioned problems by integrating the model knowledge from the source domain and a few labeled target EEG data. It possesses the powerful capability of the SMM for learning matrix-form data. Furthermore, the model knowledge of the source domain can be used to compensate for the deficiency in learning due to the lack of labeled target EEG data. Different from most current model parameter transfer learning methods, the proposed method can propagate the structural information from the source model to the target model. Hence, the generalization capability can be greatly enhanced by transferring the model knowledge and structural information of the source domain. Instead of directly using the source EEG data, the KL-SMM can afford privacy protection by leveraging only the model knowledge of the source domain. In addition, it can be efficiently optimized through the ADMM method. We conducted extensive experiments on two publicly available EEG datasets to validate the effectiveness of the proposed method. As demonstrated by the experimental results, the KL-SMM can achieve promising results in scenarios with few labeled target EEG data.

The remainder of this paper is organized as follows: Section "Related Works" is a review of related works. In Section "Matrix Learning Preliminaries", the notations and preliminaries of the SMM are introduced. The KL-SMM model and its learning algorithm are described in Section "Knowledge-Leverage-Based SMM". In Section "Experiments", the details of extensive experiments and analyses are presented. The conclusions of the paper are presented in Section "Conclusion".

RELATED WORKS

Transfer learning has emerged as a novel technique for retaining and reusing knowledge learned from historical tasks for new tasks. As described above, transfer learning generally refers to the knowledge-leverage-based learning mechanism, which can extract useful knowledge from the source domain and propagate them as the supervision information for modeling the target domain. According to the types of transferred knowledge of the source domain, most current research on transfer learning for EEG classification can be broadly divided into the following categories: (1) instance transfer, (2) feature representation transfer, and (3) model parameter transfer (Wang et al., 2015).

For the first category, it is assumed that the partial source EEG data can be selected and considered together with few labeled target EEG data. The source EEG data are obtained through either instance selection or importance sampling cross-validation (Li et al., 2010; Hossain et al., 2016, 2018; Zanini et al., 2018). For example, Hossain et al. (2016) proposed an instance selection strategy based on active learning. The selected source EEG data were then used together with available target-labeled EEG data to train the target model. Li et al. (2010) demonstrated the possibility of weighing the source EEG data through the importance sampling cross-validation strategy, following which the source data with high weights were used to estimate the target classifier.

The aim of the feature representation transfer method is to learn a good feature representation, which has some relevant source knowledge encoded within it, for the target subject. Most feature representation transfer learning methods were developed based on the common spatial patterns (CSP) through the modification of the covariance matrix or optimization function (Kang et al., 2009; Lotte and Guan, 2010; Samek et al., 2013). For example, Samek et al. (2013) developed an extension of the CSP. They proposed learning a stationary subspace in which the stationary information of multiple subjects can be transferred. In addition to the above-mentioned shallow feature representation transfer learning methods, several deep transfer learning methods (Fahimi et al., 2019; Hang et al., 2019) have been proposed. In general, these methods apply the domain adaptation techniques in a task-specific layer to incorporate the learned source and target deep features into a common feature space. For example, Hang et al. (2019) proposed leveraging the maximum mean discrepancy and the center-based discriminative feature learning techniques simultaneously to reduce the domain shift, demonstrating a performance improvement in the MI-based BCI.

The third category is the model parameter transfer, which assumes that the source subjects and target subjects share some parameters or prior distributions of the models. Model parameter transfer learning methods always leverage source models to model the target subjects in EEG classification. For example, Azab et al. (2019) proposed a logistic regression-based transfer learning method. The linear combination of multiple-source models was transferred for the construction of the target domain. In Alamgir et al. (2010); Jayaram et al. (2016), Alamgir et al. proposed a multi-task learning method to improve the generalization performance of the EEG classification for individual subjects using subject-specific information, as well as the shared model knowledge inherent in all available subjects.

Despite these successes, most current transfer learning methods require the direct use of source EEG data, which may cause the issue of privacy disclosure, especially for biomedical information. Furthermore, existing transfer learning methods used for EEG recognition always built on that the input data are vectors. However, transforming EEG data, which are naturally represented as matrices, into vectors will destroy their structural information. The proposed method belongs to the third category. Unlike the previous transfer learning methods, the KL-SMM can incorporate model knowledge from the source domain, thereby guaranteeing privacy protection to some extent; it can also directly handle matrix-form EEG data.

MATRIX LEARNING PRELIMINARIES

Among the current matrix learning methods, the SMM (Luo et al., 2015) and its variants [e.g., (Zheng et al., 2018a)] are applied in many fields, owing to their simplicity and effectiveness. In this section, we present some notations and preliminary knowledge on the SMM, which are the foundation of the proposed KL-SMM method.

Mathematical Notations

Matrices are denoted by bold uppercase letters (i.e., $\mathbf{X}$) in the following. For a matrix $\mathbf{X} \in \mathbb{R}^{d_1 \times d_2}$ of rank r, it can be expressed as $rank(\mathbf{X}) = r$. The condensed singular value decomposition (SVD) of $\mathbf{X}$ is denoted as $\mathbf{X} = \mathbf{U}_\mathbf{X} \sum_\mathbf{X} \mathbf{V}_\mathbf{X}^T$, where $\mathbf{U}_X \in \mathbb{R}^{d_1 \times r}$ and $\mathbf{V}_X \in \mathbb{R}^{d_2 \times r}$ satisfy $\mathbf{U}_\mathbf{X}^T \mathbf{U}_\mathbf{X} = \mathbf{I}_r$ and $\mathbf{V}_\mathbf{X}^T \mathbf{V}_\mathbf{X} = \mathbf{I}_r$, and $\sum_\mathbf{X} = \mathrm{diag}(\sigma_1(\mathbf{X}), \sigma_2(\mathbf{X}), \ldots, \sigma_r(\mathbf{X}))$ with $\sigma_1(\mathbf{X}) \geq \sigma_2(\mathbf{X}) \geq \cdots \geq \sigma_r(\mathbf{X}) > 0$.

Definition 1. Given any $\tau > 0$, the singular value thresholding (SVT) (Cai et al., 2010) of matrix $\mathbf{X}$ is defined as

$$D_\tau[\mathbf{X}] = \mathbf{U}_\mathbf{X} \mathbf{S}_\tau \left[\sum_\mathbf{X}\right] \mathbf{V}_\mathbf{X}^T \tag{1}$$

where $S_\tau\left[\sum_\mathbf{X}\right] = \mathrm{diag}\left(\{\sigma_1(\mathbf{X}) - \tau\}_+, \{\sigma_2(\mathbf{X}) - \tau\}_+, \ldots, \{\sigma_r(\mathbf{X}) - \tau\}_+\right)$ and $\{z\}_+ = \max(z, 0)$.

Let $\| \mathbf{X} \|_F = \sqrt{\sum_{i=1}^r \sigma_i(\mathbf{X})^2}$ be the Frobenius norm of $\mathbf{X}$, $\| \mathbf{X} \|_* = \sum_{i=1}^r \sigma_i(\mathbf{X})$ denotes the nuclear norm of $\mathbf{X}$, and the subdifferential of $\| \mathbf{X} \|_*$ can be defined as follows.

Definition 2. The subdifferential of $\| \mathbf{X} \|_*$, that is, $\partial \| \mathbf{X} \|_*$ (Candes and Recht, 2009), can be formulated as

$$\partial \| \mathbf{X} \|_* = \left\{ \mathbf{U}_\mathbf{X} \mathbf{V}_\mathbf{X}^T + \mathbf{Z} \,\middle|\, \mathbf{Z} \in \mathbb{R}^{d_1 \times d_2},\ \mathbf{U}_\mathbf{X}^T \mathbf{Z} = \mathbf{0},\ \mathbf{Z}\mathbf{V}_\mathbf{X} = 0,\ \| \mathbf{Z} \|_2 \leq 1 \right\}, \tag{2}$$

where $\| \mathbf{Z} \|_2 = \sigma_1(\mathbf{Z})$ denotes the spectral norm of $\mathbf{Z}$.

SMM

The matrix classifier, SMM, is defined as a penalty function plus a hinge loss. The penalty function, i.e., spectral elastic net, which

enjoys the property of grouping effect as well as keeping a low-rank representation. The hinge loss enjoys the property of large margin while contributing to the sparseness and robustness of the classifier. The objective function of the SMM can be formulated as follows:

$$\begin{aligned} &\min_{\mathbf{w},b} \frac{1}{2} tr\left(\mathbf{W}^T\mathbf{W}\right) + \tau \parallel \mathbf{W} \parallel_* + C\sum_{i=1}^{N} \xi_i \\ &\text{s.t.} \quad y_i\left[tr\left(\mathbf{W}^T\mathbf{X}_i\right) + b\right] \geq 1 - \xi_i, \xi_i \geq 0, \ \forall i = 1, 2, \ldots, N \end{aligned} \tag{3}$$

Specifically, the spectral elastic net can be represented as a combination of the squared Frobenius matrix norm $\parallel \mathbf{W} \parallel_F^2 = tr\left(\mathbf{W}^T\mathbf{W}\right)$ and nuclear norm $\parallel \mathbf{W} \parallel_*$ on the regression matrix W.

The objective function of the SMM can be solved through the ADMM method; thus, Eq. (3) is reformulated as

$$\begin{aligned} &\min_{\mathbf{W},b,S} F\left(\mathbf{W}, b\right) + G\left(\mathbf{S}\right) \\ &\text{s.t.} \ \mathbf{S} - \mathbf{W} = \mathbf{0} \end{aligned}, \tag{4}$$

where $F\left(\mathbf{W}, b\right) = \frac{1}{2} tr\left(\mathbf{W}^T\mathbf{W}\right) + C\sum_{i=1}^{N}\{1 - y_i[tr(\mathbf{W}^T\mathbf{X}_i) + b]\}_+$ and $G\left(\mathbf{S}\right) = \tau \parallel \mathbf{S} \parallel_*$.

According to the augmented Lagrangian function in Eq. (4), $\left(\mathbf{W}, b\right)$ and $\mathbf{S}$ can be iteratively computed in two steps:

$$\begin{aligned} (\mathbf{W}^{(k)}, b^{(k)}) = &\underset{(\mathbf{W},b)}{\operatorname{argmin}} F(\mathbf{W}, b) - tr((\mathbf{\Lambda}^{(k-1)})^T\mathbf{W}) \\ &+ \frac{\rho}{2} \parallel \mathbf{W} - \mathbf{S}^{(k-1)} \parallel_F^2, \end{aligned} \tag{5}$$

$$\mathbf{S}^{(k)} = \arg\min_{\mathbf{S}} G(\mathbf{S}) + tr((\mathbf{\Lambda}^{(k-1)})^T\mathbf{S}) + \frac{\rho}{2} \parallel \mathbf{W}^{(k)} - \mathbf{S} \parallel_F^2, \tag{6}$$

where k denotes the iteration index. $\rho > 0$ is a hyperparameter, and $\mathbf{\Lambda}$ is a Lagrangian multiplier.

Knowledge-Leverage-Based SMM

Generally, the current SMM and its variants belong to the data-driven method that always focuses on achieving impressive classification performance with sufficient training data. In practice, it is necessary to collect sufficient EEG data for each subject to establish a subject-specific classifier. However, long-term recording EEG data may exhaust the subject. Therefore, to model the target domain using insufficient EEG data, we proposed a novel algorithm to enhance the generalization capability of the SMM on the target domain by leveraging the useful knowledge underlying the source domain.

The framework of the KL-SMM for an EEG-based MI BCI is illustrated in **Figure 1**. To model the target domain, two main types of information, the model knowledge of the source domain and few labeled target EEG data, are used simultaneously.

KL-SMM Model

A dataset $D_s = \left\{\left(\mathbf{X}_{s,1}, y_{s,1}\right), \left(\mathbf{X}_{s,2}, y_{s,2}\right), \cdots, \left(\mathbf{X}_{s,N_s}, y_{s,N_s}\right)\right\}$ in source domain, it consists of N_s trials labeled EEG signals. $\mathbf{X}_{s,i} \in \mathbb{R}^{p\times q}$ denotes the ith trial with $p \times q$ dimension. $y_{s,i}$ is the corresponding class label of $\mathbf{X}_{s,i}$. A dataset $D_t = \left\{\left(\mathbf{X}_{t,1}, y_{t,1}\right), \cdots, \left(\mathbf{X}_{t,N}, y_{t,N}\right), \mathbf{X}_{t,N+1}, \cdots, \mathbf{X}_{t,N_t}\right\}$ in the target domain, it consists of N labeled EEG trials and $(N_t - N)$ unlabeled trials, where $N \ll (N_t - N)$.

For modeling the target domain, we proposed to integrate the labeled target EEG data and source model as follows:

$$\min_{f} \sum_{i=1}^{N} L\left(f\left(\mathbf{X}_{t,i}\right), y_{t,i}\right) + \lambda tr\left[\left(\mathbf{W}_s - \mathbf{W}_t\right)^T\left(\mathbf{W}_s - \mathbf{W}_t\right)\right], \tag{7}$$

Here, $L(\cdot, \cdot)$ denotes the loss function. $f\left(\mathbf{X}_{t,i}\right) = tr\left(\mathbf{W}_t^T\mathbf{X}_{t,i}\right) + b$ denotes the matrix classifier to be learned. Eq. (7) includes two terms, where the first term is used to learn from labeled target EEG data, and the second term is designed to leverage the model knowledge (i.e., $\mathbf{W}_s$) underlying the source domain. The goal is to exploit the desired KL-SMM by approximating its model to the source model. The parameter λ is adopted to balance the influence between the two terms above.

As in the SMM, we introduced the spectral elastic net penalty to capture the correlation information within the matrix-form

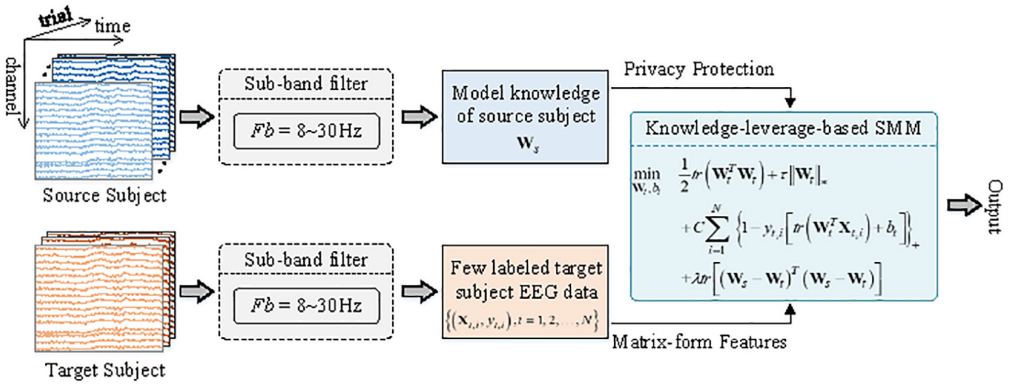

FIGURE 1 | Framework of the proposed KL-SMM for EEG-based motor imagery BCI. Both source EEG data and target EEG data are first bandpass filtered in the frequency range of 8∼30 Hz. SMM is then applied to learn source model $\boldsymbol{W_s}$. The source model (only needed) enables the classification model realize the privacy protection. An objective function of the proposed KL-SMM is then implemented by using the source model and the matrix-form features extracted from few labeled target data.

EEG data. Furthermore, the hinge loss function was adopted, owing to its inherent characteristic of sparseness and robustness. Above all, the objective function of the proposed KL-SMM can be formulated as follows:

$$\begin{aligned}\min_{\mathbf{W}_t,b_t}\ & \frac{1}{2}tr(\mathbf{W}_t^T\mathbf{W}_t)+\tau\parallel\mathbf{W}_t\parallel_*+C\sum_{i=1}^{N}\xi_i^t \\ & +\lambda tr[(\mathbf{W}_s-\mathbf{W}_t)^T(\mathbf{W}_s-\mathbf{W}_t)] \\ \text{s.t.}\quad & y_{t,i}[tr(\mathbf{W}_t^T\mathbf{X}_{t,i})+b_t]\geq 1-\xi_i^t,\xi_i^t\geq 0, \\ & \forall i=1,2,\ldots,N\end{aligned}, \tag{8}$$

where the parameter $C>0$ is used to maintain a balance between fitting the labeled target EEG data and minimizing the complexity of the solution.

Parameter Learning for KL-SMM

Because the Eq. (8) is convex in both $\mathbf{W}_t$ and b_t, an alternating iterative strategy based on the ADMM method can be used to derive the learning algorithm of the KL-SMM. Specifically, by introducing an auxiliary variable S_t, the objective function of the KL-SMM can be equivalently reformulated as

$$\begin{aligned}\min_{\mathbf{W}_t,b_t,\mathbf{S}_t}\ & F\left(\mathbf{W}_t,b_t\right)+G\left(\mathbf{S}_t\right) \\ \text{s.t.}\quad & \mathbf{S}_t-\mathbf{W}_t=\mathbf{0}\end{aligned}, \tag{9}$$

where $F\left(\mathbf{W}_t,b_t\right)=\frac{1}{2}tr\left(\mathbf{W}_t^T\mathbf{W}_t\right)+C\sum_{i=1}^{N}\{1-y_{t,i}[tr\left(\mathbf{W}_t^T\mathbf{X}_{t,i}\right)+b_t]\}_+ +\lambda tr\left[\left(\mathbf{W}_s-\mathbf{W}_t\right)^T\left(\mathbf{W}_s-\mathbf{W}_t\right)\right]$ and $G\left(\mathbf{S}_t\right)=\tau\parallel\mathbf{S}_t\parallel_*$.

The parameter optimization of Eq. (9) can be solved using the augmented Lagrangian algorithm

$$\begin{aligned}L_a\left(\mathbf{W}_t,b_t,\mathbf{S}_t,\mathbf{\Lambda}\right)=&F(\mathbf{W}_t,b_t)+G\left(\mathbf{S}_t\right)+tr[\mathbf{\Lambda}^T(\mathbf{S}_t-\mathbf{W}_t)] \\ &+\frac{\rho}{2}\parallel\mathbf{S}_t-\mathbf{W}_t\parallel_F^2,\end{aligned} \tag{10}$$

where $\mathbf{\Lambda}$ is the Lagrangian multiplier, and $\rho>0$ is a hyperparameter. Theorems 1 and 2 provide the calculations of parameters $\mathbf{S}_t$ and $\left(\mathbf{W}_t,b_t\right)$.

Theorem 1. For the fixed $\mathbf{W}_t$, using the Lagrangian multiplier $\mathbf{\Lambda}$ and any positive scalar $\tau>0$, $\rho>0$ in Eq. (10), $\mathbf{S}_t$ can be optimized using the following update rule:

$$\mathbf{S}_t=D_\tau\left[\rho\mathbf{W}_t-\mathbf{\Lambda}\right]. \tag{11}$$

Proof of Theorem 1: Supposing $\mathbf{W}_t$ is fixed, the optimization problem in Eq. (10) is equivalent to minimizing the function as follows:

$$J\left(\mathbf{S}_t\right)=\tau\parallel\mathbf{S}_t\parallel_*+tr(\mathbf{\Lambda}^T\mathbf{S}_t)+\frac{\rho}{2}\parallel\mathbf{S}_t-\mathbf{W}_t\parallel_F^2. \tag{12}$$

Because $J\left(\mathbf{S}_t\right)$ is convex, with respect to $\mathbf{S}_t$, if $0\in\partial J\left(\mathbf{S}_t^*\right)$ with $\mathbf{S}_t^*=\left(1/\rho\right)\cdot D_\tau\left[\rho\mathbf{W}_t-\mathbf{\Lambda}\right]$ can be proven, we can conclude that $\mathbf{S}_t^*$ is a solution to Eq. (12). The derivation of $J\left(\mathbf{S}_t\right)$ with respect to $\mathbf{S}_t$ can be expressed as

$$\partial J\left(\mathbf{S}_t\right)=\mathbf{\Lambda}-\rho\mathbf{W}_t+\rho\mathbf{S}_t+\tau\cdot\partial\parallel\mathbf{S}_t\parallel_*. \tag{13}$$

To further simplify this equation, let the SVD of $(\rho\mathbf{W}_t-\mathbf{\Lambda})$ be denoted as $\rho\mathbf{W}_t-\mathbf{\Lambda}=\mathbf{U}_a\sum_a\mathbf{V}_a^T+\mathbf{U}_b\sum_b\mathbf{V}_b^T$. In the equation, $\sum_a$ represents the diagonal matrix with diagonal entries greater than τ. $\sum_b$ represents the remaining part of the SVD with diagonal entries less than or equal to τ. $\mathbf{U}_a$ and $\mathbf{V}_a$ ($\mathbf{U}_b$ and $\mathbf{V}_b$) are matrices that correspond to the left and right singular vectors of the diagonal matrix $\sum_a$ ($\sum_b$). In terms of Definition 1, $\mathbf{S}_t^*$ can be reformulated as $\left(1/\rho\right)\cdot\mathbf{U}_a\left(\sum_a-\tau\mathbf{I}\right)\mathbf{V}_a^T$. Substituting $\mathbf{S}_t^*$ into Eq. (13), we have

$$\begin{aligned}\partial J\left(\mathbf{S}_t\right)|_{\mathbf{S}_t^*}&=\mathbf{\Lambda}-\rho\mathbf{W}_t+\rho\mathbf{S}_t^*+\tau\cdot\partial\parallel\mathbf{S}_t^*\parallel_* \\ &=-\tau\left(\mathbf{U}_a\mathbf{V}_a^T+\tfrac{1}{\tau}\mathbf{U}_b\sum_b\mathbf{V}_b^T\right)+\tau\cdot\partial\parallel\mathbf{S}_t^*\parallel_*.\end{aligned} \tag{14}$$

Let $\mathbf{Z}=(1/\tau)\cdot\mathbf{U}_b\sum_b\mathbf{V}_b^T$, because $\mathbf{U}_a$, $\mathbf{U}_b$, $\mathbf{V}_a$, $\mathbf{V}_b$ are column orthogonal, we can easily verify that $\mathbf{U}_a^T\mathbf{Z}=0$, $\mathbf{Z}\mathbf{V}_a=0$, and $\parallel\mathbf{Z}\parallel_2\leq 1$. Thus, we have $0\in\partial J\left(\mathbf{S}_t^*\right)$. Theorem 1 is proved.

Theorem 2. For the fixed $\mathbf{S}_t$, $\left(\mathbf{W}_t,b_t\right)$ can be optimized using the following update rule:

$$\mathbf{W}_t=\frac{1}{2\lambda+\rho+1}\left(\mathbf{\Lambda}+\rho\mathbf{S}_t+2\lambda\mathbf{W}_s+\sum_{i=1}^{N_t}\alpha_i y_{t,i}\mathbf{X}_{t,i}\right), \tag{15}$$

$$b_t=\frac{1}{|\Delta|}\sum_{i\in\Delta}\left\{y_{t,i}-[tr(\mathbf{W}_t^T\mathbf{X}_{t,i})]\right\}, \tag{16}$$

where $\Delta=\{i\,|0\leq\alpha_i\leq C,\forall i=1,2,\ldots,N\}$ refers to the Lagrangian multipliers, and$\alpha=[\alpha_1,\alpha_2,\cdots,\alpha_N]^T\in\mathbb{R}^N$ can be obtained using the box constraint quadratic programming solver:

$$\begin{aligned}\max_{\alpha}\ & -\frac{1}{2}\boldsymbol{\alpha}^T\mathbf{K}\boldsymbol{\alpha}+\mathbf{H}^T\boldsymbol{\alpha} \\ \text{s.t.}\ & 0\leq\boldsymbol{\alpha}\leq C,\boldsymbol{\alpha}^T\mathbf{Y}=0\end{aligned}, \tag{17}$$

where $\mathbf{K}=\left[K_{ij}\right]\in\mathbb{R}^{N\times N}$ and $\mathbf{H}=\left[\mathrm{h}_i\right]\in\mathbb{R}^N$ with

$$K_{ij}=\frac{1}{2\lambda+\rho+1}y_{t,i}y_{t,j}tr(\mathbf{X}_{t,i}^T\mathbf{X}_{t,j}), \tag{18}$$

$$\mathrm{h}_i=1-\frac{1}{2\lambda+\rho+1}y_{t,i}tr[(\mathbf{\Lambda}+\rho\mathbf{S}_t+2\lambda\mathbf{W}_s)^T\mathbf{X}_{t,i}]. \tag{19}$$

Proof of Theorem 2: Given the fixed variable $\mathbf{S}_t$, the optimization problem in Eq. (10) equals to optimize the following objective function:

$$\begin{aligned}\min_{\mathbf{W}_t,b_t}\ & \frac{1}{2}tr(\mathbf{W}_t^T\mathbf{W}_t)+C\sum_{i=1}^{N}\xi_i^t-tr(\mathbf{\Lambda}^T\mathbf{W}_t)+\frac{\rho}{2}\parallel\mathbf{S}_t-\mathbf{W}_t\parallel_F^2 \\ & +\lambda tr\left[\left(\mathbf{W}_s-\mathbf{W}_t\right)^T\left(\mathbf{W}_s-\mathbf{W}_t\right)\right] \\ \text{s.t.}\quad & y_{t,i}\left[tr\left(\mathbf{W}_t^T\mathbf{X}_{t,i}\right)+b_t\right]\geq 1-\xi_i^t,\ \xi_i^t\geq 0,\forall i=1,2,\ldots,N\end{aligned}. \tag{20}$$

The augmented Lagrangian function of Eq. (20) is denoted as

$$\begin{aligned}L_a'=&\frac{1}{2}tr\left(\mathbf{W}_t^T\mathbf{W}_t\right)+C\sum_{i=1}^{N}\xi_i^t-tr(\mathbf{\Lambda}^T\mathbf{W}_t)+\frac{\rho}{2}\parallel\mathbf{S}_t-\mathbf{W}_t\parallel_F^2 \\ &+\lambda tr\left[\left(\mathbf{W}_s-\mathbf{W}_t\right)^T\left(\mathbf{W}_s-\mathbf{W}_t\right)\right] \\ &-\sum_{i=1}^{N}\alpha_i\left\{y_{t,i}\left[tr\left(\mathbf{W}_t^T\mathbf{X}_{t,i}\right)+b_t\right]-1+\xi_i^t\right\}-\sum_{i=1}^{N}\beta_i\xi_i^t\end{aligned}. \tag{21}$$

Setting the derivative of L_a' with respect to ξ_i^t and b_t, to 0, we can obtain

$$\frac{\partial L_a'}{\partial \xi_i^t} = 0 \Rightarrow C - \alpha_i - \beta_i = 0 \text{ and } \frac{\partial L_a'}{\partial b_t} = 0 \Rightarrow \sum_{i=1}^{N} \alpha_i y_{t,i} = 0. \tag{22}$$

Substituting Eq. (22) into Eq. (21), and then setting the derivative of L_a' with respect to W_t to 0, we obtain

$$\frac{\partial L_a'}{\partial \mathbf{W}_t} = 0 \Rightarrow \mathbf{W}_t = \frac{1}{2\lambda + \rho + 1}\left(\mathbf{\Lambda} + \rho \mathbf{S}_t + 2\lambda \mathbf{W}_s + \sum_{i=1}^{N} \alpha_i y_{t,i} \mathbf{X}_{t,i}\right). \tag{23}$$

Substituting Eq. (22) and Eq. (23) into Eq. (21),

$$L_a' = \sum_{i=1}^{N}\left(1 - \frac{1}{2\lambda + \rho + 1} y_{t,i} tr\left[\left(\mathbf{\Lambda} + \rho \mathbf{S}_t + 2\lambda \mathbf{W}_s\right)^T \mathbf{X}_i\right]\right)\alpha_i - \frac{1}{2(2\lambda + \rho + 1)} \sum_{i=1}^{N}\sum_{j=1}^{N} \alpha_i \alpha_j y_{t,i} y_{t,j} tr(\mathbf{X}_{t,i}^T \mathbf{X}_{t,j}) + \theta. \tag{24}$$

Here, $\theta$is a constant, which can be represented as $\theta = \frac{\rho}{2} tr\left(\mathbf{S}_t^T \mathbf{S}_t\right) + \lambda tr\left(\mathbf{W}_s^T \mathbf{W}_s\right) - \frac{1}{2(2\lambda+\rho+1)} \parallel \mathbf{\Lambda} + \rho \mathbf{S}_t + 2\lambda \mathbf{W}_s \parallel_F^2$. Thus, the dual problem of Eq. (24) can be denoted as

$$\begin{aligned} \max_{\alpha} & \sum_{i=1}^{N}\left(1 - \frac{1}{2\lambda + \rho + 1} y_{t,i} tr\left[\left(\mathbf{\Lambda} + \rho \mathbf{S}_t + 2\lambda \mathbf{W}_s\right)^T \mathbf{X}_i\right]\right)\alpha_i \\ & - \frac{1}{2(2\lambda + \rho + 1)} \sum_{i=1}^{N}\sum_{j=1}^{N} \alpha_i \alpha_j y_{t,i} y_{t,j} tr(\mathbf{X}_{t,i}^T \mathbf{X}_{t,j}) \\ \text{s.t.} & \sum_{i=1}^{N} \alpha_i y_{t,i} = 0, 0 \le \alpha_i \le C, \forall i = 1, 2, \ldots, N \end{aligned} \tag{25}$$

Algorithm 1: The learning procedure for KL-SMM

Input: Training dataset $D_T = \left\{\mathbf{X}_{t,i}, y_{t,i}\right\}_{i=1}^{N}$, source model $\mathbf{W}_s$, parameter τ and λ;

Output: $\mathbf{W}_t$, b_t;

Initialize: $\mathbf{S}_t^{(-1)} = \hat{\mathbf{S}}_t^{(0)} \in \mathbf{R}^{p \times q}$, $\mathbf{\Lambda}^{(-1)} = \hat{\mathbf{\Lambda}}^{(0)} \in \mathbf{R}^{p \times q}$, $\nu^{(1)} = 1$, $\eta \in (0, 1)$, $\rho > 0, l = 1$

Repeat

Computing $\mathbf{W}_t^{(l)}$, $b_t^{(l)}$ with $\hat{\mathbf{S}}_t^{(l)}$ and $\hat{\mathbf{\Lambda}}^{(l)}$ using Theorem 2;

Computing $\mathbf{S}_t^{(l)}$with $\mathbf{W}_t^{(l)}$ and $\hat{\mathbf{\Lambda}}^{(l)}$ using Theorem 1;

Update $\mathbf{\Lambda}^{(l)} \leftarrow \hat{\mathbf{\Lambda}}^{(l)} + \rho\left(\mathbf{S}_t^{(l)} - \mathbf{W}_t^{(l)}\right)$;

$l \leftarrow l + 1$.

Until convergence

The optimization problem of Eq. (21) can finally be transformed into a QP problem. Substituting the obtained optimal solution α into Eq. (23), it is easy to obtain the value of $\mathbf{W}_t$. Finally, the optimal b_t can be calculated as follows:

$$b_t = y_{t,i} - \left[tr\left(\mathbf{W}_t^T \mathbf{X}_{t,i}\right)\right]. \tag{26}$$

In practice, averaging these optimal solutions, we can obtain

$$b_t = \frac{1}{|\Delta|} \sum_{i \in \Delta}\left\{y_{t,i} - \left[\text{tr}\left(\left(\mathbf{W}_t\right)^T \mathbf{X}_{t,i}\right)\right]\right\}, \tag{27}$$

where $\Delta = \{i \,|\, 0 \le \alpha_i \le C, \forall i = 1, 2, \ldots, N\}$. Theorem 2 is proved.

For the fixed $\mathbf{W}_t$ and $\mathbf{S}_t$, the Lagrangian multiplier $\mathbf{\Lambda}$ in Eq. (10) can be updated as follows:

$$\mathbf{\Lambda}^{(k)} = \mathbf{\Lambda}^{(k-1)} + \rho\left(\mathbf{S}_t - \mathbf{W}_t\right). \tag{28}$$

The optimal solution is estimated iteratively. The learning procedure for the KL-SMM is given in Algorithm 1.

Computational Complexity

We further analyzed the computational complexity of the KL-SMM. In Algorithm 1, Step 1 computes the parameter $\left(\mathbf{W}_t, b_t\right)$ by solving a QP problem in Eq. (17), which takes time $O\left(N^2 pq\right)$ with Nsamples of $p \times q$ dimension. Step 2 computes the eigen decomposition for $\mathbf{S}_t$ in Eq. (11), which takes time $O\left(\min\left(p^2 q, pq^2\right)\right)$. In practice, the dimensions, p and q, of the extracted EEG features are not too high. Thus, the computational complexity of the KL-SMM is dominated by the QP, that is, $O\left(I \cdot N^2 pq\right)$, where I denotes the iteration number.

EXPERIMENTS

In this section, we evaluate the proposed KL-SMM on two publicly available MI EEG datasets [i.e., Datasets IIa and IIb of the BCI competition (Hang et al., 2020)], which can be found in http://www.bbci.de/competition/iv/. We first describe the EEG datasets. Then, the compared methods and corresponding parameter settings are provided. Finally, we present and discuss the experimental results.

EEG Data Description and Preprocessing

(1) *BCI competition IV Dataset IIa (Exp.1)*: This dataset includes 22-channel EEG signals recorded from nine subjects (denoted as *S01–S09*). During the experiment, each subject was required to perform four kinds of MI tasks, hand (left and right), foot, and tongue. A total of 576 trials of two sessions on different days were collected for each subject. In our experiment, we used the left-hand and right-hand EEG data. In addition, the EEG trials collected from the second day were adopted. Thus, the training and test datasets each contained 72 EEG trials.

(2) *BCI competition IV Dataset IIb (Exp.2)*: This dataset also contains the EEG signals of nine subjects (denoted as *B01–B09*), which were recorded using three electrodes, *C3*, *Cz*, and *C4*. During the experiment, each subject was instructed to perform left- and right-hand MI tasks for 4.5 s. For each subject, there were five sessions. Sessions 1, 2, and 3 were collected on the first day, and 4 and 5 were collected on the second day. Similar to *Exp.1*, the EEG trials collected from the second day were used. Specifically, Session 4 was used as the training data, and Session 5 was used as the test data.

With reference to Hang et al. (2020), there was a time interval of *[0.5, 3]*s after the visual cues in each trial for all the datasets. We bandpass-filtered the EEG signals to 8–30 Hz through a five-order Butterworth filter, which covers the dominated frequency band for MI tasks (Nam et al., 2011). Then, we adopted the spatial filters to detect the MI-related desynchronization/synchronization (ERD/ERS) patterns. Finally, the widely used band-power estimation method (Vidaurre et al., 2005) was used to extract the matrix-form EEG features for all the subjects. To construct the transfer learning tasks, each subject was considered the target domain, and the training data of the remaining subjects constituted the source domain. To evaluate the performance of the KL-SMM, we set three different numbers of labeled target EEG data, that is, the first 8, 14, and 20 training trials. The classification performances on the test data of all the subjects were reported.

Experimental Setup

Baseline Methods

To evaluate the classification performance of the aforementioned transfer tasks, the proposed method was compared with four methods in the experiments: (1) SVM (Vapnik, 1995), (2) BSVM (Pirsiavash et al., 2009), (3) SMM (Luo et al., 2015), and (4) Adaptive SVM (ASVM) (Yang et al., 2007).

Implementation Details

It is known that the format of the input data of both the SVM and ASVM should be vectors or scalars. Thus, we first had to reshape the extracted two-dimensional matrix features into vector features. For the BSVM, SMM, and proposed KL-SMM, the matrix features can be inputted directly. To evaluate the effect of the transfer learning mechanism, because the SVM, BSVM, and SMM are no-transfer baselines, we simply used the labeled target EEG trials as the training data to build these classification models. In addition, for the ASVM and KL-SMM, we also leveraged the source model knowledge in constructing the target classifier. However, unlike the ASVM, the traditional transfer learning method, the KL-SMM can directly process EEG matrix features and fully exploit the structural information.

The optimal parameters were selected using a five-fold cross-validation method on the training group for all comparison methods. Parameter C was assigned by selecting the value from the set $\{1e-6, 1e-5, 1e-4, 1e-3, 1e-2, 1e-1, 1e0, 1e1\}$. For the SMM and KL-SMM, we tuned the parameter τ from the set $\{1e-5,\ 2e-5,\ 5e-5,\ 1e-4,\ 2e-4,\ 5e-4,\ 1e-3,\ 2e-3,\ 5e-3,\ 1e-2,\ 2e-2,\ 5e-2,\ 1e-1,\ 2e-1,\ 5e-1,\ 1e0\}$. To ensure a fair comparison with the ASVM, an adjustable parameter λ_A was added to the term of knowledge transfer, which can control how much the knowledge of source domain to transfer. For the KL-SMM and ASVM, parameters λ and λ_A were set by selecting the value from set $\{1e-4,\ 5e-4,\ 1e-3,\ 5e-3,\ 1e-2,\ 5e-2,\ 1e-1,\ 5e-1,\ 1e0\}$. To validate the classification performance of our method, we used the following metrics on the test dataset, i.e., Accuracy (ACC), $F1$ score (F1), and the area under the receiver operating characteristics curve (AUC). Herein, $\mathrm{ACC} = (\mathrm{TP}+\mathrm{TN}) \big/ (\mathrm{TP}+\mathrm{FN}+\mathrm{FP}+\mathrm{TN})$ and $\mathrm{F1} = 2 \times \mathrm{PPV} \times \mathrm{SEN} \big/ (\mathrm{PPV}+\mathrm{SEN})$, where the positive predictive value $(\mathrm{PPV}) = \mathrm{TP} \big/ (\mathrm{TP}+\mathrm{FP})$ and sensitivity $(\mathrm{SEN}) = \mathrm{TP} \big/ (\mathrm{TP}+\mathrm{FN})$.

Experimental Results Analysis

The classification performances of all the comparison methods on 14 labeled target EEG trials on two datasets are given in **Tables 1–6**. The performance comparison of the KL-SMM with the compared methods in *Exp.1* is shown in **Tables 1–3**. The classification results of all compared methods in *Exp. 2* are shown in **Tables 4–6**. The best classification performance values are highlighted in bold. According to the results, the following conclusions can be drawn.

From the classification performances of all the comparison methods on the 14 labeled target EEG trials, we found that the proposed KL-SMM method achieved the highest average results in terms of the ACC, AUC, and F1. As shown in **Tables 1–3**, the proposed KL-SMM outperformed the baseline SMM on average by 5.87%, 5.66%, and 8.85% based on the ACC, AUC, and F1, respectively. As can be observed from the classification results in **Tables 4–6**, the KL-SMM outperformed the SMM on average by 3.68%, 3.78%, and 5.83% based on the ACC, AUC, and F1, respectively. The promising performances prove that the KL-SMM can leverage the model knowledge of the source subject to boost the generalization capability of the SMM when there are limited labeled EEG trials. In addition, the KL-SMM boosted the classification accuracy for six out of nine subjects in Exp.1, and eight out of nine subjects in Exp.2, respectively. These experimental results further demonstrate the effectiveness of the proposed KL-SMM that leveraged the knowledge underlying the source domain.

The BSVM and SMM outperformed the SVM in most cases. This confirms the ability of the BSVM and SMM to exploit the correlations between rows or columns of EEG matrix features.

TABLE 1 | Comparison of ACC using 14 labeled target EEG data in *Exp.1*.

	Target subjects									
Methods	**S01**	**S02**	**S03**	**S04**	**S05**	**S06**	**S07**	**S08**	**S09**	**Avg.**
SVM	0.5972	0.5000	0.9583	0.5556	0.5139	0.5556	0.5972	0.9306	0.8472	0.6728
BSVM	0.5556	0.4861	0.9583	0.5278	0.5972	0.5417	0.5972	**1.0000**	0.8472	0.6790
SMM	0.6111	0.5000	**0.9722**	0.5556	0.5556	0.5556	0.6111	0.9444	0.8472	0.6836
ASVM	0.6111	**0.5139**	0.9167	0.6667	0.6389	0.5972	0.7222	0.9444	0.8472	0.7176
KL-SMM	**0.6528**	0.5000	0.9306	**0.7361**	**0.6944**	**0.6111**	**0.7361**	0.9583	**0.8611**	**0.7423**

TABLE 2 | Comparison of AUC using 14 labeled target EEG data in *Exp.1*.

	Target subjects									
Methods	**S01**	**S02**	**S03**	**S04**	**S05**	**S06**	**S07**	**S08**	**S09**	**Avg.**
SVM	0.6265	0.5015	0.9776	0.5640	0.5316	0.5548	0.6019	0.9228	0.9190	0.6889
BSVM	0.5980	0.5023	0.9367	0.5239	0.6019	0.5579	0.6181	**1.0000**	0.9190	0.6953
SMM	0.6273	0.5015	**0.9830**	0.5640	0.5733	0.5548	0.6142	0.9406	0.9190	0.6975
ASVM	0.6273	**0.5177**	0.9313	0.6790	0.6481	0.6142	0.7261	0.9406	0.9190	0.7337
KL-SMM	**0.6744**	0.5015	0.9375	**0.7261**	**0.7068**	**0.6173**	**0.7415**	0.9606	**0.9213**	**0.7541**

TABLE 3 | Comparison of F1 using 14 labeled target EEG data in *Exp. 1*.

	Target subjects									
Methods	**S01**	**S02**	**S03**	**S04**	**S05**	**S06**	**S07**	**S08**	**S09**	**Avg.**
SVM	0.3256	0.5385	0.9589	0.4483	0.3636	0.4667	0.6234	0.9275	0.8308	0.6092
BSVM	0.2000	0.5195	0.9565	0.3462	0.5538	0.4407	0.5397	**1.0000**	0.8308	0.5986
SMM	0.3636	0.5385	**0.9722**	0.4483	0.4286	0.4667	0.6410	0.9429	0.8308	0.6258
ASVM	0.3636	**0.5570**	0.9091	0.6842	0.6579	**0.5672**	0.6970	0.9429	0.8308	0.6900
KL-SMM	**0.4681**	0.5385	0.9254	**0.7397**	**0.7027**	0.5333	**0.7164**	0.9565	**0.8485**	**0.7143**

TABLE 4 | Comparison of ACC using 14 labeled target EEG data in *Exp. 2*.

	Target subjects									
Methods	**B01**	**B02**	**B03**	**B04**	**B05**	**B06**	**B07**	**B08**	**B09**	**Avg.**
SVM	0.4750	0.5125	0.4500	0.8688	0.5813	0.6688	0.7000	0.9500	0.7250	0.6590
BSVM	0.5125	0.5125	0.4813	0.8750	0.5688	0.5813	0.6250	0.9375	0.7188	0.6458
SMM	0.4875	**0.5313**	0.4500	0.8750	0.5938	0.6750	0.6813	0.9563	0.7625	0.6681
ASVM	0.6063	0.5000	**0.5000**	0.9125	0.6063	0.6938	0.6813	0.9500	0.6688	0.6799
KL-SMM	**0.6125**	**0.5313**	0.4625	**0.9563**	**0.6438**	**0.7125**	**0.7250**	**0.9625**	**0.7375**	**0.7049**

TABLE 5 | Comparison of AUC using 14 labeled target EEG data in *Exp. 2*.

	Target subjects									
Methods	**B01**	**B02**	**B03**	**B04**	**B05**	**B06**	**B07**	**B08**	**B09**	**Avg.**
SVM	0.4614	0.5247	0.4655	0.8698	0.5948	0.6761	0.6980	0.9577	0.7263	0.6638
BSVM	0.4963	0.5102	0.5048	0.8652	0.5781	0.5833	0.6159	0.9453	0.7080	0.6452
SMM	0.4747	0.5431	0.4655	0.8814	0.6081	0.6825	0.6841	0.9605	**0.7678**	0.6742
ASVM	0.5922	0.5103	**0.5356**	0.9377	0.6172	0.7138	0.6664	0.9577	0.6580	0.6876
KL-SMM	**0.5939**	**0.5470**	0.4697	**0.9673**	**0.6627**	**0.7389**	**0.7202**	**0.9670**	0.7416	**0.7120**

TABLE 6 | Comparison of F1 using 14 labeled target EEG data in *Exp. 2*.

	Target subjects									
Methods	**B01**	**B02**	**B03**	**B04**	**B05**	**B06**	**B07**	**B08**	**B09**	**Avg.**
SVM	0.5172	0.4348	0.3125	0.8800	0.6082	0.6788	0.7303	0.9518	0.7755	0.6544
BSVM	0.6100	**0.5938**	0.3566	0.8837	0.5767	0.5839	0.7170	0.9390	0.7368	0.6664
SMM	0.5119	0.4604	0.3125	0.8851	0.6061	0.6829	0.7052	0.9576	**0.7935**	0.6572
ASVM	0.6358	0.3651	**0.5918**	0.9176	0.6557	0.7322	0.7243	0.9518	0.7039	0.6976
KL-SMM	**0.6702**	0.4000	0.4691	**0.9571**	**0.6885**	**0.7527**	**0.7528**	**0.9634**	0.7857	**0.7155**

Notably, the SMM has better classification performance than the BSVM because of its convex objective function that can be effectively optimized by the ADMM method. Furthermore, it can be observed that, owing to its ability to leverage the source model knowledge in modeling the target domain when the labeled target EEG data is very limited, the ASVM yielded

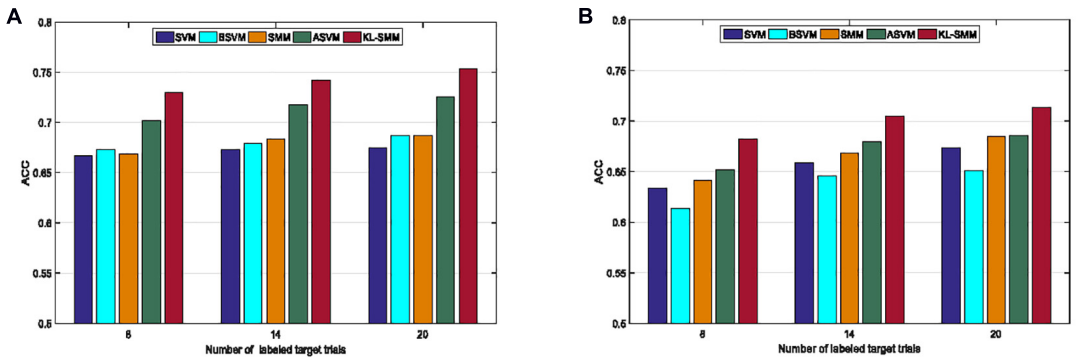

FIGURE 2 | Average classification ACCs of comparison methods with different numbers of labeled target EEG trials in *Exp.1* **(A)** and *Exp.2* **(B)**.

TABLE 7 | Statistical significance comparisons of ACC of KL-SMM and other methods in *Exp.1* and *Exp.2*.

	Exp.1				Exp.2			
Num. of labeled trials	**KL-SMM vs. SVM**	**KL-SMM vs. BSVM**	**KL-SMM vs. SMM**	**KL-SMM vs. ASVM**	**KL-SMM vs. SVM**	**KL-SMM vs. BSVM**	**KL-SMM vs. SMM**	**KL-SMM vs. ASVM**
8	**0.0167**	**0.0116**	**0.0085**	**0.0085**	**0.0164**	**0.0107**	**0.0465**	**0.0307**
14	**0.0287**	**0.0485**	**0.0442**	**0.0207**	**0.0129**	**0.0074**	**0.0419**	**0.0376**
20	**0.0039**	**0.0227**	**0.0060**	**0.0249**	**0.0014**	**0.0053**	**0.0215**	**0.0328**

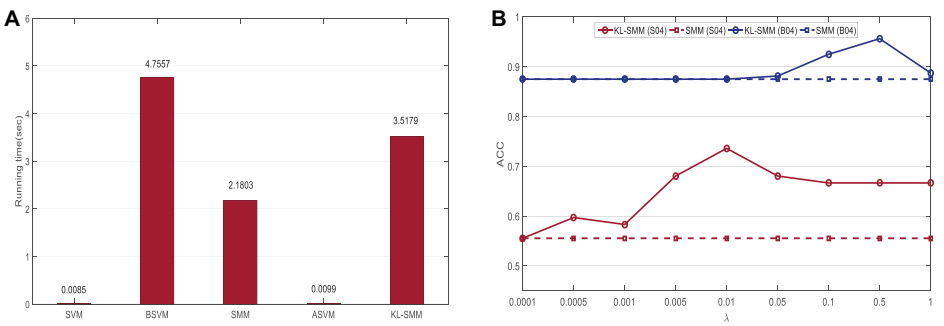

FIGURE 3 | (A) Running time for subject *S01* using 14 labeled target EEG trials in *Exp.1*; **(B)** Parameter sensitivity of KL-SMM for the transfer tasks *S04* in *Exp.1* and *B04* in *Exp.2* using 14 labeled target EEG trials, respectively.

better classification results than the SVM. The foundation of the KL-SMM is the SMM, which can leverage the source model knowledge and exploit the structural information within the EEG feature matrices. The experimental results prove that structural information can indeed improve classification performance.

We further studied the effects of different numbers of labeled target EEG instances on the classification performance of the KL-SMM. **Figure 2** shows the average classification ACCs when 8, 14, and 20 labeled target EEG trials were available from the target subject. **Figures 2A,B** show the average classification results of all the compared methods for *Exp.1* and *Exp.2*, respectively. It can be observed that the KL-SMM outperformed the other methods in all the cases. Specifically, the improvement was more pronounced when few labeled target EEG trials were available, as shown in **Figure 2B**. From these results, we can observe that increasing the number of the labeled target EEG instances improved the average classification ACCs of all the compared methods. This is mainly because more training data may enhance the generalization performance of the classification model. The average ACC of the KL-SMM was significantly better than those of the other methods when there was no knowledge transfer, especially when the labeled target EEG instances were very limited. Overall, compared to other methods, the classification performance of the proposed KL-SMM was superior. The encouraging results were mainly attributed to the fact that the KL-SMM method possessed the matrix learning capability derived from the matrix learning machine, which allowed it to directly handle the matrix-form features, thus retaining the structural information of EEG data. In addition, the KL-SMM achieved a more outstanding classification performance because of its ability to leverage the useful model knowledge of the source domain.

DISCUSSION

Statistical Analysis

We further performed a t-test statistical analysis to verify whether there was a significant difference with a confidence level of 95% between the KL-SMM and the other methods. The results of the t-test using different numbers of labeled target EEG trials are shown in **Table 3**. A p-value less than 0.05 indicates that there are significant differences between the KL-SMM and the other methods. We highlighted the statistically significant differences in boldface. From **Table 7**, it can be observed that in all cases, the null hypothesis can be rejected. This proves that the KL-SMM significantly outperformed the other methods. This further demonstrated the ability of the KL-SMM to capture the structural information within the EEG data, in addition to a strong transfer learning capability. Therefore, it is suitable for the classification of complex matrix-form EEG data with cross-subject variability.

Running Time

Figure 3A shows the running time of the KL-SMM and other methods on a subject, *S01*, in *Exp.1* using 14 labeled target EEG trials. Except for the SVM and ASVM, the KL-SMM achieved comparable computational cost with the traditional matrix leaning method SMM. Furthermore, the KL-SMM required less computational time, compared to the BSVM. It was proven that the running time of the KL-SMM was approximately 1.6 times less that of the SMM. The KL-SMM achieved better classification results, without the increase in computational costs becoming unacceptable. This shows the potential value of the KL-SMM for real-world BCI applications.

Parameter Sensitivity

We further show the effect of free parameter on the performance of KL-SMM, i.e., the knowledge transfer penalty λ. We conduct parameter sensitivity experiments on the transfer tasks *S04* in *Exp.1* and *B04* in *Exp.2* using 14 labeled target EEG trials, respectively. We vary the parameter of interest in $\{1e-4, 5e-4, 1e-3, 5e-3, 1e-2, 5e-2, 1e-1, 5e-1, 1e0\}$. **Figure 3B** shows the classification accuracy of our KL-SMM in contrast to SMM represented as dashed lines. It can be found that the accuracy of KL-SMM is improved with the increase of parameter λ, suggesting that taking the model knowledge of source domain into account can benefit for EEG classification. As the parameter value is further increased, the classification performance will decrease due to the distribution discrepancy between the source domain and the target domain.

CONCLUSION

In this study, we proposed a KL-SMM method for MI-based BCIs. The proposed KL-SMM belongs to the matrix classifier, which can exploit the structural information of EEG data in matrix form. Furthermore, it can leverage the existing source model knowledge in modeling the construction of the target subjects in scenarios of limited labeled target training data. Similar to the SMM, the KL-SMM can be easily optimized using the ADMM. Extensive experimental results on two publicly available MI datasets demonstrate the superiority of the KL-SMM to the compared methods in most cases. However, despite its promising performance, there is still room for improvement. For example, adaptively controlling the penalty λ is critical to determining how much knowledge is transferred. In addition, how to extend KL-SMM to multi-class classification will be investigated in future work.

DATA AVAILABILITY STATEMENT

Publicly available datasets were analyzed in this study. This data can be found here: http://www.bbci.de/competition/iv/.

AUTHOR CONTRIBUTIONS

YC is responsible for data processing and data analysis. WH and SL are responsible for manuscript writing. XL and QW is responsible for study design. GL is responsible for experimental design. JQ and K-SC are responsible for manuscript editing. All authors contributed to the article and approved the submitted version.

FUNDING

This work was supported in part by the Key R&D Program of Guangdong Province, China under Grant (2018B030339001), the National Natural Science Foundation of China under Grants (61802177 and 62072452), the Fundamental Research Funds for the Central Universities under Grant (CDLS-2019-04), the CAS Key Laboratory of Human-Machine Intelligence-Synergy Systems (2014DP173025), and the Hong Kong Research Grants Council under Grant (PolyU 152006/19E).

REFERENCES

Agarwal, A., Dowsley, R., McKinney, N. D., Wu, D., Lin, C. T., De Cock, M., et al. (2019). Protecting privacy of users in brain-computer interface applications. *IEEE Trans. Neural Syst. Rehabil. Eng.* 27, 1546–1555. doi: 10.1109/tnsre.2019.2926965

Alamgir, M., Grosse-Wentrup, M., and Altun, Y. (2010). "Multitask learning for brain-computer interfaces," in *Processing of the 13th International Conference on Artificial Intelligence and Statistics. (AISTATS)*, Vol. 9, Washington, DC, 17–24.

Allison, B. Z., McFarland, D. J., Schalk, G., Zheng, S. D., Jackson, M. M., and Wolpaw, J. R. (2008). Towards an independent brain–computer interface using steady state visual evoked potentials. *Clin. Neurophysiol.* 119, 399–408. doi: 10.1016/j.clinph.2007.09.121

Al-Qaysi, Z. T., Zaidan, B. B., Zaidan, A. A., and Suzani, M. S. (2018). A review of disability EEG based wheelchair control system: coherent taxonomy, open challenges and recommendations. *Comput. Methods Progr. Biomed.* 164, 221–237. doi: 10.1016/j.cmpb.2018.06.012

Ang, K. K., Guan, C., Chua, K. S. G., Ang, B. T., Kuah, C. W. K., Wang, C., et al. (2011). A large clinical study on the ability of stroke patients to use an

EEG-based motor imagery brain-computer interface. *Clin. EEG Neurosci.* 42, 253–258. doi: 10.1177/155005941104200411

Azab, A. M., Mihaylova, L., Ang, K. K., and Arvaneh, M. (2019). Weighted transfer learning for improving motor imagery-based brain–computer interface. *IEEE Trans. Neural Syst. Rehabil. Eng.* 27, 1352–1359. doi: 10.1109/tnsre.2019.2923315

Cai, J. F., Candès, E. J., and Shen, Z. (2010). A singular value thresholding algorithm for matrix completion. *SIAM J. Optim.* 20, 1956–1982. doi: 10.1137/080738970

Candes, E. J., and Recht, B. (2009). Exact matrix completion via convex optimization. *Found. Comput. Math.* 9, 717–772. doi: 10.1007/s10208-009-9045-5

Deng, Z., Jiang, Y., Choi, K.-S., Chung, F.-L., and Wang, S. (2013). Knowledge-leverage-based TSK fuzzy system modeling. *IEEE Trans. Neural Netw. Learn. Syst.* 24, 1200–1212. doi: 10.1109/tnnls.2013.2253617

Fahimi, F., Zhang, Z., Goh, W. B., Lee, T.-S., Ang, K. K., and Guan, C. (2019). Inter-subject transfer learning with an end-to-end deep convolutional neural network for EEG-based BCI. *J. Neural Eng.* 16:026007. doi: 10.1088/1741-2552/aaf3f6

Hang, W., Feng, W., Du, R., Liang, S., Chen, Y., Wang, Q., et al. (2019). Cross-subject EEG signal recognition using deep domain adaptation network. *IEEE Access* 7, 273–282. doi: 10.1109/ACCESS.2019.2939288

Hang, W., Feng, W., Liang, S., Wang, Q., Liu, X., and Choi, K. S. (2020). Deep stacked support matrix machine based representation learning for motor imagery EEG classification. *Compu. Methods Prog. Biomed.* 193:105466. doi: 10.1016/j.cmpb.2020.105466

Hossain, I., Khosravi, A., Hettiarachchi, I., and Nahavandi, S. (2018). Multiclass informative instance transfer learning framework for motor imagery-based brain-computer interface. *Comput. Intell. Neurosci.* 2018:6323414. doi: 10.1155/2018/6323414

Hossain, I., Khosravi, A., and Nahavandhi, S. (2016). "Active transfer learning and selective instance transfer with active learning for motor imagery based BCI," in *Proceeding of the IEEE International Joint Conference on Neural Networks (IJCNN)*, Vancouver, BC, 4048–4055. doi: 10.1109/IJCNN.2016.7727726

Jayaram, V., Alamgir, M., Altun, Y., Scholkopf, B., and Grosse-Wentrup, M. (2016). Transfer learning in brain-computer interfaces. *IEEE Comput. Intell. Mag.* 11, 20–31. doi: 10.1109/MCI.2015.2501545

Kang, H., Nam, Y., and Choi, S. (2009). Composite common spatial pattern for subject-to-subject transfer. *IEEE Signal Process. Lett.* 16, 683–686. doi: 10.1109/lsp.2009.2022557

Li, Y., Kambara, H., Koike, Y., and Sugiyama, M. (2010). Application of covariate shift adaptation techniques in brain–computer interfaces. *IEEE Trans. Biomed. Eng.* 57, 1318–1324. doi: 10.1109/tbme.2009.2039997

Lotte, F., and Guan, C. (2010). "Learning from other subjects helps reducing brain-computer interface calibration time," in *Proceeding of the 2010 IEEE International Conference on Acoustics, Speech and Signal Processing (ICASSP)*, Dallas, TX, 614–617. doi: 10.1109/ICASSP.2010.5495183

Luo, L., Xie, Y., Zhang, Z., and Li, W. J. (2015). "Support matrix machines," in *Proceeding of the International Conference on International Conference on Machine Learning*, France, 938–947.

Morioka, H., Kanemura, A., Hirayama, J.-I., Shikauchi, M., Ogawa, T., Ikeda, S., et al. (2015). Learning a common dictionary for subject-transfer decoding with resting calibration. *NeuroImage* 111, 167–178. doi: 10.1016/j.neuroimage.2015.02.015

Nam, C. S., Jeon, Y., Kim, Y. J., Lee, I., and Park, K. (2011). Movement imagery-related lateralization of event-related (de) synchronization (ERD/ERS): motor-imagery duration effects. *Clin. Neurophysiol.* 122, 567–577. doi: 10.1016/j.clinph.2010.08.002

Pan, S., and Yang, Q. (2009). A survey on transfer learning. *IEEE Trans. Knowl. Data Eng.* 22, 1345–1359. doi: 10.1109/TKDE.2009.191

Pfurtscheller, G., and Da Silva, F. L. (1999). Event-related EEG/MEG synchronization and desynchronization: basic principles. *Clin. Neurophysiol.* 110, 1842–1857. doi: 10.1016/s1388-2457(99)00141-8

Pfurtscheller, G., and Neuper, C. (2001). Motor imagery and direct brain-computer communication. *Proc. IEEE* 89, 1123–1134. doi: 10.1109/5.939829

Pirsiavash, H., Ramanan, D., and Fowlkes, C. C. (2009). Bilinear classifiers for visual recognition. *Adv. Neural Inform. Process. Syst.* 22, 1482–1490.

Salvaris, M., and Sepulveda, F. (2009). Visual modifications on the P300 speller BCI paradigm. *J. Neural Eng.* 6:046011. doi: 10.1088/1741-2560/6/4/046011

Samek, W., Meinecke, F. C., and Müller, K.-R. (2013). Transferring subspaces between subjects in brain–computer interfacing. *IEEE Trans. Biomed. Eng.* 60, 2289–2298. doi: 10.1109/tbme.2013.2253608

Vapnik, V. (1995). *The Nature of Statistical Learning*. Berlin: Springer-Verlag. doi: 10.1007/978-1-4757-2440-0

Vidaurre, C., Schlögl, A., Cabeza, R., Scherer, R., and Pfurtscheller, G. (2005). Adaptive on-line classification for EEG-based brain computer interfaces with AAR parameters and band power estimates. *Biomed. Technik Biomed. Eng.* 50, 350–354. doi: 10.1515/bmt.2005.049

Vourvopoulos, A., Badia, S. B. I., and Liarokapis, F. (2017). EEG correlates of video game experience and user profile in motor-imagery-based brain–computer interaction. *Vis. Comput.* 33, 533–546. doi: 10.1007/s00371-016-1304-2

Wang, P., Lu, J., Zhang, B., and Tang, Z. (2015). "A review on transfer learning for brain-computer interface classification," in *Proceeding of the 2015 5th International Conference on Information Science and Technology (ICIST)*, Piscataway, NJ: IEEE, 315–322. doi: 10.1109/ICIST.2015.7288989

Wang, Z., Yu, Y., Xu, M., Liu, Y., Yin, E., and Zhou, Z. (2019). Towards a hybrid BCI gaming paradigm based on motor imagery and SSVEP. *Int. J. of Hum. Comput. Interact.* 35, 197–205. doi: 10.1080/10447318.2018.1445068

Wolf, L., Jhuang, H., and Hazan, T. (2007). "Modeling appearances with low rank svm," in *Proceeding of the IEEE Conference on Computer Vision and Pattern Recognition*, Minneapolis, MN, 1–6. doi: 10.1007/978-3-319-12000-3_1

Yang, J., Yan, R., and Hauptmann, A. G. (2007). "Adapting SVM classifiers to data with shifted distributions," in *Proceeding of the Seventh IEEE International Conference on Data Mining Workshops*, Omaha, NE, 69–76. doi: 10.1109/ICDMW.2007.37

Zanini, P., Congedo, M., Jutten, C., Said, S., and Berthoumieu, Y. (2018). Transfer learning: a riemannian geometry framework with applications to brain–computer interfaces. *IEEE Trans. Biomed. Eng.* 65, 1107–1116. doi: 10.1109/tbme.2017.2742541

Zheng, Q., Zhu, F., and Heng, P. A. (2018a). Robust support matrix machine for single trial EEG classification. *IEEE Trans. Neural Syst. Rehabil. Eng.* 26, 551–562. doi: 10.1109/tnsre.2018.2794534

Zheng, Q., Zhu, F., Qin, J., Chen, B. D., and Heng, P. A. (2018b). Sparse support matrix machine. *Pattern Recognit.* 76, 715–726. doi: 10.1016/j.patcog.2017.10.003

Zheng, Q., Zhu, F., Qin, J., and Heng, P. (2018c). Multiclass support matrix machine for single trial EEG classification. *Neurocomputing* 275, 869–880. doi: 10.1016/j.neucom.2017.09.030

Conflict of Interest: The authors declare that the research was conducted in the absence of any commercial or financial relationships that could be construed as a potential conflict of interest.

frontiers in Neuroscience

ORIGINAL RESEARCH
published: 10 December 2020
doi: 10.3389/fnins.2020.578126

A One-Dimensional CNN-LSTM Model for Epileptic Seizure Recognition Using EEG Signal Analysis

Gaowei Xu[1], Tianhe Ren[2], Yu Chen[3]* and Wenliang Che[1]**

[1] Department of Cardiology, Shanghai Tenth People's Hospital, Tongji University School of Medicine, Shanghai, China, [2] School of Informatics, Xiamen University, Xiamen, China, [3] Department of Dermatology & STD, Nantong First People's Hospital, Nantong, China

Frequent epileptic seizures cause damage to the human brain, resulting in memory impairment, mental decline, and so on. Therefore, it is important to detect epileptic seizures and provide medical treatment in a timely manner. Currently, medical experts recognize epileptic seizure activity through the visual inspection of electroencephalographic (EEG) signal recordings of patients based on their experience, which takes much time and effort. In view of this, this paper proposes a one-dimensional convolutional neural network-long short-term memory (1D CNN-LSTM) model for automatic recognition of epileptic seizures through EEG signal analysis. Firstly, the raw EEG signal data are pre-processed and normalized. Then, a 1D convolutional neural network (CNN) is designed to effectively extract the features of the normalized EEG sequence data. In addition, the extracted features are then processed by the LSTM layers in order to further extract the temporal features. After that, the output features are fed into several fully connected layers for final epileptic seizure recognition. The performance of the proposed 1D CNN-LSTM model is verified on the public UCI epileptic seizure recognition data set. Experiments results show that the proposed method achieves high recognition accuracies of 99.39% and 82.00% on the binary and five-class epileptic seizure recognition tasks, respectively. Comparing results with traditional machine learning methods including k-nearest neighbors, support vector machines, and decision trees, other deep learning methods including standard deep neural network and CNN further verify the superiority of the proposed method.

Keywords: convolutional neural network, electroencephalographic, epileptic seizure recognition, long short-term memory, signal analysis

OPEN ACCESS

Edited by:
Yizhang Jiang,
Jiangnan University, China

Reviewed by:
Guodong Sun,
Hubei University of Technology, China
Lingfei Cai,
Shanghai Business School, China

***Correspondence:**
Tianhe Ren
596106517@qq.com
Yu Chen
961643503@qq.com
Wenliang Che
chewenliang@tongji.edu.cn

Specialty section:
This article was submitted to Neuroprosthetics, a section of the journal Frontiers in Neuroscience

Received: *30 June 2020*
Accepted: *10 November 2020*
Published: *10 December 2020*

Citation:
Xu G, Ren T, Chen Y and Che W (2020) A One-Dimensional CNN-LSTM Model for Epileptic Seizure Recognition Using EEG Signal Analysis. Front. Neurosci. 14:578126. doi: 10.3389/fnins.2020.578126

INTRODUCTION

Epilepsy is a neurological disorder, caused by various genetic and acquired factors, which has affected over 50 million people all over the world (Galanopoulou et al., 2012; Abraira et al., 2019; San-Segundo et al., 2019). Usually, epilepsy is caused by the abnormal activities in the brain, it leads to various symptoms, including temporary confusion, loss of consciousness or awareness,

uncontrollable jerking movements and so on. Epilepsy seriously affects both the physical and mental health of patients, and in some extreme cases, it even poses a threat to patients' life. Therefore, it is urgent and important to provide timely and effective protective measures for people with epilepsy and thus improve life quality of patients (Tsubouchi et al., 2019).

Electroencephalographic (EEG) provides a noninvasive biophysical examination method for medical experts to studying the characteristics of epilepsy, which can offer much detailed information of epilepsy patients that cannot be obtained by other physiological methods (Adeli et al., 2007; Jiang et al., 2017a,b). Traditionally, medical experts diagnose epilepsy and determine the cause of seizures through visually analyzing the EEG signal data based on their experience, which takes much time and effort. To date, there have been many attempts to automatically recognize epileptic seizure activity using advanced deep learning techniques (Adeli et al., 2007; Jiang et al., 2015; Schmidhuber, 2015; Jiang et al., 2020a,b).

In recent years, deep learning has developed tremendously and is widely used in various fields, especially in image processing and natural language processing (Acharya et al., 2013; Jiang et al., 2015; LeCun et al., 2015). Convolutional neural network (CNN), as one of the most famous deep learning models, can extract abundant features by using various filters in the convolutional layers, pooling layers, normalization layers, and fully connected layers, thereby improving the execution performance of various tasks (Radenovic et al., 2019). However, CNN cannot retain memory of previous time series patterns and thus, it is challenging for CNN to directly learn the most important and representative features from EEG biomedical signals in the form of time series. Consequently, CNN has difficulty in accurately constructing the relationship between the raw EEG signals and the epileptic seizure recognition results.

Recurrent neural network (RNN), as a specific type of neural networks, uses previous outputs as inputs and thus can remember information from the past (Choi et al., 2016; Kong et al., 2019). Recently, there have been many researches applying the RNN in the fields of natural language processing and speech recognition. Long short-term memory (LSTM) is one of RNN architectures (Hanson et al., 2016; Jiang et al., 2019) and has been widely adopted for time series processing. Its design specifically solves the gradient vanishing problem in the basic RNN and helps to learn long-term dependencies, which can acquire the temporal features of sequential data more effectively. In order to model the sequence temporally and improve the modeling capabilities of the deep neural networks, T. Sainath et al. combined the advantages of CNN and RNN to form a convolutional LSTM neural network (Sainath et al., 2015) and applied it on a variety of large vocabulary tasks, which provides a 4–6% relative improvement over an LSTM. In addition, there are also many other studies focusing on extracting temporal and spatial features by combining CNN and LSTM models, which proves the effectiveness and superiority of this solution (Jiang et al., 2019). Therefore, in this paper, in order to improve the performance of EEG signal classification, a CNN-LSTM model is proposed for features extraction of EEG signals and automatic recognition and detection of epileptic seizure (Sun et al., 2019).

The rest of this paper is organized as follows: section "Dataset Description" introduces the UCI epileptic seizure recognition data set. Section "Proposed Method" presents the proposed method, including data pre-processing, 1D CNN, LSTM structure, the 1D CNN-LSTM model, and model application. Section "Method Evaluation" presents the experimental results and provides experimental analysis. Finally, the conclusion and future works are discussed in section "Conclusion and Future Work."

DATA SET DESCRIPTION

The data set used in this paper is the public UCI epileptic seizure recognition data set (Andrzejak et al., 2001). In the original data set, there are five different folders with 100 files for each folder. To be specific, each file represents a recording sample of the brain activity from one subject. In each file, there is a recording of brain activity with 4097 data points, which is sampled for 23.5 s. That is to say, there is a total of 500 subjects in this data set, each has a recording sample with 4097 data points.

The original dataset is first pre-processed by the UCI and then published online. Each sample with 4097 data points is divided into 23 data chunks and each chunk has 178 data points of 1 s. After that, the 23 data chunks are shuffled. Finally, for the 500 subjects, 11,500 time-series EEG signal data samples are obtained.

There are five health conditions in the UCI epileptic seizure recognition data set, they include one epileptic seizure condition and four normal conditions where subjects do not have epileptic seizures. The details of them are as follows:

(1) Epileptic seizure condition: the recordings of subjects who have epileptic seizures;
(2) First normal condition: the recordings of subjects who opened their eyes when they were recording the EEG signals;
(3) Second normal condition: the recordings of subjects who closed their eyes when they were recording the EEG signals;
(4) Third normal condition: the recordings of EEG signals collected from the healthy brain area of subjects;
(5) Fourth normal condition: the recordings of EEG signals collected from the tumor area in the brain of subjects.

The raw EEG signal data of the subjects' five health conditions is shown in **Figure 1**. The difference between the raw EEG signal waveform of the epileptic seizure condition and the normal condition can be easily observed, while the difference between the raw EEG signal waveform of the different normal conditions can hardly be observed. Therefore, in this paper, binary and five-class epileptic seizure recognition tasks are both considered in order to thoroughly evaluate the performance of the proposed method.

PROPOSED METHOD

In this section, the proposed epileptic seizure recognition method based on the 1D CNN-LSTM model is presented. Firstly, the raw EEG signal data is pre-processed; then, the 1D CNN and LSTM

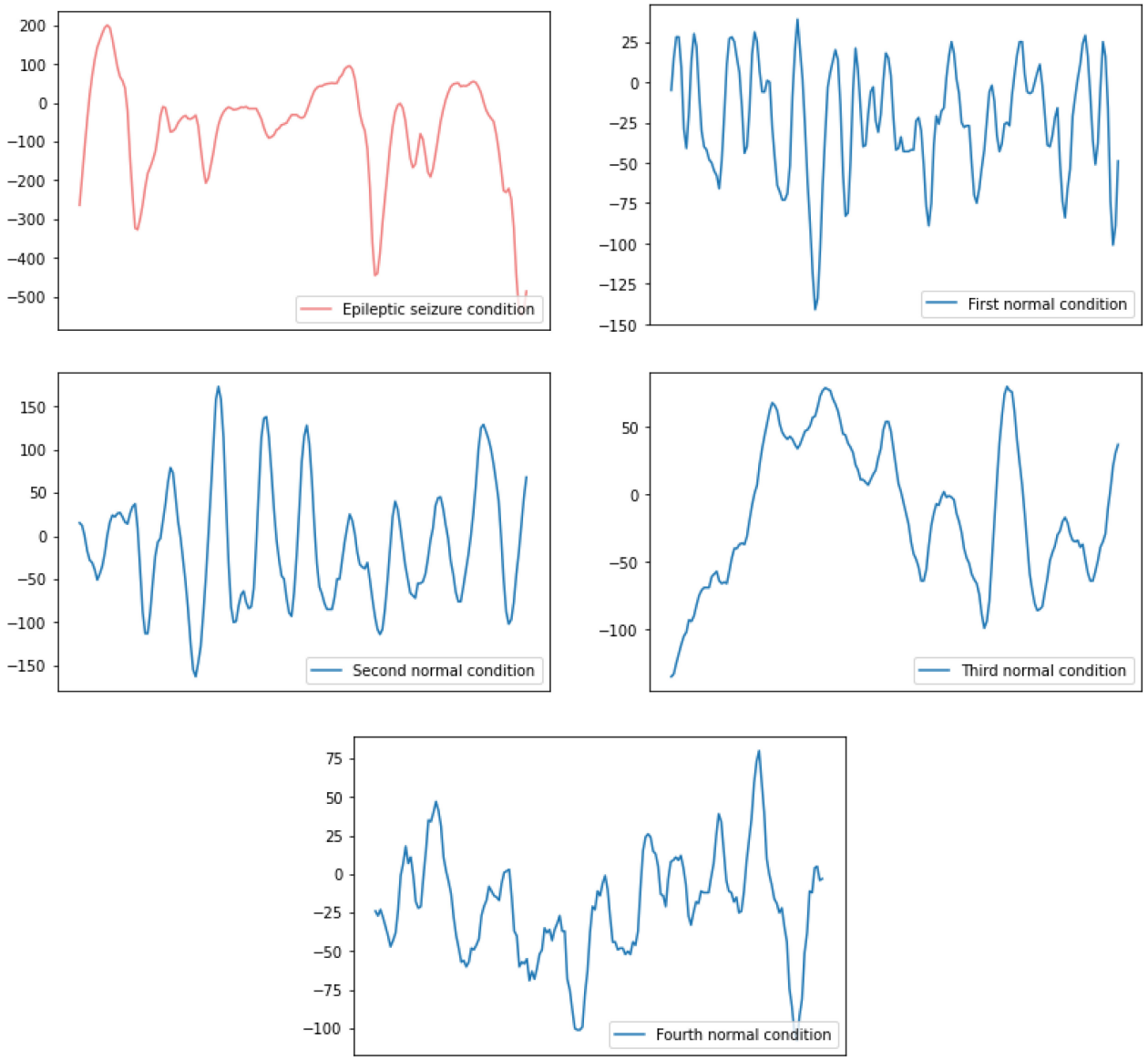

FIGURE 1 | The raw EEG signal waveform of one epileptic seizure condition and four normal conditions.

are introduced, respectively; finally, the 1D CNN-LSTM model is designed and applied for epileptic seizure recognition.

Data Pre-processing

As we introduced in section "Dataset Description," the original data set has been processed and re-structured in advance by a UCI official. Thus, in the data pre-processing process, we only normalized the EEG signal data provided by the UCI official data set before feeding it into the neural network.

1D CNN

The 1D CNN can extract the effective and representative features of 1D time-series sequence data through performing 1D convolution operations using multiple filters. In this paper, the convolutional filters and feature maps of the 1D CNN are all one-dimensional, thus it can match the one-dimensional characteristic of raw EEG signal data, the details of the 1D convolution operation are shown in **Figure 2**. By deepening the number of convolutional layers, the CNN can gradually extract higher-level features which are robust and discriminative for the epileptic seizure recognition tasks.

LSTM Structure

The typical structure of an LSTM block is shown in **Figure 3** (Yuan et al., 2020). There are four gates in the LSTM block, which are cell state gate z which remembers the information over time, forget gate z^f which controls the extent of the value kept in the

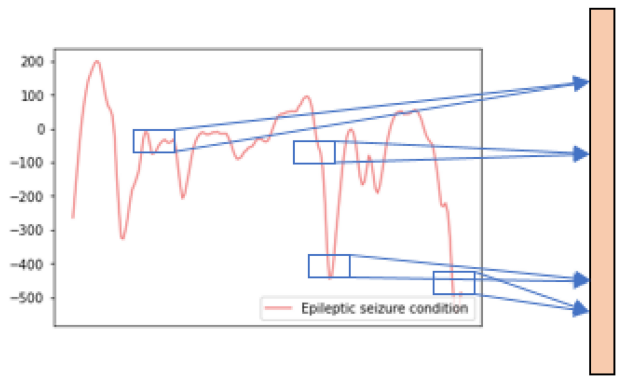

FIGURE 2 | The details of the 1D convolution operation.

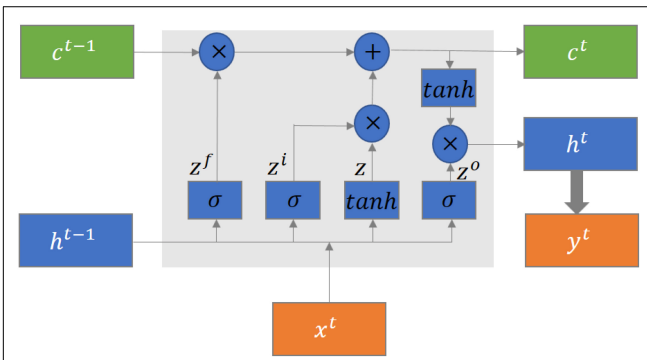

FIGURE 3 | The typical structure of an LSTM block.

cell, input gate z^i which controls the extent of the value flow in the cell, and output gate z^o which controls the extent of the value in the cell to be used for computing the output. Each gate contains a fully connected layer and an activation function. In addition, there are three inputs, which are cell state c^{t-1}, previously hidden state h^{t-1}, and current input x^t, and three outputs, which are cell state c^t, hidden state h^{t-1}, and current output y^t, in the LSTM block. The current output is generated based on the hidden state. The mathematical formulation of the LSTM units is defined as follows:

$$z^f = \sigma\left(W^f\left[x_t, h_{t-1}\right]\right)$$

$$z^i = \sigma\left(W^i\left[x_t, h_{t-1}\right]\right)$$

$$z = tanh\left(W\left[x_t, h_{t-1}\right]\right)$$

$$z^o = \sigma\left(W^o\left[x_t, h_{t-1}\right]\right)$$

$$c^t = z^f \times c^{t-1} + z^i \times z$$

$$h^t = z^o \times \tanh(c^t)$$

$$y^t = \sigma\left(W' h_t\right)$$

1D CNN-LSTM Model

The proposed 1D CNN-LSTM model is composed of an input layer, four convolutional layers, one pooling layer, two LSTM layers, four fully connected (FC) layers, and a soft-max output layer. The detailed network structure is shown in **Figure 4** (Jiang et al., 2015; Zhao et al., 2019; Cura et al., 2020).

Firstly, the 1D EEG signal data is directly used as the input of the proposed model, and the shape of the input data is 178 × 1. Then, the input data is passed through the first convolutional layer in order to extract abstract features of raw signal data, where the number of 1D convolutional kernels in the Conv Layer1 is 64, the shape of each convolutional kernel is 3 × 1 and the stride of convolutional kernels is 1. This convolutional layer is followed by a Rectified Linear Unit (ReLU) activation layer which can introduce non-linearity to the proposed model. Here, the mathematical definition of the 1D convolutional operation and the ReLU activation is described as follows:

$$y_j^l = \sigma\left(\sum_{i=1}^{N_{l-1}} conv1D(w_{i,j}^l, x_i^{l-1}) + b_j^l\right)$$

where x_i^{l-1} represents the ith feature map in the $(l-1)$th layer; y_j^l represents the jth feature map in the lth layer; $w_{i,j}^l$ represents the trainable convolutional kernel; N_{l-1} represents the number of feature maps in the (l-1)th layer; *conv1D* represents the 1D convolution operation without zero-padding, therefore, the dimension of the feature map in the lth layer is less than that in the *l-1*th layer; b_j^l represents the bias of the jth feature map in the lth layer; σ() represents the ReLU activation function, which can help avoid the overfitting problem. It is defined as follows:

$$\sigma(x) = \begin{cases} 0, & x \leq 0 \\ x, & x > 0 \end{cases}$$

After the convolution and activation, 64 feature maps with the size of 176 × 1 are outputted. After that, the output of the Conv Layer1 is then passed through a max-pooling layer. Here, the mathematical definition of the 1D max-pooling operation is described as follows:

$$p_i^a = \max(p_i^{a'} : a \leq a' < a + s)$$

where $p_i^{a'}$ is the a'th neuron in the ith feature map before max-pooling operation and p_i^a is the ath neuron in the ith feature map after max-pooling operation, and s is the size of pooling window. In the Pooling Layer1, the size of pooling window is 2 and the stride of windows is also 2. It can significantly reduce the number of training parameters in the proposed model and accelerate the training process. After the pooling operation, 64 feature maps with the size of 88 × 1 are outputted. Then, three convolutional layers are followed to further extract higher-level features which can facilitate the classification. They are Conv Layer2, Conv Layer3, Conv Layer4, there are 128 kernels in the shape of 3 × 1 in the Conv Layer 2, 512 kernels in the same shape in the Conv Layer3, and 1024 kernels in the same shape in the Conv Layer4. Similarly, the convolution operation is the

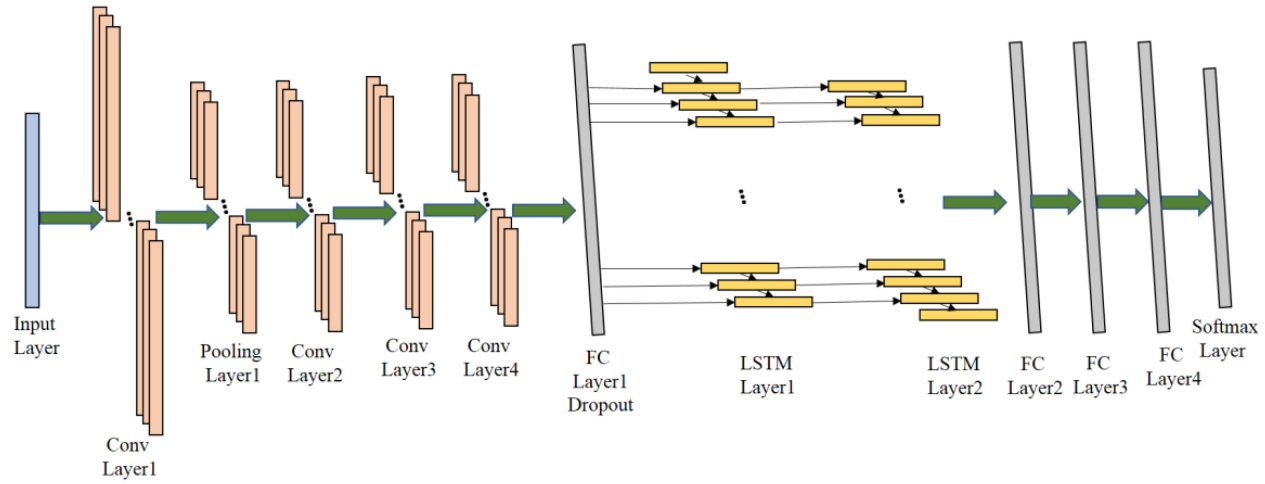

FIGURE 4 | The structure of the 1D CNN-LSTM model.

same as that in the Conv Layer1, and ReLU is also applied for non-linear activation.

After the feature maps passing through all the 1D convolutional layers, the obtained 1024 feature maps with the size of 82 × 1 will be fed into one FC layer with 256 neurons and dropout is then applied to the output of the FC layer. FC Layer1 can concatenate the output from the convolution layers and reduce the dimension of feature maps in order to fit the input of LSTM layers, and dropout can alleviate the overfitting concerns to some extent.

After passing through the FC Layer1, the output features are fed into the LSTM layers which is capable of avoiding the long-term dependency problem in the standard RNN. There are four gates including the cell state gate, forget gate, input data, output gate, in the LSTM cell. They can collaborate with each other to preserve the previous information and further improve the ability of learning useful information from EEG time-series data. There are 64 neurons in both the LSTM Layer1 and the LSTM Layer2.

After the features passing through the LSTM layers, the output features will then be fed into three FC layers. FC Layer2, FC Layer3 and FC Layer4 are fully connected layers with 256, 128, and 64 neurons, respectively. Finally, a softmax output layer is added to the proposed model for final recognition. The detailed configuration of the proposed model can be adjusted according to the specific epileptic seizure recognition task.

Model Application

After the proposed model is successfully built and trained, the 1D CNN-LSTM model is applied to recognize epileptic seizure activity.

METHOD EVALUATION

In this section, the performance of the proposed method is evaluated by the experiments conducted on the public UCI epileptic seizure recognition data set and the training and testing results of the proposed method are given. Additionally, comparative experimental results with traditional machine learning methods and other deep learning methods are also given in order to show its superiority. All the experiments are conducted on a deep learning workstation equipped with an Intel 12-core 3.5-GHz CPU, a GTX1080TI GPU, 256 GB SSD, and 96 GB Memory.

Experimental Setup

During the whole process of the experiment, we selected 90% of the data as the training set and 10% of the data as the test set. As for the deep neural network (DNN), CNN and, 1D convolutional LSTM models, the number of training epochs is set as 100. In order to improve the generalization performance and avoid the overfitting problem, the dropout technique is used in the proposed method.

It should be pointed out that the data are randomly shuffled before training and then fed into the network. During training, at the end of each epoch, the accuracy of the proposed 1D CNN-LSTM model on the training data set and test data set are both calculated, which can help us to judge whether the model is overfitting and thereby verify the generalization ability of the current model. In addition, we add checkpoints during the training process, if the generalization ability of the model has not improved within the 10 training processes, the learning rate will be changed.

Two types of epileptic seizure recognition tasks are considered in this paper, namely binary and five-class recognition tasks. To be specific, the epileptic seizure condition and the normal condition are included in the binary task, and the epileptic seizure condition and the four normal conditions, including eyes open, eyes closed, EEG activity from the healthy brain area, and EEG activity from the tumor area, are included in the five-class task.

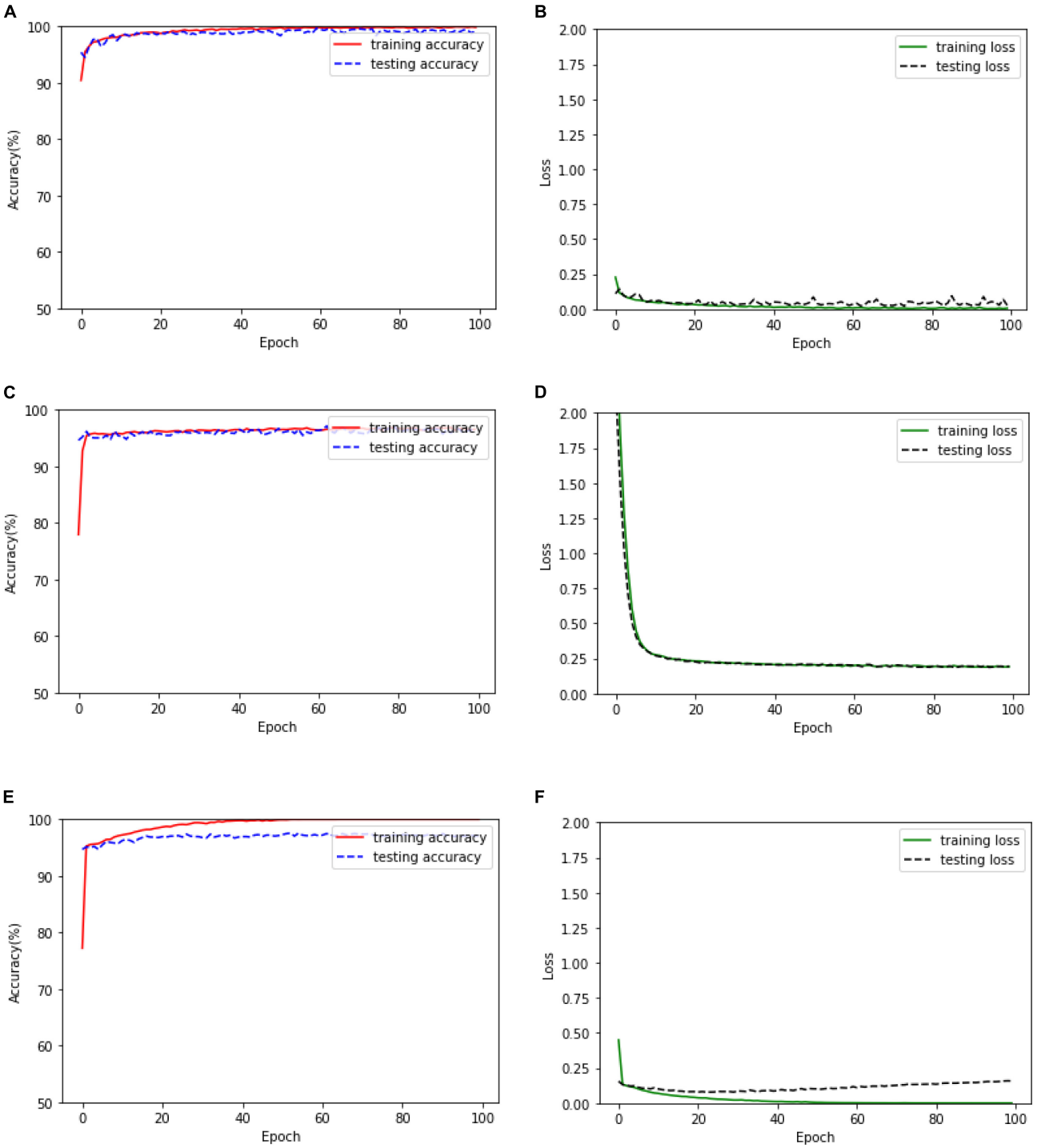

FIGURE 5 | Training and testing results of the binary recognition task. **(A)** The training and test accuracy of the proposed model. **(B)** The training and test loss of the proposed model. **(C)** The training and test accuracy of the DNN. **(D)** The training and test loss of the DNN. **(E)** The training and test accuracy of the standard CNN. **(F)** The training and test loss of the standard CNN.

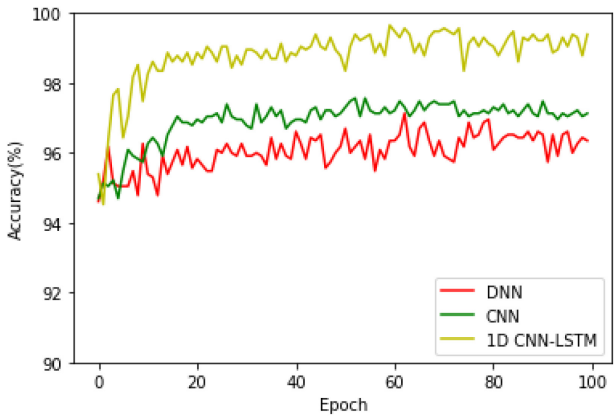

FIGURE 6 | Testing accuracies of these three models on the binary recognition task.

Experimental Results and Analysis

Binary Recognition Task

In this subsection, firstly, the training accuracy, testing accuracy, training loss, and testing loss of the proposed method based on the 1D CNN-LSTM model when it is applied to the binary recognition task is given in **Figure 5**. In addition, two deep learning models are also realized for epileptic seizure recognition in order to compare them with the proposed model, which are the DNN and standard CNN. The training and testing results of the DNN and the standard CNN are also given in **Figure 5**.

It can be seen from **Figure 5** that the DNN has the fastest convergence speed, while the training loss and testing loss of the proposed model decrease at the lowest speed. Therefore, the proposed model needs more training time. On the other hand, the training and testing loss values of the proposed model are obviously smaller than the values of the DNN model, thus obtaining better training and testing accuracies. However, although the training performance of the standard CNN is similar to that of the proposed model, the testing performance of the standard CNN degrades seriously after the early stage of the training process, which is significantly inferior to the proposed model.

After that, in order to see the accuracy superiority of the proposed 1D CNN-LSTM model over the DNN and CNN models in more detail, the testing accuracies of these three models on the binary recognition tasks are shown in **Figure 6**. It can be seen from **Figure 6** that the proposed model achieves the highest testing accuracy throughout most of the training process. Therefore, it can be concluded that the proposed model is superior to the DNN model and standard CNN model in both the training and testing processes.

Finally, in order to further evaluate the seizure classification performance of these three models, the accuracy, precision, recall, and F1-score metrics are calculated and compared in **Table 1**. These performance metrics are briefly introduced as follows:

$$\text{Accuracy} = \frac{TP + TN}{TP + TN + FP + FN}$$

TABLE 1 | The performance of DNN, CNN, and the proposed 1D CNN-LSTM model on the binary classification task.

Methods	Accuracy	Precision	Recall	F1-score
DNN	96.35%	95.18%	87.50%	0.9118
CNN	97.13%	94.24%	92.34%	0.9328
Proposed model	99.39%	98.39%	98.79%	0.9859

$$\text{Precision} = \frac{TP}{TP + FP}$$

$$\text{Recall} = \frac{TP}{TP + FN}$$

$$\text{F1} - \text{Score} = 2 \times \frac{\text{Precision} \times \text{Recall}}{\text{Precision} + \text{Recall}}$$

where the values of *TP* and *FN* represent the number of a given seizure recognition task being correctly classified and incorrectly classified, respectively; *TN* represents the number of seizure recognition tasks not belonging to a given class not being classified as this class; *FP* represents the number of a given seizure recognition task being incorrectly classified as this type.

It can be seen from **Table 1** that the accuracy, precision, recall, and the F1-score of the proposed model are 99.39%, 98.39%, 98.79%, and 0.9859%, respectively, which is significantly better than the DNN and standard CNN models. To be specific, compared with the DNN model and the standard CNN model, the proposed model obtains accuracy improvements of 3.04% and 2.26%, precision improvements of 3.21% and 4.15%, recall improvements of 11.29% and 6.45%, and F1-score improvements of 0.074 and 0.053.

Five-Class Recognition Task

Then, the training and testing processes of the above-mentioned three models when they are applied to the five-class recognition task are conducted, and the testing accuracies of these three models are given in **Figure 7**. It can be found that the DNN and CNN models exhibit a similar accuracy performance, while the proposed 1D CNN-LSTM model obtains the best recognition performance regardless of the different recognition tasks.

Table 2 provides the accuracy, precision, recall, and F1-score of the DNN, CNN, and the proposed model. From **Table 2**, it can be seen that the proposed model significantly outperforms the DNN and CNN models in terms of all the metrics.

TABLE 2 | The performance of DNN, CNN, and the proposed 1D CNN-LSTM model on the five-class classification task.

Methods	Accuracy	Precision	Recall	F1-score
DNN	68.78%	67.63%	67.67%	0.6691
CNN	67.30%	67.73%	66.76%	0.6705
Proposed model	82.00%	81.78%	81.70%	0.8156

Additional Analysis

In this subsection, two additional analysis experiments are conducted. The first one is to determine the most suitable number of neurons in the hidden LSTM layer. Therefore, the number of neurons in the hidden LSTM layer is changed. The accuracy comparison results of the proposed 1D CNN-LSTM model with 32, 64, 128, 192, and 256 neurons in the hidden LSTM layer are given in **Table 3**.

TABLE 3 | Test accuracies of the proposed 1D CNN-LSTM model with different numbers of neurons in the hidden LSTM layer.

The number of neurons in the hidden LSTM layer	32	64	128	192	256
Accuracy on binary recognition task	99.22%	99.39%	99.04%	99.39%	99.39%
Accuracy on five-class recognition task	80.78%	82.00%	79.48%	80.70%	78.61%

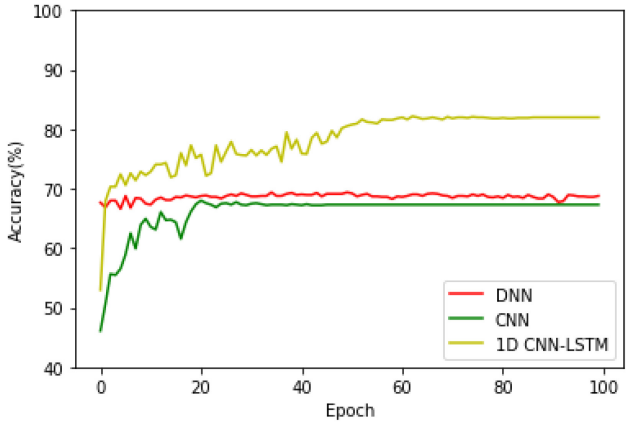

FIGURE 7 | Testing accuracies of the three models on the five-class recognition task.

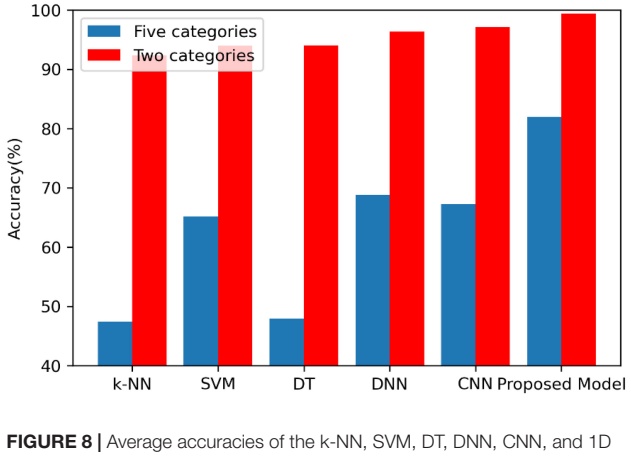

FIGURE 8 | Average accuracies of the k-NN, SVM, DT, DNN, CNN, and 1D CNN-LSTM models.

It can be found that the when the number of neurons in the LSTM layer equals 64, the test accuracy of the proposed model reaches 99.39% on the binary recognition task, which is higher than others. On the other hand, when the number of neurons in the LSTM layer equals 64, the best accuracy of 82.00% is achieved on the five-class recognition task.

The second analysis experiment is to further verify the accuracy superiority of the proposed model. In this paper, apart from the deep learning model, the following three machine learning-based approaches are also realized to compare them with the proposed method in order to further test the superiority of the proposed model, which are k-nearest neighbor (k-NN), decision tree (DT), and support vector machine (SVM) models. All the experiments of these models are carried out 10 times, and the average accuracies of the k-NN, SVM, DT, DNN, CNN, and 1D CNN-LSTM models are shown in **Figure 8**.

On the binary recognition task, the accuracy of the proposed model is 99.39%, which is 7.09% higher than k-NN, 5.43% higher than SVM, and 5.35% higher than DT. On the five-class recognition task, the accuracy of the proposed model is 82.00%, which is 34.57% higher than k-NN, 16.87% higher than SVM, and 34.05% higher than DT. All these results prove the strong potential of the proposed 1D CNN-LSTM model in the research area of EEG-based epileptic seizure recognition.

CONCLUSION AND FUTURE WORK

In this paper, a 1D CNN-LSTM model is proposed for epileptic seizure recognition through EEG signal analysis. The proposed model combines a 1D CNN and an LSTM to construct an end-to-end network that can accurately classify normal and epileptic seizure EEG signals. The 1D CNN has the strong ability of EEG signal feature extraction and the LSTM network is able to memorize and recognize the sequential EEG signals. The performance of the proposed model is verified by the experiments conducted on the well-known UCI epileptic seizure recognition data set. Two epileptic seizure recognition tasks, including binary and five-class recognition tasks, are carried out. The proposed model achieves high accuracies of 99.39% and 82.00% on the two tasks, respectively. In addition, taking the binary recognition task for example, the proposed model achieves accuracy improvements of 3.04%, 2.26%, 7.09%, 5.43%, and 5.35% compared with the other methods including DNN, CNN, k-NN, SVM, and DT, respectively.

Although the proposed model has achieved considerable progress in the area of epileptic seizure recognition, there are still two limitations that need to be further addressed in the future. First, the recognition performance of the proposed model on the multi-class tasks is not very satisfying. Second, the supervised training of the proposed model needs a large amount of labeled EEG signal data. However, collecting sufficient labeled data is time-consuming and laborious. Based on these limitations, the future work will focus on two aspects: first, the proposed model

can be further modified and optimized in order to improve its performance on the more complex epileptic seizure recognition tasks, which will improve its classification ability on different data sets; second, the transfer learning technique can be introduced to the proposed model in order to alleviate the dependence on the labeled signal data.

DATA AVAILABILITY STATEMENT

Publicly available datasets were analyzed in this study. This data can be found here: https://archive.ics.uci.edu/ml/datasets/Epileptic+Seizure+Recognition.

AUTHOR CONTRIBUTIONS

GX supervised this research and revised the manuscript. TR conducted the experiments and drafted the manuscript writing. YC and WC checked for grammatical errors of the manuscript and discussed difficult problems in the manuscript with GX. All authors contributed to the article and approved the submitted version.

FUNDING

This work was supported in part by the Fundamental Research Funds for the Central Universities under Grant 22120190211.

REFERENCES

Abraira, L., Gramegna, L. L., Quintana, M., Santamarina, E., Salas-Puig, J., Sarria, S., et al. (2019). Cerebrovascular disease burden in late-onset non-lesional focal epilepsy. *Seizure* 66, 31–35. doi: 10.1016/j.seizure.2019.02.004

Acharya, U. R., Vinitha Sree, S., Swapna, G., Martis, R. J., and Suri, J. S. (2013). Automated EEG analysis of epilepsy: a review. *Knowl. Based Syst.* 45, 147–165. doi: 10.1016/j.knosys.2013.02.014

Adeli, H., Ghosh-Dastidar, S., and Dadmehr, N. (2007). A wavelet-chaos methodology for analysis of EEGs and EEG subbands to detect seizure and epilepsy. *IEEE Trans. Biomed. Eng.* 54, 205–211. doi: 10.1109/tbme.2006.886855

Andrzejak, R. G., Lehnertz, K., Rieke, C., Mormann, F., David, P., and Elger, C. E. (2001). Indications of nonlinear deterministic and finite dimensional structures in time series of brain electrical activity: dependence on recording region and brain state. *Phys. Rev. E Stat. Nonlin. Soft. Matter Phys.* 64: 061907.

Choi, E., Schuetz, A., Stewart, W. F., and Sun, J. (2016). Using recurrent neural network models for early detection of heart failure onset. *J. Am. Med. Inf. Assoc.* 24, 361–370. doi: 10.1093/jamia/ocw112

Cura, A., Kucuk, H., Ergen, E., and Oksuzoglu, I. B. (2020). "Driver profiling using long short term memory (LSTM) and convolutional neural network (CNN) methods," in *Preceding of the IEEE Transactions on Intelligent Transportation Systems (Early Access)*, Piscataway, NJ: IEEE, 1–11. doi: 10.1109/tits.2020.2995722

Galanopoulou, A. S., Buckmaster, P. S., Staley, K. J., Moshé, S. L., Perucca, E., Engel, J., et al. (2012). Simonato for the American epilepsy, identification of new epilepsy treatments: issues in preclinical methodology. *Epilepsia* 53, 571–582. doi: 10.1111/j.1528-1167.2011.03391.x

Hanson, J., Yang, Y., Paliwal, K., and Zhou, Y. (2016). Improving protein disorder prediction by deep bidirectional long short-term memory recurrent neural networks. *Bioinformatics* 33, 685–692.

Jiang, Y., Chung, F.-L., Wang, S., Deng, Z., Wang, J., and Qian, P. (2015). Collaborative fuzzy clustering from multiple weighted views. *IEEE Trans. Cybernet.* 45, 688–701. doi: 10.1109/tcyb.2014.2334595

Jiang, Y., Gu, X., Wu, D., Hang, W., Xue, J., Qiu, S., et al. (2020a). "Novel negative-transfer-resistant fuzzy clustering model with a shared cross-domain transfer latent space and its application to brain CT image segmentation," in *Preceding of the IEEE/ACM Transactions on Computational Biology and Bioinformatics*, Piscataway, NJ: IEEE, doi: 10.1109/TCBB.2019.2963873

Jiang, Y., Zhang, Y., Lin, C., Wu, D., and Lin, C.-T. (2020b). "EEG-based driver drowsiness estimation using an online multi-view and transfer TSK fuzzy system," in *IEEE Transactions on Intelligent Transportation Systems*, Piscataway, NJ: IEEE, doi: 10.1109/TITS.2020.2973673

Jiang, Y., Deng, Z., Chung, F.-L., Wang, G., Qian, P., Choi, K.-S., et al. (2017a). Recognition of Epileptic EEG signals using a novel multi-view TSK fuzzy system. *IEEE Trans. Fuzzy Syst.* 25, 3–20. doi: 10.1109/tfuzz.2016.2637405

Jiang, Y., Wu, D., Deng, Z., Qian, P., Wang, J., Wang, G., et al. (2017b). Seizure classification from EEG signals using transfer learning, semi-supervised learning and TSK fuzzy system. *IEEE Trans. Neural Syst. Rehabil. Eng.* 25, 2270–2284. doi: 10.1109/tnsre.2017.2748388

Jiang, Y., Zhao, K., Xia, K., Xue, J., Zhou, L., Ding, Y., et al. (2019). A novel distributed multitask fuzzy clustering algorithm for automatic MR brain image segmentation. *J. Med. Syst.* 43:118.

Kong, W., Dong, Z. Y., Jia, Y., Hill, D. J., Xu, Y., and Zhang, Y. (2019). Short-term residential load forecasting based on LSTM recurrent neural network. *IEEE Trans. Smart Grid.* 10, 841–851. doi: 10.1109/tsg.2017.2753802

LeCun, Y., Bengio, Y., and Hinton, G. (2015). Deep learning. *Nature* 521, 436–444.

Radenovic, F., Tolias, G., and Chum, O. (2019). Fine-tuning CNN image retrieval with no human annotation. *IEEE Trans. Pattern Anal. Mach. Intell.* 41, 1655–1668. doi: 10.1109/tpami.2018.2846566

Sainath, T. N., Vinyals, O., Senior, A., and Sak, H. (2015). "Convolutional, long short-term memory, fully connected deep neural networks, ICASSP," in *Preceding of the IEEE International Conference on Acoustics, Speech and Signal Processing (ICASSP)*, Brisbane, QLD, 4580–4584.

San-Segundo, R., Gil-Martín, M., D'Haro-Enríquez, L. F., and Pardo, J. M. (2019). Classification of epileptic EEG recordings using signal transforms and convolutional neural networks. *Comput. Biol. Med.* 109, 148–158. doi: 10.1016/j.compbiomed.2019.04.031

Schmidhuber, J. (2015). Deep Learning in neural networks: an overview. *Neural Netw.* 61, 5–117.

Sun, Y., Lo, F. P.-W., and Lo, B. (2019). EEG-based user identification system using 1D-convolutional long short-term memory neural networks. *Expert Syst. Appl.* 125, 259–267. doi: 10.1016/j.eswa.2019.01.080

Tsubouchi, Y., Tanabe, A., Saito, Y., Noma, H., and Maegaki, Y. (2019). Long−term prognosis of epilepsy in patients with cerebral palsy. *Dev. Med. Child Neurol.* 61, 1067–1073. doi: 10.1111/dmcn.14188

Yuan, X., Li, L., and Wang, Y. (2020). "Nonlinear dynamic soft sensor modeling with supervised long short-term memory network," in *Preceding of the IEEE Transactions on Industrial Informatics*, Piscataway, NJ: IEEE, 3168–3176. doi: 10.1109/tii.2019.2902129

Zhao, J., Mao, X., and Chen, L. (2019). Speech emotion recognition using deep 1D & 2D CNN LSTM networks. *Biomed. Signal. Process. Control* 47, 312–323. doi: 10.1016/j.bspc.2018.08.035

Conflict of Interest: The authors declare that the research was conducted in the absence of any commercial or financial relationships that could be construed as a potential conflict of interest.

frontiers in Neuroscience

ORIGINAL RESEARCH
published: 23 December 2020
doi: 10.3389/fnins.2020.622759

An Investigation of Deep Learning Models for EEG-Based Emotion Recognition

Yaqing Zhang[1,2], Jinling Chen[2], Jen Hong Tan[3], Yuxuan Chen[2], Yunyi Chen[2], Dihan Li[2], Lei Yang[2], Jian Su[4], Xin Huang[5]* and Wenliang Che[1]**

[1] Department of Cardiology, Shanghai Tenth People's Hospital, Tongji University School of Medicine, Shanghai, China, [2] Department of Software Engineering, School of Informatics Xiamen University (National Demonstative Software School), Xiamen, China, [3] Department of Computer and Software, Institute of System Science, National University of Singapore, Singapore, Singapore, [4] Nanjing University of Information Science and Technology, Nanjing, China, [5] School of Software, Jiangxi Normal University, Nanchang, China

Emotion is the human brain reacting to objective things. In real life, human emotions are complex and changeable, so research into emotion recognition is of great significance in real life applications. Recently, many deep learning and machine learning methods have been widely applied in emotion recognition based on EEG signals. However, the traditional machine learning method has a major disadvantage in that the feature extraction process is usually cumbersome, which relies heavily on human experts. Then, end-to-end deep learning methods emerged as an effective method to address this disadvantage with the help of raw signal features and time-frequency spectrums. Here, we investigated the application of several deep learning models to the research field of EEG-based emotion recognition, including deep neural networks (DNN), convolutional neural networks (CNN), long short-term memory (LSTM), and a hybrid model of CNN and LSTM (CNN-LSTM). The experiments were carried on the well-known DEAP dataset. Experimental results show that the CNN and CNN-LSTM models had high classification performance in EEG-based emotion recognition, and their accurate extraction rate of RAW data reached 90.12 and 94.17%, respectively. The performance of the DNN model was not as accurate as other models, but the training speed was fast. The LSTM model was not as stable as the CNN and CNN-LSTM models. Moreover, with the same number of parameters, the training speed of the LSTM was much slower and it was difficult to achieve convergence. Additional parameter comparison experiments with other models, including epoch, learning rate, and dropout probability, were also conducted in the paper. Comparison results prove that the DNN model converged to optimal with fewer epochs and a higher learning rate. In contrast, the CNN model needed more epochs to learn. As for dropout probability, reducing the parameters by ∼50% each time was appropriate.

Keywords: EEG, emotion recognition, DNN (deep neural network), CNN (convolutional neural network), CNN-LSTM

OPEN ACCESS

Edited by:
Yizhang Jiang,
Jiangnan University, China

Reviewed by:
Yuanpeng Zhang,
Nantong University, China
Shan Zhong,
Changshu Institute of Technology, China

****Correspondence:***
Jian Su
sj890718@gmail.com
Xin Huang
xinhuang@jxnu.edu.cn
Wenliang Che
chewenliang@tongji.edu.cn

Specialty section:
This article was submitted to Neuroprosthetics, a section of the journal Frontiers in Neuroscience

Received: *29 October 2020*
Accepted: *26 November 2020*
Published: *23 December 2020*

Citation:
Zhang Y, Chen J, Tan JH, Chen Y, Chen Y, Li D, Yang L, Su J, Huang X and Che W (2020) An Investigation of Deep Learning Models for EEG-Based Emotion Recognition. Front. Neurosci. 14:622759. doi: 10.3389/fnins.2020.622759

INTRODUCTION

There are many research methods applied to real-time emotion recognition. For example, researchers use electroencephalogram (EEG) signals and peripheral physiological such as ECG, respiration, skin resistance, and blood pressure to carry out emotion recognition research (Horlings et al., 2008). Among them, the EEG signal in the objective physiological signal is directly generated

by the central nervous system, which is closely related to human emotional states (Jiang et al., 2020b).

There are usually two machine learning strategies for analyzing EEG signals: step-by-step machine learning and end-to-end deep learning (Yang et al., 2020). Step-by-step machine learning mainly involves three steps: the first step is to obtain the digital data by sampling the analog signals, known as signal preprocessing. The second step is artificial feature extraction, which is to calculate the features using feature extraction formulas. Finally, the features are classified using mechine learning methods to achieve the emotion classification result. Wavelet transform and entropy measures are widely used in feature extraction (Zhang et al., 2018). Murugappan et al. (2010) used the "db4" wavelet function for deriving a set of conventional and modified energy-based features from EEG signals for classifying emotions. Paul et al. (2015) used the multifractral detrended fluctuation analysis (MFDFA) method to extract features and used a support vector machine (SVM) to categorize the EEG feature space related to various emotional states into their respective classes. Jiang et al. (2020a) used transfer learning to reduce the differences in data distribution between the training and testing data (Yang et al., 2016; Jiang et al., 2017). Besides, they proposed a novel negative-transfer-resistant fuzzy clustering model (Jiang et al., 2015) with a shared cross-domain transfer latent space (Jiang et al., 2019).

However, it is difficult to cover all the implied features by manual extraction, and the formulae used to extract time-domain and frequency-domain features are often very complex. In addition, EEG signals are susceptible to noises such as electromyographic artifacts, which create serious interference in the progressive machine learning approach. In view of the above situations, some end-to-end deep learning methods are used to solve these problems. Alhagry et al. (2017) proposed a long short-term memory (LSTM) model to learn features from EEG signals. The classification accuracy reached 85.65, 85.45, and 87.99% for different labels. Schirrmeister et al. (2017) used convolutional neural networks (CNN) for EEG decoding and visualization which have shown great potential when applied to end-to-end emotion recognition based on EEG-signals. Zhang et al. (2017) improved the entirely automatic feature extraction of MWL classification which then had effective high performance compared with traditional machine learning methods.

Since the deep learning models for EEG-based emotion recognition are still in their infancy, there is still a lot of room for adjustment in model structure and parameter settings. In this paper, we investigated the application of existing deep learning models widely used in this field, and implemented several popular deep learning models including deep neural networks (DNN), convolutional neural networks (CNN), long short-term memory (LSTM), and a hybrid model of convolutional neural networks and long short-term memory (CNN-LSTM) for EEG emotion recognition.

Firstly, we extracted 63 s of 32-channel EEG data from 40 trials of 32 subjects. In order to improve the classification efficiency, we selected 14 channels which were most suitable for EEG emotion classification. We built two feature datasets, including RAW data and standard (STD) data. STD data were extracted by calculating eight eigenvalues including the maximum, standard deviation, kurtosis, and so on. In order to make efficient use of the data, we used a 10-fold cross-validation method to build the dataset for each sample before training the model. We put the pre-processed feature datasets into four deep learning models, classifying the emotion in the valence dimension and arousal dimension to four labels by one-hot encoding. In terms of model design selection, we adjusted the learning rate, epoch, and dropout probability, and compared the applicable values of different models. Finally, we obtained the comparison results of the four models.

The rest of this article is organized as follows:

Data description, data preprocessing, deep learning models for emotion recognition, experiments, conclusion, and references.

DATA DESCRIPTION

The experiment was carried out on the DEAP dataset (Koelstra et al., 2012). The dataset was developed by a team of researchers at Queen Mary University of London and is a large multimodal database for the analysis of spontaneous emotions. It contains EEG, ECG, EMG, and other peripheral physiological signals. To collect the signals, 32 subjects were asked to watch 40 segments of 1-min music videos which represented different emotions. Their corresponding brain signals were collected as they watched the videos. After watching each video, participants rated their emotional responses to the 40 music videos on a scale of one to nine based on excitement, control, and how much they liked and were familiar with the videos.

The DEAP database includes two parts: online evaluation and physiological experiment. The online evaluation mainly contains basic information about the initial stimulus material. The physiological experiment mainly contains information on the experiment, including the number of experimental subjects, the rating values, and the recorded signals. The rating scales include arousal, valence, dominance, liking, and familiarity. The rating value from small to large indicates that each index is from negative to positive, from weak to strong.

The DEAP dataset contains 32 groups of EEG data in total, corresponding to the experimental data of 32 subjects (s01–s32). The data of each subject contains two arrays: ***data*** and ***labels***.

DATA PREPROCESSING

The Pre-processing of RAW Data

In this paper, the ***data*** array we used had already been preprocessed, in which the EEG data were desampled, the sampling frequency became 128 Hz, and then the signal was filtered to 4–45 Hz through a band-pass filter. Then the EEG data were averaged to the same reference. We chose 63 s as the reference length of each trail, of which the first 3 s were the preparing time, and the other 60 s were collected during the watching of the video. Therefore, in every separate trail, there were 63 s*128 Hz = 8,064 sampling points for each channel.

In order to simplify the training difficulty and improve the accuracy of emotion recognition, we selected 14 corresponding electrodes of the channels which had the most significant

TABLE 1 | The selected EEG channels.

Channel no.	Channel content
1	Fp1
2	AF3
3	F3
4	F7
7	C3
11	P3
13	PO3
17	Fp2
18	AF4
20	F4
21	F8
25	C4
29	P4
31	PO4

impact on the generation of emotion. **Table 1** shows the 14 selected channels and their corresponding electrodes. **Figure 1** shows the international 10–20 standard system electrode position distribution map, in which the 14 selected electrodes were labeled with different colors to indicate the different influence on emotion generation.

The total EEG cycles were 40 tests per subject. We set the data dimension of the dataset to 40 (epochs)*14 (channels)*8,064 (time points). In order to distinguish from the feature extraction data indicated later, we used RAW data to represent this 40 × 14 × 8,064 data array.

The Pre-processing of STD Data

Feature extraction is necessary in the construction of a deep learning neural network for an emotion recognition task. Of all the domains, we chose the characteristics of time and frequency as the data features. Taking the time point of the raw data array processed in the previous section as the raw time domain feature forms **RAW** data.

We used eight statistical methods to extract the features of the time domain. The following mathematical formula shows how these features were calculated, where E(n) stands for the signal value of the *n* time points.

The mean of the original signal:

$$\mu_E = \frac{1}{N}\sum_{n=1}^{N} E(n) \tag{1}$$

The standard deviation of the original signal:

$$\sigma_E = \sqrt{\frac{1}{N}\sum_{n=1}^{N}(E(n) - \mu_E)^2} \tag{2}$$

The maximum of the original signal:

$$E_{max} = \max E(n) \tag{3}$$

The minimum of the original signal:

$$E_{min} = \min E(n) \tag{4}$$

Average absolute value of the first difference:

$$\delta_E = \frac{1}{N-1}\sum_{n=1}^{N-1} |E(n+1) - E(n)| \tag{5}$$

Average absolute value of the second difference:

$$\lambda_E = \frac{1}{N-2}\sum_{n=1}^{N-2} \left|E(n+2) - 2E(n+1) + E(n)\right| \tag{6}$$

The skewness of the original signal (Mardia, 1970):

$$Skew = \frac{1}{N}\sum_{n=1}^{N}\left[\left(\frac{E(n) - \mu_E}{\sigma_E}\right)^3\right] \tag{7}$$

The kurtosis of the original signal (deCarlo, 1997):

$$Kurtosis = \frac{N(N+1)}{(N-1)(N-2)(N-3)}\sum_{n=1}^{N}\left(\frac{E(n) - \mu_E}{\sigma_E}\right)^4 - \frac{3(N-1)^2}{(N-2)(N-3)} \tag{8}$$

The combination of the eight statistical features into an eigenvector to represent the time domain features are known as the **STD** data. We divided the 63 s of each trail into 1 s segments, each segment contained 128 sampling points. Then the **STD** data array shape was 40(epoch) * 14 (channel) * 63 (time segment) * 128 (sampling point).

To compare the performance of different feature extraction methods under different deep learning neural networks, we used **RAW** and **STD** as two different features to train the models.

The Description of Data and Label

The labels array was a 40 × 4 two-dimensional array, which represented the video/trial × label (valence, arousal, dominance, liking) corresponding to the self-evaluation of each MV. The **valence** level (on a scale of 1 to 9) indicated how happy people felt. People with a happier mood were tested in a higher valence. The **arousal** level (on a scale of 1 to 9) represented the activation of feeling in people. People with a high level of activation generated a higher arousal rating. In this paper, we considered **valence** and **arousal** as the two dimensions of measurement to classify the emotions of the subjects.

In order to transform the continuous rating into a discrete tag form, we used the one-hot encoding form to classify the four types of emotions, as shown in **Figure 2**. The emotions of the subjects were divided into four categories: high arousal/high valence, high arousal/low valence, low arousal/high valence, and low arousal/low valence, which were expressed as [0,0,0,1], [0,1,0,0], [0,0,1,0], and [1,0,0,0]. Thus, the shape of the ***Labels*** array was 40 (epochs) × 4 (label category).

This paper uses ***RAW data***, ***STD data,*** and ***Labels*** as inputs for the neural network. The array description is shown in **Table 2**.

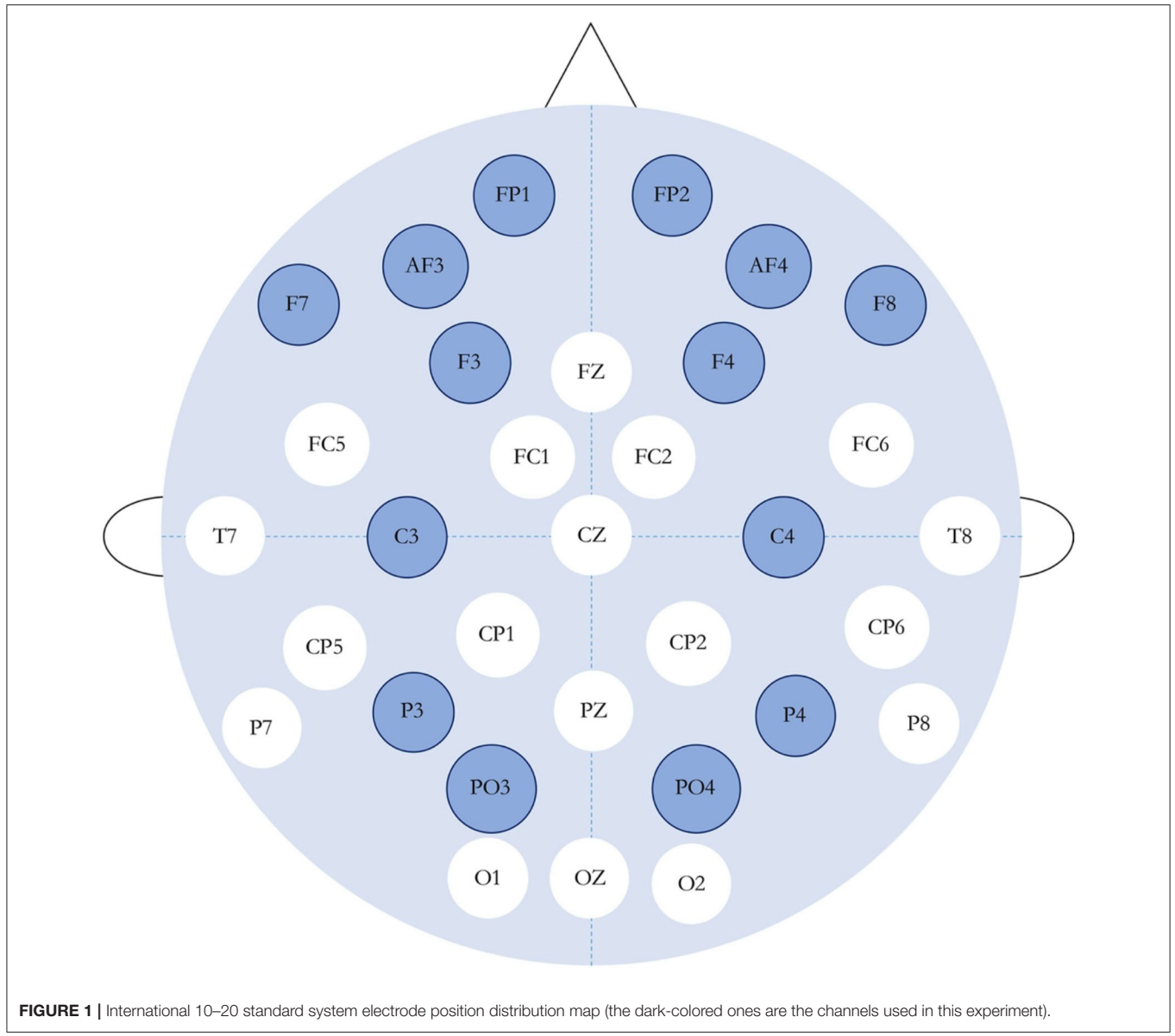

FIGURE 1 | International 10–20 standard system electrode position distribution map (the dark-colored ones are the channels used in this experiment).

DEEP LEARNING MODELS FOR EMOTION RECOGNITION

In this paper, we investigated widely used deep learning models for emotion recognition based on EEG signals. We implemented several popular deep learning models including a DNN, CNN, and LSTM for RAW data classification, and designed CNN-LSTM models for higher performance.

Deep Neural Network Model

In the traditional sense, the neural network is also called a multi-layer perceptron. It is composed of an input layer, an output layer, and a number of hidden layers. Continuous functions such as Sigmoid or Tanh are used to simulate the response of neurons to excitation. The multi-layer perceptron can remove the constraint of the earlier discrete transmission function. However, as the number of layers increases, the optimization function is more and more likely to fall into the local optimal solution. On the basis of the multi-layer perceptron, the DNN replaces the *Sigmoid* function with *ReLU*, *maxout,* and other activation functions, effectively overcoming the gradient disappearance problem (Hanin, 2019).

In this paper, we mainly used a fully connected **DNN** model as the basic model in emotion classification.

Convolutional Neural Network Model

A convolutional neural network (CNN) has been applied widely in original signal processing and image recognition. A CNN has three significant characteristics: a local sensing field, weight sharing, and down sampling, which can decrease the complexity of the network. The high accuracy of the

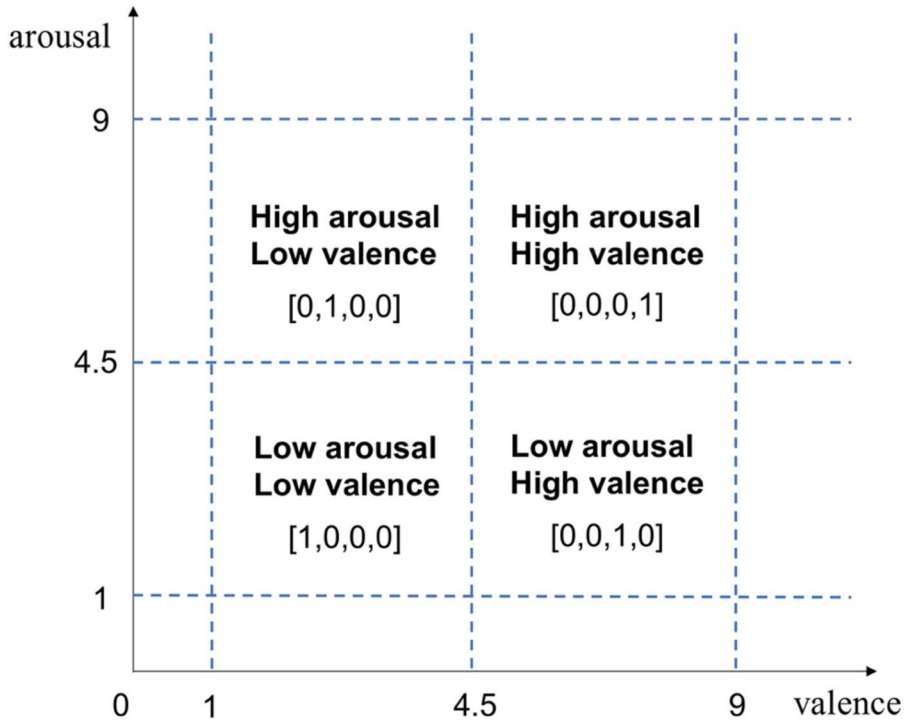

FIGURE 2 | Valence/arousal measurement and one-hot encoding labels.

TABLE 2 | Data description.

Array name	Array shape	Array contents
RAW data	40 × 14 × 8,064	trial no. × channel data
STD data	40 × 14 × 63 × 128	trial no. × time segment × sampling point
Label	40 × 4	trial no. × label (one-hot encoding)

recognition tasks is mainly because it can learn local non-linear features by convolution and non-linear activation functions, and express high-level features as the combination of low-level features. In addition, many CNNs use a pooling layer to create a rough representation of intermediate features, which makes the CNN more translation invariant (Chen et al., 2019).

For the CNN model, the convolution kernel is the key to automatic feature extraction (Cheng and Parhi, 2020). **Figure 3** shows the 1D-convolution kernel for the automatic feature extraction of our model.

The ReLU function is usually used as the activation function due to its simplicity of implementation. It can speed up calculation and convergence. The ReLU function has the following formula:

$$f\ (x) = \max(0,\ x) \tag{9}$$

The pooling layer is a structure for down sampling the features obtained from the convolutional layers, which can reduce the amount of computation and the degree of over-fitting of the network to some extent, thus improving the peKrformance of the CNN model. The convolution-max-pooling process is shown in **Figure 4**.

Our CNN model has four convolution-max-pooling blocks, then a Flatten layer to expand the convolution results, followed by two full-connection layers, and a dense softmax layer. This configuration is the optimal model for the DEAP emotion classification dataset. **Figure 5** shows the structure of our deep CNN model.

Long Short-Term Memory Model

A recurrent neural network (RNN) is a type of recursive neural network that inputs sequential data and performs recursion in the evolutionary direction of a sequence, connected by a chain of all the recurrent units (Graves et al., 2013). An LSTM network is a variant of the recurrent neural network, which is mainly used to process sequence information with a long time difference.

Figure 6 is the schematic diagram of the LSTM unit. The LSTM unit inputs four variables from one input entry and three other gates, which is different from the neuron univariate input of other models. For each neuron in the neural network, the door is opened or closed by the value of input data and parameter weight, and these parameters can be obtained by model training. An LSTM network can solve the problem of gradient vanishing in back propagation by adding three gates. Many of these units are linked together in time series and can form an LSTM model, as the **Figure 7** shows.

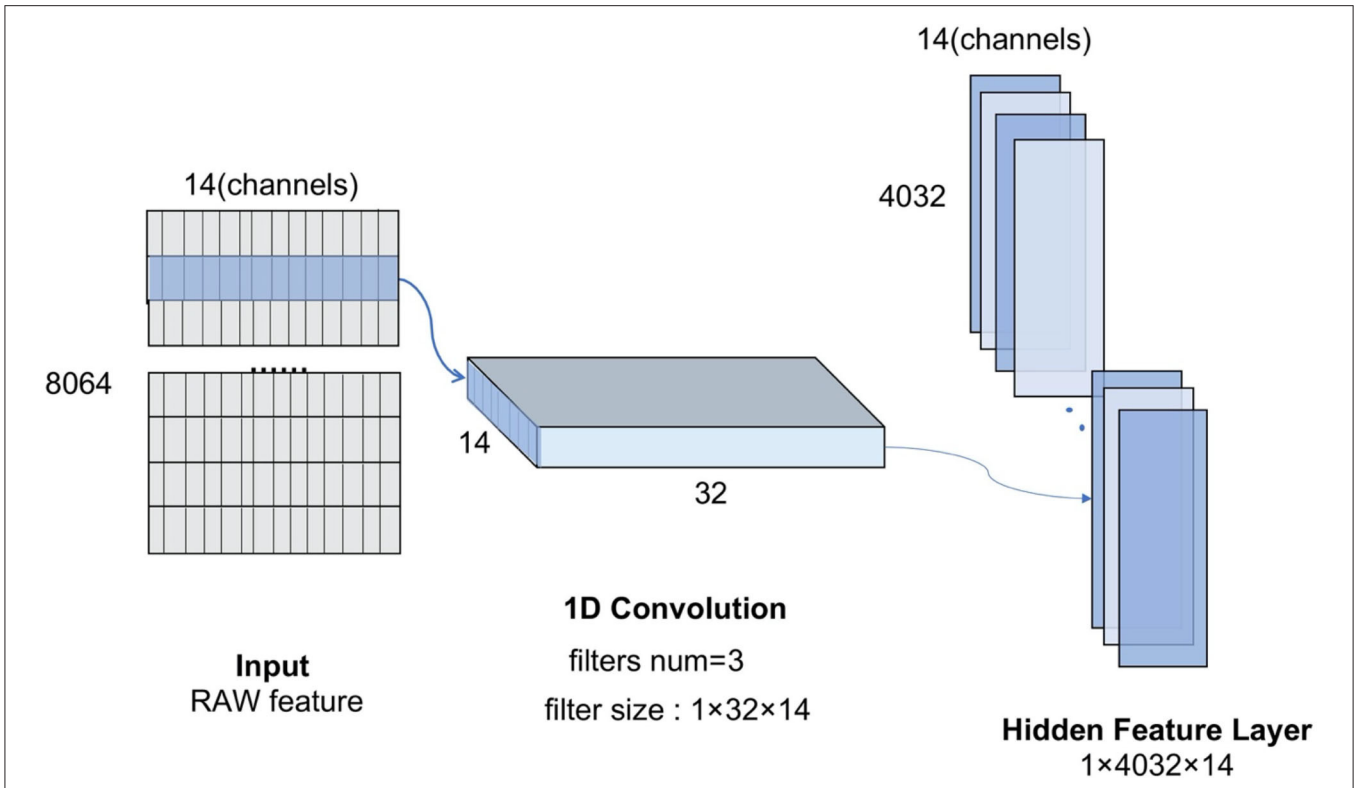

FIGURE 3 | The convolution-max process diagram.

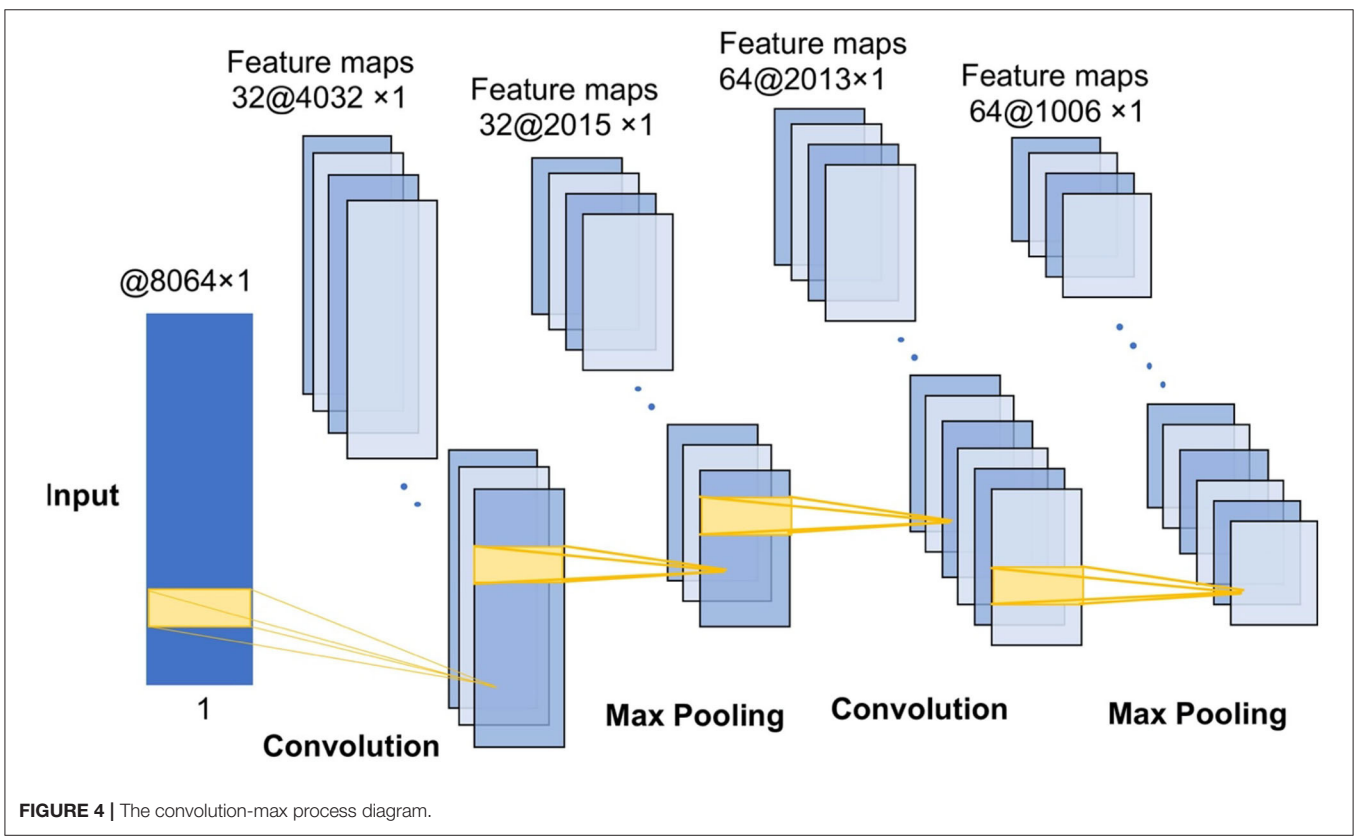

FIGURE 4 | The convolution-max process diagram.

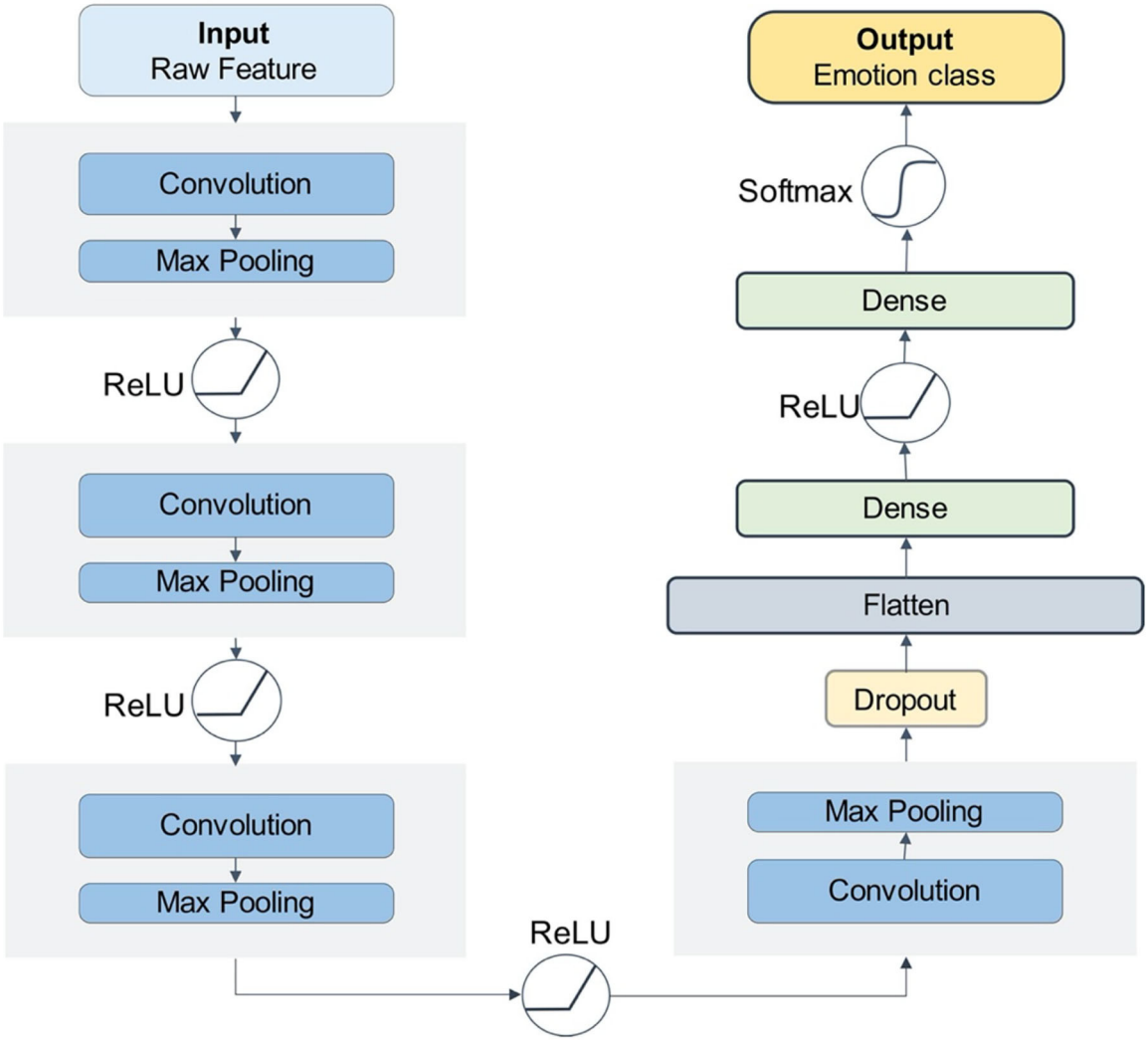

FIGURE 5 | The CNN model structure.

In this paper, we designed a four-layer LSTM network structure. The model takes **RAW** data as input, passes through four layers of the one-way LSTM network, then connects to a dropout layer, and finally reaches the full connection classification layer.

CNN-LSTM Model

The CNN is good at extracting the spatial local relevant features of data, but it struggles to capture the long-term dependence relationship in sequence data, which can be remedied by the LSTM. So, a hybrid model of the CNN and LSTM have been proven to have good performance in natural signal recognition (Ma and Hovy, 2016; Zhao et al., 2019). Therefore, this paper proposed a CNN-LSTM hybrid network model of the CNN and LSTM serial.

In the **CNN-LSTM model**, the **RAW data** were taken as input and used the CNN model for feature extraction before entering the LSTM. After taking the input from the CNN layer, the LSTM units connected as a link and passed the result to the next layer, usually the fully connected dense layer and the softmax classification layer, see **Figure 8**.

The LSTM of the first layer contained 64 units and the second layer contained 32 units. We chose ReLU as the activation function of the LSTM layer in order to prevent the gradient vanishing. In addition, since the LSTM model had many more parameters than the other deep learning models, we added two dropout layers to prevent over-fitting of the training data. Finally, the full connection layer and the softmax function were used as the classification output layer.

EXPERIMENTS

Experimental Setup

In the experiments, we implemented the DNN, CNN, LSTM, and CNN-LSTM, respectively, adjusted the structural design of

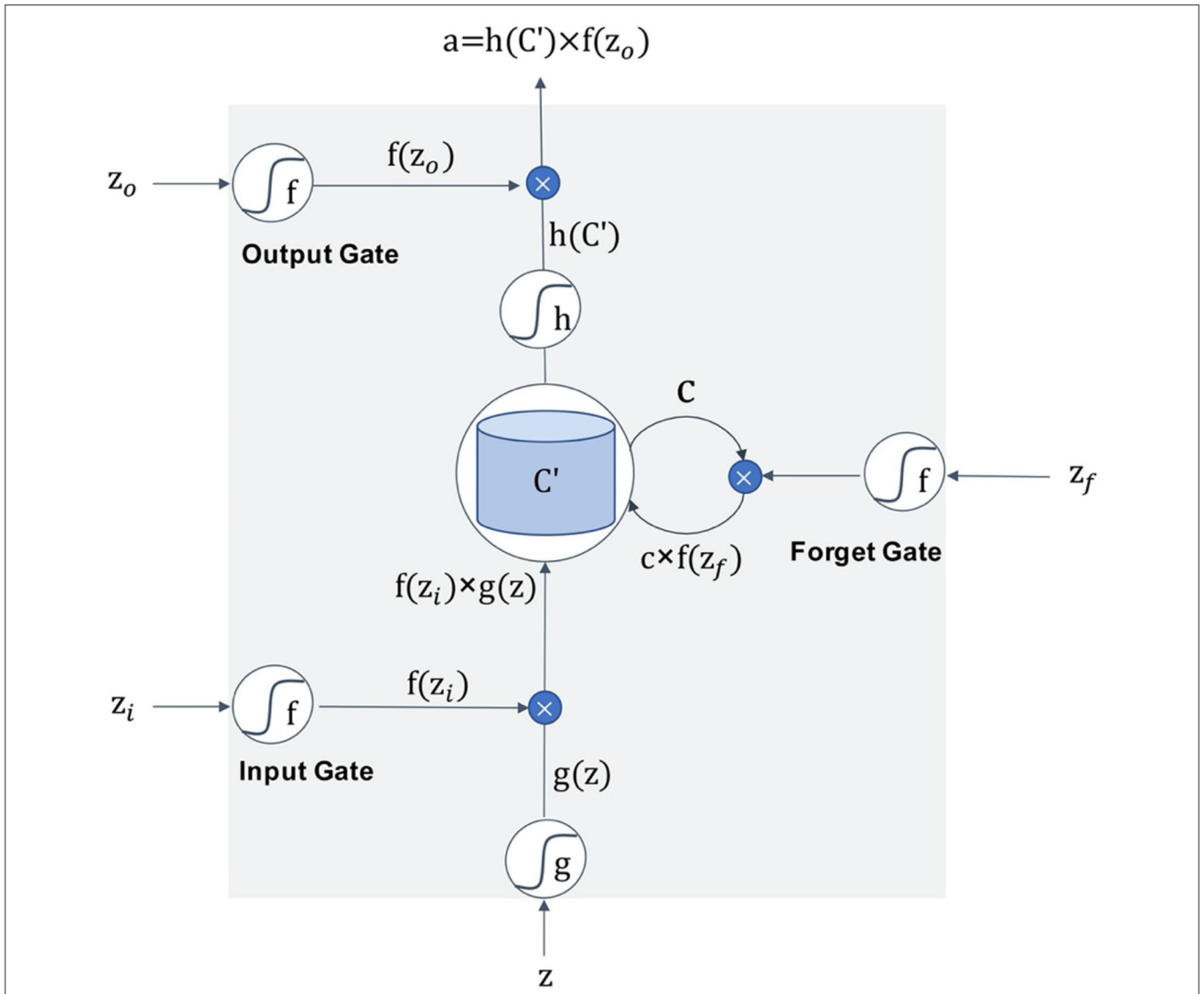

FIGURE 6 | The schematic diagram of the LSTM unit.

the model, and optimized the parameters. In addition, it was mentioned that there are two machine learning strategies for analyzing EEG signals: step-by-step machine learning and end-to-end deep learning. In order to compare the two feature extracting methods, we took the **RAW** data and **STD** features, which had been pre-processed, as the input data of the models, respectively.

In terms of training models, we used the method of ***10-fold cross-validation*** to train the classifier. The original data were divided into 10 subsamples, with one subsample retained as the validation set and the other nine samples used as the training set. The cross-validation was repeated 10 times to create an average of the estimation results. This validation method helped us obtain a more reliable and stable model by using limited label data. We chose ***Adam*** as the optimizer of the models (Shindjalova et al., 2014).

To evaluate the classification performance of the model, we used ***Acc*** and ***Loss*** to represent the accuracy and loss. The calculation formula of ***Acc*** is:

$$Acc = \frac{CP + CN}{CP + CN + MN + MP} \tag{10}$$

In this formula, CP is the number of positive examples that were correctly classified, CN is the number of negative examples that were correctly classified, MN is the number of positive examples that were misclassified, and MP is the number of negative examples that were misclassified.

Because the classification options are one-hot encoding multi-dimensional vectors, we used ***multi-classification cross-entropy*** as the loss function for all the models (de Boer et al., 2005). The Loss of the model can be calculated by the following formula

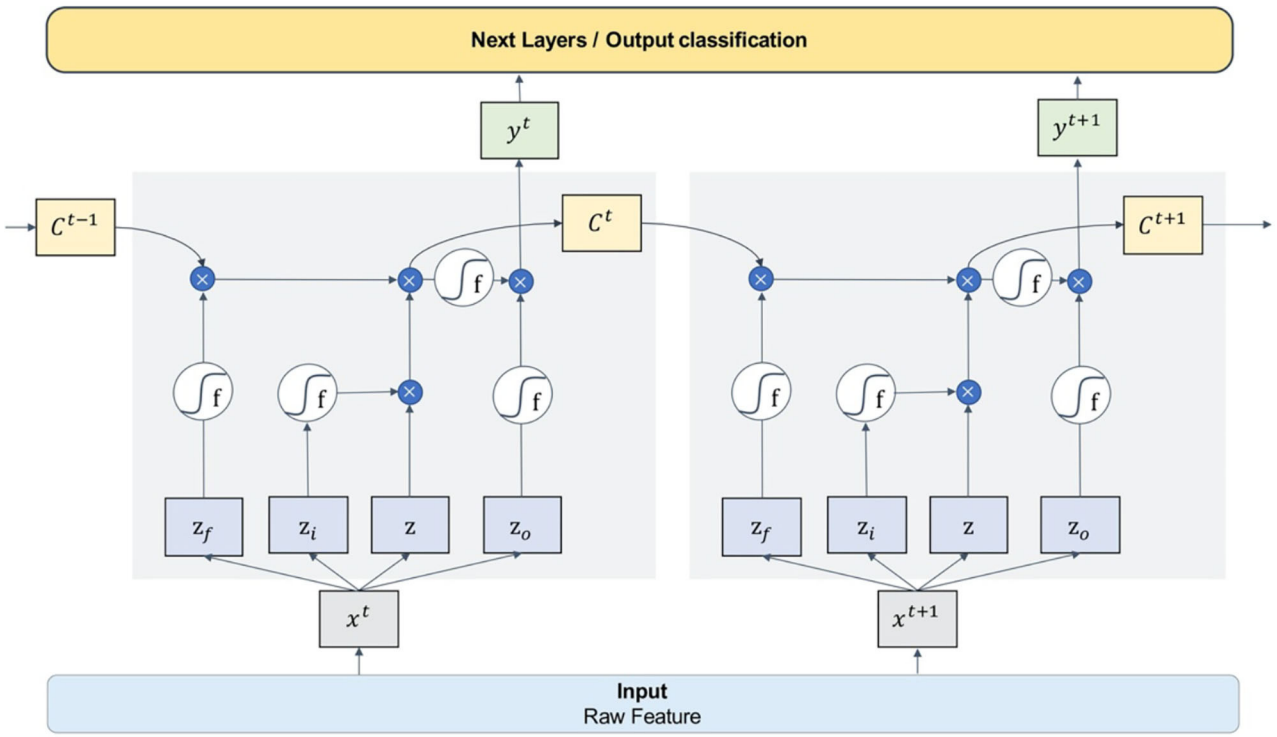

FIGURE 7 | The connection mode and working principle of the LSTM model.

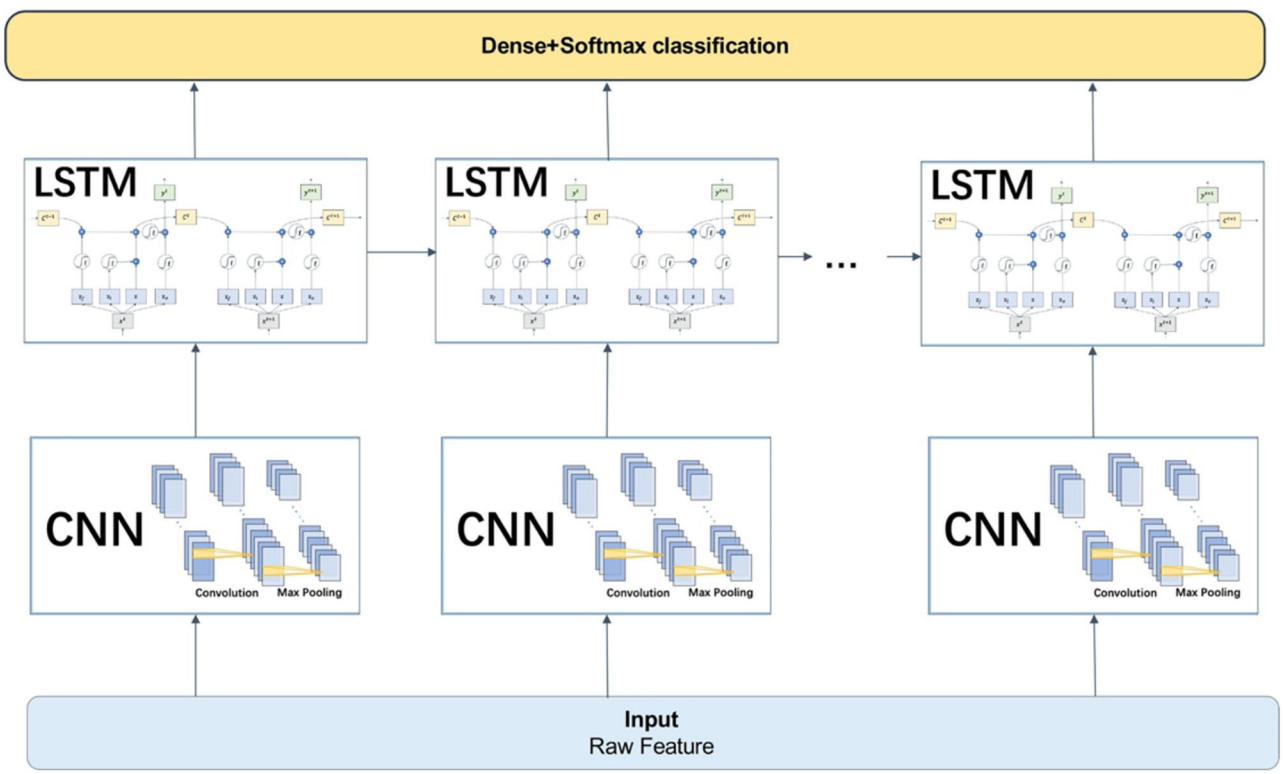

FIGURE 8 | The connection mode and working principle of the CNN-LSTM model.

TABLE 3 | The *Acc* result of different models and different features.

Features \ Models	DNN	CNN	LSTM	CNN-LSTM
RAW	0.6399	0. 9012	0.6747	0.9417
STD	0.7900	0. 8224	0.7500	0. 8887

TABLE 4 | The *Loss* result of different models and different features.

Features \ Models	DNN	CNN	LSTM	CNN-LSTM
RAW	9.5678	0.4953	3.4232	0.3012
STD	6.8361	0.3476	5.3459	0.4243

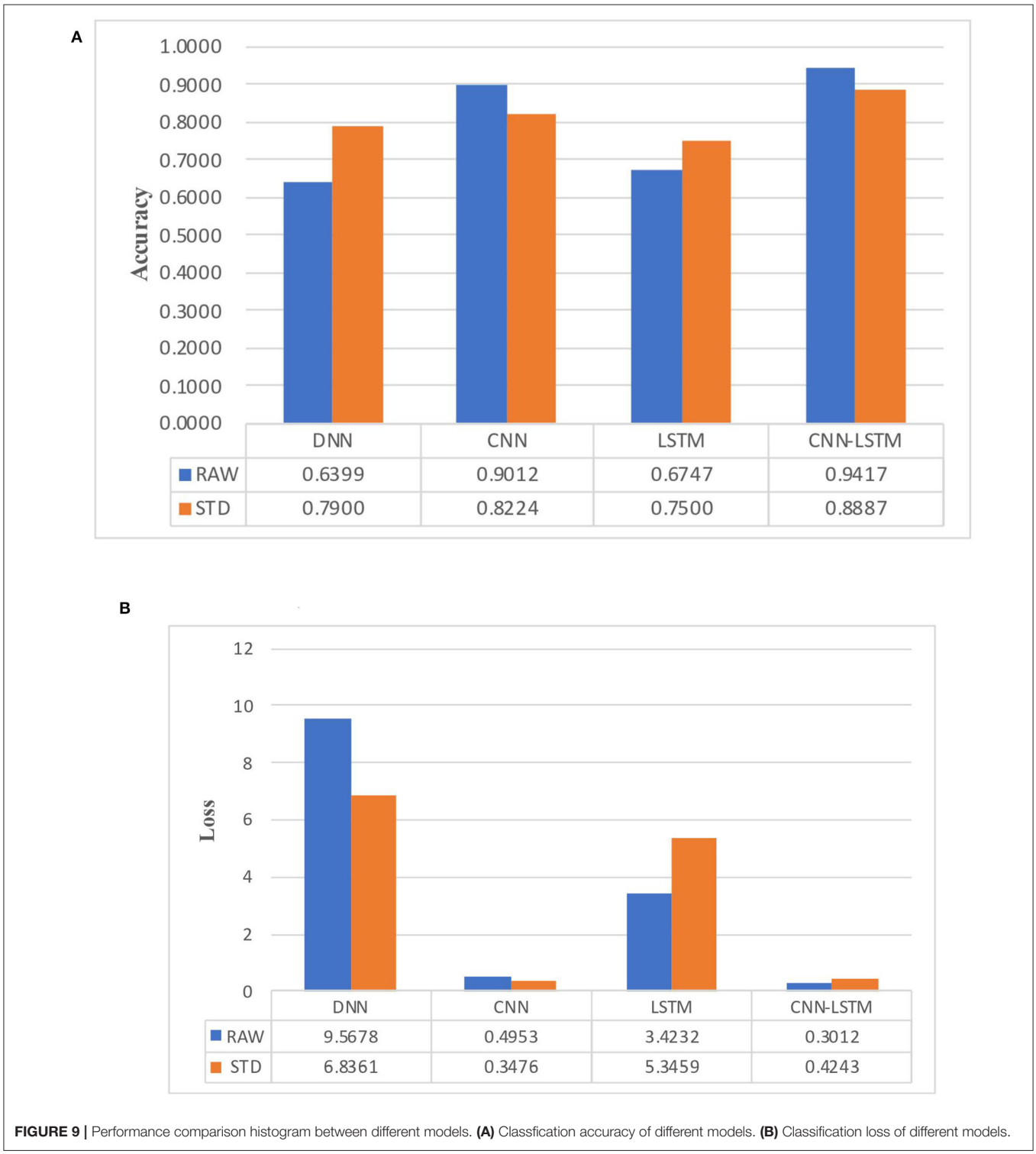

FIGURE 9 | Performance comparison histogram between different models. **(A)** Classfication accuracy of different models. **(B)** Classification loss of different models.

TABLE 5 | The influence of different epoch and learning rates for the DNN and CNN models.

Epoch	Learning rate	DNN	CNN
3	0.001	55.3	26.3
3	0.05	59.2	35.9
3	0.01	62.5	43.2
10	0.001	63.3	58.3
10	0.05	63.4	62.5
10	0.01	63.4	75.4
20	0.001	63.3	80.3
20	0.05	63.4	78.5
20	0.01	63.4	79.2

(Zhang et al., 2021):

$$\boldsymbol{Loss} = -\sum_{j=1}^{T} y_i log P_j \tag{11}$$

where y_j is the classification of the j th sample and P_j is the probability of the j th sample to be recognized as y_j.

Accuracy and Comparison Results

The training and test set included 55% positive samples and 45% negative samples, so it can be considered that the number of positive and negative samples was basically consistent. We repeated each model testing five times and averaged the results of those tests. The **Tables 3**, **4** show the experimental results of ***Acc*** and ***Loss***. **Figure 9** shows a bar chart comparison of them.

Additional Analysis and Results

During the training of the model, we compared the selection of some parameters and fine tuned the models. For the four architectures described above, we evaluated several design choices including learning rate, epoch, and dropout probability.

Epoch and Learning Rate

The epoch is the number of iterations during training. The learning rate determines the convergence speed and result accuracy of the model. Taking the CNN and LSTM as examples, the training results of different epochs and learning rates were adjusted and shown in **Table 5**.

It can be seen that the DNN model converged to optimal with fewer epochs and a higher learning rate. In contrast, the CNN model needed more epochs to learn. We chose 10 epoches and 0.01 as the learning rate for the DNN model. For the CNN model, we set 20 epoches and used the self-regulated learning rate callback function to autonomously adjust according to the training condition.

Dropout Probability

Since the dropout setting is very important for the gradient descent process of the LSTM model, we set the dropout probability at 20, 50, and 80%, respectively, and tested the LSTM model and CNN-LSTM model.

TABLE 6 | The influence of dropout probability for the LSTM and CNN-LSTM models.

Dropout probability (%)	LSTM	CNN-LSTM
20	0.58	0.62
50	0.71	0.89
90	0.51	0.48

It can be seen in **Table 6** that reducing the parameters by ∼50% each time was appropriate.

Result Discussion

The experimental results show that the CNN model and CNN-LSTM had better performance in emotion recognition classification, and were consistently more stable and had higher accuracy in RAW data than STD data. This result verified the advantages of the end-to-end deep learning mode we mentioned earlier, and proved that the CNN can be regarded as a feature extractor in end-to-end classification, which can automatically extract hidden features in EEG signals. It comes to a conclusion that the CNN feature extracter is more suitable for emotion recognition than manual feature extraction in emotion recognition based on EEG signals of the DEAP dataset.

The performance of the DNN model was not as good as the other complex models, but the training speed was fast. The DNN model could achieve optimal performance in fewer epochs and at a faster learning rate. The LSTM model was not as stable as the CNN and CNN-LSTM models. Moreover, with the same number of parameters, the training speed of the LSTM was much slower and it struggled to achieve convergence.

In addition, we found that the DNN model only needed a few training epochs to achieve convergence. The method of automatically adjusting the learning rate was suitable for the CNN and CNN-LSTM models. It was better to set the dropout rate of the LSTM at a medium level.

CONCLUSION

In this paper, several deep learning models for the classification of emotions were established and their performance was verified on the DEAP dataset. It was concluded that the CNN model or CNN-LSTM hybrid models were more effective in emotional classification than traditional machine learning methods. In particular, the automatical feature extraction of EEG signals was proven to have high performance in end-to-end multi-dimensional emotion recognition.

In the next step of research, we will try to obtain more data on EEG signals and implement other EEG-based emotional recognition models with more variables considered.

DATA AVAILABILITY STATEMENT

Publicly available datasets were analyzed in this study. This data can be found at: DEAPdataset http://www.eecs.qmul.ac.uk/mmv/datasets/deap/index.html.

AUTHOR CONTRIBUTIONS

YZ was responsible for writing the manuscript and carrying out experiments. JC, YuxC, YunC, and DL collected data for the experiments. LY checked the English grammer of the article. All authors contributed to the article and approved the submitted version.

FUNDING

This work was supported by the Fundamental Research Funds for the Central Universities, Grant No. 22120190211.

REFERENCES

Alhagry, S., Aly, A., and El-Khoribi, R. A. (2017). Emotion recognition based on EEG using LSTM recurrent neural network. *Int. J. Adv. Comput. Sci. Appl.* 8, 355–358. doi: 10.14569/IJACSA.2017.081046

Chen, J. X., Zhang, P. W., Mao, Z. J., Huang, Y. F., Jiang, D. M., and Zhang, Y. N. (2019). Accurate EEG-based emotion recognition on combined features using deep convolutional neural networks. *IEEE Access. IEEE* 7, 44317–44328. doi: 10.1109/ACCESS.2019.2908285

Cheng, C., and Parhi, K. K. (2020). Fast 2D convolution algorithms for convolutional neural networks. *IEEE Trans. Circuits Syst. I Regular Pap.* 67, 1678–1691. doi: 10.1109/TCSI.2020.2964748

de Boer, P. T., Kroese, D. P., Mannor, S., and Rubinstein, R. Y. (2005). A tutorial on the cross-entropy method. *Ann. Operat. Res.* 134, 19–67. doi: 10.1007/s10479-005-5724-z

deCarlo, L. T. (1997). On the meaning and use of kurtosis. *Psychol. Methods* 2, 292–307. doi: 10.1037/1082-989X.2.3.292

Graves, A., Mohamed, A., and Hinton, G. (2013). "Speech recognition with deep recurrent neural networks," in *2013 IEEE International Conference on Acoustics, Speech and Signal Processing*. (*IEEE),* 6645–6649.

Hanin, B. (2019). Universal function approximation by deep neural nets with bounded width and ReLU activations. *Mathematics* 7:992. doi: 10.3390/math7100992

Horlings, R., Datcu, D., and Rothkrantz, L. J. M. (2008). "Emotion recognition using brain activity," in *Proceedings of the 9th International Conference on Computer Systems and Technologies and Workshop for PhD Students in Computing - CompSysTech '08* (New York, NY: ACM Press).

Jiang, Y., Chung, F. L., Wang, S., Deng, Z., Wang, J., and Qian, P. (2015). Collaborative fuzzy clustering from multiple weighted views. *IEEE Trans. Cybernet.* 45, 688–701. doi: 10.1109/TCYB.2014.2334595

Jiang, Y., Gu, X., Wu, D., Hang, W., Xue, J., Qiu, S., et al. (2020a). "A novel negative-transfer-resistant fuzzy clustering model with a shared cross-domain transfer latent space and its application to brain CT image segmentation," in *IEEE/ACM Transactions on Computational Biology and Bioinformatics* (IEEE).

Jiang, Y., Wu, D., Deng, Z., Qian, P., Wang, J., Wang, G., et al. (2017). Seizure classification From EEG signals using transfer learning, semi-supervised learning and TSK fuzzy system. *IEEE Trans. Neural Syst. Rehabil. Eng.* 25, 2270–2284. doi: 10.1109/TNSRE.2017.2748388

Jiang, Y., Zhang, Y., Lin, C., Wu, D., and Lin, C. T. (2020b). "EEG-based driver drowsiness estimation using an online multi-view and transfer TSK fuzzy system," in *IEEE Transactions on Intelligent Transportation Systems* (IEEE), 1–13.

Jiang, Y., Zhao, K., Xia, K., Xue, J., Zhou, L., Ding, Y., et al. (2019). A novel distributed multitask fuzzy clustering algorithm for automatic MR brain image segmentation. *J. Med. Syst.* 43:118. doi: 10.1007/s10916-019-1245-1

Koelstra, S., Muhl, C., Soleymani, M., Lee, J. S., Yazdani, A., Ebrahimi, T., et al. (2012). DEAP: a database for emotion analysis; using physiological signals. *IEEE Trans. Affect. Comput.* 3, 18–31. doi: 10.1109/T-AFFC.2011.15

Ma, X., and Hovy, E. (2016). "End-to-end Sequence Labeling via Bi-directional LSTM-CNNs-CRF," in *Proceedings of the 54th Annual Meeting of the Association for Computational Linguistics (Volume 1: Long Papers)* (Stroudsburg, PA: Association for Computational Linguistics), 1064–1074. doi: 10.18653/v1/P16-1101

Mardia, K. V. (1970). Measures of multivariate skewness and kurtosis with applications. *Biometrika* 57, 519–530. doi: 10.1093/biomet/57.3.519

Murugappan, M., Ramachandran, N., and Sazali, Y. (2010). Classification of human emotion from EEG using discrete wavelet transform. *J. Biomed. Sci. Eng.* 3, 390–396. doi: 10.4236/jbise.2010.34054

Paul, S., Mazumder, A., Ghosh, P., Tibarewala, D. N., and Vimalarani, G. (2015). "EEG based emotion recognition system using MFDFA as feature extractor," in *2015 International Conference on Robotics, Automation, Control and Embedded Systems (RACE)* (IEEE).

Schirrmeister, R. T., Springenberg, J. T., Fiederer, L. D. J., Glasstetter, M., Eggensperger, K., Tangermann, M., et al. (2017). Deep learning with convolutional neural networks for EEG decoding and visualization. *Hum. Brain Mapp.* 38, 5391–5420. doi: 10.1002/hbm.23730

Shindjalova, R., Prodanova, K., and Svechtarov, V. (2014). "Modeling data for tilted implants in grafted with bio-oss maxillary sinuses using logistic regression," in *Energy Education Science and Technol Part B Social and Educational Studies*, 58–62.

Yang, C., Deng, Z., Choi, K. S., and Wang, S. (2016). Takagi–sugeno–kang transfer learning fuzzy logic system for the adaptive recognition of epileptic electroencephalogram signals. *IEEE Trans. Fuzzy Syst.* 24, 1079–1094. doi: 10.1109/TFUZZ.2015.2501438

Yang, P., Wang, D., Kagn, Z. J., Li, T., Fu, L. H., and Yu, Y. R. (2020). Prediction model of paroxysmal atrial fibrillation based on pattern recognition and ensemble CNN-LSTM. *Zhejiang Daxue Xuebao* 54, 1039–1048.

Zhang, J., Li, S., and Yin, Z. (2017). Pattern classification of instantaneous mental workload using ensemble of convolutional neural networks. *IFAC PapersOnLine* 50, 14896–14901. doi: 10.1016/j.ifacol.2017.08.2534

Zhang, Y., Ishibuchi, H., and Wang, S. (2018). Deep Takagi–sugeno–kang fuzzy classifier with shared linguistic fuzzy rules. *IEEE Trans. Fuzzy Syst.* 26, 1535–1549. doi: 10.1109/TFUZZ.2017.2729507

Zhang, Y., Wang, S., Xia, K., Jiang, Y., Qian, P., and Alzheimer's Disease Neuroimaging Initiative. (2021). Alzheimer's disease multiclass diagnosis via multimodal neuroimaging embedding feature selection and fusion. *Inform. Fusion* 66, 170–183. doi: 10.1016/j.inffus.2020.09.002

Zhao, J., Mao, X., and Chen, L. (2019). Speech emotion recognition using deep 1D & 2D CNN LSTM networks. *Biomed. Signal Process. Control* 47, 312–323. doi: 10.1016/j.bspc.2018.08.035

Conflict of Interest: The authors declare that the research was conducted in the absence of any commercial or financial relationships that could be construed as a potential conflict of interest.

frontiers in Neuroscience

ORIGINAL RESEARCH
published: 13 January 2021
doi: 10.3389/fnins.2020.578255

A Dynamic Multi-Scale Network for EEG Signal Classification

Guokai Zhang[1], Jihao Luo[2], Letong Han[2], Zhuyin Lu[2], Rong Hua[3], Jianqing Chen[4]* and Wenliang Che[5]**

[1] School of Optical-Electrical and Computer Engineering, University of Shanghai for Science and Technology, Shanghai, China, [2] School of Software Engineering, Tongji University, Shanghai, China, [3] College of Computer Science and Engineering, Shandong University of Science and Technology, Qingdao, China, [4] Department of Otolaryngology, Head & Neck Surgery, Shanghai Ninth People's Hospital, Affiliated to Shanghai Jiaotong University School of Medicine, Shanghai, China, [5] Department of Cardiology, Shanghai Tenth People's Hospital, Tongji University School of Medicine, Shanghai, China*

Accurate and automatic classification of the speech imagery electroencephalography (EEG) signals from a Brain-Computer Interface (BCI) system is highly demanded in clinical diagnosis. The key factor in designing an automatic classification system is to extract essential features from the original input; though many methods have achieved great success in this domain, they may fail to process the multi-scale representations from different receptive fields and thus hinder the model from achieving a higher performance. To address this challenge, in this paper, we propose a novel dynamic multi-scale network to achieve the EEG signal classification. The whole classification network is based on ResNet, and the input signal first encodes the features by the Short-time Fourier Transform (STFT); then, to further improve the multi-scale feature extraction ability, we incorporate a dynamic multi-scale (DMS) layer, which allows the network to learn multi-scale features from different receptive fields at a more granular level. To validate the effectiveness of our designed network, we conduct extensive experiments on public dataset III of BCI competition II, and the experimental results demonstrate that our proposed dynamic multi-scale network could achieve promising classification performance in this task.

Keywords: brain-computer interface, electroencephalography, multi-scale, Fourier transform, dynamic learning

OPEN ACCESS

Edited by:
Yizhang Jiang,
Jiangnan University, China

Reviewed by:
Lifeng Ma,
Nanjing University of Science and Technology, China
Hongwei Chen,
Donghua University, China

****Correspondence:***
Rong Hua
huarong@sdust.edu.cn
Jianqing Chen
chen.christophe@yahoo.com
Wenliang Che
chewenliang@tongji.edu.cn

Specialty section:
This article was submitted to Neuroprosthetics, a section of the journal Frontiers in Neuroscience

Received: *30 June 2020*
Accepted: *09 November 2020*
Published: *13 January 2021*

Citation:
Zhang G, Luo J, Han L, Lu Z, Hua R, Chen J and Che W (2021) A Dynamic Multi-Scale Network for EEG Signal Classification. Front. Neurosci. 14:578255. doi: 10.3389/fnins.2020.578255

1. INTRODUCTION

The brain sends brainwaves (Shahid et al., 2010) that enable human beings to think and act. During this process, people's motion intention can be captured by collecting EEG signals [called motor imagery (MI) EEG] from the cerebral cortex (Schlögl et al., 2005). To make MI possible, the BCI system creates a pathway between the brain and external devices (Zich et al., 2015) and converts the EEG signals into electrical signals to control peripheral devices, such as an electrically propelled wheelchair. For people suffering from physical inconveniences caused by paralysis or stroke, BCI system can help them act autonomously; this can not only help patients achieve self-care but also be a means of rehabilitation therapy (Schlögl et al., 2005; Padfield et al., 2019).

The EEG-based BCI system is divided into BCI based on steady-state visual evoked potential (SSVEP) and that based on sensorimotor rhythm (SMR) according to the type of EEG signals, and the latter is related to MI (Schlögl et al., 2005; Zich et al., 2015). The imagination of body movements affects the rhythmic activity recorded in the sensorimotor cortex. For example, when subjects are imagining movement to the left, the amplitude of mu and beta rhythm decreases

on the right side of the sensorimotor areas of the brain (Shahid et al., 2010). These increases and decreases in sensorimotor rhythms are called event-related synchronization (ERS) and event-related desynchronization (ERD) respectively (Shahid et al., 2010; Padfield et al., 2019). By analyzing the characteristics of these signals and rhythms, these features can be converted into output instructions for the control of BCI system.

Focusing on the state-of-the-art MI-based EEG systems, most of them consist of two parts: feature extraction and classification (Dose et al., 2018; Padfield et al., 2019). Some systems divide the first part into feature extraction and feature selection (Bashivan et al., 2015; Schirrmeister et al., 2017; Tang et al., 2017). In the feature extraction part, informative and non-redundant features are extracted from the original EEG data. Useful features are then sent to the feature selection step to obtain less computation complexity and higher classification accuracy. Finally, the classification step matches the characteristics of the EEG signals to different categories.

For the feature extraction part, the most basic techniques are divided into time-domain, frequency-domain, and spatial domain analysis (Padfield et al., 2019). As a typical time-domain approach, autoregressive (AR) modeling used the AR coefficients or spectrum as signal features (Krusienski et al., 2006). Though it has been improved into vector autoregressive (VAR) modeling, this method was not always effective when encountering an unstable sequence (Haboub et al., 2020). As for the frequency-domain analysis, the Fast Fourier transform (FFT) and Welch's method were both widely used in this field (Oikonomou et al., 2017; Li et al., 2020). Compared to FFT, Welch's method reduced the noise information of the original data but offered lower frequency resolution. Besides, time-frequency analysis methods such as the Short-time Fourier Transform (STFT), the discrete wavelet transform (DWT), and the flexible analytic wavelet transform (FAWT) were more powerful because they related the spectral information to the temporal domain and derived dynamic features, but they also required manual screening at the same time (Kumar et al., 2014; Tabar and Halici, 2016; You et al., 2020). In terms of spatial domain analysis, common spatial pattern (CSP) was the most common method thar uses spatial filters to transform EEG signals into a new space to precisely extract useful information from different frequency bands. However, CSP was time consuming since the optimal frequency band was subject specific and had to process redundant data to find the final solution (Lotte and Guan, 2010; Yang et al., 2015; Wankar et al., 2017).

Classification methods such as support vector machine (SVM), linear discriminant analysis (LDA), Bayesian classifiers, k-nearest neighbors (k-NN), and regression trees were widely used in recent literature (Kumar et al., 2017; Oikonomou et al., 2017). Among these techniques, the LDA and the SVM approaches both had the problem of overfitting, and k-NN was memory consuming since it had to process all the datasets at once. Beyond that, logistic regression outperformed SVM, k-NN, and artificial neural network (ANNs) approaches in classification accuracy.

In addition to the classification techniques mentioned above, computational intelligence methods, including the recurrent neural network (RNN) and convolutional neural network (CNN), were also widely used (Cheng et al., 2018; Zhou et al., 2018; Tang et al., 2020). The performance of deep learning methods was compared to traditional SVM and LDA classifiers, and it was proven that neural networks can improve the classification accuracy because they can automatically select informative features and constantly adjust parameters through backpropagation (Yang et al., 2015). For example, Cheng et al. performed an experiment to improve the classification accuracy of stroke patients using deep neural networks (DNN). They found that the features selected from sub-bands by DNN outperformed traditional feature extraction methods, and the DNN classifier also performed better than SVM (Cheng et al., 2018). Except for basic CNN, a modified one-dimensional multi-scaled CNN (1DMSCNN) was proposed by Tang to classify the preprocessed EEG signals, and it proved to have a better performance compared with algorithms, including CSP and long short-term memory with Discrete Wavelet Transform (DWT-LSTM) (Tang et al., 2020). To sum up, supervised learning methods are much preferred compared to methods based on unsupervised learning, and the latter ones are mainly used for the feature selection part.

In recent years, networks like the CNN, RNN, stacked autoencoders (SAE), deep belief networks (DBN), and VGGNet (Visual Geometry Group) were widely used in MI EEG systems (Schirrmeister et al., 2017; Tang et al., 2017; Li et al., 2020). These neural networks can complete all the above-mentioned steps because the network layers can extract feature maps from original data and learn to classify according to training labels. As one of the most popular networks in MI EEG systems, the CNN was often combined with other techniques such as the WT and STFT in practical experiments. For instance, (Li et al., 2020) segmented the EEG data by time windows then employed FFT to transform each time window to spectrum. By using the modified VGG called mVGG, a complicated image containing time-frequency features was generated, and its accuracy reached 88.62, 92.28, and 96.86% on three datasets-higher than that of the state-of-the-art imaging methods (Li et al., 2020). In addition, Chaudhary et al. introduced STFT and continuous wavelet transform (CWT) into CNN and drew the conclusion that the CWT approach yields better results than the other existing methods with accuracy score of 99.35% (Chaudhary et al., 2019).

While those previous works have achieved satisfying performance on the EEG classification task, they may be limited to the ignorance of extracting the multi-scale features from different receptive fields and resolutions, and those could be an important factor in learning the contextual characteristic of the EEG signal. To handle this problem, in this paper, we propose a dynamic multi-scale network for the EEG signal classification. The proposed method is mainly based on ResNet; before we input the EEG signal to the network, we first encoded it by STFT to obtain the feature representations and decrease the influence of the noise. Moreover, to extract the multi-scale and contextual characteristic from the input signal, a novel dynamic multi-scale (DMS) layer was designed as one part of the network. Finally, we conducted extensive experiments on public dataset III of BCI competition II to validate the effectiveness of our

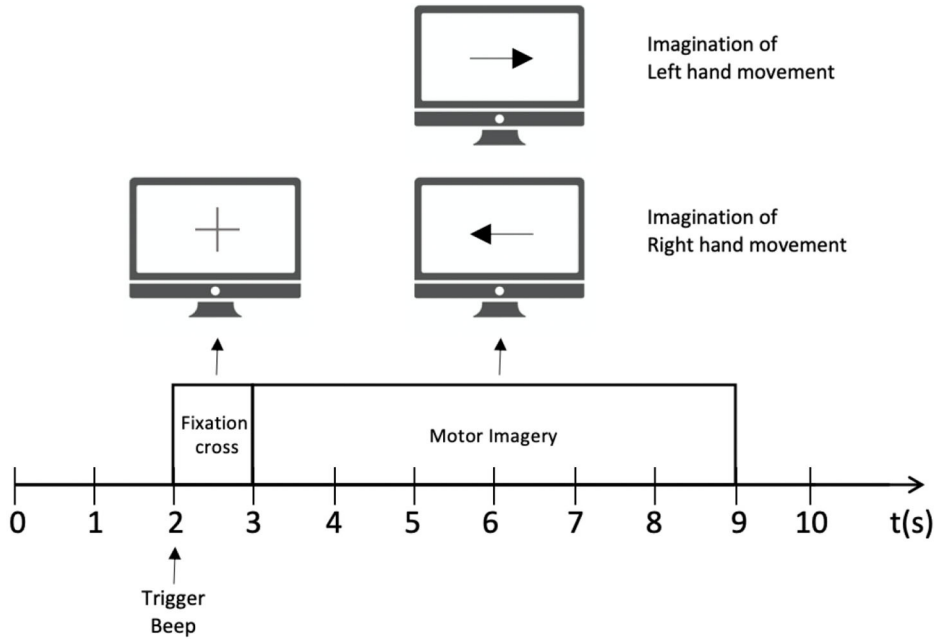

FIGURE 1 | The experimental paradigm for each trial.

proposed method, and the experimental results demonstrate that our method could achieve promising results compared with other ones.

The rest of this paper is organized as follows. Section 2 describes the experimental data, the preprocessing procedure, as well as the proposed network architecture. Section 3 then introduces the evaluation metrics and presents the experiment results of different channels and network architectures. Finally, the overall conclusion of this paper is summarized in section 4.

2. METHODOLOGY

2.1. Data Description

Public dataset III of BCI competition II is adopted to train the MI BCI model. This dataset was collected from a 25-year-old female subjects during a feedback session. This experiment is constitutive of 280 trials in total, and each trial has a length of 9 s. As shown in **Figure 1**, the first 2 s of the experiment was quiet. An acoustic stimulus and a cross "+," which indicates the beginning of the trial, was then displayed in the following 1s. After that, at $t = 3$ s, an arrow (left or right, randomly) was shown on the screen as a cue. At the same time, the subject was asked to finish the motor imagery task according to the cue. The trial data were collected by three EEG channels C3, Cz, and C4, which were sampled with 128 Hz and filtered between 0.5 and 30 Hz. The diagram of source EEG data is shown in **Figure 2**.

2.2. Network Architecture

The main backbone of our proposed network is based on ResNet, which has proven its effectiveness in many computer-vision tasks. Given an input signal, we first used the STFT to gain the feature representations of the input signal and achieving the goal of noise reduction simultaneously. Furthermore, to better improve the ability of learning multi-scale features of the network, we incorporated a DMS layer after each residual block stage, which enables the network to learn the multi-scale features from the granular level. The overall structure of our designed network is shown in **Figure 3**, and it is sequentially composed of a series of convolution layers, max-pooling layers, residual blocks, and DMS layers. Note that for learning more non-linear information from input signals, the network uses the ReLU activation function after each convolution layer, and we omit this unit in **Figure 3** for simplicity. We replace the original ResNet, which adopts average-pooling as the next to last layer, with the max-pooling layer, which can provide more salient representation and thus further improve the classification performance of the network. Finally, the extracted representations from the network pass through a fully connected layer with the softmax activation function to output the prediction probabilities of the two classes (left or right). In the following subsections, we will give a detailed description of the residual block, the data prepossessed by the STFT, and the designed DMS layer.

2.2.1. Residual Block

Since the whole network architecture is based on ResNet and the core unit of it is the residual block, we will in this section first give a brief retrospect of the residual block. As shown in **Figure 4A**, the input feature of the residual block is denoted as x. The residual block uses skip connection to reduce the influence of vanishing gradient problem of the network. During the process, the residual function $F(x)$ is

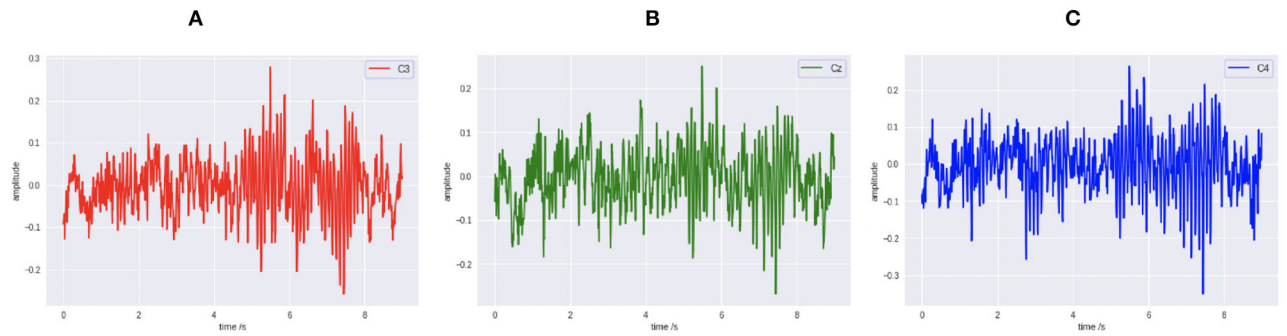

FIGURE 2 | The original EEG signal data diagram. **(A)** C3. **(B)** Cz. **(C)** C4.

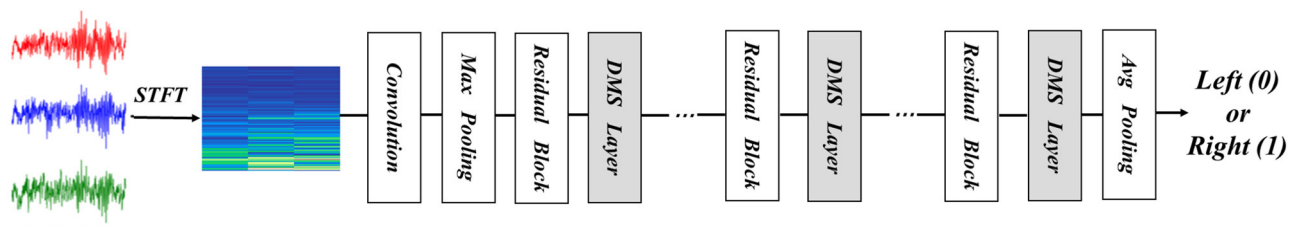

FIGURE 3 | The overview of our proposed dynamic multi-scale network.

learned by using the labeled data to train the weight layer as shown below:

$$F(x) = F'(x) - x \tag{1}$$

where the $F'(x)$ is the desired underlying mapping and the weight layer can be composed of any type of neural network layer, including convolutional layers or fully connected layers. Through setting the residual function $F(x)$ to zero, the help from residual blocks to skip certain parts of the network can enable the network compose of many different feature extracting layers that capture different possible features of the data. The bottleneck architecture, as shown in **Figure 4B**, aims to achieve the function of controlling the dimension of feature map by adding up two 1×1 convolution layers before and after the weight layer.

2.3. Feature Encoding by STFT

Fourier Transform is a form of transforming the signal from the time domain to the frequency domain. It is an important analysis tool in the fields of acoustics, speech, telecommunications, and signal processing. In our approach, before inputting the signal into the network, we first encoded the signal by STFT. We first give a detailed description of the Discrete Fourier Transform (DFT), FFT, and STFT. DFT is a representation of continuous Fourier Transform in discrete systems, and FFT is a fast algorithm for efficiently realizing DFT. Supposing $t(n)$ is a finite length sequence of length N, then the N-point DFT of $T(k)$ is the following:

$$T(k) = \sum_{n=0}^{N-1} t(n) W_N^{nk}, k = 0, 1, \ldots N-1 \tag{2}$$

Among which the rotation factor W_N is defined as follows:

$$W_N = e^{-j2\pi/N} \tag{3}$$

When $t(n)$ is a complex sequence, directly calculating $T(k)$ according to the above formula based on a certain value of k requires N complex multiplications and $N-1$ complex numbers addition. For all k values, a total of N^2 complex multiplications and $N(N-1)$ complex additions are thus required, which requires a huge workload. However the rotation factor $W_N = e^{-j2\pi/N}$ has its symmetrical and periodic characteristics as follows:

$$W_N^k = -W_N^{k+N/2} \tag{4}$$

$$W_N^k = -W_N^{k+N} \tag{5}$$

By applying these properties, FFT decomposes the long-sequence DFT into smaller DFTs and uses these small DFT calculations to replace large DFT calculations to achieve the purpose of improving efficiency. Nevertheless, since DFT has higher requirements for sampling the entire period of the signal where non-integer sampling will cause analysis errors including spectral leakage and fence effects, the STFT is applied to solve these

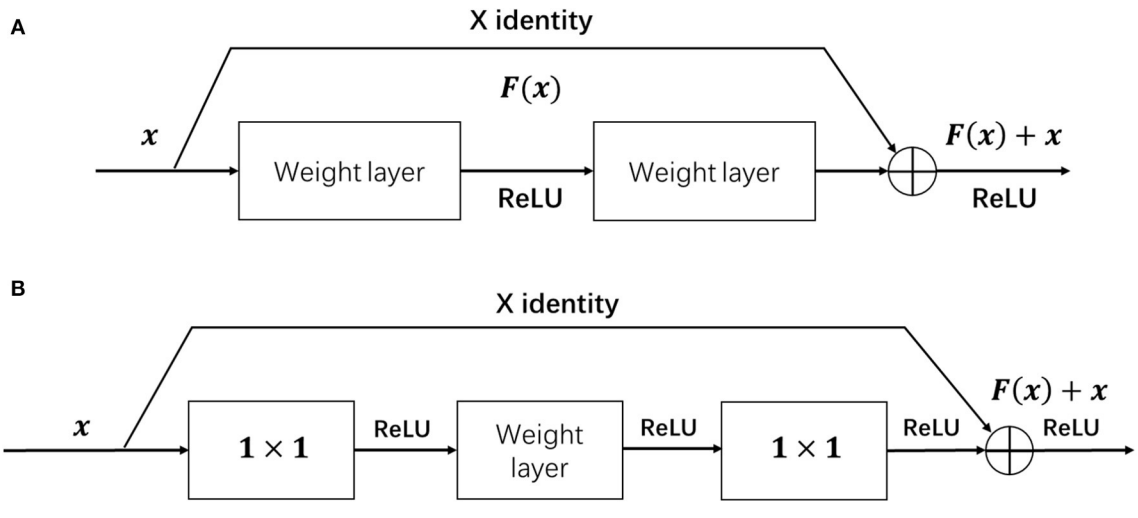

FIGURE 4 | The structure of the residual block **(A)** and residual bottleneck **(B)**.

problems. STFT defines a time and frequency distribution class, which specifies the complex amplitude of any signal changing with time and frequency to get more accurate spectrum information. It uses a sliding window mechanism as well to set the window size and step size, allowing the window slide on the time domain signal and calculating the Fourier Transform of each window separately to form the frequency domain signal corresponding to different time windows, which is expressed as follows:

$$s_N(n) = s(n)g(n - mR) \tag{6}$$

$$S_{STFT}(n, \mathcal{F}) = \sum_{n=0}^{N-1} s_N(n)e^{-j\mathcal{F}n} = \sum_{n=0}^{N-1} s(n)g(n - mR)e^{-j\mathcal{F}n} \tag{7}$$

among which, the signal sequence at time n is defined as $s(n)$. And the $g(n-mR)$ represents the selected window of size $n-mR$, along with the time axis m and the hop size of R. The frequency axis is defined as $\mathcal{F}$. After applying STFT to the input signal, the feature representation of the data is shown as **Figure 5**.

2.4. Dynamic Multi-Scale Layer

The multi-scale features describe the contextual characteristics of the input from different scales, which are of great importance to the vision classification tasks. However, due to the fixed sizes of filters, the classical ResNet fails to learn the multi-scale features from different receptive fields, which hinders the model from achieving a better classification performance. To address this challenge, in this section, we designed a novel dynamic multi-scale (DMS) layer that could extract the multi-scale features more efficiently, and the structure of the DMS layer is shown in **Figure 6**. Given an input feature F, a channel split function $f(\cdot)$ is utilized to divide the feature map to four equal numbers of sub-maps, and each of them could be denoted as s_i where $i \in \{1, 2, 3, 4\}$. Then, to learn multi-scale features from the granular level, a dynamic multi-scale learning module M_i is designed as shown in the right part of **Figure 6**, which uses three dynamic sizes of 2D convolutions to extract the multi-scale features from different receptive fields. To balance the computational complexities and the final model performance, three sizes of M_i are adopted, $d \times d$, $\frac{d}{2} \times \frac{d}{2}$, and $\frac{d}{4} \times \frac{d}{4}$, respectively, and here d represents the dimension of feature map s_i. After passing through those three convolution layers, the output features are then concatenated as one. Furthermore, to reduce the numbers of the feature maps, a convolution layer with the size of 1×1 is utilized to output the final feature map z_i. Specifically, inspired by the previous work (Gao et al., 2019), we add $\{z_1, z_2, z_3\}$ to $\{s_2, s_3, s_4\}$ for combining more information from different scales. After the processing from each M_i, the learned multi-scale feature map z_i is gained, and the final output feature map of the DMS layer is obtained by fusing those four sub-maps z_1, z_2, z_3, and z_4 with channel shuffling. Since different feature map resolutions can contain discriminative information, and the DMS layer aims to make the network more conducive for learning multi-scale and contextual features, we located the DMS layer after each stage's last residual block for obtaining the multi-scale features more efficiently. The algorithm of dynamic multi-scale feature learning process is illustrated in Algorithm 1.

2.5. Implementation Details

The experiment runs on Nvidia GTX1080 GPU and is implemented by Keras 2.2.5. The categorical cross-entropy loss function is adopted to train the CNN model, which assesses the difference between the real label and the predicted label. As for the network optimizer, the Adam optimizer was chosen to adaptively optimize the learning rate based on the initial setting of 0.0003. Except for that, we also use the callback function ReduceLROnPlateau to monitor the decline in learning rate according to validation accuracy, and the lower boundary of

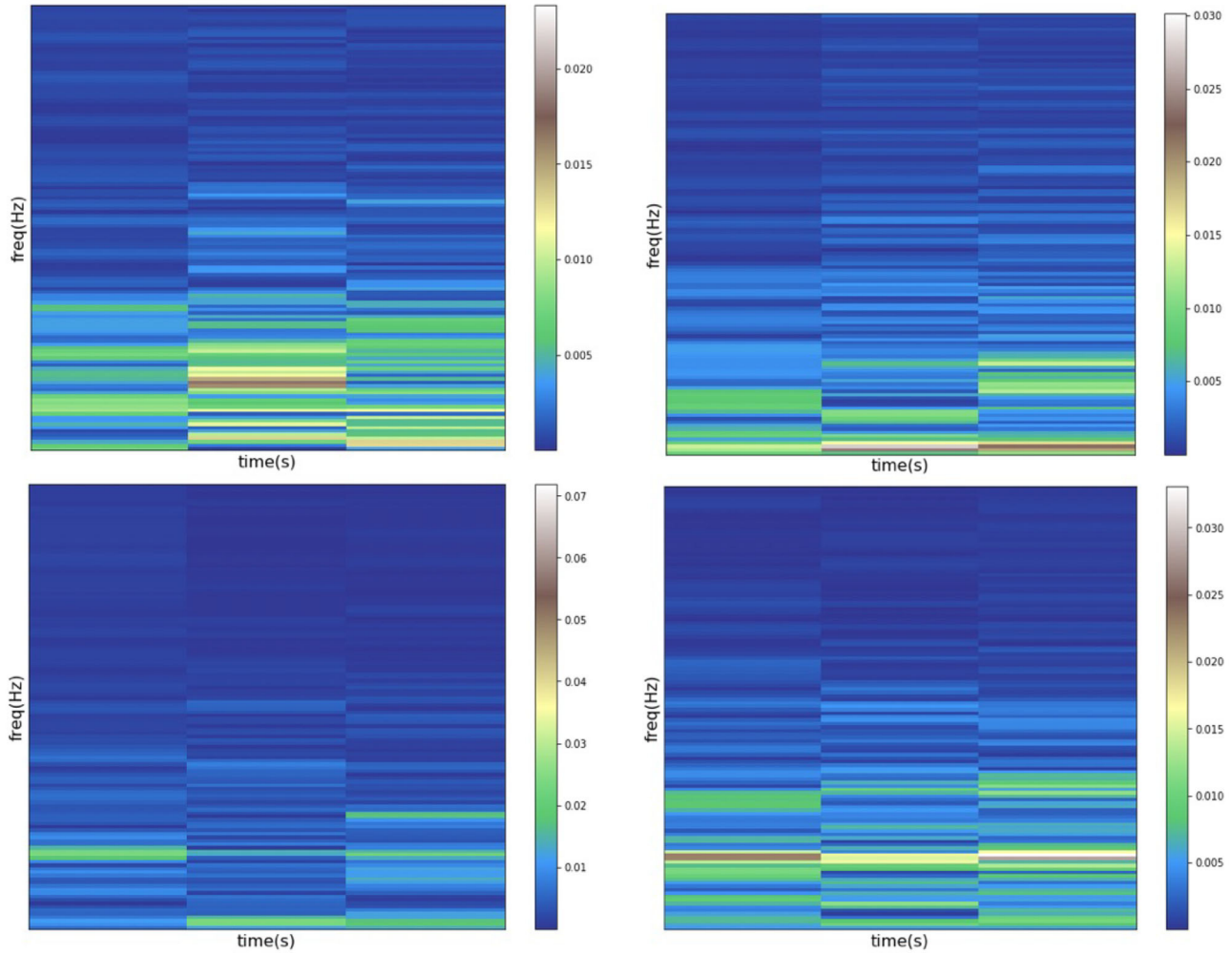

FIGURE 5 | Data diagram after STFT processing.

learning rate was then set to 0.0001 and the patience set to 10 epochs. The training set and the validation set were divided according to the scale of 0.3, and the former was trained with a batch size of 8 for each epoch. By using softmax as our classifier, the checkpoint with the best accuracy was selected as the final model.

3. EXPERIMENTAL RESULTS

3.1. Evaluation Metrics

For evaluation of experimental results, the commonly used accuracy metric was adopted. In this experiment, accuracy was evaluated by judging the classification results of two classes of the model, and the metric is defined as below:

$$Accuracy = \frac{TP + TN}{TP + TN + FP + FN} \tag{8}$$

where TP (True Positives) refers to the number of the EEG records that indicate left and identified as left; TN (True Negatives) denotes the number of the EEG records that are left and identified as right; FP (False Positives) is the number of the EEG records that are right but are predicted as left; and FN (False Negatives) refers to the number of the EEG records that are right but are predicted as right. By using this metric, the performance of the proposed model could be evaluated quantitatively.

3.2. Performance of Different Channels and Window Functions

In this section, an experiment of different channel combinations and STFT windows was conducted to compare the corresponding performance. The selected channel combinations included 2-channel (C3 and C4) and 3-channel (C3, Cz, and C4). STFT windows are adopted to reduce the leakage of the spectrum during signal interception. There are some widely used STFT window functions from which we adopted boxcar, triang, hamming, hann, and bartlett in this experiment.

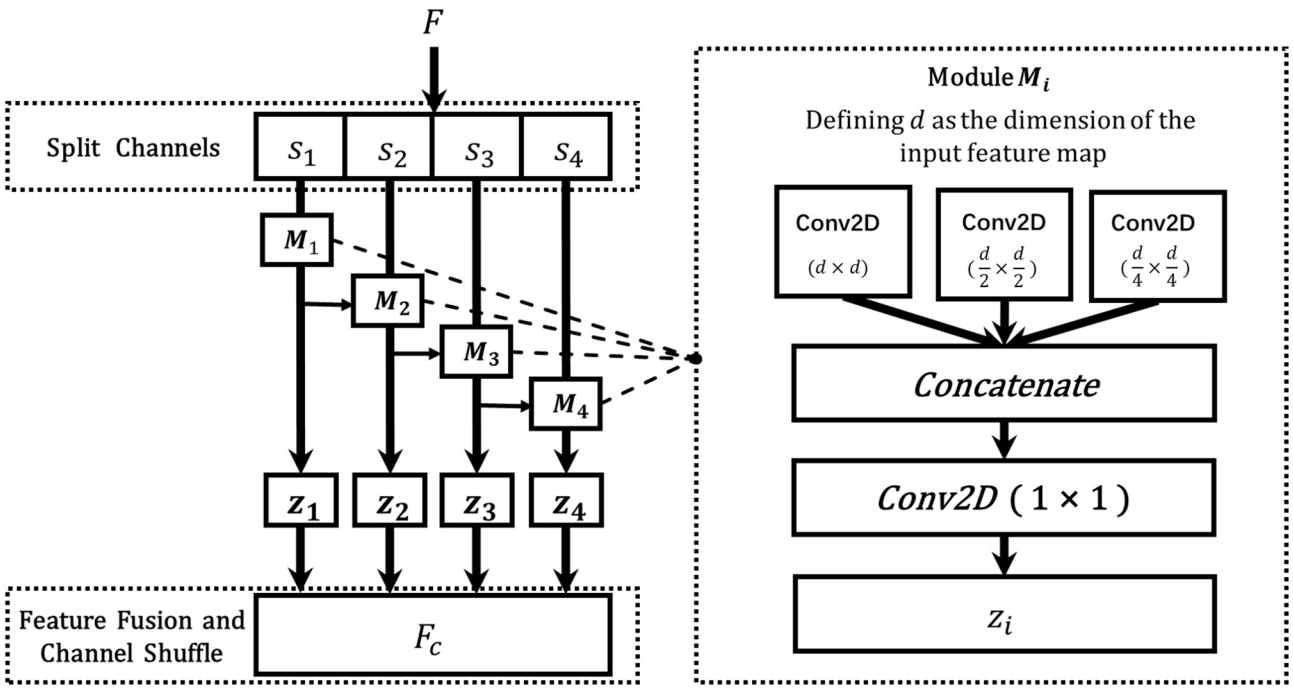

FIGURE 6 | The architecture of the DMS layer. The **F** is the input feature map from the previous layer, and $\mathbf{s_1}, \mathbf{s_2}, \mathbf{s_3}$, *and* $\mathbf{s_4}$ are the split feature maps from **F**, $\mathbf{M_i}$ denotes the dynamic multi-scale module, which consists of three 2D convolutions with different sizes ($\mathbf{d} \times \mathbf{d}$, $\frac{\mathbf{d}}{\mathbf{2}} \times \frac{\mathbf{d}}{\mathbf{2}}$, $\frac{\mathbf{d}}{\mathbf{4}} \times \frac{\mathbf{d}}{\mathbf{4}}$), where **d** is the dimension of feature $\mathbf{s_i}$, and $\mathbf{z_i}$ is the fused output features of $\mathbf{M_i}$, and $\mathbf{F_C}$ represents the final output of the DMS layer.

The comparison result is shown in **Table 1**. It demonstrates that the best performance is achieved on the combination of 2-channel and hann window function with the accuracy of 90.47%, and the hardest classification is 3-channel boxcar function with the accuracy of 65.48%. We also notice that the overall performance of 2-channel input data is relatively better, which means that the EEG signals under the Cz region contain less informative characteristics but more noise. Meanwhile, the hann window achieves higher accuracy than other STFT window functions, which means this default Fourier function indeed has the best performance. Overall, the accuracy performance of different window combinations of 2-channel is above 77%, which indicates that the proposed network architecture is relatively effective in this classification scenario.

3.3. Comparison With Different Sampling Intervals

As the experimental paradigm shown in **Figure 1**, the cue of the arrow appears after 3 s, and the motor imagery begins directly after. The informative EEG signals from 3 to 9 s are therefore adopted as input data in this paper. However, the signals of the whole period of 6 s contains unrelated noise. Meanwhile, considering the delay between the time when the subject receives the cue and when she starts to imagine, the sliding window of the time duration is introduced to bring as little irrelevant noise as possible into this experiment. As shown in **Table 2**, the durations of each 3 s after the first 3 s are selected as input data, and the comparison results show that the classification accuracy between the period of 3–6 s is the best. Correspondingly, the accuracy based on the 5–8 s section performs the worst, which suggests that there is indeed a short delay before the subject conduct the motor imagery after receiving the cue. Comparing the overall results of different time durations, the accuracy decreases together with time interval is all above 78%, and it can thus be considered that motion imagination mainly occurs in a short period after receiving the cue. According to this part of the experiment, we find that the classification accuracy is indeed related to the time interval sliding window. However, due to the differences of delay time in each subject, specific experiments and analyses need to be conducted.

3.4. Comparison With Different Combinations of Convolutions

Different combinations of convolutions in the DMS layer could give various representations from different receptive fields. Thus, in this section, we conduct the experiments to explore the effectiveness of different combinations of convolutions. Since we have adopted three sizes of convolutions in DMS layer, here we denote Conv_1, Conv_2, and Conv_3 as the convolution with the sizes $d \times d$, $\frac{d}{2} \times \frac{d}{2}$, and $\frac{d}{4} \times \frac{d}{4}$, respectively, where d is the dimension of the input feature map from the previous layer. The detailed comparison result is shown in **Table 3**, from the result we can see that the best performance is gained by the combination of Conv_1, Conv_2, and Conv_3, simultaneously, which with the accuracy of 90.47%. Meanwhile, for single size of the convolution, the best

Algorithm 1: The algorithm of dynamic multi-scale feature learning

Input: F: Input Feature
Output: F_c: Final output feature map of DMS layer

function $MS(P)$:
  $F_d \leftarrow Conv2D(d, d)(P)$
  $F_{\frac{d}{2}} \leftarrow Conv2D(\frac{d}{2}, \frac{d}{2})(P)$
  $F_{\frac{d}{4}} \leftarrow Conv2D(\frac{d}{4}, \frac{d}{4})(P)$
  $P_F \leftarrow Concatenate(F_d, F_{\frac{d}{2}}, F_{\frac{d}{4}})$
  $P_F \leftarrow Conv2D(1, 1)(P_F)$
  return P_F
end function
$S = \{s_1, s_2, s_3, s_4\} \leftarrow f(F)$
for *each* $s_i \in S$ **do**
  if $s_i == s_1$ *or* s_4 **then**
    $z_i = MS(s_i)$
  else
    $z_i = MS(add[z_{i-1}, s_i])$
  endif
endfor
$F_C \leftarrow concatenate(z_1, z_2, z_3, z_4)$
$F_C \leftarrow$ channel shuffle(F_C);

TABLE 1 | The overall performance of different channel and window combinations.

Method	Accuracy (%)
boxcar + C3/C4	83.33
triang + C3/C4	89.28
hamming + C3/C4	86.90
hann + C3/C4	90.47
bartlett + C3/C4	77.38
boxcar + C3/Cz/C4	65.48
triang + C3/Cz/C4	70.24
hamming + C3/Cz/C4	67.86
hann + C3/Cz/C4	66.67
bartlett + C3/Cz/C4	77.35

TABLE 2 | The overall performance of different sampling intervals.

Duration (s)	Accuracy (%)
3–6	90.47
3.5–6.5	86.90
4–7	84.52
4.5–7.5	79.76
5–8	78.57

result is achieved by $Conv_2$, which indicates that the medium size of the convolution can be crucial in this classification task.

TABLE 3 | The overall performance of different combinations of convolutions.

Method	Accuracy (%)
$Conv_1$	86.97
$Conv_2$	88.21
$Conv_3$	87.32
$Conv_1$ + $Conv_2$	89.73
$Conv_1$ + $Conv_3$	89.22
$Conv_2$ + $Conv_3$	89.65
$Conv_1$ + $Conv_2$ + $Conv_3$	90.47

TABLE 4 | The overall performance of different methods.

Method	Accuracy (%)
PSD+LDA	65.60
Discriminative area selection+FHNN	83.10
STFT based features+ResNet	85.09
STFT based features+Res2Net	89.73
DWT and AR model+LDA	90.00
Wavelet based features+FSVM	87.86
Wavelet based features+SVM	89.83
Wavelet based features+CNN	84.09
Multiple auto correlation+LVQ	90.00
Morlet wavelet+Bayes quadratic	89.29
Higher order features+LDA	89.29
Higher order features+Neural network	90.00
STFT based features+CNN	80.95
Our Proposed Method	90.47

3.5. The Effectiveness of Different Split Channel Numbers

In our proposed method, different split numbers of the feature channels could provide various influences on the final result. Therefore, in this section, we implement 1 to 6 split-channel numbers to explore its effects on the final classification performance. As illustrated in **Table 5**, with the split-channel number increasing, the performance of the classification model is improved. Specifically, when the split-channel number is more than 4, the boosted performance is not as comparative as the previous ones. Thus, considering to balance the model performance and complexities, we adopt the split channel number of 4 as our final experimental setting.

3.6. Compare With Other Methods

To further evaluate the effectiveness of our proposed network, we compared our method with other previous works, including STFT based features+ResNet (He et al., 2016), STFT based features+CNN (Li et al., 2014), STFT based features+Res2Net (Gao et al., 2019), PSD+LDA (Solhjoo and Moradi, 2004), Discriminative area selection+FHN (Hsu, 2015), DWT and AR model+LDA (Xu et al., 2009), Wavelet based features+FSVM/SVM/CMM (Xu et al., 2019), Multiple auto correlation+LVQ (Wang et al., 2014), Morlet

TABLE 5 | The overall performance of different split channel numbers.

Split Channel Numbers	Accuracy (%)
Ch-1	87.61
Ch-2	88.53
Ch-3	89.79
Ch-4	90.47
Ch-5	90.50
Ch-6	90.51

wavelet+Bayes quadratic (Lemm et al., 2004), Higher order features+LDA/Neural network (Zhou et al., 2008). **Table 4** shows the comparison results of networks above. According to the classification accuracy demonstrated in **Table 4**, it can be observed that the proposed network performs better in this EEG classification task than the other two ones. The best performance of our method can achieve the accuracy of 90.47% since we adopt STFT for preprocessing and incorporate the DMS layer to our network. In conclusion, it is proved that with the adoption of DMS layer, our proposed method can achieve a promising performance compared to other common networks.

4. CONCLUSION

In this paper, we propose a dynamic multi-scale network for the motor imagery EEG signals classification, which could help patients achieve self-care and rehabilitation therapy potentially. The main backbone of the proposed network is based on ResNet, and, given input from the network, we first encoded the feature representations by STFT; to further learn the multi-scale features from a more granular level, the proposed network incorporates a dynamic multi-scale layer that enables us to learn more contextual information from different receptive fields. To evaluate the performance of our proposed method, we conducted extensive experiments on public dataset III of BCI competition II. The experimental results demonstrate that our proposed method could achieve a competitive result, which further proves the effectiveness of the designed network. In future work, we will focus on exploring the combination of pre-defined features with the deep convolution features.

DATA AVAILABILITY STATEMENT

Publicly available datasets were analyzed in this study. This data can be found here: http://www.bbci.de/competition/ii/.

AUTHOR CONTRIBUTIONS

GZ, JL, and LH conceived the idea and designed the algorithm. GZ and JL conducted the experiments and validated its effectiveness. LH wrote the initial paper. All authors contributed to refining the ideas and revised the manuscript.

REFERENCES

Bashivan, P., Rish, I., Yeasin, M., and Codella, N. (2015). Learning representations from EEG with deep recurrent-convolutional neural networks. *arXiv preprint arXiv:1511.06448*.

Chaudhary, S., Taran, S., Bajaj, V., and Sengur, A. (2019). Convolutional neural network based approach towards motor imagery tasks EEG signals classification. *IEEE Sens. J.* 19, 4494–4500. doi: 10.1109/JSEN.2019.2899645

Cheng, D., Liu, Y., and Zhang, L. (2018). "Exploring motor imagery EEG patterns for stroke patients with deep neural networks," in *2018 IEEE International Conference on Acoustics, Speech and Signal Processing (ICASSP)* (Calgary, AB: IEEE), 2561–2565. doi: 10.1109/ICASSP.2018.8461525

Dose, H., Møller, J. S., Iversen, H. K., and Puthusserypady, S. (2018). An end-to-end deep learning approach to mi-EEG signal classification for BCIs. *Expert Syst. Appl.* 114, 532–542. doi: 10.1016/j.eswa.2018.08.031

Gao, S., Cheng, M.-M., Zhao, K., Zhang, X.-Y., Yang, M.-H., and Torr, P. H. S. (2019). Res2net: a new multi-scale backbone architecture. *IEEE Trans. Pattern Anal. Machine Intellig.* doi: 10.1109/TPAMI.2019.2938758

Haboub, A., Baali, H., and Bouzerdoum, A. (2020). "Multichannel signal classification using vector autoregression," in *ICASSP 2020 - 2020 IEEE International Conference on Acoustics, Speech and Signal Processing (ICASSP)* (Barcelona), 1021–1025. doi: 10.1109/ICASSP40776.2020.9054144

He, K., Zhang, X., Ren, S., and Sun, J. (2016). "Deep residual learning for image recognition," in *Proceedings of the IEEE Conference on Computer Vision and Pattern Recognition*, 770–778.

Hsu, W.-Y. (2015). Brain–computer interface: the next frontier of telemedicine in human–computer interaction. *Telemat. Inf.* 32, 180–192. doi: 10.1016/j.tele.2014.07.001

Krusienski, D. J., McFarland, D. J., and Wolpaw, J. R. (2006). "An evaluation of autoregressive spectral estimation model order for brain-computer interface applications," in *2006 International Conference of the IEEE Engineering in Medicine and Biology Society* (New York, NY: IEEE), 1323–1326. doi: 10.1109/IEMBS.2006.259822

Kumar, S., Sharma, A., and Tsunoda, T. (2017). An improved discriminative filter bank selection approach for motor imagery EEG signal classification using mutual information. *BMC Bioinform.* 18:545. doi: 10.1186/s12859-017-1964-6

Kumar, Y., Dewal, M., and Anand, R. (2014). Epileptic seizures detection in EEG using DWT-based apen and artificial neural network. *Signal Image Video Process.* 8, 1323–1334. doi: 10.1007/s11760-012-0362-9

Lemm, S., Schafer, C., and Curio, G. (2004). BCI competition 2003-data set III: probabilistic modeling of sensorimotor/spl mu/rhythms for classification of imaginary hand movements. *IEEE Trans. Biomed. Eng.* 51, 1077–1080. doi: 10.1109/TBME.2004.827076

Li, M., Han, J., and Duan, L. (2020). "A novel MI-EEG imaging with the location information of electrodes," in *IEEE Access*, Vol. 8, 3197–3211. doi: 10.1109/ACCESS.2019.2962740

Li, Q., Cai, W., Wang, X., Zhou, Y., Feng, D. D., and Chen, M. (2014). "Medical image classification with convolutional neural network," in *2014 13th International Conference on Control Automation Robotics & Vision (ICARCV)* (IEEE), 844–848.

Lotte, F., and Guan, C. (2010). "Spatially regularized common spatial patterns for EEG classification," in *2010 20th International Conference on Pattern Recognition* (Istanbul: IEEE), 3712–3715. doi: 10.1109/ICPR.2010.904

Oikonomou, V. P., Georgiadis, K., Liaros, G., Nikolopoulos, S., and Kompatsiaris, I. (2017). "A comparison study on EEG signal processing techniques using motor imagery EEG data," in *2017 IEEE 30th International Symposium on Computer-Based Medical Systems (CBMS)* (Thessaloniki: IEEE), 781–786. doi: 10.1109/CBMS.2017.113

Padfield, N., Zabalza, J., Zhao, H., Masero, V., and Ren, J. (2019). EEG-based brain-computer interfaces using motor-imagery: techniques and challenges. *Sensors* 19:1423. doi: 10.3390/s19061423

Schirrmeister, R. T., Springenberg, J. T., Fiederer, L. D. J., Glasstetter, M., Eggensperger, K., Tangermann, M., et al. (2017). Deep learning with convolutional neural networks for EEG decoding and visualization. *Hum. Brain Mapp*. 38, 5391–5420. doi: 10.1002/hbm.23730

Schlögl, A., Lee, F., Bischof, H., and Pfurtscheller, G. (2005). Characterization of four-class motor imagery EEG data for the BCI-competition 2005. *J. Neural Eng*. 2:L14–L22.

Shahid, S., Sinha, R. K., and Prasad, G. (2010). Mu and beta rhythm modulations in motor imagery related post-stroke EEG: a study under BCI framework for post-stroke rehabilitation. *BMC Neurosci*. 11:P127. doi: 10.1186/1471-2202-11-S1-P127

Solhjoo, S., and Moradi, M. H. (2004). "Mental task recognition: a comparison between some of classification methods," in *BIOSIGNAL 2004 International EURASIP Conference*, 24–26.

Tabar, Y. R., and Halici, U. (2016). A novel deep learning approach for classification of EEG motor imagery signals. *J. Neural Eng*. 14:016003. doi: 10.1088/1741-2560/14/1/016003

Tang, X., Li, W., Li, X., Ma, W., and Dang, X. (2020). Motor imagery EEG recognition based on conditional optimization empirical mode decomposition and multi-scale convolutional neural network. *Expert Syst. Appl*. 149:113285. doi: 10.1016/j.eswa.2020.113285

Tang, Z., Li, C., and Sun, S. (2017). Single-trial EEG classification of motor imagery using deep convolutional neural networks. *Optik* 130, 11–18. doi: 10.1016/j.ijleo.2016.10.117

Wang, X., Wang, A., Zheng, S., Lin, Y., and Yu, M. (2014). "A multiple autocorrelation analysis method for motor imagery EEG feature extraction," in *The 26th Chinese Control and Decision Conference (2014 CCDC)* (IEEE), 3000–3004.

Wankar, R. V., Shah, P., and Sutar, R. (2017). "Feature extraction and selection methods for motor imagery EEG signals: a review," in *2017 International Conference on Intelligent Computing and Control (I2C2)* (Coimbatore: IEEE), 1–9. doi: 10.1109/I2C2.2017.8321831

Xu, B., Zhang, L., Song, A., Wu, C., Li, W., Zhang, D., et al. (2019). Wavelet transform time-frequency image and convolutional network-based motor imagery EEG classification. *IEEE Access* 7, 6084–6093. doi: 10.1109/ACCESS.2018.2889093

Xu, Q., Zhou, H., Wang, Y., and Huang, J. (2009). Fuzzy support vector machine for classification of EEG signals using wavelet-based features. *Med. Eng. Phys*. 31, 858–865. doi: 10.1016/j.medengphy.2009.04.005

Yang, H., Sakhavi, S., Ang, K. K., and Guan, C. (2015). "On the use of convolutional neural networks and augmented CSP features for multi-class motor imagery of EEG signals classification," in *2015 37th Annual International Conference of the IEEE Engineering in Medicine and Biology Society (EMBC)* (Milan: IEEE), 2620–2623.

You, Y., Chen, W., and Zhang, T. (2020). Motor imagery EEG classification based on flexible analytic wavelet transform. *Biomed. Signal Process. Control* 62:102069. doi: 10.1016/j.bspc.2020.102069

Zhou, J., Meng, M., Gao, Y., Ma, Y., and Zhang, Q. (2018). "Classification of motor imagery EEG using wavelet envelope analysis and LSTM networks," in *2018 Chinese Control and Decision Conference (CCDC)* (Shenyang: IEEE), 5600–5605. doi: 10.1109/CCDC.2018.8408108

Zhou, S.-M., Gan, J. Q., and Sepulveda, F. (2008). Classifying mental tasks based on features of higher-order statistics from EEG signals in brain–computer interface. *Inf. Sci*. 178, 1629–1640. doi: 10.1016/j.ins.2007.11.012

Zich, C., Debener, S., Kranczioch, C., Bleichner, M. G., Gutberlet, I., and De Vos, M. (2015). Real-time EEG feedback during simultaneous EEG-fMRI identifies the cortical signature of motor imagery. *Neuroimage* 114, 438–447. doi: 10.1016/j.neuroimage.2015.04.020

Conflict of Interest: The authors declare that the research was conducted in the absence of any commercial or financial relationships that could be construed as a potential conflict of interest.

frontiers in Neuroscience

ORIGINAL RESEARCH
published: 25 January 2021
doi: 10.3389/fnins.2021.638638

Closed-Loop Phase-Dependent Vibration Stimulation Improves Motor Imagery-Based Brain-Computer Interface Performance

Wenbin Zhang[1], Aiguo Song[1], Hong Zeng[1], Baoguo Xu[1] and Minmin Miao[2]*

[1] The State Key Laboratory of Bioelectronics, School of Instrument Science and Engineering, Southeast University, Nanjing, China, [2] School of Information Engineering, Huzhou University, Huzhou, China

The motor imagery (MI) paradigm has been wildly used in brain-computer interface (BCI), but the difficulties in performing imagery tasks limit its application. Mechanical vibration stimulus has been increasingly used to enhance the MI performance, but its improvement consistence is still under debate. To develop more effective vibration stimulus methods for consistently enhancing MI, this study proposes an EEG phase-dependent closed-loop mechanical vibration stimulation method. The subject's index finger of the non-dominant hand was given 4 different vibration stimulation conditions (i.e., continuous open-loop vibration stimulus, two different phase-dependent closed-loop vibration stimuli and no stimulus) when performing two tasks of imagining movement and rest of the index finger from his/her dominant hand. We compared MI performance and brain oscillatory patterns under different conditions to verify the effectiveness of this method. The subjects performed 80 trials of each type in a random order, and the average phase-lock value of closed-loop stimulus conditions was 0.71. It was found that the closed-loop vibration stimulus applied in the falling phase helped the subjects to produce stronger event-related desynchronization (ERD) and sustain longer. Moreover, the classification accuracy was improved by about 9% compared with MI without any vibration stimulation (p = 0.012, paired t-test). This method helps to modulate the mu rhythm and make subjects more concentrated on the imagery and without negative enhancement during rest tasks, ultimately improves MI-based BCI performance. Participants reported that the tactile fatigue under closed-loop stimulation conditions was significantly less than continuous stimulation. This novel method is an improvement to the traditional vibration stimulation enhancement research and helps to make stimulation more precise and efficient.

Keywords: brain-computer interface, closed-loop system, phase-dependent, motor imagery, vibration stimulation

OPEN ACCESS

Edited by:
Yizhang Jiang,
Jiangnan University, China

Reviewed by:
Yuanpeng Zhang,
Nantong University, China
Wenlong Hang,
Nanjing Tech University, China

****Correspondence:***
Aiguo Song
a.g.song@seu.edu.cn

Specialty section:
This article was submitted to Neuroprosthetics, a section of the journal Frontiers in Neuroscience

Received: *07 December 2020*
Accepted: *06 January 2021*
Published: *25 January 2021*

Citation:
Zhang W, Song A, Zeng H, Xu B and Miao M (2021) Closed-Loop Phase-Dependent Vibration Stimulation Improves Motor Imagery-Based Brain-Computer Interface Performance. Front. Neurosci. 15:638638. doi: 10.3389/fnins.2021.638638

INTRODUCTION

Brain-computer interface (BCI) systems provide users with a non-muscular channel to send messages or instructions to external devices using brain activities (Wolpaw et al., 2002). Moreover, BCI based on electroencephalography (EEG) signal has attracted wide attention due to its non-invasiveness, convenience, and high time resolution. The widely used EEG-based BCI paradigms

include event-related P300 potentials, steady-state visually evoked potentials (SSVEPs), motor imagery (MI), etc. (Sharma et al., 2006; Polich, 2007; Vialatte et al., 2010; Zhang et al., 2017, 2019; Jiang et al., 2019, 2020). Among these paradigms, MI is an active BCI that allows users to adjust their alpha/beta rhythm to generate features by imagining limb movements (Pfurtscheller and Neuper, 2001). Extensive research has proved that the neurophysiological basis of motor imagery is that when subjects imagine the left- or right-hand movement, they will generate event-related desynchronization (ERD) in the specific frequency bands (commonly mu and beta) of the contralateral sensorimotor areas and event-related synchronization (ERS) on the ipsilateral side (Pfurtscheller and Lopes da Silva, 1999; Pfurtscheller et al., 2006; Tecchio et al., 2006).

However, researchers indicate that there are about 15–30% of the subjects who cannot reach proficiency in using BCI, which is called "BCI-illiteracy" (Guger et al., 2003; Minkyu et al., 2013). And the MI-based BCI has some other problems, such as the imbalance between the dominant and non-dominant hands (Maruff et al., 1999), inconsistent individual performance (Ahn and Jun, 2015), etc. Therefore, more and more researchers are devoted to improving MI-based BCI performance. The main research directions include improving MI decoding accuracy through optimizing feature extraction and classification algorithms (Lotte et al., 2018; Chen et al., 2020; Hang et al., 2020); proposing new hybrid BCI by introducing additional neural signals (such as EMG (electromyogram) (Vaughan et al., 1998; Leeb et al., 2011), fNIRS (functional near-infrared spectroscopy) (Wang et al., 2019), and gaze (Punsawad et al., 2010; Zeng et al., 2017), multiple brain modes (such as P300 and SSVEP) or multiple sensory stimuli (visual, auditory, tactile, etc.) (Pfurtscheller et al., 2010).

Among them, the study of combining sensory input with MI has achieved many exciting results, Allison et al. designed a hybrid BCI that combines the SSVEP and ERD features, which improves the decoding rate by about 6% compared to the traditional MI-based BCI (Allison et al., 2010). Cincotti et al. (2007) compared the effects of visual and vibrotactile feedback on subjects. Compared with visual feedback, the advantage of tactile feedback for MI is that it does not occupy the visual channel and retains the advantage of the MI paradigm. Meanwhile, it allows subjects to adjust their brain activities by themselves, especially for users with impaired or missing vision. Muller et al. demonstrated the feasibility of the tactile-based BCI paradigm and achieved 70% accuracy by selectively sensation of the vibration stimulation applied to the left and right index fingers (Muller-Putz et al., 2006). The fusion of tactile stimuli and MI has been proved in previous studies to improve MI-based BCI performance, specifically in reducing imagination time, increasing decoding accuracy, etc. (Chatterjee et al., 2007; Yao et al., 2014, 2015; Yi et al., 2017). Furthermore, physiological studies have found that tactile stimuli applied to the hand on the imaginary side can enhance the activation of the contralateral cortex (Nobuaki et al., 2011; Mizuguchi et al., 2012). Shu et al. (2017) found that applying unilateral tactile stimulation to non-dominant/paralyzed hands could increase MI-induced ERD lateralization potential.

Nevertheless, most researches on hybrid BCI that combine tactile and MI uses continuous, open-loop stimulation, often applied at a fixed time with a pre-set frequency and intensity (Pfurtscheller et al., 2010; Yi et al., 2017). It cannot be adjusted according to the real-time state of the subjects. In contrast, the closed-loop system can apply stimulation with the changes in the subject's status. In such a system, the phase has essential effects on the real-time state of the brain. Many studies have shown that stimulation for the brain will produce different effects according to the applied phase. For example, the application of transcranial magnetic stimulation (TMS) pulses at the peak or trough of the mu rhythm of the motor cortex have opposite plastic effects (Zrenner et al., 2017). Fehér et al. (2017) demonstrated a phase-dependent modulatory mechanism of tACS at a cortical network level. Similarly, Holt et al., 2019 used intracranial electrical stimulation based on the β-rhythm of EEG in patients with Parkinson's disease to adjust the amplitude of β-oscillation (Holt et al., 2019). The frequency and phase-specific effects of transcranial alternating current stimulation have also been shown in many experiments involving motor activity (Guerra et al., 2016; Nakazono et al., 2016), cognitive (Polanía et al., 2012), and auditory systems (Riecke et al., 2015; Polanía et al., 2018).

Among the phase-dependent researches, the alpha oscillations is particularly concerned. Lindsley first proposed that the brain state might be reflected by the phase of alpha oscillations in a phasic form (Lindsley, 1952). A phase-dependent stimulation system may potentially make a stronger effect of the stimulation on the subject or make the direction of the effect more precise, but it still lacks relevant research. Ai and Ro's (2014) research proves that 8–12 Hz neural oscillations in the somatosensory areas can affect tactile perception, and that pulsed inhibition by these oscillations shapes the state of brain activity necessary for conscious perception. Therefore, whether the close-loop vibration stimulation based on the alpha phase will affect the performance of MI-based BCI or not is worth studying.

In order to investigate the effect of vibration stimuli applied on a specific phase interval on MI BCI, we proposed a phase-based closed-loop vibration stimulation method and designed a comparative experiment to compare the difference between this method and the traditional continuous open-loop vibration stimulation methods independent of EEG phase on motor imagery. These experiments include pure motor imagery without stimulation (PMI), open-loop continuous vibration stimulation (CVS), vibration stimulation in the rising phase (RPS), and vibration stimulation in the falling phase (FPS). The oscillation modes and time-frequency characteristics of EEG under different stimulation conditions were compared, and feature extraction was performed using the FBCSP algorithm to verify whether this method based on closed-loop vibration stimulation can improve the performance of the MI-based BCI.

MATERIALS AND METHODS

Subjects

Ten healthy right-handed subjects (8 males, 2 females, aged range 21–28 years) participated in the experiment. The hand

dominance of subjects was determined by the Edinburgh Handedness Inventory. None of the subjects have prior experience with BCIs. Before the experiment, they were informed about the experimental procedure and signed the informed consent before participating in the experiment. They were not informed of the purpose of applying vibration stimulation to avoid the subject's psychological state bias when performing the imagination task. The study was approved by the Ethics Committee of Southeast University. All subjects received experimental compensation.

Tactile Stimulation

A total of three stimulation methods were designed: continuous vibration stimulation, vibration stimulation applied to the rising phase or the falling phase. Vibration stimulation provided by C2 voice coil tactor from Engineering Acoustics, Inc. (Winter Park, FL), applied to the fingertip of the non-dominant hand of the subject. The tactor was placed in a customized rubber soft base to reduce the noise generated by the desktop's resonance when stimulating. The Pacinian corpuscles and Meissner corpuscles in the mechanical receptor of human fingertips are sensitive to frequencies above 100 and 20–50 Hz, respectively (Breitwieser et al., 2012). To drive the tactor, the PC soundcard produced a 23 Hz sine wave modulated with a 200 Hz sine carrier wave and amplified with an audio amplifier. The vibration intensity was controlled by changing the volume until the subject feel the vibration obviously without affecting the imagination.

The phase-dependent vibration stimulation is applied to the rising ($[-\pi/6, \pi/3]$) or falling ($[5 \times \pi/6, 4 \times \pi/3]$) phase of the alpha oscillations in the C4 channel. Each trigger vibrates at 200 Hz frequency for 20 ms. This study used MATLAB to collect data and calculate the current phase once every 40 ms. Whether to trigger the stimulus or not is determined by the predicted current phase. The interval between each stimulation is more than 100 ms. Using the "tic-tic-toc" pattern (Severens et al., 2010) (the amplitude of the third vibration after every two beats is increased by 50%) to help the subjects maintain their attention to the vibration.

Experimental Procedure

In this study, subjects executed the tasks of motor imagery under different stimulus conditions, as shown in **Figure 2**. The experiment was divided into 4 sessions, namely, motor imagery without stimulus (PMI), motor imagery with continuous vibration stimulus (CVS), and motor imagery with phase-dependent vibration stimulus in rising (RPS) or falling intervals (FPS). Each session contains two runs, each run contains 40 trials, in which the non-dominant hand finger-tapping task and the relaxation task were executed in random order of 20 each. Each run lasted about 7 min, the subjects had about 10 min break between every two runs. Before the start of the formal experiment, the subjects were required to complete one run of the motor execution task and one run of the MI task for training, to help the subjects familiarize themselves with the experimental procedure and adequately understand the motor imagery task. In order to avoid learning effects, each subject completed four sessions in random order and completed all experiments on the same day.

During the experiment, all subjects were sitting in a comfortable chair about 1 meter away from the monitor. Put the non-dominant hand wrist on the platform and put the index finger on the tactor, both hands were relaxed as shown in **Figure 1**. To avoid placebo effects, the subjects were asked to place their fingers on the tactor through all sessions. **Figure 2** illustrates the experimental paradigm of four different sessions (PMI/CVS/RPS/FPS). The time structure of all sessions is the same as the MI task, but the applied vibration stimuli were different. At the beginning of each trial, there was a white cross displayed in the center of the screen, the subjects can relax, and a white circle appears in the middle of the cross at the 4th second, prompting the subjects to pay attention to the imagination task that was about to start for 1 s. At the 5th second, the subjects perform the motion imagery task according to the arrow or cross displayed on the screen. If the arrow pointing to the left appeared, the subject performs the imagination of the non-dominant hand index finger tapping. If the white cross appeared, the subject performs the rest task, which continued for 4 s. Then the screen was black, the subjects can relax until the white cross appears at the 11th second to prompt the start of the next trial. To minimize artifacts, subjects were asked to avoid physical movements and blinking during the task. The time structure of all sessions was the same, only the tactile stimulus applied during the 5–9 s is different.

EEG Recording and Phase-Tracking Approach

A SynAmps2 amplifier (Neuroscan Compumedics, United States) and a 64-channel active electrode cap (BrainAmp, ActiCap, BrainProducts, Munich, Germany) were used to acquire the EEG signal. We recorded 27 channels (Fp1, Fp2, F1, Fz, F2, FC1-6, FCz, C1-6, Cz, CP1-6, CPz, P1, P2, Pz) based on International 10/20 system (see **Figure 2**). The reference electrode was placed on the left mastoid and the electrode located on the forehead served as the ground. All the impedance of electrodes was kept below 10 kΩ during the recordings. An analog bandwidth filter with 0.1–100 Hz and a notch filter with 50 Hz were applied to the EEG signals. The EEG sampling rate was set to 1,000 Hz.

In order to deliver tactile stimulation output at a specified phase interval of a given frequency, we have adopted a previously proposed method based on Fast Fourier Transform (FFT) to track the phase of the EEG signal in real-time (Farrokh et al., 2017). The EEG signals were transmitted from the amplifier to MATLAB (MathWorks, United States) in real-time through the TCP / IP protocol for real-time phase tracking. Starting from the 5th second of each trial, extract the latest 300 ms data of the C4 channel every 40 ms and perform the following steps to predict the phase of the current time point: First, a 10th order elliptical infinite impulse response (IIR) filter is used to perform 8–12 Hz bandpass filtering the data; second, the FFT of this data segment is calculated; third, calculate the frequency and phase of the dominant

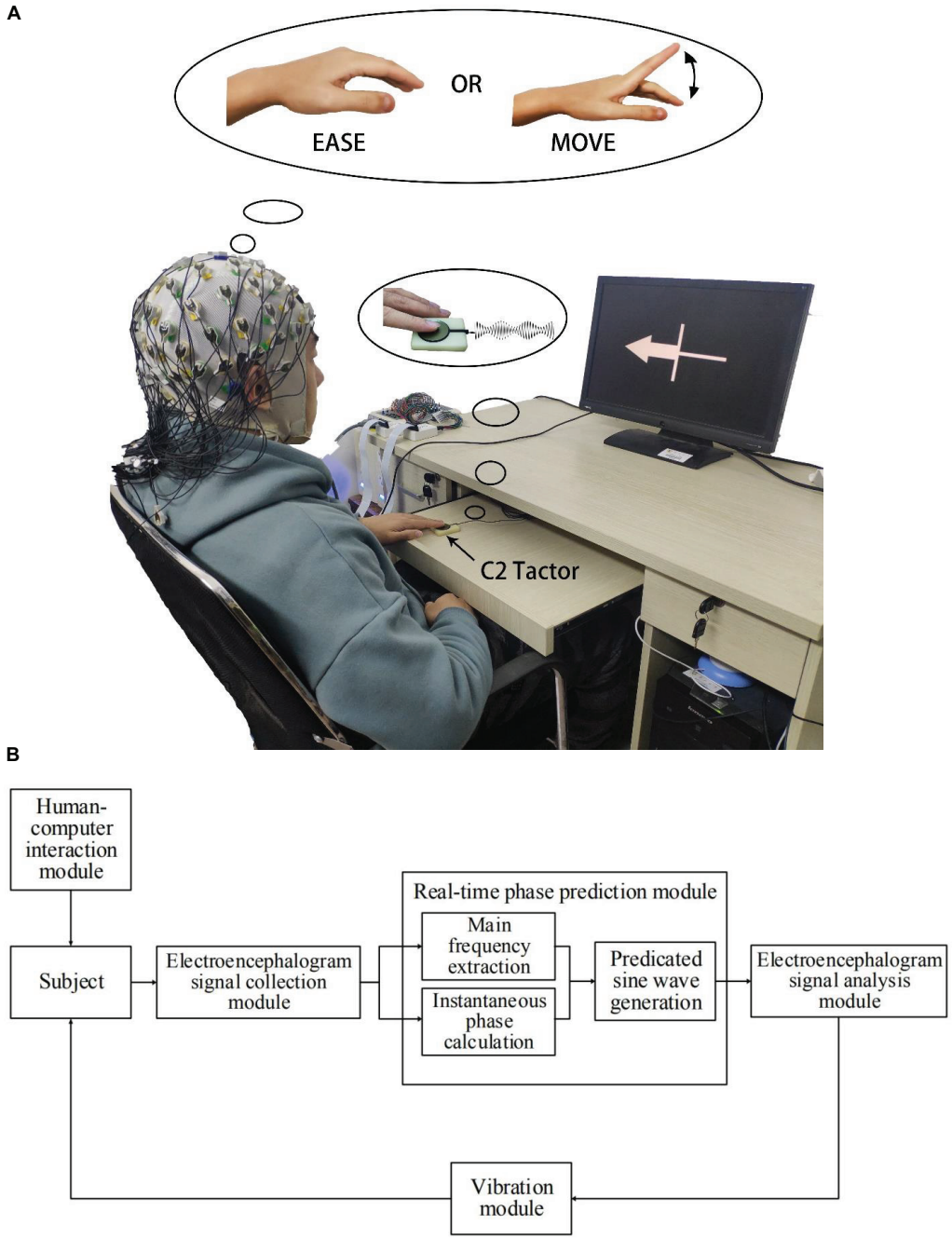

FIGURE 1 | (A) Experimental setup: The subjects were seated in a comfortable chair. Their non-dominant hand's index finger was placed on the C2 tactor, and they performed imagination tasks according to the instructions displayed on the screen. The tactor provides corresponding vibration stimulation according to the experimental settings. **(B)** Flowchart of the closed-loop stimulation system.

component of the signal from the FFT; finally, using a simple sine function to forecast the signal by using the calculated phase and frequency.

Algorithms and Analysis Methods

In this study, the data were analyzed off-line using customized MATLAB programs and the MATLAB-based EEGLAB toolbox (Delorme and Makeig, 2004). To remove the artifacts caused by eye movements, the automatic artifact removal (AAR) toolbox with the SOBI algorithm was used (Gómez-Herrero, 2007). Afterward, common average reference (CAR) was adopted to re-reference the data. Event-related spectral perturbation (ERSP) was used to evaluate the mean spectral power changes in time-frequency and spatial

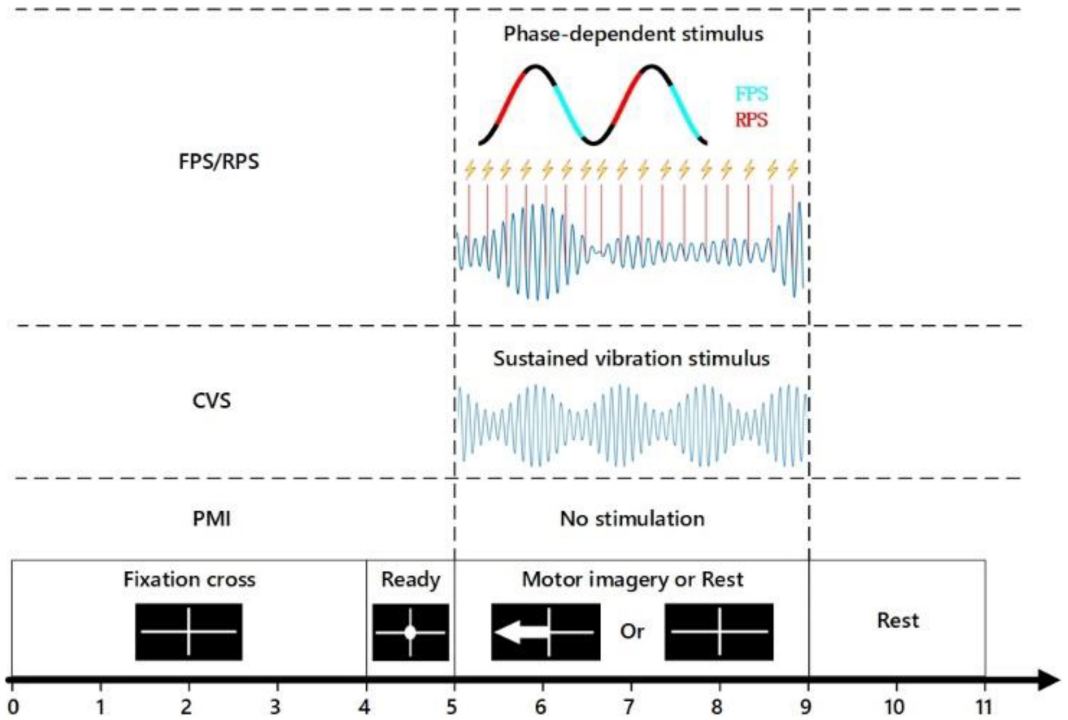

FIGURE 2 | Experimental procedure of the four different sessions, all sessions use the same time structure. The only difference is the way the mechanical vibration stimulus applied to the subject's fingertip within 5–9 s: under FPS/RPS conditions, a 20 ms vibration stimulus was applied each time according to the phase of EEG alpha wave. Under FPS/RPS conditions, the constant 23 Hz vibration stimulus with 200 Hz as the carrier frequency was applied to the fingertip of the subjects. No stimulation was applied under PMI conditions.

domains. In this work, the ERSP of n trials was calculated by Eq. (1):

$$ERSP(f,t) = \frac{1}{n}\sum_{k=1}^{n}(F_k(f,t)^2) \quad (1)$$

Where $F_k(f,t)$ indicates the spectral estimation of kth trial at frequency f and time t, n is the number of trials. We use EEGLAB to compute the ERSP (dB), the short-time Fourier transform (STFT) was applied with a Hanning-tapered window which was length 200 ms. To normalize the baseline, each spectral estimation subtracted the mean power changes in [3 4] s (the 1 s epoch before attention cue appear). The key electrodes C3 and C4 were selected to display the time courses from 0 to 9 s between 1 and 30 Hz. The ERD/ERS values were calculated in alpha (8–13 Hz) and beta (14–30 Hz) respectively.

To compare the MI-BCI classification performance under different feedback conditions, all 27 channels data were utilized for pattern classification, and the data of 0.5–4 s after imagine task onset were extracted for feature extraction and pattern classification. The specific effect of tactile stimulation is not clear, and we cannot make the *priori* choice of the relevant frequency band(s), so the Filter Bank Common Spatial Pattern (FBCSP) algorithm (Ang et al., 2008; Keng et al., 2012) was utilized to extract the features from the narrowband EEG signals for classification. FBCSP divides each epoch of EEG data into sub-bands with different frequency bands and then implement the CSP algorithm on the filtered signals at each sub-band to calculate the corresponding features. In this study, the sub-bands are chosen from the range 8–32 Hz with bandwidth of 4 Hz (8–12, 12–16, 16–20, 20–24, 24–28, 28–32 Hz). After that, we use Fisher's linear discriminative analysis (LDA) for the 2-class classification.

For statistical analysis, a 10 × 10-fold cross-validation strategy was utilized to evaluate the classification performance. Every group includes two runs, 80 trials and corresponding categories were randomly divided into 10 sets, each consist of 8 trials. Among the 10 sets, each 9 parts (72 trials) were for training the LDA classifier and the remaining one part (8 trials) was for testing. Repeating 10 times to get 100 results, and finally get the average classification accuracy. To evaluate the performance of the phase-tracking algorithm, we calculated the Hilbert transformation offline and compared the phase using the Phase Locking Value (PLV).

RESULTS

The main purpose of this study is to investigate whether phase-based closed-loop vibration tactile stimulation can improve the performance of the MI paradigm BCI. The MI-BCI applied with closed-loop vibration stimulation based on the rising or falling phase of the EEG signal in real-time was compared with the MI-BCI without stimulation or with open-loop stimulation,

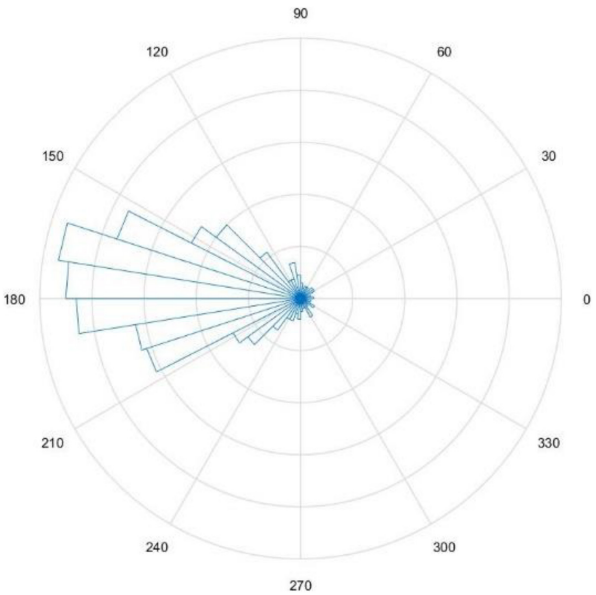

FIGURE 3 | Rose plot under FPS conditions, shows the actual phase of the vibration stimulus.

respectively. The offline analysis evaluated the phase-tracking algorithm based on FFT was used to obtain PLV = 0.71, and the trials with more errors in the applied stimulation position were removed. **Figure 3** shows a rose plot of the stimulus phase of one subject's FPS run.

Event-Related Spectral Perturbation (ERSP)

Figure 4 shows the ERSP distributions across time-frequency (A) and spatial domains (B) from one representative subject (S2). The C3 and C4 channels were selected to cover the left and right sensorimotor cortices in time-frequency analysis. No obvious desynchronization was observed for the imagery tasks in the alpha and beta bands of the PMI task. In contrast, CVS, RPS, and FPS all enhance the activation of the sensorimotor cortex to varying degrees. However, the frequency band of continuous stimulus activation is narrow, mainly concentrated in the alpha band, and the level of activation is not as deep as the closed-loop stimulus. And FPS shows some time accumulation effects, the activation is broader and stronger as the imagine time progresses. Regarding closed-loop stimulation, it can be observed that the FPS task has a better effect on cortical activation than RPS, especially in the C4 channel. But for the rest task, it showed no obvious cortical activation in C3 and C4, and even more obvious ERS phenomenon was observed on both sides of the FPS task. CVS and RPS tasks can observe some discrete activations in the alpha band, but the range and intensity are smaller than imagery. Moreover, through the topographic maps, it is clearly shown that, compared with the weak ERD of the PMI task, the three tasks that introduce vibration stimulation significantly enhance the activation of the contralateral and ipsilateral sensorimotor cortex. The enhancement of the closed-loop stimulation's activation range and intensity are more obvious than those of the CVS task. As observed, CVS did not produce strong enough activation on the contralateral side, while FPS produced the strongest activation on both C3 and C4 channels. Meanwhile, no matter whether vibration stimulation was applied or not, no obvious cortical activation was observed during the rest. Only PMI and FPS tasks observed slight ERS on the ipsilateral sensorimotor cortex. It can be seen that tactile stimulation does not directly activate the sensorimotor cortex, but rather promotes and enhances the cortical activation induced by motor imagery.

The averaged topographical distributions of ERD topographic maps across all subjects are shown in **Figure 5**. The first row shows the activation patterns of motor imagery under four different conditions, and the second row is the rest. There are three frequency ranges under each condition (8–12, 13–30, and 8–30 Hz correspond to the alpha, beta, and alpha-beta rhythms, respectively), which makes the effects of different tactile stimuli on MI-based BCI at different frequencies more intuitively. During the left-hand motor imagery, the contralateral sensorimotor cortex shows a certain degree of activation in all conditions. All three kinds of vibration stimulation significantly enhanced the desynchronization of this area. Clear cortical desynchronization can be observed at both alpha and beta rhythm. Simultaneously, the ipsilateral sensorimotor cortex activation is also enhanced to a certain extent, especially in the beta band. Importantly, a significant desynchronization of the bilateral sensorimotor cortex is observed in the alpha band of the CVS task in the rest class, which is significantly stronger than the activation during motor imagery. This may indicate that some subjects were directly activated by continuous vibration stimulation, or involuntarily imagine the movement of their limbs during the stimulation. Besides, some activation of the contralateral sensorimotor cortex can be seen in the alpha band under the FPS and RPS tasks, but the intensity is much lower than that of CVS and the activation of motor imagery under the same conditions.

Classification Performance

Off-line classification accuracies across all the subjects with their mean accuracies are shown in **Figure 6**, and the best averaged classification accuracy of cross-validation is chosen as the performance. It is observed that the classification performance in FPS tasks is significantly better than that of PMI tasks ($p = 0.012$, paired t-test), but there is no significant difference in performance between PMI and CVS tasks, nor between FPS and RPS tasks. Compared with PMI tasks, the average performance of FPS tasks increased by about 9%, and compared with CVS and RPS tasks, it increased by about 4%. In FPS tasks, the number of BIC-illiterate subjects (accuracy < 70%) decreased from 6 to 3 out of 10 subjects. Nevertheless, under other task conditions, the number has not decreased significantly. In terms of average classification performance, tactile vibration stimulation generally enhances MI-based BCI, but individual performance is different. Among them, the performance of two subjects on the PMI task

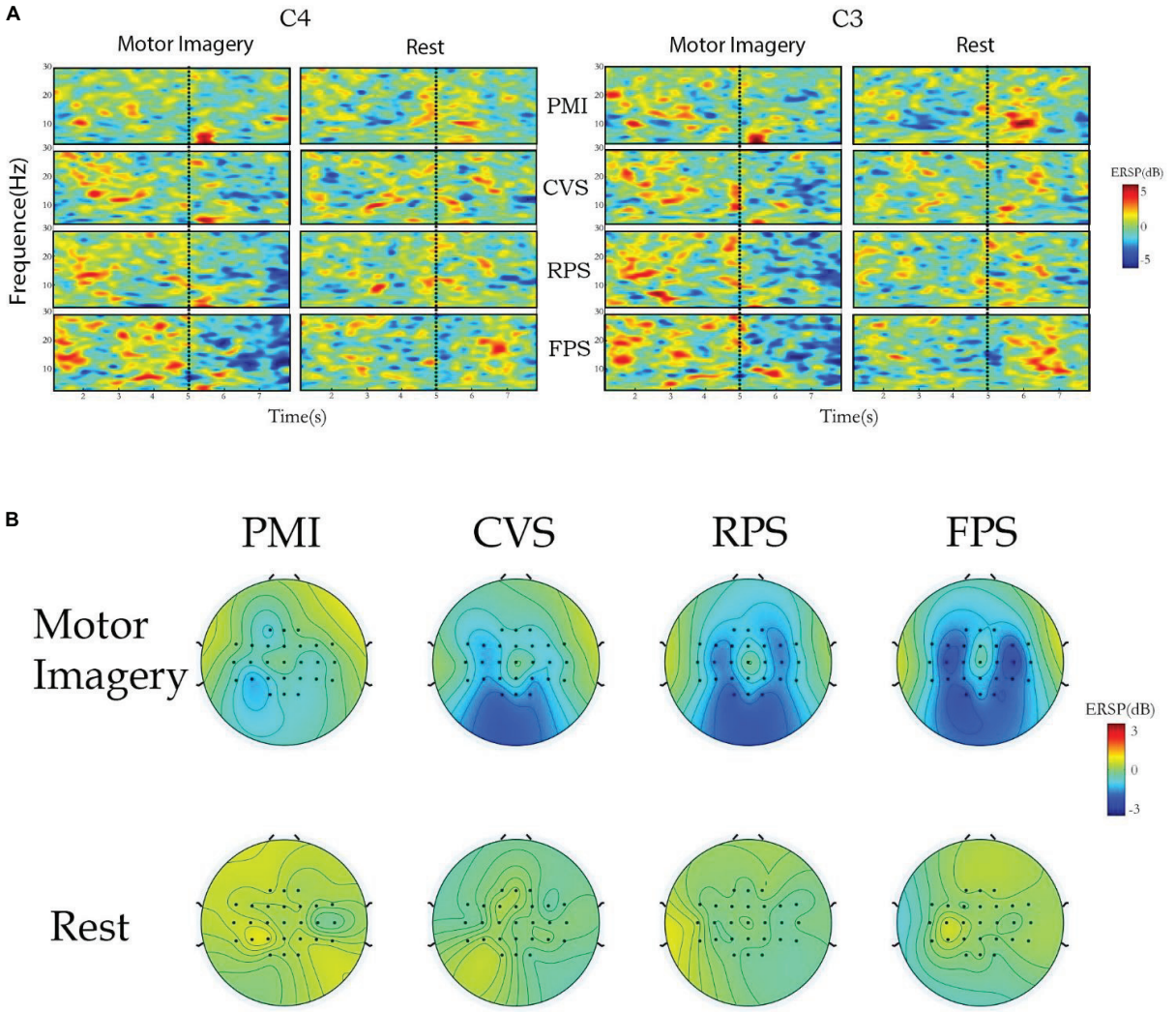

FIGURE 4 | The cortical activations in time-frequency **(A)** and spatial **(B)** domains for subject S2.

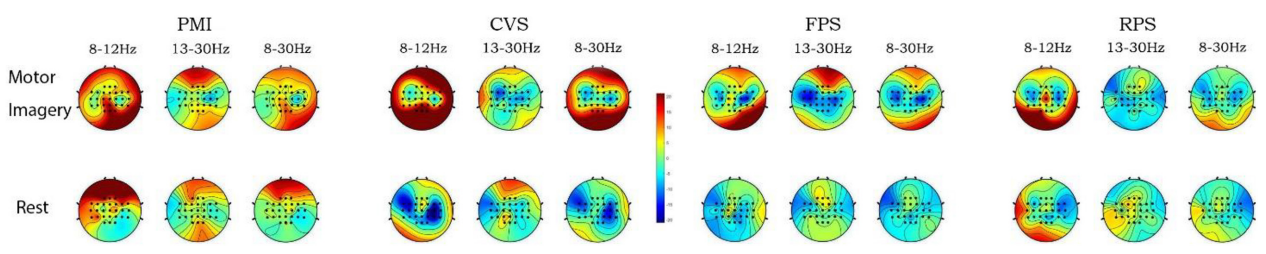

FIGURE 5 | Grand-averaged distributions of ERD patterns of all subjects for each class. The EEG power was averaged from three representative frequency bands (8–12; 13–30; 8–30 Hz) over 4 after the imagery task begins.

is higher than that of the other vibration stimulation tasks, while the classification performance of three subjects in the CVS tasks is significantly higher than the closed-loop vibration stimulation tasks and PMI tasks, which will be discussed further in the discussion section.

DISCUSSION

Effects of Tactile Stimulation on MI-BCI

In this study, we explored the impact of vibration stimulation on MI-BCI. Tactile feedback has been increasingly used in

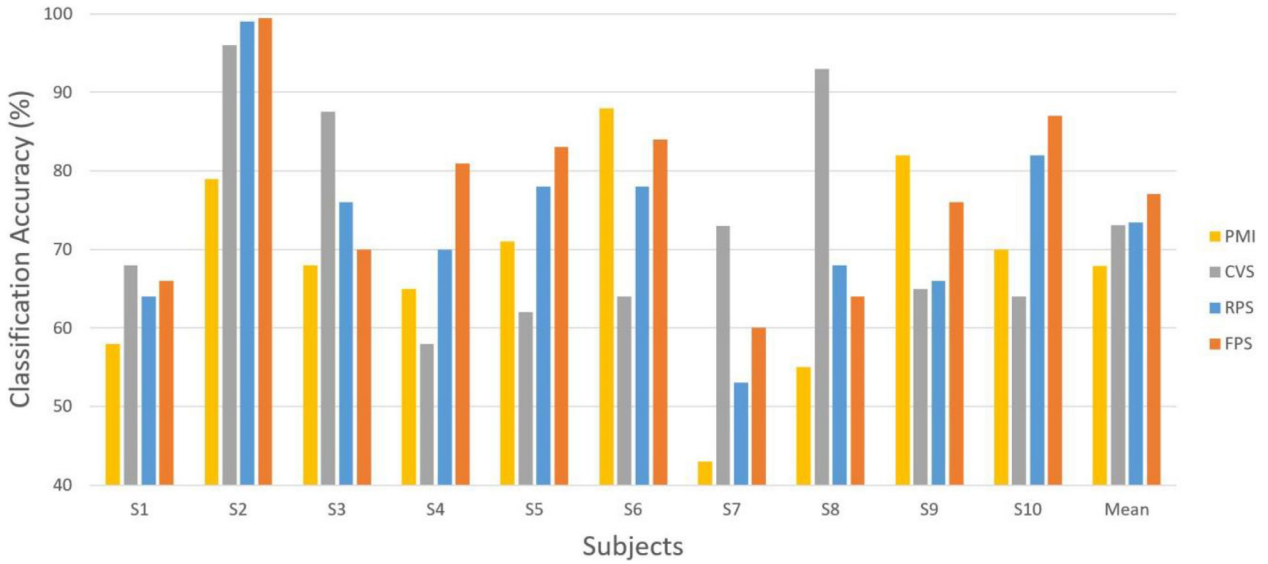

FIGURE 6 | Classification accuracies and mean accuracies in four conditions over 10 subjects.

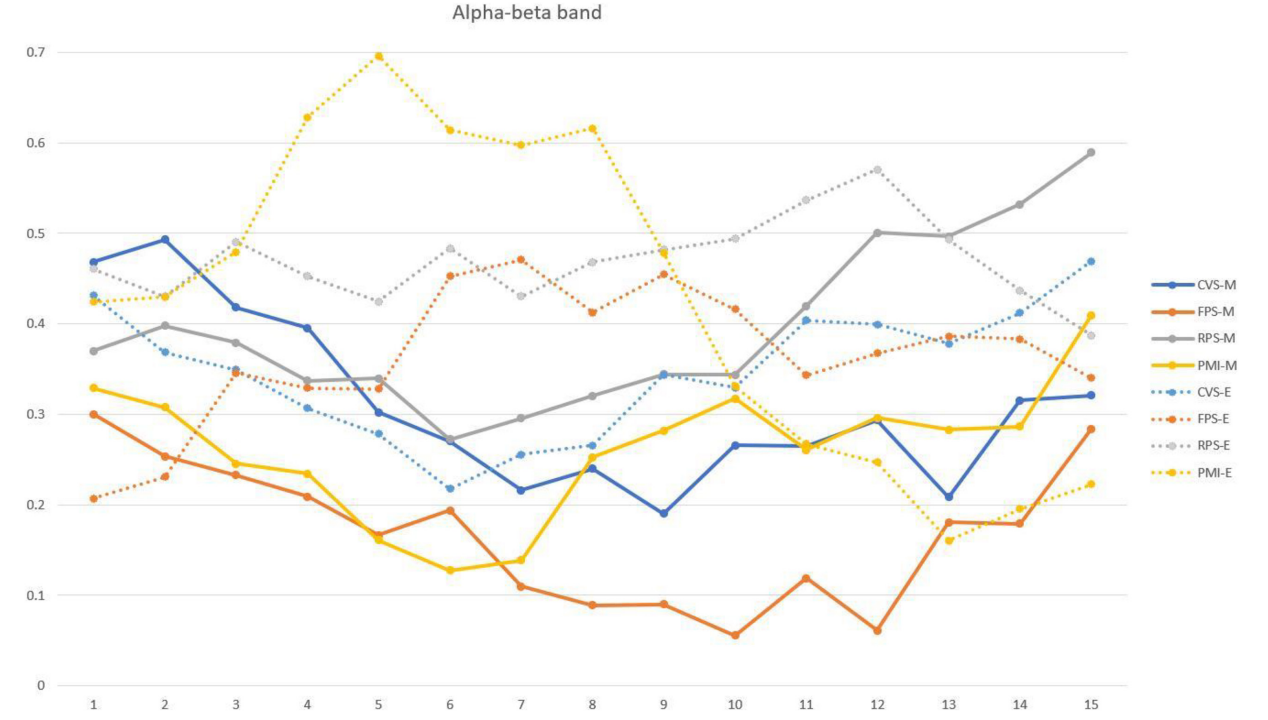

FIGURE 7 | The average energy fluctuation graph of all subjects in the alpha-beta frequency band (8–30 Hz) within 4 s after the start of the imagery task. A window with a length of 1 s is calculated every 200 ms. The solid lines correspond to imagery tasks under different conditions, and the dashed lines correspond to rest tasks.

BCI research due to its good human-computer interaction and the characteristics of reducing dependence on visual channels. There is mainly mechanical vibration stimulation, kinesthetic stimulation, electrical stimulation, and so on in terms of stimulation types. Among them, somatokinetic stimulation is more natural than other methods, which is in line with people's understanding and expectations of actual actions. However, it often requires the assistance of larger devices or is placed in a specific environment. Electrical stimulation is more powerful than vibration stimulation and can transmit the stimulation to nerves more effectively, but many subjects have fear and resistance to it. In contrast, the vibration stimulation selected

in this study has the advantages of easy wearing, low cost, and high acceptance by subjects, and is more suitable for MI-based BCI. Many studies have demonstrated that the introduction of vibrotactile stimulation can increase the excitability of the motion-related cortex (Mizuguchi et al., 2013), and have proved that the vibration stimulation can enhance the performance of the motor imagination paradigm, but further research is needed on the details of the application method.

First of all, the stimulus application method: Some studies use short-term vibration stimuli to prompt the beginning and ending of the imagery task or to inform the users of the classification results (Chatterjee et al., 2007; McCreadie et al., 2014; Jeunet et al., 2015). This kind of stimulus feedback method is often used to replace visual feedback and has little effect on classification performance. Therefore, many recent studies have focused on applying continuous tactile stimulation during imagination, and the effect of enhancing the performance of pure MI-BCI is different. Yao et al. (2013) designed a hybrid BCI that combines motor imagery and selective sensation using vibration stimuli applied by both hands simultaneously based on selective perception. Compared with the PMI task, the performance of hybrid BCI was not significantly improved. However, most of the subjects whose classification accuracy had not improved were subjects who had performed well in PMI. The subjects whose MI classification accuracy was below 60% had a visible improvement after the introduction of vibration stimulation. Similarly, Ahn et al. (2014) also studied a tactile hybrid BCI based on selective sensation. It also showed no enhancement of MI performance under bilateral vibration stimulation conditions, but the classification accuracy of MI that was executed after 3 seconds of selective sensation to vibration stimulation was about 10% higher than that of pure MI. Combined with the fact that in this study, under CVS conditions, the classification accuracy of some subjects was significantly decreased, which may be due to the difficulty of the subjects to focus on the two tasks of selective sensation and motor imagery at the same time. In this case, the vibration stimulation interfered with the participants' imagination of the action. However, under the same conditions of continuous stimulation of the hands, Yi et al. (2017) used continuous electrical stimulation and combined selective sensation with MI, but improved the overall performance of an MI-based BCI, achieving 14% improvement in total relative to the MI task alone. The reason is that continuous electrical stimulation induces additional steady-state somatosensory evoked potentials (SSSEP). The SSSEP does not directly enhance ERD, but motor imagery will affect SSSEP, resulting in more selective sensation results and making the hybrid BCI perform better. It can be seen that the effects of applying continuous vibration stimulation while performing MI may be both pros and cons. On the one hand, it has been shown that tactile stimulation can directly induce alpha/beta ERD (Gaetz and Cheyne, 2006). And the spatial attention to tactile stimulation can further regulate the activation of the cortex (Bauer et al., 2006; Dockstader et al., 2010). High-intensity tactile stimulation combined with selective sensation to induce SSSEP can further generate more features to improve classification performance. However, it is worth noting that most of the pure selective sensation paradigms using vibration stimulation only achieve a decoding rate of about 60% (Yao et al., 2013; Ahn et al., 2014; Shu et al., 2018), which shows that the ERD and other features produced by MI still play an important role in hybrid BCI. On the other hand, vibration stimulation may not induce SSSEP due to insufficient intensity or different individual adaptation frequencies. At the same time, it may distract the subjects and interfere with the subjects' imagery tasks.

Compared with stimulating both hands at the same time and then combined with selective sensation, it seems more effective to apply tactile stimuli to the imaginary ipsilateral hand (Chatterjee et al., 2007). Shu et al. (2017) applied constant tactile stimulation to the non-dominant hand improved the imbalance of MI ability between the dominant hand and the non-dominant hand, and improved the classification accuracy of MI-BCI by about 11%. This study also applied vibration stimuli to the non-dominant hand, but unlike other studies, it distinguished between imagining non-dominant hand movement and rest. Physiological studies have proved that applying tactile stimuli on the side of imagery can enhance the activation of the contralateral cortex, but no obvious cortical changes are observed on the contralateral hand. Vibration stimulation has a higher intensity than somatosensory stimulation, such as holding a ball. In addition to providing subjects with a more vivid imagination environment and increasing the excitability of the motor cortex (de Moraes Silva et al., 2015), vibration stimulation itself will also activate the sensory cortex (Gaetz and Cheyne, 2006; Tu-Chan et al., 2017). Therefore, applying a fixed vibration stimulus to one hand will definitely affect the EEG mode of the rest state and affect the classification effect.

Enhancement of Closed-Loop Vibration Stimulation on MI

In this work, our research focuses on the impact of closed-loop vibration stimulation on MI-BCI. Compared with open-loop vibration stimulation, closed-loop stimulation shows better performance in classification accuracy and the magnitude of ERD. The physiological basis for phase-based closed-loop vibration stimulation to be effective for MI is that neural oscillations in the range of 8–12 Hz can affect tactile perception (Ai and Ro, 2014), and pulses of the sensorimotor cortex alpha rhythm can promote corticospinal excitability. Previous studies on non-invasive precise phase stimulation generally used electrical stimulation, TMS, and other stimulation methods. However, sensory stimuli such as vision and hearing are increasingly used in real-time stimulation, and the effect is pronounced (Dijk et al., 2008; Romei et al., 2010). This study used the algorithm proposed by Farrokh et al. (2017) to estimate the real-time phase of the EEG of the contralateral sensorimotor cortex (C4 channel) and distinguished the rising and falling intervals to apply vibration stimulation. Studies have shown that the perception of vibration stimuli at the alpha peak is inhibited in terms of the impact on stimulus perception, while the valley is more sensitive (Ai and Ro, 2014). Schaworonkow et al. (2018) found that the MEP amplitude is modulated by the mu phase in a wide range of stimulation intensity, and the stimulation applied to the negative peak has the best effect. The intensity of

the stimulation will also affect the regulation of the mu rhythm cortex excitability. In addition, in terms of attention, even in a continuous spatial attention state, the perception results will change with phase changes (Helfrich et al., 2018). It can be seen from **Figure 5** that the motor imagery task under FES conditions exhibits the strongest ERD mode, which means that FES conditions have the best effect on the enhancement of exercise-related cortical excitability, followed by RPS conditions. At the same time, it has been observed that imagining the non-dominant hand movement will cause the activation of the ipsilateral sensorimotor cortex, which is consistent with the results of previous studies (Porro et al., 2000). Furthermore, many studies have found that applying a stimulus before the trough helps to reduce the trough, while the stimulus applied at the rising phase cannot effectively increase the peak. Moreover, the descending phase interval stimulus has a cumulative effect, and continuous multiple stimuli can further reduce the amplitude (Holt et al., 2019). That may contribute to the continuation and enhancement of ERD to a certain extent. In order to verify this, we compared the average energy changes of all subjects during the motor imagery or rest task. As shown in **Figure 7**, in the MI task, the energy of the C4 channel under FPS conditions is the lowest, and it shows a downward trend as time progresses, which may be caused by the cumulative effect of stimulation mentioned before. In contrast, the energy decrease of pure MI in the first 2 s is not much different from FPS, but it does not continue to decrease, which may be due to the participant's inability to keep focusing on their imagination. Energy reduction is also observed under CVS conditions and there is no rebound over time, but it is worth noting that the rest task under CVS conditions also shows energy decline, which is similar to the imagery task. This may be the main reason for the poor effect of CVS classification. The highest energy is observed in the rest task without stimulation, which indicates that vibration stimulation will induce the activation of the contralateral sensorimotor cortex no matter imagined or not. Among them, FPS makes the most prominent energy difference because an increase of task complexity or attention results in an increased magnitude of ERD (Boiten et al., 1992; Mashat et al., 2019).

The disadvantage of continuous open-loop vibration stimulation is that some subjects are not sensitive to mechanical vibration stimulation or only sensitive to specific vibration frequencies. In addition, the mechanical vibration stimulation of the same part for a long time will make some subjects feel tired and make the skin numb. To make the short-term vibration stimulation more easily perceivable, we applied 200 ms vibration stimulation every time and used the "tic-tic-toc" stimulation mode to enhance the participant's attention to the stimulation (Gescheider et al., 2010; Choi et al., 2015). After completing the experiment, all the subjects reported that the closed-loop stimulation method could be clearly felt compared with CVS, and the degree of fatigue is lower. Besides, the frequency of stimulation may also be one of the reasons for the enhanced MI performance. The closed-loop stimulation is applied according to the phase of the alpha rhythm, so the actual stimulation frequency is also about 10 Hz. Previous research has shown that incoming tactile stimuli at an alpha frequency can enhance task-related alpha desynchronization (Long et al., 2016). Zhang et al. (2020) experimented with enhancing MI by electrically stimulating the ulnar nerve of the contralateral wrist at the alpha frequency (10 Hz), and improved the classification accuracy of left- and right-hand MI by about 15%. But in the actual application of motor imagery, the imagination task is often initiated by people subjectively rather than pre-set. Therefore, compared with online applications, it may be more suitable for assisting the training of MI. But this proves the effectiveness of alpha frequency tactile stimulation for MI-BCI enhancement from the side.

Application Prospects and Future Works

This article tried to apply vibration stimuli in different phase intervals of real-time EEG signals, but the estimation algorithm of EEG real-time phase still has room for improvement in accuracy and computational efficiency. Physiological studies (Ai and Ro, 2014) have proved that the neural oscillation of the alpha band can affect sensory perception, so in addition to the phase information, we can try to monitor the activation of the sensory-motor cortex of the subject according to the activation state of the cerebral cortex and cortical energy. Further enhance the robustness and effectiveness of the closed-loop stimulation system and reduce vibration stimulation interference on the concentration of MI. Besides, because vibration stimulation may be particularly effective for BCI-illiteracy groups, while subjects with better MI performance are likely to have the opposite effect, the intensity or frequency of vibration stimulation should be adjusted adaptively according to the actual performance of the subjects (Bergmann et al., 2019).

In addition, some studies have shown that somatosensory stimulation can improve the motor function training effect of stroke patients (Sawaki et al., 2006; Bastos Conforto et al., 2010). The activation of the contralateral cortex during MI enhanced by vibration stimulation is also considered helpful to the neural reorganization of stroke patients, so closed-loop vibration stimulation can be further applied to assist stroke rehabilitation training. Limited by the small number of subjects, the effect of vibration stimulation applied in different intervals on cortical activation and energy changes is still unclear. In future works, more subjects should be recruited to further study the changes in cortical energy caused by vibration stimulation in different phase intervals, and to conduct long-term experiments to explore whether vibration stimulation has a long-term effective effect on MI-BCI.

CONCLUSION

In this work, a closed-loop vibration stimulation method based on real-time phase prediction is proposed to improve MI-based BCI's overall performance. The effects of continuous vibration stimulation and closed-loop vibration stimulation in two different phase intervals on the non-dominant hand imagination movement and rest classification performance are compared and analyzed. We found that the closed-loop vibration stimulation in the descending interval can deepen the contralateral ERD of MI to a greater extent than other

conditions, thereby significantly improving the classification accuracy. Subjects generally report that closed-loop stimulation methods can better assist the execution of MI and are less prone to tactile fatigue. The method proposed in this paper is an improvement to the existing BCI enhancement methods. It may be expected to benefit people with complete somatosensory systems but impaired motor functions in the future.

DATA AVAILABILITY STATEMENT

The raw data supporting the conclusions of this article will be made available by the authors, without undue reservation.

ETHICS STATEMENT

The studies involving human participants were reviewed and approved by the Ethics Committee of Southeast University. The patients/participants provided their written informed consent to participate in this study.

AUTHOR CONTRIBUTIONS

WZ, AS, and HZ designed the study. WZ set up the experiment platform. BX and WZ performed the experiment. WZ and MM analyzed the data and wrote the manuscript. AS, HZ, and BX were involved in critical revision of the manuscript. All the authors read and approved the final manuscript.

FUNDING

This paper was supported by the NSFC under grant no. 91648206 and Basic Research Project of leading Technology of Jiangsu Province under grant no. BK20192004.

REFERENCES

Ahn, M., and Jun, S. C. (2015). Performance variation in motor imagery brain–computer interface: a brief review. *J. Neurosci. Methods* 243, 103–110. doi: 10.1016/j.jneumeth.2015.01.033

Ahn, S., Ahn, M., Cho, H., and Jun, S. C. (2014). Achieving a hybrid brain–computer interface with tactile selective attention and motor imagery. *J. Neural Eng.* 11:066004. doi: 10.1088/1741-2560/11/6/066004

Ai, L., and Ro, T. (2014). The phase of prestimulus alpha oscillations affects tactile perception. *J. Neurophysiol.* 111, 1300–1307. doi: 10.1152/jn.00125.2013

Allison, B. Z., Brunner, C., Kaiser, V., Müller-Putz, G. R., Neuper, C., and Pfurtscheller, G. (2010). Toward a hybrid brain-computer interface based on imagined movement and visual attention. *J. Neural Eng.* 7:26007.

Ang, K. K., Chin, Z. Y., Zhang, H., and Guan, C. (2008). "Filter bank common spatial pattern (FBCSP) in brain-computer interface," in *Proceedings of the IEEE International Joint Conference on Neural Networks*, (Hong Kong: IEEE).

Bastos Conforto, A., Nocelo Ferreiro, K., Tomasi, C., dos Santos, R. L., Loureiro Moreira, V., Nagahashi Marie, S. K., et al. (2010). Effects of somatosensory stimulation on motor function after subacute stroke. *Neurorehabil. Neural Rep.* 24, 263–272. doi: 10.1177/15459683093 49946

Bauer, M., Oostenveld, R., Peeters, M., and Fries, P. (2006). Tactile spatial attention enhances gamma-band activity in somatosensory cortex and reduces low-frequency activity in parieto-occipital areas. *Neuroscience* 26, 490–501. doi: 10.1523/jneurosci.5228-04.2006

Bergmann, T. O., Lieb, A., Zrenner, C., and Ziemann, U. (2019). Pulsed facilitation of corticospinal excitability by the sensorimotor mu-alpha rhythm. *J. Neurosci.* 39, 10034–10043. doi: 10.1523/jneurosci.1730-19.2019

Boiten, F., Sergeant, J., and Geuze, R. (1992). Event-related desynchronization: the effects of energetic and computational demands. *Electroencephalogr. Clin. Neurophysiol.* 82, 302–309. doi: 10.1016/0013-4694(92)90110-4

Breitwieser, C., Kaiser, V., Neuper, C., and Müller-Putz, G. R. (2012). Stability and distribution of steady-state somatosensory evoked potentials elicited by vibro-tactile stimulation. *Med. Biol. Eng. Comput.* 50, 347–357. doi: 10.1007/s11517-012-0877-9

Chatterjee, A., Aggarwal, V., Ramos, A., Acharya, S., and Thakor, N. V. (2007). A brain-computer interface with vibrotactile biofeedback for haptic information. *J. Neuroeng. Rehabil.* 4:40.

Chen, Y., Hang, W., Liang, S., Liu, X., Li, G., Wang, Q., et al. (2020). A novel transfer support matrix machine for motor imagery-based brain computer interface. *Front. Neurosci.* 14:606949. doi: 10.3389/fnins.2020.606949

Choi, I., Bond, K. A., Krusienski, D. J., and Nam, C. S. (2015). "Comparison of stimulation patterns to elicit steady-state somatosensory evoked potentials (SSSEPs): implications for hybrid and SSSEP-based BCIs," in *Proceedings of the 2015 IEEE International Conference on Systems, Man, and Cybernetics (SMC)*, (Kowloon Tong: IEEE).

Cincotti, F., Kauhanen, L., Aloise, F., Palomäki, T., Capurusso, N., Jylänki, P., et al. (2007). Vibrotactile feedback for brain-computer interface operation. *Comput. Intell. Neurosci.* 2007:48937.

de Moraes Silva, J., Lima, F. P. S., de Paula Júnior, A. R., Teixeira, S., Lima, S. T., Bastos, V. H., et al. (2015). Assessing vibratory stimulation-induced cortical activity during a motor task-a randomized clinical study. *Neurosci. Lett.* 608, 64–70. doi: 10.1016/j.neulet.2015.09.032

Delorme, A., and Makeig, S. (2004). EEGLAB: an open source toolbox for analysis of single-trial EEG dynamics including independent component analysis. *Neurosci. Methods* 134, 9–21. doi: 10.1016/j.jneumeth.2003.10.009

Dijk, H. V., Schoffelen, J. M., Oostenveld, R., and Jensen, O. (2008). Prestimulus oscillatory activity in the alpha band predicts visual discrimination ability. *J. Neuroence Official J. Soc. Neurosci.* 28, 1816–1823. doi: 10.1523/jneurosci.1853-07.2008

Dockstader, C., Cheyne, D., and Tannock, R. (2010). Cortical dynamics of selective attention to somatosensory events. *Neuroimage* 49, 1777–1785. doi: 10.1016/j.neuroimage.2009.09.035

Farrokh, M., Katharine, D., Peter, G., Jonathan, D., and Zariffa, J. (2017). A fast eeg forecasting algorithm for phase-locked transcranial electrical stimulation of the human brain. *Front. Neurosci.* 11:401. doi: 10.3389/fnins.2017.00401

Fehér, K. D., Nakataki, M., and Morishima, Y. (2017). Phase-dependent modulation of signal transmission in cortical networks through tACS-induced neural oscillations. *Front. Hum. Neurosci.* 11:471. doi: 10.3389/fnhum.2017.00471

Gaetz, W., and Cheyne, D. (2006). Localization of sensorimotor cortical rhythms induced by tactile stimulation using spatially filtered MEG. *Neuroimage* 30, 899–908. doi: 10.1016/j.neuroimage.2005.10.009

Gescheider, G. A., Wright, J. H., and Verrillo, R. T. (2010). *Information-processing Channels in the Tactile Sensory System: A Psychophysical and Physiological Analysis*. Hove: Psychology Press.

Gómez-Herrero, G. (2007). *Automatic Artifact Removal (AAR) Toolbox v1.3*. Tampere: Tampere University of Technology.

Guerra, A., Pogosyan, A., Nowak, M., Tan, H., Ferreri, F., Di Lazzaro, V., et al. (2016). Phase dependency of the human primary motor cortex and cholinergic inhibition cancelation during beta tACS. *Cereb. Cortex* 26, 3977–3990. doi: 10.1093/cercor/bhw245

Guger, C., Edlinger, G., Harkam, W., Niedermayer, I., and Pfurtscheller, G. (2003). How many people are able to operate an eeg-based brain-computer interface (bci)? *IEEE Trans. Neural Syst. Rehabil. Eng.* 11, 145–147. doi: 10.1109/tnsre.2003.814481

Hang, W., Feng, W., Liang, S., Wang, Q., and Choi, K. S. (2020). Deep stacked support matrix machine based representation learning for motor imagery eeg classification. *Comp. Methods Programs Biomed.* 193:105466. doi: 10.1016/j.cmpb.2020.105466

Helfrich, R. F., Fiebelkorn, I. C., Szczepanski, S. M., Lin, J. J., Parvizi, J., Knight, R. T., et al. (2018). Neural mechanisms of sustained attention are rhythmic. *Neuron* 99, 854–865.e5.

Holt, A. B., Kormann, E., Gulberti, A., Pötter-Nerger, M., McNamara, C. G., Cagnan, H., et al. (2019). Phase-dependent suppression of beta oscillations in Parkinson's disease patients. *J. Neurosci.* 39, 1119–1134. doi: 10.1523/jneurosci.1913-18.2018

Jeunet, C., Vi, C., Spelmezan, D., N'Kaoua, B., Lotte, F., and Subramanian, S. (2015). "Continuous tactile feedback for motor-imagery based brain-computer interaction in a multitasking context," in *Paper presented at INTERACT 2015, Bamberg, Germany*, (Bamberg: Springer International Publishing).

Jiang, Y., Zhang, Y., Lin, C., Wu, D., and Lin, C. T. (2020). Eeg-based driver drowsiness estimation using an online multi-view and transfer tsk fuzzy system. *IEEE Trans. Intell. Transport. Syst.* 1–13.

Jiang, Y., Zhao, K., Xia, K., Xue, J., Zhou, L., Ding, Y., et al. (2019). A novel distributed multitask fuzzy clustering algorithm for automatic mr brain image segmentation. *J. Med. Syst.* 43:118.

Keng, A. K., Yang, C. Z., Chuanchu, W., Cuntai, G., and Haihong, Z. (2012). Filter bank common spatial pattern algorithm on bci competition iv datasets 2a and 2b. *Front. Neurosci.* 6:39. doi: 10.3389/fnins.2012.00039

Leeb, R., Sagha, H., Chavarriaga, R., and Millán, J. R. (2011). A hybrid brain-computer interface based on the fusion of electroencephalographic and electromyographic activities. *J. Neural Eng.* 8:025011. doi: 10.1088/1741-2560/8/2/025011

Lindsley, D. B. (1952). Psychological phenomena and the electroencephalogram. *Electroencephalogr. Clin. Neurophysiol.* 4:443. doi: 10.1016/0013-4694(52)90075-8

Long, J., Tazoe, T., Soteropoulos, D. S., and Perez, M. A. (2016). Interhemispheric connectivity during bimanual isometric force generation. *J. Neurophysiol.* 115:00876.2015.

Lotte, F., Bougrain, L., Cichocki, A., Clerc, M., Congedo, M., Rakotomamonjy, A., et al. (2018). A review of classification algorithms for EEG-based brain-computer interfaces: a 10 year update. *J. Neural Eng.* 15:031005

Maruff, P., Wilson, P. H., Fazio, J. D., Cerritelli, B., and Currie, J. (1999). Asymmetries between dominant and non-dominant hands in real and imagined motor task performance. *Neuropsychologia* 37, 379–384. doi: 10.1016/s0028-3932(98)00064-5

Mashat, M. E. M., Lin, C. T., and Zhang, D. (2019). Effects of task complexity on motor imagery based brain-computer interface. *IEEE Trans. Neural Syst. Rehabil. Eng.* 27, 2178–2185. doi: 10.1109/tnsre.2019.2936987

McCreadie, K. A., Coyle, D. H., and Prasad, G. (2014). Is sensorimotor BCI performance influenced differently by mono, stereo, or 3-D auditory feedback? *IEEE Trans. Neur. Syst. Rehab.* 22, 431–440. doi: 10.1109/tnsre.2014.2312270

Minkyu, A., Hohyun, C., Sangtae, A., Chan, J. S., and Dewen, H. (2013). High theta and low alpha powers may be indicative of bci-illiteracy in motor imagery. *PLoS One* 8:e80886. doi: 10.1371/journal.pone.0080886

Mizuguchi, N., Nakata, H., Hayashi, T., Sakamoto, M., Muraoka, T., Uchida, Y., et al. (2013). Brain activity during motor imagery of an action with an object: a functional magnetic resonance imaging study. *Neurosci. Res.* 76, 150–155. doi: 10.1016/j.neures.2013.03.012

Mizuguchi, N., Sakamoto, M., Muraoka, T., Moriyama, N., and Kanosue, K. (2012). Influence of somatosensory input on corticospinal excitability during motor imagery. *Neurosci. Lett.* 514, 127–130. doi: 10.1016/j.neulet.2012.02.073

Muller-Putz, G. R., Scherer, R., Neuper, C., and Pfurtscheller, G. (2006). Steady-state somatosensory evoked potentials: suitable brain signals for brain-computer interfaces? *IEEE Trans. Neural Syst. Rehabil. Eng.* 14, 30–37. doi: 10.1109/tnsre.2005.863842

Nakazono, H., Ogata, K., Kuroda, T., and Tobimatsu, S. (2016). Phase and frequency-dependent effects of transcranial alternating current stimulation on motor cortical excitability. *PLoS One* 11:e0162521. doi: 10.1371/journal.pone.0162521

Nobuaki, M., Masanori, S., Tetsuro, M., Kento, N., Shoichi, K., Hiroki, N., et al. (2011). The modulation of corticospinal excitability during motor imagery of actions with objects. *PLoS One* 6:e26006. doi: 10.1371/journal.pone.0026006

Pfurtscheller, G., Allison, B. Z., Brunner, C., Bauernfeind, G., and Birbaumer, N. (2010). The hybrid bci. *Front. Neurosci.* 4:30. doi: 10.3389/fnpro.2010.00003

Pfurtscheller, G., Brunner, C., Schlögl, A., and Lopes da Silva, F. H. (2006). Mu rhythm (de)synchronization and EEG single-trial classification of different motor imagery tasks. *Neuroimage* 31, 153–159. doi: 10.1016/j.neuroimage.2005.12.003

Pfurtscheller, G., and Lopes da Silva, F. H. (1999). Event-related EEG/MEG synchronization and desynchronization: basic principles. *Clin. Neurophysiol.* 110, 1842–1857. doi: 10.1016/s1388-2457(99)00141-8

Pfurtscheller, G., and Neuper, C. (2001). Motor imagery and direct brain-computer communication. *Proc. IEEE* 89, 1123–1134. doi: 10.1109/5.939829

Polanía, R., Nitsche, M. A., Korman, C., Batsikadze, G., and Paulus, W. (2012). The importance of timing in segregated theta phase-coupling for cognitive performance. *Curr. Biol.* 22, 1314–1318. doi: 10.1016/j.cub.2012.05.021

Polanía, R., Nitsche, M. A., and Ruff, C. C. (2018). Studying and modifying brain function with non-invasive brain stimulation. *Nat. Neurosci.* 21, 174–187. doi: 10.1038/s41593-017-0054-4

Polich, J. (2007). Updating p300: an integrative theory of p3a and p3b. *Clin. Neurophysiol.* 118, 2128–2148. doi: 10.1016/j.clinph.2007.04.019

Porro, C. A., Cettolo, V., Francescato, M. P., and Baraldi, P. (2000). Ipsilateral involvement of primary motor cortex during motor imagery. *Eur. J. Neurosci.* 12, 3059–3063. doi: 10.1046/j.1460-9568.2000.00182.x

Punsawad, Y., Wongsawat, Y., and Parnichkun, M. (2010). "Hybrid EEG-EOG brain-computer interface system for practical machine control," in *Proceedings of the International Conference of the IEEE Engineering in Medicine & Biology* (Buenos Aires: IEEE).

Riecke, L., Formisano, E., Herrmann, C. S., and Sack, A. T. (2015). 4-Hz transcranial alternating current stimulation phase modulates hearing. *Brain Stimul.* 8, 777–783. doi: 10.1016/j.brs.2015.04.004

Romei, V., Gross, J., and Thut, G. (2010). On the role of prestimulus alpha rhythms over occipito-parietal areas in visual input regulation: correlation or causation? *J. Neurosci.* 30, 8692–8697. doi: 10.1523/jneurosci.0160-10.2010

Sawaki, L., Wu, C. W.-H., Kaelin-Lang, A., and Cohen, L. G. (2006). Effects of somatosensory stimulation on use-dependent plasticity in chronic stroke. *Stroke* 37, 246–247. doi: 10.1161/01.str.0000195130.16843.ac

Schaworonkow, N., Triesch, J., Ziemann, U., and Zrenner, C. (2018). Eeg-triggered tms reveals stronger brain state-dependent modulation of motor evoked potentials at weaker stimulation intensities. *Brain Stimul.* 12, 110–118. doi: 10.1016/j.brs.2018.09.009

Severens, M., Farquhar, J., Desain, P., Duysens, J., and Gielen, C. (2010). Transient and steady-state responses to mechanical stimulation of different fingers reveal interactions based on lateral inhibition. *Clin. Neurophysiol.* 121, 2090–2096. doi: 10.1016/j.clinph.2010.05.016

Sharma, N., Pomeroy, V. M., and Baron, J. C. (2006). Motor imagery: a backdoor to the motor system after stroke? *Stroke* 37, 1941–1952. doi: 10.1161/01.str.0000226902.43357.fc

Shu, X., Chen, S., Meng, J., Yao, L., Sheng, X., Jia, J., et al. (2018). Tactile stimulation improves sensorimotor rhythm-based bci performance in stroke patients. *IEEE Trans. Bio Med. Eng.* 66, 1987–1995. doi: 10.1109/tbme.2018.2882075

Shu, X., Yao, L., Sheng, X., Zhang, D., and Zhu, X. (2017). Enhanced motor imagery-based BCI performance via tactile stimulation on unilateral hand. *Front. Hum. Neurosci.* 11:585. doi: 10.3389/fnhum.2017.00585

Tecchio, F., Zappasodi, F., Melgari, J. M., Porcaro, C., and Rossini, P. M. (2006). Sensory-motor interaction in primary hand cortical areas: a magnetoencephalography assessment. *Neuroscience* 141, 533–542. doi: 10.1016/j.neuroscience.2006.03.059

Tu-Chan, A. P., Natraj, N., Godlove, J., Abrams, G., and Ganguly, K. (2017). Effects of somatosensory electrical stimulation on motor function and cortical oscillations. *J. Neuroeng. Rehabil.* 14:113.

Vaughan, T. M., Miner, L. A., Mcfarland, D. J., and Wolpaw, J. R. (1998). Eeg-based communication: analysis of concurrent emg activity. *Electroencephalogr. Clin. Neurophysiol.* 107, 428–433. doi: 10.1016/s0013-4694(98)00107-2

Vialatte, F.-B., Maurice, M., Dauwels, J., and Cichocki, A. (2010). Steady-state visually evoked potentials: focus on essential paradigms and future perspectives. *Prog. Neurobiol.* 90, 418–438. doi: 10.1016/j.pneurobio.2009.11.005

Wang, Z., Zhou, Y., Chen, L., Gu, B., Yi, W., Liu, W., et al. (2019). Bci monitor enhances electroencephalographic and cerebral hemodynamic activations during motor training. *IEEE Trans. Neural Syst. Rehabil. Eng.* 27, 780–787. doi: 10.1109/tnsre.2019.2903685

Wolpaw, J. R., Birbaumer, N., and Mcfarland, D. J. (2002). Brain-computer interfaces for communication and control. *Clin. Neurophysiol.* 113, 767–791.

Yao, L., Jianjun, M., Sheng, X., Zhang, D., and Zhu, X. (2015). A novel calibration and task guidance framework for motor imagery bci via a tendon vibration induced sensation with kinesthesia illusion. *J. Neural Eng.* 12, 113–123.

Yao, L., Meng, J., Zhang, D., Sheng, X., and Zhu, X. (2013). Selective sensation based brain-computer interface via mechanical vibrotactile stimulation. *PLoS One* 8:e64784. doi: 10.1371/journal.pone.0064784

Yao, L., Meng, J., Zhang, D., Sheng, X., and Zhu, X. (2014). Combining motor imagery with selective sensation toward a hybrid-modality bci. *Biomed. Eng. IEEE Trans.* 61, 2304–2312. doi: 10.1109/tbme.2013.2287245

Yi, W., Qiu, S., Wang, K., Qi, H., Zhao, X., He, F., et al. (2017). Enhancing performance of a motor imagery based brain–computer interface by incorporating electrical stimulation-induced sssep. *J. Neural Eng.* 14:026002. doi: 10.1088/1741-2552/aa5559

Zeng, H., Wang, Y., Wu, C., Song, A., Liu, J., Ji, P., et al. (2017). Closed-loop hybridgaze brain-machine interface based robotic arm control with augmented reality feedback. *Front. Neurorobot.* 11:60. doi: 10.3389/fnbot.2017.00060

Zhang, X., Guo, Y., Gao, B., and Long, J. (2020). Alpha frequency intervention by electrical stimulation to improve performance in mu-based bci. *IEEE Trans. Neural Syst. Rehabil. Eng.* 28, 1–1. doi: 10.1155/2019/7030286

Zhang, Y., Chung, F. L., and Wang, S. (2019). A multiview and multiexemplar fuzzy clustering approach: theoretical analysis and experimental studies. *IEEE Trans. Fuzzy Syst.* 27, 1543–1557. doi: 10.1109/tfuzz.2018.2883022

Zhang, Y., Ishibuchi, H., and Wang, S. (2017). Deep takagi–sugeno–kang fuzzy classifier with shared linguistic fuzzy rules. *IEEE Trans. Fuzzy Syst.* 26:1. doi: 10.1109/tcyb.2020.3016972

Zrenner, C., Desideri, D., Belardinelli, P., and Ziemann, U. (2017). Real-time eeg-defined excitability states determine efficacy of tms-induced plasticity in human motor cortex. *Brain Stimul.* 11, 374–389. doi: 10.1016/j.brs.2017.11.016

Conflict of Interest: The authors declare that the research was conducted in the absence of any commercial or financial relationships that could be construed as a potential conflict of interest.

frontiers in Neuroscience

METHODS
published: 24 March 2021
doi: 10.3389/fnins.2021.647393

Transferred Subspace Learning Based on Non-negative Matrix Factorization for EEG Signal Classification

Aimei Dong, Zhigang Li† and Qiuyu Zheng†*

School of Computer Science and Technology, Qilu University of Technology (Shandong Academy of Science), Jinan, China

EEG signal classification has been a research hotspot recently. The combination of EEG signal classification with machine learning technology is very popular. Traditional machine leaning methods for EEG signal classification assume that the EEG signals are drawn from the same distribution. However, the assumption is not always satisfied with the practical applications. In practical applications, the training dataset and the testing dataset are from different but related domains. How to make best use of the training dataset knowledge to improve the testing dataset is critical for these circumstances. In this paper, a novel method combining the non-negative matrix factorization technology and the transfer learning (NMF-TL) is proposed for EEG signal classification. Specifically, the shared subspace is extracted from the testing dataset and training dataset using non-negative matrix factorization firstly and then the shared subspace and the original feature space are combined to obtain the final EEG signal classification results. On the one hand, the non-negative matrix factorization can assure to obtain essential information between the testing and the training dataset; on the other hand, the combination of shared subspace and the original feature space can fully use all the signals including the testing and the training dataset. Extensive experiments on Bonn EEG confirmed the effectiveness of the proposed method.

Keywords: non-negative factorization, transfer learning, shared hidden subspace, EEG signal, classification

OPEN ACCESS

Edited by:
Yizhang Jiang,
Jiangnan University, China

Reviewed by:
Xiaodan Sui,
The Chinese University of Hong Kong, China
Xin Liu,
Xuzhou Medical University, China

****Correspondence:***
Aimei Dong
amdong@qlu.edu.cn

† These authors have contributed equally to this work

Specialty section:
This article was submitted to Neuroprosthetics, a section of the journal Frontiers in Neuroscience

Received: *29 December 2020*
Accepted: *22 February 2021*
Published: *24 March 2021*

Citation:
Dong A, Li Z and Zheng Q (2021) Transferred Subspace Learning Based on Non-negative Matrix Factorization for EEG Signal Classification. Front. Neurosci. 15:647393. doi: 10.3389/fnins.2021.647393

INTRODUCTION

Epilepsy (Talevi et al., 2007) is a chronic disease with sudden abnormal discharge of brain neurons, which leads to transient brain dysfunction. Existing studies (Subasi and Gursoy, 2010) have proved that epileptic seizures are caused by sudden abnormal discharge of brain neurons, and the use of EEG signals can effectively improve the progress of epilepsy line detection and diagnosis in order to facilitate the timely treatment of relevant medical staff. Due to its recurrent characteristics, it brings great inconvenience to patients' daily life. At present, there are about 50 million epileptic patients in the world; most of them come from developing countries. Meanwhile, there are about 2.4 million new patients every year. Epilepsy can occur in all ages, and about 50% of the patients in the world occur in adolescence or childhood. Compared with normal people, the mortality of epileptic patients has increased by 2–3 times.

It is one of the important means to identify and diagnose epilepsy patients with computer-aided therapy according to pathological information contained in the EEG signals. In the classical epilepsy recognition (Guler and Ubeyli, 2007; Tazllas et al., 2009; Dorai and Ponnambalam, 2010; Iscan et al., 2011; Acharya et al., 2013; Fouad et al., 2015) methods, we usually train a classifier to recognize and diagnose epilepsy based on the existing data. The core steps are feature extraction and classifier training. The quality of feature representation is directly related to the training of classifiers. Therefore, in the classification of EEG signals, many methods are generally used to extract the features of EEG signals, such as principal component analysis (PCA) (Subasi and Gursoy, 2010), Kernel principal component analysis (KPCA) (Patel et al., 2018), and wavelet packet decomposition (WPD) (Ting et al., 2008).

With the wide applications of computer-aided diagnosis technology, more and more methods have been applied to EEG signal detection in recent years, such as support vector machine (SVM) (Temko et al., 2011), linear discriminant analysis (LDA) (Subasi and Gursoy, 2010), empirical mode decomposition (EMD) (Bajaj and Pachori, 2012), and fuzzy system (Aarabi et al., 2009). The common characteristic of these methods is that they usually train classifiers to recognize EEG signals according to the existing labeled data. In such cases, great challenges have always been encountered in the process of EEG signal classification. Firstly, the EEG signal is a highly non-linear and non-stationary signal. It is normal situation that different EEG acquisition equipment, different patients, and even the same patient at a different time have different data with diverse characteristics, which leads to the inapplicability of the training model. Second, the number of EEG signals is always insufficient due to the patient's body or privacy, which also leads to the problems of robustness and generalization of traditional classification methods in EEG signals detection.

To this end, the transfer learning (Dong and Wang, 2014) method is proposed. Transfer learning is a new machine learning method that uses existing knowledge to solve problems in different but related fields. It relaxes two basic assumptions in traditional machine learning: (1) training samples and new testing samples for learning satisfy the condition of independent and identically distribution; (2) the number of samples in the auxiliary domain is much more than that in the target domain. Its purpose is to improve the performance for the target domain with the aid of the auxiliary domain. For the application of epileptic EEG signal classification, health signals and/or signals during seizures are used for training while the testing samples are the signals during seizure-free intervals.

In this paper, we try to solve the problem of epileptic seizure classification with the framework of transfer learning. It is obvious that EEG signals in different fields contain some shared knowledge independent of the data. We reconstruct the EEG signals of different fields to find the shared hidden features between the auxiliary domain and the target domain. In order to improve the recognition ability of the target domain, we augment the dimension of the data and combine the original data with the obtained shared features.

In summary, we propose a novel method called transferred SVM based on non-negative matrix factorization (Lee and Seung, 1999) (NMF-TL). Specifically, we use a variety of methods to extract the features of EEG signals firstly, and then non-negative matrix factorization is used to extract the shared potential features between the auxiliary domain and the target domain; finally, the augmented dimension is used to train the final classification model in order to improve the discrimination ability of the target domain. The principle of the proposed method is shown in **Figure 1**.

The rest of the paper is organized as follows. We introduce the feature extraction of EEG signals and the latest transfer learning achievements in Section "Related Work." In Section "Proposed Method," the proposed method is formulated in detail. The German EEG data set is used to carry out extensive experiments in Section "Experiments." Finally, we summarize our method.

RELATED WORK

In this section, we review the application of feature extraction and transfer learning in EEG signal processing in recent years, as well as the research on non-negative matrix factorization.

Feature Extraction Methods About EEG Signals

One of the challenges of EEG signal processing is feature extraction. EEG signals have the characteristic of being non-stationary, i.e., the EEG signal is non-linear in nature. At present, there are four EEG signal processing methods: (1) time domain analysis; (2) frequency domain analysis; (3) combination of time and frequency domain; and (4) non-linear method.

Time domain analysis mainly extracts the waveform characteristics of EEG, such as linear prediction (Altunay et al., 2010; Joshi et al., 2014), principal component analysis (Ghosh-Dastidar et al., 2008), independent component analysis (Jung et al., 2001; Viola et al., 2009), and linear discriminant analysis (Jung et al., 2001). Frequency domain analysis uses Fourier transform to extract the frequency characteristics of the EEG signal. Frequency domain analysis can be divided into parametric method and non-parametric method. The non-parametric method extracts frequency domain information of time series. The Welch (Welch, 1967; Polat and Güne, 2007; Faust et al., 2008) method is a typical method. For the non-parametric method's disadvantage of information loss, the parametric method is proposed. The parametric method mainly includes moving average model, autoregressive (Deryaübeyl and Güler, 2004) model, and autoregressive moving average. Time domain analysis and frequency domain analysis cannot get all the information of the EEG signal separately. So the methods of combining time and frequency domain are proposed, such as wavelet transform (Subasi, 2007) and Hilbert Huang transform (Oweis and Abdulhay, 2011). Non-linear technology can be used to describe the biological system effectively. It is also applicable to EEG signal analysis. Non-linear methods mainly use various parameters of EEG which can describe biological information

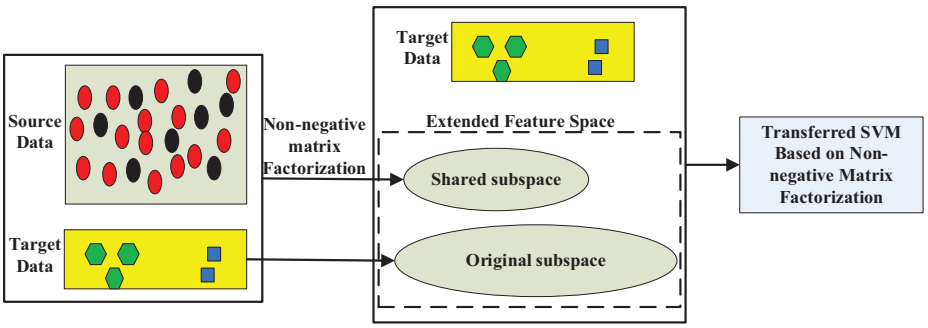

FIGURE 1 | Principle of the proposed transferred SVM based on non-negative matrix factorization.

to extract the features of EEG, such as maximum Lyapunov exponent, correlation dimension, fractal dimension, Hurst index, approximate entropy and sample entropy, and recursive quantitative analysis.

Non-negative Matrix Factorization

In the process of signal processing, it is an important problem to construct a method that multidimensional data can be better detected. To this end, non-negative matrix factorization (NMF) is proposed; it can extract the potential feature structure of data and reduce the dimension of features.

NMF was proposed by Lee and Sueng (Lee and Seung, 1999). It has obtained great achievements in many fields such as signal processing, biomedical engineering, pattern recognition, computer vision, and image engineering. In recent years, many scholars have improved it from different views. In order to overcome the problem of local and sparse optimization, some scholars (Chen et al., 2001; Li et al., 2001) combine the sparse penalty term with sed as the objective function. However, the local NMF algorithm has poor ability to describe the data. Xu et al. (2003) optimized and proposed a restricted NMF. Wang et al. (2004) added Fisher discriminant information (the difference between intraclass divergence and interclass divergence) into GKLD to form an objective function, and constructed the Fisher NMF algorithm. In order to eliminate the influence of sample uncertainty on data, some weighted NMF (Wang et al., 2006) were also proposed.

For a given domain dataset $\mathbf{X} = [\boldsymbol{x}_1, \boldsymbol{x}_2, \cdots, \boldsymbol{x}_N] \in \mathbb{R}^{d\times N}$, $x_i = [x_{i1}, x_{i2}, \cdots, x_{id}] \in \mathbb{R}^{d\times 1}$, where N is the number of samples and d is the number of dimensionality. The goal of non-negative matrix factorization is to find out two non-negative and low-rank matrices: one is coefficient matrix$\mathbf{W} \in \mathbb{R}_+^{d\times r}$ and the other is base matrix$\mathbf{H} \in \mathbb{R}_+^{r\times N}$, which satisfy$\mathbf{X} \approx \mathbf{WH}$, where$r <$ min $\{d, N\}$. So the objective function can be defined as follows:

$$\begin{aligned} &\min_{W,H} ||\mathbf{X}\text{-}\mathbf{WH}||_F^2 \\ &s.t. \mathbf{W} \geq 0, \mathbf{H} \geq 0 \end{aligned} \tag{1}$$

Lee and Sueng proposed an iterative multiplicative update algorithm and obtained the following update rules:

$$\mathbf{W}_{i,j} \leftarrow \mathbf{W}_{i,j} \frac{(\mathbf{XH}^T)_{i,j}}{(\mathbf{WHH}^T)_{i,j}} \tag{2}$$

$$\mathbf{H}_{i,j} \leftarrow \mathbf{H}_{i,j} \frac{(\mathbf{W}^T\mathbf{X})_{i,j}}{(\mathbf{W}^T\mathbf{WH})_{i,j}} \tag{3}$$

Transfer Learning

In the task of EEG signal classification, the traditional machine learning method assumes that all data have the same data distribution. However, due to the non-stationarity of EEG signals, this assumption does not exist, which makes it difficult for traditional methods to achieve good results in practical applications. In order to overcome this problem, transfer learning is put forward.

Transfer learning is proposed to solve small sample problems and personalized problems and has been widely used in BCI classification in recent years. A dual-filter framework (Tu and Sun, 2012) is proposed, which can be used to learn the common knowledge of source domain and target domain. Transfer learning, semi-supervised learning, and TSK fuzzy system are combined (Jiang et al., 2017) to improve the interpretability of transfer learning. In literacy (Yang et al., 2014), with the adoption of the large projection support vector machine, the useful knowledge between the training domain and test domain is learned by calculating the maximum average deviation. In literacy (Raghu et al., 2020), two different classification methods are proposed based on convolutional neural networks: (1) transfer learning by a pre-training network and (2) image feature extraction by a pre-training network and classification by a support vector machine classifier.

PROPOSED METHOD

In this paper, we propose a transfer learning method based on subspace learning. Our method is mainly divided into three steps: the first step is to extract the feature of the EEG signal; the second step is to use non-negative matrix factorization to learn

the shared knowledge of the auxiliary domain and target domain; thirdly, the dimension of data is augmented by the combination of the original feature space with the obtained shared feature space. Finally, we use the augmented data space for transfer learning. The principle of the proposed method is shown in **Figure 1**.

Notations

(1) Let domain $D = \{x_i, y_i\} \in \mathbf{X} \times \mathbf{Y}: i = 1, 2, \cdots, n$, where $\mathbf{X}$ represents the domain sample instance space, Y represents the domain sample label space, and $\{x_i, y_i\}$ represents an instance in domain D.

(2) Let $P(D) = P(\mathbf{X}, \mathbf{Y})$ be the data distribution in domain D. There are two domainsD_s and D_t; if $D_s \neq D_t$, then D_s and D_t are different domains.

(3) Let $D_s = \{(\boldsymbol{x}_i^s, y_i^s) \in \mathbf{X}^s \times \mathbf{Y}^s, i = 1, 2, \cdots, n_s\}$represent the source domain and $D_t = \{(\boldsymbol{x}_i^t, y_i^t) \in \mathbf{X}^t \times \mathbf{Y}^t, i = 1, 2, \cdots, n_t\}$ represent the target domain, where $n_s \geq n_t$, the superscript represents the domain, and the subscript represents the index of the sample.

This proposed method is based on the following assumptions: (1) There is only one source domain and one target domain. (2) The data distribution is different but related, and two different domains share a low-dimensional shared hidden subspace through non-negative matrix factorization. (3) The source domain includes a large amount of data and label information, and the target domain includes a small amount of tagged data. The learning task is to make full use of the source domain information to train a classifier with better generalization performance for the target domain.

Low-Dimensional Shared Hidden Subspace Learning

Given source domain and target domain data $\mathbf{X} = \{\mathbf{X}^s, \mathbf{X}^t\}$, where $\mathbf{X}^s = \{\boldsymbol{x}_1^s, \boldsymbol{x}_2^s, \cdots, \boldsymbol{x}_{n_s}^s\} \in \mathbb{R}^{d_s \times n_s}$ and $\mathbf{X}^t = \{\boldsymbol{x}_1^t, \boldsymbol{x}_2^t, \cdots, x_{n_t}^t\} \in \mathbb{R}^{d_t \times n_t}$, d_s and d_t are the numbers of dimensionality in the source domain and target domain, respectively, andn_s andn_t are the numbers of samples in the source domain and target domain, respectively. With the adoption of non-negative matrix factorization, we construct the objective function as Eq. (4):

$$\begin{aligned} &\min_{W^s, W^t, H} \alpha^s ||\mathbf{X}^s - \mathbf{W}^s\mathbf{H}||_F^2 + \alpha^t \left|\left|\mathbf{X}^t - \mathbf{W}^t\mathbf{H}\right|\right|_F^2 \\ &s.t. \alpha^s + \alpha^t = 1, 0 < \alpha^s, \alpha^t < 1 \\ &\mathbf{W}^s, \mathbf{W}^t, \mathbf{H} > 0 \end{aligned} \tag{4}$$

where$\mathbf{W}^s \in \mathbb{R}^{d_s \times r}$ and $\mathbf{W}^t \in \mathbb{R}^{d_t \times r}$ are the projection matrices for the source domain and target domain data, respectively, which can map the data from a low-dimensional shared hidden space to the original feature space.$r$is the dimensionality of the low-dimensional shared hidden space and$1 \leq r \leq \min\{d_s, d_t\}$.$\mathbf{H}$ is the low-dimensional shared hidden space between the source and the target domain. α^s andα^t are the weight parameters for the source and target domain and satisfies$\alpha^s + \alpha^t = 1$. With the adoption of ADMM and literature [27], we obtain the following update rules:

$$\left(\mathbf{W}^s\right)_{i,j} \leftarrow \frac{\left(\mathbf{X}^s\mathbf{H}^T\right)_{i,j}}{\left(\mathbf{W}^s\mathbf{H}\mathbf{H}^T\right)_{i,j}} \left(\mathbf{W}^s\right)_{i,j} \tag{5}$$

$$\left(\mathbf{W}^t\right)_{i,j} \leftarrow \frac{\left(\mathbf{X}^t\mathbf{H}^T\right)_{i,j}}{\left(\mathbf{W}^t\mathbf{H}\mathbf{H}^T\right)_{i,j}} \left(\mathbf{W}^t\right)_{i,j} \tag{6}$$

$$(\mathbf{H})_{i,j} \leftarrow \frac{\alpha^s \left(\left(\mathbf{W}^s\right)^T \mathbf{X}^s\right)_{i,j} + \alpha^t \left(\left(\mathbf{W}^t\right)^T \mathbf{X}^t\right)_{i,j}}{\alpha^s \left(\left(\mathbf{W}^s\right)^T \mathbf{W}^s\mathbf{H}\right)_{i,j} + \alpha^t \left(\left(\mathbf{W}^t\right)^T \mathbf{W}^t\mathbf{H}\right)_{i,j}} (\mathbf{H})_{i,j} \tag{7}$$

Based on the above analysis and derivation, low-dimensional shared hidden subspace learning is obtained. The algorithm description is summarized as shown in **Table 1**.

The Process of Training and Testing

After the low-dimensional shared hidden subspace H is obtained, we use H as the shared knowledge between source domain and target domain to transfer information. With the large margin principle, we combine the shared information and SVM conception to learn the final classifier. That is to say, for the training data (source domain data), the classified decision function consists of two parts: the original feature space and the shared hidden space. Specifically, the classified decision function is rewritten based on the classical SVM in the form of Eq. (8):

$$f_s(\boldsymbol{x}) = \left(\boldsymbol{w}^s\right)^T \boldsymbol{x}^s + \left(\boldsymbol{v}^s\right)^T \mathbf{H}\mathbf{x}^s + b^s \tag{8}$$

where$\boldsymbol{w}^s$ and $\boldsymbol{v}^s$ represent the classification parameter in the original feature space and shared hidden subspace, respectively. Finally, we use the learned parameters $\boldsymbol{w}^s$, $\boldsymbol{v}^s$, and b^s to classify the testing data (target domain data).

TABLE 1 | The description of the low-dimensional shared hidden subspace learning.

Algorithm NMF-TL

1. **Parameters:** Dimensions of shared hidden space r, weight parameters for source and target domain α^s, α^t

2. **Input:** source domain data $\{(\boldsymbol{x}_k^s, y_k^s)|k = 1, 2, \cdots, n_s\}$, target domain data $\{(\boldsymbol{x}_k^t, y_k^t)|k = 1, 2, \cdots, n_t\}$

3. **Initialization:** set $\mathbf{W}_0^s$, $\mathbf{W}_0^t$, H_0 satisfying $\mathbf{X}^s = \mathbf{W}_0^s\mathbf{H}_0$, $\mathbf{X}^t = \mathbf{W}_0^t\mathbf{H}_0$, *iter* = 1 set the maximum number *itermax* of iterations and the threshold of error ε

4. **Repeat:**

4-1:update $(\mathbf{H}_{iter})_{i,j}$ using Eq.(7)

4-2:update $((\mathbf{W}_{iter})^s)_{i,j}$ using Eq. (5)

4-3:update $((\mathbf{W}_{iter})^t)_{i,j}$ using Eq. (6)

4-4: $iter = iter + 1$

textbfUntil:

$\| (\mathbf{H}_{iter})_{i,j} - (\mathbf{H}_{iter-1})_{i,j} \| < \varepsilon$ or $\| ((W_{iter})^s)_{i,j} - ((W_{iter-1})^s)_{i,j} \| < \varepsilon$ *or* $\| ((W_{iter})^t)_{i,j} - ((W_{iter-1})^t)_{i,j} \| < \varepsilon$ *or* (*iter* > *itermax*)

5. **Output:** low dimensional shared hidden space $H \in \mathbb{R}^{r \times d}$

EXPERIMENTS

In this section, to evaluate the effectiveness of the proposed method NMF-TL which combines the conception of non-negative matrix factorization, transfer learning, and the large margin principle, we did extensive experiments with EEG signals. All the methods were carried out in MATLAB (R2016b) on a computer with Intel(R) Core (TM) i7-4510U 2.50 GHz CPU and 16GB RAM.

Dataset and Compared Methods

The dataset used in the experiments can be publicly downloaded from the web http://www.meb.unibonn.de/epileptologie/science/physik/eegdata.html. The original data contains five groups of data (denoted as A–E), and the details are described in **Figure 2**. Each group contains 100 single-channel EEG segments of 23.6 s duration. The sampling rate of all datasets was 173.6 Hz. Since there are 100 EEG signals in each group of data, it is not very easy to visualize all their characteristics simultaneously. **Figure 3** shows one typical signal in each group to facilitate intuitive observation of the differences in the signals among the five groups of data. The original EEG signals are processed by feature extraction using wavelet packet decomposition (WPD), short-time Fourier transform (SIFT), and kernel principle component analysis (KPCA), and then the EEG signals are used to train and test different classifiers in the experiment.

According to the EEG data described in **Figure 2**, we designed 10 groups of datasets and each dataset is related with different distributions from two scenarios to compare the performance and effectiveness of the proposed method. In the

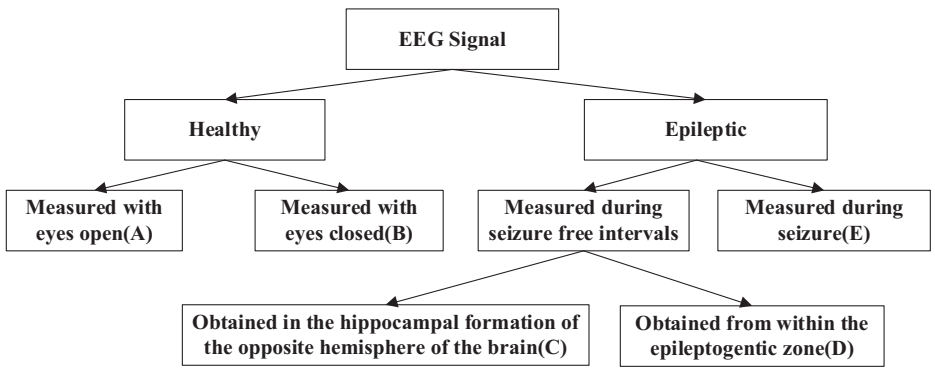

FIGURE 2 | Description of the EEG data.

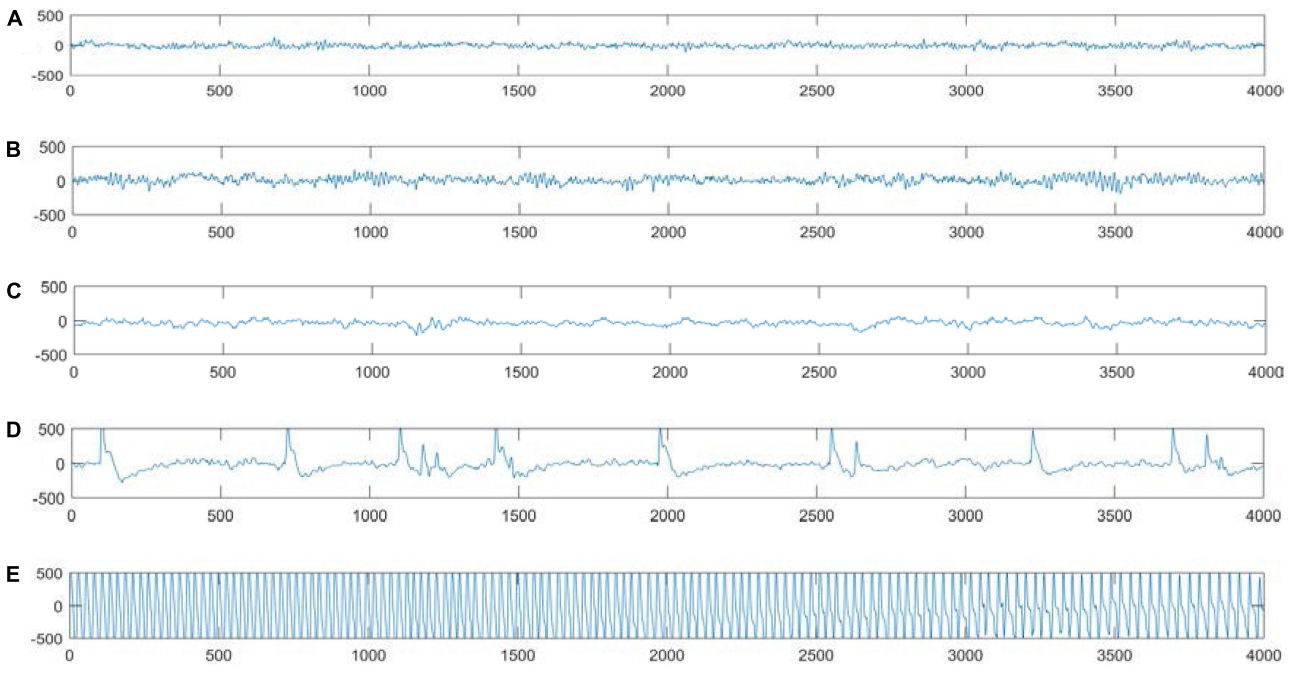

FIGURE 3 | Typical EEG signals in groups **(A–E)**.

first scenario, the source domain (i.e., the training dataset) and the target domain (i.e., the testing dataset) are drawn from the identical distribution, while in the second scenario the data distribution is different. The detailed information is summarized in **Table 2**. Specifically, in scenario 1, dataset 1# is designed for binary classification while dataset 2# is designed for multiclass classification; in scenario 2, datasets 3#–6# are designed for binary classification while datasets 7# and 8# are designed for multiclass classification. For binary classification, we designated the healthy subjects (A or B) as positive class and the epileptic subjects (C, D, or E) as negative class. For multiclass classification, the classification task is to identify different classes according to **Figure 2A–E**.

A 10-fold cross-validation strategy was used to obtain the final results for scenario 1. For scenario 2, one cross-validation-like strategy was adopted. Specifically, for each dataset in scenario 2, firstly, source data and target data were sampled separately satisfying different distributions to obtain the one classifier; secondly, the source data and the target data are swapped to obtain another classifier. The one-round result is obtained based on the two classifiers. The process is similar to the traditional twofold cross validation strategy. The above procedure was repeated 10 times. For both scenarios, the average result is recorded.

The proposed method is compared with other seven different classification methods, namely, SVM (Guler and Ubeyli, 2007), LDA (Peng and Lu, 2012), DT (Goker et al., 2012), NB (Tazllas et al., 2009), KNN (Cover and Hart, 1967), MTLF (Xu et al., 2017), and LMPROJ (Quanz and Huan, 2009).

Results and Analysis

The results on classification accuracy of 8 classifiers on 8 different datasets are recorded in **Tables 3–5**.

In **Table 3**, we give the comparison results of the proposed method and other compared methods based on WPD feature extraction. It can be seen that our method is obviously better than other results. In the results of A/E, B/C, and B/D classification, our method has little improvement effect compared with other methods, with an increase of about 6%. However, in other group classifications, our method improves the effect obviously, and it improves the accuracy by more than 10%. This also proves that our method can better learn the shared knowledge between source domain and target domain.

TABLE 2 | The description of the 8 groups of datasets.

Scenario	Datasets	Source domain (training dataset)	Target domain (testing dataset)
Scenario 1: same distribution	1#	A(75),E(75)	A(25),E(25)
	2#	A(75),B(75),E(75)	A(25),B(25),E(25)
Scenario 2: different distribution	3#	A(75),E(75)	A(25),C(25)
	4#	A(75),E(75)	A(25),D(25)
	5#	B(75),E(75)	B(25),C(25)
	6#	B(75),E(75)	B(25),D (25)
	7#	A(75),B(75),E(75)	A(25),B(25),C(25)
	8#	A(75),B(75),E(75)	A(25),B(25),D(25)

TABLE 3 | Classification accuracy comparison of 8 classifiers on datasets based on WPD feature extraction.

Method	1#	2#	3#	4#	5#	6#	7#	8#
SVM	0.9150	0.6733	0.6842	0.6987	0.9550	0.9650	0.6433	0.6667
LDA	0.9150	0.8600	0.8350	0.8450	0.7850	0.8050	0.8367	0.8300
DT	0.8950	0.7933	0.8500	0.8300	0.9500	0.9300	0.7300	0.7267
NB	0.8700	0.7799	0.5800	0.5600	0.7600	0.7450	0.5799	0.6167
KNN	0.9150	0.8533	0.7650	0.8050	0.9600	0.9500	0.7500	0.7467
MTLF	0.9600	0.8800	0.6950	0.7000	0.9000	0.8850	0.7433	0.7564
LMPROJ	0.8700	0.7767	0.7950	0.8750	0.8000	0.9200	0.6800	0.6700
NMF-TL	0.9700	0.9800	0.9500	0.9500	0.9700	0.9750	0.9699	0.9467

TABLE 4 | Classification accuracy comparison of 8 classifiers on datasets based on SIFT feature extraction.

Method	1#	2#	3#	4#	5#	6#	7#	8#
SVM	0.9800	0.6908	0.5600	0.5800	0.7150	0.7700	0.7187	0.7033
LDA	0.9900	0.8900	0.5050	0.5650	0.6300	0.6650	0.5700	0.6100
DT	0.9764	0.9300	0.6500	0.7200	0.5600	0.6450	0.6467	0.7067
NB	0.9450	0.9367	0.5800	0.5800	0.5650	0.6400	0.6499	0.6233
KNN	0.9864	0.9367	0.5100	0.5650	0.5100	0.5400	0.6100	0.6333
MTLF	0.9850	0.9833	0.5125	0.5800	0.8450	0.8400	0.6634	0.7067
LMPROJ	0.9800	0.7933	0.6000	0.8750	0.8700	0.8750	0.6700	0.6750
NMF-TL	0.9950	0.9933	0.9700	0.9650	0.9700	0.9650	0.9467	0.9500

TABLE 5 | Classification accuracy comparison of 8 classifiers on datasets based on KPCA feature extraction.

Method	1#	2#	3#	4#	5#	6#	7#	8#
SVM	0.9300	0.8300	0.5700	0.5645	0.7500	0.7700	0.5933	0.6267
LDA	0.9050	0.5467	0.8900	0.9530	0.9150	0.9150	0.6467	0.6733
DT	0.9800	0.8533	0.8950	0.9725	0.8400	0.8650	0.7767	0.8700
NB	0.8950	0.8149	0.6300	0.7900	0.7900	0.7550	0.6367	0.6700
KNN	0.9400	0.7767	0.8450	0.8950	0.8850	0.9050	0.7400	0.7467
MTLF	0.9350	0.9400	0.7750	0.8500	0.7650	0.8150	0.8199	0.8400
LMPROJ	0.9550	0.9233	0.7717	0.7700	0.8900	0.8400	0.8633	0.8700
NMF-TL	0.9870	0.9500	0.9650	0.9800	0.9800	0.9600	0.9600	0.9767

In the STFT feature classification results shown in **Table 4**, we can see that our method has achieved good results in other groups of experiments except the A/E group. This is because A/E classification is a traditional binary classification and the proposed method has not demonstrated the superiority over other compared method. For the A/B/E group experiment, our method has improved the accuracy of about 9% compared with the other non-transfer learning methods and improved about 5% compared with the other two transfer learning methods. In all the other group experiments, the proposed method achieved a better range of results.

From **Table 5**, we can see that our method has improved by about 4% compared with other methods in the A/E group classification. In other groups of experiments, our method has

improved about 12% accuracy compared with several baseline methods and also improved about 5% accuracy compared with the other two transfer learning methods.

In summary, from **Tables 3–5**, we can draw the following conclusion:

(1) For the traditional scenario, i.e., the scenario where the training dataset and the testing dataset are drawn from the same distribution, the proposed method could not demonstrate the superiority over other compared methods, especially for binary classification tasks.
(2) For the transfer learning scenario, the i.e., scenario where the training dataset and the testing dataset are drawn from different but related domains, the transfer learning methods can achieve better results compared with the non-transfer learning methods. The results display that the transfer learning method can exert the positive transfer ability to the best advantage.
(3) For the transfer learning scenario, i.e., the scenario where the training dataset and the testing dataset are drawn from different but related domains, the proposed method shows better performance compared with the other two transfer learning methods. These results show that the proposed method can not only find the shared hidden knowledge but also find the potential relationship between the source domain and the target domain.

At the same time, in order to make our experimental results more visual, we give a broken line chart of the accuracy of our experimental results as shown in **Figures 4–6**. From **Figures 4–6**, we can clearly see that our experimental method is obviously better than other experiments in accuracy, and our experimental method has greatly improved the experimental accuracy compared with other methods.

Besides the classification accuracy, we also performed experiments with measurements of F1 score and Recall.

In **Table 6**, we compare the F1_score results of our method with other methods based on WPD feature extraction. It can be seen that our method is superior to other methods except the B/C and B/D dataset. In the comparison between A/C and A/D, our method only improves about 0.25%. But in other comparison results, the F1_score of this method is improved by about 7%.The proposed method can find the potential relationship between the source and the target domain by non-negative matrix factorization and balance the performance between accuracy and recall. LDA has also achieved good results in this experiment, which shows that LDA classification has good generalization ability.

The F1_score comparison results of 8 classification methods based on KPCA feature extraction are shown in **Table 7**. The proposed method has achieved good results except A/E and A/C groups. Compared with other baseline methods, the F1_score of the proposed method in the A/B/E, B/C, and B/D groups increased by about 5%, and that in the A/B/C and A/B/D groups increased by about 15%; compared with the other two transfer learning methods, the F1_score of our method in the A/C and A/D groups increased by about 18%, and that in the B/D, A/B/C, and A/B/D groups increased by about 4.5%.

In **Table 8**, we show the F1_score comparison of eight classification methods based on STFT feature extraction. It can be seen that compared with the other baseline methods, the proposed method has increased by about 8% in the A/B/E and

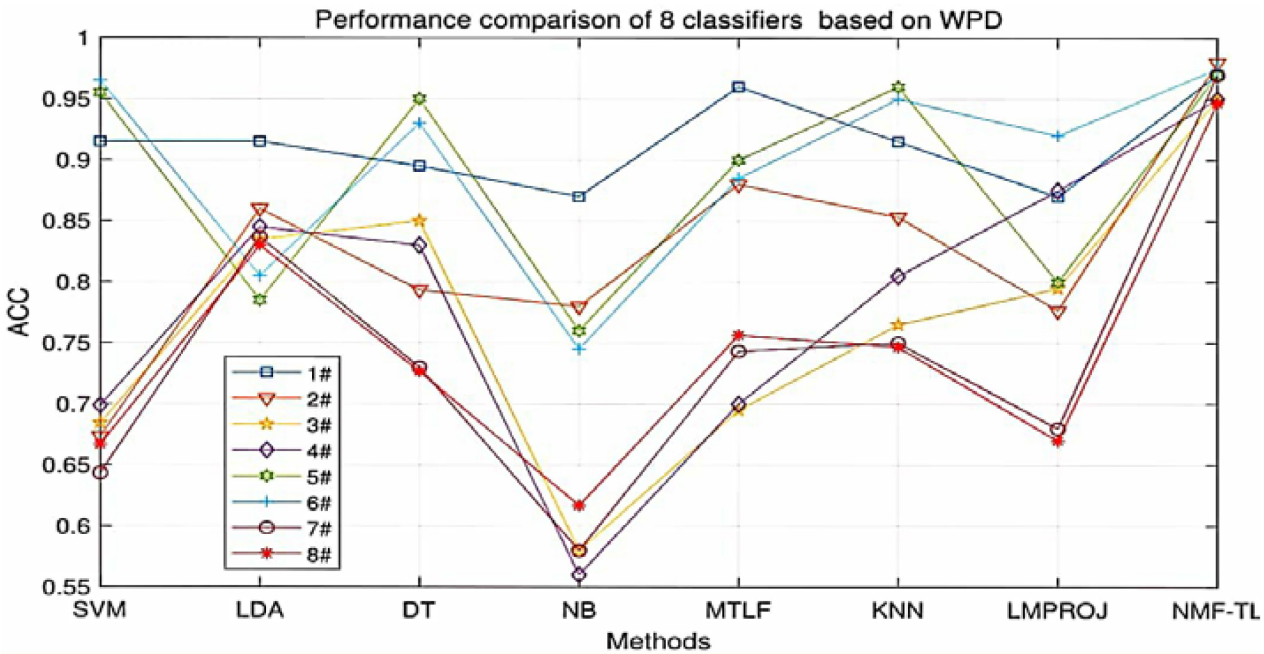

FIGURE 4 | Classification accuracy comparison of 8 classifiers on datasets based on WPD feature extraction.

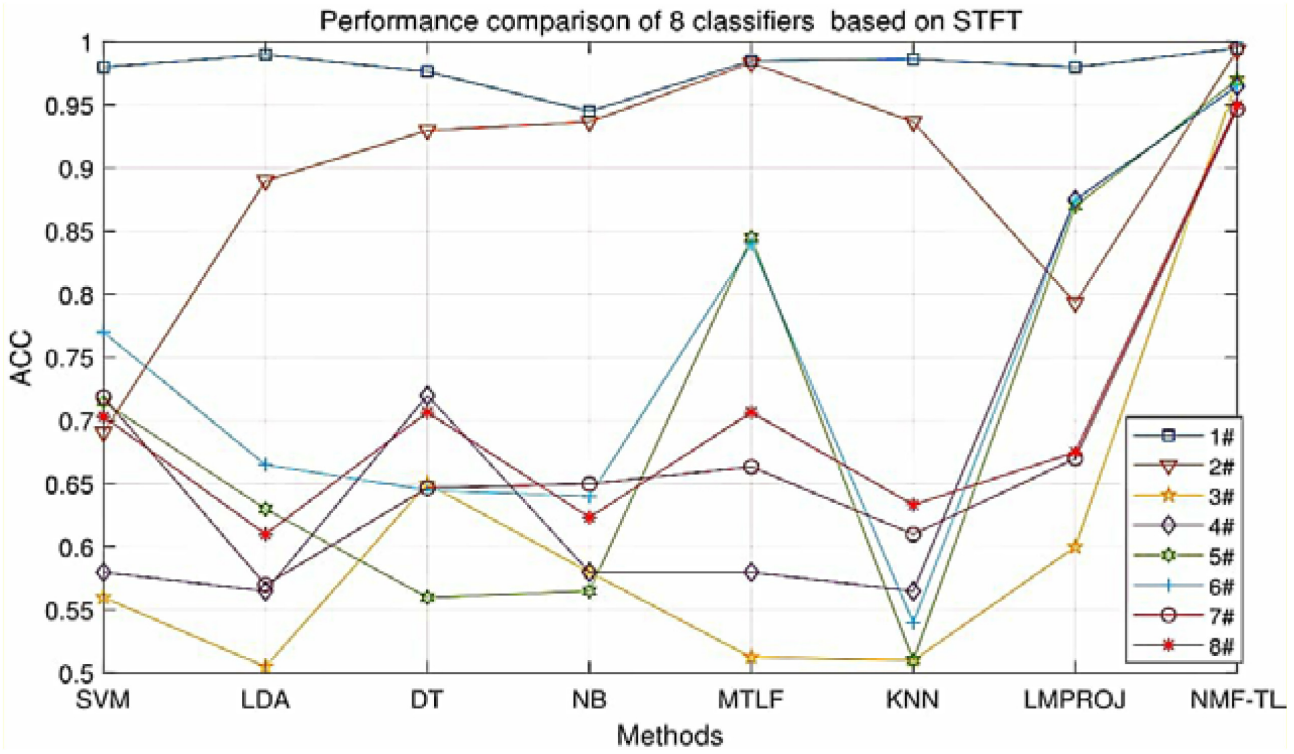

FIGURE 5 | Classification accuracy comparison of 8 classifiers on datasets based on SIFT feature extraction.

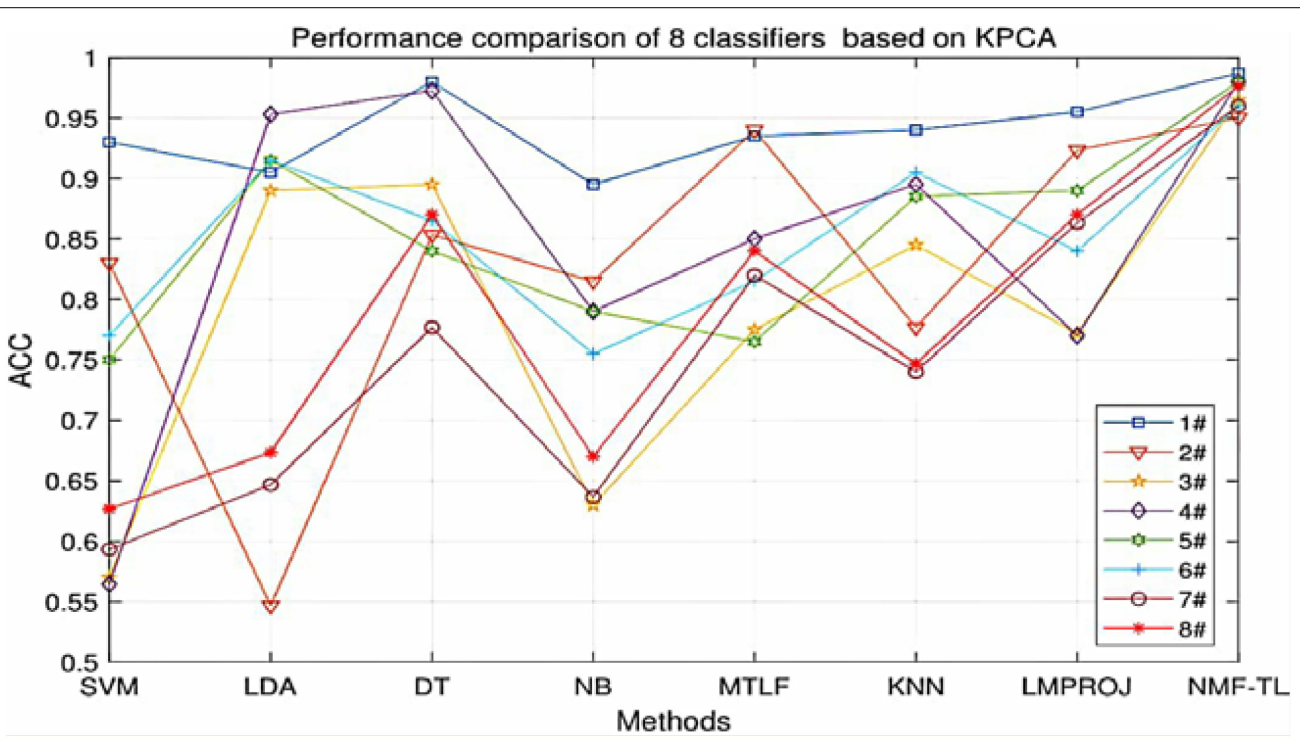

FIGURE 6 | Classification accuracy comparison of 8 classifiers on datasets based on KPCA feature extraction.

TABLE 6 | F1_score of 8 classifiers on datasets based on WPD feature extraction.

Method	1#	2#	3#	4#	5#	6#	7#	8#
SVM	0.9364	0.8033	0.9784	0.9685	0.9562	0.9587	0.6877	0.6954
LDA	0.9600	0.9100	0.9000	0.9000	0.9700	0.9700	0.9100	0.9100
DT	0.9000	0.7600	0.8700	0.8700	0.9500	0.9500	0.7600	0.7600
NB	0.8659	0.8050	0.2092	0.3303	0.8022	0.7922	0.8050	0.7850
KNN	0.9600	0.8550	0.9000	0.9700	0.9900	0.9800	0.8450	0.8450
MTLF	0.9559	0.8850	0.5578	0.5994	0.8888	0.8885	0.8700	0.8700
LMPROJ	0.8678	0.8535	0.8109	0.8725	0.8260	0.9126	0.8025	0.7684
NMF-TL	0.9987	0.9850	0.9800	0.9700	0.9800	0.9800	0.9850	0.9800

TABLE 7 | F1_score of 8 classifiers on datasets based on PCA feature extraction.

Method	1#	2#	3#	4#	5#	6#	7#	8#
SVM	0.9014	0.8840	0.9572	0.9685	0.6503	0.6462	0.5972	0.6211
LDA	0.9100	0.5100	0.9000	0.9100	0.8700	0.8700	0.5300	0.5300
DT	0.9890	0.8450	0.9767	0.9823	0.8500	0.8500	0.8100	0.8200
NB	0.7930	0.8150	0.4302	0.7403	0.7759	0.7562	0.8152	0.4850
KNN	0.9800	0.7700	0.9300	0.9400	0.9100	0.9000	0.7700	0.7700
MTLF	0.9341	0.9200	0.7046	0.8131	0.8374	0.8274	0.9200	0.9200
LMPROJ	0.9566	0.9434	0.7806	0.8066	0.8984	0.8376	0.9037	0.9078
NMF-TL	0.9800	0.9450	0.9700	0.9980	0.9800	0.9400	0.9700	0.9700

TABLE 8 | F1_score of 8 classifiers on datasets based on SIFT feature extraction.

Method	1#	2#	3#	4#	5#	6#	7#	8#
SVM	0.9796	0.8264	0.9796	0.9765	0.8042	0.8218	0.7239	0.7470
LDA	0.9898	0.8500	0.9672	0.9801	0.9600	0.9765	0.8500	0.8500
DT	0.9987	0.9050	0.9253	0.9645	0.9900	0.9900	0.9050	0.9050
NB	0.9667	0.8850	0.4248	0.4247	0.6927	0.6972	0.8850	0.8900
KNN	0.9845	0.9150	0.9632	0.9754	0.9847	0.9667	0.9100	0.9100
MTLF	0.9900	0.9800	0.2720	0.3995	0.6766	0.8626	0.9391	0.9066
LMPROJ	0.9649	0.8661	0.3307	0.8871	0.8803	0.8812	0.8816	0.8016
NMF-TL	0.9920	0.9950	0.9987	0.9600	0.9800	0.9900	0.9700	0.9950

TABLE 9 | Recall of 8 classifiers on datasets based on WPD feature extraction.

Method	1#	2#	3#	4#	5#	6#	7#	8#
SVM	0.9600	0.9980	0.9700	0.9600	0.9700	0.9700	0.5100	0.5100
LDA	0.8700	0.7600	0.7700	0.7900	0.6000	0.6400	0.6900	0.6700
DT	0.8900	0.8600	0.8300	0.7900	0.9500	0.9100	0.6700	0.6600
NB	0.8400	0.8581	0.1200	0.2200	0.9600	0.9600	0.6521	0.6674
KNN	0.8700	0.8500	0.6300	0.6400	0.9300	0.9200	0.5600	0.5500
MTLF	0.9700	0.9393	0.5150	0.5300	0.9100	0.9050	0.7815	0.7757
LMPROJ	0.8600	0.9750	0.8700	0.8600	0.9200	0.8400	0.9750	0.9750
NMF-TL	0.9400	0.9700	0.9200	0.9300	0.9600	0.9700	0.9400	0.8800

A/B/D experimental groups, and that in the A/B/C experimental group increased by about 6%; compared with the other two transfer learning methods, it increased by about 66% in the A/C experimental group and in other experimental groups obvious improvement has also been observed.

We record the recall results of 8 classification methods based on WPD feature extraction in **Table 9**. As shown in **Table 9**, compared with the baseline method, the recall rate of the proposed method in the A/B/C and A/B/D groups increased by about 22%; compared with the two transfer learning methods, the recall rate of our method in the A/C and B/C experimental groups increased by about 4%, and the recall rate in the A/D, B/D, and A/B/C experimental groups increased by about 6.5%.

TABLE 10 | Recall of 8 classifiers on datasets based on SITF feature extraction.

Method	1#	2#	3#	4#	5#	6#	7#	8#
SVM	0.9800	0.8350	0.8650	0.9650	0.9750	0.9850	0.6300	0.6650
LDA	0.9800	0.9700	0.0400	0.1300	0.2600	0.3300	0.0400	0.1300
DT	0.9900	0.9800	0.3000	0.4400	0.1300	0.3000	0.1300	0.3100
NB	0.9875	0.9548	0.4100	0.4100	0.9750	0.9800	0.6618	0.6594
KNN	0.9900	0.9870	0.0400	0.1300	0.0400	0.0800	0.0400	0.0800
MTLF	0.9850	0.9847	0.2391	0.3000	0.9750	0.9635	0.6588	0.7049
LMPROJ	0.9700	0.9550	0.2000	0.9575	0.9200	0.9125	0.9525	0.9675
NMF-TL	0.9987	0.9900	0.9400	0.9700	0.9600	0.9400	0.9000	0.8600

TABLE 11 | Recall of 8 classifiers on datasets based on PCA feature extraction.

Method	1#	2#	3#	4#	5#	6#	7#	8#
SVM	0.9550	0.9650	0.9200	0.9400	0.5600	0.5600	0.4600	0.4600
LDA	0.9000	0.6200	0.8800	0.9600	0.9600	0.9600	0.8800	0.9600
DT	0.9600	0.8700	0.7900	0.9800	0.8300	0.8800	0.7100	0.9700
NB	0.7700	0.8643	0.2800	0.7500	0.7100	0.7100	0.6809	0.8060
KNN	0.9800	0.7700	0.9300	0.9400	0.9100	0.9000	0.7700	0.7700
MTLF	0.9200	0.9898	0.7000	0.7000	0.9500	0.9525	0.7898	0.8534
LMPROJ	0.9600	0.9450	0.9500	0.9550	0.9700	0.9200	0.9600	0.9600
NMF-TL	0.9700	0.9600	0.9900	0.9600	0.9800	0.9800	0.9300	0.9700

TABLE 12 | Friedman values for 8 different methods on datasets based on WPD feature extraction.

Method	1#	2#	3#	4#	5#	6#	7#	8#
SVM	1.420	37.81	36.01	36.64	0.4300	1.200	38.14	27.41
LDA	7.128	11.42	1.48	3.528	9.148	3.020	3.045	12.23
DT	0.7375	3.788	0.6325	1.418	0.5150	0.8775	0.2700	1.408
NB	1.818	6.735	25.40	17.75	9.423	11.36	28.11	20.25
KNN	2.260	2.368	3.562	1.470	9.910	1.628	13.25	3.648
MTLF	0.1725	0.4475	12.60	10.80	3.980	5.590	12.16	10.86
LMPROJ	2.250	14.74	1.788	0.3450	5.288	3.245	28.73	30.51
NMF-TL	0.8150	0.3700	2.853	1.178	1.255	0.3225	1.238	1.023

TABLE 13 | Friedman values for 8 different methods on datasets based on SIFT feature extraction.

Method	1#	2#	3#	4#	5#	6#	7#	8#
SVM	0.430	35.27	36.06	36.64	27.27	11.71	15.88	9.250
LDA	16.50	16.00	14.52	13.55	18.67	21.72	18.12	17.78
DT	8.593	23.98	7.800	12.89	8.280	15.47	14.95	30.32
NB	0.1075	1.283	23.04	25.43	31.86	25.96	25.13	33.13
KNN	16.80	35.85	17.12	27.64	16.65	31.67	15.76	28.85
LMPROJ	1.00	14.00	26.10	4.310	1.010	0.9300	21.73	38.74
MTLF	0.4125	0.085	35.11	28.40	8.670	8.648	33.47	26.43
NMF-TL	0.4300	0.2850	6.195	0.7825	0.5150	3.300	3.865	2.028

TABLE 14 | Friedman values for 8 different methods on datasets based on KPCA feature extraction.

Method	1#	2#	3#	4#	5#	6#	7#	8#
SVM	14.75	37.46	28.83	7.850	9.773	33.44	8.365	27.28
LDA	1.565	0.9150	2.570	4.422	2.220	0.6975	0.7675	2.165
DT	1.223	1.010	2.085	2.727	2.143	2.800	2.433	4.095
NB	2.213	21.05	5.057	21.55	2.513	1.095	13.15	2.580
KNN	1.165	0.3075	3.162	0.8975	1.445	0.3050	0.2450	4.475
LMPROJ	0.5450	0.4900	11.59	8.845	2.665	5.875	4.033	35.63
MTLF	0.1725	0.3825	12.73	7.200	7.773	5.955	11.04	5.973
NMF-TL	0.3625	0.7600	0.2575	0.6225	0.8150	2.307	0.2150	2.545

In **Table 10**, we can see that the proposed method has achieved good results in terms of recall rate. In the B/C group, the difference is only 1.5% compared with the optimal result. In A/E, the proposed method is 0.87% higher than the optimal value. In the A/B/E, A/C, A/D, and A/B/C groups, the NMF-TL method has achieved the best results. In the B/C group, the proposed method is only 1.5% lower than the optimal value, which indicates that the NMF-TL method is good in this group of experiments.

From **Table 11**, we can see that except the A/B/E and A/B/C groups, the proposed method has achieved the best results. At the same time, in the A/B/E group the proposed method is only 1% lower than the optimal value and in A/B/C group, the difference is more, which is a decrease by 3%.

In summary, from the recall results shown in **Tables 9–11**, we can draw the following conclusion:

(1) Recall rate means the probability of being predicted as a positive sample in the actual positive sample. In **Table 9**, we can clearly see that our method has achieved good results, which also proves that our method rarely has misdiagnosis results in the detection process and improves the accuracy of our diagnosis results.
(2) In the diagnosis of diseases, there will be misdiagnosis. A good detection method can greatly reduce the incidence of misdiagnosis. In this experiment, our method is obviously better than other methods.
(3) The higher the recall rate, the lower the misdiagnosis rate of the correct samples. The lower the misdiagnosis rate in medical diagnosis, the more conducive it is to the relevant practitioners to make judgment as soon as possible. In this group of experiments, our method has achieved good results, which shows that compared with other methods, our algorithm has a lower misdiagnosis rate.

Friedman and Nemenyi Tests

Friedman and Nemenyi tests are used to compare several algorithms on 8 different datasets. The Friedman test can analyze whether there exist obvious differences between all comparison algorithms on multiple data sets. Nemenyi was used to further analyze whether those pairs of algorithms have significant differences. In **Tables 12–14**, we report Friedman values for each algorithm on 8 datasets with three different feature extraction methods. **Figures 7–9** show the Nemenyi test chart for each algorithm on 8 datasets with three different feature extraction methods.

From **Tables 12–14**, we draw the following conclusions.

(1) For WPD feature extraction, it can be seen that the proposed method has achieved good results in several groups. In the experiments of the A/B/E, B/D, and A/B/D groups, our results have won the first place; in the comparison of the A/E, A/C, and B/C groups, ours got the third place; and in the rest of the groups, ours got the second place. We can see that the proposed method has obvious differences with other algorithms, especially with SVM, LDA, NB, and KNN. This is because the traditional classification method is not suitable for transfer learning circumstances which need to find the potential relationship between the source and the target domain.

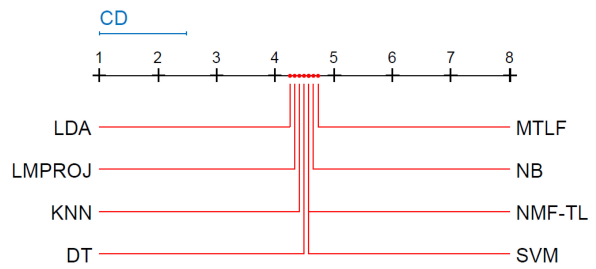

FIGURE 7 | Nemenyi test chart of 8 different methods on datasets based on WPD feature extraction.

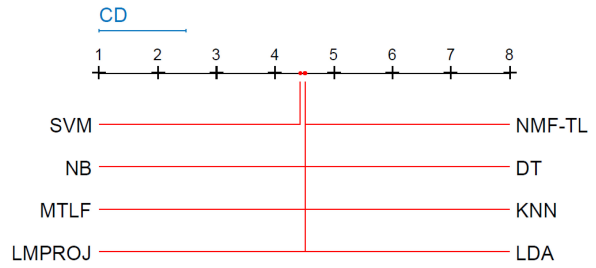

FIGURE 8 | Nemenyi test chart of 8 different methods on datasets based on SIFT feature extraction.

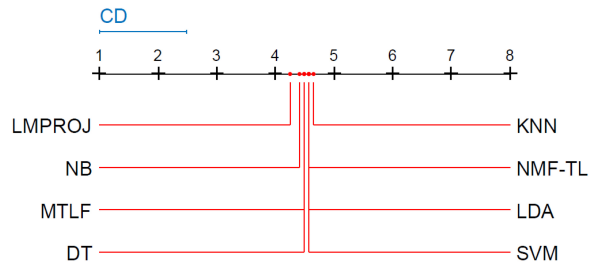

FIGURE 9 | Nemenyi test chart of 8 different methods on datasets based on KPCA feature extraction.

(2) For SIFT feature extraction, our method got the first place in most of the experiments, the third place in the A/E group, and the second place in the B/D group.
(3) For KPCA feature extraction, our experimental results are almost the same as those of other feature extractions and we also get the best results in many groups, but the results in the A/B/E and B/D groups are not very ideal, and our results are not as good as those of other experiments.

The horizontal line in **Figure 7** indicates the size of the average order value. The solid dot on the horizontal line represents the average order value of each corresponding algorithm. The blue line represents the size of the CD value. The red line represents the CD value of each algorithm. The more there are overlapping red lines, the more similar the performance of the two algorithms. From **Figure 7**, we can see that our method is significantly higher than the critical value CD compared with other methods, and it also shows that our method has a completely different performance from other methods.

From Figure8, we can see that the values of several models are significantly larger than the CD value, which also shows that our method is significantly different from other methods based on SITF feature extraction, and there is no model similar to our experimental model. At the same time, in addition to SVM, other models are similar.

From **Figure 9**, we can see that compared with other groups of experiments, the *p*-value we obtained in this group of experiments is the largest, which shows that compared with WPD and SIFT feature extraction, there are greater differences in the models of this group of experiments. We can see that the performance of our method is not as good as other methods, such as LMPROJ, NB, MTLF, and DT. This is because our method needs to extract the shared potential features between the source and the target domain, which leads to the performance degradation of our method. In terms of performance, LDA and SVM are most similar to our method.

CONCLUSION

In this paper, we proposed new transfer learning methods based on non-negative matrix factorization with the large margin principle for EEG signal classification. Specifically, we first learned the shared hidden subspace data between the source domain and the target domain, then we trained the SVM classifier on the augmented feature space consisting of the original feature space and the shared hidden subspace, and finally we use the learned classifier to classify the new target domain data. Extensive experiments confirmed the effectiveness of the proposed method. As future work, we will evaluate the proposed method on more new datasets, such as the Chinese physiological signal challenge dataset on electrocardiogram classification.

DATA AVAILABILITY STATEMENT

The dataset analyzed for this study can be found in the Department of Epileptology University of 19 Bonn (http://epileptologie-bonn.de/cms/upload/workgroup/lehnertz/eegdata.html).

AUTHOR CONTRIBUTIONS

AD developed the theoretical framework and model in this work and drafted and revised the manuscript. ZL and QZ implemented the algorithm and performed experiments and result analysis.

FUNDING

This study was supported by the National Natural Science Foundation of China under Grant (Nos. 61703219 and 61702292).

REFERENCES

Aarabi, A., Fazel-Rezai, R., and Aghakhani, Y. (2009). A fuzzy rule-based system for epileptic seizure detection in intracranial EEG. *Clin. Neurophysiol.* 120, 1648–1657. doi: 10.1016/j.clinph.2009.07.002

Acharya, U. R., Sree, S. V., Swapna, G., Martis, R. J., and Suri, J. S. (2013). Automated EEG analysis of epilepsy: a review. *Knowl. Based Syst.* 45, 147–165. doi: 10.1016/j.knosys.2013.02.014

Altunay, S., Telatar, Z., and Erogul, O. (2010). Epileptic EEG detection using the linear prediction error energy. *Expert Syst. Appl.* 37, 5661–5665. doi: 10.1016/j.eswa.2010.02.045

Bajaj, V., and Pachori, R. B. (2012). Classification of seizure and nonseizure EEG signals using empirical mode decomposition. *IEEE Trans. Inform. Technol. Biomed.* 16, 1135–1142. doi: 10.1109/titb.2011.2181403

Chen, X., Gu, L., Li, S. Z., and Zhang, H.-J. (2001). "Learning representative local features for face detection," in *Proceedigs of the IEEE Computer Society Conference on Computer Vision and Pattern Recognition. CVPR 2001* (Kauai, HI: IEEE).

Cover, T. M., and Hart, P. E. (1967). Nearest neighbor pattern classification. *IEEE Trans. Inform. Theory* 13, 21–27.

Deryaübeyl, E., and Güler, I. (2004). Spectral analysis of internal carotid arterial Doppler signals using FFT. AR, MA, and ARMA methods. *Comput. Biol. Med.* 34, 293–306. doi: 10.1016/s0010-4825(03)00060-x

Dong, A. M., and Wang, S. T. (2014). A shared latent subspace transfer learning algorithm using SVM. *Acta Automatica Sinica* 40, 2276–2287.

Dorai, A., and Ponnambalam, K. (2010). "Automated epileptic seizure onset detection," in *Proceedings of the International Conference On Autonomous and Intelligent Systems (AIS), 2010* (Piscataway, NJ: IEEE), 1–4. doi: 10.3233/jifs-200800

Faust, O., Acharya, R. U., Allen, A. R., and Lin, C. M. (2008). Analysis of EEG signals during epileptic and alcoholic states using AR modeling techniques. *Irbm* 29, 44–52. doi: 10.1016/j.rbmret.2007.11.003

Fouad, M., Amin, K. M., El-Bendary, N., and Hassanien, A. E. (2015). "Brain computer interface: a review," in *Brain-Computer Interfaces. Intelligent Systems Reference Library*, Vol. 74, eds A. Hassanien and A. Azar (Cham: Springer), 3–30.

Ghosh-Dastidar, S., Adeli, H., and Dadmehr, N. (2008). Principal component analysis-enhanced cosine radial basis function neural network for robust epilepsy and seizure detection. *IEEE Trans. Biomed. Eng.* 55, 512–518. doi: 10.1109/tbme.2007.905490

Goker, I., Osman, I., Ozekes, S., Baslo, M. B., Ertas, M., and Ulgen, Y. (2012). Classification of junenile myoclonic epilepsy data acquired through scanning electromyography with machine learning algorithms. *J. Med. Syst.* 36, 2705–2711. doi: 10.1007/s10916-011-9746-6

Guler, I., and Ubeyli, E. D. (2007). Multiclass support vector machines for EEG-signals classification. *IEEE Trans. Inform. Technol. Biomed.* 11, 117–126. doi: 10.1109/titb.2006.879600

Iscan, Z., Dokur, Z., and Demiralp, T. (2011). Classification of electroencephalogram signals with combined time and frequency features. *Expert Syst. Appl.* 38, 10499–10505. doi: 10.1016/j.eswa.2011.02.110

Jiang, Y., Wu, D., Deng, Z., Pengjiang Qian, P., Wang, J., Wang, G., et al. (2017). Seizure classification from EEG signals using transfer learning. Semi-Supervised Learning and TSK Fuzzy System. *IEEE Trans. Neural Syst. Rehabil. Eng.* 25, 2270–2284. doi: 10.1109/tnsre.2017.2748388

Joshi, V., Pachiori, R. B., and Vijesh, A. (2014). Classification of ictal and seizure-free EEG signals using fractional linear prediction. *Biomed. Signal Process. Control* 9, 1–5. doi: 10.1016/j.bspc.2013.08.006

Jung, T. P., Makeig, S., Mckeown, M. J., Bell, A. J., Lee, T. W., and Sejnowski, T. J. (2001). Imaging brain dynamics using independent component analysis. *Proc. IEEE Inst. Electr. Electron. Eng.* 89, 1107–1122. doi: 10.1109/5.939827

Lee, D. D., and Seung, H. S. (1999). Learning the parts of objects by non-negative matrix factorization. *Nature* 401, 788–791. doi: 10.1038/44565

Li, S. Z., Hou, X. W., Zhang, H. J., and Cheng, Q. S. (2001). "Learning spatially localized, parts-based representation," in *Proceedings of the 2001 IEEE Computer Society Conference on Computer Vision and Pattern Recognition. CVPR 2001* (Kauai, HI: IEEE).

Oweis, R. J., and Abdulhay, E. W. (2011). Seizure classification in EEG signals utilizing Hilbert–Huang transform. *BioMed. Eng. OnLine* 10:38. doi: 10.1186/1475-925x-10-38

Patel, R., Gireesan, K., and Sengottuvel, S. (2018). Decoding non-linearity for effective extraction of the eye-blink artifact pattern from EEG recordings. *Pattern Recognit. Lett.* 139, 42–49.

Peng, P., and Lu, B. L. (2012). "Immune clonal algorithm based feature selection for epileptic EEG signal classification," in *Proceedings of the 11th International Conference on Information Science, Signal Processing and their Applications (ISSPA)* (Montreal, QC: IEEE), 848–853.

Polat, K., and Güne, S. (2007). Classification of epileptiform EEG using a hybrid system based on decision tree classifier and fast Fourier transform. *Appl. Math. Comput.* 187, 1017–1026. doi: 10.1016/j.amc.2006.09.022

Quanz, B., and Huan, J. (2009). "Large margin transductive transfer learning," in *Proceedings of the .18th ACM Conference on Information And Knowledge Management* (New York, NY: Association for Computing Machinery), 1327–1336.

Raghu, A. B. S., Sriraam, N., Temel, Y., Rao, S. V., and Kubben, P. L. (2020). EEG based multi-class seizure type classification using convolutional neural network and transfer learning. *Neural Netw.* 124, 202–212. doi: 10.1016/j.neunet.2020.01.017

Subasi, A. (2007). EEG signal classification using wavelet feature extraction and a mixture of expert model. *Expert Syst. Appl.* 32, 1084–1093. doi: 10.1016/j.eswa.2006.02.005

Subasi, A., and Gursoy, M. I. (2010). EEG signal classification using PCA. ICA, LDA and support vector machines. *Experts Syst. Appl.* 37, 8659–8666. doi: 10.1016/j.eswa.2010.06.065

Talevi, A., Cravero, M. S., and Castro, E. A. (2007). Discovery of antivonvulsant activity of abietic acid through application of linear discriminant analysis. *Bioorg. Med. Chem. Lett.* 17, 1684–1690. doi: 10.1016/j.bmcl.2006.12.098

Tazllas, A. T., Tsipouras, M. G., and Fotiadis, D. I. (2009). Epileptic seizure detection in EEGs using time-frequency features. *IEEE Trans. Inf. Technol. Biomed.* 13, 703–710. doi: 10.1109/titb.2009.2017939

Temko, A., Thomas, E., Marnane, W., Lightbody, G., and Boylan, G. (2011). EEG-based neonatal seizure detection with support vector machines. *Clin. Neurophysiol.* 22, 464–473. doi: 10.1016/j.clinph.2010.06.034

Ting, W., Guo-Zheng, Y., Bang-Hua, Y., and Hong, S. (2008). EEG feature extraction based on wavelet packet decomposition for brain computer interface. *Measurement* 41, 618–625. doi: 10.1016/j.measurement.2007.07.007

Tu, W. T., and Sun, S. L. (2012). A subject transfer framework for EEG classification. *Neurocomputing* 82, 109–116. doi: 10.1016/j.neucom.2011.10.024

Viola, F. C., Thorne, J., Edmonds, B., Schneider, T., Eichele, T., and Debener, S. (2009). Semi-automatic identification of independent components representing EEG artifact. *Clin. Neurophysiol.* 48, 1470–1480.

Wang, G., Kossenkov, A. V., and Ochs, M. F. (2006). LS-NMF: a modified non-negative matrix factorization algorithm utilizing uncertainty estimates. *BMC Bioinformatics* 7:175. doi: 10.1186/1471-2105-7-175

Wang, Y., Jia, Y., Hu, C., and Turk, M. (2004). Fisher non-negative matrix factorization for learning local features. *Res. Gate* 2004, 27–30.

Welch, P. D. (1967). The use of fast Fourier transform for the estimation of power spectra: a method based on time averaging over short, modified periodograms. *IEEE Trans. Audio Electroacoust.* 15, 70–73. doi: 10.1109/tau.1967.1161901

Xu, B., Lu, J., and Huang, G. (2003). "A constrained non-negative matrix factorization in information retrieval," in *Proceedings of the IEEE International Conference on Information Reuse and Integration IRI 2003*, Las Vegas, NV: IEEE.

Xu, Y. H., Pan, S. J. L., Xiong, H., Wu, Q., Luo, R., Min, H., et al. (2017). A unified framework for metric transfer learning. *IEEE Trans. Knowl. Data Eng.* 29, 1158–1171.

Yang, C. J., Deng, Z., Choi, K. S., Jiang, Y., and Wang, S. (2014). Transductive domain adaptive learning for epileptic electroencephalogram recognition. *Artif. Intell. Med.* 62, 165–177. doi: 10.1016/j.artmed.2014.10.002

Conflict of Interest: The authors declare that the research was conducted in the absence of any commercial or financial relationships that could be construed as a potential conflict of interest.

frontiers in Neuroscience

ORIGINAL RESEARCH
published: 01 April 2021
doi: 10.3389/fnins.2021.669345

Constructing Dynamic Brain Functional Networks via Hyper-Graph Manifold Regularization for Mild Cognitive Impairment Classification

Yixin Ji[1,2], Yutao Zhang[1], Haifeng Shi[3], Zhuqing Jiao[1,2], Shui-Hua Wang[4]* and Chuang Wang[5]**

[1] School of Microelectronics and Control Engineering, Changzhou University, Changzhou, China, [2] School of Computer Science and Artificial Intelligence, Changzhou University, Changzhou, China, [3] Department of Radiology, Changzhou Second People's Hospital Affiliated to Nanjing Medical University, Changzhou, China, [4] School of Informatics, University of Leicester, Leicester, United Kingdom, [5] School of Medicine, Ningbo University, Ningbo, China

OPEN ACCESS

Edited by:
Mohammad Khosravi, Persian Gulf University, Iran

Reviewed by:
Xia-an Bi, Hunan Normal University, China
Weikai Li, Nanjing University of Aeronautics and Astronautics, China

***Correspondence:**
Zhuqing Jiao
jzq@cczu.edu.cn
Shui-Hua Wang
shuihuawang@ieee.org
Chuang Wang
wangchuang@nbu.edu.cn

Specialty section:
This article was submitted to Neuroprosthetics, a section of the journal Frontiers in Neuroscience

Received: *18 February 2021*
Accepted: *11 March 2021*
Published: *01 April 2021*

Citation:
Ji Y, Zhang Y, Shi H, Jiao Z, Wang S-H and Wang C (2021) Constructing Dynamic Brain Functional Networks via Hyper-Graph Manifold Regularization for Mild Cognitive Impairment Classification. Front. Neurosci. 15:669345. doi: 10.3389/fnins.2021.669345

Brain functional networks (BFNs) constructed via manifold regularization (MR) have emerged as a powerful tool in finding new biomarkers for brain disease diagnosis. However, they only describe the pair-wise relationship between two brain regions, and cannot describe the functional interaction between multiple brain regions, or the high-order relationship, well. To solve this issue, we propose a method to construct dynamic BFNs (DBFNs) via hyper-graph MR (HMR) and employ it to classify mild cognitive impairment (MCI) subjects. First, we construct DBFNs via *Pearson*'s correlation (PC) method and remodel the PC method as an optimization model. Then, we use *k*-nearest neighbor (KNN) algorithm to construct the hyper-graph and obtain the hyper-graph manifold regularizer based on the hyper-graph. We introduce the hyper-graph manifold regularizer and the $L1$-norm regularizer into the PC-based optimization model to optimize DBFNs and obtain the final sparse DBFNs (SDBFNs). Finally, we conduct classification experiments to classify MCI subjects from normal subjects to verify the effectiveness of our method. Experimental results show that the proposed method achieves better classification performance compared with other state-of-the-art methods, and the classification accuracy (ACC), the sensitivity (SEN), the specificity (SPE), and the area under the curve (AUC) reach $82.4946 \pm 0.2827\%$, $77.2473 \pm 0.5747\%$, $87.7419 \pm 0.2286\%$, and 0.9021 ± 0.0007, respectively. This method expands the MR method and DBFNs with more biological significance. It can effectively improve the classification performance of DBFNs for MCI, and has certain reference value for the research and auxiliary diagnosis of Alzheimer's disease (AD).

Keywords: mild cognitive impairment, Alzheimer's disease, dynamic brain functional network, manifold regularization, hyper-graph

INTRODUCTION

Alzheimer's disease (AD) is a primary degenerative brain disease that occurs in senectitude and presenium (Lu et al., 2019; Bi et al., 2021). AD creates issues in memory, thinking, analysis, judgment, visual and spatial recognition, and emotional regulation. However, there are currently no specific treatments or therapeutic drugs to reverse disease progression. Mild cognitive impairment (MCI) is also a type of dementia, and is an intermediate stage between normal people and AD patients. In clinical practice, MCI is mostly manifested as a decline in cognitive function and memory, but it does not affect the daily life of patients (Muldoon and Bassett, 2016). Related research has shown that the annual conversion rate of MCI to AD is about 10–15% (Jiao et al., 2014; Zhang et al., 2015b). MCI due to AD provides a potential window to detect and diagnose AD before significant neurodegeneration has begun. Early active intervention treatment for MCI can improve or delay its cognitive decline and even the development of AD (Alzheimer's Association, 2012). Therefore, the accurate identification of MCI and the intervention of MCI through drug and non-drug pathways to reduce the AD conversion rate have attracted great attention from researchers (Gauthier et al., 2006; Tobia et al., 2017). It is important to explore which subjects will progress from MCI to AD, as there are predictors of progression that will indicate a more rapid rate of progression in MCI subjects.

Nowadays, neuroimaging technology is widely used in the detection and research of brain diseases. Some existing brain imaging techniques include magnetic resonance imaging (MRI) technology (Zhang et al., 2015a), functional MRI (fMRI) (Zhang Y. D. et al., 2016), and diffusion MRI (Basser and Pierpaoli, 2011). Electrophysiology techniques, including electroencephalogram (EEG) (Jung et al., 2000), magnetoencephalography (MEG) (Smythies et al., 2005), and positron emission technology (PET) (Mourik et al., 2009), provide effective and non-invasive methods to explore the brain and its connection patterns, revealing brain functions and brain structures that could not be revealed before. Many medical and biological studies have shown that human cognitive processes usually rely on pair-wise relationships between different neurons and brain regions (Ou et al., 2015). The brain functional network (BFN) can describe the function or structural interaction of the brain at the entire brain connection level (Rubinov and Sporns, 2010); thus, it provides a new tool for exploring the function and structure of the brain. In the research based on resting-state fMRI, the BFN is generally constructed through the full time series of resting state. Most recent studies have shown that brain neural activity changes dynamically over time, and this dynamic change will contain more abundant information (Chang and Glover, 2010). Therefore, research on dynamic BFN (DBFN) will help us further explore the operation mode of the whole brain, and it is conducive to the auxiliary diagnosis of brain diseases.

In research based on BFNs, how to construct BFNs is a very important procedure. Researchers have proposed many methods for constructing BFNs, from the simplest method for constructing BFNs based on *Pearson*'s correlation (PC) (Jiang et al., 2019), to the partial correlation method (Jiang et al., 2019), to the dynamic causal model method (Roebroeck et al., 2005), etc. However, these methods have their shortcomings. For example, the PC method can only calculate the full correlation, and it cannot remove the redundant effects of other brain regions. The BFN construction method based on partial correlation may lead to ill-posed problems (Li et al., 2019). Now, adding regularizers to the PC method or the partial method can result in better BFNs. Regularizers mainly reflect some prior information of the brain, such as sparsity (Qiao et al., 2016), modularity (Qiao et al., 2016), group sparsity (Wee et al., 2014), scale-free property (Li et al., 2017), etc. These properties are transformed into corresponding regularizers embedded in the construction of BFNs through certain transformations to obtain BFNs containing more prior information.

Recently, BFNs via manifold regularization (MR) have been widely used in studies. About MR, Li et al. (2020c) proposed a hypothesis: if two brain regions are very close in space, then the functional connections between them and other brain regions may share similar connection patterns. It means that these brain regions have similar topological properties. Li et al. (2020c) transformed this similarity into a manifold regularizer and introduced it to construct BFNs. Xue et al. (2020) constructed BFNs based on the same idea, and introduced the distance information between brain regions into the manifold regularizers. However, most studies just consider the pair correlation between brain regions, but ignore the high-order relationship which reflects interactive information between multiple brain regions. This could be a drawback because the BFN itself is a complex network. Recent studies have shown that a brain region usually directly interacts with several neighboring brain regions, forming a complex interactive relationship. Therefore, the high-order relationship between brain regions may contain some discriminative information to improve the classification performance. Hyper-graph is a good choice to describe the high-order relationship between multiple nodes in a graph (Yu et al., 2014), and has been successfully applied in many fields. In traditional graphs, one edge of the graph can only connect two related vertices. In practice, the relationship between objects is much more complicated than the pairwise relationship. Hyper-graph is an extension of traditional graphs. In a hyper-graph, a hyper-edge is a collection of any number of nodes, which can connect any number of nodes, so it is natural to use hyper-graphs to model high-order relationships. Zhou et al. (2007) proposed a hyper-graph learning method for clustering, classification, and embedding learning, and the hyper-graph Laplacian operator was used to describe the complex relationship between multiple samples. Jie et al. (2016) used sparse representation (SR) method to construct hyper-graph and applied it to the diagnosis of AD and MCI patients.

Most of the above studies performed feature extraction, feature selection, and classification for hyper-graph directly. But few studies convert the hyper-graph into a regularizer and introduce it into the construction of BFNs. To solve these problems, we propose a method for constructing DBFNs via hyper-graph MR (HMR) and apply this method to differentiate MCI subjects from normal subjects. First, we construct DBFNs and transform the PC method into an optimization model.

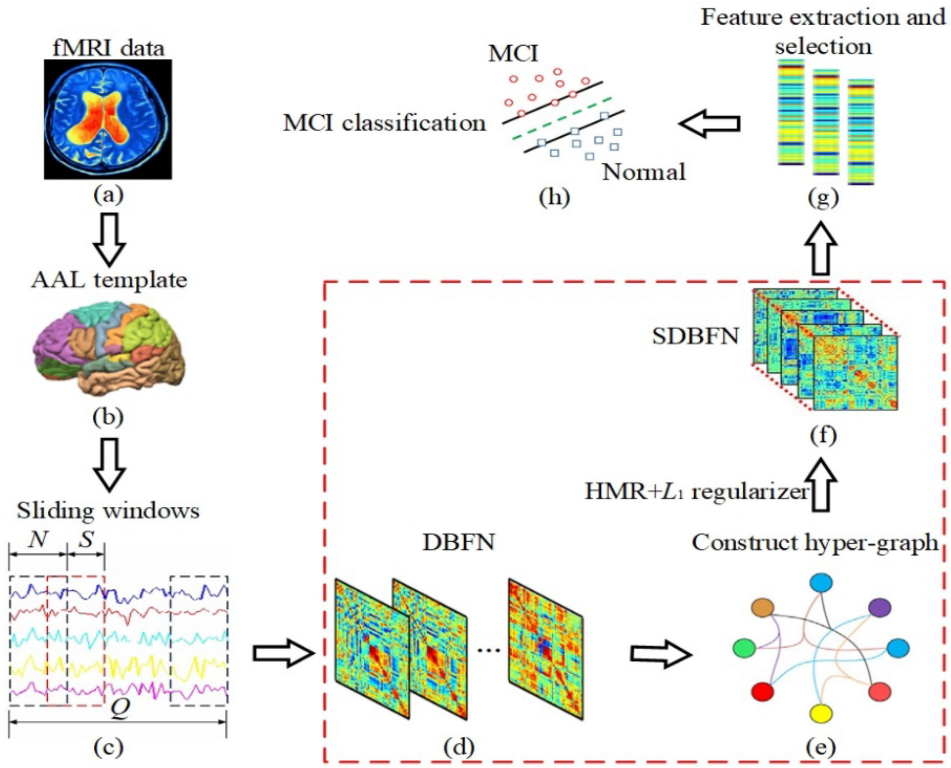

FIGURE 1 | The framework of constructing SDBFNs via SHMR for MCI classification. The area marked in red box is the key research part. **(a)** Preprocessing the obtained resting-state fMRI data of two types of subjects; **(b)** registering the preprocessed resting-state fMRI data to 90 brain regions according to the AAL template, and obtaining the time series of all brain regions; **(c)** dividing the entire time series into multiple overlapping sub-sequence segments by sliding window method; **(d)** constructing DBFNs based on the PC method and transforming it into an optimized model; **(e)** constructing hyper-graphs based on DBFNs and obtaining hyper-graph Laplacian matrices; **(f)** constructing the manifold regularizer by hyper-graph Laplacian matrices, and introducing the manifold regularizer and $L1$-norm regularizer into the optimization model of the PC method to obtain SDBFNs; **(g)** extracting the weighted-graph local clustering coefficient of each brain region in SDBFNs, and using the t-test for feature selection; and **(h)** training a linear kernel SVM classifier to classify the SDBFNs of all subjects and analyzing the classification performance.

Next, we construct hyper-graphs based on DBFNs and obtain the hyper-graph manifold regularizer. Then, we introduce the hyper-graph manifold regularizer and $L1$-norm regularizer into the optimization model of the PC method to obtain the sparse DBFNs (SDBFNs). After that, we extract the weighted-graph local clustering coefficient of each brain region in two types of subjects' SDBFNs as an effective feature and use t-test for feature selection from SDBFNs. Finally, we train a linear kernel support vector machine (SVM) to classify the SDBFNs of all subjects and analyze the classification performance. Furthermore, we also investigate the parameter sensitivities on classification performance and some discriminative brain regions.

MATERIALS AND METHODS

Data Acquisition and Processing

The subjects were recruited through local newspapers and media in North Carolina[1] (Qiao et al., 2016; Li et al., 2020b). They are all right-handed and have no history of neurological or mental illness, and no history of alcohol or drug abuse. Excluding these who frequently use psychotropic drugs, stimulants, and β-blockers, all subjects received standard neuropsychological assessments and responses.

Raw fMRI images are scanned by the 3T Siemens TRIO scanner. The image size is 74 × 74 × 45, the voxel size is 2.97 × 2.97 × 3 mm^3, and the repetition time (TR) is 3000 ms with 180 volumes. The raw resting-state fMRI data are preprocessed by using the SPM toolbox[2] and DPARSFA[3] toolbox of Matlab R2012a software. In order to avoid signals dithering, the first 10 fMRI images are discarded. The remaining images are first corrected in time layer and head motion, and then the images are spatially normalized and linear drift removed. Band-pass filtering is performed with 0.01–0.08 Hz to remove the interference of blood flow and power frequency. In addition, the generalized linear model is used to remove covariates such as head movement parameters, white matter, gray matter, and

[1]http://www.nitrc.org/projects/modularbrain/

[2]http://www.fil.ion.ucl.ac.uk/spm/

[3]http://rfmri.org/dparsf/

TABLE 1 | The specific group characteristics of the subjects.

Group characteristic	MCI	Normal
Gender (male/female)	25M / 20F	14M / 32F
Age (mean ± SD)	74.13 ± 6.68	73.5 ± 3.50
MMSE (mean ± SD)	27.71 ± 1.73	28.10 ± 1.35

cerebrospinal fluid. Finally, we clean the data with frame-wise displacements (FD) > 0.5. Data are registered through the Anatomical Automatic Labeling (AAL) atlas (Tzourio-Mazoyer et al., 2002), and blood oxygenation level-dependent (BOLD) signals in each brain region are extracted by means of mean value. Screened by data time points are greater than 80, and BOLD signals of 91 subjects (45 MCI subjects and 46 normal subjects) are retained. **Table 1** shows the specific group characteristics of the subjects, including their Mini-Mental State Examination (MMSE) scores.

Conventional DBFN Construction

Suppose $\mathbf{X} = \left[\boldsymbol{x}_1, \boldsymbol{x}_2, ..., \boldsymbol{x}_p\right] \in \mathbb{R}^{Q\times P}$ is a time series matrix, Q is the total number of time points, P is the number of brain regions, and $\boldsymbol{x}_i, \boldsymbol{x}_j \in \mathbb{R}^{Q\times 1}$ are the time series vectors of the ith brain region and the jth brain region. We use the sliding window method to divide the entire time series into several overlapping time sub-segments (Chen et al., 2016). Assuming that the window width is N and the step size is S, defining $\boldsymbol{x}_i^{(l)}(k) \in \mathbb{R}^{N\times 1}$ as the k-th sub-segment extracted from the time series of the lth subject. The total number of windows K is expressed as:

$$K = \frac{Q-N}{S} + 1, 1 \le k \le K \tag{1}$$

Then we calculate the PC coefficient between each sub-segment and construct DBFNs. $\boldsymbol{x}_i^k \in \mathbb{R}^N, \left(k = 1, ..., K\right)$ denotes the time series of the ith brain region in the kth window, and the time series matrix $\boldsymbol{X}^{(k)} = \left[\boldsymbol{x}_1^k, \boldsymbol{x}_2^k, ..., \boldsymbol{x}_P^k\right] \in \mathbb{R}^{N\times P}$ in the kth window concatenate $\mathbf{x}_i^k$ in series. The correlation coefficient matrix of BFN $W^{(k)}$ in the kth window is $\boldsymbol{W}^{(k)} = \left(\boldsymbol{X}^{(k)}\right)^T \boldsymbol{X}^{(k)}$. Convert this formula to the optimized form as:

$$\min_{\boldsymbol{W}^{(k)}} ||\boldsymbol{W}^{(k)} - \boldsymbol{X}^{(k)^T}\boldsymbol{X}^{(k)}||_F^2 \tag{2}$$

BFN Construction Based on MR

Li et al. (2020c) were inspired by the existence of similar connection patterns (i.e., similar internal structures) in BFNs and proposed a method for constructing sparse BFNs via MR. Li et al. (2020c) also extended MR, embedded the sparse prior information, and obtained the extended method SMR. The objective function of SMR can be formulated as:

$$\min_{\boldsymbol{W}} ||\boldsymbol{X}\text{-}\boldsymbol{X}\boldsymbol{W}||_F^2 + \lambda||\boldsymbol{W}||_1 + \beta tr\left(\boldsymbol{W}^T\boldsymbol{L}\boldsymbol{W}\right) \tag{3}$$

where $||.||_F^2$ represents the square of the F-norm, $||.||_1$ represents the $L1$-norm, λ is a regularization parameter of $L1$-norm regularizer, and β is the regularization parameter of manifold regularizer. tr(.) represents the trace of the matrix, $\boldsymbol{L}$ is the Laplacian matrix, and its solution method is $\boldsymbol{L} = \boldsymbol{I} - \boldsymbol{D}^{-\frac{1}{2}}\boldsymbol{S}\boldsymbol{D}^{-\frac{1}{2}}$. $\boldsymbol{I}$ is the identity matrix and $\boldsymbol{D}$ is a diagonal matrix. The diagonal elements in $\boldsymbol{D}$ are expressed as $D_{ii} = \sum_{j=1}^{N} W_{ij}$. $\boldsymbol{S}$ is the correlation coefficient matrix of the BFN constructed based on the PC method. When $\lambda = 0$, this method changes into the BFN construction method based on MR.

DBFN Construction Based on HMR

Hyper-graph is an extension of conventional graph. Denote a hyper-graph as $\boldsymbol{G}(\boldsymbol{V}, \boldsymbol{E}, \boldsymbol{A})$, where $\boldsymbol{V}$ represents the set of vertices, $\boldsymbol{E}$ represents the set of hyper-edges, and $\boldsymbol{A}$ represents the set of weights of each hyper-edge. For the hyper-graph $\boldsymbol{G}$, we use the correlation matrix $\boldsymbol{H}\in\mathbb{R}^{|\mathbf{V}|\times|\mathbf{E}|}$ to describe the relationship between vertices and hyper-edges; it can be formulated as:

$$H(v, e) = \begin{cases} 1, if\ v \in e \\ 0, if\ v \notin e \end{cases} \tag{4}$$

where $v \in \boldsymbol{V}$ is a node in $\boldsymbol{G}$ and $e \in \mathbf{E}$ is a hyper-edge in $\boldsymbol{G}$.

For the correlation matrix $\boldsymbol{H}$, the node degree of each node and the edge degree of each hyper-edge can be formulated as:

$$d(v) = \sum_{e\in E} a(e_b)\ h(v, e_b),\ b = 1, ..., M \tag{5}$$

$$\delta(e_b) = \sum_{v\in V} h(v, e_b),\ b = 1, ..., M \tag{6}$$

where e_b (b = 1,..., M and M represents the number of hyper-edges) represents the bth hyper-edge and $a(e_b)$ represents the weight of e_b. MR explores the internal geometric structure of the graph by means of the Laplacian matrix. Similarly, the Laplacian matrix of the hyper-graph can better reflect the high-order relationship between multiple samples for HMR. Many methods of calculating the Laplacian matrix of the hyper-graph can be roughly divided into two categories: one category is to construct a simple graph based on the original hyper-graph, and then calculate the Laplacian matrix on the simple graph (Zien et al., 1999); another category is to directly derive the Laplacian matrix of the hyper-graph based on the Laplacian matrix of the simple graph (Zhou et al., 2007). By comparison, we use the second method to calculate the Laplacian matrix of the hyper-graph:

$$\boldsymbol{L}^h = \boldsymbol{I} - \Theta \tag{7}$$

where $\boldsymbol{L}^h$ is the Laplacian matrix of the hyper-graph, $\boldsymbol{I}$ is the identity matrix, and $\Theta = \boldsymbol{D}_v^{-\frac{1}{2}}\boldsymbol{H}\boldsymbol{A}\boldsymbol{D}_e^{-1}\boldsymbol{H}^T\boldsymbol{D}_v^{-\frac{1}{2}}$, $\boldsymbol{D}v$ represents the diagonal matrix and its diagonal elements are $d(v)$, and $\boldsymbol{D}e$ represents the diagonal matrix and its diagonal elements are $\delta(e_b)$. $\boldsymbol{A}$ represents the diagonal matrix and its diagonal elements are hyper-edge weights. Referring to the methods of Zhou et al. (2007) and Shao et al. (2019), we adopt k-nearest neighbor (KNN) algorithm to construct the hyper-graph based on DBFNs.

Inspired by the research of Li et al. (2017), we propose a method for constructing DBFNs based on HMR, and add the $L1$-norm regularizer based on HMR, and obtain a new DBFN

TABLE 2 | Classification performance of different window widths and step sizes.

Method	ACC (%) ± STD	SEN (%) ± STD	SPE (%) ± STD	AUC ± STD
V = 1,S = 50	**81.0570 ± 0.2551**	**77.2975 ± 0.3529**	86.4165 ± 0.3682	0.8986 ± 0.0026
V = 2,S = 50	76.4275 ± 0.4389	66.9583 ± 0.5456	85.8976 ± 0.5863	0.8409 ± 0.0023
V = 1,S = 60	80.7219 ± 0.4070	71.1746 ± 0.4867	**90.2692 ± 0.4831**	0.9025 ± 0.0021
V = 2,S = 60	73.4818 ± 0.7597	59.4141 ± 1.0188	87.5494 ± 0.8488	0.8191 ± 0.0039
V = 1,S = 70	77.0553 ± 0.6533	66.3636 ± 1.1438	87.7470 ± 1.1023	0.8409 ± 0.0059
V = 2,S = 70	65.7299 ± 0.8631	43.8148 ± 1.7895	87.6449 ± 0.5250	0.7483 ± 0.0062
V = 1,S = 80	48.7391 ± 4.2414	14.0000 ± 3.1514	83.4783 ± 7.6827	0.5307 ± 0.0493
V = 2,S = 80	47.2440 ± 2.4217	16.4444 ± 2.3888	78.0435 ± 3.8956	0.5053 ± 0.0221

TABLE 3 | Classification performance of different neighbor numbers.

Method	ACC (%) ± STD	SEN (%) ± STD	SPE (%) ± STD	AUC ± STD
k = 1	81.5969 ± 0.2353	77.2330 ± 0.2969	85.9607 ± 0.4100	0.8984 ± 0.0018
k = 3	82.1424 ± 0.3034	76.7742 ± 0.3528	87.5105 ± 0.4055	0.8988 ± 0.0011
k = 5	82.2696 ± 0.2158	77.1900 ± 0.4619	87.3492 ± 0.2770	0.8984 ± 0.0010
k = 6	81.9266 ± 0.3825	76.2796 ± 0.6879	87.5736 ± 0.2972	0.9001 ± 0.0015
k = 7	**82.4946 ± 0.2827**	**77.2473 ± 0.5747**	**87.7419 ± 0.2286**	**0.9021 ± 0.0007**
k = 8	82.2076 ± 0.1873	76.9677 ± 0.4484	87.4474 ± 0.2582	0.9003 ± 0.0013
k = 9	81.9021 ± 0.2479	76.2867 ± 0.3729	87.5175 ± 0.2706	0.8997 ± 0.0015
k = 10	81.6502 ± 0.3456	76.0143 ± 0.3929	87.2861 ± 0.4948	0.8977 ± 0.0014
k = 15	81.5525 ± 0.2362	75.7348 ± 0.2989	87.3703 ± 0.2506	0.8954 ± 0.0011

construction method, namely, SHMR. The objective function of SHMR is as follows:

$$\min_{\boldsymbol{W}^{(k)}} ||\boldsymbol{W}^{(k)} - \boldsymbol{X}^{(k)^{\mathrm{T}}}\boldsymbol{X}^{(k)}||_F^2 + \lambda||\boldsymbol{W}^{(k)}||_1 + \beta tr\left(\boldsymbol{W}^{(k)\mathrm{T}}\boldsymbol{L}^h\boldsymbol{W}^{(k)}\right) \quad (8)$$

where $\boldsymbol{X}^{(k)}$ represents the time series matrix of the kth window, λ represents the regularization parameter of $L1$-norm, and β represents the regularization parameter of manifold regularizer. When $\lambda = 0$, the method changes into the DBFN construction method based on HMR.

In Formula (8), the derivable part is the fitting term and the manifold regularizer and the non-derivable part is the L1-norm regularizer. We use the proximal operator method (Yan et al., 2013) to optimize and solve the non-derivable part. Then the gradient of the fitting term $f = ||\boldsymbol{W}^{(k)} - \boldsymbol{X}^{(k)^{\mathrm{T}}}\boldsymbol{X}^{(k)}||_F^2$ is calculated as:

$$\nabla_{\boldsymbol{W}^{(k)}} f\left(\boldsymbol{X}^{(k)}, \boldsymbol{W}^{(k)}\right) = 2\left(\boldsymbol{W}^{(k)} - \boldsymbol{X}^{(k)^{\mathrm{T}}}\boldsymbol{X}^{(k)}\right) \quad (9)$$

Then we update $\boldsymbol{W}^{(k)}$ m times:

$$\boldsymbol{W}_m^{(k)} = \boldsymbol{W}_{m-1}^{(k)} - \alpha_m\left(\nabla_{\boldsymbol{W}^{(k)}} f\left(\boldsymbol{X}^{(k)}, \boldsymbol{W}_{m-1}^{(k)}\right) + \beta\boldsymbol{L}^h\boldsymbol{W}^{(k)}\right) \quad (10)$$

where α_m represents the step size in gradient descent.

Then we calculate the proximal operator of the L1-norm regularizer which can be formulated as:

$$proximal_{\lambda||.||_1}\left(\boldsymbol{W}_m^{(k)}\right) = \left[sgn\left(W_{ij}^{(k)}\right) \times max\left(abs\left(W_{ij}^{(k)}\right) - \lambda\right), 0\right]_{N\times N} \quad (11)$$

The intention of Formula (11) is to apply a soft threshold operation to the elements in $\boldsymbol{W}_m^{(k)}$. After each gradient descent calculation is completed, we use the proximal operator to solve the constraint of $\boldsymbol{W}^{(k)}$.

Accordingly, we adopt the same strategy as in the study of Elhamifar and Vidal (2013) and symmetrize $\boldsymbol{W}^{(k)}$; finally, we obtain $\boldsymbol{W}^{*(k)} = \frac{\boldsymbol{W}^{(k)} + \boldsymbol{W}^{(k)^T}}{2}$. We use $\boldsymbol{W}^{*(k)}$ to represent the DBFN constructed by SHMR, namely, SDBFN.

Feature Extraction, Feature Selection, and Classification via SDBFN

The weighted-graph local clustering coefficient has been widely used in the analysis of BFN, and related studies have also shown that the clustering properties of BFN have changed in neurological diseases (such as AD and MCI) (Jiao et al., 2019). Giving a network of N nodes, the weighted-graph local clustering coefficient of node i can be formulated as:

$$C_i = \frac{2\sum_{i,j\in v_i}\left(\omega_{ij}\right)^{\frac{1}{3}}}{|\boldsymbol{v}_i|\left(|\boldsymbol{v}_i| - 1\right)} \quad (12)$$

where ω_{ij} represents the weight of the connection edge between node i and node j, $\boldsymbol{v}_i$ represents the set of nodes directly

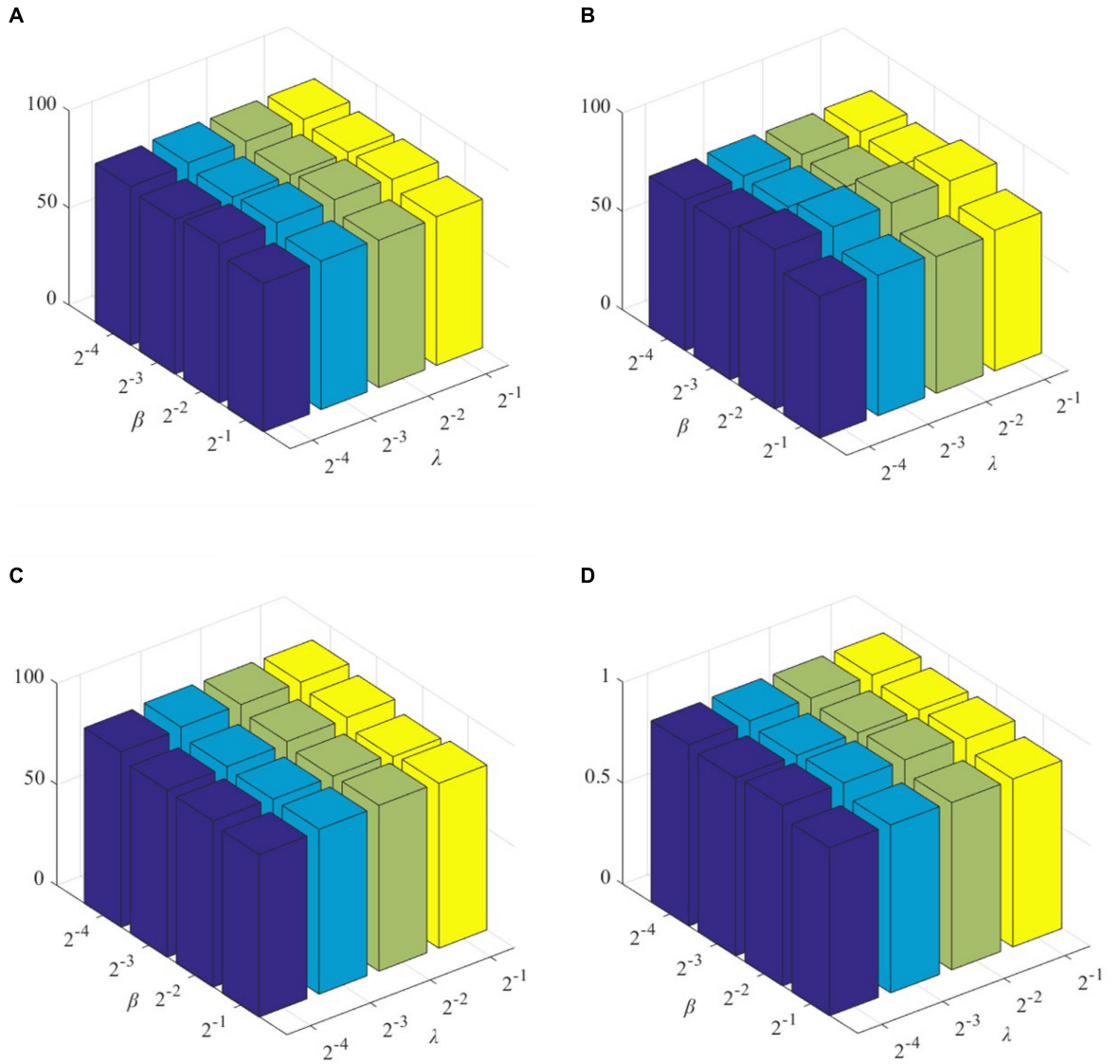

FIGURE 2 | Classification performance of SDBFNs obtained by different regularization parameters: **(A)** ACC, **(B)** SEN, **(C)** SPE, and **(D)** AUC.

connected to node i, and $|\boldsymbol{v}_i|$ represents the number of elements in $\boldsymbol{v}_i$.

The generalization ability of SVM is excellent, and the process of transformation from non-linear problem to linear problem can be realized by kernel function. SVM solves the local optimal problem and curse of dimensionality problem in small sample non-linear space. In order to avoid the confusing effect of feature extraction and the selection of the classifier on the classification performance, we calculate the weighted-graph local clustering coefficients in SDBFNs as effective features and use the t-test method for feature selection, and finally we train a linear kernel SVM to classify the SDBFNs of all subjects. We use four metrics to evaluate the classification performance: accuracy (ACC), sensitivity (SEN), specificity (SPE), and area under the curve (AUC) (Li et al., 2018).

EXPERIMENTAL RESULTS

Parameter Sensitivity on Classification Performance

In this section, we discuss the sensitivities of different parameters on MCI classification performance. Since there are multiple parameters in our method, the grid search method cannot be used directly to find the optimal parameter. Our strategy is to find the optimal parameter separately, that is, to find each optimal parameter step by step.

Sensitivity of Different Window Width and Step Size

The window width S and step size V have an important influence on constructing DBFNs and SDBFNs. Since SDBFN is optimized

TABLE 4 | Classification performance of different regularization parameter values.

Method	ACC (%) ± STD	SEN (%) ± STD	SPE (%) ± STD	AUC ± STD
$\lambda = 2^{-4}, \beta = 2^{-4}$	81.7265 ± 0.2902	76.5806 ± 0.3397	86.8724 ± 0.4542	0.8980 ± 0.0013
$\lambda = 2^{-4}, \beta = 2^{-3}$	**82.4946 ± 0.2827**	77.2473 ± 0.5747	**87.7419 ± 0.2286**	**0.9021 ± 0.0007**
$\lambda = 2^{-4}, \beta = 2^{-2}$	82.1426 ± 0.2041	76.7957 ± 0.2552	87.4895 ± 0.2789	0.9008 ± 0.0018
$\lambda = 2^{-4}, \beta = 2^{-1}$	82.1063 ± 0.2744	77.0036 ± 0.4272	87.2090 ± 0.2886	0.9016 ± 0.0007
$\lambda = 2^{-3}, \beta = 2^{-4}$	79.5965 ± 0.3622	76.4301 ± 0.3820	82.7630 ± 0.5875	0.8818 ± 0.0022
$\lambda = 2^{-3}, \beta = 2^{-3}$	79.7052 ± 0.4198	76.4229 ± 0.7407	82.9874 ± 0.5474	0.8796 ± 0.0021
$\lambda = 2^{-3}, \beta = 2^{-2}$	79.7154 ± 0.3038	75.4265 ± 0.4231	84.0042 ± 0.4187	0.8770 ± 0.0024
$\lambda = 2^{-3}, \beta = 2^{-1}$	80.0542 ± 0.2779	75.6344 ± 0.5218	84.4741 ± 0.5414	0.8768 ± 0.0027
$\lambda = 2^{-2}, \beta = 2^{-4}$	81.5949 ± 0.3644	80.9247 ± 0.6929	82.2651 ± 0.4942	0.8930 ± 0.0018
$\lambda = 2^{-2}, \beta = 2^{-3}$	81.3470 ± 0.2691	81.0251 ± 0.3718	81.6690 ± 0.7053	0.8910 ± 0.0019
$\lambda = 2^{-2}, \beta = 2^{-2}$	81.7879 ± 0.2006	**81.9068 ± 0.4611**	81.6690 ± 0.3105	0.8918 ± 0.0014
$\lambda = 2^{-2}, \beta = 2^{-1}$	80.8248 ± 0.5051	81.6918 ± 0.5472	79.9579 ± 0.7180	0.8821 ± 0.0037
$\lambda = 2^{-1}, \beta = 2^{-4}$	76.2415 ± 0.2577	71.9570 ± 0.2883	80.5259 ± 0.4664	0.8321 ± 0.0015
$\lambda = 2^{-1}, \beta = 2^{-3}$	76.4409 ± 0.3330	71.2688 ± 0.3996	81.6129 ± 0.4470	0.8312 ± 0.0021
$\lambda = 2^{-1}, \beta = 2^{-2}$	75.7620 ± 0.4170	69.4552 ± 0.5639	82.0687 ± 0.5143	0.8283 ± 0.0017
$\lambda = 2^{-1}, \beta = 2^{-1}$	76.4985 ± 0.2997	71.4122 ± 0.3636	81.5849 ± 0.3956	0.8313 ± 0.0018

based on DBFN, we first classify DBFN of all subjects based on different window widths and step sizes to determine the optimal window width and step size. The specific process of classification is as follows. First, we extract the weighted-graph local clustering coefficients in DBFNs of all subjects, which are constructed with different window widths and step sizes. Then we use the *t*-test method for feature selection, with the significance level of 0.05. Finally, we choose linear kernel SVM classifier to classify all subjects, and the linear kernel SVM classifier is implemented using the LIBSVM toolbox (Chang and Lin, 2011). In classification, MCI subjects are generally regarded as positive samples, and normal subjects are regarded as negative samples. We use ACC, SEN, SPE, and AUC to measure the classification performance of different methods, and we also use 10-fold cross validation to verify the classification results (Li et al., 2020a; Xu et al., 2020) by taking the mean value of each classification index after 10 times of 10-fold cross-validation as the final results. We analyze the classification performance of multiple groups of window widths and step sizes to find the optimal parameter. The classification performance of different window widths and step sizes and the standard deviation (STD) of each index are shown in **Table 2**. The best classification performance is highlighted in black. Among them, the step size varies from 1 to 2 with an interval of 1 and the window width varies from 50 to 80 with an interval of 10.

From **Table 2**, we can see that the ACC and SEN are better when the window length is 50 and the step size is 1. As the window width and step size increase, the classification performance becomes worse gradually. This is consistent with the conclusions in the research of Jiao et al. (2019) and Li et al. (2018). The reason may be that using a larger window width and larger step size will ignore the functional connections between some brain regions and part of the dynamic information that changes over time, so that the classification performance starts to decrease.

Sensitivity of the Number of Neighbors

We use the KNN algorithm to construct the hyper-graph. The specific process is to use the KNN algorithm to select the *k* nearest vertices to the center vertex to form a hyper-edge. The classification results of different neighbor numbers are shown in **Table 3**, and the values of *k* are set as 1, 3, 5, 7, 8, 9, 10, and 15 (Shao et al., 2019). When $k = 1$, it does not construct a hyper-graph. We can find that ACC, SEN, SPE, and AUC are the best when the value of *k* is 7, which is consistent with the conclusion in the study of Shao et al. (2019). When the value of *k* is larger than 7, the classification performance begins to decline. The possible reason for this is that when the value of *k* is larger, it describes the global structure information of the sample rather than the local distribution information. When the value of *k* is larger, the hyper-edge may contain many different types of samples, so it cannot reflect the real data structure well. In addition, when $k = 1$, the classification performance is slightly lower, indicating that the introduction of hyper-graph helps to improve the classification performance.

Sensitivity of Regularization Parameters

The role of L1-norm regularizer is mainly to remove redundant features and make DBFNs sparser. The hyper-graph manifold regularizer retains the discriminative information of each subject, thereby inducing more discriminative features. The regularization parameters λ and β are used to adjust the complexity of constructing DBFNs. We test the values of various classification indices for Normal and MCI subjects under different regularization parameters. The classification performance of SDBFNs obtained by different regularization parameters are shown in **Figure 2**, and the specific results are shown in **Table 4**, where the ranges of λ and β are both $\{2^{-4}, 2^{-3}, 2^{-2}, 2^{-1}\}$.

From **Figure 2** and **Table 4**, we can find that the ACC, SEN, SPE, and AUC are best when $\lambda = 2^{-4}$ and $\beta = 2^{-3}$. With

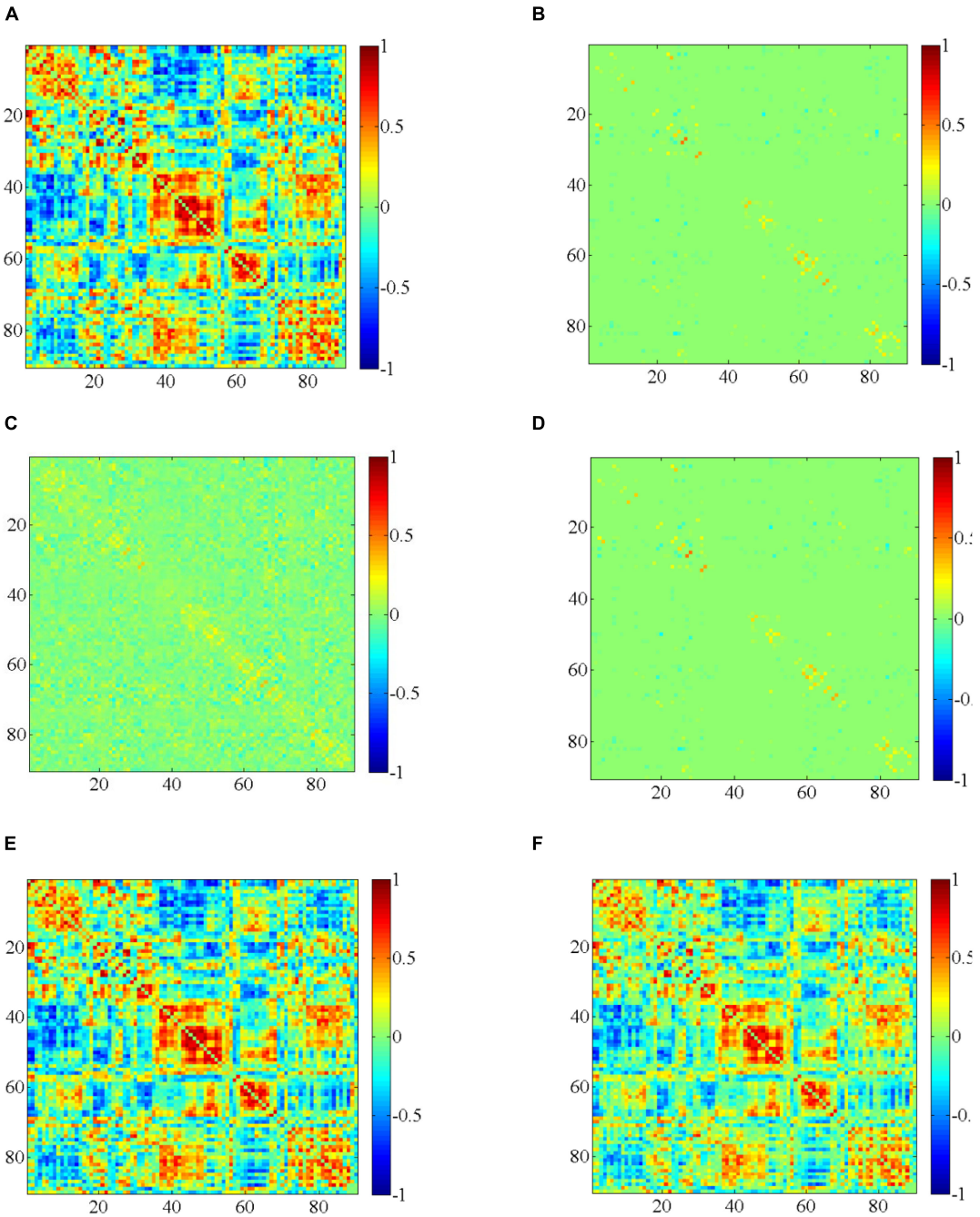

FIGURE 3 | Visualization results of constructing the BFN in the same time window by different methods. **(A)** PC, **(B)** SR, **(C)** MR, **(D)** SMR, **(E)** HMR, and **(F)** SHMR.

TABLE 5 | Classification performance of different methods.

Method	ACC (%) ± STD	SEN (%) ± STD	SPE (%) ± STD	AUC ± STD
PC (Jiang et al., 2019)	81.0570 ± 0.2551	77.2975 ± 0.3529	86.4165 ± 0.3682	0.8986 ± 0.0026
SR (Jiang et al., 2019)	73.9135 ± 0.2756	68.7518 ± 0.3423	79.0753 ± 0.5537	0.8237 ± 0.0009
MR (Li et al., 2020c)	49.8402 ± 1.1050	**96.3184 ± 5.3426**	3.3620 ± 4.3518	0.8291 ± 0.0404
SMR (Li et al., 2020c)	74.3410 ± 0.3876	68.9902 ± 0.4506	79.6918 ± 0.5397	0.8275 ± 0.0022
HMR	81.4570 ± 0.2727	76.6237 ± 0.3087	86.2903 ± 0.3670	0.9005 ± 0.0017
SHMR	**82.4946 ± 0.2827**	77.2473 ± 0.5747	**87.7419 ± 0.2286**	**0.9021 ± 0.0007**

the increase of λ and β, the classification performance starts to decrease. According to the above experiments, we set the window width to 50, the step size to 1, the number of neighbors to 7, and $\lambda = 2^{-4}$ and $\beta = 2^{-3}$ to construct SDBFNs.

Visualization of BFNs

We randomly select a subject, then we use different methods to construct DBFNs, and visualize the BFN in the same time window. These comparison methods are related to our method, as shown in **Figure 3**. The compared methods that we employ include the PC method (Jiang et al., 2019), the SR method (the regularization parameter corresponding to the optimal classification performance is 2^4) (Jiang et al., 2019), the MR method (the regularization parameter corresponding to the optimal classification performance is 2^{-4}) (Li et al., 2020c), the SMR method (the regularization parameters corresponding to the optimal classification performance are 2^4 and 2^{-1}), and the HMR method (the regularization parameter corresponding to the optimal classification performance is 2^{-3}). **Figures 3A–F** are the visualized results of constructing the BFN in the same time window by different methods.

Figure 3 shows the visualization results of constructing the BFN in the same time window by different methods. From these visualization results, we can find that the BFN constructed based on the PC method in the same time window is often dense, while the BFN constructed based on the SR method in the same time window is sparse. **Figure 3D** is sparser than **Figure 3A** and the topological structure is clearer, while **Figures 3B,C** have stronger functional connection strength.

Classification Performance for MCI by Different Methods

We compare the classification performance of different DBFN construction methods for MCI identification, where the best classification performance is highlighted. As shown in **Table 5**, the classification performance of SHMR for MCI is better than other methods, expect SEN. In particular, its ACC, SEN, SPE, and AUC are 82.4946 ± 0.2827%, 77.2473 ± 0.5747%, 87.7419 ± 0.2286%, and 0.9021 ± 0.0007, respectively. The best classification performance among the compared methods is the HMR method, and its ACC, SEN, SPE, and AUC are 81.4570 ± 0.2727%, 76.6237 ± 0.3087%, 86.2903 ± 0.3670%, and 0.9005 ± 0.0017, respectively. The classification performance of the SMR method is better than that of the SR method, but the classification performance of MR is worse than that of the SR method. It shows that the simultaneous introduction of L1-norm regularizer and manifold regularizer based on the SR method can effectively improve the quality of DBFNs and enhance the classification ACC effectively, while the introduction of L1-norm regularizer alone cannot improve the classification performance. This result is similar to the research of Li et al. (2020c). The classification performances of the SHMR method and the HMR method are all better than that of the PC method; it indicates the effectiveness of introducing the hyper-graph manifold regularizer.

Discriminative Brain Regions

In each 10-fold cross-validation, the number of selected features determines the quality of the DBFN. If the number of selected features is larger, the DBFN constructed by the corresponding method may contain more potential information. Therefore, in 10-fold cross-validation, we counted the number of selected features in different methods, that is, the number of selected weighted-graph local clustering coefficients, as shown in **Figure 4**. We can find that the SHMR method has more features selected in the 10-fold cross-validation than other methods, so the SHMR method can select more stable features.

In order to find some biomarkers for MCI diagnosis, we search for discriminative features and consider that features with higher frequency in 10-fold cross-validation are discriminative features. Therefore, we count features with high frequency in 10-fold cross-validation. There are 21 brain regions corresponding to these features, which are called discriminative brain regions. The details of the discriminative brain regions are shown in **Table 6**. Then we use the BrainNet Viewer toolbox[4] (Xia et al., 2013) to visualize the discriminative brain regions. These discriminative brain regions are mapped to the ICBML52 template, and we use the JET template for color marking. The visualization results are shown in **Figure 5**.

From **Table 6** and **Figure 5**, we can find that some selected discriminative brain regions, including the left posterior cingulate gyrus (PCG.L), right posterior cingulate gyrus (PCG.R), left hippocampus (HIP.L), left inferior parietal, supramarginal, and angular gyri (IPL.L), right inferior parietal, supramarginal, and angular gyri (IPL.R), right precuneus (PCUN.R), left inferior temporal gyrus (ITG.L), and right inferior temporal gyrus (ITG.R), belong to the regions in the default mode network (DMN) (Bi et al., 2020a,b; Jiao et al., 2020). Most of the selected brain regions have been widely considered to be related to AD and MCI, which is consistent with the results of previous related research. Take the PCG.L, PCG.R, HIP.L, PCUN.R, ITG.L,

[4]https://www.nitrc.org/projects/bnv/

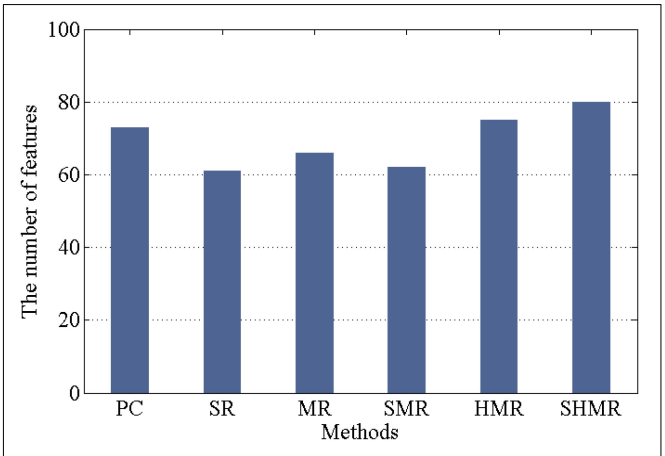

FIGURE 4 | Number of features selected by different methods in 10-fold cross-validation.

TABLE 6 | Discriminative brain regions.

ID	Regions	Abbreviations (L:left R:right)	MNI coordinates			References
			X(mm)	*Y*(mm)	*Z*(mm)	
1	Precentral_L	PreCG.L	−38.65	−5.68	50.94	
2	Precentral_R	PreCG.R	41.37	−8.21	52.09	Zhang H. et al., 2016
9	Frontal_Mid_Orb_L	ORBmid.L	−30.65	50.43	−9.62	Zhang et al., 2018
12	Frontal_Inf_Oper_R	IFGoperc.R	50.20	14.98	21.41	Chen et al., 2016
14	Frontal_Inf_Tri_R	IFGtriang.R	50.33	30.16	14.17	Salvatore et al., 2015
16	Frontal_Inf_Orb_R	ORBinf.R	41.22	32.23	−11.91	Salvatore et al., 2015
22	Olfactory_R	OLF.R	10.43	15.91	−11.26	Sun et al., 2012
28	Rectus_R	REC.R	8.35	35.64	−18.04	
35	Cingulum_Post_L	PCG.L	−4.85	−42.92	24.67	Zhang et al., 2018
36	Cingulum_Post_R	PCG.R	7.44	−41.81	21.87	Wee et al., 2012
37	Hippocampus_L	HIP.L	−25.03	−20.74	−10.13	Salvatore et al., 2015
43	Calcarine_L	CAL.L	−7.14	−78.67	6.44	Xu et al., 2016
44	Calcarine_R	CAL.R	15.99	−73.15	9.40	
47	Lingual_L	LING.L	−14.62	−67.56	−4.63	
57	Postcentral_L	PoCG.L	−31.16	−40.30	−20.23	Xu et al., 2016
61	Parietal_Inf_L	IPL.L	−42.80	−45.82	46.74	
62	Parietal_Inf_R	IPL.R	46.46	−46.29	49.54	Salvatore et al., 2015
68	Precuneus_R	PCUN.R	9.98	−56.05	43.77	
71	Caudate_L	CAU.L	−11.46	11.00	9.24	Salvatore et al., 2015
89	Temporal_Inf_L	ITG.L	−49.77	−28.05	−23.17	Zhang et al., 2018
90	Temporal_Inf_R	ITG.R	53.69	−31.07	−22.32	

and ITG.R as examples. Both PCG.L and PCG.R are involved in the formation of memory, and HIP.L is responsible for the storage, conversion, and orientation of long-term memory. PCUN.R is associated with many high-level cognitive functions, such as episodic memory, self-related information processing, and consciousness generation. ITG.L and ITG.R belong to the temporal lobe, which have the function of processing auditory information, and they are also related to memory and emotion. If ITG.L and ITG.R are damaged, it will cause personality changes. PCUN.R, ITG.L, and ITG.R demonstrate that DMN plays an important role in cognitive function and neuromodulation (Jiao et al., 2017a,b). In addition, some brain regions belonging to the prefrontal and occipital lobes are extracted, such as ORBmid.L, IFGoperc.R, and LING.L. It indicates that the language, vision, and motor perception of MCI patients have changed compared with people without MCI (Wee et al., 2011).

DISCUSSION

In recent years, researchers have shown an increased interest in the epidemiology, clinical characteristics, neuroimaging, biomarkers, mechanism of disease, neuropathology, and clinical trials of MCI. The challenges remain around the borders of the condition, i.e., between normal aging and early MCI and between MCI and clinical AD. However, with the development new neuroimaging techniques, these transitional states may be clarified. A major study indicates an annual rate of progression from cognitively healthy to the aMCI state of 3% per year. In addition, 26% of aMCI subjects have progressed to AD over 12 months, while another 4% of the aMCI subjects have reverted to a cognitively healthy status (Petrella and Doraiswamy, 2005). To date, relatively little research has been carried out on the MCI classification. Herein, our study proposes a DBFN construction method via HMR. We then apply this method to MCI classification. In this method, the DBFN construction method based on PC method is first transformed into an optimization model, and we construct SDBFNs by adding a hyper-graph manifold regularizer into the optimization model. The classification performance of SDBFNs for MCI patients and normal subjects outperforms other comparable methods.

Most research only considers the pair-wise relationship between brain regions and ignores the high-order relationship between multiple brain regions. This high-order relationship can also be regarded as the relationship between functional connections, which is important prior information. Nowadays, related research has explored this high-order relationship. For example, Chen et al. (2016) used correlation's correlation to construct high-order functional networks, and reduced the dimensionality of high-order functional networks through k-means clustering method. The effectiveness of this method is verified in identifying MCI. Zhou et al. (2018) proposed a high-order functional network construction method based on matrix variate normal distribution (MVND). This method uses BFNs as samples and assumes that features in these samples follow MVND. Then, the maximum-likelihood estimation (MLE) for

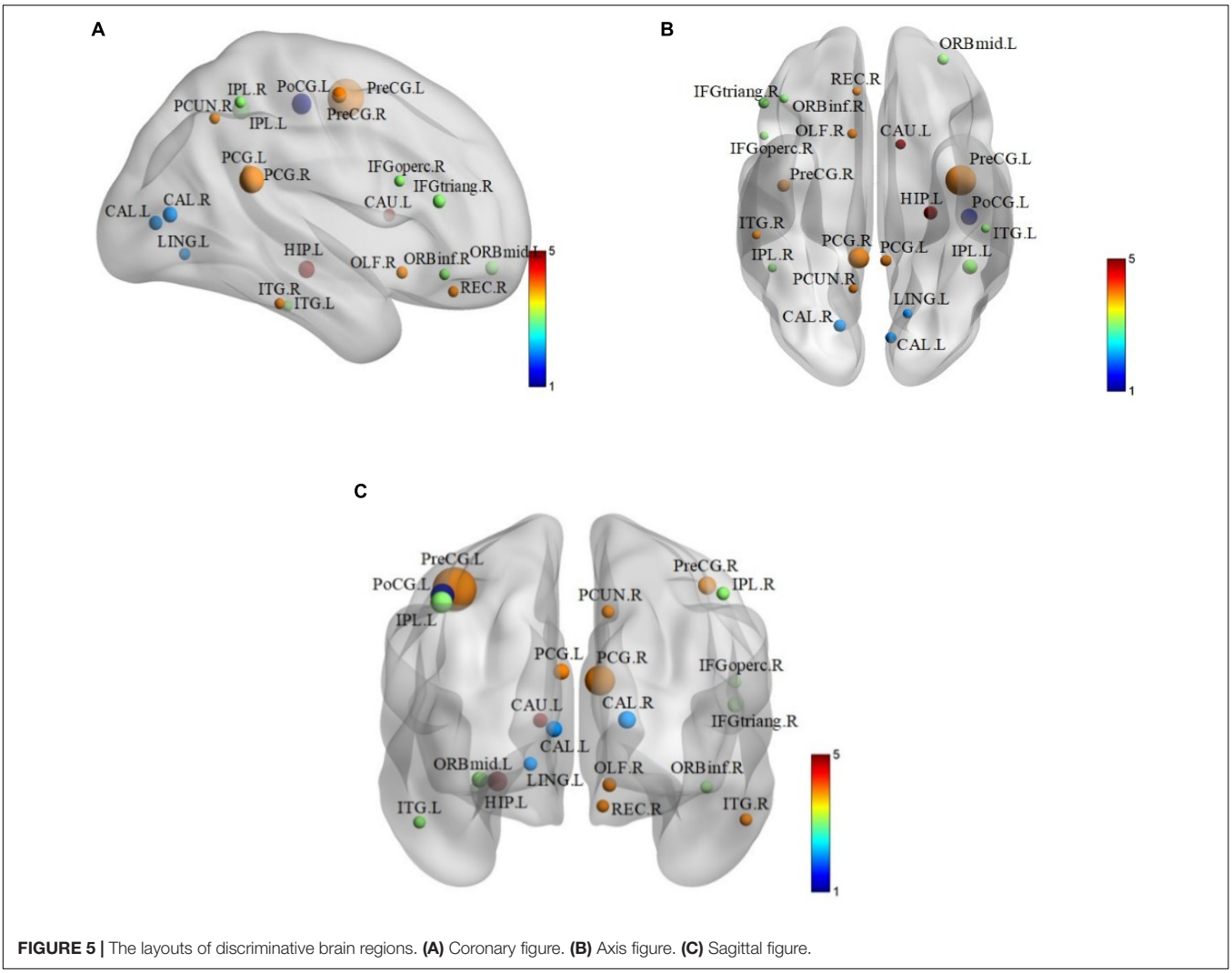

FIGURE 5 | The layouts of discriminative brain regions. **(A)** Coronary figure. **(B)** Axis figure. **(C)** Sagittal figure.

MVND is calculated to obtain the final high-order functional networks. However, these two methods have some shortcomings. The method of Chen et al. (2016) involves many parameters, which may easily lead to overfitting when the number of training data is limited, and this method is not supported by a mathematical model. The method of Zhou et al. (2018) requires strict assumptions before the subsequent conclusions can be established, so describing this complex relationship is very important. In a hyper-graph, a hyper-edge can connect more than two vertices, so the hyper-graph can naturally model this high-order relationship well.

However, our method also has issues which need to be improved. First, it is a very important step to construct the hyper-graph. Hence, we use the KNN method to construct the hyper-graph, which is not interpretable in the field of neuroimaging. Inspired by the work of Jie et al. (2016), we can use the SR method to construct the hyper-graph in future. Second, the main work of this study focuses on the DBFN construction method and we use the *t*-test method to select features. The improvement strategies for feature selection include simple improvement of feature selection method. The training set is combined with the test set to iteratively select the features which improve the classification performance step by step.

In summary, our method makes up for the problem that most methods for BFN construction cannot reflect the pair-wise relationship between multiple brain regions well. We apply this method to MCI classification, and have achieved the best classification ACC which outperforms the compared methods. Moreover, the discriminative brain regions obtained by our method can better reflect the pathogenic mechanism of MCI. Our future work will solve the following problems. First, we only classify Normal subjects and MCI subjects, and consider the binary problem. In the future, we can set up multi-class classifications, such as adding AD subjects to form a three-class problem and verifying our method. In addition, the dataset we used is relatively small, which may affect the promotion performance of the classifier. In practical applications, we will try to use other methods,

such as transfer learning, to design specific methods for BFNs and further improve classification performance.

DATA AVAILABILITY STATEMENT

The original contributions presented in the study are included in the article/supplementary material. Further inquiries can be directed to the corresponding author/s.

ETHICS STATEMENT

Ethical review and approval was not required for the study on human participants in accordance with the local legislation and institutional requirements. Written informed consent for participation was not required for this study in accordance with the national legislation and the institutional requirements.

AUTHOR CONTRIBUTIONS

ZJ, S-HW, and CW designed the research. YJ, YZ, and HS performed the study. YJ and HS analyzed the data. YJ wrote the manuscript. ZJ and CW revised the manuscript. All authors read and approved the final manuscript.

FUNDING

This work was supported by the National Natural Science Foundation of China under Grant No. 51877013, the Natural Science Foundation of Jiangsu Province under Grant No. BK20181463, the Key Research and Development Program of Jiangsu Province under Grant No. BE2018638, the Science and Technology Project of Changzhou City under Grant No. CE20205056, and the Natural Science Funds for Distinguished Young Scholar of Zhejiang under Grant No. LR20H090001. This work was also sponsored by Qing Lan Project of Jiangsu Province.

REFERENCES

Alzheimer's Association, (2012). Alzheimer's disease facts and figures. *Alzheimers Dement.* 8, 131–168.

Basser, P. J., and Pierpaoli, C. (2011). Microstructural and physiological features of tissues elucidated by quantitative-diffusion-tensor MRI. *J. Magn. Reson.* 213, 560–570. doi: 10.1016/j.jmr.2011.09.022

Bi, X. A., Hu, X., Wu, H., and Wang, Y. (2020a). Multimodal data analysis of Alzheimer's disease based on clustering evolutionary random forest. *IEEE J. Biomed. Health Inform.* 24, 2973–2983. doi: 10.1109/jbhi.2020.2973324

Bi, X. A., Hu, X., Xie, Y. M., and Wu, H. (2021). A novel CERNNE approach for predicting Parkinson's Disease-associated genes and brain regions based on multimodal imaging genetics data. *Med. Image Anal.* 67:101830. doi: 10.1016/j.media.2020.101830

Bi, X. A., Liu, Y. C., Xie, Y. M., Hu, X., and Jiang, Q. H. (2020b). Morbigenous brain region and gene detection with a genetically evolved random neural network cluster approach in late mild cognitive impairment. *Bioinformatics* 36, 2561–2568. doi: 10.1093/bioinformatics/btz967

Chang, C. C., and Lin, C. J. (2011). LIBSVM: a library for support vector machines. *ACM Trans. Intell. Syst. Technol.* 2, 389–396.

Chang, C. T., and Glover, G. H. (2010). Time-frequency dynamics of resting-state brain connectivity measured with fMRI. *Neuroimage* 50, 81–98. doi: 10.1016/j.neuroimage.2009.12.011

Chen, X. B., Zhang, H., Gao, Y., Wee, C. Y., Li, G., and Shen, D. G. (2016). High-order resting-state functional connectivity network for MCI classification. *Hum. Brain Mapp.* 37, 3282–3296. doi: 10.1002/hbm.23240

Elhamifar, E., and Vidal, R. (2013). Sparse subspace clustering: algorithm, theory, and applications. *IEEE Trans. Pattern Anal. Mach. Intell.* 35, 2765–2781. doi: 10.1109/tpami.2013.57

Gauthier, S., Reisberg, B., Zaudig, M., Petersen, R., Ritchie, K., Broich, K., et al. (2006). Mild cognitive impairment. *Lancet* 367, 1262–1270.

Jiang, X., Zhang, L. M., Qiao, L. S., and Shen, D. G. (2019). Estimating functional connectivity networks via low-rank tensor approximation with applications to MCI identification. *IEEE Trans. Biomed. Eng.* 67, 1912–1920.

Jiao, Z. Q., Ji, Y. X., Zhang, J. H., Shi, H. F., and Wang, C. (2020). Constructing dynamic functional networks via weighted regularization and tensor low-rank approximation for early mild cognitive impairment classification. *Front. Cell Dev. Biol.* 8:610569. doi: 10.3389/fcell.2020.610569

Jiao, Z. Q., Wang, H., Ma, K., Zou, L., and Xiang, J. B. (2017a). Directed connectivity of brain default networks in resting state using GCA and motif. *Front. Biosci. Landmark* 22:1634–1643. doi: 10.2741/4562

Jiao, Z. Q., Wang, H., Ma, K., Zou, L., Xiang, J. B., and Wang, S. H. (2017b). Effective connectivity in the default network using Granger causal analysis. *J. Med. Imaging Health Inform.* 7, 407–415. doi: 10.1166/jmihi.2017.2029

Jiao, Z. Q., Xia, Z. W., Ming, X. L., Cheng, C., and Wang, S. H. (2019). Multi-scale feature combination of brain functional network for eMCI classification. *IEEE Access* 7, 74263–74273. doi: 10.1109/access.2019.2920978

Jiao, Z. Q., Zou, L., Cao, Y., Qian, N., and Ma, Z. H. (2014). Effective connectivity analysis of fMRI data based on network motifs. *J. Supercomput.* 67, 809–819.

Jie, B., Wee, C. Y., Shen, D. G., and Zhang, D. Q. (2016). Hyper-connectivity of functional networks for brain disease diagnosis. *Med. Image Anal.* 32, 84–100. doi: 10.1016/j.media.2016.03.003

Jung, T. P., Makeig, S., Humphries, C., Lee, T. W., Mckeown, M. J., Iragui, V., et al. (2000). Removing electroencephalographic artifacts by blind source separation. *Psychophysiology* 37, 163–178. doi: 10.1111/1469-8986.3720163

Li, W. K., Geng, C. X., and Chen, S. C. (2020a). Leave zero out: towards a no-cross-validation approach for model selection. *arXiv* [preprint] arXiv:2012.13309

Li, W. K., Qiao, L. S., and Shen, D. G. (2020b). Towards a better estimation of functional brain network for MCI identification: a transfer learning view. *IEEE J. Biomed. Health Inform.* 24, 1160–1168. doi: 10.1109/jbhi.2019.2934230

Li, W. K., Wang, Z. X., Qiao, L. S., and Shen, D. G. (2019). Functional brain network estimation with time series self-scrubbing. *IEEE J. Biomed. Health Inform.* 23, 2494–2504. doi: 10.1109/jbhi.2019.2893880

Li, W. K., Wang, Z. X., Zhang, L. M., Qiao, L. S., and Shen, D. G. (2017). Remodeling pearson's correlation for functional brain network estimation and autism spectrum disorder identification. *Front. Neuroinform.* 11:55. doi: 10.3389/fninf.2017.00055

Li, W. K., Xu, X. W., Jiang, W., Wang, P. J., and Gao, X. (2020c). Functional connectivity network estimation with an inter-similarity prior for mild cognitive impairment classification. *Aging* 12:17328. doi: 10.18632/aging.103719

Li, Y., Liu, J. Y., Gao, X. Q., Jie, B., Minjeong, K., Pew-Thian, Y., et al. (2018). Multimodal hyper-connectivity of functional networks using functionally-weighted LASSO for MCI classification. *Med. Image Anal.* 52, 80–96. doi: 10.1016/j.media.2018.11.006

Lu, S. Y., Lu, Z. H., and Zhang, Y. D. (2019). Pathological brain detection based on AlexNet and transfer learning. *J. Comput. Sci.* 30, 41–47. doi: 10.1016/j.jocs.2018.11.008

Mourik, J. E. M., Lubberink, M., Schuitemaker, A., Tolboom, N., and Boellaard, R. (2009). Image-derived input functions for PET brain studies. *Eur. J. Nuclear Med. Mol. Imaging* 36, 463–471. doi: 10.1007/s00259-008-0986-8

Muldoon, S. F., and Bassett, D. S. (2016). Network and multilayer network approaches to understanding human brain dynamics. *Philos. Sci.* 83, 710–720. doi: 10.1086/687857

Ou, J. L., Lian, Z. C., Xie, L., Xiang, L., Wang, P., Hao, Y., et al. (2015). Atomic dynamic functional interaction patterns for characterization of ADHD. *Hum. Brain Mapp.* 35, 5262–5278. doi: 10.1002/hbm.22548

Petrella, J. R., and Doraiswamy, P. M. (2005). Alzheimer's disease: 100 years of progress. *Neuroimaging Clin. N. Am.* 15, 13–14.

Qiao, L. S., Zhang, H., Kim, M. J., Teng, S. H., Zhang, L. M., and Shen, D. G. (2016). Estimating functional brain networks by incorporating a modularity prior. *Neuroimage* 141, 399–407. doi: 10.1016/j.neuroimage.2016.07.058

Roebroeck, A., Formisano, E., and Goebel, R. (2005). Mapping directed influence over the brain using Granger causality and fMRI. *Neuroimage* 25, 230–242. doi: 10.1016/j.neuroimage.2004.11.017

Rubinov, M., and Sporns, O. (2010). Complex network measures of brain connectivity: uses and interpretations. *Neuroimage* 52, 1059–1069. doi: 10.1016/j.neuroimage.2009.10.003

Salvatore, C., Cerasa, A., Battista, P., Gilardi, M. C., Quattrone, A., and Castiglioni, I. (2015). Magnetic resonance imaging biomarkers for the early diagnosis of Alzheimer's disease: a machine learning approach. *Front. Neurosci.* 9:307. doi: 10.3389/fnins.2015.00307

Shao, W., Peng, Y., Zu, C., Wang, M. L., Zhang, D. Q., and the Alzheimer's Disease Neuroimaging Initiative (2019). Hypergraph based multi-task feature selection for multimodal classification of Alzheimer's disease. *Comput. Med. Imaging Graph.* 80:101663. doi: 10.1016/j.compmedimag.2019.101663

Smythies, L. E., Sellers, M., Clements, R. H., Mosteller-Barnum, M., Meng, G., Benjamin, W. H., et al. (2005). Human intestinal macrophages display profound inflammatory anergy despite avid phagocytic and bacteriocidal activity. *J. Clin. Invest.* 115, 66–75. doi: 10.1172/jci200519229

Sun, G. H., Raji, C. A., MacEachern, M. P., and Burke, J. F. (2012). Olfactory identification testing as a predictor of the development of Alzheimer's dementia: a systematic review. *Laryngoscope* 122, 1455–1462. doi: 10.1002/lary.23365

Tobia, M. J., Hayashi, K., Ballard, G., Gotlib, I. H., and Waugh, C. E. (2017). Dynamic functional connectivity and individual differences in emotions during social stress. *Hum. Brain Mapp.* 38, 6185–6205. doi: 10.1002/hbm.23821

Tzourio-Mazoyer, N., Landeau, B., Papathanassiou, D., Crivello, F., Etard, O., Delcroix, N., et al. (2002). Automated anatomical labeling of activations in SPM using a macroscopic anatomical parcellation of the MNI MRI single-subject brain. *Neuroimage* 15, 273–289. doi: 10.1006/nimg.2001.0978

Wee, C. Y., Yap, P. T., Li, W. B., Kevin, D., Jeffrey, N. B., Guy, G. P., et al. (2011). Enriched white matter connectivity networks for accurate identification of MCI patients. *Neuroimage* 54, 1812–1822. doi: 10.1016/j.neuroimage.2010.10.026

Wee, C. Y., Yap, P. T., Zhang, D. Q., Denny, K., Browndyke, J. N., Potter, G. G., et al. (2012). Identification of MCI individuals using structural and functional connectivity networks. *Neuroimage* 59, 2045–2056. doi: 10.1016/j.neuroimage.2011.10.015

Wee, C. Y., Yap, P. T., Zhang, D. Q., Wang, L. H., and Shen, D. G. (2014). Group-constrained sparse fMRI connectivity modeling for mild cognitive impairment identification. *Brain Struct. Funct.* 219, 641–656. doi: 10.1007/s00429-013-0524-8

Xia, M. R., Wang, J. H., and He, Y. (2013). BrainNet Viewer: a network visualization tool for human brain connectomics. *PLoS One* 8:e68910. doi: 10.1371/journal.pone.0068910

Xu, L. L., Wu, X., Li, R., Chen, K. W., Long, Z. Y., Zhang, J. C., et al. (2016). Prediction of Progressive Mild Cognitive Impairment by multi-modal neuroimaging biomarkers. *J. Alzheimers Dis.* 51, 1045–1056. doi: 10.3233/jad-151010

Xu, X. W., Li, W. K., Mei, J., Tao, M. L., Wang, X. B., Zhao, Q. H., et al. (2020). Feature selection and combination of information in the functional brain connectome for discrimination of Mild Cognitive Impairment and analysis of altered brain patterns. *Front. Aging Neurosci.* 12:28. doi: 10.3389/fnagi.2020.00028

Xue, Y. F., Zhang, L. M., Qiao, L. S., and Shen, D. G. (2020). Estimating sparse functional brain networks with spatial constraints for MCI identification. *PLoS One* 15:e0235039. doi: 10.1371/journal.pone.0235039

Yan, C. G., Cheung, B., Kelly, C., Colcombe, S., Cameron Craddock, R., Martino, A. D., et al. (2013). A comprehensive assessment of regional variation in the impact of head micromovements on functional connectomics. *Neuroimage* 76, 183–201. doi: 10.1016/j.neuroimage.2013.03.004

Yu, J., Rui, Y., Tang, Y. Y., and Tao, D. C. (2014). High-order distance-based multiview stochastic learning in image classification. *IEEE Trans. Cybern.* 44, 2431–2442. doi: 10.1109/tcyb.2014.2307862

Zhang, H., Chen, X. B., Shi, F., Gang, L., Kim, M. J., Giannakopoulos, P., et al. (2016). Topographical information-based high-order functional connectivity and its application in abnormality detection for Mild Cognitive Impairment. *J. Alzheimers Dis.* 54, 1095–1112. doi: 10.3233/jad-160092

Zhang, Y., Zhang, H., Chen, X. B., Liu, M. X., Zhu, X. F., Lee, S. W., et al. (2018). Strength and similarity guided group-level brain functional network construction for MCI diagnosis. *Pattern Recogn.* 88, 421–430. doi: 10.1016/j.patcog.2018.12.001

Zhang, Y. D., Dong, Z. C., Ji, G. L., and Wang, S. H. (2015a). Effect of spider-web-plot in MR brain image classification. *Pattern Recogn. Lett.* 62, 14–16. doi: 10.1016/j.patrec.2015.04.016

Zhang, Y. D., Dong, Z. C., Liu, A. J., Wang, S. H., and Ji, G. L. (2015b). Magnetic resonance brain image classification via stationary wavelet transform and generalized eigenvalue proximal support vector machine. *Med. Imaging Health Inform.* 5, 1395–1403. doi: 10.1166/jmihi.2015.1542

Zhang, Y. D., Wang, S. H., Phillips, P., Yang, J., and Yuan, T. F. (2016). Three-Dimensional eigenbrain for the detection of subjects and brain regions related with Alzheimer's disease. *J. Alzheimers Dis.* 50, 1163–1179. doi: 10.3233/jad-150988

Zhou, D., Huang, J., and Scholkopf, B. (2007). "Learning with hypergraphs: clustering, classification, and embedding," in *Proceedings of the 19th International Conference on Neural Information Processing Systems*, Vancouver, BC, 1601–1608.

Zhou, Y. Y., Qiao, L. S., Li, W. K., Zhang, L. M., and Shen, D. G. (2018). Simultaneous estimation of low- and high-order functional connectivity for identifying mild cognitive impairment. *Front. Neuroinform.* 12:3. doi: 10.3389/fninf.2018.00003

Zien, J. Y., Schlag, M. D. F., and Chan, P. K. (1999). Multilevel spectral hypergraph partitioning with arbitrary vertex sizes. *IEEE Trans. Comput. Aided Design Integr. Circuits Syst.* 18, 1389–1399. doi: 10.1109/43.784130

Conflict of Interest: The authors declare that the research was conducted in the absence of any commercial or financial relationships that could be construed as a potential conflict of interest.

frontiers in Neuroscience

ORIGINAL RESEARCH
published: 23 April 2021
doi: 10.3389/fnins.2021.670745

Sleep Quality Detection Based on EEG Signals Using Transfer Support Vector Machine Algorithm

*Wu Wen**

Chongqing Technology and Business Institute, Chongqing, China

Background: In recent years, with the acceleration of life rhythm and increased pressure, the problem of sleep disorders has become more and more serious. It affects people's quality of life and reduces work efficiency, so the monitoring and evaluation of sleep quality is of great significance. Sleep staging has an important reference value in sleep quality assessment. This article starts with the study of sleep staging to detect and analyze sleep quality. For the purpose of sleep quality detection, this article proposes a sleep quality detection method based on electroencephalography (EEG) signals.

Materials and Methods: This method first preprocesses the EEG signals and then uses the discrete wavelet transform (DWT) for feature extraction. Finally, the transfer support vector machine (TSVM) algorithm is used to classify the feature data.

Results: The proposed algorithm was tested using 60 pieces of data from the National Sleep Research Resource Library of the United States, and sleep quality was evaluated using three indicators: sensitivity, specificity, and accuracy. Experimental results show that the classification performance of the TSVM classifier is significantly higher than those of other comparison algorithms. This further validated the effectiveness of the proposed sleep quality detection method.

Keywords: sleep quality detection, EEG signal, discrete wavelet transform, transfer support vector machine, national sleep research resource library

OPEN ACCESS

Edited by:
Yizhang Jiang,
Jiangnan University, China

Reviewed by:
Tongguang Ni,
Changzhou University, China
Shan Zhong,
Changshu Institute of Technology, China

***Correspondence:**
Wu Wen
kevin983913@163.com

Specialty section:
This article was submitted to Neuroprosthetics, a section of the journal Frontiers in Neuroscience

Received: *22 February 2021*
Accepted: *15 March 2021*
Published: *23 April 2021*

Citation:
Wen W (2021) Sleep Quality Detection Based on EEG Signals Using Transfer Support Vector Machine Algorithm. Front. Neurosci. 15:670745. doi: 10.3389/fnins.2021.670745

INTRODUCTION

As an important physiological phenomenon and a necessary physiological process, sleep is considered to be a resting state with a greatly reduced response capacity (Siegel, 2005). The body eliminates fatigue through sleep, restores mental and physical strength, and maintains a good state. At present, the pace of social life is fast, and sleep disorders have become an increasingly common problem. The problem of sleep disturbance will have a negative impact on the body's alertness and attention, causing patients to have adverse consequences due to reduced alertness. Many physiological functions change during sleep, such as decreased skeletal muscle tension, slower breathing, and decreased visual, auditory, tactile, and other sensory sensitivities. These changes also vary in different sleep stages. Changes in physiological functions during sleep lead to corresponding changes in electrophysiological signals, and sleep research has also been carried out.

Sleep quality assessment is an important branch of sleep research and an integral part of sleep neurobiology research. Because sleep neurobiology is closely related to cognitive neuroscience, sleep quality assessment also helps in studying various neurocognitive functions such as learning

and memory. This shows that sleep quality assessment plays an important role in sleep research. Surveys indicate that most people suffer from poor sleep quality due to physical or psychological problems. And poor sleep quality will produce further positive feedback on the original physical and psychological problems, which will continue to deteriorate. At present, the burden on doctors for the diagnosis and detection of such diseases is relatively heavy. Especially for the acquisition and processing of patients' night sleep data, the help of automation and digital technology is very much needed. Therefore, the research in this paper will have irreplaceable clinical value and practical significance. At present, the research direction of sleep quality mainly focuses on the study of sleep staging. With the continuous development of computer technology, many machine learning methods had been proposed and used in the medical applications (Bezdek, 1980, 1981; Hall et al., 1992; Ahmed et al., 2002; Pedrycz, 2002; Chen and Zhang, 2004; Chuang et al., 2006; Weijer and Gevers, 2006; Jing et al., 2007; Cleuziou et al., 2009; Gu and Zhou, 2009; Zhu et al., 2009; Krinidis and Chatzis, 2010; Hall and Goldgof, 2011; Ji et al., 2011; Jiang et al., 2012, 2014, 2020; Yu et al., 2012; Chen et al., 2013; Gong et al., 2013; Thanh and Wu, 2013; Li et al., 2014; Elazab et al., 2015; Okita et al., 2015; Qian et al., 2015; Wang et al., 2015, 2019; Zheng et al., 2015; Devi and Setty, 2018; Lee et al., 2018; Rosati et al., 2018; Cai et al., 2019; Gu et al., 2019; Chrobak et al., 2020; Kumar et al., 2020; Liu et al., 2020; Singh et al., 2020; Sunjana and Azizah, 2020; Yin et al., 2020; Zhang et al., 2020). The sleep staging method has evolved from the traditional visual observation method to the automatic staging method based on extracting physiological signal features. The accuracy and efficiency of sleep staging are greatly improved. The process of automatic sleep staging algorithm mainly includes signal preprocessing, feature extraction, sleep stage classification, and result output. The commonly used models for sleep stage classification are machine learning algorithms such as support vector machine (SVM) (Doroshenkov et al., 2007; Hsu and Yang, 2013; Qian et al., 2016a,b, 2017, 2018a,b, 2020; Jiang et al., 2017a,b, 2019; Xia et al., 2019). The methods commonly used to extract the characteristic parameters of sleep staging from electroencephalography (EEG) data mainly include wavelet transform and other methods (Alessandro et al., 2001; Kannathal et al., 2005; Srinivasan et al., 2005; Mohseni et al., 2006; Subasi, 2007; Bruzzo et al., 2008; Albayrak and Koklukaya, 2009; Yuen et al., 2009; Fathima et al., 2010; Geng et al., 2011; Gandhi et al., 2012; Sen and Peker, 2013). **Table 1** shows the progress of sleep staging research in recent years.

In this study, EEG signals were selected. After preprocessing and feature extraction, the signals were classified using the transfer support vector machine (TSVM) classifier. The performance of the algorithm is evaluated from the three indicators of sensitivity, specificity, and accuracy. The work of this paper is summarized as follows:

(1) The transfer mechanism is introduced into the classic SVM algorithm to obtain the transfer learning SVM (TL-SVM) classification model. Since the model can use the source domain dataset to guide the classification of the target domain dataset, the accuracy of the classification is improved to a certain extent.
(2) A sleep EEG recognition method based on TL-SVM is proposed. Experiments show that this method is feasible and effective for sleep quality detection.

TABLE 1 | Research progress in sleep staging.

References	Type of data	Characteristic parameters	Classification model
Huang et al. (2014)	EEG	STFT	RVM
Fraiwan et al. (2010)	EEG	Multiwavelet time–frequency entropy	LDA
Fraiwan et al. (2012)	EEG	Time–frequency analysis	RF
Baja and Pachori (2013)	EEG	Pseudo Wigner–Ville distribution	LS-SVM
Long et al. (2014)	EEG	Viewable	SVM
Koch and Christensen (2014)	Respiratory signal	Amplitude, depth characteristics	LDA
Kayikcioglu et al. (2015)	EEG, EOG	Dirichlet distribution	SVM
Hassan and Bhuiyan (2016)	EEG	AR coefficient	PLS
Hassan and Bhuiyan (2016)	EEG	EMD	AdaBoost
Lajnef et al. (2015)	EMG, EOG	Energy characteristics	SVM

EEG, electroencephalography; EOG, electrooculography; EMG, electromyography; STFT, short-time Fourier transform; AR, autoregressive; EMD, empirical mode decomposition; RVM, relevance vector machine; LDA, linear discriminant analysis; RF, radiofrequency; LS-SVM, least squares support vector machine; PLS, partial least squares.

BACKGROUND

Introduction to Sleep Staging

This article selects EEG signals for the study of sleep quality; therefore, here, we focus on analyzing the role of EEG in sleep staging. We mainly describe sleep staging and the relationship between EEG and sleep.

According to the American Academy of Sleep Medicine (AASM) staging criteria, a normal sleep cycle can be divided into two stages, namely, the non-rapid eye movement (NREM) period and the rapid eye movement (REM) period. According to the depth of sleep, NREM is further divided into stages I–III. The above-mentioned stages recur periodically during sleep of normal people all night. When going to sleep, a normal person's sleep stage first enters the NREM stage, gradually transitioning from stage I to III, and then enters the REM stage at stage II or III of NREM. The sleep stage enters the REM stage from the NREM stage, representing a complete sleep cycle. Normal adults have about four to six sleep cycles all night. Under normal circumstances, the sleep time of stage I in normal adults accounts for about 5% of a whole night's sleep, stage III in NRE accounts for about 50%, stage II in NRE accounts for 20%, and the REM stage accounts for 25%. **Figure 1** is a normal adult sleep structure diagram.

The red area in **Figure 1** represents the NREMIII stage, which is the stage of deep sleep. The yellow area is the REM

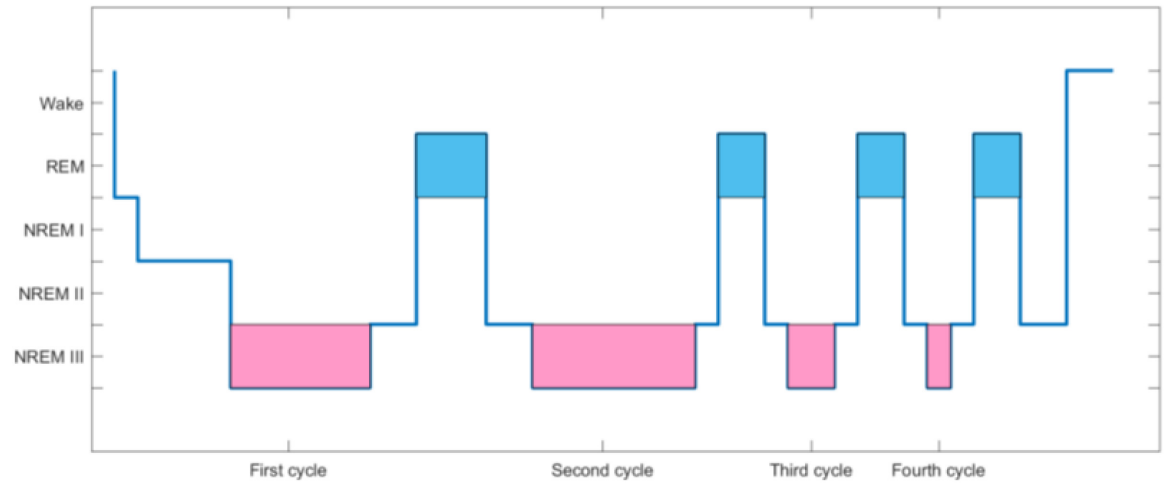

FIGURE 1 | Adult sleep structure diagram.

period where "dreams" often appear. As the black line drops, it means deeper sleep. The higher the position of the black line, the lighter the sleep. During the sleep cycle, EEG will change correspondingly with the change of sleep stage.

Sleep EEG Signal

During sleep, the brain often has rhythm, amplitude, frequency, and other EEG rhythms. The thalamus is the generating part of the EEG rhythm. Its main function is to receive excitement from the brain stem to form a thalamus cortical circuit, thereby regulating the level of neuron excitement. Thalamic neurons have low-threshold calcium channels. During human sleep, thalamic afferent stimulation is low and membrane potential is low, causing calcium channel opening, a large amount of calcium ion influx, forming a short excitatory postsynaptic potential (EPSP). Because a large number of inhibitory neurons in the thalamus block the afferent stimulation, a series of longer inhibitory postsynaptic potentials (IPSP) will follow the EPSP to form a group of EPSP–IPSP. This goes on repeatedly to form the EEG rhythm. The EEG rhythm with typical characteristics during sleep can be used as a basis for judging the sleep stage and diagnosing sleep diseases. Taking adults as an example, **Table 2** shows five typical rhythms. It can be seen from these five types of rhythms that different EEG rhythms have large differences in frequency, amplitude, shape, etc., which is a good electrophysiological basis for sleep staging.

SLEEP QUALITY DETECTION BASED ON EEG SIGNALS

Sleep Quality Testing Process

The core of sleep quality detection lies in sleep staging. Being able to design a highly accurate sleep staging algorithm can effectively promote the inspection of sleep quality. The flow of the sleep staging method is shown in **Figure 2**. In this study, EEG signals were selected as the input signal source, and preprocessing and feature extraction were performed on the EEG signals. Finally, the TSVM classifier and preliminary staging results were corrected to complete the sleep staging.

Brainwave Pretreatment

EEG is an electrophysiological signal with weak amplitude and is extremely susceptible to noise interference. Therefore, before signal analysis, it needs to be preprocessed to reduce high-frequency noise, baseline drift, and artifact interference. The signal preprocessing process is shown in **Figure 3**.

TABLE 2 | Introduction to five types of rhythm.

Slow wave Θ	During the transition period from just falling asleep to light sleep, slow-wave Θ activity repeatedly bursts. And, often adjacent to the top wave, there is no specific shape standard. The average frequency is generally 5–7 Hz, and it appears more in the center of the head and in the top area.
Top wave	The top wave is a sign of the N1 phase, which can be extended to the N2 phase. The maximum amplitude often appears in the cranial region, and the frequency is generally 3–8 Hz. A typical top wave is symmetrically synchronized on both sides and has a sharp shape.
σ rhythm	The σ rhythm is a sign of the N2 period and can be continued to the N3 period, which lasts more than 0.5 s. Its maximum amplitude often appears in the cranial area and can reach the frontal area, central area, and apical area on both sides of the head. The σ rhythm is generally a 12- to 14-Hz spindle-shaped wave, so it is also called a spindle wave.
κ synthetic wave	κ synthetic waves often appear in the N2 phase and can continue to the N3 phase, mainly distributed in the apical or frontal area of the head. The waveform is similar to the top wave, but is wider. It is a steep negative wave followed by a positive wave, often followed by a series of 12- to 14-Hz σ rhythms. Synthetic waves are often induced by external stimuli such as sound and touch.
α rhythm	The α rhythm is a symbolic rhythm of awake state. It often appears in the back of the head and can spread to the central region, the middle temporal region, or the troubled roof. The α rhythm is generally 9–11 Hz.

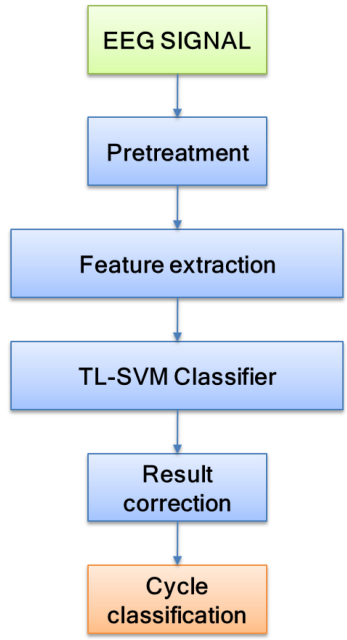

FIGURE 2 | Flowchart of the sleep staging method.

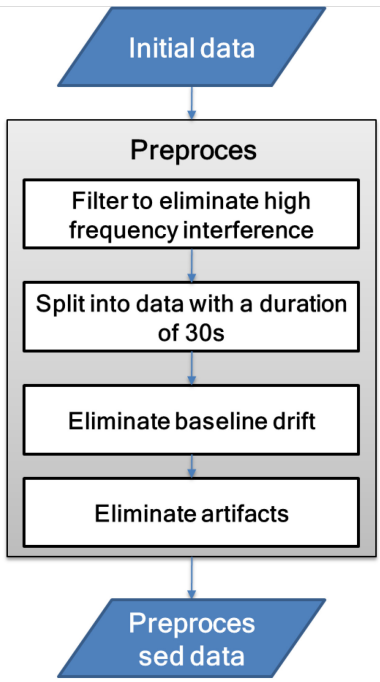

FIGURE 3 | Signal preprocessing flowchart.

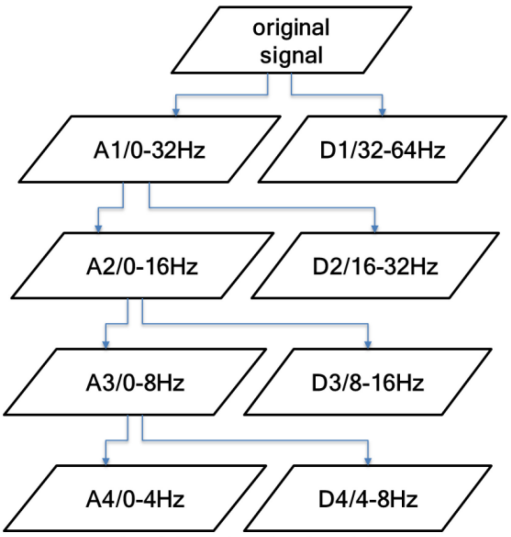

FIGURE 4 | Frequency range of the sub-bands obtained by a four-layer discrete wavelet transform (DWT) decomposition.

Brain Wave Feature Extraction

This study uses discrete wavelet transform (DWT) for feature extraction. When extracting, the artificial sleep staging results obtained according to the AASM rules are used as the reference standards. When DWT analyzes the EEG signals, the main problem to be solved is the choice of decomposition layers and wavelet basis, where the decomposition layers are determined by the original signal frequency. The power of the EEG signal is mainly concentrated in the range of 0–30 Hz, so the decomposition frequency is set to 4 to extract all the characteristic frequency bands of the EEG signal. The signal is decomposed into D1–D4 components with detailed information and A4 components with low-frequency information.

Figure 4 shows the frequency range of the sub-band obtained by a four-layer DWT decomposition of the EEG signal. It can be seen from the figure that the A4 component contains the δ frequency band (0–4 Hz), the D4 component contains the θ frequency band (4–8 Hz), the D3 component contains the α frequency band (8–13 Hz) and part of the β frequency band, and the D2 component contains the β frequency band (13–30 Hz). The D1 component has frequency information higher than 30 Hz, which basically contains no information about the EEG signal. Therefore, in this study, the D2–D4 detailed component and the low-frequency component A4 are used.

In this paper, the db4 wavelet is used to decompose the EEG signal into four layers, and the mean and standard deviation of the absolute values of the D2–D4 and A4 components are counted. Because of the particularity of wavelet decomposition, first calculate the wavelet coefficients on the 25-s timescale and then use the sliding window to obtain the parameters of 80, 140, and 200 s by calculating the mean. In this paper, the four-layer wavelet decomposition of the db4 wavelet is used to process the EEG signals, and the wavelet coefficients of the four frequency bands shown in **Table 3** are extracted.

Sleep Brain Wave Classifier Training

The classifier used in this paper is TSVM. It uses relevant knowledge of the source domain to assist the target domain in establishing a classification model. Among them, a large number of labeled sample sets (T_s) in the source domain are similar to the

TABLE 3 | Correlation between wavelet components and the EEG signal frequency band.

Component	Frequency range (Hz)
A4	δ frequency band
D2	β frequency band
D3	α and part of β frequency band
D4	θ frequency band

target domain test set (Test), and a small number of the labeled sample sets in the target domain (T_t) are the same as the Test. By "transferring" T_s's knowledge, w_s, to T_t, a classification model was obtained, f:$X \rightarrow Y$, so that f could correctly classify Test.

The SVM classifier consists of (w, b), the discriminant function is $f(x) = wT_x + b$, and the classification decision function is $L(x) = \text{sign}(f(x))$. The theoretical basis of the algorithm in this paper is that, if the two domains are related, the respective values of the two domain classifiers should be similar. By adding $\mu \parallel w_t - w_s \parallel^2$ to the SVM objective formula, transfer learning between the two domains can be achieved, where $\parallel w_t - w_s \parallel^2$ represents the degree of difference between the two-domain classifiers. The larger the value, the greater the difference between the classifiers. Parameter μ controls the penalty level. The principle of TSVM can be expressed in **Figure 5**.

There is a source domain SVM classifier (w_s, b_s). Use the source domain classifier knowledge, w_s, to carry out transfer learning on the target domain. The optimization goal problem is as follows:

$$\begin{aligned} \min_{w_t, b_t} \ & \frac{1}{2} \parallel w_t \parallel^2 + C_t \sum_{i=1}^{n} \xi_i^t + \mu \parallel w_t - w_s \parallel^2 \\ s.t. \ & y_i^t \left(\left(w_t \cdot x_i^t \right) + b_t \right) \geq 1 - \xi_i^t, \ i = 1, 2, \ldots, n \\ & \xi_i^t \geq 0, \ i = 1, 2, \ldots n. \end{aligned} \tag{1}$$

where $\beta = (\beta_1, \beta_2, ..., \beta_n)^T$ and $\gamma = (\gamma_1, \gamma_2, ..., \gamma_n)^T$ are the Lagrange multiplier column vectors. Find the partial derivatives of the original variables w_t, ξ_i^t, and b_t and set to 0.

$$\frac{\partial L}{\partial \xi_i^t} = C_t - \beta_i - \lambda_i = 0 \Rightarrow 0 \leq \beta_i \leq C_t \tag{2}$$

$$\frac{\partial L}{\partial w_t} = 0 \Rightarrow w_t = \frac{2\mu w_s + \sum_{i=1}^{n} \beta_i \left(y_i^t \cdot x_i^t \right)}{2\mu + 1} \tag{3}$$

$$\frac{\partial L}{\partial b_t} = 0 \Rightarrow \sum_{i=1}^{n} \beta_i y_i^t = 0 \tag{4}$$

Substituting Equations (3, 4) into the objective function (1), the dual form of the original problem is

$$\begin{aligned} & \min_{\beta} \frac{1}{2(2\mu + 1)} \sum_{i=1}^{n} \sum_{j=1}^{n} \beta_i \beta_j y_i^t y_j^t \left(x_i^t \cdot x_j^t \right) \\ & + \sum_{i=1}^{n} \left(\frac{2\mu y_i^t \left(x_i^t \cdot w_s \right)}{2\mu + 1} - 1 \right) \beta_i - \frac{\mu}{2\mu + 1} \parallel w_s \parallel^2 \\ & s.t. \ 0 \leq \beta_i \leq C_t, \ \sum_{i=1}^{n} \beta_i y_i^t = 0, \ i = 1, 2, \ldots, n. \end{aligned} \tag{5}$$

The specific algorithm of the transfer learning target domain classifier is as follows:

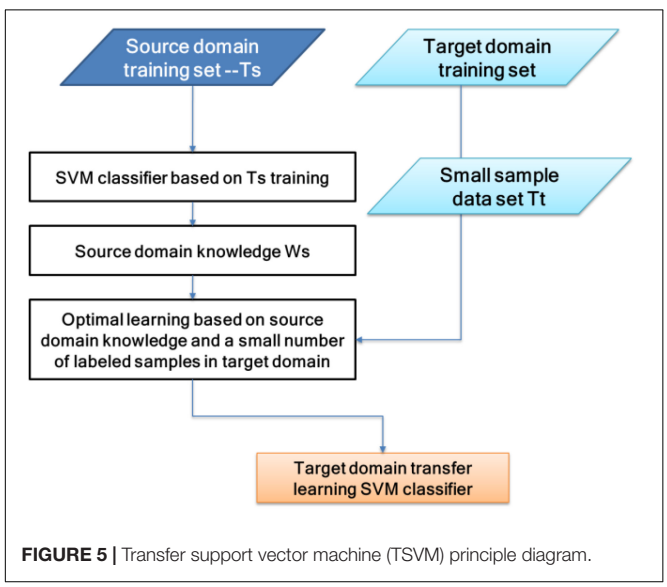

FIGURE 5 | Transfer support vector machine (TSVM) principle diagram.

TABLE 4 | Evaluation indicators.

Index	Index calculation formula	Description
True positive rate (recall)	$TPR = \frac{TP}{TP+FN}$	TP: true positive TN: true negative FP: false positive FN: false negative
True negative rate (specificity)	$TNR = \frac{TN}{TN+FP}$	
Precision	$precision = \frac{TP}{TP+FP}$	

TABLE 5 | TPR indicators of the different classifiers on the test dataset (in percent).

Number model	SVM	BC	DT	TCA	JDA	TSVM
200070	87.71	81.20	78.73	91.32	91.56	90.57
200071	83.39	77.88	80.21	90.74	93.91	93.20
200072	82.81	78.70	77.75	86.51	86.67	85.70
200073	82.78	82.32	83.31	85.93	86.38	87.11
200077	83.22	58.98	81.23	89.39	89.51	88.87
200076	87.35	78.87	75.32	86.63	85.22	85.05
200077	83.57	83.38	80.27	90.12	87.09	86.18
200078	82.83	80.20	79.57	86.78	86.43	87.20
200078	83.21	72.32	83.53	84.35	87.58	86.78
200079	83.20	78.57	81.10	88.96	87.77	87.00
200080	82.87	80.55	83.37	89.23	88.80	87.27
200081	83.57	81.79	87.38	87.10	89.92	89.85
200082	87.78	75.37	75.77	86.54	89.53	90.33
200083	87.79	57.94	57.73	87.96	91.22	91.78
200084	83.52	81.18	78.75	88.92	92.81	90.80
200085	82.27	78.78	81.33	88.61	87.62	87.07
200086	83.72	81.10	82.10	87.43	86.32	88.17
200087	82.51	78.75	78.75	82.89	84.46	83.37
200088	83.23	81.52	78.80	86.37	86.59	85.78
200089	83.78	77.88	87.23	86.66	88.11	89.00
Mean	84.06	77.36	79.61	87.62	88.38	88.05

TPR, true positive rate; SVM, support vector machine; BC, Bayes classifier; DT, decision tree; TCA, transfer component analysis; JDA, joint distribution adaptation; TSVM, transfer support vector machine.

(1) Gain knowledge of the source domain w_s, choose the appropriate penalty parameters C_t, μ.
(2) Construct Equation (5) convex quadratic programming problem, obtain the solution $\beta^* = (\beta_1^*, \beta_2^*, ..., \beta_n^*)^T$, and obtain w_t^* by Equation (3).
(3) Select the β^* component β_j^* in the open interval $(0, C_t)$ and calculate $b_t^* = y_j^t - (w_t^* \cdot x_t^j)$.
(4) Construct a hyperplane $(w_t^* \cdot x_t) + b_t^* = 0$. From this, the decision function $f(x^e) = \text{sign}(g(x^e))$ is obtained, where $g(x^e) = (w_t^* \cdot xe) + b^*$.

EXPERIMENTAL VERIFICATION AND RESULTS ANALYSIS

Experimental Data

The experimental data for this study come from the National Sleep Research Resource Library (NSRR). The resource library provides a large number of physiological signal data of clinical trials. The collected physiological signal data from The Sleep Heart Health Study (SHHS) implemented by the National Heart Lung & Blood Institute (NHLBI) of the United States are shared by the resource library. The samples of the polysomnography (PSG) experiment in the Sleep Heart Health Study (SHHS) dataset originated from 6, 441 individuals collected from 1995 to 1998. The subjects were all over 40 years old and in good health. In this paper, the first 60 sets of samples in the Sleep Heart Health Study (SHHS) dataset will be used as the experimental test data. We randomly selected 40 as the training set and the remaining 20 as the test set.

Evaluation Index

The evaluation indicators used in this article are shown in **Table 4**.

Experimental Results and Analysis

In order to verify the effectiveness of the sleep staging method proposed in this paper, we used the DWT feature extraction method. The comparative classifiers used are SVM (Melgani and Bruzzone, 2004), Bayes classifier (BC) (Moraes et al., 2020), decision tree (DT) classifier (Friedl and Brodley, 1997), transfer component analysis (TCA) (Abid et al., 2016), and joint distribution adaptation (JDA) (Xie et al., 2018). The parameters of the TCA algorithm are set as: regularization parameter $\lambda \in \{0.01, ..., 100\}$ and dimension parameter $\dim \in \{10, ..., 100\}$. The parameters of the JDA algorithm are set as: regularization parameter $\lambda \in \{0.01, ..., 100\}$, dimension parameter $\dim \in \{10, ..., 100\}$, and iteration parameter iter = {1,3,5}. The value range of the parameter μ in the TSVM algorithm is {0.001, 0.005, 0.1, 0.3, 0.5, 0.7, 0.9, 0.99}. **Tables 5–7** are comparisons of the evaluation indexes TPR, TNR, and precision of the test dataset under different classifiers. Only some use cases are given in each table.

An algorithm with excellent performance should have higher TPR, TNR, and precision. As can be seen from the data in **Tables 5–7**, on the indicator TPR, the TSVM algorithm improves

TABLE 6 | TNR indicators of the different classifiers on the test dataset (in percent).

Number model	SVM	BC	DT	TCA	JDA	TSVM
200070	91.12	92.20	91.03	95.82	95.95	94.55
200071	93.39	89.99	91.21	94.91	95.03	96.22
200072	92.91	93.10	91.15	93.23	93.56	95.00
200073	90.29	92.32	92.30	93.68	95.11	94.18
200077	91.20	89.99	90.26	93.85	97.36	96.91
200076	92.35	92.91	94.32	96.35	96.94	97.05
200077	93.55	94.39	92.51	97.10	96.12	96.17
200078	95.43	94.27	93.51	98.51	98.79	96.20
200078	93.21	91.32	93.43	96.56	97.20	97.57
200079	94.20	89.51	90.00	96.02	97.46	96.00
200080	92.91	90.55	93.22	95.44	98.02	97.21
200081	93.52	92.17	91.47	93.87	95.33	96.95
200082	90.59	94.31	93.11	94.67	96.63	96.33
200083	91.37	92.94	91.13	94.90	95.35	95.19
200084	93.52	91.16	93.15	95.34	95.76	96.90
200085	92.20	94.19	94.03	95.89	96.54	97.01
200086	93.12	91.10	92.30	94.17	96.10	95.11
200087	92.51	89.15	92.15	94.63	97.27	96.31
200088	95.23	91.50	93.90	93.43	96.21	95.19
200089	93.19	90.99	91.53	96.14	95.92	96.06
Mean	92.79	91.90	92.29	95.23	96.33	96.11

TNR, true negative rate; SVM, support vector machine; BC, Bayes classifier; DT, decision tree; TCA, transfer component analysis; JDA, joint distribution adaptation; TSVM, transfer support vector machine.

TABLE 7 | Precision indicators of different classifiers on the test dataset (in percent).

Number model	SVM	BC	DT	TCA	JDA	TSVM
200070	72.45	71.20	67.43	74.60	73.47	73.54
200071	73.10	69.78	70.21	73.75	74.07	74.20
200072	72.71	68.90	69.65	72.08	72.84	73.90
200073	72.67	72.32	73.31	72.43	75.85	74.11
200077	73.22	58.67	71.23	73.66	74.11	74.89
200076	74.35	68.89	65.32	75.28	75.23	75.05
200077	73.56	73.37	70.26	73.60	74.81	75.17
200078	72.73	70.20	69.56	73.98	75.92	74.20
200078	73.21	62.32	73.53	75.73	72.35	74.98
200079	73.20	68.59	71.10	73.68	74.22	75.00
200080	72.76	80.56	73.34	73.52	75.02	74.29
200081	73.54	71.44	74.38	73.80	74.33	74.85
200082	76.48	65.34	65.94	75.74	76.94	78.33
200083	76.64	59.69	59.43	75.47	78.90	77.97
200084	73.52	71.17	68.65	76.38	75.87	75.80
200085	72.19	68.98	71.33	74.11	75.68	74.09
200086	73.92	81.10	72.10	75.92	75.05	76.16
200087	72.41	68.65	67.45	74.22	74.88	73.39
200088	73.26	71.52	68.80	74.26	76.43	75.98
200089	73.48	69.78	74.23	75.89	77.31	76.00
Mean	73.47	69.62	69.86	74.41	75.16	75.10

SVM, support vector machine; BC, Bayes classifier; DT, decision tree; TCA, transfer component analysis; JDA, joint distribution adaptation; TSVM, transfer support vector machine.

the traditional SVM, BC, and DT by 4.7, 13.8, and 11.0%, respectively. On the indicator TNR, it increased by 3.6, 4.6, and 4.1%, respectively. On the indicator precision, it increased by 2.2, 7.9, and 5.2%, respectively. The performance of the SVM algorithm is more stable and better than those of the BC and DT algorithms, which is why we chose SVM as the basic algorithm. The performance of the TSVM algorithm used in this article is ahead of the comparison algorithm in all three evaluation indicators. This is because the introduction of the transfer mechanism can effectively utilize useful information from the source domain data and improve the classification performance.

Comparing the three migration learning algorithms TCA, JDA, and TSVM, the performance gap of each algorithm is not big. Among them, the performance of the JDA algorithm is the best, the TSVM used in this article is the second, and TCA is the worst. The reasons for choosing TSVM in this article are as follows: firstly, the TSVM algorithm is more widely used, and the mathematical principles and implementation process are relatively simple. Secondly, compared with other migration algorithms, TSVM has little performance gap, and the recognition results based on TSVM can fully meet the needs of reality. Thirdly, TSVM needs to optimize and set a few parameters, but JDA, which has the best classification effect, needs to optimize and set many parameters. If the parameters are selected differently, the final operation effect of the algorithm will be very different. Based on the above reasons, it is feasible to choose TSVM as the final classifier in this paper.

CONCLUSION

In order to check the quality of sleep, this paper mainly carried out research work on sleep staging. The innovation of this research lies in the introduction of a transfer learning classifier, which can effectively improve the classification performance of the data. The transfer learning classifier introduces the transfer learning mechanism based on the traditional SVM classifier. The introduction of the transfer learning mechanism can effectively use the knowledge of the source domain to guide the classification task of the target domain. In sleep staging research work, the EEG signal is first preprocessed, then DWT is used for feature extraction, and, finally, the TSVM with transfer learning mechanism is used to classify the feature data. The experimental results on the public dataset show that the method in this paper has greatly improved the performance of classification and can achieve the detection of sleep quality to a certain extent. However, this article only uses EEG signals for research, which has limitations. The research on sleep quality based on multimodal physiological signals can be expanded in the future.

DATA AVAILABILITY STATEMENT

The original contributions presented in the study are included in the article/supplementary material, further inquiries can be directed to the corresponding author/s.

AUTHOR CONTRIBUTIONS

WW independently conceived and designed the framework of the manuscript. From the determination of the research problem, the selection and implementation of the solution are all done independently by WW. During the implementation of the solution, the main tasks include model training, experimental data evaluation and analysis, and manuscript preparation. WW was independently responsible for the entire process from conception to the completion of the manuscript.

REFERENCES

Abid, F., Hassan, A., Abid, A., Niazi, I. K., and Jochumsen, M. (2016). "Transfer learning for electroencephalogram signals," in *Proceedings of the 9th International Conference on Computer and Electrical Engineering (ICCEE)*, Barcelona.

Ahmed, M. N., Yamany, S. M., Mohamed, N., Farag, A. A., and Moriarty, T. (2002). Amodified fuzzy c-means algorithm for bias field estimation and segmentation of MRI data. *IEEE Trans. Med. Imaging* 21, 193–199. doi: 10.1109/42.996338

Albayrak, M., and Koklukaya, E. (2009). The detection of an epileptiform activity on EEG signals by using data mining process. *E J. New World Sci. Acad.* 4, 1–12.

Alessandro, M. D., Vachtsevanos, G., Hinson, A., and Esteller, R. (2001). "A genetic approach to selecting the optimal feature for epileptic seizure prediction," in *Proceedings of the 23rd Annual International Conference of the IEEE on Engineering in Medicine and Biology Society*, Istanbul.

Baja, V., and Pachori, R. B. (2013). Analysis and classification of sleep stages based on difference visibility graphs from a single-channel EEG signal. *Comput. Methods Program. Biomed.* 112, 320–328.

Bezdek, J. C. (1980). A convergence theorem for the fuzzy ISODATA clustering algorithm. *IEEE Trans. Pattern Analys. Mach. Intellig.* 1, 1–8. doi: 10.1109/TPAMI.1980.4766964

Bezdek, J. C. (1981). *Pattern Recognition with Fuzzy Objective Function Algorithms*. New York, NY: Plenum Press.

Bruzzo, A. A., Gesierich, B., Santi, M., and Tassinari, C. A. (2008). Permutation entropy to detect vigilance changes and preictal states from scalp EEG in epileptic patients-A preliminary study. *Neurol. Sci.* 29, 3–9.

Cai, T. T., Ma, J., and Zhang, L. (2019). Chime: clustering of high-dimensional Gaussian mixtures with EM algorithm and its optimality. *Ann. Statist.* 47, 1234–1267. doi: 10.1214/18-AOS1711

Chen, S., and Zhang, D. (2004). Robust image segmentation using FCM with spatialconstraints based on new kernel-induced distance measure. *IEEE Trans. Syst. Man Cybernet. Part B Cybernet.* 34, 1907–1916. doi: 10.1109/TSMCB.2004.831165

Chen, X., Xu, X., Huang, J. Z., and Ye, Y. (2013). TW-k-means: automated two-level variable weighting clustering algorithm for multiview data. *IEEE Trans. Knowl. Data Eng.* 25, 932–944. doi: 10.1109/TKDE.2011.262

Chrobak, M., Dürr, C., Aleksander, F., and Nilsson, B. J. (2020). Online clique clustering. *Algorithmica* 82, 938–965. doi: 10.1007/s00453-019-00625-1

Chuang, K. S., Tzeng, H. L., Chen, S., Wu, J., and Chen, T. J. (2006). Fuzzy c-means clustering with spatial information for image segmentation. *Comput. Med. Imaging Graph. Off. J. Comput. Med. Imaging Soc.* 30, 9–15. doi: 10.1016/j.compmedimag.2005.10.001

Cleuziou, G., Exbrayat, M., Martin, L., and Sublemontier, J. H. (2009). "Co FKM: a centralized method for multiple-view clustering," in *Proceedings of the 9th International Conference on Data Mining*, Miami FL, doi: 10.1109/ICDM.2009.138

Devi, B. R., and Setty, S. P. (2018). Hybrid clustering algorithm 'KCu' for combining the features of K-means and CURE Algorithm for efficient outliers handling. *Adv. Model. Analys. B* 61, 76–79. doi: 10.18280/ama_b.610204

Doroshenkov, L. G., Konyshev, V. A., and Selishchev, S. V. (2007). Classification of human sleep stages based on EEG processing using hidden markov models. *Biomed. Eng.* 41, 25–28.

Elazab, A., Wang, C., Jia, F., Wu, J., Li, G., and Hu, Q. (2015). Segmentation of brain tissues from magnetic resonance images using adaptively regularized kernel-based fuzzy c-means clustering. *Comput. Math. Methods Med.* 2015, 1–12. doi: 10.1155/2015/485495

Fathima, T., Bedeeuzzaman, M., and Farooq, O. (2010). Wavelet based features for epileptic seizure detection. *MES J. Technol. Manag.* 2, 108–112.

Fraiwan, L., Lweesy, K., Khasawneh, N., Fraiwan, M., Wenz, H., and Dickhaus, H. (2010). Classification of sleep stages using multi-wavelet time frequency entropy and LDA. *Methods Inform. Med.* 49:230.

Fraiwan, L., Lweesy, K., Khasawneh, N., Wenz, H., and Dickhaus, H. (2012). Automated sleep stage identification system based on time-frequency analysis of a single EEG channel and random forest classifier. *Comput. Methods Prog. Biomed.* 108, 10–19.

Friedl, M. A., and Brodley, C. E. (1997). Decision tree classification of land cover from remotely sensed data. *Remote Sens. Environ.* 61, 399–409.

Gandhi, T. K., Chakraborty, P., Roy, G. G., and Panigrahi, B. K. (2012). Discrete harmony search based expert model for epileptic seizure detection in electroencephalography. *Expert Syst. Appl.* 39, 4055–4062.

Geng, S., Zhou, W., Yuan, Q., Cai, D., and Zeng, Y. (2011). EEG non-linear feature extraction using correlation dimension and Hurst exponent. *Neurol. Res.* 33, 908–912.

Gong, M., Liang, Y., Shi, J., Ma, W., and Ma, J. (2013). Fuzzy c-means clustering with local information and kernel metric for image segmentation. *IEEE Trans. Image Process.* 22, 573–584. doi: 10.1109/TIP.2012.2219547

Gu, J., Cheng, T., Hua, L., Wang, J., Zhao, J., and Cao, Y. (2019). Overview of image segmentation and registration for spine biological modeling. *J. Syst. Simulat.* 31, 167–173. doi: 10.16182/j.issn1004731x.joss.18-0806

Gu, Q., and Zhou, J. (2009). "Learning the shared subspace for multi-task clustering and transductive transfer classification," in *Proceedings of the IEEE International Conference on Data Mining*, Miami Beach, FL, doi: 10.1109/ICDM.2009.32

Hall, L. O., Bensaid, A. M., and Clarke, L. P. (1992). A comparison of neural network and fuzzy clustering techniques in segmenting magnetic resonance images of the brain. *IEEE Trans. Neural Netw.* 3, 672–681. doi: 10.1109/72.159057

Hall, L. O., and Goldgof, D. B. (2011). Convergence of the single-pass and online fuzzy C-means algorithms. *IEEE Trans. Fuzzy Syst.* 19, 792–794. doi: 10.1109/TFUZZ.2011.2143418

Hassan, A. R., and Bhuiyan, M. I. H. (2016). Automatic sleep scoring using statistical features in the EMD domain and ensemble methods. *Biocybernet. Biomed. Eng.* 36, 248–255.

Hsu, Y. L., and Yang, Y. T. (2013). Automatic sleep stage recurrent neural classifier using energy features of EEG signals. *Neurocomputing* 104, 105–114.

Huang, C. S., Lin, C. L., Ko, L. W., Liu, S. Y., Su, T. P., and Lin, C. T. (2014). Knowledge-based identification of sleep stages based on two forehead electroencephalogram channels. *Front. Neurosci.* 8:263. doi: 10.3389/fnins.2014.00263

Ji, Z. X., Sun, Q. S., and Xia, D. S. (2011). A modified possibilisticfuzzy c-means clustering algorithm for bias field estimation and segmentation of brain MR image. *Comput. Med. Imag. Graph.* 35, 383–397. doi: 10.1016/j.compmedimag.2010.12.001

Jiang, C. F., Chang, C. C., and Huang, S. H. (2012). Regions of interest extraction fromspect images for neural degeneration assessment using multimodality image fusion. *Multidimens. Syst. Signal. Process.* 23, 437–449. doi: 10.1007/s11045-011-0162-3

Jiang, Y., Bi, A., Xia, K., Xue, J., and Qian, P. (2020). Exemplar-based data stream clustering toward internet of things. *J. Supercomput.* 76, 2929–2957. doi: 10.1007/s11227-019-03080-5

Jiang, Y., Chung, F. L., Wang, S., Deng, Z., Wang, J., and Qian, P. (2014). Collaborative fuzzy clustering from multiple weighted views. *IEEE Trans. Cybernet.* 45, 688–701. doi: 10.1109/TCYB.2014.2334595

Jiang, Y., Deng, Z., Chung, F. L., Wang, G., Qian, P., Choi, K. S., et al. (2017a). Recognition of epileptic EEG signals using a novel multiview TSK fuzzy system. *IEEE Trans. Fuzzy Syst.* 25, 3–20.

Jiang, Y., Wu, D., Deng, Z., Qian, P., Wang, J., Wang, G., et al. (2017b). Seizure classification from EEG Signals using transfer learning, semi-supervised learning and TSK fuzzy system. *IEEE Trans. Neural Syst. Rehabil. Eng.* 25, 2270–2284.

Jiang, Y., Zhao, K., Xia, K., Xue, J., Zhou, L., Ding, Y., et al. (2019). A Novel distributed multitask fuzzy clustering algorithm for automatic MR brain image segmentation. *J. Med. Syst.* 43:118. doi: 10.1007/s10916-019-1245-1

Jing, L. P., Ng, M. K., and Huang, J. Z. (2007). An entropy weighting k-means algorithm for subspace clustering of high-dimensional sparse data. *IEEE Trans. Knowl. Data Eng.* 19, 1026–1041. doi: 10.1109/TKDE.2007.1048

Kannathal, N., Choo, M., Acharya, U., and Sadasivan, P. (2005). Entropies for detectio of epilepsy in EEG. *Comput. Methods Prog. Biomed.* 80, 187–194.

Kayikcioglu, T., Maleki, M., and Eroglu, K. (2015). Fast and accurated PLS-based classification of EEG sleep using single channel data. *Expert Syst. Appl.* 42, 7825–7830.

Koch, H., and Christensen, J. A. (2014). Automatic sleep classification using a data-driven topic model reveals latent sleep states. *J. Neurosci. Methods* 235, 130–137.

Krinidis, S., and Chatzis, V. (2010). A robust fuzzy local information C-means clustering algorithm. *IEEE Trans. Image Process.* 19, 1328–1337. doi: 10.1109/TIP.2010.2040763

Kumar, S. N., Lenin, F. A., and Sebastin, V. P. (2020). An overview of segmentation algorithms for the analysis of anomalies on medical images. *J. Intellig. Syst.* 29, 612–625. doi: 10.1515/jisys-2017-0629

Lajnef, T., Chaibi, S., Ruby, P., Aguera, P. E., Eichenlaub, J. B., and Samet, M. (2015). Learning machines and sleeping brains: automatic sleep stage classification using decision-tree multi-class support vector machines. *J. Neurosci. Methods* 250, 94–105.

Lee, K., Moon, C., and Nam, Y. (2018). Diagnosing vocal disorders using cobweb clustering of the jitter, shimmer, and harmonics-to-noise ratio. *KSII Trans. Internet Inform. Syst.* 12, 5541–5554. doi: 10.3837/tiis.2018.11.020

Li, C., Gore, J. C., and Davatzikos, C. (2014). Multiplicative intrinsic component optimization(MICO). for MRI bias field estimation and tissue segmentation. *Magnet. Resonan. Imaging* 32, 413–439. doi: 10.1016/j.mri.2014.03.010

Liu, L., Kuang, L., and Ji, Y. (2020). Multimodal MRI brain tumor image segmentation using sparse subspace clustering algorithm. *Computat. Math. Methods Med.* 2020:8620403. doi: 10.1155/2020/8620403

Long, X., Foussier, J., Fonseca, P., Haakma, R., and Aarts, R. M. (2014). Analyzing resporatory effort amplitude for automated sleep stage classification. *Biomedical Signal Process. Control* 14, 197–205.

Melgani, F., and Bruzzone, I. (2004). Classification of hyperspectral remote sensing images with support vector machines. *IEEE Transgeosci. Remote Sens.* 42, 1778–1790.

Mohseni, H. R., Maghsoudi, A., and Shamsollah, I. M. B. (2006). "Seizure detection in EEG signals: a comparison of different approaches," in *Proceedings of the 28th Annual International Conference of the IEEE on Engineering in Medicine and Biology Society*, New York, NY.

Moraes, R. M., Soare, E. A. M. G., Machado, L. S., Machado, L. S., and Kahraman, C. (2020). A double weighted fuzzy gamma naive bayes classifier. *J. Intellig. Fuzzy Syst.* 38, 577–588.

Okita, Y., Miyata, A. H., Motomura, B. N., and Takamoto, S. (2015). A study of brain protection during total arch replacement comparing antegrade cerebral perfusion versus hypothermic circulatory arrest, with or without retrograde cerebral perfusion: analysis based on the Japan adult cardiovascular surgery database. *J. Thorac. Cardiovasc. Surg.* 149, 65–73. doi: 10.1016/j.jtcvs.2014.08.070

Pedrycz, W. (2002). Collaborative fuzzy clustering. *Pattern Recogn. Lett.* 23, 1675–1686. doi: 10.1016/S0167-865502.00130-7

Qian, P., Chen, Y., Kuo, J. W., Zhang, Y. D., Jiang, Y., Zhao, K., et al. (2020). mDixon-based synthetic CT generation for PET attenuation correction on abdomen and pelvis jointly using transfer fuzzy clustering and active learning-based classification. *IEEE Trans. Med. Imaging* 39, 819–832.

Qian, P., Jiang, Y., Deng, Z., Hu, L., Sun, S., Wang, S., et al. (2015). Cluster prototypes and fuzzy memberships jointly leveraged cross-domain maximum

entropy clustering. *IEEE Trans. Cybernet.* 46, 181–193. doi: 10.1109/TCYB.2015.2399351

Qian, P., Jiang, Y., Wang, S., Su, K. H., Wang, J., Hu, L., et al. (2016a). Affinity and penalty jointly constrained spectral clustering with all-compatibility, flexibility, and robustness. *IEEE Trans. Neural Netw. Learn. Syst.* 28, 1123–1138. doi: 10.1109/TNNLS.2015.2511179

Qian, P., Sun, S., Jiang, Y., Su, K. H., Ni, T., Wang, S., et al. (2016b). Cross-domain, soft-partition clustering with diversity measure and knowledge reference. *Pattern Recogn.* 50, 155–177.

Qian, P., Xi, C., Xu, M., Jiang, Y., Su, K. H., Wang, S., et al. (2018a). SSC-EKE: semi-supervised classification with extensive knowledge exploitation. *Inform. Sci.* 422, 51–76.

Qian, P., Zhou, J., Jiang, Y., Liang, F., and Muzic, R. F. (2018b). Multi-view maximum entropy clustering by jointly leveraging inter-view collaborations and intra-view-weighted attributes. *IEEE Access.* 6, 28594–28610. doi: 10.1109/ACCESS.2018.2825352

Qian, P., Zhao, K., Jiang, Y., Su, K. H., Deng, Z., Wang, S., et al. (2017). Knowledge-leveraged transfer fuzzy C -Means for texture image segmentation with self-adaptive cluster prototype matching. *Knowl. Based Syst.* 130, 33–50.

Rosati, P., Lupascu, C. A., and Tegolo, D. (2018). Analysis of low-correlated spatial gene expression patterns: a clustering approach in the mouse brain data hosted in the Allen Brain Atlas. *IET Comput. Vis.* 12, 996–1006. doi: 10.1049/iet-cvi.2018.5217

Sen, B., and Peker, M. (2013). Novel approaches for automated epileptic diagnosis using FCBF feature selection and classification algorithms. *Turk. J. Electric. Eng. Comput. Sci.* 21, 2092–2109.

Siegel, J. M. (2005). Clues to the functions of mammalian sleep. *Nature* 437, 1264–1271.

Singh, M., Vishal, V., Verma, A., and Sharma, N. (2020). Segmentation of MRI data using multi-objective antlion based improved fuzzy c-means. *Biocybernet. Biomed. Eng.* 40, 1250–1266. doi: 10.1016/j.bbe.2020.07.001

Srinivasan, V., Eswaran, C., and Sriraam, N. (2005). Artificial neural network based epileptic detection using time domain and frequency domain features. *J. Med. Syst.* 29, 647–660.

Subasi, A. (2007). EEG signal classification using wavelet feature extraction and a mixture of expert model. *Expert Syst. Appl.* 32, 1084–1093.

Sunjana, and Azizah, Z. (2020). Outlier detection of transaction data using DBSCAN Algorithm. *Intern. J. Psychosoc. Rehabil.* 24, 3232–3340. doi: 10.37200/IJPR/V24I2/PR200632

Thanh, M. N., and Wu, Q. M. J. (2013). A fuzzy logic model based Markov random field for medical image segmentation. *Evolv. Syst.* 4, 171–181. doi: 10.1007/s12530-012-9066-1

Wang, J., Schreiber, D. K., Bailey, N., Hosemann, P., and Toloczko, M. B. (2019). The application of the OPTICS algorithm to cluster analysis in atom probe tomography data. *Microsc. Microanalys.* 25, 338–348. doi: 10.1017/S1431927618015386

Wang, X. Y., Zhang, D. D., and Wei, N. (2015). Fractal image coding algorithm using particle swarm optimisation and hybrid quadtree partition scheme. *IET Image Process.* 9, 153–161. doi: 10.1049/iet-ipr.2014.0001

Weijer, J., and Gevers, T. (2006). Boosting color saliency in image feature. *IEEE Trans. Pattern Analys. Mach. Intellig.* 28, 150–156. doi: 10.1109/TPAMI.2006.3

Xia, K. J., Zhong, X., Zhang, L., and Wang, J. (2019). Optimization of diagnosis and treatment of chronic diseases based on association analysis under the background of regional integration. *J. Med. Syst.* 43:46.

Xie, L., Deng, Z., Xu, P., Choi, K. S., and Wang, S. (2018). Generalized Hidden-mapping transductive transfer learning for recognition of epileptic electroencephalogram signals. *IEEE Trans. Cybernet.* 49, 2200–2214.

Yin, S., Li, H., Liu, D., and Karim, S. (2020). Active contour modal based on density-oriented BIRCH clustering method for medical image segmentation. *Multimed. Tools Appl.* 79, 31049–31068. doi: 10.1016/j.ijleo.2018.01.004

Yu, S., Tranchevent, L., Liu, X., Glanzel, W., Suykens, J. A. K., De Moor, B., et al. (2012). Optimized data fusion for kernel k-means clustering. *IEEE Trans. Pattern Analys. Mach Intellig.* 34, 1031–1039. doi: 10.1109/TPAMI.2011.255

Yuen, C. T., San, W. S., Rizoni, M., and Seong, T. C. (2009). Classification of human emotions from EEG signals using statistical features and neural network. *Intern. J. Integrat. Eng.* 1, 71–79.

Zhang, C., Churazov, E., and Zhuravleva, I. (2020). Pairs of giant shock waves (N-waves). in merging galaxy clusters. *Mon. Notic. R. Astron. Soc.* 501, 1038–1045. doi: 10.1093/mnras/staa3718

Zheng, Y., Byeungwoo, J., Xu, D., Wu, Q. M. J., and Hu, Z. (2015). Image segmentation by generalized hierarchical fuzzy C- means algorithm. *J. Intellig. Fuzzy Syst.* 28, 4024–4028. doi: 10.3233/IFS-141378

Zhu, L., Chung, F. L., and Wang, S. T. (2009). Generalized fuzzy k-means clustering algorithm with improved fuzzy partitions. *IEEE Trans. Syst. Man Cybernet.* 39, 578–591. doi: 10.1109/TSMCB.2008.2004818

Conflict of Interest: The author declares that the research was conducted in the absence of any commercial or financial relationships that could be construed as a potential conflict of interest.

Advantages of publishing in Frontiers

OPEN ACCESS
Articles are free to read for greatest visibility and readership

FAST PUBLICATION
Around 90 days from submission to decision

HIGH QUALITY PEER-REVIEW
Rigorous, collaborative, and constructive peer-review

TRANSPARENT PEER-REVIEW
Editors and reviewers acknowledged by name on published articles

Frontiers
Avenue du Tribunal-Fédéral 34
1005 Lausanne | Switzerland

Visit us: www.frontiersin.org
Contact us: frontiersin.org/about/contact

REPRODUCIBILITY OF RESEARCH
Support open data and methods to enhance research reproducibility

DIGITAL PUBLISHING
Articles designed for optimal readership across devices

FOLLOW US
@frontiersin

IMPACT METRICS
Advanced article metrics track visibility across digital media

EXTENSIVE PROMOTION
Marketing and promotion of impactful research

LOOP RESEARCH NETWORK
Our network increases your article's readership